Bourban, Sébastien (Hg.)

Proceedings of the XXIIIrd TELEMAC-MASCARET User Conference 2016, 11 to 13 October 2016, Paris, France

HR Wallingford
Working with water

Proceedings of the

XXIII[rd] TELEMAC-MASCARET User Conference

11 to 13 October 2016, Paris, France

Assembled and edited by Sébastien Bourban and members of the Scientific Committee

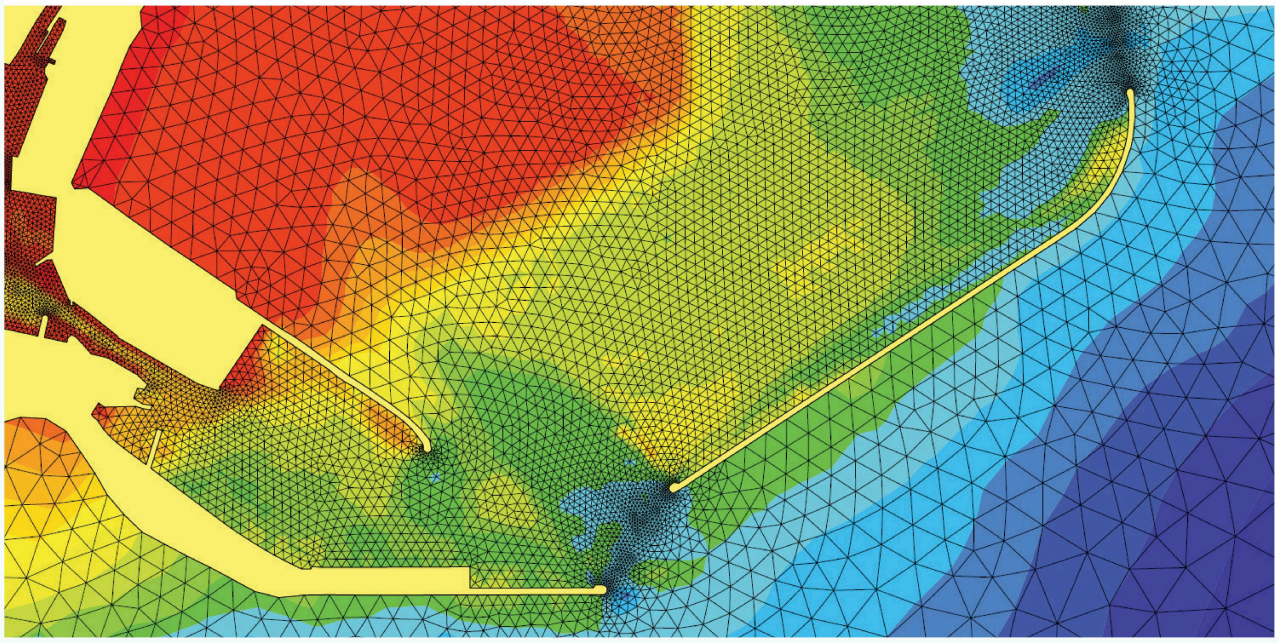

HR Wallingford Working with water
ARTELIA
Cerema
EDF
BAW Bundesanstalt für Wasserbau Federal Waterways Engineering and Research Institute
Science & Technology Facilities Council Daresbury Laboratory

HR Wallingford
Working with water

Proceedings of the

XXIII[rd] TELEMAC-MASCARET User Conference

11 to 13 October 2016, Paris, France

Assembled and edited by Sébastien Bourban,
and members of the Scientific Committee of the TELEMAC-MASCARET Consortium

Proceedings of the

XXIII[rd] TELEMAC-MASCARET User Conference

11 to 13 October 2016, Paris, France

Organised by

Cerema Eau, Mer et Fleuves
Division Mesures et Modélisations Hydrauliques
134 rue de Beauvais, CS 60039
60280 Margny Lès Compiègne

Assembled and edited by

Sébastien Bourban,
and the members of the Scientific Committee of the TELEMAC-MASCARET Consortium

Credits

Published by HR Wallingford

Published by HR Wallingford Ltd, Howbery Park, Wallingford, Oxfordshire OX10 8BA
Telephone +44 (0)1491 835381, Fax +44 (0)1491 832233
www.hrwallingford.com

Contents

** (Paper not available at time of publication)*

Day 1

Session 1 - River and urban flood

Session 2 - Sediment processes

Session 3 - Sediment processes

Session 4 - Water quality

Day 2

Session 5 - Numerical methods

Session 6 - Sediment processes

Session 7 - Numerical methods

Session 8 - Sediments, sustainability, data assimilation, flood forecasting

A regional model for South East Asia in TELEMAC 2D

Li Wang, Boudewijn Decrop, Thijs Lanckriet,
Alexander Breugem
IMDC NV
Antwerp, Belgium
abr@imdc.be

***Abstract*—In this paper a TELEMAC 2D model of the Southeast Asian waters is presented, including the Andaman sea, Gulf of Thailand, South China Sea and Java Sea. The model uses boundary conditions from OSU-TPXO, whereas atmospheric data (wind and air pressure) are used from the GFS model. The results of the model are compared with the data from OSU-TPXO in order to show that the large scale tidal pattern is predicted correctly by the model. Further, the model is compared to water level observations collected by the University of Hawaii, showing that accurate results are obtained in the whole model domain. An outlook is given of further developments that IMDC will undertake in order to extend the model to three dimensions.**

I. INTRODUCTION

The Southeast Asian waters (including Andaman Sea, Gulf of Thailand, South China Sea and Java Sea) are located between the Indian Ocean and Pacific Ocean. Due to tidal transformation on the shallow areas, as well as the important influence of seasonal wind patterns in this area, the TPXO Global Tidal Solution datasets are less suited to provide boundary conditions to local models in these waters. In addition to the tides, the prevailing monsoon winds also have a direct effect on the surface water currents of the shelf region. Over the South China Sea, the south-westward monsoon prevails from November to February (winter), whereas north-eastward monsoon occurs from June to August (summer). Primary or climatological current patterns in summer and winter are shown in Figure 1. Therefore a TELEMAC-2D finite element coastal ocean model was developed to simulate the transformation of the tides from the ocean to the shelf sea.

In this paper, the South Asian Sea model is discussed. Special attention in this discussion is given to code developments that are being performed by IMDC.

This paper is set up as follows. First the model setup is described. This is followed by a description of the results of the model, which are compared to the results of the OSU-TPXO water level elevation data base, as well as to the water level observations collected by the University of Hawaii. In this section, an extension to Telemac is described, which can be used to export time series in NetCDF format. Then an outlook is given of future developments to the Southeast Asia model, as well as Telemac developments that are being performed related to these future developments. The paper is ended with some conclusions.

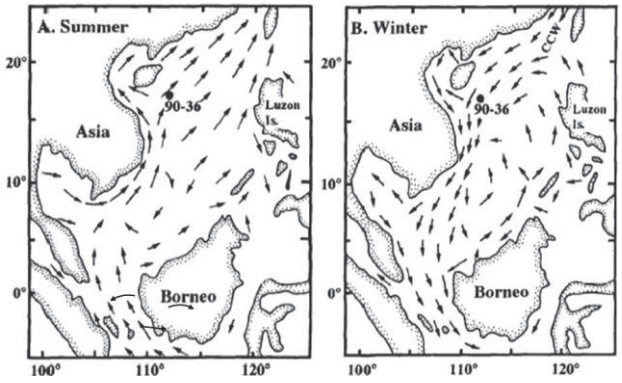

Figure 1. Primary currents during the summer and winter monsoon periods [1]

II. MODEL SETUP

This model is built on an unstructured mesh which allows to closely fit the complex geometry of numerous islands in the region and easily adjust resolution for different areas (). The resolution of the mesh ranges from 2 km to 40 km. The model consists of 49595 nodes and 94953 elements. The bathymetry used in this study comes from GEBCO (General Bathymetric Chart of the Oceans), which is freely available and has a 30-second resolution. This global grid is largely generated by combining quality-controlled ship depth soundings with interpolation between sounding points guided by satellite-derived gravity data. The bathymetric data are interpolated onto the mesh using linear interpolation. The resulting bathymetry is shown in Figure 3. The mesh is set-up in the Mercator coordinate system, but uses TELEMAC's spherical coordinates, which is needed due to the large spatial extent of the model.

The model is supplied with water level boundary conditions from the OSU-TPXO Global Tidal Solution [2] at the eastern and western model boundaries.

The physical process included in the model are the Coriolis force (using a spatially varying Coriolis coefficient), tidal boundary forces and bottom friction using the Manning equation. The model uses atmospheric pressure and wind velocities to take the atmospheric influence into account. Atmospheric data is used from the GFS model [3]. This data has a time interval of 3 hours and a spatial resolution of 0.5

Figure 2. Computational mesh of the Southeast Asia model

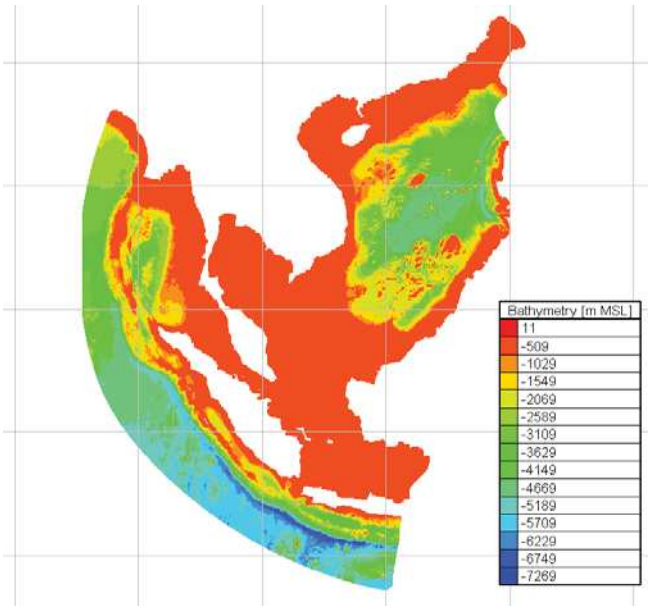

Figure 3. Bathymetry of the Southeast Asia model.

degrees. The resolution is sufficient to resolve the influence of the seasonally occurring monsoon periods. However, during extreme conditions such as typhoons, higher resolution wind data is needed. The wind drag coefficient from the British Admiralty is used. This drag coefficient is wind-speed dependent, with higher drag coefficients during higher wind velocities. A time step of 200 s is used.

The model is calibrated against tidal amplitude and phases at 60 tidal gauges over the model domain [4]. The model calibration is performed by adjusting the bed roughness and the wind drag coefficient using a multiplication factor as a calibration coefficient.

III. MODEL RESULTS

A. Tidal flow

First, the tidal flow is validated by performing a simulation without wind influence and atmospheric pressure gradients. The simulation had a duration 30 days with an additional spin-up period of 7 days, which is sufficient to distinguish the main tidal components. The results of the model are compared with those from OSU-TPXO as well as with those from water level measurements.

The model results are shown in Figure 4 to Figure 7. These figures shown the tidal amplitude as well as cotidal maps for the K1, M2, S2, M4, M6, N2 and O1 tidal components from the model results as well as those components from OSU-TPXO.

The model results compare generally well with those from OSU-TPXO. In the South China Sea, the tide is diurnal (a decreased M2 amplitude in combination with a larger K1), whereas in the rest of the domain, the tide is semi-diurnal (with larger M2 components). The transition between the diurnal and semi diurnal tides is predicted well by the TELEMAC model. There is an amphidromic point in the South China Sea, whose location is predicted well by the model (Figure 5).

B. Time series comparison

Time series of the water levels observation collected by the University of Hawaii [4] are used to compare with time series extracted in the model. This dataset containing hourly water level measurements spans many years and is freely available for download from http://uhslc.soest.hawaii.edu/data/rqh. Reconstructed (tide-only) time series from harmonic analysis were used, which were obtained by means of harmonic analysis using the UTide package.

In order to easily obtain time series from TELEMAC, a module was developed that writes time series in NetCDF format. Each station is exported to a separate NetCDF file. This module uses bi-linear interpolation inside a triangle. It is possible to specify different output periods, each within a different time interval, which must be an integer multiple of the time step in the model. All variables defined the parameter "VARIABLES FOR GRAPHIC PRINTOUTS" in the cas file are exported to the NetCDF files. In case of TELEMAC 3D, a profile is written for each location, containing all vertical nodes.

The module uses an input file called "coordinates.txt", which contains the following information:

- Number of output periods and number of output points
- Start time, end time of each output period in seconds since the start of the model) and output interval (in seconds)
- x and y coordinates, station id and station name of each output location

An example of the coordinate file is shown in Figure 8.

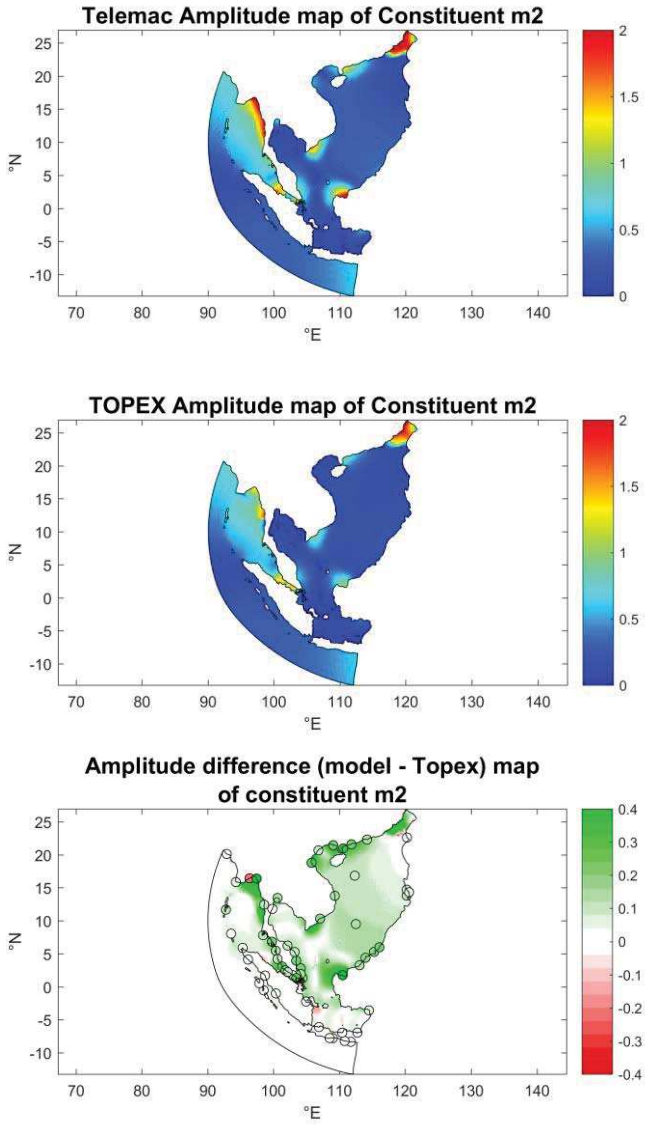

Figure 4. Comparison of the amplitude of the M2 component between OSU-TPXO and the Southeast-Asia model.

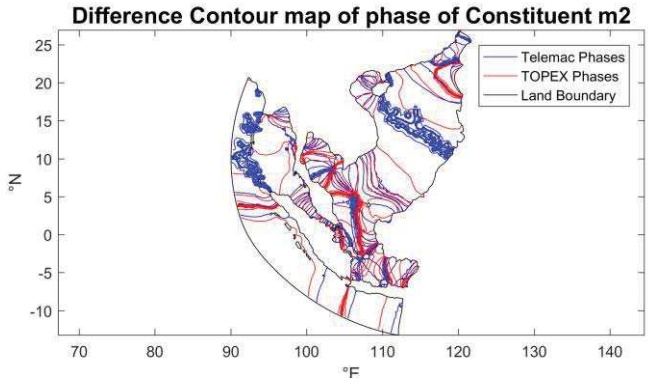

Figure 5. Cotidal maps comparing the phase of the M2 component between OSU-TPXO and the Southeast-Asia model.

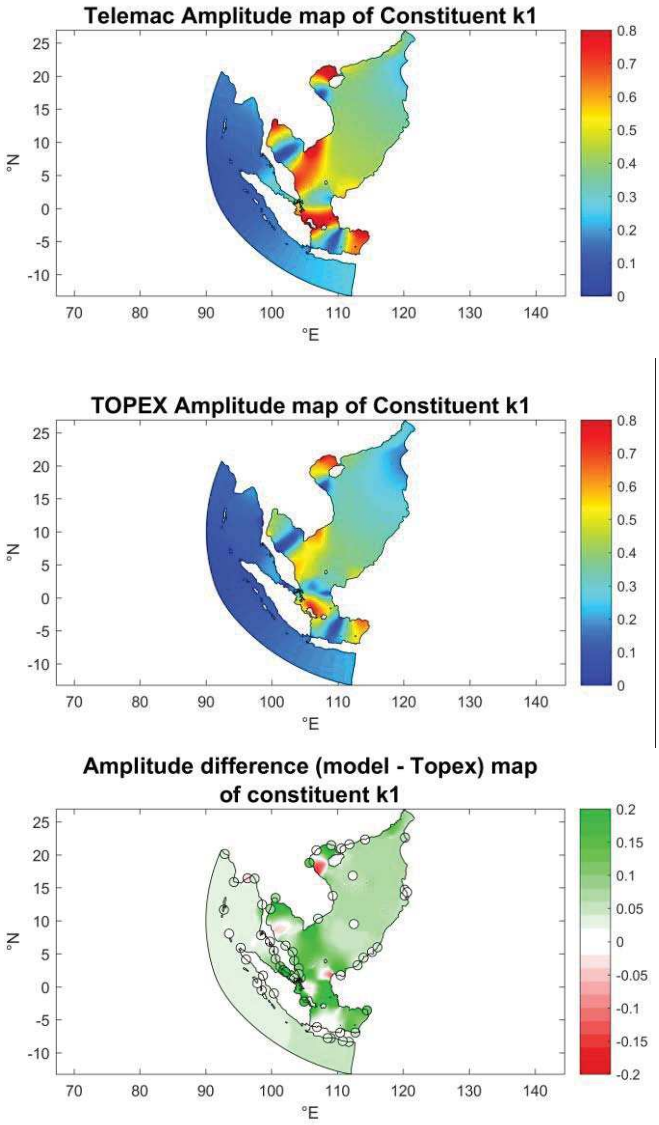

Figure 6. Comparison of the amplitude of the K1 component between OSU-TPXO and the Southeast-Asia model.

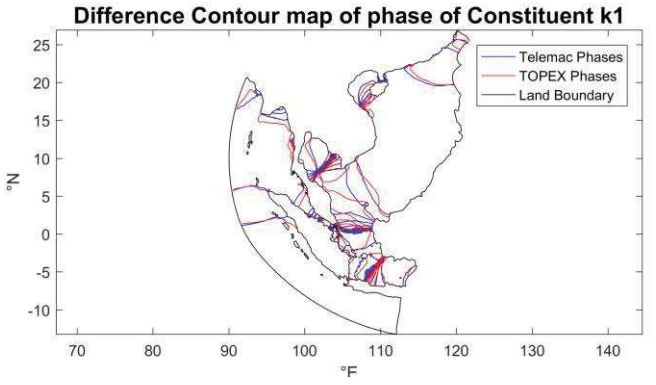

Figure 7. Cotidal maps comparing the phase of the K1 component between OSU-TPXO and the Southeast-Asia model.

```
1 6
0 2937600 200
-1295690.359065 -863961.005882 1 Padang (Telu Bayuk)
-1477772.837081 -569317.385227 2 Sibolga
-1849332.074272 -106230.577457 3 Sabang
-29646.642158 -1688115.573839 4 Prigi
-1188385.218977 -416318.867026 5 Kelang
-1095098.112518 -511245.896952 6 Keling
```

Figure 8. Example of an input file for generating NetCDF output

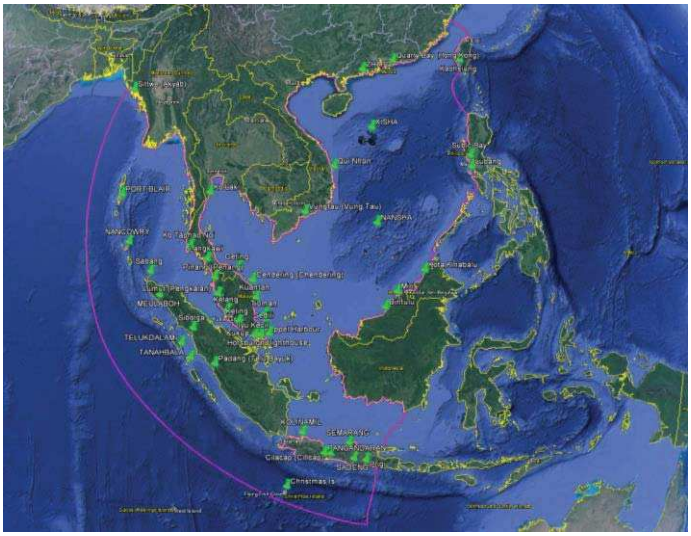

Figure 9. Location of UHSLC research-quality hourly tide stations (green pins)

The time series at Lumut in the Malacca Strait and at Kuantan in the South Chinese Sea (see Figure 9) are shown in Figure 10 and Figure 11. These figures show that the model predicts the water levels due to the tide well, in areas with a predominantly semi-diurnal tide as well as in areas with a diurnal tide.

C. *Influence of the monsoon*

The model is run for two different periods: the summer period (July to September), during which the North-eastern monsoon occurs in the South China Sea, and the winter period (December to January) during which the South-western monsoon occurs. These monsoons are important, because they lead to wind setup and set-down in the South China Sea and the Strait of Malacca, leading to a net flow in the Singapore Strait.

In order to test the model performance during wind, the meteo-induced water level anomaly is plotted for the model results as well as for the measurements in Figure 12 and Figure 13. The anomaly was obtained by performing an harmonic analysis on the data. The reconstructed signal obtained from the harmonic analysis was subtracted from the real time series in order to obtain the anomaly.

In general, the model is capable of predicting the trends in the water level anomaly in the observations. The model clearly shows peaks in the anomaly in the South China Sea in winter. This peak is somewhat overestimated by the model due to remaining frequency content. The summer monsoon setdowns around August 8th and September 15th are captured by the model.

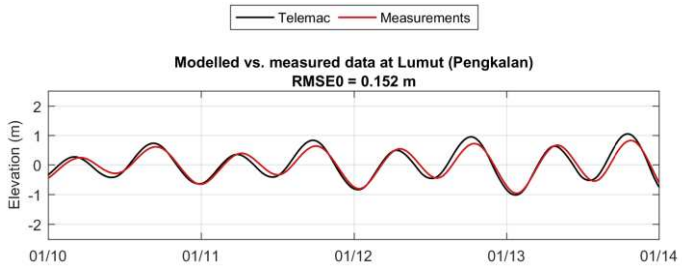

Figure 10. Time series of the water levels in Lumut (located in the Malacca Strait. There is a clear semi-diurnal pattern.

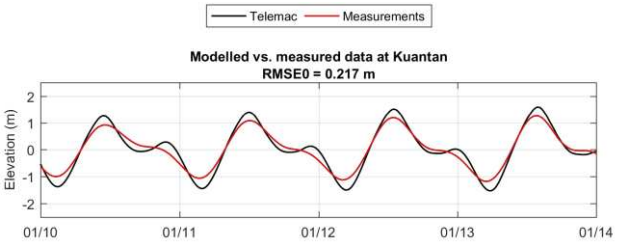

Figure 11. Time series of the water levels in Kuantan (located in the South China Sea). There is a clear diurnal pattern.

IV. OUTLOOK

Apart from predicting water levels, the model is also intended to obtain flow velocities. Unfortunately, it is not possible to test the performance of the model due to the lack of available velocity data in the area. In deep areas, wind driven flows have a strong three dimensional character, because the wind influence is mainly limited to the top of the water column. In order to apply TELEMAC 3D for such a model, IMDC is currently performing two developments, which are described briefly below.

A. *Three dimensional nesting*

In order to be able to prescribe three-dimensional open boundary conditions (for example obtained from an oceanic model such as HYCOM), a module was developed that reads boundary data (water level, three-dimensional velocity profile data and three-dimensional tracer data) from an ASCII file. The ASCII file contains the following information:

- Header line containing the text “OBCFILE3D”
- Number of boundary points in the file
- Node number of the boundary points
- Data for each time step consisting of :
  - Time (in seconds since the start time of the model)
  - Water level data (one value per node)
  - U-velocity profile data (first all values)
  - V-velocity profile data (format as for U-velocities)
  - Tracer profile data (format as for U velocities; only in case a tracer is used in the model).

The data are read, and then are interpolated linearly in time. The velocity data can be added to the water levels and velocities from OSU-TPXO, thus combining the influence in case this is necessary. In this way, space and time varying boundary conditions can be read in TELEMAC without the need for a user to do any FORTRAN programming.

B. GOTM for TELEMAC 3D

GOTM [5] is an open source 1DV turbulence model, specially aimed at oceanic applications. It contains different turbulence models typically used in oceanography, such as the Mellor-Yamada [6] model, and the KPP [7] model. GOTM is especially designed to be easily coupled to other models. The advantage of using GOTM over the existing turbulence models in TELEMAC is that the turbulence models are more suited to use in oceanography.

Presently, a coupling between GOTM and TELEMAC 3D is developed, such that the turbulence models in GOTM can be used to calculate the vertical mixing. Apart from that, it is the intension to use the equation of state from Unesco [8] within GOTM, rather than the linearized equation of states currently available in TELEMAC.

V. SUMMERY AND CONCLUSIONS

In this paper, a TELEMAC 2D model was presented for the Southeast ocean sea including the South China Sea, the Andaman sea, the Gulf of Thailand and the Java Sea. This model was compared with data from OSU-TPXO and with water level observations. This comparison shows that the model delivers good results predicting the diurnal tide in the South China Sea and the semi-diurnal tide in the rest of the model domain. An overview is given of the TELEMAC developments at IMDC, which are considered useful in order to perform three-dimensional ocean modelling.

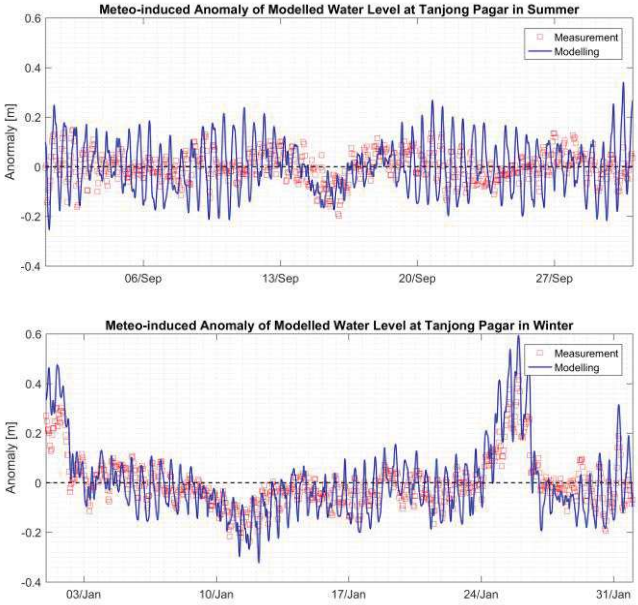

Figure 12. Meteorological water level anomaly in Tanjong Pagar (located in the Singapore Strait). Top: during the summer (North-eastern Monsoon). Bottom: during the winter (South-eastern monsoon).

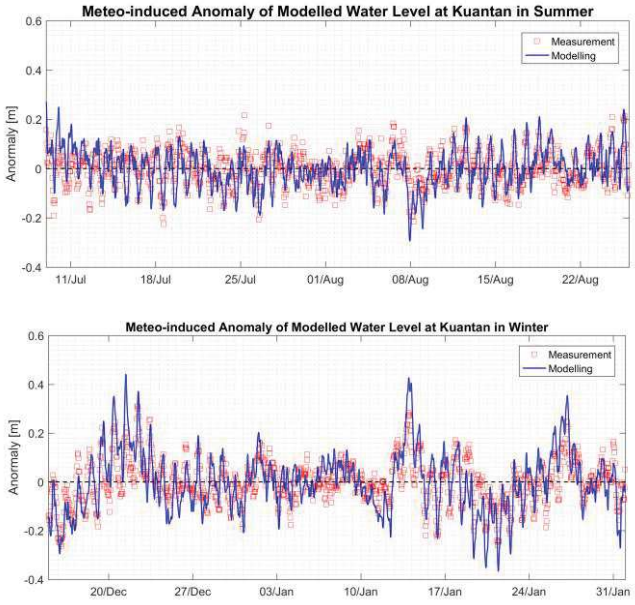

Figure 13. Meteorological water level anomaly in Kuantan (located in the South China Sea). Top: during the summer (North-eastern Monsoon). Bottom: during the winter (South-eastern monsoon).

REFERENCES

[1] Chen, L.-T., Z. Jin, and S. Luo, 1985: The variability of SST over the Indian Ocean and the South China Sea and its linkage with the atmospheric circulation. Acta Oceanol. Sin., 7, 103-110 (in Chinese).

[2] Egbert, G. D., & Erofeeva, S. Y. (2002). Efficient inverse modeling of barotropic ocean tides. Journal of Atmospheric and Oceanic Technology, 19(2), 183-204.

[3] Kistler, R., Collins, W., Saha, S., White, G., Woollen, J., Kalnay, E., ... & van den Dool, H. (2001). The NCEP-NCAR 50-year reanalysis: Monthly means CD-ROM and documentation. Bulletin of the American Meteorological society, 82(2), 247-267.

[4] University of Hawaii sea level center, http://uhslc.soest.hawaii.edu/data/?rq

[5] Burchard, H., Bolding, K., & Villarreal, M. R. (1999). GOTM, a general ocean turbulence model: theory, implementation and test cases. Space Applications Institute.

[6] Mellor, G. L., & Yamada, T. (1982). Development of a turbulence closure model for geophysical fluid problems. Reviews of Geophysics, 20(4), 851-875.

[7] Canuto, V. M., Howard, A., Cheng, Y., & Dubovikov, M. S. (1999). Ocean Turbulence I: One-Point Closure Model Momentum and Heat Vertical Diffusivities.

[8] Unesco (1981). Background papers and supporting data on the international equation of state of seawater 1980

Optimization of Bed Shear Stresses at the Head of a Reservoir to Prevent Future Sediment Deposition

Gabriele Harb
VERBUND Hydro Power
Austria
Email: gabriele.harb@gmx.at

Hannes Badura
VERBUND Hydro Power
Austria
Email: hannes.badura@verbund.com

***Abstract*—**

In reservoirs the flow velocities, the turbulence and the bed shear stresses are reduced in case of backwater. This effect leads to the settlement of sediment particles in the reservoir. In further consequence the bed levels rise and the storage volume is being reduced by filling up the reservoir with sediments. In Alpine run-off river and diversion plants the water depth are usually lower than in reservoirs of storage and pump-storage hydro power plants. A large part of the suspended sediments is thus transported through the reservoir and deposition of bed load fractions is the main problem. The deposition of coarse sediments at the head of the reservoir may cause problems regarding flood protection by raising the bed level and thus, raising the water level too. In the selected case study, the widening of the river bed at the head of the reservoir worsens this problem and lead to sediment depositions in the reservoir. Additionally the values of the design flood events for flood protection have been increased since the hydro power plan was built and the state of the art of flood modeling has changed in the last decades. These three facts together lead to a flood protection problem for the surrounding areas. The paper presents the application of Telemac2D to solve this issues. The numerical analysis showed that the removal of the sediment depositions and the implementation of a berm increases the shear stresses for reducing sediment deposition in the future.

I. Introduction

The construction of dams and reservoirs influence the natural sediment transport processes and affect the sediment connectivity. Due to the increase in water depth in reservoirs, the flow velocities, turbulences and bed shear stresses are reduced variably. This leads to deposition of the transported sediments, increases the bed level and often reduces the storage volume by filling up the reservoir. A decreased reservoir volume reduces, and in extreme cases eliminates the capacity of hydropower, water supply, irrigation and flood control benefits [1]. However, reservoirs with less than 20 m height are usually shallow and morphological evolution develops relatively quick compared to large reservoirs [2].

Reservoir sedimentation is a common problem in dam engineering today. At any reservoir where a sustainable long-term use is required, it will be necessary to manage sediments as well as water [1].

Traditionally, reservoirs have been designed and operated with the assumption of a usable life of about 100 years, which will eventually be terminated by sediment deposition in the reservoir. The reservoirs have often been planned with a large volume of dead storage, which provided enough space for the sediment depositions of 20 - 40 years. Usually little thought was given to the fact that the reservoirs would have to be replaced, if the storage is lost. The assumption was always made that someone else in a future generation, will find a solution for the sedimentation problem. Reservoir sedimentation is thus an increasing problem worldwide. Sediment management in reservoirs is not longer a problem that can put off to be dealt with in the future; it has become a contemporary problem. Traditional approaches of sediment management have not taken into account the need for a sustainable sediment management [1].

The main factors in reservoir sedimentation are the reduced transport capacity of coarse solids as bed load, the transport of fine fractions in a stochastic distribution, and in some cases the transport of fine fractions in the form of density currents. The occurring sedimentation pattern reflects these processes and therefore it is essential to know the processes determining the sedimentation in order to choose the adequate management method [3].

The implementation of a successful sediment management requires appropriate knowledge of the sedimentation and erosion processes in reservoirs, because every reservoir is unique regarding the purpose, the geometry, and other boundary conditions like hydrological and hydraulic conditions. Consequently not every management method is suitable for every reservoir. Additionally in the case of a chain of river plants it is essential to know the operation method of upstream plants and reservoirs. The management methods have to be coordinated in time and space for a successful sediment management.

The success of the different management methods is often investigated using theoretical approaches and physical models. The problem is, that all theoretical approaches and physical models may contain uncertainties or scaling effects. Therefore it is important to include a sensitivity analysis in the investigations of the reservoir management methods. There is a large amount of literature available concerning sediment management methods, e.g., [1], [4], [5] or [6], the focus here is on the principles behind the problems of reservoir sedimentation and on large storage reservoirs.

Over the past few decades physical models have been used to analyze processes and improve knowledge regarding water flow and sediment transport in rivers and reservoirs. Due to the rapid development of computational fluid dynamics (CFD), the increased computer power and the availability of clusters and parallel processing, numerical modeling has become an

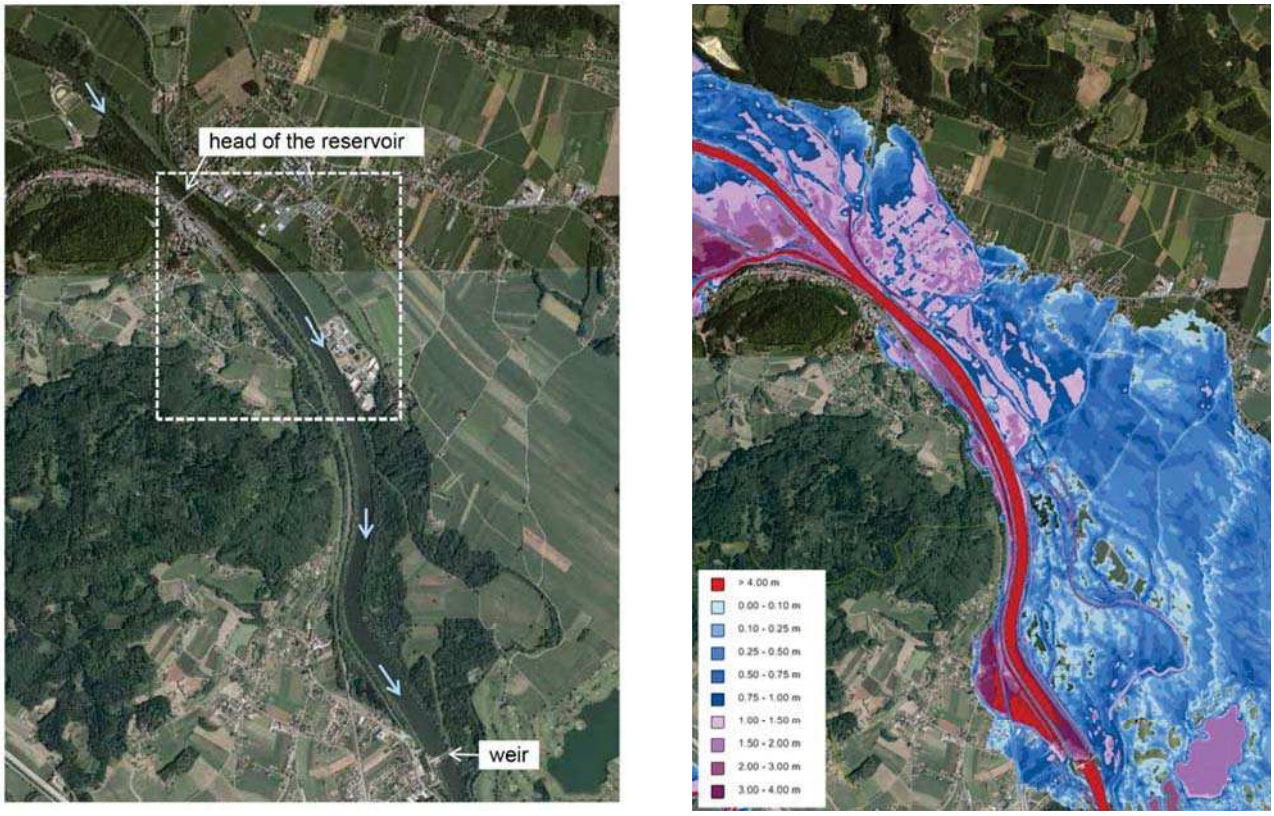

(a) Overview of the project area

(b) Water depth in the project area in case of the 100-year flood

Fig. 1: Project area

important tool in fields of hydraulics. There are various numerical models available which are able to handle hydraulic problems. However, numerical models with implemented and tested sediment transport algorithms are relatively rare.

In the present case study, the adaption of the hydraulic design of reservoir layout, singular excavation measure and reservoir operation adaption leads to an optimized and sustainable state of the art sediment management in a chain of power plants. This paper describes the hydraulic design development for a sensitive and urbanized flood plain area.

II. Project Area and Background

The project area is a reservoir at the river Mur in lower Styria, Austria (Figure 1a). The reservoir is approximately 5 km long and a width of river bed of 60-150m. Since beginning of operation in 1988 the reservoir was operated without flushing permissions. The head of the reservoir is located in an urban area. The plant design includes flood protection measures like levees on both sides of the river. But since the start of operation of the hydro power plant the values of the design flood events for flood protection have been increased, and the state of the art of flood modeling has changed in the last decades. The plant is located in an area of natural floodplain, these facts together lead to a flood protection problem for these areas.

Upstream of the reservoir, the bankfull flow of the river Mur is reached between the 5-year flood event and the 20-year flood event. In the case of a 100-year flood event the floodplains are filled up and several villages and the railway are flooded. Figure 1b shows the calculated water depth in the project area.

The head of the reservoir is next to the bridge shown in Figure 1a. Upstream of this bridge the river Kainach flows into the river Mur. Downstream of the bridge the flow profile of

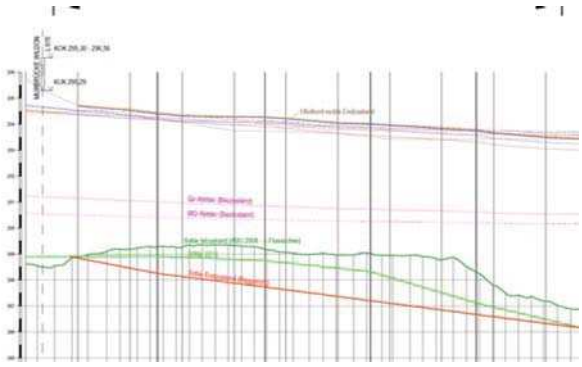

Fig. 2: Bed levels in the reservoir; the dark green line denotes the river bed in 2008 in the middle of the bed, the light green line denotes the thalweg in 2013 after a high flood event and the red line is the planned dredged river bed

(a) Freeze core taken at the head of the reservoir

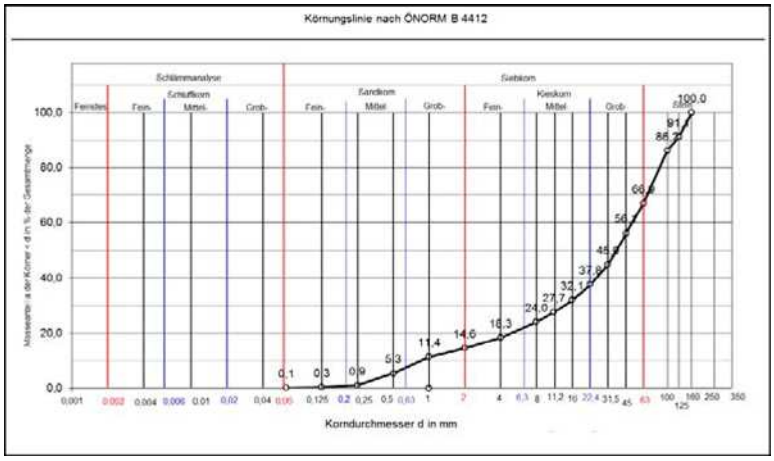

(b) Corresponding grain-size distribution

Fig. 3: Freeze core and grain-size distribution from the head of the reservoir

the River Mur widens up from approx. 50-60m to 70-80m.

Table I shows the hydrological conditions of the river Mur in the project area.

TABLE I: Hydrological conditions in the project area

Flow condition	Q Mur [m^3/s]	Q Kainach [m^3/s]	Q total [m^3/s]
mean discharge	110	10	120
design discharge	190	10	200
1-year flood	460	90	550
5-year flood	735	75	810
10-year flood	800	200	1000
30-year flood	1050	200	1250
100-year flood	1400	150	1550

A. Sedimentation in the Reservoir

The widening in the river downstream of the bridge at the head of the reservoir lead to an aprupt deceleration of the velocities. Transported sediment at flood events or higher discharges thus deposits in the reservoir. Echo-soundings showed the rising of the bed levels at the head of the reservoir (Figure 2).

According to the shear stress conditions in the reservoir, the fine sediments are transported to the weir, while coarse sediments (gravel and cobbles) mainly deposit at the head of the reservoir. The coarse sediment depositions at the head of the reservoir increase the water level additionally. Hence, the rising of the bed levels at the head of the reservoir creates additional problems concerning flood safety for the surrounding areas.

In 2014 the freeze-core method was used to take sediment samples in the reservoir. The samples were sieved according to the Austrian Standard. The freeze-core taken at the head of the reservoir is shown in Figure 3. The mean diameter d_m of the sample is about 40 mm, whereas the d_{90} is about 125 mm, which is still relatively coarse for a reservoir in an lower Alpine river.

B. Description of the Project

The idea behind the project was first to dredge the sediment depositions at the head of the reservoir and second to enhance the shear stresses sustainable to prevent future sediment depositions and to create a stable river bed solution. The dredging of the sediment deposition expand the river section downstream of the bridge additionally. The implementation of a submerged intermediate berm should thus concentrate the flow field and enhance the flow velocities and the sediment transport. Additionally the levee on the orographic right side downstream of the bridge will be heightened to prevent future flooding of the orographic right floodplains. To obtain a official approval for the heightening of the levee it has to be ensured that the cutting of the retention area does not influence the flood wave in the downstream of the project area significantly. Figure 4 gives an overview over the planned measures. A cross section of the planned submerged intermediate berm is shown in Figure 5.

To avoid an increase flooding of the orographic left floodplains, existing water levels for the 30-year flood and the 100-year flood, respectively, should not be increased. This was a the main technical term for the project design. Therefore, a numerical model was applied to model

- the current state in the project area to calibrate the model,
- the final state with the optimized submerged intermediate berm and the heightening of the levees on the orographic right side downstream of the bridge,
- and additional construction stages.

To enhance the sediment transport in this reservoir, the permission regarding the operation of the hydro power plant

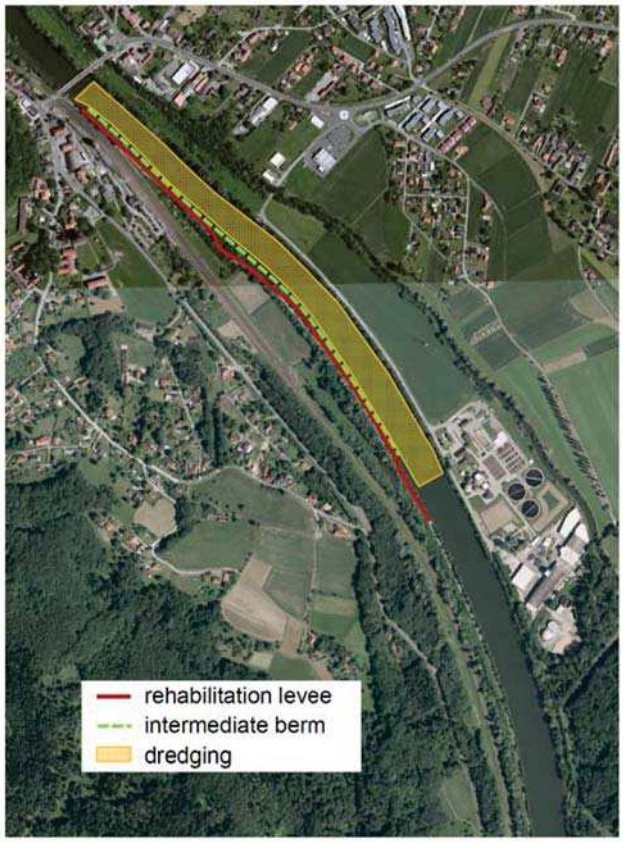

Fig. 4: Overview over the project

has been changed to allow the lowering of the water level at higher discharges and enable free flow conditions at the weir in case of discharges which are higher than the 5-year flood.

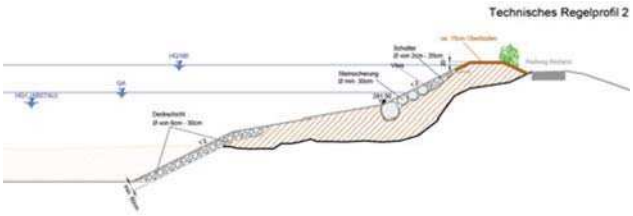

Fig. 5: Cross section of the submerged intermediate berm

III. Numerical Model

In the present study the hydrodynamic model TELEMAC-2D v7p1 from the TELEMAC-MASCARTE suite [7] was used to simulate the flood wave and analyses the effect of the submerged intermediate berm. The mesh with approximately 245,000 triangular cells and an average edge length of 5-10 m was based on an existing SMS-mesh and edited using BlueKenue [8]. Figure 6 shows the generated mesh with the conserved break lines of the river banks.

The roughness values in the model were set according to the land use in the area, the friction law after Strickler was used. The water levels were calibrated using the measurement

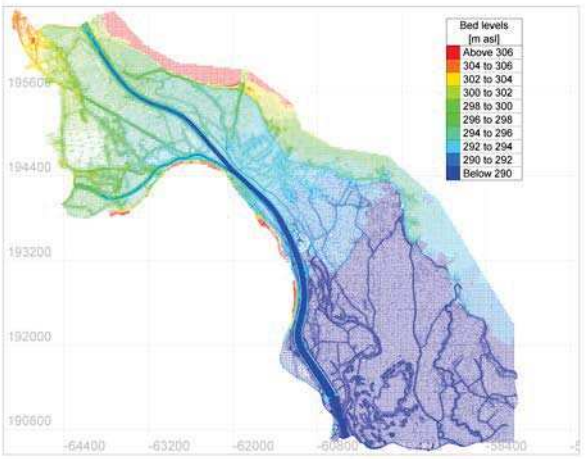

Fig. 6: Bed levels of the generated mesh of the project area

data of existing gauges. Based on the calibration results, the turbulence was modeled using the Elder Model. The standard secondary currents algorithm was applied.

IV. Results

Several runs with modified settings (width, height) of the intermediate berm were necessary to increase the shear stress as much as possible but do not heighten the water levels. The final setup is presented here.

Figure 7 shows the comparison of calculated shear stresses for a 1-year flood with a discharge of 550 m^3/s (a) in the current state with maximum operation level and (b) with the implemented submerged intermediate berm, dredging and draw down of the water level of 1.5m at the weir. The draw-down of the water level increases the flow velocities and the bed shear stresses in the reservoir. Because of the low water depths and the movement of the head of the reservoir due to the change in the water level, the bed shear stresses increases not only at the weir but in the whole reservoir. The implementation of the submerged intermediate berm enhances the shear stress at the head of the reservoir additionally.

The differences in the water levels between the current state and the planned state with the submerged intermediate berm for the 100-year flood event are indicated in 8. The water levels decrease next to the bridge and in the southern part on the project area. The orographic right side of the river stays dry, therefore the differences in the water level are equal to the former water depth.

V. Conclusion

In the present study the effects of the implementation of a submerged intermediate berm together with dredging actions on the water level, flow field and bed shear stresses have been analyzed with a two-dimensional numerical model. The model has been calibrated using gauge data. The results show that the modification of the river section at the head of the reservoir and the draw-down of the water level lead to enhanced the bed shear stresses not only next to the weir but also up to the head of the reservoir. The bed shear stresses are significant

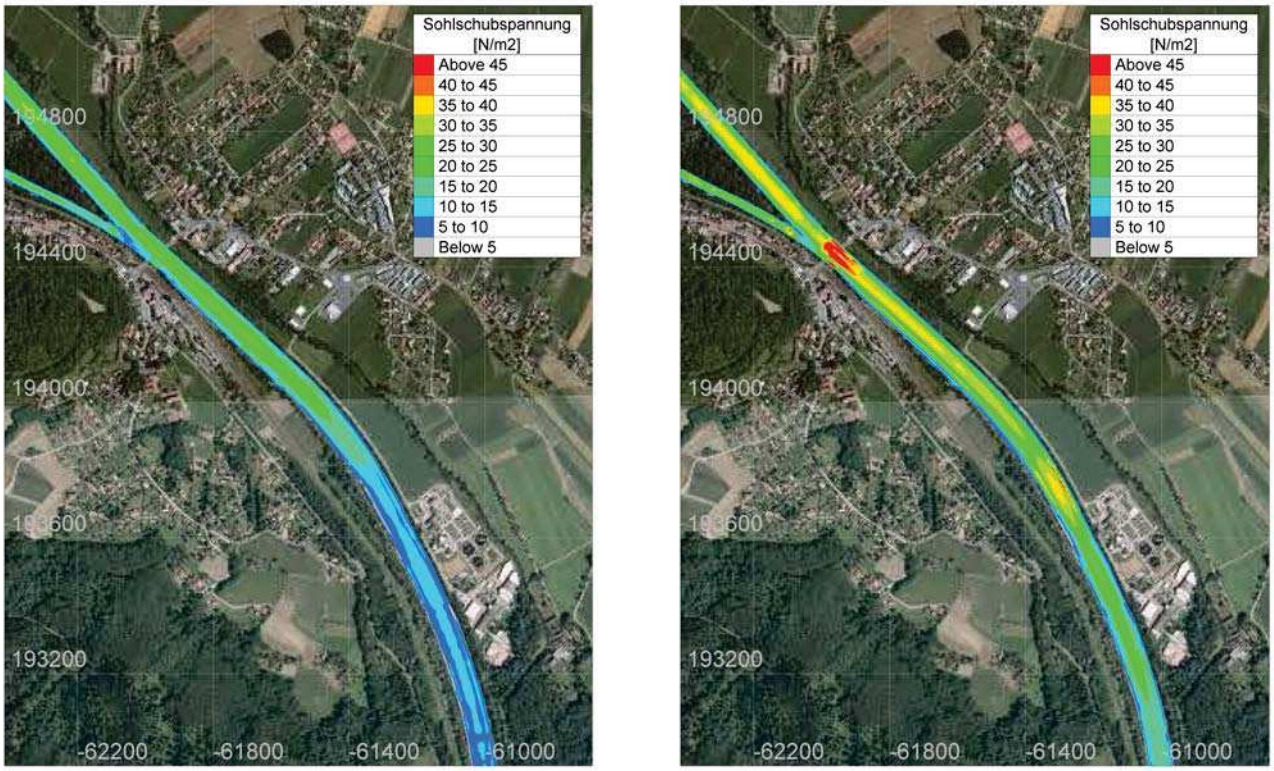

(a) Calculated shear stresses in the current state [(N/m^2) with maximum operation level at the weir (292 m asl)

(b) Calculated shear stresses in the final state (N/m^2) with submerged intermediate berm, dredging and lowering of the water level at the weir to 290.5 m asl

Fig. 7: Comparison of calculated shear stresses for the current and the final state

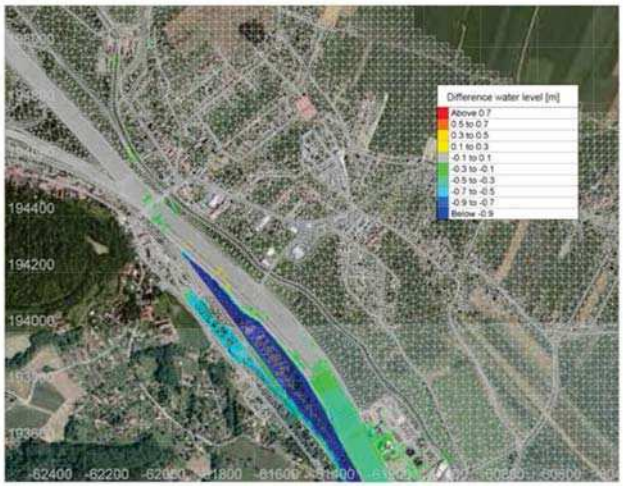

Fig. 8: Differences in the water levels for the 100-year flood

higher with the modified geometry than in the current state due to the increase of the energy slope resulting of the lowering of the water level. The elimination of the deceleration effect caused by the widening of the river bed enhances the bed shear stresses at the head of the reservoir too. The combined measures can thus reduce the sedimentation at the head of the reservoir and facilitate the erosion of the sediment depositions in the middle of the reservoir and next to the weir as well as enable the sediment pass through the reservoir at higher flood event.

REFERENCES

[1] G. Morris and J. Fan, *Reservoir Sedimentation Handbook*. McGraw-Hill Book Co., New York, 1998.

[2] W. Wu, *Computational River Dynamics*. Taylor & Francis Group, London, UK, 2008.

[3] W. Bechteler, "The purposes of impounding facilities," in *ALPRESERV - Sediment Management Methods - Technical and legal aspects*. Universitt der Bundeswehr Mnchen, Volume 4/2006, ISSN 1862-9636, 2006.

[4] D. Batuca and J. Jordaan, *Silting and Desilting of Reservoirs*. A.A. Balkema, Rotterdam, 2000.

[5] R. White, *Evacuation of sediments from reservoirs*. Thomas Telford Publishing, 2001.

[6] E. Atkinson, *The Feasibility of Flushing Sediment from Reservoirs*. TDR Project R5839, Report OD 137, HR Wallingford, 1996.

[7] J.-M. Hervouet, *Hydrodynamics of Free Surface Flows: modelling with the finite element method*. Wiley, 2007.

[8] C. H. C. CHC, "Blue Kenue - Reference Manual," Homepage of the National Research Council Canada, 2011.

Implementation of a rainfall-runoff model in TELEMAC-2D

Pierre-Louis Ligier[1]

[1] Sweco Energuide AB, Hydropower and Dams Department, Stockholm, Sweden (pierre-louis.ligier@sweco.se)

Abstract— **Since version v6p2 it is possible to model rain or evaporation in TELEMAC-2D and TELEMAC-3D. However, this feature does not include dynamic modelling of the infiltration processes during a rainfall event. In Sweden, 2D hydraulic models are starting to be widely used for rainfall simulations with applications in urban planning and sewage system design, natural hazards risk assessments (flooding, debris-flow) and in the mining industry (tailing dams). In all of the above, infiltration can be of utmost importance. The possibility to dynamically model the infiltration process during a rainfall event will therefore increase the suitability of 2D hydraulic models for such applications. With that objective, a rainfall-runoff model has been implemented in TELEMAC-2D. The model is based on the Method of Abstractions, developed by USA's Soil Conservation Service, in which the infiltration potential is characterized by a coefficient called Curve Number (CN). This coefficient is a function of four major runoff properties (hydrological soil groups, land use, hydrologic surface condition of native pasture and antecedent moisture conditions). The Curve Number runoff model implemented in TELEMAC-2D offers the possibility to define spatially varying CN values at each computational node. The model also includes the possibility to account for the actual terrain slope by adjusting the CN values locally. Finally, options making it possible to read a block-type hyetograph from a formatted data file as well as applying a so-called Chicago Design Storm hyetograph from Intensity-Duration-Frequency equation parameters have been implemented. The Curve Number runoff model will be available in the next release of the open TELEMAC-MASCARET suite (version v7p2).**

I. INTRODUCTION

Since version v6p2 it is possible to model rain or evaporation in TELEMAC-2D and TELEMAC-3D. However, this feature does not include dynamic modelling of the infiltration processes during a rainfall event. In Sweden, 2D hydraulic models are starting to be widely used for rainfall simulations with applications in urban planning and sewage system design, natural hazards risk assessments (flooding, debris-flow) and in the mining industry (tailing dams). In all of the above, infiltration can be of utmost importance. The possibility to dynamically model the infiltration process during a rainfall event will therefore increase the suitability of 2D hydraulic models for such applications. With that objective, the Curve Number runoff model has been implemented in TELEMAC-2D.

This paper is articulated in three parts. In the first part, the Curve Number runoff model is presented. The second part describes how the model and its options have been implemented in TELEMAC-2D, the different methods for rainfall definition and a new validation case. Finally, an example of application is presented.

II. THE CURVE NUMBER RUNOFF MODEL

A. Method

The Curve Number runoff model, also known as the SCS Method of Abstractions, has been developed from 1954 by USA's Soil Conservation Service (SCS). This method, which is widely used in the world, aims at computing abstractions from storm rainfall using a spatially and temporally lumped infiltration loss model. It gives best results in agricultural watersheds with negligible baseflow [1].

The conversion from rainfall to runoff can be expressed by the following conservation equation:

$$P = P_e + F \quad (1)$$

With P the rainfall depth (mm), P_e the runoff depth (mm) and F the hydrologic abstractions (mm).

The aim of runoff modelling is to assess the hydrologic abstractions F which are composed of (i) interception storage (vegetation foliage…), (ii) surface storage, (iii) infiltration, (iv) evaporation and (v) evapotranspiration. For short-term storm modelling, which is the Curve Number runoff model's field of application, abstractions due to infiltration are largely predominant over other forms which are then disregarded [1].

Runoff analysis has shown that runoff begins after that a certain amount of rainfall, called "initial abstraction", is abs-

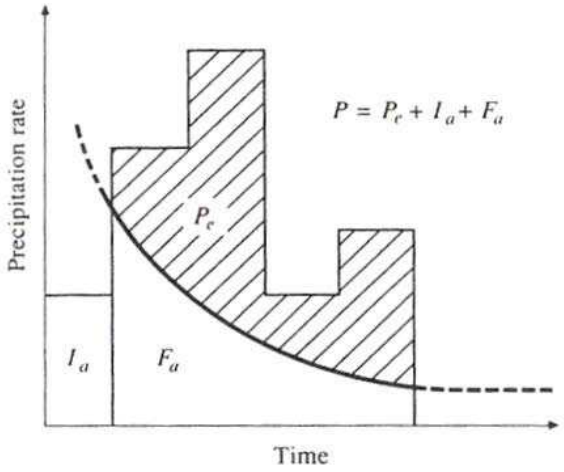

Figure 1. Variables in the Curve Number runoff model [3].

tracted as interception, infiltration and surface storage [2]. The conservation equation can also be written as:

$$P = P_e + I_a + F_a \quad (2)$$

With I_a the initial abstraction (mm) and F_a the hydrologic abstraction (mm) corresponding to infiltration and also called "continuing abstraction". The different variables in the Curve Number runoff model are illustrated in Fig. 1.

The Curve Number runoff model is based on the assumption that retention is proportional to runoff:

$$\frac{F_a}{S} = \frac{P_e}{(P-I_a)} \quad (3)$$

With S the potential maximal retention (mm). The expression of the runoff P_e can then be obtained by combining (2) and (3):

$$P_e = \frac{(P-I_a)^2}{P-I_a+S} \; for \; P > I_a$$
$$P_e = 0 \; for \; P \leq I_a \quad (4)$$

This expression is the main equation of the Curve Number runoff model and is based on two parameters, I_a and S. A relation between I_a and S was developed using rainfall and runoff data from experimental watersheds [2]:

$$I_a = \lambda \cdot S \quad (5)$$

The coefficient λ, known as the initial abstraction ratio, has been originally defined as 0.2 (-) [2]. It can be noted that more recent studies have pointed out that this value is probably high, as presented in the next section. The runoff equation relies then on only one parameter, the potential maximal retention S. It is however difficult to estimate this parameter which is function of geological and hydrological conditions and which theoretically varies between 0 and infinity. For practical reasons, the Curve Number (CN, dimensionless) has then been defined as:

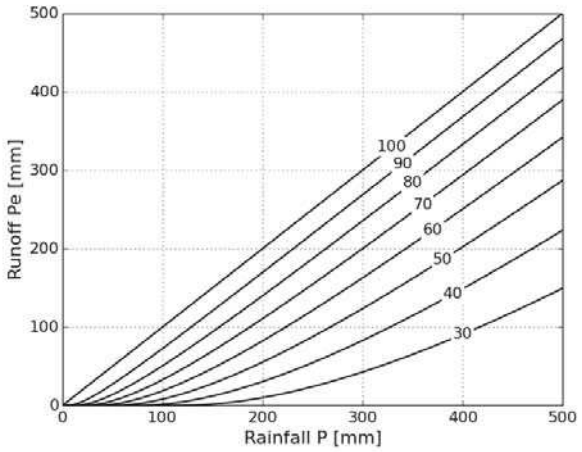

Figure 2. Solutions of the runoff equation (4) for CN values varying between 30 and 100 and for λ = 0.2.

$$S = 25.4 \cdot \left(\frac{1000}{CN} - 10\right) \quad (6)$$

Curve Number values vary between 0 (infinite potential maximal retention i.e. no runoff) and 100 (no retention i.e. no infiltration) and are function of geology, land use and antecedent moisture conditions. Solutions of (4) for CN values varying between 30 and 100 and for λ = 0.2 are presented in Fig. 2.

The SCS has defined Curve Number values for different types of land use classes and for four different hydrological soil groups: Group A (deep sands, deep loess and aggregated silts), Group B (shallow loess, sandy loams), Group C (clay loams, shallow sandy loams, soils low in organic content and soils usually high in clay) and Group D (soils that swell significantly when wet, heavy plastic clays and certain saline soils) and for three type of hydrologic surface condition of native pasture (poor, fair, and good). These values, which are presented in tables and are available in handbooks (for example [3, 4]), have been determined for an initial abstraction ratio λ = 0.2 and for normal antecedent moisture conditions (referred as AMC II) are referred as CN(II).

For dry antecedent moisture conditions (AMC I, lowest runoff potential) and wet antecedent moisture conditions (AMC III, highest runoff potential), CN(II) values can be converted with the following equations (also illustrated in Fig. 3) [3]:

$$CN(I) = \frac{4.2 \cdot CN(II)}{10 - 0.058 \cdot CN(II)} \quad (7)$$

$$CN(III) = \frac{23 \cdot CN(II)}{10 + 0.13 \cdot CN(II)} \quad (8)$$

The antecedent moisture condition classes has been initially defined based on the 5-day antecedent rainfall for the dormant and growing season [2, 3]. However, more recent analyses have shown that there is no apparent relationship between antecedent rainfall and CN values [5]. Despite a

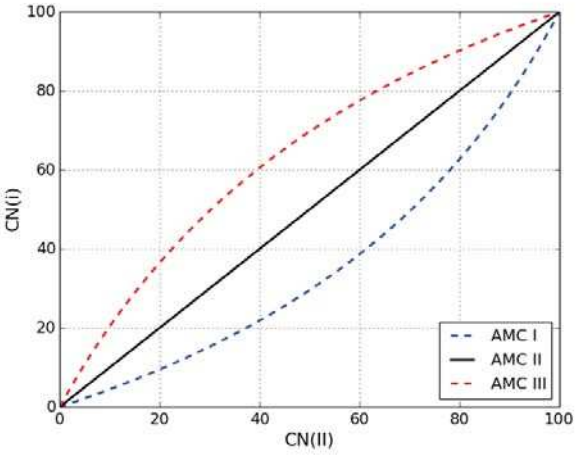

Figure 3. Curve Number conversion based on antecedent moisture condition classes (AMC).

relative lack of guidance, antecedent moisture condition classes can be used as a calibration or design parameter.

Although being a lumped method, the Curve Number runoff equation (4) can be time distributed to simulate infiltration during a storm. Equations (2) and (3) can be combined to obtain the accumulated continuing abstraction F_a [3, 5]:

$$F_a = \frac{S\cdot(P-I_a)}{P-I_a+S} \quad for\ P > I_a$$
$$F_a = 0 \quad for\ P \leq I_a \tag{9}$$

With P being the accumulated rainfall depth (mm) at a given time step. The corresponding accumulated runoff depth P_e can then be determined using (2).

B. Reanalysis of the initial abstraction ratio

The initial abstraction ratio was analysed through rainfall-runoff data measured on 307 watersheds or plots in the USA [6]. The results have shown that the ratio λ varies from storm to storm and that the original value of 0.2 is unusually high. The study concluded that the value of λ can be re-estimated to 0.05 and that more than 90% of the values were lower than 0.2. Changing the initial abstraction ratio from the original method implies that the potential maximal retention and hence the Curve Number should be adjusted. The study proposed a relationship giving CN(II) values expressed in terms of λ = 0.05 as a function of the standard CN(II) values expressed in terms of λ = 0.2 (see also Fig. 4):

$$CN(II)_{\lambda=0.05} = \frac{100}{1.879\cdot(100/CN(II)_{\lambda=0.2}-1)^{1.15}+1} \tag{10}$$

This new formulation implies that runoff occurs earlier than with the standard method (λ = 0.2). The greater effect is found on storms with low P/S ratios, i.e. for either small storms or storms with low CN values, for example forest, for which the peak discharge tends to increase. For a more detailed

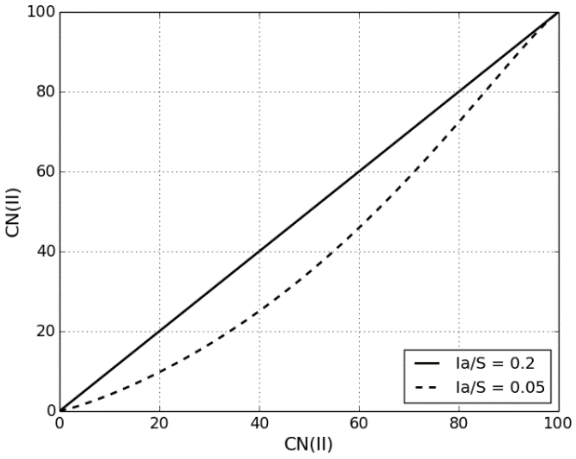

Figure 4. Curve Number conversion for an initial abstraction ratio λ = 0.05.

analysis, please refer to [6].

C. Effect of steep slopes

The terrain slope has not been incorporated in the original Curve Number runoff model which is believed to be valid primarily for low slope terrains. However, it has been demonstrated that increasing terrain slopes generate increasing runoff volumes [7]. An experimental study performed on a watershed located in the Loess Plateau of China has proposed a relation to adjust the standard Curve Number for slopes between 0.14 and 1.4 m/m [7]:

$$CN(II)_\alpha = CN(II)\cdot\frac{322.79+15.63\cdot\alpha}{\alpha+323.52} \tag{11}$$

With α the terrain slope in m/m ($0.14 \leq \alpha \leq 1.4$). The standard CN values can then be increased by up to approximatively 6% for a slope α = 1.4.

D. Remark

It has been common practice to use the Curve Number runoff model using a weighted CN value over the whole watershed. This was done mainly to limit the number of calculations. The use of computers with the possibility to define several CN values within the watershed based on local geological and hydrological characteristics has removed this constraint. As the runoff depth does not evolve linearly with the potential maximal retention (and therefore the Curve Number), see (4), differences will be observed between the two methods on a same watershed (weighted CN value or spatially defined CN values).

E. Advantages and disadvantages of the Curve Number runoff model

In [1], V. Ponce and R. Hawkins have done a critique of the Curve Number runoff model listing up its advantages and disadvantages. The most important points are recalled hereafter.

Advantages:

- The method is simple, stable, predictable and based on empirical data.
- It relies on only one parameter (CN) which varies as a function of four major runoff properties (hydrological soil groups, land use, hydrologic surface condition of native pasture and antecedent moisture conditions).
- It is well established and used worldwide.

Disadvantages:

- The method was developed using regional field data from the United States. Certain caution is therefore required for use in different regions.
- The results are very sensitive to the antecedent moisture condition classes. Furthermore, there is no clear guidance on how to determine which class to use.
- The method assumes an initial abstraction ratio $\lambda = 0.2$ which was shown to be overestimated (see above).
- The method should be used with caution on large watersheds (> 250 km^2).

III. IMPLEMENTATION IN TELEMAC-2D

A. Overview

In TELEMAC-2D, rain or evaporation is modelled as a source term implemented in subroutine `prosou.f`. The Curve Number runoff model has been implemented in a new subroutine called `runoff_scs_cn.f` (available from version v7p2). The model is activated thanks to a new keyword RAINFALL-RUNOFF MODEL whose value should be set to 1 (default is 0, no runoff model) and assuming that the keyword RAIN OR EVAPORATION is set to YES. The input data consist in rainfall and the standard CN(II) values that can be defined at each node of the computational domain.

The standard method for defining the CN(II) values is a spatial interpolation performed from a user defined set of points defining polygons with constant CN(II) values. This data is to be provided in a formatted data file. Note that each polygon must have unique point coordinates (polygons cannot share vertices with identical coordinates).

CN values can also be defined directly in the geometry file as an additional variable. This variable is read by TELEMAC-2D when the keywords NAMES OF PRIVATE VARIABLES and NUMBER OF PRIVATE ARRAYS are included in the steering file. Examples of application for both methods are provided in a new validation case (see next section).

The antecedent moisture conditions can be defined with the new keyword ANTECEDENT MOISTURE CONDITIONS (1: AMC I, dry antecedent moisture conditions; 2: AMC II, normal antecedent moisture conditions [default]; 3: AMC III, wet antecedent moisture conditions). When choosing the option 1 or 3, CN(II) input values are converted to either CN(I) or CN(III) using (7) and (8).

The user can also choose between the original initial abstraction ratio ($\lambda = 0.2$) and the revised formulation ($\lambda = 0.05$) with the new keyword OPTION FOR INITIAL ABSTRACTION RATIO (1: $\lambda = 0.2$ [default]; 2: $\lambda = 0.05$). When choosing the option 2, CN(II) input values are converted using (10).

Finally, it is possible to adjust CN(II) values to account for steep slopes using (11). This option should be activated manually directly in `runoff_scs_cn.f` (local variable `STEEPSLOPECOR`, not activated by default).

The Curve Number runoff model requires that the tidal flats option is activated (TIDAL FLATS = YES).

B. Options for rainfall definition

Rainfall can be defined in three different ways in the Curve Number runoff model. The standard method consists in using a rainfall with constant intensity defined by the existing keyword RAIN OR EVAPORATION IN MM PER DAY (method activated by default). A new keyword has been introduced to define the duration of rain (or evaporation): DURATION OF RAIN OR EVAPORATION IN HOURS (units: hours, default is infinite). This keyword can also be used with the standard rain or evaporation function (without runoff model).

Rainfall can also be defined by a user specified block-type hyetograph giving the rainfall depth (mm) between two consecutive times provided in a formatted data file.

Finally, rainfall can also be defined as a so-called Chicago Design Storm (CDS) hyetograph computed automatically from user defined Intensity-Duration-Frequency (IDF) parameters.

The IDF relationship used is [3]:

$$i = \frac{a}{t^b + c} \tag{12}$$

With i the rainfall intensity over a duration t (mm/h), t the rainfall duration (hours), a, b and c are the IDF parameters. The instantaneous rainfall intensity i (mm/h) is then obtained from the following expression [3]:

$$i = \frac{a \cdot \left((1-b) \cdot t_R^b + c \right)}{\left(t_R^b + c \right)^2} \tag{13}$$

With t_R the time relative to rainfall peak (hours):

$$t_R = \frac{t_{peak} - t}{R} \quad for\ t < t_{peak}$$
$$t_R = \frac{t - t_{peak}}{1-R} \quad for\ t \geq t_{peak} \tag{14}$$

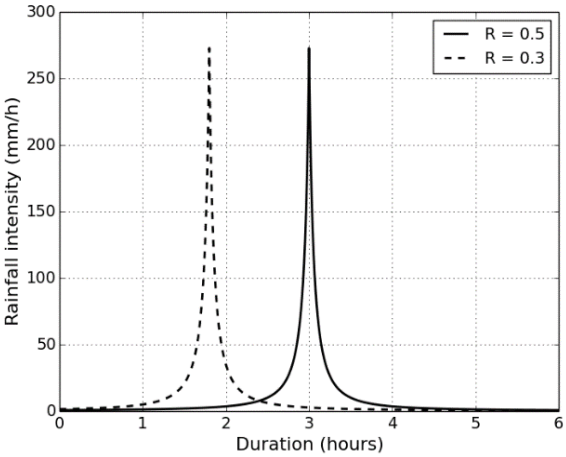

Figure 5. Example of CDS-type hyetographs (a = 60.0 – b = 0.97 – c = 0.22) expressed in rainfall intensity (mm/h).

With t the current time step (hours), t_{peak} the time of the rainfall peak (hours) and R the peak decentring parameter (dimensionless, varies between 0 and 1). The time of peak is defined as:

$$t_{peak} = R \cdot t_{rainfall} \quad (15)$$

With $t_{rainfall}$ the duration of the rainfall event provided by the new keyword DURATION OF RAIN OR EVAPORATION IN HOURS.

Examples of CDS-type hyetographs are given in Fig. 5 for a rainfall duration of six hours and with two different decentring parameters (R = 0.5, symmetrical hyetograph and R = 0.3).

Block-type or CDS-type hyetograph can be chosen manually directly in `runoff_scs_cn.f` (local variable `RAINDEF`).

Evaporation is not supported by the Curve Number runoff model.

C. Validation case

A new validation case called "pluie" has been added to the TELEMAC-2D library and will be available from version v7p2 (…/examples/telemac2d/pluie). Three examples are provided with (i) a classic rainfall defined by a constant rainfall intensity without runoff model, (ii) a classic rainfall defined by a constant rainfall intensity with Curve Number runoff model using CN(II) values interpolated from a set of points provided in a formatted data file and (iii) a rainfall defined by a hyetograph read from a formatted data file with Curve Number runoff model using CN(II) values stocked in the geometry file as an additional variable.

The classic rainfall is defined using the existing keyword RAIN OR EVAPORATION IN MM PER DAY = 100.0 and for a duration of 6 hours (DURATION OF RAIN OR EVAPORATION IN HOURS = 6.0) so that the total rainfall depth is 25 mm. The hyetograph defined in the last example has an irregular time distribution but has the same total rainfall depth.

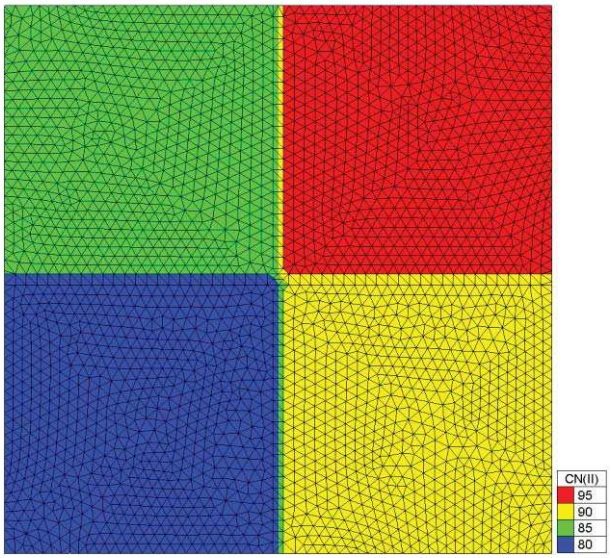

Figure 6. Computational domain used for the validation case with spatial repartition of CN(II) values.

The Curve Number runoff model is used with default settings (ANTECEDENT MOISTURE CONDITIONS = 2 and OPTION FOR INITIAL ABSTRACTION RATIO = 1).

The model geometry is a square with a side length of 100 meters composed of 5412 triangular elements with no open boundaries and with a constant bathymetry. The computational domain is divided in four parts with CN(II) values of 80, 85, 90 and 95, see Fig. 6. All the examples are run over a simulation period of 8 hours with a time-step of 200 seconds.

Results from the first example show, as expected, a constant water depth of 0.025 m at the end of the simulation corresponding to the total rainfall depth applied (no infiltration).

Results from the second and third examples show similar runoff depths at the end of the simulation for each CN(II) value. This result is expected since the rainfall depth is only function of the CN(II) values and of the total rainfall depth. The runoff depths are saved as an additional user variable in the result files named "ACC. RUNOFF". The final runoff depths obtained from the simulations for each CN(II) value are presented in Table I.

TABLE I. TOTAL RAINFALL AND RUNOFF DEPTHS FOR THE VALIDATION CASE.

Rainfall (mm)	**Runoff (mm)**			
	CN(II) = 80	***CN(II) = 85***	***CN(II) = 90***	***CN(II) = 95***
25.0	2.0	4.2	7.9	14.0

Their values are identical to the analytical solutions of (4) with a precision of 10^{-9} m. The CPU times of the provided examples are a few seconds in scalar mode on a laptop machine.

D. Additional computational cost

The additional computational cost of the new Curve Number runoff model has been estimated by comparing CPU times of the following simulations:

- Classic rainfall defined by a constant rainfall intensity without runoff model.
- Classic rainfall defined by a constant rainfall intensity with Curve Number runoff model used with CN(II) = 100 over the whole computation domain. The CN values are assigned using the default method, for instance a spatial interpolation from a set of points provided in a formatted data file.
- Similar case as above but with CN(II) values stocked and read from the geometry file.

Using CN(II) = 100 (i.e. no infiltration) ensures that the rainfall depth added in the domain at each time step is identical for all the simulations which makes it possible to assess the computational cost added by the new model only independently of the hydrodynamics conditions.

The model geometry used is a square with a side length of 1000 meters composed of 581 130 triangular elements with no open boundaries and with a constant bathymetry. The simulations have been performed using the same settings than those defined in the validation examples except for the time step which has been chosen to 20 seconds. The machine used was a DELL laptop (Windows 7 64-bit) with a processor of 2.5 GHz and 16 GB of RAM. The Fortran compiler used was gfortran version 4.7.0. Simulations have been performed in scalar mode. Results are presented in Table II.

TABLE II. ESTIMATION OF THE ADDITIONAL COMPUTATIONAL COST.

Simulation	**CPU time**	**Cost**
No runoff model	1407 s	-
CN runoff model with spatial interpolation of CN(II) values	1515 s	7.7%
CN runoff model with CN(II) values stocked in geometry file	1417 s	0.7%

Results show that the CPU time of the reference case (no runoff model) is increased by 7.7% when using the default method for assigning the CN(II) values at each node (spatial interpolation) whereas the additional computational cost can be considered as negligible when CN(II) values are stocked and read from the geometry file (0.7%). The cost generated by the spatial interpolation step is function of the model size and simulation duration.

IV. EXAMPLE OF APPLICATION

The Curve Number runoff model has been used to model runoff conditions in a watershed located on the eastern coast of the Lake Vättern in Sweden, approximatively 8 km in the North-East of the city of Jönköping. Lake Vättern's eastern coast is characterized by 200 to 300 m high hills with locally steep slopes along the shoreline. The hills are mainly covered by forest and by agricultural land. Soils are composed mainly of sandy to silty moraine. Bedrock outcrops are present in the steeper slopes. The drainage system is composed of ditches. In the southern part of the watershed, where the steeper slopes are located, the ditches transform into ravines characterized by bed slopes up to 30-35 degrees. The time of concentration of these ravines is approximatively 30 minutes. The aim of the study was to assess the runoff potential in the watershed as part of a debris-flow risk assessment and to define flooding maps.

A TELEMAC-2D model covering the 5 km^2 watershed has been set up with element sizes varying between 1 and 2 m and totalling approximatively 2 800 000 elements. Model boundary on land corresponds with the watershed's bound. The model has one open boundary, Lake Vättern, defined with a constant water level (mean water level). Eight pipes or culverts located under the existing roads have been included in the model.

One of the main difficulties of two-dimensional rainfall modelling is the definition of bottom friction as runoff is typically characterized by small water depths (so-called "sheet flow"), usually much smaller than the mesh size. An interesting approach would be to use a friction coefficient defined as a function of bottom asperities' submergence ratio [8, 9]. However, in this application, friction was modelled using the classic Strickler equation and with assumed coefficients of 5 $m^{1/3}/s$ for natural terrain [10] and of 50 $m^{1/3}/s$ for hard surfaces. For such applications it can be considered that the Strickler coefficients for natural terrains are independent of the land use and therefore of the CN values.

Rainfall was defined as Chicago Design Storm (CDS) hyetographs with a duration of 6 hours for return periods between 10 and 500 years. A frequency analysis has been performed on data from four meteorological stations located

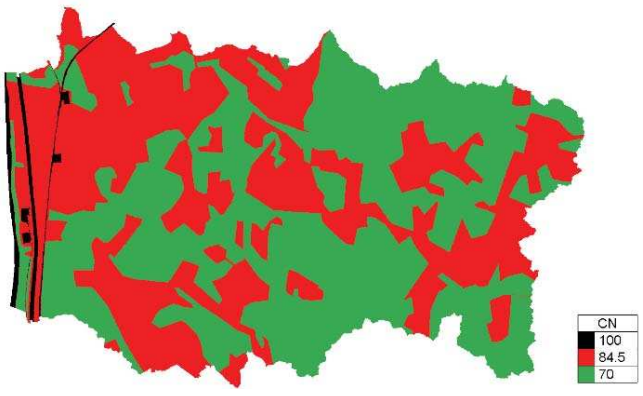

Figure 7. Repartition of CN(II) values over the computational domain.

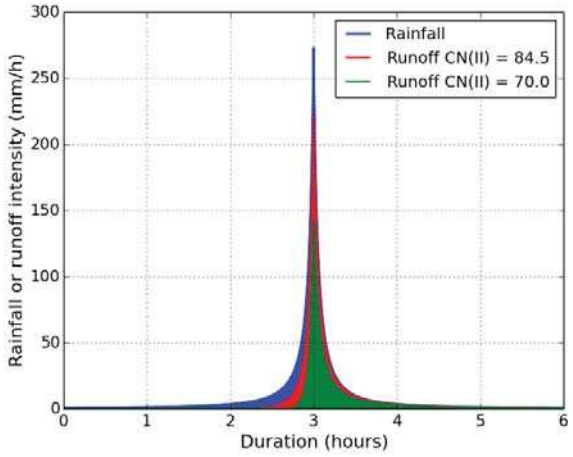

Figure 8. Rainfall hyetograph and corresponding runoff hyetographs for CN(II) = 70 and 84.5 and AMC III expressed in intensity (mm/h). The rainfall hyetograph has been defined using similar IDF parameters than on Fig.5.

around the watershed in order to define Intensity-Duration-Frequency (IDF) curves. Finally, these curves have been approximated with three-parameter IDF equations (11) by least-square fitting. Rainfall was defined as symmetrical hyetographs (peak decentring parameter $R = 0.5$).

CN values have been defined for three land use types: (i) forest, (ii) agricultural land and (iii) roads and other types of hard surfaces or lakes. The CN(II) values were defined for the hydrological soil groups C and D and the antecedent moisture conditions were considered to be wet (AMC III, highest runoff potential). The model was used with the standard initial abstraction ratio formulation ($\lambda = 0.2$). The CN(II) values have also been corrected to account for steep slopes.

The CN(II) values were eventually calibrated against estimations of specific discharges for 100-year return period flow available in the same area (no hydraulic calibration data was available). The simulations have been performed with CN(II) values of (i) 70 for forest, (ii) 84.5 for agricultural land and (iii) 100 for roads and other types of hard surfaces or lakes, see Fig. 7.

An example of calculated 100-year return period runoff hyetographs for CN(II) = 70 and 84.5 and for AMC III is presented on Fig. 8. The corresponding rainfall and runoff depths, computed with (4) to (8), are presented in Table III.

TABLE III. TOTAL RAINFALL AND RUNOFF DEPTHS FOR THE HYETOGRAPHS OF FIG. 8.

Rainfall (mm)	**Runoff (mm)**	
	CN(II) = 70	***CN(II) = 84.5***
61.0	26.8	42.0

V. SUMMARY AND CONCLUSIONS

A runoff model has been implemented in TELEMAC-2D in order to take spatially varying infiltration processes into account during storm rainfall modelling. The model is the Curve Number runoff model, also known as the SCS Method of Abstractions, which has been developed from 1954 by USA's Soil Conservation Service (SCS) and is widely used worldwide. The main advantage of this model relies in its simplicity since infiltration is defined by only one parameter function of four major runoff properties (hydrological soil groups, land use, hydrologic surface condition of native pasture and antecedent moisture conditions). The model has been implemented along with two options regarding the definition of the initial abstraction ratio and a correction to account for steep slopes. Rainfall can be defined in three different ways (with a constant rainfall intensity, with a user defined hyetograph or with a so-called Chicago Design Storm hyetograph based on a three-parameter Intensity-Duration-Frequency equation). The Curve Number runoff model will be available in the version v7p2 of the TELEMAC-MASCARET suite along with a validation case.

ACKNOWLEDGEMENTS

This development was funded by the Hydropower and Dams Department at Sweco Energuide AB through its "Innovation project" program. The author would also like to thank Riadh ATA at EDF R&D for his support in integrating the Curve Number runoff model to the TELEMAC-MASCARET suite.

REFERENCES

[1] U.S. Department of Agriculture, Soil Conservation Service, National Engineering Handbook, Section 4, Hydrology, Chapter 10 Estimation of direct runoff from storm rainfall, NEH Notice 4-102, August 1972.

[2] V. T. Chow, D. R. Maidment, L. W. Mays, Applied Hydrology, McGraph-Hill International Editions, 1988.

[3] U.S. Department of Agriculture, National Resources Conservation Service, National Engineering Handbook, Part 630 Hydrology, Chapter 9 Hydrologic soil-cover complexes, July 2004.

[4] U.S. Department of Agriculture, National Resources Conservation Service, National Engineering Handbook, Part 630 Hydrology, Chapter 10 Estimation of direct runoff from storm rainfall, July 2004.

[5] D. E. Woodward, R. H. Hawkins, R. Jiang, A. T. Hjelmfelt, Jr., J. A. Van Mullem, Q. D. Quan, "Runoff Curve Number method: Examination of the initial abstraction ratio", World Water & Environmental Resources Congress, 2003.

[6] M. Huang, J. Gallichand, Z. Wang, M. Goulet, "A modification of the Soil Conservation Service curve number method for steep slopes in the Loess Plateau of China", Hydrological Processes. Vol. 20, pp. 579-589, 2006.

[7] F. Taccone, G. Antoine, "Numerical modeling of sediment transfers at the catchment scale with TELEMAC", Proceedings of the 22nd Telemac & Mascaret User Club, Warrington, UK, 13-15 October 2015.

[8] D. S. L. Lawrence, "Macroscale surface roughness and frictional resistance in overland flow", Earth Surface Processes and Landforms, Vol. 22, pp. 365-382, 1997.

[9] R. García Díaz, "Analysis of Manning coefficient for small-depth flows on vegetated beds", Hydrological Processes, Vol. 19, pp. 3221-3233, 2005.

Culverts modelling in TELEMAC-2D and TELEMAC-3D

Sven Smolders[1], Agnès Leroy[2], Maria João Teles[3], Tatiana Maximova[1], Joris Vanlede[1]

[1] Flanders Hydraulics Research, Flemisch Government, Antwerp, Belgium. (svensmolders@gmail.com)
[2] LNHE, EDF R&D, Chatou, France. (agnes.leroy@edf.fr)
[3] Egis Ports, Saint-Quentin-en-Yvelines Cedex, France.

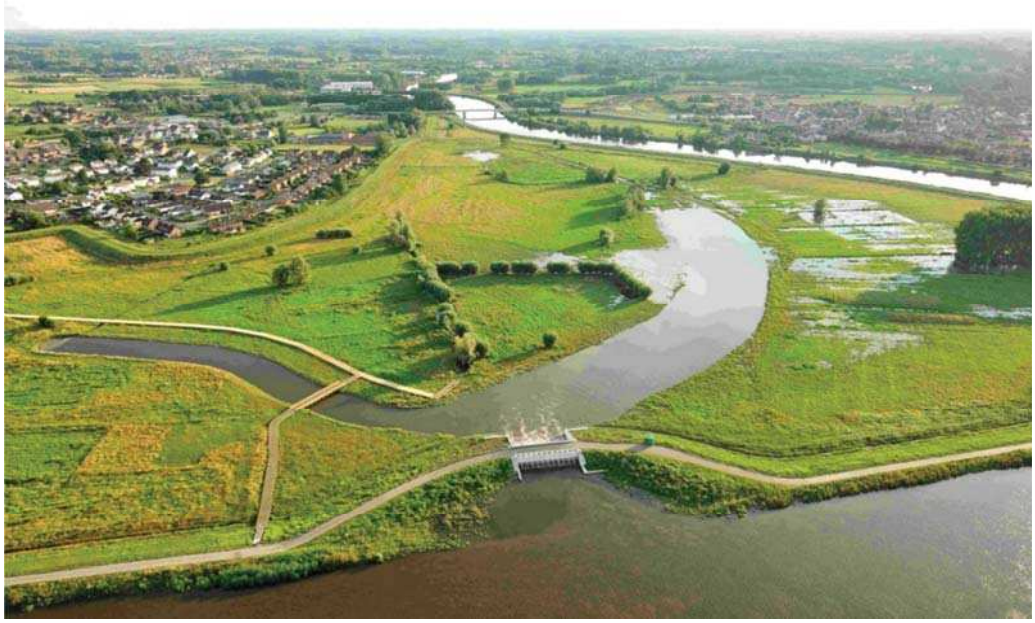

Figure 1 - Bergenmeersen: Flood control area (FCA) with controlled reduced tide (CRT) along the Scheldt estuary, Belgium (picture: www.sigmaplan.be)

***Abstract* – The numerical simulation of flows between (tidal) rivers and floodplains often requires the representation of hydraulic structures such as culverts. The aim of this work is to enable TELEMAC-3D to represent such structures. A model for culverts had already been implemented in TELEMAC-2D, and a new one was added through this work, with discharge configurations. A file describing the culverts positions and characteristics must be provided by the user in TELEMAC-3D in the same way as in TELEMAC-2D. Each culvert is constituted of two source (/sink) points at which the discharge rates have opposite signs. The culvert paires are thus treated exactly like source / sink points in TELEMAC-3D, and the discharge rates are computed by the same subroutine as in TELEMAC-2D. The model was validated on two test-cases with TELEMAC-3D. One of those test-cases is the flood control area, Bergenmeersen (picture here above), situated along the Scheldt estuary. The culverts were calibrated for a data set measured in 2014. The code was validated on water level measurements of this area during the storm of December 6th, 2013. The modelled water levels fitted very well the measured ones.**

I. INTRODUCTION

The Scheldt estuary and its tributaries in Flanders, Belgium, are influenced by the tides of the North Sea until far upstream. In case of extreme weather conditions like storm tides and heavy rainfall, this could lead to extreme water levels and even floods.

In 1976 large parts of the region of the Scheldt estuary in Flanders were flooded after a storm tide. To protect the region from such disaster in the future, the Flemish government presented the Sigma-plan (S for Scheldt) in 1977. Originally this plan aimed at strengthening and elevate the dikes, building flood control areas (FCA) and building a storm surge barrier on the Scheldt near Antwerp. The storm surge barrier was never built, but the flood control areas were. In 2005 the Sigma-plan was updated with the newest scientific developments and to account for climate change and integrated water management. Furthermore, the Sigma-plan wanted to contribute to important European nature goals for the Flanders region.

To create more tidal habitat in the Scheldt estuary, some of the flood control areas were adapted so that the tide could enter and leave these areas in a reduced way (the tide has to be reduced because most of the land surrounding the Scheldt estuary in Flanders has a low elevation)[1]. New structures were built to allow water to flow in and out of these areas every tide.

When in 2013 a new large scale TELEMAC-3D model of the entire Scheldt estuary was made (*i.e.* the Scaldis model [2]), there was a need to model also the water exchange between the river and these flood control areas. At that time there was no subroutine in TELEMAC-3D to model this kind of flow interactions. The Fortran code that was developed for this model in 2014 and presented that year at the TELEMAC-MASCARET User Club conference [3] is now implemented in the main code of TELEMAC so that it is available for all users.

This paper will give a description of how the code was developed and how it was implemented in TELEMAC. It further provides an elaborate description of the parameters of this code by applying it to a test-case called Bergenmeersen (also available amongst the TELEMAC validation test cases).

II. FLOW THROUGH CULVERTS

A number of studies regarding the description of flows through culverts refer to the work of *Bodhaine* [4]. Bodhaine categorized the flow through a culvert into six types, and for each type the discharge is calculated in a different way. The equations are deduced from the continuity and energy equations between the approach section (Figure 2) and the exit (downstream) section of the culvert. The type of flow depends on whether the culvert flows full and whether the flow is controlled by the entrance or exit part of the culvert. Figure 2 shows a sketch for the culvert flow definition.

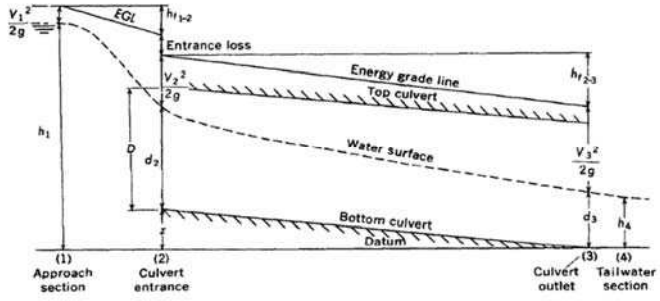

Figure 2 - Sketch of the general flow through a culvert [4].

Let z be the elevation of the culvert entrance relative to the datum through the culvert exit. The gravitational constant is given by g and h_{f12} is the head loss due to friction from the approach section to the culvert entrance; h_{f23} is the head loss due to friction inside the culvert, d_2 and d_3 are the water depths at the culvert entrance and exit, respectively; V_1, V_2 and V_3 are the velocities at the approach section, culvert entrance and culvert exit, respectively; D is the culvert height; and h_1 and h_4 are the water depths upstream and downstream of the culvert structure.

The six types of flows classified by Bodhaine [4] depend on the water depths upstream and downstream of the culvert. These types are discussed below:

Flow Type 1 – Critical depth at inlet – supercritical flow inside the culvert

In Flow Type 1 the critical depth occurs at the entrance of the culvert and the flow is supercritical inside the culvert. The culvert slope (S_0) has to be greater than the critical slope (S_c) and the culvert flows partially full. For the Froude number $Fr=1$ (which is the case at the entrance section for a Flow Type 1), the discharge coefficient is typically C_D=0.95. The discharge is calculated according to the following formula:

$$Q = C_D A_c \sqrt{2g\left(h_1 - z - h_c - h_{f12} + \alpha \frac{V_1^2}{2g}\right)} \qquad (1)$$

with:
- C_D the discharge coefficient
- A_c flow area at critical water depth
- g the gravitational constant
- h_1 upstream water depth
- z elevation of the culvert entrance
- h_c critical water depth
- h_{f12} head loss due to friction from the approach section to the culvert entrance
- α kinetic energy correction coefficient for the approach section
- V_1 average flow velocity at the approach section of the culvert

Flow Type 2 – Critical depth at outlet – subcritical flow inside the culvert

In Flow Type 2 the flow is tranquil (i.e. subcritical) inside the culvert. The critical depth is located at the culvert outlet. The culvert flows partially full. Here the culvert slope S_0 has to be smaller than the critical slope S_c. The discharge coefficient is similar to Flow Type 1. The discharge is calculated according to the following formula:

$$Q = C_D A_c \sqrt{2g * \left(h_1 - h_c - h_{f12} - h_{f23} + \alpha \frac{V_1^2}{2g}\right)} \qquad (2)$$

with: h_{f23} head loss due to friction inside the culvert.

Flow Type 3 – Tranquil flow – subcritical flow throughout the culvert

In Flow Type 3 the flow is subcritical throughout the culvert. There is no critical depth. The culvert flows partially full. Like Flow Types 1 and 2, the discharge coefficient varies in function of the Froude number, being typically between C_D=0.82 – 0.95. The discharge is calculated according to the following formula:

$$Q = C_D A_3 \sqrt{2g\left(h_1 - d_3 - h_{f12} - h_{f23} + \alpha \frac{V_1'^2}{2g}\right)} \quad (3)$$

with: A_3 flow area at the culvert outlet
d_3 water depth at the culvert outlet

Flow Type 4 – Submerged inlet and outlet

In Flow Type 4 the culvert inlet and outlet are submerged. The culvert flows full. The discharge coefficient varies in function of the culvert geometry, ranging typically between C_D=0.75 and C_D=0.95. The discharge is calculated according to the following formula:

$$Q = C_D A_0 \sqrt{\frac{2g(h_1 - h_4)}{1 + 29 C_D{}^2 n^2 L / R^{4/3}}} \quad (4)$$

with: A_0 flow area at the culvert entrance
h_4 downstream water depth
n Manning coefficient
L length of the culvert
R hydraulic radius

The user must be aware that, in [4], imperial units are used. In equation 4 here above the factor 29 is an artefact of the imperial units.

Flow Type 5 – Rapid flow at inlet

In Flow Type 5, the flow is supercritical at the inlet to the culvert. The culvert flows partially full. Flow Type 5 are rare. When it occurs, the discharge coefficient is in general lower than the other types.

$$Q = C_D A_0 \sqrt{2g(h_1 - z)} \quad (5)$$

Flow Type 6 – Full flow with free outfall

In Flow Type 6 the culvert flows full. The discharge coefficient is similar to the one obtained for the Flow Type 4. The discharge is calculated according to the following formula:

$$Q = C_D A_0 \sqrt{2g\left(h_1 - d_3 - h_{f23}\right)} \quad (6)$$

The indices might seem a bit confusing, but it was chosen to take the formulas from Bodhaine [4] as they are. Bodhaine differentiated between the following six flow type based on conditions given in Table 1.

Table 1. Flow types as defined by Bodhaine (1968).

Flow Type 1	$\frac{h_1 - z}{D} < 1.5$	$\frac{h_4}{h_c} < 1.0$	$S_0 > S_c$
Flow Type 2	$\frac{h_1 - z}{D} < 1.5$	$\frac{h_4}{h_c} < 1.0$	$S_0 < S_c$
Flow Type 3	$\frac{h_1 - z}{D} < 1.5$	$\frac{h_4}{D} \leq 1.0$	
Flow Type 4	$\frac{h_1 - z}{D} > 1.0$	$\frac{h_4}{D} > 1.0$	
Flow Type 5	$\frac{h_1 - z}{D} \geq 1.5$	$\frac{h_4}{D} \leq 1.0$	
Flow Type 6	$\frac{h_1 - z}{D} \geq 1.5$	$\frac{h_4}{D} \leq 1.0$	

Different culvert geometry will affect the choice between Flow Type 5 or 6. To differentiate between both types, Bodhaine suggests to use the relations given in Figure 3, in which r denotes the radius of curvature of a rounded entrance and w is the measure of a chamfered entrance. First a curve corresponding to r/D, w/D is chosen. Then a point is set using the value for the culvert slope and for the ratio between the culvert length and height. If the point lies to the right of the chosen curve, the discharge is of Flow Type 6, if it lies to the left of the curve, the discharge is of Flow Type 5.

The head loss coefficients are topics of different studies made through laboratory experiments. A number of authors have arrived to different values or empirical relationships for the head loss coefficients. [4] suggests different values for the discharge coefficient (C_D) for each Flow Type and depending on a number of culvert geometric features. The discharge coefficients can vary from 0.39 to 0.98. Another example is given by [5] who proposes a non-dimensional coefficient μ, also referred to as a discharge coefficient that, for hydraulic structures made of only one culvert, can be written as follows:

$$\mu = \frac{1}{\sqrt{C_1 + C_2 + C_3}} \quad (7)$$

with: C_1 head loss coefficient at the entrance of the hydraulic structure
C_2 head loss coefficient in the hydraulic structure
C_3 head loss coefficient at the exit of the hydraulic structure

If the general expression for the discharge $Q = \mu A \sqrt{2g\Delta H}$ proposed by [5] is compared with the formulae

given by [4], it can be seen that the non-dimensional discharge coefficient (μ), incorporates both the effect of the discharge coefficient (C_D) and the continuous and local head losses. ΔH is the head for each type of flow.

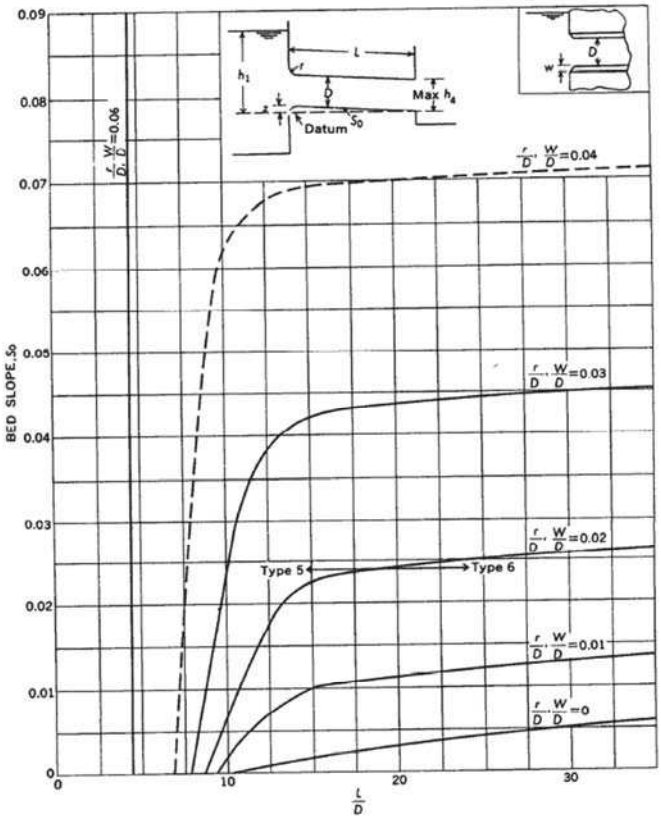

Figure 3 - Criterion for classifying flow types 5 and 6 in concrete box or pipe culverts with square, rounded, or beveled entrances, either with or without wing walls [4]

III. TRANSLATION INTO CODE

Following the proposition of [5] the equations proposed by [4] are translated into equations that could be implemented in the TELEMAC Fortran code. Flow Type 1 was not implemented because it only occurs when the culvert slope is larger than the critical flow slope, which only happens in very rare occasions.

Flow Type 2 – Critical depth at outlet:

$$Q = \mu h_c W \sqrt{2g * \left(S_1 - (z_2 + h_c)\right)} \quad (8)$$

Flow Type 3 – Tranquil flow:

$$Q = \mu (S_2 - z_2) W \sqrt{2g(S_1 - S_2)} \quad (9)$$

Flow Type 4 – Submerged outlet:

$$Q = \mu D W \sqrt{2g(S_1 - S_2)} \quad (10)$$

Flow Type 5 – Rapid flow at inlet:

$$Q = \mu D W \sqrt{2g h_1} \quad (11)$$

Flow Type 6 – Full flow with free outfall:

$$Q = \mu D W \sqrt{2g * \left(S_1 - (z_2 + D)\right)} \quad (12)$$

with:
- Q discharge through the culvert,
- W culvert width,
- D culvert height,
- μ total head loss coefficient,
- S_1 water level on side 1,
- S_2 water level on the side 2,
- h_1 water level above the culvert base on side 1,
- h_2 water level above the culvert base on side 2,
- h_c critical water level inside the culvert (this will be assumed to be close to 2/3 of h_1),
- z_1 base level of the culvert at side 1, and
- z_2 base level of the culvert at side 2.

Most of these variables are shown in a schematic representation of the culvert in [6].

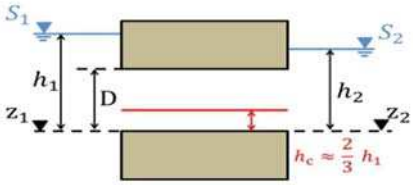

Figure 4 - Schematic representation of a culvert with the different parameters [6]

The conditions for which each type of flow occurs are summarized in Table 2. To distinguish Flow Type 5 from Flow Type 6 a constant C56 is defined that is dependent on the culvert slope and the ratio W/D. Using Figure 3, the curve (W/D) is chosen and the point for which the value of the slope (S_0) encounters the curve will have as abscissa the value C56. Then if L/D < C56, flow type 5 occurs, otherwise Flow Type 6 is used [4].

Table 2 - Conditions for each type of flow used in TELEMAC

	$\frac{S_1 - z_1}{D}$	$\frac{S_2 - z_2}{D}$	$S_2 - z_2$	**L/D**
Flow Type 2	<1.5		h_c	
Flow Type 3	<1.5	≤ 1.0	h_c	
Flow Type 4	>1.0	1.0		
Flow Type 5	≥ 1.5	≤ 1.0		C56
Flow Type 6	≥ 1.5	≤ 1.0		≥C56

To use the culverts in our model, additional features had to be incorporated in the code:

- Wooden beams can be placed in front of the culverts to control the timing when water can start flowing in the flood control areas with controlled reduced tide.
- Most culvert structures have trash screens in front and behind them to prevent garbage and drift wood from clogging the hydraulic structure.
- On the outlet culverts there are one-way valves present to prevent the water from entering the FCA's through these culverts.

Most of these structures are incorporated in the code as an extra head loss coefficient, except the wooden beams that act as a small weir. To incorporate these into the code, the geometric features of the culvert presented in Figure 4 are modified and presented in Figure 5. An equivalent culvert bottom elevation was used replacing both the bottom elevations z_1 and z_2 in the formulae described above. The mean between z_1 and z_2 is taken as equivalent bottom elevation of the culvert. The diameter of the culvert used in the equations will be the one corresponding to the entrance of the culvert, *i.e.* like in Figure 5. If the flow goes from left to the right D will be replaced by D_1 and on the opposite direction, the value of D_2 will be used. For the start of the water flow into the FCA the z_1 and z_2 bottom elevations are still used so that the start and end of water flow through the culverts remain as close as possible to reality.

By using this equivalent bottom elevation, the culverts' frictional head losses are overestimated and the local larger head losses due to the presence of the weir are not exactly taken into account. These complicated structures are difficult to model exactly and this assumption keeps things simple. There are many head loss coefficients in the equations and together with the parameters that describe the dimensions of the culverts, the user can tune the modeled discharges.

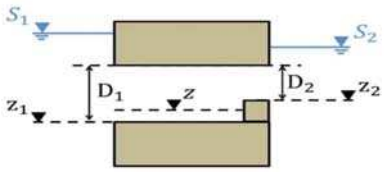

Figure 5 - Representation of the different variables used to calculate the discharges for each type of flow[6]

The head loss coefficient (μ) was adapted from the one computed in TELEMAC-2D, based on [5] and is used as main head loss coefficient. Features of the structure that caused additional head loss, such as one-way valves, trash screens or pillars are added in the computation of (μ), which contributes to the flexibility of the implementation of many types of culvert structures.

The head loss due to singularities can be obtained by the general relation from [7,5]:

$$\Delta H = C\frac{U^2}{2g} \text{or} U = \mu\sqrt{2g\Delta H} \quad (13)$$

with: $\mu = \frac{1}{\sqrt{C}}$ (14)

The coefficient C represents the sum of the different contributions for the head loss due to singularities:

$$C = C_1 + C_p + C_2 + C_3 + C_V + C_{Trash} \quad (15)$$

The different contributions to this head loss coefficient C will be discussed separately and in detail below.

C_1 – the entrance head loss

C_1 represents the head loss due to the contraction of the flow at the entrance of the hydraulic structure. Usually, there is an abrupt contraction at the culvert entrance that will cause a head loss due to the deceleration of the flow immediately after the vena contracta.

Figure 6 is extracted from [8] and for a culvert between a river and a floodplain the contraction can be seen as very large, so the parameter on the x axis in Figure 6 will be close to zero and are head loss coefficient will be 0.5.

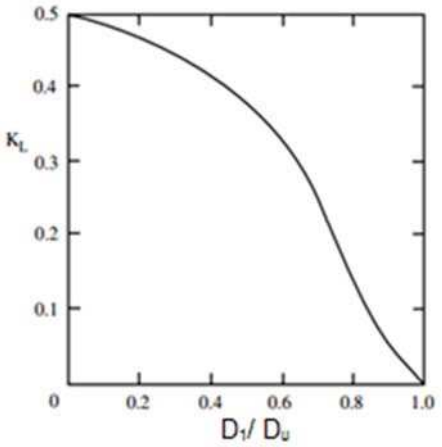

Figure 6 - Local loss coefficient for a sudden contraction as a function of diameter ratio between the diameter after the contraction (D_1) and before the contraction D_u [8].

Bodhaine [4] noticed that the discharge coefficient (C_D) for Flow Type 5 had to be lowered comparatively with the other Flow Types. The calculated discharge seemed to be overestimated when the default equation is used. Therefore

a correction coefficient is taken into account. The correction coefficient, C5 is applied to C_1 when Flow Type 5 occurs, such that:

$$\Delta H_1 = C5 * C_1 \frac{U^2}{2g} \quad (16)$$

Bodhaine proposes an interval for the value of this correction coefficient: $4 \leq C5 \leq 10$.

C_p – the head loss due to pillars in the culvert

Sometimes at the entrance of culverts the flow is divided into two sections by a pillar. This pillar causes additional head loss and is taken into account. According to [5] the head loss caused by parallel pillars is given by:

$$\Delta H_p = C_p \frac{U^2}{2g} \quad (17)$$

and $C_p = \beta \left(\frac{L_p}{b}\right)^{4/3} sin\theta \quad (18)$

with C_p represents the head loss coefficient due to the presence of pillars
L_p thickness of the pillars,
b the distance between two consecutive pillars
β is a coefficient dependent on cross-sectional area of the pillar.

According to [5] β will be 2.42 for rectangular pillars and 1.67 for rounded pillars. θ stands for the angle of the pillar with the horizontal plane. In most cases this will be 90° and $sin\theta$ will be equal to 1. The code does not use this head loss coefficient on its own: its value was added to the C_1 head loss coefficient.

C_2 – the head loss due to internal friction

C_2 represents the head loss coefficient due to the friction in the structure and is expressed by [7]:

$$\Delta H_2 = C_2 \frac{U^2}{2g} = \frac{2gLn^2}{R^{4/3}} \frac{U^2}{2g} \quad (19)$$

with L length of the structure,
n the Manning Strickler coefficient of the structure (material) and
R the wet cross-sectional area in the structure.

In the code, an assumption was made to calculate the hydraulic radius for each type of flow, since the code does not make any kind of backwater analysis to get the precise water depths that occur in the culvert.

C_3 – the exit head loss

C_3 is the head loss coefficient due to expansion of the flow exiting the culvert. It is given by [7]:

$$\Delta H_3 = \left(1 - \frac{A_s}{A_{s2}}\right)^2 \frac{U^2}{2g} = C_3 \frac{U^2}{2g} \quad (20)$$

with A_s, A_{s2} sections in and just outside at the downstream part of the structure.

Usually C_3 is equal to 1 for a sudden enlargement.

C_V – head loss due to one-way valve

C_V is the head loss coefficient due to the presence of a valve. The head loss due to valves (ΔH_v) is given by:

$$\Delta H_v = C_v \frac{U^2}{2g} \quad (21)$$

with C_V depends on the type of valve and the degree of opening.

For a flap gate valve (rotating around to hinges at its upper edge), some values were obtained experimentally, and they depend on the opening angle of the valve [8]:

Table 3 - Values for the head loss coefficient depending on the opening of a gate valve according to [7].

	Wide open	¾ open	½ open	¼ open
C_V	0.2	1.	5.6	17

Like with C_1 a correction coefficient ($C_{v,5}$) is applied to this head loss coefficient to take into account the increase of the head loss with Flow Type 5. Through a number of laboratory experiments with a physical scale model at Flanders Hydraulics Research [1], it was clear that when Flow Type 5 occurs, there is a greater influence of the head loss coefficient of the valve.

$$\Delta H_{v,5} = C_{v,5} C_v \frac{U^2}{2g} \quad (22)$$

C_{Trash} – head loss due to trash screen

Trash screens are usually present at the inlet of culverts to prevent garbage from entering or blocking the culvert. The head loss due to the presence of these screens (ΔH_t) can be estimated by its relationship with the velocity head through the net flow area. A number of expressions were obtained in the past by several authors. The expression given by [9] is used:

$$\Delta H_t = \left(1.45 - 0.45A_{trash} - {A_{trash}}^2\right)\frac{U^2}{2g} = C_{trash}\frac{U^2}{2g} \quad (23)$$

with U net flow velocity

$A_{trash} = \frac{A_{net}}{A_{gross}}$ provides the ratio of net flow area to gross rack area.

The value for C_{trash} can vary between C_{trash}= 0 (for A_{trash} = 1, equivalent to not having any trash screens) to approximately C_{trash}= 1.4 (for A_{trash} = 0, for which the net flow area is negligible small compared to the gross rack area).

IV. IMPLEMENTATION IN TELEMAC

The goal of the implementation of this code in TELEMAC was to use the same subroutine for culverts in TELEMAC-2D and TELEMAC-3D.

Culverts were already implemented in TELEMAC-2D in the subroutine BUSE (file buse.f). The existing code has four equations, three of which are similar to the equations presented here (Flow Types 3, 5 and 6). In order to ensure backward compatibility while keeping the implementation within the same subroutine, a new keyword, OPTION FOR CULVERTS (OPTBUSE), was created to let the user choose between both sets of equations. This keyword can be added to the steering file. If the user wants to use the existing code in TELEMAC-2D or 3D, the value is 1. If the user wants to use the equations presented here, the value is 2.

The existing capability of TELEMAC to set source and sink terms anywhere in the domain was useful to implement a culvert function. The inflow and outflow of a culvert then act as a pair of source / sink points. For instance, when the flow is going from the river to the floodplain side, a source term is added on the floodplain side (positive discharge), and at the same time a sink term is set in the river (opposite discharge). By doing this, the culverts are assumed short and the water that leaves the river enters the floodplain at the same time. The computed discharges in BUSE (file buse.f) are simply added at the end of the sources matrix as follows:

```
QSCE2(NPTSCE+I)                =-DBUS%R(I)
   QSCE2(NPTSCE+NBUSE+I)= DBUS%R(I)
```

with NPTSCE is the number of punctual sources and DBUS(I) is the discharge computed for culvert number I

In TELEMAC-3D the total number of source points, NSCE, is now the sum of the punctual sources (NPTSCE, that existed before these developments) and twice the number of culverts.

Equations 8 to 12 are implemented in the code based on the conditions given in Table 2. Figure 7 gives a flow chart of the part of the algorithm once the OPTION FOR CULVERTS (OPTBUSE) is switched on.

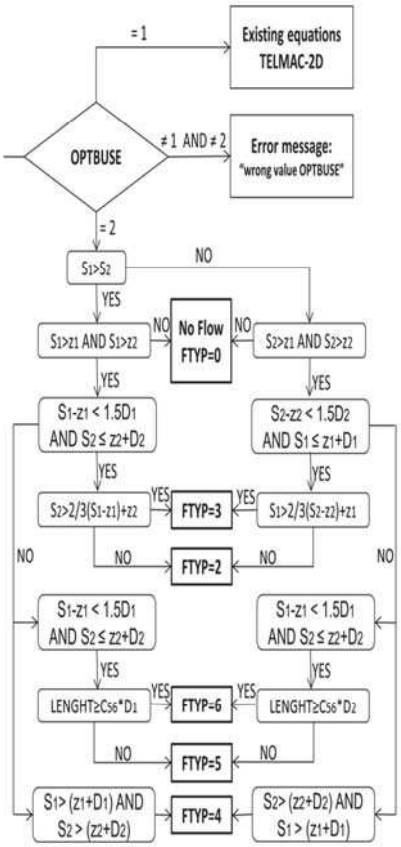

Figure 7 - Flow chart showing the conditions for every type of flow in the BUSE (file buse.f) subroutine.

The user has to specify all the parameters related to the culverts in a text file, through the keyword: CULVERTS DATA FILE. This text file will be read by the subroutine LECBUS (file lecbus.f). The text file and the existing subroutine LECBUS were extended to take extra parameters into account.

The first and third lines of the text file are comment lines and these are not read. On the second line the first variable is the relaxation parameter (RELAXB). This relaxation parameter will give a weight to the discharge calculated at the current time step. This is a value between 0 and 1. The result is a weighted averaged discharge based on the discharge of this and the previous time step. After the relaxation parameter there is a number indicating the number of culverts. The number of culverts needs to be given in the steering file through the keyword NUMBER OF CULVERTS (NBUSE) and this number will be checked with the number in the text file as an extra control parameter. The third line is commented and contains the names of all the parameters used in BUSE. They are separated by a tab. The flow through a culvert can go in both directions.

In the following the index 1 is used for the river side and the index 2 for the floodplain side of the culvert. The following parameters must be listed in the culverts data file:

I1 node number of culvert on side 1 (river)
I2 node number of the culvert on side 2 (floodplain)
CE1 entrance head loss coefficient for the culvert on side 1 (this corresponds to the head loss coefficient C_1)
CE2 entrance head loss coefficient for the culvert on side 2 (this corresponds to the head loss coefficient C_1)
CS1 exit head loss coefficient for the culvert on side 1 (this corresponds to the head loss coefficent C_3)
CS2 exit head loss coefficient for the culvert on side 2 (this corresponds to the head loss coefficent C_3)
LARG the width of the culvert
HAUT1 height of the culvert on side 1
CLP coefficient to restrict the flow direction (0 both directions are possible; 1 = only flow from side 1 to 2; 2 = only flow from side 2 to 1; 3 = no flow)
L linear head loss coefficient used only when OPTBUSE=1; If OPTBUSE=2, **L** is calculated
RD1 culvert bottom elevation on side 1(z_1)
RD2 culvert bottom elevation on side 2(z_2)
CV head loss coefficient when a valve is present
C56 factor to differentiate between flow types 5 and 6
CV5 correction factor for C_V when flow type 5 is used
C5 correction factor for CE_1 and CE_2 with Flow Type 5
TRASH head loss coefficient when trash screen are present
HAUT2 height of the culvert on side 2
FRIC Manning strickler coefficient used in equation 19
LONG length of the culvert (not necessarily based on the position of the source / sink nodes)
CIR parameter to determine if the culvert is rectangular (=1) or circular (=0); in case of a circular culvert the height is taken to calculate the wet section.

The computed discharge is positive for the flow from side 1 to side 2. When the discharge is computed by BUSE based on the above parameters, it undergoes three possible changes.

- First, the relaxation is computed. Based on the weight and the difference with the discharge in the previous time step, this can change the computed discharge of the current time step.
- Then, a test is performed to check if there is enough water present at the current time step to extract the anticipated discharge. A maximum of 90% of the available water is allowed to leave.
- Finally, the code checks that the culvert configuration allows the water to flow in the computed direction, and if not blocks the flow by setting the discharge to zero.

In the culvert data file, the user can choose the direction of the flow through a culvert by setting the parameter CLP (for example if there is a one-way valve in the culvert).

It is possible to use passive or active tracers when using culverts. The following equation describing the evolution of tracer concentration (T) is solved:

$$\frac{\partial T}{\partial t} + U\frac{\partial T}{\partial x} + V\frac{\partial T}{\partial y} + W\frac{\partial T}{\partial z} = v_t \Delta(T) + Q' \qquad (24)$$

The tracer diffusion coefficient is given by v_t and Q' represents the source terms for tracers. In order to take the transport of tracers into account when using culverts, the user only has to specify the keywords related to the tracers in the steering file.

The subroutines BUSE and LECBUS are both called from TELEMAC-2D and TELEMAC-3D in the same way.

V. TEST-CASE BERGENMEERSEN

Bergenmeersen is the name of a flood control area with controlled reduced tide. An aerial photograph is shown in. It is located far upstream in the Scheldt estuary. Figure 8 shows the location of Bergenmeersen in the Scheldt estuary, represented as a mesh of the Scaldis model [2,10].

Figure 9 shows Bergenmeersen in more detail. It shows the mesh of the small model that was used to test the culvert code presented in this paper. The mesh size is about 7 m. Bergenmeersen is also available as a TELEMAC-3D validation case, but with a coarser mesh.

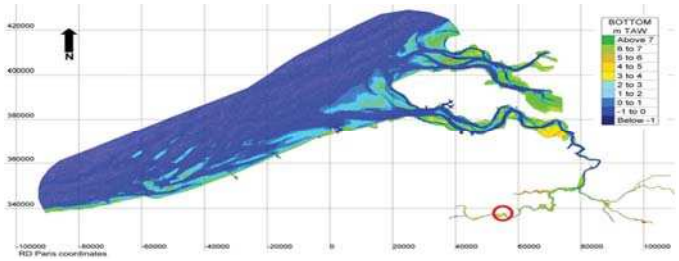

Figure 8 - red circle indicating the location of Bergenmeersen in the Scheldt estuary. The map shown represents the grid of the Scaldis model [2]

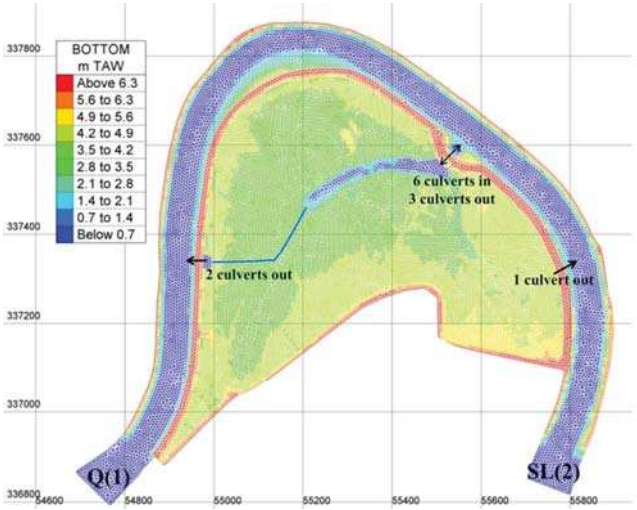

Figure 9 - Detailed view of the mesh and bathymetry of the small model of Bergenmeersen.

Bergenmeersen was first a flood control area only. In the summer of 2013 the inlet culverts became operational making it a flood control area with controlled reduced tide. Twice a day the tide can enter the area, creating new tidal nature. There are 6 inlet culverts, which are built above three outlet culverts.

Figure 10 shows an aerial view on this construction. On two other sides of the area are three old outlet culverts (locations given in Figure 9). The dike between the Scheldt river and the floodplain is an overflow dike. When high storm surges enter the estuary, at a critical level the water can flow over this dike. The level of this overflow dike at Bergenmeersen is 6.4 m TAW (i.e. 0 m TAW is about low water at sea) [11]. The other dikes are 8.0 m TAW. The floodplain is then buffering the excess surge water and prevents floods upstream and downstream from this area.

Every year around September, a 13-hour measurement campaign is executed (13 hours to capture one tidal cycle), measuring the inlet and outlet discharges. Water levels are constantly measured using a diver on the floodplain side and another one at the Scheldt side of the large inlet-outlet structure. Moreover on December 6th 2013 there was a storm surge entering the estuary and water levels inside and outside Bergenmeersen were measured with these divers and a helicopter picture shows that the flood plain was almost completely filled (Figure 10). All these data are available to calibrate the parameters used for the culverts.

Figure 10 - Bergenmeersen at December 6th 2013 filled with water from the storm surge

Figure 11 shows an image of the cross section seen from the side of the Bergenmeersen inlet and outlet structure. In this view the Scheldt river is on the left and the floodplain is on the right. The inlet culverts are built on top of the outlet culverts. The outlet culverts have a one-way valve (nr 1 in Figure 11) to prevent water from entering the floodplain too soon. There are trash screens (nr 2 in Figure 11) on both sides of the construction. They keep large debris and driftwood from clogging the culverts. Just in front of the inlet culvert there is a possibility to place wooden beams (nr 3 in Figure 11) that act as a weir. These are used to fine tune the amount of water entering daily in the flood plain. The height of the weir determines the moment at which water can start flowing in. Inside the inlet culvert there is also a sliding valve (nr 4 in Figure 11) that can close the inlet culvert. These valves were meant to close the inlet culverts in case of a storm surge to keep the full buffer capacity of the floodplain, but they are currently also used to control the amount of water entering the area. Their positions are known for the 13 hour measurement of September 11, 2014. This data set is used to calibrate the culvert parameters.

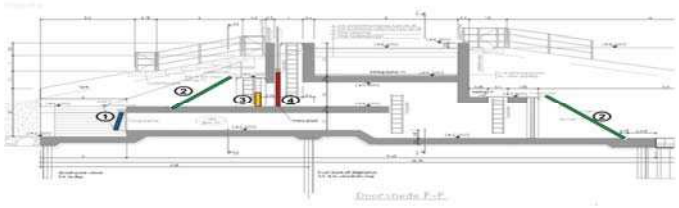

Figure 11 - side section showing the internal construction of the inlet and outlet structure at Bergenmeersen. Number 1 is the one-way valve of the outlet culvert; 2 are the trash screens at both sides of the structure; 3 is the log weir; 4 is a sliding valve that can close the inlet culvert.

Table 4 provides an overview of the parameter values that were used. There are three sets of parameters values given: the first is a start set where a first guess is made for all parameters while remaining as close as possible to the

physical values. The second set is the parameter set following calibration against the 13 hour measurement on Bergenmeersen on September 11, 2014. Comparing the first two data sets provides an overview of the changes made to get a better result. Finally set 3 gives the parameters that were used for the simulation of the December 6, 2013 storm surge.

For each set of parameters some variables are not shown in Table 4 because they were not changed or were not dependent on the construction of the structure. Through physical experiments the value of $C_{v,5}$, the correction factor for the head loss due to the presence of a valve when flow type 5 occurs, was set to be 1.5. This value is set to 1.5 only for the outlet culverts who have the one-way valve. The inlet culverts don't have this valve so for them the value of $C_{v,5}$ is set to zero. C_5 was given a value of 6, *i.e.* a value in the interval proposed by [4]. According to Figure 3 the culverts have no bed slope and no wing walls (W=0), so a value of 10 is found for the C_{56} parameter. The parameter `L` is computed with `OPTION FOR CULVERTS`=2 (The user value of `L` will be ignored in this case). These parameters are not listed in Table 4.

For the start set of the culvert parameters the following values were chosen: for CE_1 and CE_2 the value of 0.5 was selected according to Figure 6. For the 6 inlet culverts for CE_1 the head loss coefficient due to the presence of a pillar was also added. According to equation 18 (with $\theta = 90°$, $\beta = 2.42$, L_p=0.4 and b=1.35, C_p=0.47 which is rounded to 0.5) 0.5 was chosen for CE_1 which gives us 1. There are 6 inlet culverts and 6 outlet culverts, but because the outlet culvert parameters are the same for all 6 culverts only one set of parameters is shown. There are also three old outlet culverts present. Their exact measurements are not known, but the parameters were taken the same for all three of them and are only shown for one. For a sudden enlargement C_S is taken equal to 1. The inlet culverts have a width of 3 m, but because of the presence of a pillar in each culvert, their width is taken equal to 2.7 m (LARG = 2.7 m). For the outlet culverts, LARG = 1.35 m. For the older outlet culverts LARG was taken equal to 1.5 m. The bottom level of the inlet culverts was 4.2 m TAW according to the as built plans. So RD1 and RD2 were set to 4.2, except three inlet culverts had wooden beams in front of them (their height was 0.25 m, 0.25 m and 0.1 m). So RD1 was raised for these three culverts to 4.45, 4.45 and 4.3 respectively. The bottom level of the outlet culverts was 2.7 m TAW and for the old outlet culverts RD1 and RD2 were taken equal to 2.5 m TAW. All inlet culverts had different valve positions. This was taken into account by modifying the height of the river side (side 1). The inlet culverts have a normal height of 1.6 m. HAUT1 and HAUT2 should be equal to this 1.6 m for all inlet culverts, but HAUT1 was adapted for each inlet culvert individually taking the valve position and the wooden beams into account. It represents the amount of opening on side 1 of the structure. The outlet culverts have a height of 1.1 m. The old outlet structures were given a height of 1.5 m. The direction of flow was set: CLP was set to 0 for the inlet culverts, meaning water can flow in both directions through these culverts. For the outlet culverts CLP was set to 2, meaning only outflow due to the presence of the one-way valve.

Table 4 - Parameter values for culvert calibration

		CE1	CE2	CS1	CS2	LARG	HAUT1	CLP	RD1	RD2	CV	TRASH	HAUT2	FRIC	LONG
2014 start	inlet	1	0,5	1	1	2,7	0,35	0	4,45	4,2	0	1,5	1,6	0,015	10
	inlet	1	0,5	1	1	2,7	0,35	0	4,45	4,2	0	1,5	1,6	0,015	10
	inlet	1	0,5	1	1	2,7	0,35	0	4,3	4,2	0	1,5	1,6	0,015	10
	inlet	1	0,5	1	1	2,7	0,45	0	4,2	4,2	0	1,5	1,6	0,015	10
	inlet	1	0,5	1	1	2,7	0,25	0	4,2	4,2	0	1,5	1,6	0,015	10
	inlet	1	0,5	1	1	2,7	0,35	0	4,2	4,2	0	1,5	1,6	0,015	10
	outlet	0,5	0,5	1	1	1,35	1,1	2	2,7	2,7	1	1,5	1,1	0,015	9
	outlet old	0,5	0,5	1	1	1,5	1,5	2	2,5	2,5	1	1	1,5	0,015	30
2014 calibrated	inlet	1	0,5	1	1	2,7	0,35	0	4,45	4,45	0	1	1,3	0,015	1
	inlet	1	0,5	1	1	2,7	0,35	0	4,45	4,45	0	1	1,3	0,015	1
	inlet	1	0,5	1	1	2,7	0,35	0	4,3	4,3	0	1	1,45	0,015	1
	inlet	1	0,5	1	1	2,7	0,45	0	4,15	4,15	0	1	1,6	0,015	1
	inlet	1	0,5	1	1	2,7	0,25	0	4,15	4,15	0	1	1,6	0,015	1
	inlet	1	0,5	1	1	2,7	0,35	0	4,15	4,15	0	1	1,6	0,015	1
	outlet	0,5	0,5	1	1	1,35	1,1	2	2,65	2,65	1,5	1	1,1	0,015	9
	outlet old	0,5	0,5	1	1	1,5	1,5	2	2,5	2,5	1,5	1	1,5	0,015	30
2013 storm	inlet	1	0,5	1	1	2,7	1,3	0	4,45	4,45	0	1	1,3	0,015	1
	inlet	1	0,5	1	1	2,7	1,3	0	4,45	4,45	0	1	1,3	0,015	1
	inlet	1	0,5	1	1	2,7	1,45	0	4,3	4,3	0	1	1,45	0,015	1
	inlet	1	0,5	1	1	2,7	1,6	0	4,15	4,15	0	1	1,6	0,015	1
	inlet	1	0,5	1	1	2,7	1,6	0	4,15	4,15	0	1	1,6	0,015	1
	inlet	1	0,5	1	1	2,7	1,6	0	4,15	4,15	0	1	1,6	0,015	1
	outlet	0,5	0,5	1	1	1,35	1,1	2	2,65	2,65	1,5	1	1,1	0,015	9
	outlet old	0,5	0,5	1	1	1,5	1,5	2	2,5	2,5	1,5	1	1,5	0,015	30
	leak	0,5	0,5	1	1	0,5	0,5	1	2,5	2,5	17	1	0,5	0,015	30

For the one-way valve, it was important to know how far this valve would open with outflowing water to determine its head loss coefficient. According to [7] in Table 3 a head loss coefficient can be found for specific opening angles of the valve. In the framework of one of projects [12], the opening angle of the one-way valve of Bergenmeersen was measured for a 13 hour period (September 2015). In Figure 12 shows the results of this measurement and at full outflow the angle measured reached 70°. So from Table 3 the head loss value is taken according to a ¾ opening of the valve, $C_V = 1$.

For the trash screen head loss equation 23 was used with a net flow area of 77% a head loss coefficient of 0.5 was calculated. This value was tripled because of the presence of debris and driftwood in front of the screens. For the friction coefficient a value was taken for smooth concrete. 0.015 was taken for the Manning Strickler value. For the length of the inlet culverts, 10 m was taken and for the outlet culverts 9 m was taken. For the old outlet culverts 30 m was taken.

With this first set of parameters for the inlet and outlet culverts, a model run can be started. A time step of 2 seconds was used. Private arrays (made available already within TELEMAC) were programmed to give the discharges of the culverts as output. One private array was programmed to give information about the type of flow that was used each time step for all culverts. The steering file used here is the same as the steering file for the Bergenmeersen validation case in the TELEMAC-3D basis.

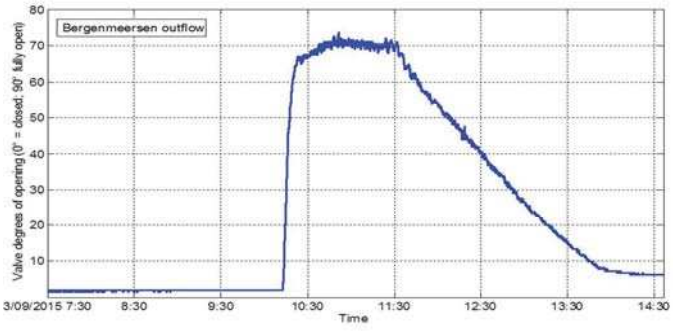

Figure 12 - Measurement of the degree of opening of the one-way valve at the outlet culverts at Bergenmeersen [12].

The red line in Figure 12 shows the water levels inside the floodplain after the first run without any calibration. The black dots indicate the measured water level in the floodplain. The squares give the water level that was measured outside the floodplain near the outlet structure. Calibration can be done in three ways: 1) the total head loss can be increased or decreased. All parameters contributing to the total head loss are always summed in the calculations. So there is little difference between increasing the head loss coefficient of the valve or the trash screen. The only difference is that not all head loss coefficients are always used. The outlet culverts use the head loss due to the one-way valve for example and the inlet culverts do not. 2) A second way to alter the discharges is to adapt the physical parameters like RD1 and RD2 or HAUT1 and HAUT2. 3) A third way is to alter the boundary conditions, like the floodplain. Because small bathymetric elements are not always very well represented in the mesh, this might cause differences in water levels inside the floodplain. To get better results, the mesh was refined only in the floodplain area, with a discretisation of 0.1 m, and a ditch that was not well represented in the model was created by changing the bottom level of some points by hand. This ditch made a connection between the two old outlet culverts on the left side (Figure 9) and the main channel in the floodplain. Creating this ditch caused a better drainage of the floodplain.

To get the best result, the head loss of the outlet culverts (blue line in Figure 13) was increased by 0.5 by increasing C_V. The bottom level of the whole construction was lowered with 0.05 m resulting in different RD values, the RD2 values of the inlet culverts were brought to the level of the wooden beams like their RD1 values (also decreasing their HAUT2 values accordingly), and the length of the inlet culverts was reduced to 1 m because of the small openings at side 1 due to the valve positions. The latter made the code switch in some situations from flow type 6 to flow type 5 resulting in different discharge values. When the model automatically modifies the discharges towards the river, the discharges towards the floodplain will change also because of a different amount of water present in the floodplain.

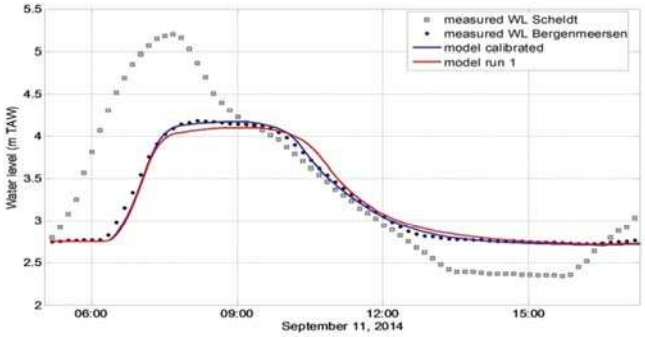

Figure 13 - measured and calibrated water levels for Bergenmeersen at September 11, 2014.

Figure 14 shows the measured (dots) and modelled (blue line) discharge going in the floodplain through the inlet culverts. The results show a very good agreement between the simulation and the measurements. Only between 7:45 and 8:15 the modelled discharges are too high.

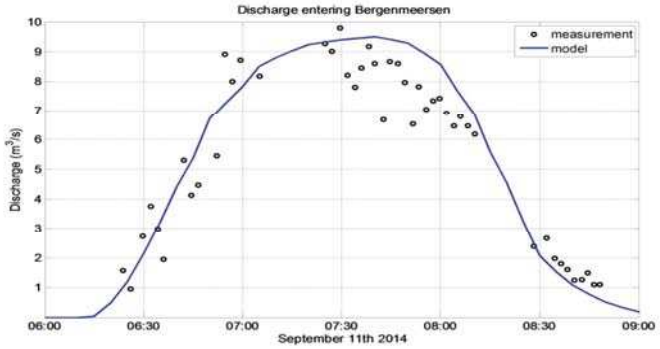

Figure 14 - Measured and modelled total discharge entering Bergenmeersen floodplain at September 11, 2014. The model results are the ones after calibration.

Figure 15 shows the measured (dots) and the modelled (blue line) discharge leaving the floodplain at the six new outlet culverts. The shape of the modeled curve fits well with the measured one, but a small time lag can be seen. The modeld curve was significantly improved by the 0.1 m increase in bottom level of the floodplain.

The second set of parameters in Table 4 is the one after the calibration effort resulting in the better results in Figure 13 (blue line), Figure 14 and Figure 15. To test if this parameter set could also deliver good results with other boundary conditions, the water elvels of a storm surge of December 6, 2013 were taken as boundary conditions. For this data set, the only available measurements are the water levels, no measurements of the discharge having been done. All other settings and parameters remained unchanged. The red line in Figure 16 shows the simulation results, while the black dots show the measured values. The model fails to reproduce the water levels in the floodplain. For the inlet culverts the wooden beams in front of them were there from the beginning, but the position of the valve was not known. The valve at that time were assumed fully opened, so this was changed in the parameter set for the inlet

culverts. It was also noticed by the people who performed the measurements that the water level in the floodplain was already rising slightly before the water level outside had reached the bottom level of the inlet culverts. So, a leakage was also assumed through the old outlet culverts. So one extra culvert was added with only flow in to represent the leakage flow. This resulted in the third parameter set given in Table 4 and gave a very good result for the modelled water levels inside the floodplain as given by the blue line in Figure 16.

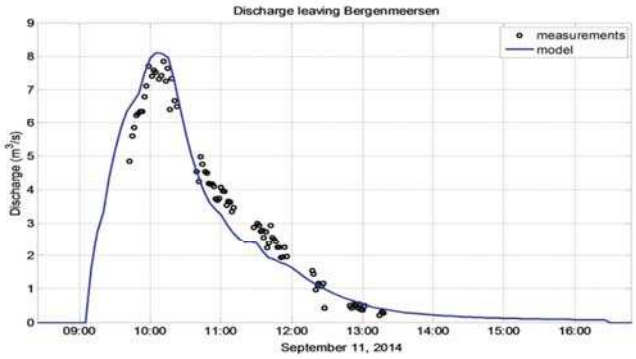

Figure 15 - Measured and modelled discharge leaving the Bergenmeersen floodplain through the new outlet structure (6 outlet culverts) at September 11, 2014. The model results are the ones after calibration.

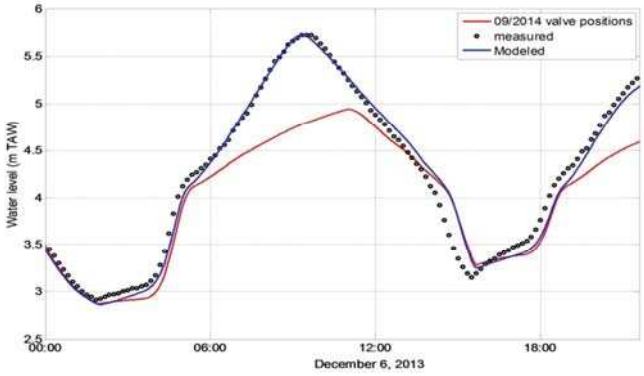

Figure 16 - Measured and modelled water levels for the storm of December 6, 2013. The Red line indicates the modelled water level when using the September 2014 valve positions in the culvert file instead of all open valves in December 2013.

The results are not perfect yet, but are coming very close. Because it is unknown if all valves were really fully open, in the absence of detailed information about the three old culverts and about the possible leakage and where it's coming from, further improvement of the results will be difficult.

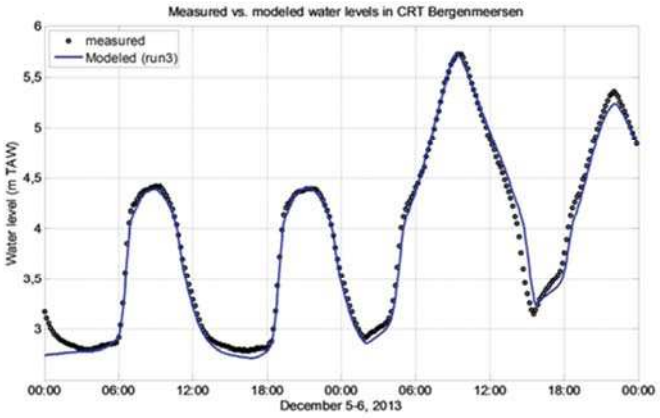

Figure 17 - Modelled and measured water levels for the period of December 5-6, 2013.

Figure 17 shows a longer time series where modelled and measured water levels are compared for the period of December 5-6, 2013. These results show the capability of the code to model the flow through these structures very well, even with trash screen, valves and wooden beams: the results are very good.

Finally, Figure 18 shows again the water levels inside and outside the floodplain on December 6, 2013, but on the bottom part of the Figure the types of flow that occur through the inlet and outlet culverts were added. This figure clearly shows that most types of flow occur during the simulation (remember that Flow Type 1 through a steep culvert was not added in the code). Negative Flow Types indicate flow going from the floodplain to the river Scheldt and vice versa for positive flow types. The figure also shows positive Flow Types for outlet culverts, but the CLP parameter, making that outlet culverts are only allowed to have flow from the floodplain to the river and not vice versa, makes sure the calculated discharge is set to zero in this case. Because of the exceptionally high water level with this storm surge we can also see negative flow types for the inlet culverts. This means that water is also leaving the floodplain through the inlet culverts. This was designed in this way to foresee extra capacity to drain the floodplain in case room is needed for a subsequent storm surge.

VI. CONCLUSIONS

This work aimed at adding a culvert functionality in TELEMAC-3D. The framework available in TELEMAC-2D was used so that the two modules are consistent. A new formulation for culverts was also added in this framework, and successfully validated against field measurements on the Bergenmeersen case. The latter is described in details in the paper.

Due to the complexity of the culvert modelling, there is a high number of parameters to provide in the formulation. The process of fitting of these parameters (head losses in

the culverts, etc.) on the Bergenmeersen test-case was described. All the developments, documentation and validation cases will be available in release V7P2 of the open TELEMAC system.

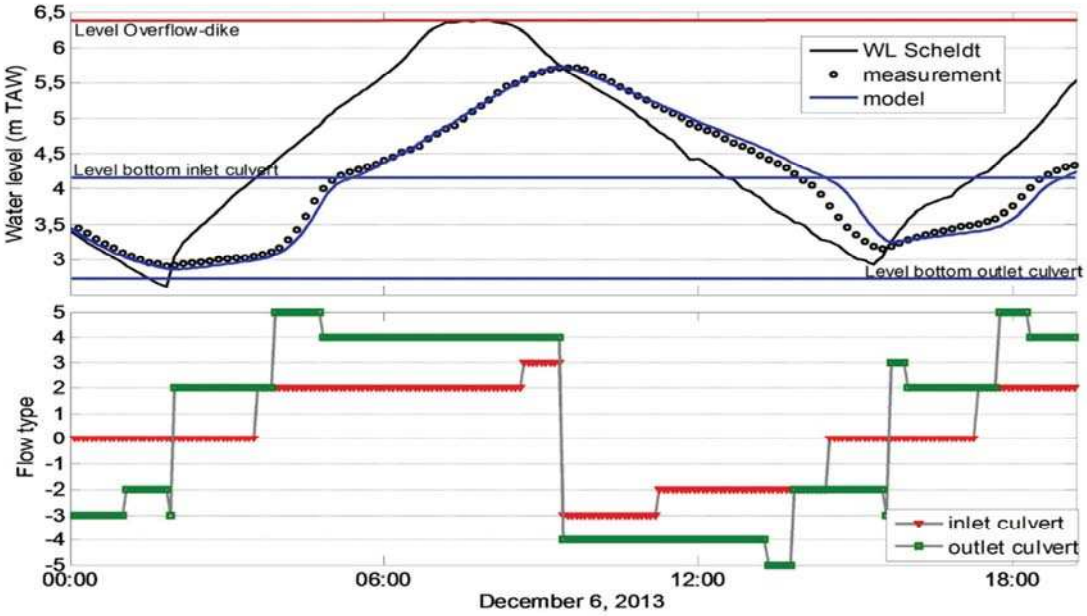

Figure 18 - modelled and measured water levels for the storm of December 6, 2013 and the type of flows that occurred through in- and outlet culverts

REFERENCES

[1] T. Cox, T. Maris, P. De Vleeschauwer, T. De Mulder, K. Soetaert, P. Meire, "Flood control areas as an opportunity to restore estuarine habitat." Ecological Engineering, Vol. 28, Issue 1, 2006, pp. 55-63.

[2] Smolders, S.; Maximova, T.; Vanlede, J.; Plancke, Y.; Verwaest, T.; Mostaert, F. (2016). Integraal Plan Bovenzeeschelde: Subreport 1 – SCALDIS: a 3D Hydrodynamic Model for the Scheldt Estuary. Version 5.0. WL Rapporten, 13_131. Flanders Hydraulics Research: Antwerp, Belgium.

[3] W. Baeyens, B. van Eck, C. Lambert, R. Wollast, L. Goeyens, "General description of the Scheldt estuary." *Hydrobiologia* 34,1998,83-107.

[4] G.L. Bodhaine, " Measurement of peak discharge at culverts by indirect methods", U.S. Geological Survey, Techniques of Water-Resources Investigations, 1968, book 3, chapter A3 60p.

[5] M. Carlier, "Hydraulique générale et appliquéé", 1972, Paris, Eyrolles

[6] Teles M. J., Smolders S., Maximova T., Rocabado I., Vanlede J., 2015. Numerical modelling of flood control areas with controlled reduced tide. Scheldt estuary physics and integrated management : proceedings of the 36th IAHR World Congress, 28 June - 3 July 2015, Delft & The Hague, the Netherlands- p. 90-99

[7] A. Lencastre, "Manuel d'hydraulique générale", 1961, Paris, Eyrolles

[8] E. Bruce Larock, W. Roland Jeppson, Z. Gary Watters, "Hydraulics of Pipeline Systems", 2000, CRC Press

[9] Wahl T.L., 1992. Trash control structures and equipment: a literature review and survey of bureau of reclamation experience. United States Department of the Interior, Bureau of Reclamation, Hydraulics Branch, Research and Laboratory Services Division, Denver, Colorado, 1992.

[10] Smolders S., Teles M.J., Maximova T., Vanlede J., 2014. Implementation of controlled reduced tide and flooding areas in the TELEMAC-3D model of the Scheldt Estuary. Proceedings of the 21st TELEMAC-MASCARET User Conference, 15th-17th October 2014. Grenoble, France, pp. 111-118. ISBN: 978-2-9548911-0-1

[11] De Beukelaer-Dossche, M.; Decleyre, D. (Ed.) (2013). Bergenmeersen: construction of a Flood Control Area with Controlled Reduced Tide as part of the Sigma Plan. Waterways and Sea Canal (W&SC)/Agency for Nature and Forest (ANB): Antwerp/Brussels. ISBN 9789040303432. 136 pp.

[12] Vercruysse, Jeroen; Visser, Klaas Pieter; Peeters, Patrik; Mostaert, Frank (2016). Vismigratie GOG/GGG: Opmeting van helling terugslagklep en debiet te Bergenmeersen. Versie 4.0. WL Rapporten, 15_034. Waterbouwkundig Laboratorium: Antwerpen, België.

Construction of a flood forecasting model on the river Odet (Finistere, France) with MASCARET

Anne-Laure Tiberi-Wadier
Cerema Eau, Mer et Fleuves
29280 PLOUZANE
FRANCE
Email: Anne-Laure.Tiberi-Wadier@cerema.fr

Michel Bueno-Ravel
Service de Prévision des Crues
Vilaine et Côtiers Bretons
DREAL Bretagne
L'Armorique - 10 Rue Maurice Fabre - CS 96515
35065 RENNES Cedex
FRANCE
Email: spc35@developpement-durable.gouv.fr

***Abstract*—A numerical model for flood and storm surge forecasting on the Odet river (Brittany) was developed by the Cerema. This model was ordered by the "Service de Prévisions des Crues Vilaine et Côtiers Bretons (SPC VCB)" (i.e. flood forecasting service for Brittany) in order to extend its tool set.**

The simulations are performed with the numerical 1D model MASCARET.

Upstream, on each tributary, the model goes up to a hydrometric station, where continuous flow and water height measurements are available. Downstream, the boundary of the model is the estuary of the river Odet, where are also available water height measurements.

The purpose of the model is the forecast of water height at the three stations Moulin Vert (river Steir), Kervir and Justice (river Odet) which are located in the city of Quimper.

At first, the model is calibrated with measurements upstream and downstream: measured flow upstream, measured water height at the estuary. Then it is tested in operational conditions. The model is thus supplied with

- **at the upstream boundaries, flows calculated by an hydrological GRP model, supplied with rain forecasts;**
- **at the downstream boundary, tide and storm surge forecasts.**

This paper focuses on the calibration and the validation of the model against data measurements.

I. Introduction

The cities of Quimper, Guengat and Ergue-Gaberic are often subject to overflows of rivers, leading to flooding in urban areas. These events result from the combination of two phenomena:

- excessive rainfall over the catchment basin, which consists in deep valleys through which flows the rivers Odet, Jet and Steir;
- high tides, sometimes increased by storm surges, which impact goes up to the upstream of Quimper.

The SPC VCB is responsible for flood forecasting in the city of Quimper. This organization wanted to develop a numerical model to extend its forecasting tools in this area. Since early 2016, the Cerema is working on the construction of a numerical 1D model with MASCARET.

II. Presentation of the geographical characteristics of the area

A. Catchment basin of the river Odet

The river Odet is a coastal river located in the department of Finistere (Brittany). It flows through the city of Quimper, and its mouth is located between the resort of Benodet and the city of Combrit. The river Odet has two tributaries: the river Jet and the river Steir. Table I summarizes the characteristics of the sub-catchment basins.

TABLE I: Characteristics of the three rivers Odet, Steir and Jet over the whole catchment basin

River	Odet	Jet	Steir
Elevation of the source of the river (IGN69)	175 m	200 m	100 m
Total length of the river (km)	66	26	29
Catchment area (km^2)	720	116	202

B. Area covered by the MASCARET model

The MASCARET model does not cover the whole catchment basin : it only focuses on urban areas. Figure 1 shows the segments of the rivers covered by the model. Table II provides the lengths of modeled river segments.

Continuous flow measurements are available at three upstream stations: Treodet (river Odet), Kerjean (river Jet) and Ty Planche (river Steir). The downstream boundary of the model is located at Plaisance near the estuary of the river. Continuous water height measurements are also available at this point. The stations at the boundaries of the model are represented in green on figure 1.

The purpose of the model is the forecast of water height at the three station Kervir, Justice (river Odet) and Moulin Vert (river Steir), represented in red on figure 1.

III. Construction of the hydraulic model

A. Geographical data

Several 1D hydraulic studies have already been made on the river Odet. Thus some topographic and bathymetric data

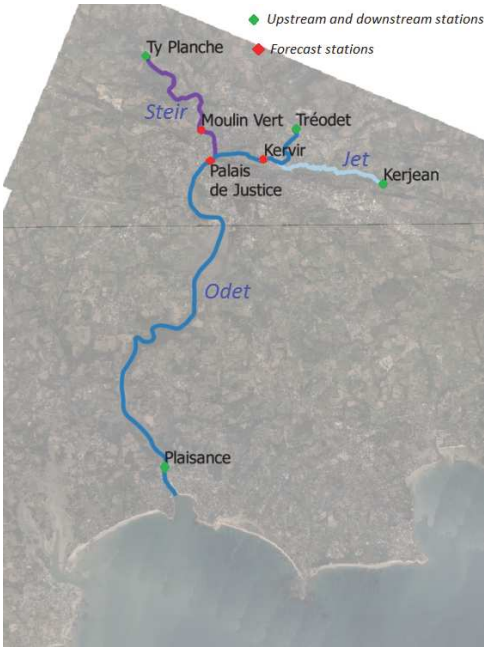

Fig. 1: The rivers Odet, Steir and Jet with the location of the hydrological stations

were available. These data were occasionnaly completed by lidar measurements.

B. Geometrical characteristics of the model

The model consists in 253 geometrical cross sections, for a total length of 35.1 km. Table II indicates the number of cross sections, bridges and weir for each river. The time step of the calculation is 180 s. The resolution of the computational mesh is 5 meters. The horizontal discretization of cross sections is 10 cm. After calibration, Strickler coefficients are between 15 and 41 in the riverbed, and between 5 ans 30 in flood plains.

TABLE II: Characteristics of the three rivers Odet, Steir and Jet considered in the model

River	Odet	Jet	Steir
Length considered in the model (km)	23.1	5.8	6.2
Number of cross sections in the model	157	14	82
Number of bridges in the model	24	1	13
Number of weir in the model	0	1	4

IV. Methodology for the calibration of the hydraulic model

A. Hydraulic data available

To calibrate the MASCARET model, continuous flow and water height measurements are available. Table III summarizes the time coverage of available data for each station.

TABLE III: Time coverage of hydraulic data used for the calibration

Station	Type of data used	Start of time coverage
Treodet (river Odet)	Flow	June, 2005
Kerjean (river Jet)	Flow	May, 2008
Ty Planche (river Steir)	Flow	June, 2005
Kervir (river Odet)	Water height	January, 2006
Justice (river Odet)	Water height	August, 2012
Moulin Vert (river Steir)	Water height	June, 2005
Plaisance (river Odet)	Water height	June, 2005

B. General methodology

In this study, the numerical model was calibrated by comparing the results of the simulations with the water height measurements at the three station Kervir, Justice and Moulin Vert. First, the model was calibrated over the period November 1st, 2013 - February 28th, 2014. This winter was characterized by numerous events of flood and storm surge. Then the model was validated over the period November 1st, 2012 - February 28th, 2013. This winter had less storms than the winter used for the calibration. We can notice that the events used for the calibration and the validation are uncorrelated.

The assessment of the adequacy of the results of the model with measurements is realized thanks to two methods:

- a visual analysis, by grahpically comparing the simulated and the measured water heights;
- a calculation of statistical parameters between the simulated and the measured data.

C. Statistical parameters

Statistical parameters are calculated from the measured and the simulated series. Let us denote:

- H_{obs}, the observed water height
- H_{mod}, the water height model forecast
- n, the number of samples

1) Statistical parameters on the whole distribution: In the first time, the calculation of statistical parameters is realized on the whole distribution, to characterize the entire simulated serie. Four statistical parameters are calculated:

- Mean error

$$\frac{1}{n}\sum_{t=1}^{n}[H_{mod}(t) - H_{obs}(t)] \quad (1)$$

- Mean absolute error

$$\frac{1}{n}\sum_{t=1}^{n}|H_{mod}(t) - H_{obs}(t)| \quad (2)$$

- Relative mean error

$$\frac{1}{n}\sum_{t=1}^{n}\frac{H_{mod}(t) - H_{obs}(t)}{H_{obs}(t)} \quad (3)$$

- Relative mean absolute error

$$\frac{1}{n}\sum_{t=1}^{n}\left|\frac{H_{mod}(t)-H_{obs}(t)}{H_{obs}(t)}\right| \quad (4)$$

These statistical parameters are calculated for all water heights and for water height classes. The boundaries of the classes are defined by the transition threshold used for public alert levels (green, yellow, orange and red).

2) Characterization of the errors on peaks of water height during events: We no longer consider the whole series. The analysis focuses on the representation of flood and storm surge events. Thus, errors concerning the value and the time offset of the peak of water height are characterized. For each event, the maximum of water height measured and simulated are compared, based on the following formula:

$$\Delta H = (H_{mod})_{max} - (H_{obs})_{max} \quad (5)$$

Thus it is possible to evaluate the model's performance on this specific topic, which is often communicated to the public.

The time offset between the two peaks is characterized in the same way by the formula:

$$\Delta T = T[(H_{mod})_{max}] - T[(H_{obs})_{max}]) \quad (6)$$

D. Periods for the calculation of statistical parameters

1) Calibration winter 2013-2014: During the calibration for winter 2013-2014, a set of 11 events were selected. Figure 2 shows the measured water height at the three stations Kervir, Moulin Vert and Justice during the winter. The events we focus on are represented in red.

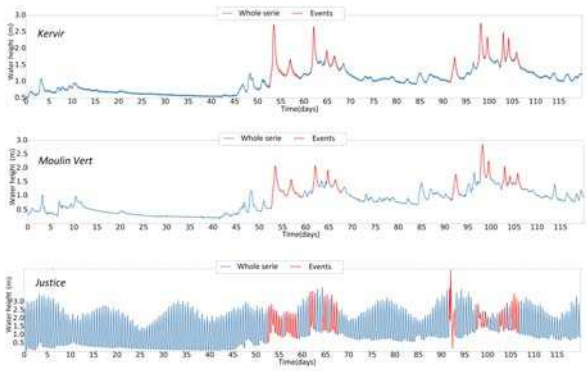

Fig. 2: Measured water height at the three stations Kervir, Moulin Vert and Justice from November 1st, 2013 to February 28th, 2014. Flood and storm surge events are represented in red.

2) Special case for the station Justice: Figure 2 highlights the fact that water height at the station Justice is dominated by tide effects, even during river floods. So for this location, it is relevant to analyze the high tide peaks. During the calibration winter, the calculation of errors on peaks is thus made on about 200 peaks of high tide.

V. Calibration and validation of the hydraulic model

A. Station Justice

1) Global analysis: Figure 3 compares the observed series in orange and the simulated serie in blue during the calibration and the validation periods. A good match can be found between the two series, for both the winters of calibration and validation.

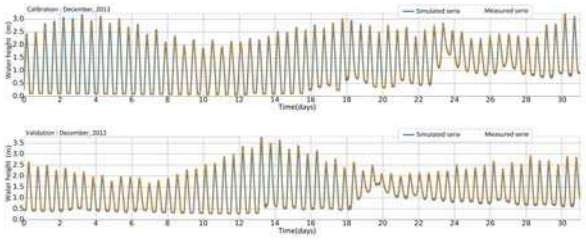

Fig. 3: Example of simulated and measured series during calibration and validation - Station Justice

Table IV represents the results of the calculation of statistics during the calibration and the validation winters (respectively denoted "CAL" in black and "VAL" in blue in the table). These results show that the performance of the model during the calibration and the validation periods are similar. The model is thus robust.

TABLE IV: Statistical parameters during calibration and validation - Station Justice

Water height class	Period	Mean error	Mean absolute error	Relative mean error	Relative mean absolute error
All water heights	CAL	-2.9 cm	6.7 cm	-0.9 %	8.9 %
	VAL	-3.6cm	6.2 cm	-3.3 %	7.1 %
Green vigilance	CAL	-2.9 cm	6.8 cm	-0.9 %	8.9 %
	VAL	-3.6 cm	6.2 cm	-3.3 %	7.1 %
Yellow vigilance	CAL	-1.1 cm	3.9 cm	-0.3 %	1.1 %
	VAL	1.2 cm	2.7 cm	0.3 %	0.8 %

2) Analysis of the peaks of high tide: Figure 4 represents the difference between water height measured and simulated, and the time offset between the two peaks for each high tide during the calibration period. These two graphics also show the water height mesaurement at the moment of the peaks. A positive value concerning the water height corresponds to an overestimation of the model relative to measurements, and a positive value concerning the offset means that the model is delayed respect to the measurements.

On this figure, regarding the errors on the water heights:

- green corresponds to a difference of less than 5 cm in absolute value
- blue corresponds to a difference between 5 cm and 10 cm in absolute value

- orange corresponds to a difference between 10 cm and 15 cm in absolute value
- red corresponds to a difference more than 15 cm in absolute value

Regarding the errors on the moment of the peak:

- green color corresponds to a difference of less than 6 minutes in absolute value
- blue color corresponds to a difference between 6 minutes and 18 minutes in absolute value
- orange color corresponds to a difference between 18 minutes and 30 minutes in absolute value
- red color corresponds to a difference more than 30 minutes in absolute value

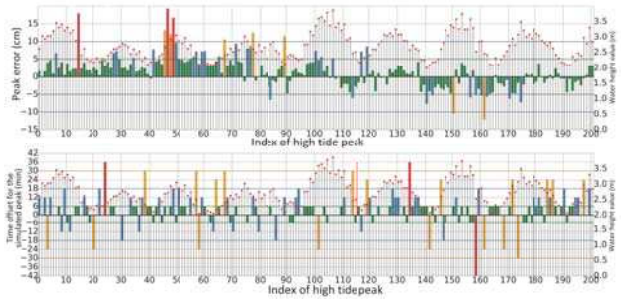

Fig. 4: Peaks errors, time offsets and associated water height for high tide during 2013-2014 winter - Station Justice

Figure 4 shows that:

- most of simulated peaks are less than 5 cm of the measures;
- for only 3 high tides, the model calculates a value with an error more than 15 cm;
- the model tends to be slightly late for the time of the peak, with an average error on the time offset of about 3 minutes;
- the high tides for which the model show an important error (colors orange or red) does not correspond to important water height at the station.

B. Station Kervir

1) Global analysis: Again, the measured and simulated series shown on figure 5 indicate that the two series match well.

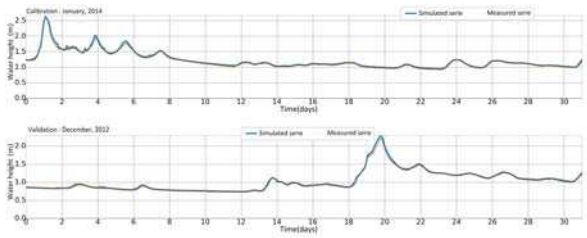

Fig. 5: Example of simulated and measured series during calibration and validation - Station Kervir

Table V represents the results of the calculation of statistics during the calibration and the validation winters. The model is robust also on this station, since its performances during the two periods are similar.

TABLE V: Statistical parameters during calibration and validation - Station Kervir

Water height class	Period	Mean error	Mean absolute error	Relative mean error	Relative mean absolute error
All water heights	CAL	-0.1 cm	2.0 cm	-0.3 %	1.9 %
	VAL	0.6 cm	2.0 cm	0.6 %	2.3 %
Green vigilance	CAL	-0.4 cm	1.7 cm	-0.5 %	1.8 %
	VAL	0.5 cm	2.0 cm	0.5 %	2.3 %
Yellow vigilance	CAL	6.3 cm	6.9 cm	3.2 %	3.6 %
	VAL	9.1 cm	9.1 cm	4.7 %	4.7 %
Orange vigilance	CAL	-5.6 cm	5.8 cm	-2.1 %	2.2 %
	VAL	no data	no data	no data	no data

2) Analysis of the peaks of events: Figure 6 represents the differences between the peaks of water height measured and simulated, and the time offset between the two peaks for the 11 events of the calibration period. These two graphics also show in grey the water height mesaurement at the moment of the peaks. The colors have the same meaning than before, on figure 4.

This figure highlights the fact that for most events, the difference is less than 10 cm between the simulated and the measured peaks. For only one event, the absolute error is between 10 and 15 cm. Regarding the time offset of the water height peaks, the differences between the model and the measurements is often less than 18 minutes.

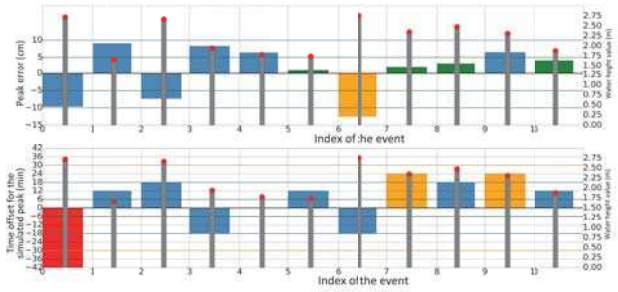

Fig. 6: Peaks errors, time offsets and associated water height for the 11 events selected during 2013-2014 winter - Station Kervir

C. Station Moulin Vert

1) Global analysis: Figure 7 also shows a general good match between the two series, during both the winters of calibration and validation. Results indicated on Table VI also confirm the robstness of the model on this station.

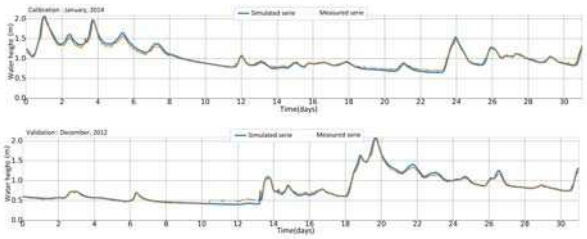

Fig. 7: Example of simulated and measured series during calibration and validation - Station Moulin Vert

TABLE VI: Statistical parameters during calibration and validation winter - Station Moulin Vert

Water height class	Period	Mean error	Mean absolute error	Relative mean error	Relative mean absolute error
All water heights	CAL	0.3 cm	3.5 cm	-0.1 %	3.3 %
	VAL	-0.2 cm	2.2 cm	-0.6 %	3.3 %
Green vigilance	CAL	0.5 cm	3.3 cm	-0.1 %	3.3 %
	VAL	-0.2 cm	2.2 cm	-0.6 %	3.3 %
Yellow vigilance	CAL	1.4 cm	5.0 cm	0.8 %	2.6 %
	VAL	1.3 cm	5.3 cm	0.8 %	2.8 %
Orange vigilance	CAL	-16.9 cm	17.5 cm	-6.5 %	6.8 %
	VAL	no data	no data	no data	no data

2) Analysis of the peaks of events: On figure 8, we can notice that most events are relatively well represented, with an absolute error lower than 10 cm. However, one event is not well reproduced by the model. Regarding the time offset, the model is in early in comparison to the measurements.

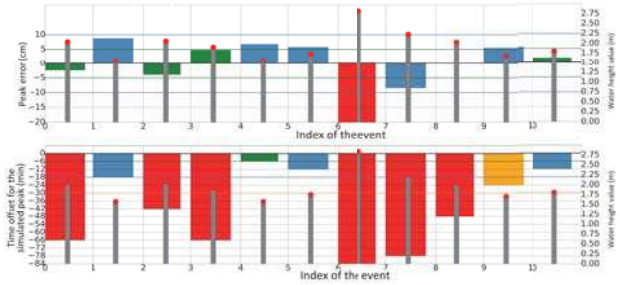

Fig. 8: Peaks errors, time offsets and associated water height for the 11 events selected during 2013-2014 winter - Station Moulin Vert

VI. Set up of an operational forecasting chain

A. Forecasting chain organization

The 1D hydraulic MASCARET model aims to fit into an overall prediction tool chain, shown on figure 9. Indeed, a hydrological model GRP is actually being calibrated. This model will calculate initial conditions for the hydraulic model using rain forecasts.

To achieve its forecasts in operational conditions, the SPC VCB has at its disposal:

- the tide prevision from the "Service Hydrographique et Océanographique de la Marine" (SHOM)
- the storm surge prevision from Meteo France
- the rain prevision from Meteo France

Thus the forecast of water height in operational conditions will be realized according to the scheme in figure 9.

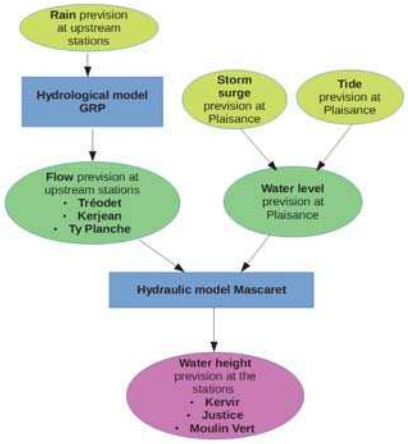

Fig. 9: Scheme of the operational forecasting chain

B. Example : event of December 23rd, 2013

Figure 10 represents the forecasts of water height at the three stations Kervir, Moulin Vert and Justice for the event which occurred on December 23rd, 2013. These results are not final, since the GRP model is still being calibrated. For this example, the GRP model is run with rain measurements.

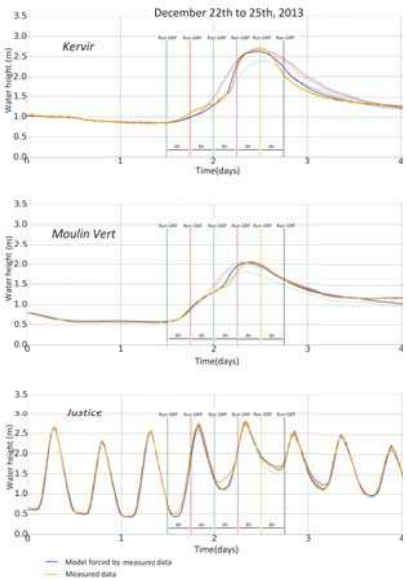

Fig. 10: Results with the global chain: the GRP model calcultes flows, fed into the MASCARET model

The hydrological model GRP is run every 6 hours. This is indicated by a vertical line on figure 10. For each run, a graph shows the prevision of water height done with MASCARET, for which:

- upstream boundaries conditions (flow) are provided by the GRP model
- downstream boundary condition (water depth) is the result of the sum of astronomical tide and storm surge predictions.

The previsions of water height results depend on the time at which the hyrological model is run. The best accuracy is not always achieved by using the latest flow forecast.

VII. Conclusion

A hydraulic numerical model for flood forecasts on the city of Quimper was build with MASCARET. It is intended to be integrated in a global forecast chain : with tide, storm surge and rain previsions, the model is able to forecast water heights in the city several hours in advance. Before this integration, tests will be carried out in real conditions on at least one season to validate or not its operationnal utilisation.

Suspended Sediment depositions in the impoundment of Iffezheim barrage effect of mesh resolution with Telemac3D

Christina Seegers,
Roy Frings and Holger Schüttrumpf
Institute for Hydraulic Engineering
and Water Resources Management
RWTH Aachen University
52056 Aachen, Germany
Email: christina.seegers@baw.de

Rebekka Kopmann
and Andrea Wahrheit-Lensing
Hydraulic Engineering in Inland Areas,
Federal Waterways Engineering and Research Institute
BAW
76187 Karlsruhe, Germany

***Abstract*—Deposition of fine sediments (mainly silt) takes place in the weir channel of the Iffezheim barrage and makes dredging a necessity, due to flood risks that develop with higher water levels. The current pattern in this area is three dimensional and turbulent structures are believed to be one key factor for the deposition of the suspended fine sediments in the weir channel (influencing quantity and pattern of deposits). The aim of this study was to prove that a detailed representation of turbulent structures enables an improved simulation of deposits. Therefore a comparison between a coarse mesh model with ∼5 m resolution and a fine mesh model with ∼1 m resolution was made. With the fine mesh a turbulence model following Smagorinsky was used and with the coarse mesh a $k-\epsilon$ turbulence model was applied. Both meshes show the presence of a large recirculation zone in the weir channel. The fine mesh shows that superposed on this recirculation zone, time-varying eddies occur, which influence the sedimentation pattern. The better resolution of turbulent structures with the fine mesh leads to depositional patterns that fit better to the observed changes in bed level. This study shows that a good representation of the turbulent structures is essential for numerical investigations of suspended sediment deposits in impoundments with three dimensional current patterns.**

I. Introduction

Deposition of fine sediments (mainly silt) takes place in the weir channel of the Iffezheim barrage producing sediment volumes of on average 100 000 m^3/a between 2005 and 2010. Although most of the sediment that enters the barrage is not being deposited, the deposited sediments lead to a higher water level and have to be dredged due to flood protection requirements. The sediment is polluted with HCB (Hexachlorobenzene - a pesticide used until 1981) leading to high disposal costs, because the material has to be removed from the weir channel and then transported to a disposal area where it can be deposited. This results in a high interest in countering measures to reduce dredging costs by the responsible authorities. To find useful measures the processes influencing the deposition of sediments in this area were to be investigated with a 3D numerical model to further improve the understanding of the system.

Several investigations ([1]- [5] at different institutes) have been conducted in this region focusing on flood risks, a recirculation zone, possible measures [5] the amount of deposited sediments, sediment processes [1] and contaminants [4]. The current pattern in the depositional area (Figure 1) is three dimensional and for flows below 2 200 m^3/s a huge recirculation zone of ∼700 m length and with varying width (∼ 80 m to 280 m) can be observed. The presence of this recirculation zone and the associated time-varying eddies in the weir channel are believed to be one key factor for the deposition of the suspended fine sediments in the weir channel (influencing quantity and pattern of deposits). It should be known that although most of the time (∼85%) there is nearly no flow in the weir channel in most of the remaining time (∼12%) a recirculation zone is present in the weir channel.

The aim of this study was to show, that the reproduction of turbulent structures in the weir channel with the numerical model has a strong impact on the deposition patterns and quantities. Two numerical models with different resolutions and different turbulence models using Telemac 3D were used to achieve this. A fine mesh with a resolution of roughly 1 m in the weir channel was set up, to allow a good representation of the recirculation zone including eddies. A turbulence model following Smagorinsky was chosen for this mesh . The hydrodynamic situation and resulting sediment deposits produced with this fine model were compared to a model using a coarser mesh with a resolution of roughly 5 m that was operated with a $k-\epsilon$ model (to include small scale turbulence that would have been omitted using the Smagorinski model).

II. Study site

The study site is located at the upper Rhine at the border between Germany and France. This barrage is the last of a group of 10 barrages built for energy production between Basel and Iffezheim. Following this barrage, that was established in 1977, the Rhine is free flowing until it reaches the North Sea. The modelled region is of 3 kilometre length with the lower boundaries being located at the barrage constructions (lock, power station and weir). In the model area the Rhine splits up in three channels leading to these constructions (Figure 1). Since 2013 most of the water in mean discharge conditions and slightly above is used for power generation. The power station

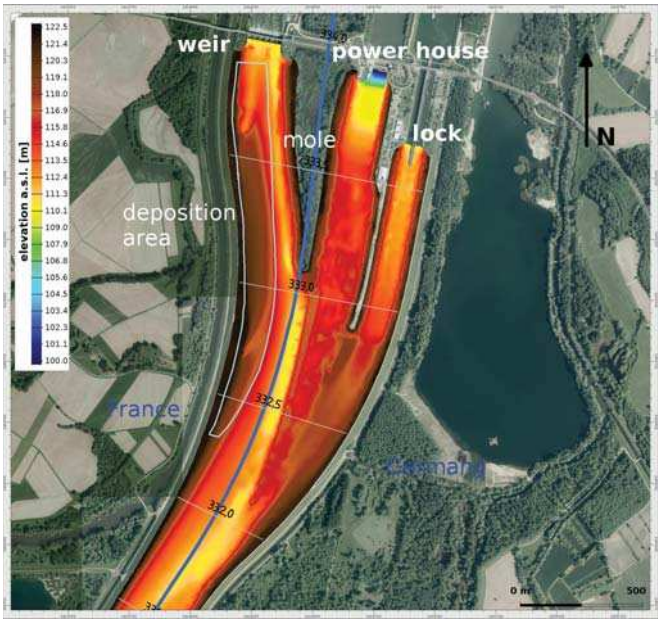

Fig. 1: The Iffezheim barrage in November 2014. Bed levels and the splitting of the Rhine into the three channels leading to lock, power house and weir. Photo images from BKG: Bundesamt fr Kartographie und Geodsie

can use up to 1 500 m^3/s of water per second, to generate 146 MW of peak power. Before 2013 1 100 m^3/s were used for power generation. Mean discharge flow means 1 250 m^3/s for the gauge at Maxau in Karlsruhe, which is roughly 30 kilometers downstream of Iffezheim. Mean low flow implies 581 m^3/s and mean high flow 3 060 m^3/s. The weir is made up of 6 weir fields, each giving the possibility to route water below or above the field. A torsion-rigid gate (fish-belly gate) is used for water flowing over the weir and allowing flow at the bottom a plain vertical rising gate is used. Each of these structures has a width of 20 m. Finding a good representation of this structure in the model proved to be challenging. Between the weir and the power station a mole was built resulting in a clear distinction of two channels, one to the power station and the other to the weir. A third channel leads to the lock, which is of no interest in this study.

The sediment deposited in the weir channel consists of a range of grain sizes from clay to sand, with most of the sediments being silt. The bed topography (Figure 1) shows two parts in the weir channel, a channel region with higher water depths (11-12 m) and a deposition area with water depths of 3-6 m.

III. Model set up and calibration

The two models were set up with different meshes having a coarser grid resolution with mean node distances in the weir channel of about 5 m and a finer grid resolution with mean node distances in the weir channel of about 1 m. In both models the angles of the elements were in the range of 30°to 90°and both were consisting of 20 layers. As boundary condition for the inlet a flow was imposed. The boundary at the power station was steered the same way, while at the weir water levels were imposed. For simplicity there was no flow at the lock. For the sediment concentration C at the inlet a condition based on the discharge was implemented in bord3d subroutine: $C = C_0 * Q^{1.95}$, with Q the inflow and C_0 a basic concentration that was a function of the node n. The sediment was distributed along the nodes in a way that more sediment was close to the bed and to the left side of the inlet. Representing the sediment distributions found in measurements. For the fine mesh model (with higher computational costs) a Smagorinski turbulence model was used, while for the coarse mesh a $k-\epsilon$ model was used. Time steps were 1 s for the fine mesh model (FM) and 2 s for the coarse mesh model (CM). The sediment was calculated including flocculation using the default coefficients and without a consolidation model.

As implemented in Telemac (subroutine tfond) the friction velocity $v_{friction}$ was calculated via

$$v_{friction}^2 = (\frac{\kappa}{\log R})^2 * (u^2 + v^2) \quad (1)$$

with κ the karman constant, $R = \max\{1.001; \frac{30*d}{k_s}\}$, d is the distance between the first two levels of the mesh, k_s the Nikuradse roughness coefficient, u and v are the velocities in x and y direction at the first level of the mesh.

The shear stresses at the bottom τ_b (see Telemac manual [7] p. 52) were calculated via $\tau_b = \rho * v_{friction}^2$ with ρ the density. The shear stresses were only depending on the friction velocity and sediment content for these computations without salinity (and thus without a special density law).

For deposition of sediments the calculation of the deposition flux $F_{deposition}$ followed Krone (1962) using:

$$F_{deposition} = P_d W_C C \quad (2)$$

with P_d probability of deposition ($P_d = 1 - (\frac{\tau_b}{\tau_{cd}})$), τ_{cd} critical shear stress for deposition W_C settling velocity and C concentration of sediments in the water.

For erosion of sediment, following Partheniades (1965) the equation

$$F_{erosion} = M(\frac{\tau_b}{\tau_{ce}} - 1) \quad (3)$$

was applied with M, erosion coefficient, and τ_{ce} critical shear stresses for erosion.

The time period chosen for the calibration of the model was August 2006 to October 2006. The corresponding hydrograph is shown in Figure 2. This time period was chosen, due to the information available about the water levels at the weir and the discharges at the power house, as well as due to the typical time distance between two measurements with deposition occurring and discharges between 900 m^3/s and 2 900 m^3/s. The maximum discharge in the weir channel was thus 1 400 m^3/s. The measured differences in bed level, after the $\sim$70 day period between August and October are shown in Figure 3. Both models with fine and coarse mesh have been calibrated with initial bed topography of august 2006 (based on echo soundings with distances of 20 m), the resulting parameter set is slightly different. Especially the critical shear stresses for deposition was different.

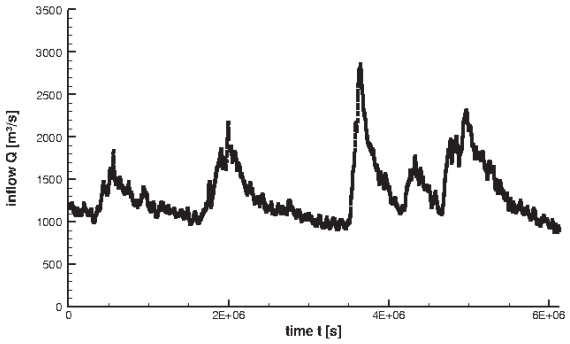

Fig. 2: The hydrograph of the calibration period August 2006 to October 2006.

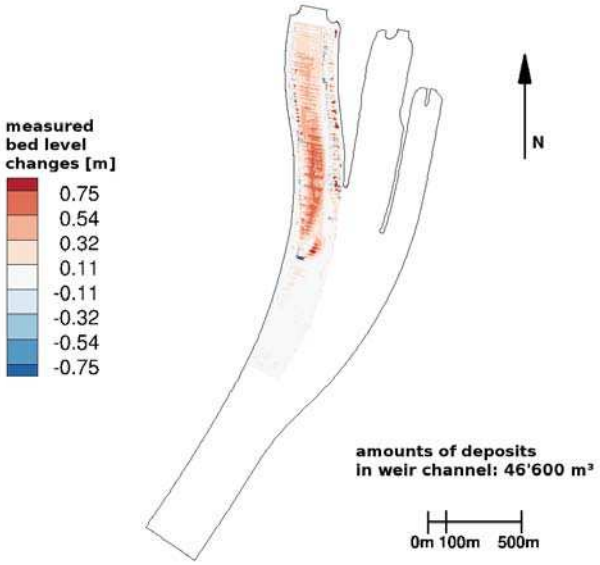

Fig. 3: The measured bed level changes between August 2006 and October 2006.

A. Coarse mesh model

In the weir channel the coarse mesh had mean node distances of about 5 m length. The minimum value for the area ratio was 0.39. For the coarse mesh, the $k-\epsilon$ model was chosen as turbulence model. The calibration parameters were decided on the basis of sediment quantities deposited in the weir channel, to fit best with the following values: For the settling velocity a value of 0.0025 m/s, corresponding to a grain size of $\sim$0.05 mm (coarse silt), following the equation of Soulsby [6], was chosen. The critical shear stress for deposition (Equation 2) was set to 0.135 N/m^2 and the critical shear stress for erosion (Equation 3) was 0.52 N/m^2, a value well within the range of measured critical shear stresses by Noack et al. [2]. The erosion constant (Equation 3) was set to 1.25×10^{-03} kg/m^2/s. The resulting bed level changes, calculated using the model with coarse mesh (Figure 4) fit reasonably well to the observed bed level changes, although for high discharges the erosion seemed to be somewhat to

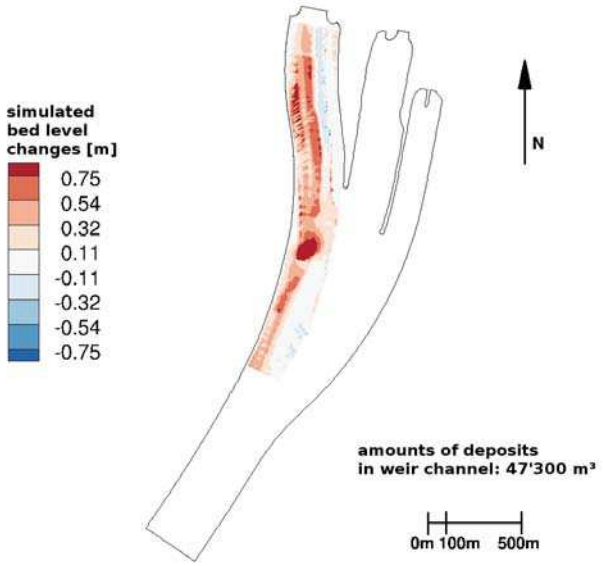

Fig. 4: The simulated bed level changes between August 2006 and October 2006, using the model with coarse mesh.

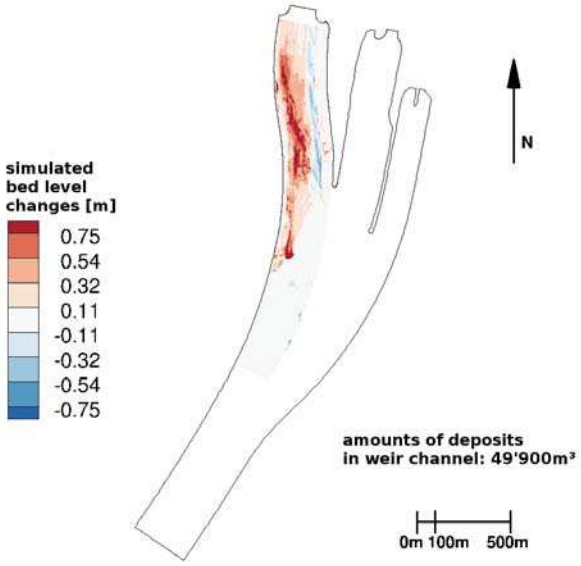

Fig. 5: The simulated bed level changes between August 2006 and October 2006, using the model with fine mesh.

strong, resulting in too much bed level erosion (not shown here).

B. Fine mesh model

The fine mesh had mean node distances in the weir channel of about 1 m with a minimal area ratio of 0.34. For the fine mesh, the Smagorinski model was chosen as turbulence model and for the settling velocity a value of 0.0013 m/s, corresponding to a grain size of 0.04 mm (coarse silt), following the equation of Soulsby [6], was chosen. The critical shear stress for deposition was 0.004 N/m^2 and the critical shear

stress for erosion was 0.59 N/m^2. The erosion constant was set to 0.80×10^{-03} kg/m^2/s. The resulting bed level changes, calculated using the model with fine mesh (Figure 5) fit well to the observed bed level changes. The erosion process during periods of peak discharges was not well reproduced by the model, which can be seen with different time periods (not shown here).

IV. Comparison of fine and coarse mesh model

Both models, the one with the fine mesh and the one with the coarse mesh showed fairly good results after calibration. It is thus justified to compare these two models with fine and coarse mesh, to get more insight in the way the models simulate deposition. This comparison is divided in two parts. The first part deals with the hydrodynamics and illustrates the numerical representation of the recirculation zone and the forces acting on the bed. The second part will deal with the morphodynamics and compare the sediment in the weir channel and the resulting deposits. The sediment was strongly affected by the hydrodynamic situation.

1) Hydrodynamics: There was a big difference regarding the representation of the recirculation zone between the two models. In the model with the coarse grid, the recirculation zone was nearly stationary in time, while in the model with the fine mesh within the recirculation zone time-varying eddies occurred and more dynamic was observed in the flow pattern. The displacement of eddies was high, depending on inflow (about 20 m in 600 s for 400 m^3/s in the weir channel) and local hydrodynamic situations differed a lot with time. Therefore a comparison with the fine model was based on averaged quantities. Time averages were done over a period of 18 000 s (5 h). Three discharges were considered. One with 1 600 m^3/s as inflow and 100 m^3/s discharge in the weir channel termed as 'lower' inflow with a huge recirculation zone, a second one with 1 900 m^3/s inflow (leaving 400 m^3/s in the weir channel) called 'moderate' and a third one with 2 200 m^3/s inflow that allowed 700 m^3/s in the weir channel. The last 'higher' flow resulted in a recirculation zone of minor extent in the weir channel. The water levels in the weir channel were set to the same level to allow model comparison.

a) flow velocities: As shown in figures 6 and 7, the flow velocities for a moderate inflow situation gave maximum flow velocities in the coarse mesh of 0.5 m/s and average velocities of 0.20 m/s in the weir channel. The huge recirculation zone with an extent of $\sim$160 m in width and $\sim$800 m in length was more detailed in the fine mesh model and consisted of several eddies. The differences in flow velocities between coarse and fine mesh models were small 0.026 m/s in average and 0.25 m/s at most. They could be found in the region next to weir and mole and in the region with higher water depth. The most prominent difference consisted in more detailed, small scale flow structures in the fine mesh model with the Smagorinski turbulence model. For higher inflow (not shown here) the dimensions of the recirculation zone were reduced to 80 m and 700 m. The flow velocity differences were still small with 0.006 m/s in average and at most 0.35 m/s. Lower inflows (not shown here) lead to smaller flow velocities (with a maximum of 0.25 m/s) and the extend of the recirculation zone increased to 190 m width and 1 000 m length (differences were on average 0.0002 m/s).

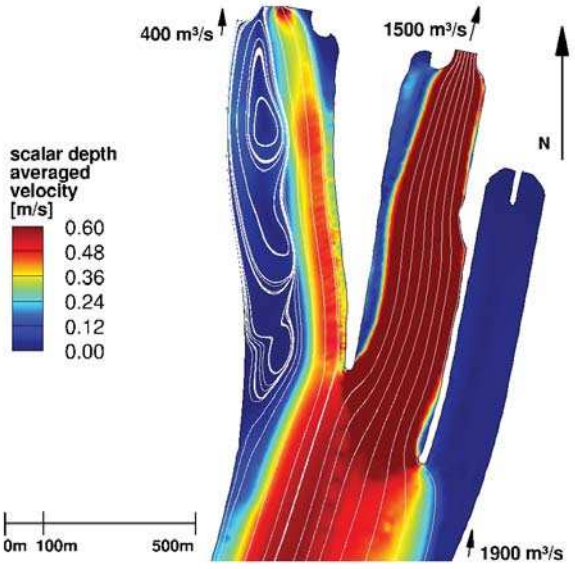

Fig. 6: Depth averaged scalar flow velocities in the weir channel. White lines represent the recirculation zone modelled with the coarse mesh model. An inflow of 1 900 m^3/s, a flow at the power house of 1 500 m^3/s and a flow at the weir of remaining 400 m^3/s, characterized as moderate flow situation, were applied.

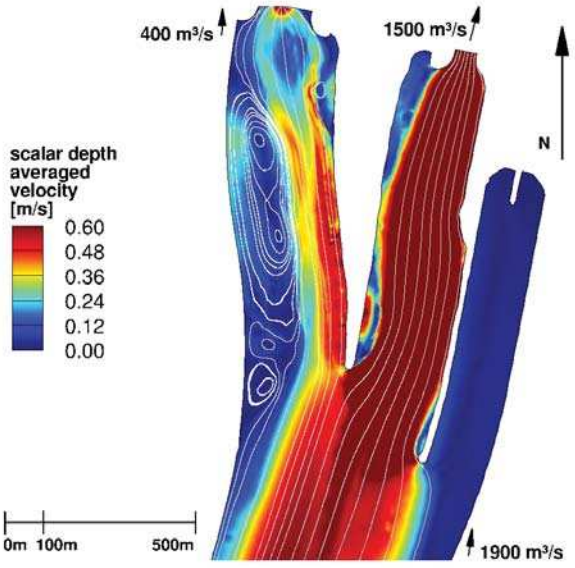

Fig. 7: Depth averaged scalar flow velocities in the weir channel. White lines represent the recirculation zone modelled with the fine mesh model for a moderate inflow situation.

b) friction velocities and shear stresses: The flow velocities led to the friction velocities, which were relevant for the sediment deposits, as can be deduced from the equations for sediment deposits (see section III). For the moderate inflow situation (leaving 400 m^3/s discharge in the weir channel) the average friction velocity with the coarse mesh model was 0.0085 m/s . With higher velocities in the deeper region with

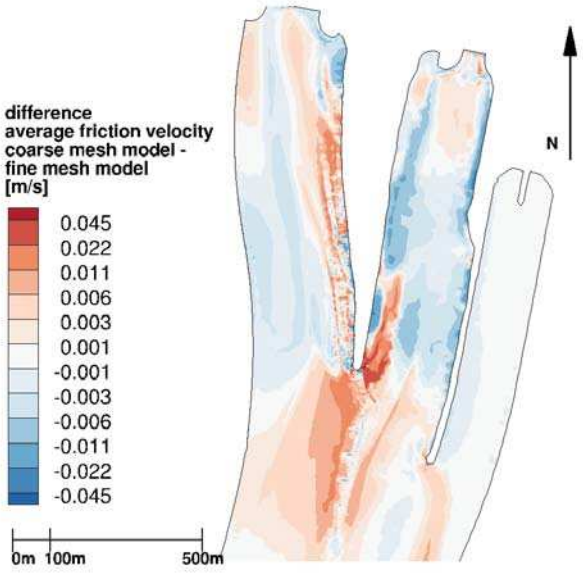

Fig. 8: The differences in the friction velocities (averaged in time) of the model with the fine mesh and the friction velocities of the model with the coarse mesh. For a moderate flow situation.

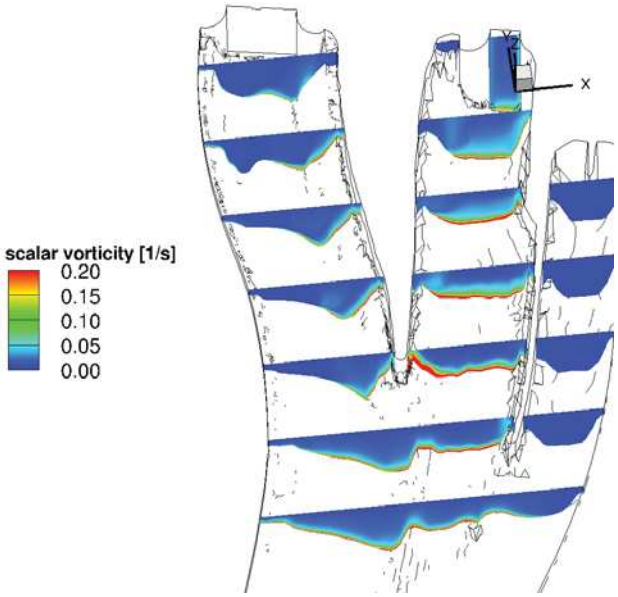

Fig. 9: The vorticity of the coarse mesh model for moderate flow situations in the weir channel.

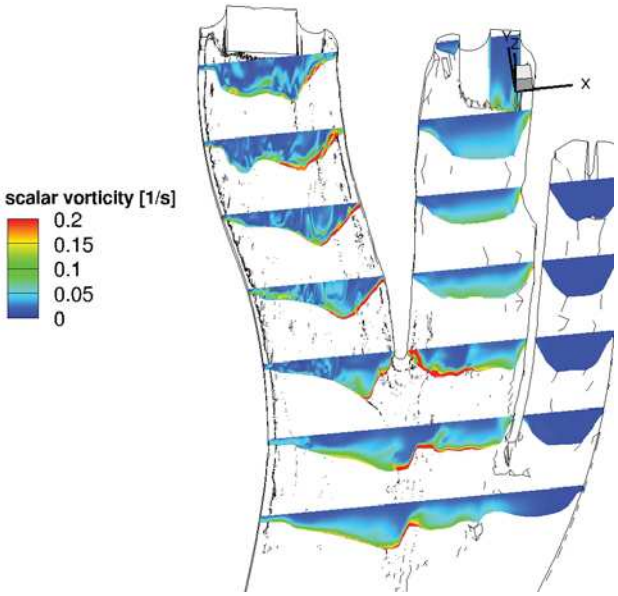

Fig. 10: The vorticity of the fine mesh model for moderate flow situations in the weir channel.

roughly 0.0177 m/s and lower velocities in the deposition area with roughly 0.0028 m/s. The fine mesh model gave an average friction velocity in the weir channel of 0.0084 m/s. It is obvious that the friction velocities mainly differ in the region close to the mole. While in the deposition region there were only small differences - see figure 8 for differences of averaged friction velocities. On average the differences were 0.0002 m/s. For higher inflow the region with higher velocities extended, while it decreased for smaller velocities so that average friction velocities in the weir channel changed to 0.0045 m/s for lower flows (0.0042 m/s FM) and to 0.0124 m/s for higher flows (0.0121 m/s FM) .

The pattern of the resulting shear stresses in the weir channel was the same as for the friction velocities with values up to 0.9 N/m^2 at the mole and lower values in the deposition area with 0.001 N/m^2 for the coarse mesh model. For higher flows the shear stresses increased. For lower flow situations they decreased to maximum values of 0.5 N/m^2 and average values of 0.06 N/m^2. The differences in shear stress were small with locally higher shear stresses, that changed positions along with the eddies in the fine mesh model.

c) vorticity: As a measure of turbulence the vorticity is shown in Figure 9 for the coarse mesh model and in Figure 10 for the fine mesh model. It is obvious that in the fine mesh model more vorticity could be observed, since more turbulence could be resolved with the fine mesh.

2) Morphodynamics:

a) sediment: The sediment in the water was given as concentrations. Figure 11 showed the sediment distribution in the model with the coarse mesh for moderate inflows. The corresponding Figure 12 with the fine mesh model illustrates the huge difference between the two models for the weir channel. The positions of the sediments in the weir channel were entirely different. For the coarse mesh model, the sediments were situated close to the mole. The sediment was held back at the boundary of the recirculation zone in case of the coarse mesh model and there the settling of the sediments took place. For higher flows the recirculation zone decreased and the sediment was distributed over a wider area in the coarse mesh model. It was the opposite for the model with the fine mesh. The sediment amounts (in the water in the weir channel) were 19 400 kg for the coarse mesh model and 55 700 kg for the fine mesh model (compared to CM: 58 000 kg and FM: 85 400 kg for the higher inflow). For lower

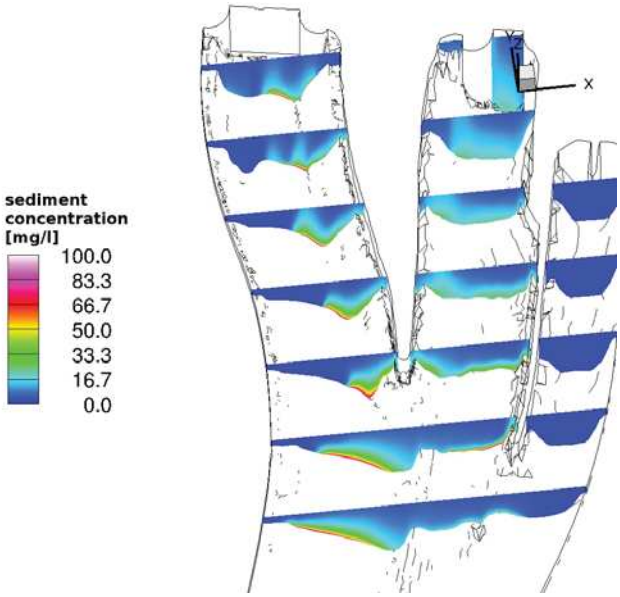

Fig. 11: The sediment concentrations using the model with the coarse mesh and a moderate flow situation.

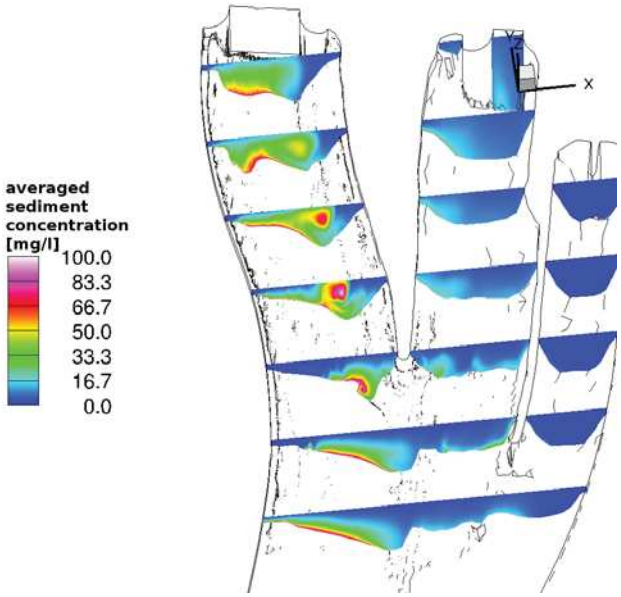

Fig. 12: The averaged sediment concentrations in the weir channel using the model with the fine mesh, for a moderate flow situation.

flows the recirculation zone increased and less sediment was present in the models (CM: 3 300 kg and FM: 12 000 kg). Not only the amounts of sediments in the weir channel changed also the position of the deposits. Sediment was present within the recirculation zone in the model with the fine mesh (see figure 12) and thus above the deposition area. While more sediment was in the deeper channel region, close to the bed in the coarse mesh model (see figure 11) and thus not above the deposition area. It is apparent that more sediment was routed along the weir channel in case of the fine mesh model compared to the coarse one.

b) sediment deposition: The sediments present in the weir channel could possibly be deposited, if the hydrodynamic situation allowed this. The resulting depositional pattern was quite different for the two models. Figure 13 shows the differences between the bed levels. The areas where the sediments were deposited for moderate inflows were at the edge of the deposition area for the coarse mesh model (with 870 m^3 of deposits) and close to the french bank for the fine mesh model (with 410 m^3 of deposits). They did not even overlap, and could be described as at the border of the recirculation zone (CM) and within the recirculation zone (FM). For higher inflows, the region were deposition took place of the coarse mesh model (with 1 700 m^3 of deposits) moved closer to the bank. The region were deposition took place of the fine mesh model nearly stayed at the same position (with 500 m^3 of deposits). For lower inflows the region were deposition took place of the fine mesh model extended and covered most of the weir channel with 180 m^3 of deposits. The coarse mesh model deposited only in the deep channel region of the weir channel and close to the weir, but mostly before the weir channel begins with 230 m^3 of deposits. Although more sediment was present in the weir channel in the fine mesh model, more sediment was deposited in the coarse mesh model for the presented inflows. While for most flow situations the amounts of deposited sediments were of the same magnitude

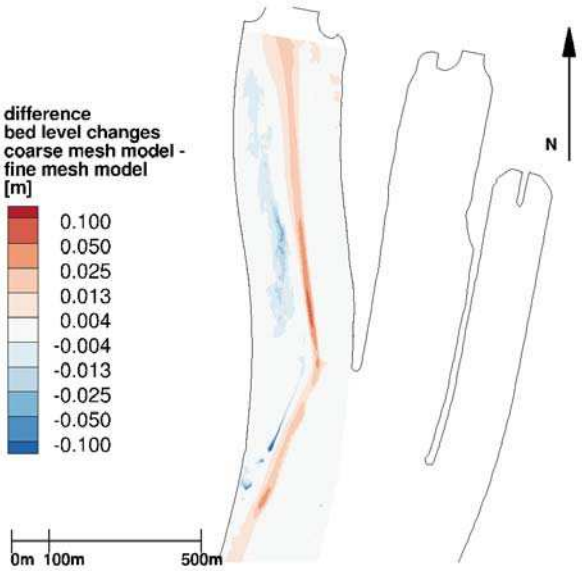

Fig. 13: The differences in bed level changes within 5 h between the models with coarse and fine mesh, for moderate inflows.

(with factors below 5) the most important result was that the positions were essentially different.

V. Discussion

The differences in the depositional patterns during periods with the presence of the recirculation zone are to be dealt with. These patterns are governed by the description of the deposition (Equation 2). In a first step the differences between the models following this description are presented and the

main causes are examined. As second step the relation to the turbulent structures is given. It will be explained why the fine mesh model is believed to better represent the deposition processes and what the effects of better representation of the turbulent structures were. The role of the eddies in this representation will be clarified.

The hydrodynamic situation was similar, but in detail there were a lot of differences between the models with coarse and fine mesh. These differences were associated with small scale flow structures and the time-varying eddies in the recirculation zone. The distribution of the sediment within the weir channel was in reaction to these small but essential hydrodynamic differences, totally different. To investigate the reasons for the different depositional patterns the underlying laws that influence the deposition are recalled here. The friction velocity was calculated via formula 1 and was thus depending on the local flow velocities and the local roughness. As described in the hydrodynamics part IV-1b, the average friction velocities were not too different between the two models. The shear stresses according $\tau_b = \rho * v^2_{friction}$ were directly depending on the friction velocities. These shear stresses were needed to calculate the deposition according to equation 2. The sediment content and settling velocity directly influenced the deposition of sediments and since the shear stresses were part of the equation to calculate the deposition of sediments also friction velocities had a control function. The sediment thus was in two ways present in the calculation of the deposits, directly as concentration and by means of density also via the shear stress calculation. The presence of sediments, that depended on the hydrodynamic situation, was the main factor for the differences between the models with coarse and fine mesh. This can be concluded since the differences in friction velocities were small in the weir channel, the differences in shear stress were also small while the differences in the sediment concentrations and position of the deposited sediments were huge with no or nearly no overlap. The positions of the deposits simulated with the fine mesh within the recirculation zone, were more plausible (Figure 13).

It is known from some measurements (done by the BfG: German Federal Institute of Hydrology) that within the recirculation zone sediments are present. Following the above process description these sediments were expected to be deposited. Although the calibration results (Figures 4 and 5) look similar the way they result from the simulations was different (not shown here). That within the recirculation zone in the coarse mesh model no sediment was being deposited was compensated by deposition at higher discharges in the weir channel at these positions. The higher sediment amount that was deposited in the deeper parts of the weir channel was compensated by higher erosion. The deposition behaviour is believed to be better captured with the fine mesh model, as indicated via sediment the mentioned concentration measurements and via application to different time periods (both not shown here).

The sediment was present in the water column due to advection and diffusion. Its distribution differed a lot between coarse and fine mesh model. The different sediment distribution in the weir channel led to a different availability of the sediment regarding the deposition. The different sediment distribution could be related to the turbulent structures and their representation in the weir channel. This can be seen by

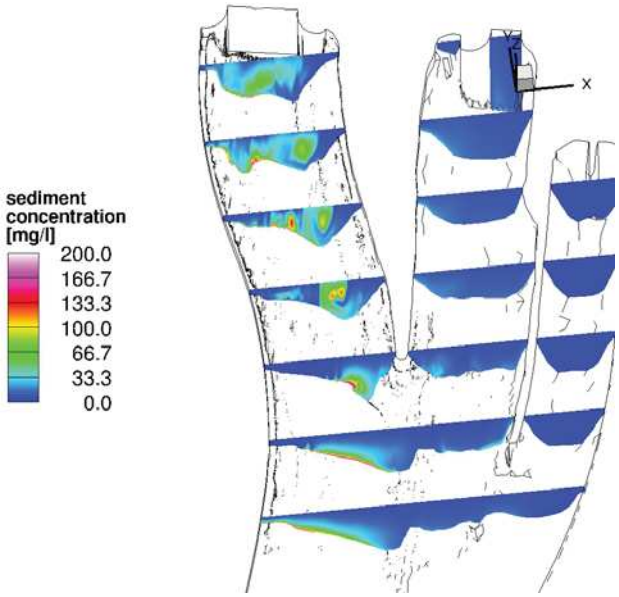

Fig. 14: The sediment distribution in the weir channel for moderate flow situations, with fine mesh model.

comparing Figure 14, showing the sediment concentrations in the weir channel calculated with the fine mesh model, with the vorticity of the fine mesh at the same time Figure 10. Regions of higher vorticity could be associated with regions of higher sediment concentrations.

The vorticity could be associated with the time-varying eddies in the weir channel, as they moved around also the regions of high vorticity with more sediment content were moved along. This is the reason why time averages over 5 h were necessary for the comparison of coarse and fine mesh (Section IV-1). For short time intervals the sediment was deposited only at some parts within the recirculation zone, since the deposition flux (Figure 15) was high at the centre of an eddy.

Thus the representation of the sediment distribution and deposition was better in the fine mesh model. This could be associated with the turbulent structures, which were better represented in the fine mesh model.

In the model the amounts of sediments deposited in relation to the inflow can be gathered. Thus the influence of the representation of the recirculation zone on the overall sediment deposits for a given hydrograph can be specified. For the coarse mesh model of Iffezheim barrage and the calibration time period 105% of the sediment was estimated to be deposited in situations associated with the recirculation zone (and 21% in situations without recirculation zone). For the fine mesh model 118% of the sediment was estimated to be deposited in situations associated with the recirculation zone and 5% in situations without recirculation zone. Some of the deposited sediment amount was being eroded in higher flow situations with no recirculation zone.

This effect of better representation of the deposition area with higher mesh resolution was not depending on the bed level topography. Assuming that recirculation zones and 3D

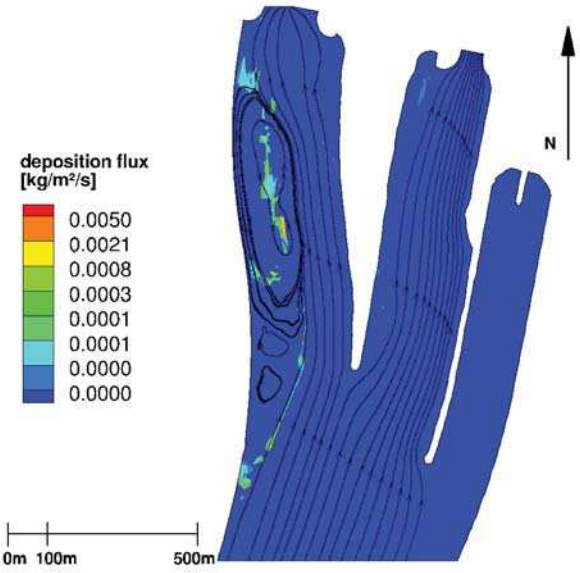

Fig. 15: The deposition flux in the weir channel for moderate flow situations, with fine mesh model. Black streamlines (of depth averaged velocities) show the recirculation zone.

turbulent structures are present in similar situations leads to the conclusion that for the numerical implementation of impoundments a good representation of turbulent structures improves the simulation of sediment deposition.

VI. Conclusion

The time-varying eddies observed in the model with the fine mesh and Smagorinski model influenced the depositional patterns in the Iffezheim barrage and led to more realistic deposition behaviour in the weir channel than the mainly static recirculation zone that could be modelled using the coarse mesh model. Leading to the conclusion that the effect of the turbulent structures, that introduces sediments into the recirculation zone, in the weir channel really is one key factor to model the sediment deposition. Yet there are still improvements regarding a realistic representation of the actual situation in the model to be achieved to gather more insight in the processes and their reactions to measures in the study site.

Generally a good representation of the turbulent structures associated with recirculation zones is essential for numerical investigations of sediment deposits in impoundments.

References

[1] *3D CFD modelling of velocities and sediment transport in the Iffezheim hydropower reservoir*, G. Hillebrand, I: Klassen and N.R.B. Olsen, Hydrology Research 2016

[2] M. Noack, G. Hillebrand, U. Seidenkranz and S. Wieprecht, *Untersuchung der Erosionsstabilitt kohsiver Sedimentablagerungen im Wehrkanal der Staustufe Iffezheim, Rhein*, Hydrologie und Wasserbewirtschaftung 60 (3),pp. 164-175, 2016

[3] T. Brudy-Zippelius and Schmidt, A., *Sedimentationsproblematik im Oberwasser der Staustufe Iffezheim–Dreidimensionale Simulation von Strömung und Schwebstofftransport*, Strmungssimulation im Wasserbau, Dresdner Wasserbaukolloquium Mrz 2006. Dresdner Wasserbauliche Mitteilungen H. 32, pp. 149-156, 2006

[4] G. Jacoub and Westrich, B., *Modelling transport dynamics of contaminated sediments in the headwater of a hydropower plant at the Upper Rhine River*, Acta hydrochimica et hydrobiologica, 34 (3),pp. 179-286, 2006

[5] A. Schmidt, T. Brudy-Zippelius, R. Kopmann and M. Imiela *Investigations to reduce sedimentation upstream of a barrage on the river Rhine*, WIT Transactions on Ecology and the Environment 80, 2005

[6] R. Soulsby, *Dynamics of marine sands: a manual for practical applications* Thomas Telford, 1997

[7] www.opentelemac.org *TELEMAC-3D Software operating manual 7.0*, January 2016.

Using an eco-friendly flushing event to calibrate 3D sediment transport model through a reservoir: the case study of Champagneux run-of-river dam on the Rhône River, France

Damien ALLIAU, Pierre NUNES, Christophe PETEUIL
Compagnie Nationale du Rhône
Lyon, France
d.alliau@cnr.tm.fr

Nicolas HUYBRECHTS
Roberval Laboratory, LHN (joint research unit UTC-CETMEF)
Compiègne, France

Abstract— **Reservoirs controlled by dam are likely to force inflowing sediments to settle. This process can be more or less temporal and intensive, depending on particle size and reservoir characteristics. To limit the reservoir sedimentation and prevent a disruption of sediment continuity, one possible option for dam operators is to recover favorable flow conditions either for routing inflowing sediments or remobilize previous deposits. For the last 30 years, the Champagneux run-of-river dam (Rhône River, France) has experienced significant deposition processes affecting mainly fine sediment fractions.**

In 2014-2015, a hybrid modelling survey has been conducted to calibrate a TELEMAC-3D model to determine hydraulic parameters, especially for vertical distribution of velocity for the knowledge of bed shear stress values in the whole reservoir [1]. Following step of this assessment consisted in calibration of sediment transport models to predict short and long term bathymetric evolutions and improve current approaches to manage sediments. Rhône River flush event permitted modelling team to calibrate a morpho-dynamic model over this period: from May 19th to 31st 2016, which CNR has lead a specific sediment operation, called eco-friendly flush [4], to limit environmental impacts by supporting operations of drawdown of Verbois Dam (downstream Geneva, Swiss). Champagneux Dam is one of six dams concerned by this operation. Thanks to intensive surveys conducted by CNR, an exhaustive sediment database has been established including: sub-surface real-time measurements of turbidity, suspended sediment concentration, grain size distribution, settling velocity measurements, bed-load tracking with an ADCP, and vertical distribution of suspended material and suspension. These data have been used to validate morpho-dynamic parameters (with mixed size classes): SEDI-3D for suspended load (using *u*, *v* and *w* velocity components) and SISYPHE for bed-load transport.

I. INTRODUCTION

By decreasing the velocity of the flow and turbulence, reservoirs controlled by dams are likely to force inflowing sediments to settle. This process can be more or less temporal and intensive, depending on particle size and the reservoir characteristics [3]. To reduce the reservoir sedimentation and prevent a disruption of sediment continuity, one possible option for dam operators is to recover favorable flow conditions either for routing inflowing sediments or to remobilize previous deposits [2]. For the last 30 years, the Champagneux run-of-river dam (Rhône River, France) has experienced significant deposition processes affecting mainly fine sediment fractions. One essential challenge that CNR has to deal with as the dam operator is to predict bathymetric state for short and long term, especially for flushing events.

To achieve this objective, the approach favored by CNR relies on a morpho-dynamic model based on a TELEMAC-3D model. This one was previously calibrated only for hydrodynamic parameters, in particular for vertical gradient of velocity [1]. The purpose of this communication is to present sediment methodology and first T-3D calibration results.

II. OBJECTIVES

A. *Context of the sediment flushing operation*

Since the Genissiat dam completion in 1948, 19 sediment flushing operations have been organized in the upper Rhone River. A French-Swiss agreement includes a definition of the frequency and of the time schedule for the operation: organization of the sediment flushing every 3 years and timing between the end of May and the beginning of June.

Several technical, environmental and administrative requirements are considered by CNR. For instance, at the Genissiat dam and further downstream, CNR has to deal with the following challenges: (1) ensure safety, (2) limit sediment deposits in the reservoirs, (3) release sediment fluxes coming from upstream, (4) significantly regulate the concentration of suspended load in order to limit the impact of the flushing operation, (5) preserve the natural sections of the Rhone River, and (6) limit the impact of sediment release on human activities closely connected with the river (Nuclear Power plant, drinking water, etc.).

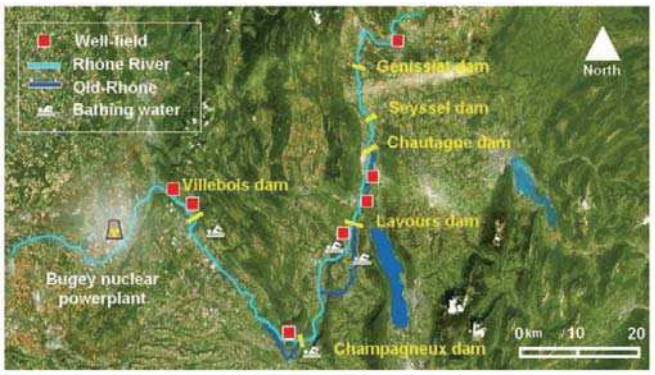

Figure 1. Location of stakes likely to be impacted by flushing

The reservoir of Champagneux is concerned by this sediment flushing operation, as shown in Fig. 1.

B. Principles of the environmentally friendly flushing

The principles of the environmentally friendly flushing carried out by CNR in the French upper Rhone River is to send only a concentration of suspended sediment downstream of the Genissiat dam, because the fluvial environment cannot withstand it [4]. The suspended load released downstream of the Genissiat dam should not exceed a maximum level of concentration: the maximum limits admitted at Seyssel gauging station are as follows: average concentration during the entire operation below 5 $g.l^{-1}$, average concentration during a continuous period of 6 hours below 10 $g.l^{-1}$ and average concentration during a continuous period of 30 minutes below 15 $g.l^{-1}$. In comparison, the maximum value observed during natural floods is around 3 $g.l^{-1}$ for the time period between 1988 and 2009.

In parallel of Genissiat specific operating conditions, the reservoirs of Chautagne, Lavours, Champagneux and Villebois have been lowered progressively (Fig. 1): these operations lead to an increase in flow speed, thus ensuring sufficient velocity to drive the sediments coming from Switzerland along the river.

C. Understanding sediment transport process for Champagneux reservoir

Even if the suspended load released by Genissiat dam is almost controlled during flushing events, downstream reservoirs are affected by sedimentation processes, Champagneux is one of them. These deposits consist of potentially cohesive fine sediment (mixture of sand, silt and clay) and lead to an aggradation of the bed reservoir. Materials can be transported in whole or in part depending on the episodes of high water and floods affecting the upstream part of the watershed. In the long term, the presence of these accumulations may be possibly detrimental. The main issues are:

- What types of hydrodynamic conditions are necessary to set these deposits in motion?
- Would an evolution of sediment management be likely to lead to the achievement of a satisfactory state of morphological balance? Otherwise, what are the preventive maintenance ways to set up?

A detailed data collection has been conducted by CNR in 2014-2016: *in situ* measurements (surface deposits for grain size distribution curves and mechanical tests, erosion tests, auscultation by subaquatic video or acoustic samplers) and hydro-dynamic hybrid modelling study [1]. This preliminary analysis also led to better determine the consequences of long term deposits for different hydrological conditions and operating conditions. A hybrid modelling step has been conducted to calibrate a TELEMAC-3D model to determine hydraulic parameters, especially for vertical distribution of velocity to assess bed shear stress values in the whole reservoir.

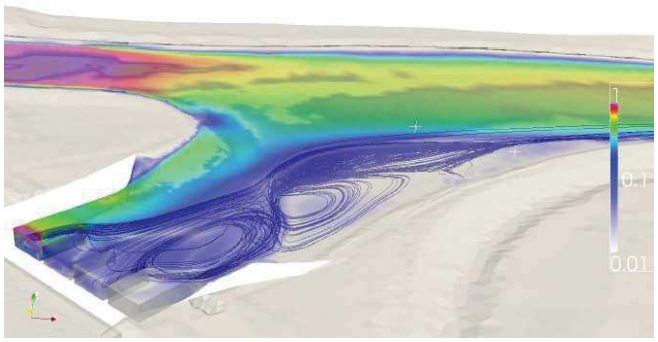

Figure 2. Overview of TELEMAC-3D model

The following step of this assessment consisted of calibration of sediment transport models to predict short and long term bathymetric evolutions and improve current approaches to manage sediments.

To complete this first work, a hydro-sedimentary model TELEMAC-3D (SISYPHE / Sedi-3D) has been implemented during eco-friendly flush (from May 19th to 31st 2016). This model was calibrated to reproduce the deposit phase during the flushing operation in spring and a specific assessment was conducted with sensitivity tests. A plausible variation range was studied with regard to the different calibration parameters.

III. AVAILABLE MEASUREMENTS

A. Monitoring network

In order to pilot the sediment flushing operation in real time, but also to evaluate its environmental impacts, CNR has carried out a comprehensive monitoring during several weeks regarding the following topics: suspended sediment concentration, bathymetry, grain size analysis, physical and chemical parameters (temperature, dissolved oxygen, pH, NH4, conductivity and turbidity), toxicity and eco-toxicity, and bacteriology. Specific surveys have been conducted concerning the following issues: well-fields for drinking water, natural reserves, by-passed river channel and refuge zones for fish. Specific sediment fluxes samplers were designed by CNR, in order to provide real time data to the Genissiat dam command center throughout the reservoir and the duration of the operation (Fig. 3).

Figure 3. Turbidity floating sensor on the Rhône River, May 2016.

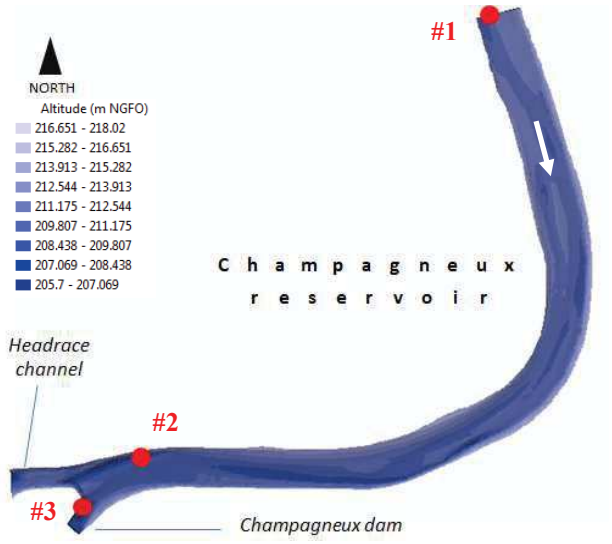

Figure 4. Location of *in situ* samplings (turbidity sensor, sediment concentration and grain size distribution curve)

Besides real time data used by the dam command center (turbidimeter, see Fig. 7 & 8), several samples were collected every 4 hours at each 3 stations to determine by laboratory tests sediment concentration (to correlate NTU signal with a solid concentration g.L^{-1}) and grain size distribution curves. With IRSTEA team, ADCP measurements and Niskin bottle samples were done for 3 cross sections to measure the bedload fluxes and vertical distribution of sediment concentration, but results were unfortunately not workable.

B. *Sediment characteristics*

Sediments analysis of Champagneux reservoir has required several measurements performed during field campaigns (April 2015, May 2016) completed by lab-tests. Surface and sub-surface pattern have been mapped with lateral sonar and sub-bottom profiler. Results showed a broad particle size range: from non-cohesive (gravels to sand) to cohesive (silt) with a proportion of clay upper than 20%.

Samples taken during the flushing event have been analysed to determine the mean diameter (d_{50}) of the suspended particles: those analyses highlighted that only cohesive sediment is transported by suspension. The mean diameter of the suspended material is around 10 µm. In addition, CNR has measured the settling velocity of *in-situ* particles (Fig; 1). Experiments by Andreansen device showed that the settling velocity is 10 time higher than the one expected with a theoretical law.

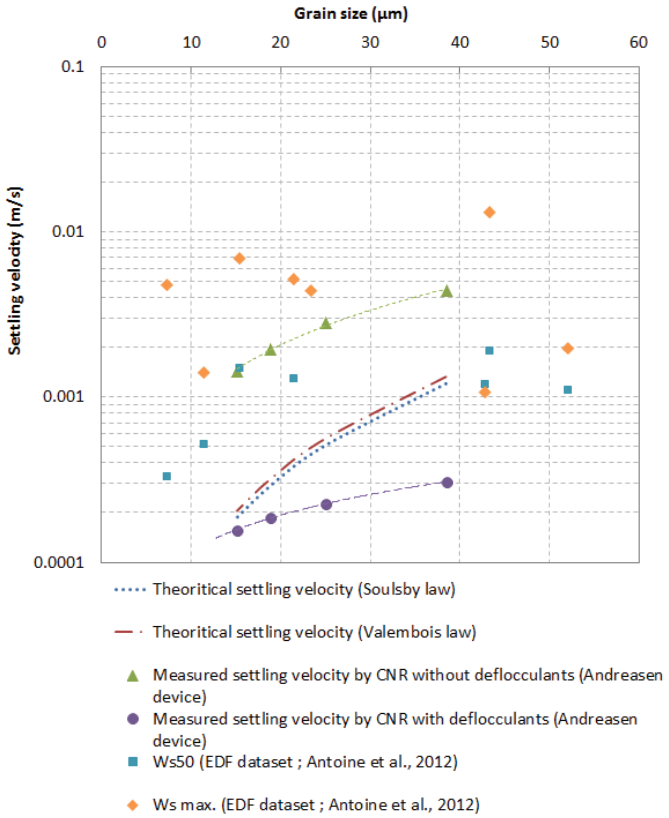

Figure 5. Settling velocities.

JET & EFA erodibility lab-tests (Jet Erosion Test & Erosion Function Apparatus) have been also conducted to determine the critical erosion shear stress (Table I) and the intensity of erosion depending on material.

TABLE I. Erosion PARAMETERS

	Sediment facies		
	Sand	**Silt**	**Clay**
Critical erosion shear stress τ_c (N.m^{-2})	0.2 - 0.3	0.7 - 2.5	4.0 – 7.0
Critical velocity (m.s^{-1})	0.2 - 0.3	0.3 - 0.7	1.0 - 1.6

IV. 3D MORPHO-DYNAMICS SIMULATION

A. *Numerical model*

The domain was 4 km long, integrating Champagneux dam and its reservoir, with the entry of the headrace channel (see Fig.4). To eliminate numerical instabilities, caused by sediment transport calculations, a derived mesh was generated excluding dry nodes (upper than 0.5 m water depth). The edge length was set to 20 m in the reservoir, but was decreased to [2-10] m nearest to the dam. The 3D model presented 10 horizontal levels describing a logarithmic profile refined near the bottom. Consequently the 3D grid comprised about 112,510 nodes and 193,050 elements.

The computational area presented 5 liquid boundaries. At the inlet, discharge and concentration measurements were

forced in TELEMAC-3D (V7P1 release). A discharge was imposed on each flap over gates of Champagneux dam. At the headrace channel outlet, water level was imposed.

The suspended load is solved by SEDI-3D whereas bottom evolution and bed-load transport are treated by SISYPHE. A time step of 2 seconds was chosen. The entire flushing process (12 days) was simulated.

B. Sediment transport, erosion and deposition modelling

Only cohesive sediments were set up in suspension with a constant profile over the depth which created an approximatively underestimation of 30% of the total concentration. Mixed size classes (sand and mud) were used to define the bottom (Fig. 6). Three different areas were defined depending on the fraction of sand/mud. Critical erosion shear stress depended on the percentage of each class. Deposition/erosion fluxes were defined by Krone & Partheniades laws [7] [8].

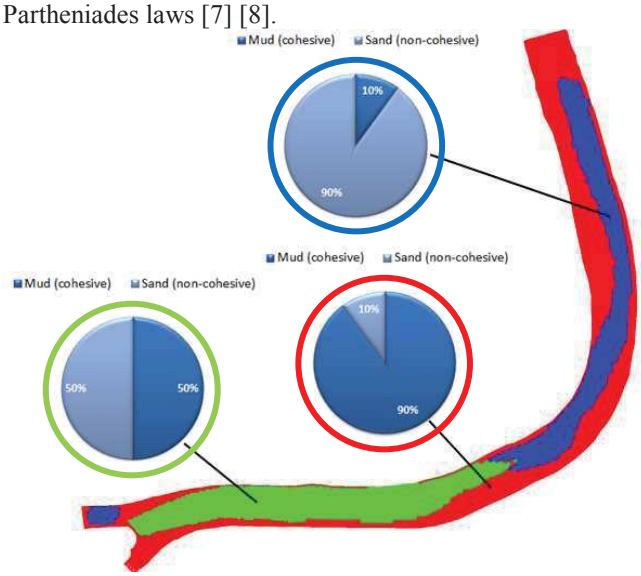

Figure 6. Map of mixed size classes (sand and mud).

Partheniades law gave erosion as a function of the effective stress and an erosion rate coefficient.

$$E = M\left(\frac{\tau}{\tau_c} - 1\right) \quad (1)$$

Where E = erosion rate (kg.m^{-2}.s^{-1}); M = Partheniades coefficient which is related to sediment erodibility (kg.m^{-2}.s^{-1}); τ_c = the critical erosion shear stress (N.m^{-2}). Krone law gave the probability of deposition where W_s = settling velocity (m.s^{-1}); C = concentration (g.L^{-1}); τ_d = the critical deposition shear stress (N.m^{-2}).

$$D = W_s C\left(1 - \frac{\tau}{\tau_d}\right) \quad (2)$$

C. Calibration step

Calibration data corresponded to the May 2016 eco-friendly flushing operation. First, the morpho-dynamic model had to be able to fit bathymetric trends and therefore average volume recording during past flushing events, which were around 75,000 to 200,000 m^3 in Champagneux whole reservoir (CNR, internal estimation by historical assessment). For 2016 flushing event, meanwhile bathymetry survey, a first approach was to estimate the volume deposited at about 300,000 tons.

Bottom evolutions were mostly impacted by the suspended load. In fact, only sand fraction was able to move with a low intensity under flush hydrodynamic conditions. ADCP profiles did not reveal any bed-load transport, but as we said before results were unfortunately not totally usable.

Focus was set on deposition rate variables, especially on τ_d and W_s. Comparing preferential deposition areas and hydraulic shear stress, a range of τ_d may be determined as [0.1-0.5] N.m^{-2}. The settling velocity parameter was set for a mean diameter of 10 µm with a theoretical law and compared with another simulation according to *in-situ* measurement. Several cases have been done to validate the morph-dynamic models on TELEMAC-3D (Table II).

TABLE II. DEPOSITION PARAMETERS

	Set 1	Set 2	Set 3	Set 4
Partheniades coefficient M (kg.m^{-2}.s^{-1})	2.10^{-5}	2.10^{-5}	2.10^{-5}	2.10^{-5}
Critical erosion shear stress τ_c (N.m^{-2})	6	6	6	6
Settling velocity W_s (m.s^{-1})	9.10^{-5}	9.10^{-5}	9.10^{-5}	9.10^{-4}
Critical deposition shear stress τ_d (N.m^{-2})	0.1	0.3	0.5	0.3

The time variation concentration was compared on downstream measurement sites previously described (Fig. 4). In the reservoir (#2), on the right bank, concentrations fitted the measured trend for sets 1, 2 and 3. Set 4 showed a very low concentration. This induced the reduction of the sediment advection (Fig. 7). Upstream of the dam (#3), model concentration was higher than field measures. It could be probably attributed to the NTU – g.L^{-1} transformation which presented an offset or there was too much diffusion in our model (Fig. 8).

Deposit volumes were computed for each simulation (Table III). The settings which had a lower settling velocity presented a lower deposition volume than the setting 4. Deposition areas changed according to the value of τ_d. A low value created a rising of the bed nearest banks. Conversely a high τ_d value allowed a larger deposition zone. Bottom evolution intensity was promoted by increasing the settling velocity (Fig. 9).

TABLE III. DEPOSITION VOLUME

	Set 1	Set 2	Set 3	Set 4
Deposition volume (m^3)	32,605	45,074	58,611	352,804

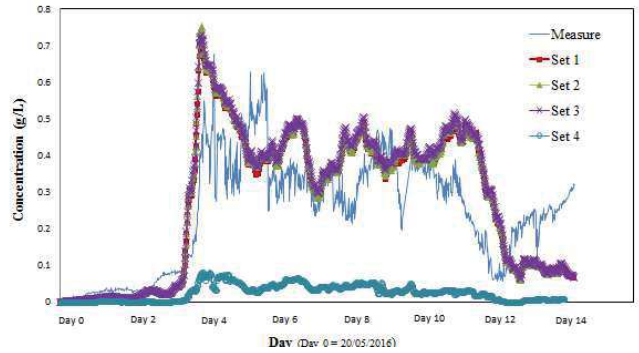

Figure 7. Time series of sediment concentration at station #2.

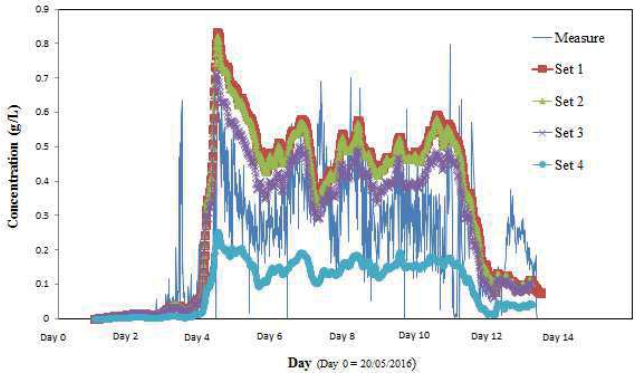

Figure 8. Time series of sediment concentration at station #3.

IV. RESULTS AND PERSPECTIVE

Results from the morpho-dynamic model showed a relative accurate correlation between calculations and measurements for sub-surface concentration. The total deposit volume was probably under the one expected but future bathymetry (*in progress*) will be able to specify volume estimation. Calibration of bed evolution and concentration were difficult due to the time variation and uncertainties of sediment parameters. Naturally, there was a large co-variance between the settling velocity, the concentration and the critical deposition shear stress. Likewise, the same phenomenon appeared while dealing with critical erosion shear stress and recent deposit. At the end of the flushing event (day 12), the concentration increased again. This peak may be correlated to the erosion of recent deposits creating "fluid mud" which was less compacted and presented a low critical erosion shear stress.

Ultimately, the model will evolve to reproduce more complex phenomena and deal with sediment dynamics by giving an input vertical concentration profile which will be able to evolve in time and change the settling velocity according to concentration.

V. CONCLUSION

A morpho-dynamic model, TELEMAC-3D/SISYPHE, was developed in order to study and reproduce the eco-friendly flushing event. As suspected, the sediment model required a comprehensive measurement dataset including sound lab-tests. A sensitivity analysis showed that the results were very influential to any variation of the parameters of Krone law. Deposition rate will indeed be more intensive according to the settling velocity and mean concentration. Deposition area depends on the critical deposition shear stress which, in our case, was estimated by locating the previous deposition area.

Further measurements such as the bathymetry resulting from the last flushing event will surely help to improve the calibration accuracy.

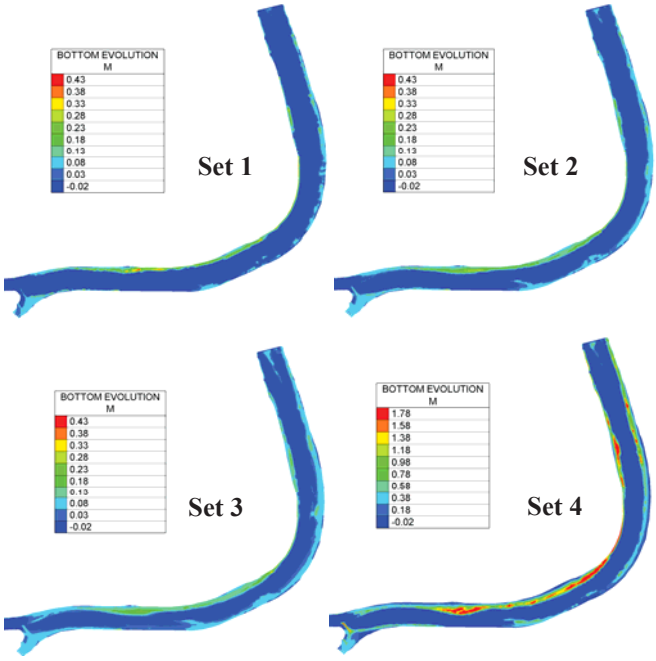

Figure 9. Bottom evolution at last frame for Set 1 to Set 4.

Figure 10.

VI. REFERENCES

[1] Alliau and al., Evaluating hydraulic conditions to favor sediment transport and erosion through a reservoir: the case study of Champagneux run-of-river dam on the Rhône River, accepted article for XXIIIrd TELEMAC-MASCARET User Conference, Paris, October 2016, 11-13th

[2] Kantoush, S. A. and Sumi, T., 2010. River morphology and sediment management strategies for sustainable reservoir in Japan and Europe Alps, Annuals of Disast. Prev. Res. Inst., Kyoto Univ., No. 53B

[3] Morris, G. L. and Fan, J., 1997. Reservoir Sedimentation Handbook: Design and Management of Dams, Reservoirs and Watersheds for Sustainable Use. New York: McGraw Hill.

[4] Fruchart, F. and Camenen B., (2012). Reservoir sedimentation: different type of flushing—friendly flushing example of Genissiat dam flushing. ICOLD International Symposium on Dams for a changing world 05/06/2012, Kyoto, Japan. 6 p.

[5] Peteuil and al., Sustainable management of sediment fluxes in reservoir by environmental friendly flushing: The case study of the Genissiat Dam on the upper Rhone River (France), 12th International Symposium on River Sedimentation, Septembre 2013 - Kyoto, Japon

[6] Partheniades, E. (1965). Erosion and deposition of cohesive soils. Journal of the Hydraulic Division, n°91, pp 105-139.

[7] Krone, R. B. (1962). Flume studies of the transport of sediment in estuarial shoaling processes. Technical report, Hydraulic Engineering Laboratory, University of Californian Berkeley.

Evaluating 3D hydraulic conditions to favor sediment transport and erosion through a reservoir: the case study of Champagneux run-of-river dam on the Rhône River, France

Damien ALLIAU, Magali DECACHARD, Carole WIRZ,
Christophe PETEUIL, Sylvain REYNAUD,
Compagnie Nationale du Rhône
Lyon, France
d.alliau@cnr.tm.fr

Antoine VOLLANT, Yannick BAUX
Optifluides
Villeurbanne, France

***Abstract*— By decreasing the velocity of the flow and turbulence, reservoirs controlled by dams are likely to force inflowing sediments to settle. This process can be more or less temporal and intensive, depending on particle size and the reservoir characteristics. To reduce the reservoir sedimentation and prevent a disruption of sediment continuity, one possible option for dam operators is to recover favorable flow conditions either for routing inflowing sediments or to remobilize previous deposits. In the case of cohesive sediments, one of the main challenges to deal with is that deposition and erosion thresholds are often radically different as a result of deposit consolidation. For the last 30 years, the Champagneux run-of-river dam (Rhône River, France) has experienced significant deposition processes affecting mainly fine sediment fractions. As a dam operator, CNR has wanted to determine hydrodynamic conditions to favor transport and erosion of fine fractions of sediment. In fact, this simple question covers many points of complexity, and thorough analyses on shear stress evaluation have been conducted by CNR. The purpose of this communication is to present hydraulic methodology and results to define those conditions in the case of the Champagneux dam.**

The evaluation of bottom shear stress throughout the reservoir and for different hydrological and operating conditions relies on a hybrid approach combining (1) a TELEMAC-3D free surface numerical model of the whole reservoir, (2) a physical scale model 1/35 limited to the downstream part of the reservoir and (3) a FLUENT CFD numerical model of the dam area. Even if those 3 models have been initially deployed in the frame of a more general project, this experience has shown that such a comprehensive approach is required to obtain relevant values of the shear stress and flow velocity close to the river bottom. Final goal is to achieve a correlation of numerical results with critical thresholds coming from core sampling lab-tests. For the dam operator, such a comprehensive survey provides useful information to enhance the management of the reservoir and feedback obtained will contribute to an optimization of the methodology for other similar cases.

I. INTRODUCTION

By decreasing the velocity of the flow and turbulence, reservoirs controlled by dams are likely to force inflowing sediments to settle. This process can be more or less temporal and intensive, depending on particle size and the reservoir characteristics [2]. To reduce the reservoir sedimentation and prevent a disruption of sediment continuity, one possible option for dam operators is to recover favorable flow conditions either for routing inflowing sediments or to remobilize previous deposits [1]. In the case of cohesive sediments, one of the main challenges to deal with is that deposition and erosion thresholds are often radically different as a result of deposit consolidation [3]. For the last 30 years, the Champagneux run-of-river dam (Rhône River, France) has experienced significant deposition processes affecting mainly fine sediment fractions. One essential challenge that CNR has to deal with as the dam operator is to determine the hydrodynamic conditions likely to ensure the remobilization of fine-grained deposits.

To achieve this objective, the approach favored by CNR relies on a hybrid model to quantify the shear stress values (τ) corresponding to different hydrologic and operating conditions. It exists several ways to know this shear stress near the bottom. On the one hand the theoretical expression of shear stress τ in turbulent boundary layer at equilibrium can be calculated with …:

$$\tau = \rho\nu\frac{\partial U}{\partial z} - \rho < u'w' > \qquad (0)$$

With ρ water density, ν kinematic viscosity, U velocity field vector and u', w' average fluctuation of velocity.

- Measurement of speed fluctuations by vertical Acoustic Doppler Velocimetry (ADV): the shear stress is related to measures *u'* and *w'* for different *z*.
- Measurement of average velocity by vertical ADV: the shear stress is connected to vertical gradient *U* (introduced in this article).

On the other hand, the development of Navier-Stokes equations with free surface assumption leads to the theoretical relation between the local hydraulic radius R_h and the energy slope J (requires measuring upstream and downstream average speed).

$$\tau = \rho g R_h J \qquad (1)$$

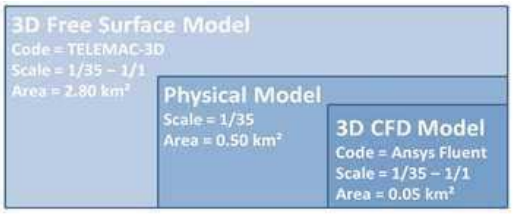

Figure 1. Hybrid modelling concept

Such issue is however far from being trivial and requires addressing following concerns:

- Even if measurements in the field should be possible, these methodologies rely on a uniform regime, which is never obtained *in situ*.
- Numerical models have to be calibrated by physical model to determine realistic shear stress values and compare it to critical shear stress values obtained from lab test on undisturbed core samples.

This communication focuses firstly on the hybrid modelling approach deployed for obtaining relevant shear stress values in the reservoir and bounding uncertainties for its evaluation. Then TELEMAC-3D methods for shear stress values are compared with outputs from Computational Fluids Dynamics (CFD) FLUENT.

II. HYBRID MODELLING

A. Overall context and methodology

First it should be specified that the results presented hereafter were obtained in the frame of a more general project which included in particular following investigations: characteristics of flow dynamics in a diversion area, evolution of spillway conveyance according to various gate openings, impact of deposits on the spillway capacity, spatial heterogeneity of reservoir deposits, and susceptibility to erosion of deposits. Due to the multiple objectives of the project, deploying a physical model only didn't appear sufficient for addressing those complex issues. Consequently, the option considered consists in a hybrid modelling approach combining (1) 3D numerical modelling of the whole reservoir, (2) a physical model at 1:35 corresponding to the downstream part of the reservoir and (3) a 3D local numerical model representing the dam area (Fig. 3). The objectives and the main principles of each model are specified in next paragraphs.

B. 3D numerical modelling of the whole reservoir

TELEMAC-3D (T-3D) is the large-scale model deployed for the whole reservoir. This model allows a suitable representation of the flow velocity distribution induced by the river bend upstream of the dam. T-3D provides also upstream boundary conditions to the physical and CFD models with regard to the flow velocity. Outputs provided correspond to situations ranging from low flows to the design flood. One of the main interests of T-3D is to calculate bottom shear stress values in the whole reservoir and with a high resolution. For shear stress calculation, a proper calibration of the vertical velocity profile is required and can be obtained from experimental measurements provided by the physical model (see Fig. 3).

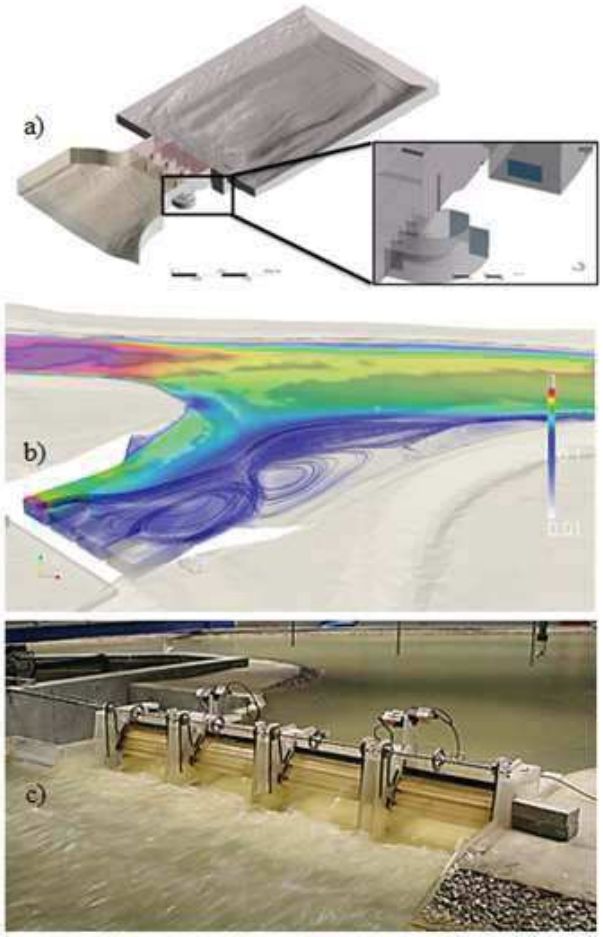

Figure 2. Hybrid model consisting of a) view of 3D CFD Fluent mesh, b) TELEMAC-3D velocity fields and c) downstream view of physical model

T-3D solves the Navier-Stokes averaged and unsteady equation (URANS) for a single incompressible fluid (including the 3 components of the average flow velocity field). The numerical method used to discretize the equations is the Finite Element Method. Friction (wall laws) includes source terms.

The domain is 4 km long, integrating Champagneux dam and its reservoir, and the entry of the headrace channel. The edge length of mesh was set to 20 m in the reservoir, but was decreased to [0.5-2] m nearest to the dam. The 3D model presented 10 horizontal levels whose spacing is ruled by a logarithmic profile refined near the bottom. Consequently the 3D grid comprises about 395,000 nodes and 776,190 elements.

The computational area presented 5 liquid boundaries. At the inlet, discharge measurements were forced in TELEMAC-3D (V6P2 release). A discharge was imposed on each 4 gates of Champagneux dam. At the headrace channel outlet, water level was imposed. Turbulence model chosen is k-ϵ, with 2

kinds of wall law (smooth friction with Reichard law, and rough friction with Nikuradse law).

C. *Physical model at 1:35*

The physical model (PM) is the local model used for determining with an appropriate accuracy the hydrodynamic flow conditions nearby dam area. Discharges considered range from frequent floods to the design flood. Investigations performed concern particularly the spillway discharge coefficient and an evaluation of its possible evolutions due to the sediment dynamics. The physical model is also used to measure the vertical velocity profile (Fig. 3) with Acoustic Doppler Velocity (ADV), to calibrate the turbulence model of T-3D and evaluate precisely the head loss due to the dam crossing. Model and natural free surface flow similarities are guaranteed according to a Froude similitude.

D. *3D numerical model of the dam area*

FLUENT (CFD) is the micro-local model deployed to simulate a broad range of flow situations with respect to the spillway gates opening. The code solves 3D URANS equations with finite volume numerical method. The domain comprises air and water so a transport equation on volume fraction is added according to the Volume of Fluid (VOF) method. Compared to T-3D, the main benefits of CFD are to (1) allow a multiphase modelling and directly account for air/water interactions at the free surface, (2) limit assumptions concerning the flow regime of the gates as the downstream of dam is simulated, and (3) obtain comprehensive modelling results with a very high spatial resolution. In the frame of this project, scale effects have been also investigated to evaluate if they can be reasonably neglected.

E. *Modelling strategy followed for minimizing uncertainties*

First, it should be kept in mind that the geometric data of the models have been unchanged during a given simulation so as to better highlight and understand the hydrodynamic processes. A mobile bed numerical model is currently operated to take into account sedimentary processes from a more detailed manner. It is also essential to note that the modelling strategy relies on cross-validation of models which requires a strict coordination between modellers throughout the calibration process. The model construction is indeed based on an iterative approach meaning in particular that assumptions specific to a given model have to be validated from outputs provided by the other ones. Such process is obviously constraining but acceptable with regard to the hydraulic safety issues at stake. In order to take full advantage of the hybrid model and facilitate interactions as well as subsequent comparisons, a formal methodology has been followed:

- All models use the same input data such as bathymetry, flow rates and gate openings observed during calibration events… Although time-consuming in the preliminary steps of the project, such approach provides huge benefits for the analysis of results in the ultimate stages of the project.
- The calibration of models is performed simultaneously and according to the same time scheme for achieving effective interactions and possibly adapting the methodology to unexpected concerns.
- The calibration process includes following steps: (1) a blind calibration of physical model and 3D numerical models using field data measured with Acoustic Doppler Current Profiler (ADCP), (2) an inter-comparison of results obtained for a given situation and (3) a reverse calibration of 3D models if significant discrepancies are eventually highlighted.
- The post processing work is performed on a common set of output parameters measured exactly at the same locations and all simulation results are compared at scale 1:1.

III. SHEAR STRESS EVALUATION BY AVERAGE VELOCITY VERTICAL PROFILES

A. *Hybrid modelling phase*

Determining the bottom shear stress is a very challenging issue, especially owing to the impossibility for measuring this parameter in situ. This parameter has been evaluated from an indirect manner using experimental observations performed on the physical model. The option considered consists in determining the friction velocity U^* from the shape of the vertical profile of velocity. In the frame of this project, the velocity profile has been measured with a Vectrino II (ADV), which can be deployed for water depth above 1 mm at 1:35. The scale 1:35 has been chosen indeed for minimizing uncertainties and this option leads finally to obtain a standard deviation of 2% when simulation results are upscaled to 1:1.

Those experimental data has been also used for validating the ability of the 3D numerical models to represent properly the whole velocity field of the flow obtained by the complete resolution of URANS system. In addition, qualitative observations demonstrate the convergence of the general flow pattern for the 3 models, with regard to the position of the recirculation cells in particular.

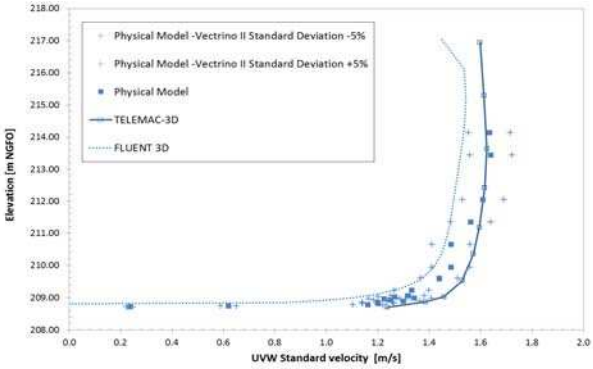

Figure 3. Inter-comparison of vertical profiles of velocity

During the calibration process, the wall law (friction coefficient) and the type of turbulence model (by an assessment of vertical evolution of velocity) have been adapted when required. A series of tests were also performed to

demonstrate that options using either a Reichard law (smooth friction plan)

$$\frac{U}{U^*} = \frac{1}{\kappa}\ln(1+\kappa y^+) + 7{,}8\left(1 - e^{\frac{y^+}{11}} - \frac{y^+}{11}e^{-0{,}33y^+}\right) \quad (2)$$

where κ=0.41 is the Von Karman constant, y^+ is the dimensionless distance to the wall, or a Nikuradse law (rough friction regime) lead to much more accurate results compared to calculation based on an vertically-averaged velocity depending on a Strickler friction law. These friction laws suppose that the speed at the wall on a mesh is not quite taking to the wall (otherwise it would be null) but it is taken into the boundary layer at a distance *y*.

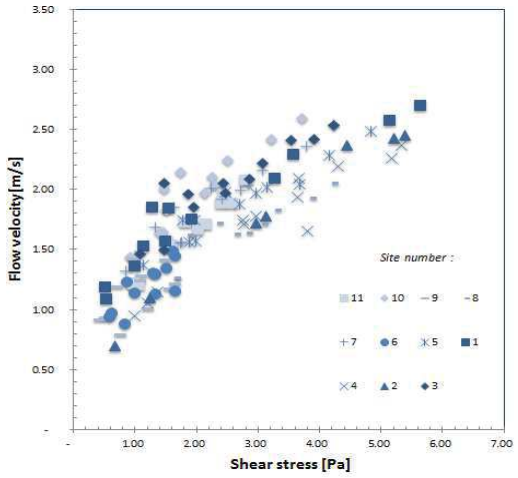

Figure 4. Flow velocity vs. shear stress at core sampling sites

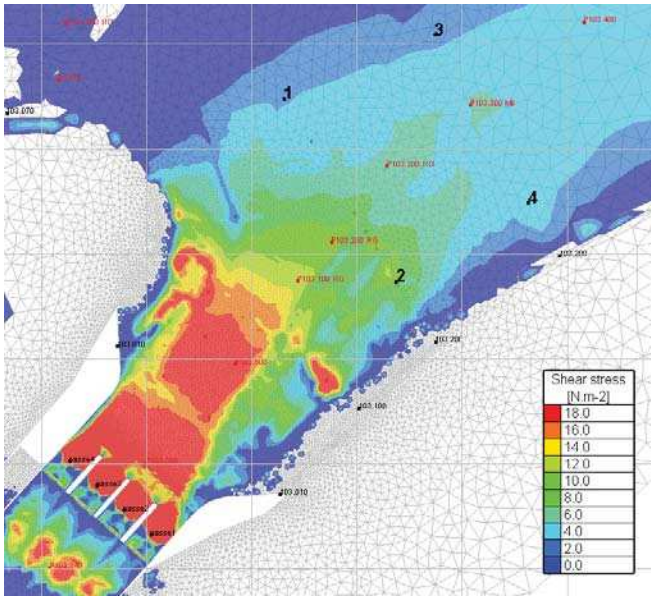

Figure 5. Shear stress distribution from T-3D calculations and location of core samples considered for erosion tests.

Concerning the maximum velocity simulated with T-3D, the main trends highlighted correspond to a −7% underestimation upstream of the dam and a +10% overestimation in the close vicinity of the spillway. The overall results are still comprised in a +/- 10% interval which is quite satisfactory. Scale effects and sensitivity tests on calibration parameters and modelling options (especially with regard to wall laws, friction regime, turbulence model, meshing…) have been also performed and results obtained lead to consider that the uncertainty on shear stress values is near 25%. Those investigations demonstrate that the major benefits of the hybrid approach deployed are (1) the possibility to calculate relevant bottom shear stress values in the entire reservoir, (2) with a high resolution and a relatively good level of confidence and (3) by taking into account a large panel of hydraulic situations (see Fig. 4 and Fig. 5).

B. Validation cases by experiment

Simulation results from T-3D were also used for comparing the *in situ* sediment dynamics understanding in the reservoir. Investigations performed have mainly focused on the possible relations between the reservoir deposits distribution and the flow pattern. In many areas, the deposition of non-cohesive particles observed in-situ is clearly explained by the limitations due to the transport capacity of the flow. The calculation of the Rouse number, which determines how a particle of a given size is likely to be transported by the water flow, provides indeed consistent results compared with the distribution of deposits within the reservoir. Similar conclusions have been obtained by comparing the sedimentation pattern with the distribution of the coarsest particles likely to be transported as bed-load.

IV. SPECIFIC ANALYSIS BASED ON CALCULATION METHOD OF SHEAR STRESS

Qualitatively, flow patterns are identical between TELEMAC-3D and FLUENT but there is a fundamental discrepancy for calculation method of shear stress value.

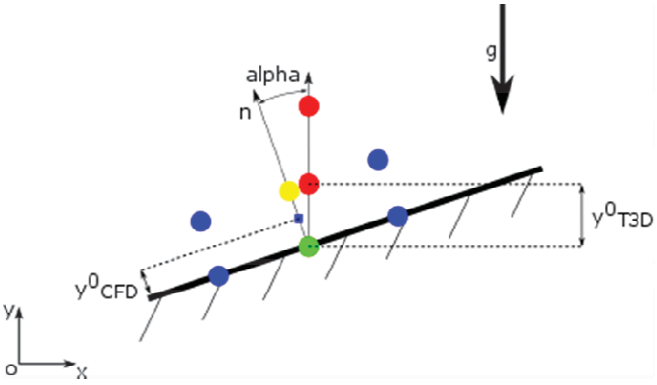

Figure 6. Diagram of positioning of computing nodes for the T3D solver (red) and FLUENT solver (blue) to calculate the stress at the wall (green).

A source of error is also the numerical method of calculating the friction velocity compared to the meshing method of numerical models. As shown in Fig. 6, T-3D has not its nodes cells directly on the normal to the walls because the extrusion of the mesh is in the direction of gravity (except in places where the normal to the sides of the river are collinear with the vertical). The definition of stress at a wall requires it to be proportional to the velocity gradient calculated in the

direction normal to the wall. Reichard's law in Eq. (2) connects the shape of the velocity profile at the wall stress: the velocity profile is fully determined by the value of the speed of the first point and the distance to the wall. The solver T-3D assimilate the height of the first layer point y_{T3D} to the distance along the normal to the wall and the velocity value of this as being the point of the yellow dot.

A retrospective correction would assume that the velocity calculated at the first node is similar to the yellow dot node and the distance to the wall is corrected by y_{T3D} cos (α), where α is the angle between the normal to the wall with the vertical direction. The shear stress would be increased as the same rate would be closer to reaching the wall. An estimate value of the relative error submitted is made by calculating the same velocity to the first cell wall of the two constraints generated by a distance y_{T3D} cos (α) and y_{T3D}. The relative error plotted in Fig.7 is therefore:

$$\frac{\left(\tau(y^0_{T3D}cos(\alpha), U) - \tau(y^0_{T3D}, U)\right)}{\tau(y^0_{T3D}, U)} \quad (3)$$

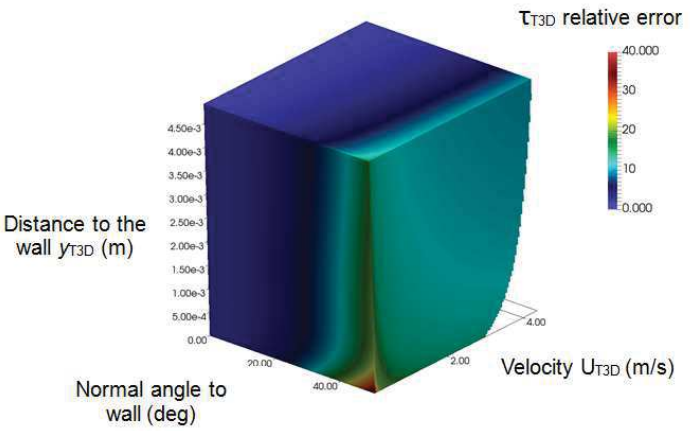

Figure 7. Relative error between the corrected stress τ (y_{T3D} cos (α), U) and stress calculated by T-3D based on a velocity range in the first compute node, the distance to the wall of the first node and the angle of the normal to the α wall.

In this parameter range and the conditions of distance to the dimensionless wall $y^+ > 1$ and wall stresses below 50 N.m^{-2}, the stress calculated by T-3D underestimates maximum of 5% of the corrected stress τ (y_{T3D} cos (α), U) for angles less than 20°, 10% for angles less than 30° and up to 40% for angles up to 50°. This source of underestimating shear stress seems to be relevant in this topic as it would mainly take place in the areas where deposits are located.

V. PERSPECTIVES

The Preston pipe method is an alternative way of directly measuring the bottom shear stress [4]. Shear stress rate U^* is connected to the difference between total and static pressure measured near the bottom. Ongoing tests at CNR laboratory based on pressure gradient measurements performed at scale 1:35 may help decreasing significantly the bounds of current uncertainties, in particular for gradually varied regime.

VI. CONCLUSION

The hybrid modelling approach deployed in the Champagneux dam case combines one physical model and two 3D numerical models used for assessing the erosion hazard of reservoir deposits. Such option is very constraining and challenging but provides unparalleled benefits for evaluating, with a high resolution and a relatively good level of confidence, relevant bottom shear stress values in the entire reservoir for a large panel of hydraulic situations. The models calibration is based on a cross-validation strategy that requires a formal organization and a strict coordination of modelling activities. It's worth noting in particular that all models use the same input data and are calibrated simultaneously and according to the same time scheme. Moreover, the post processing work is performed on a common set of output parameters measured exactly at the same locations and all simulation results are compared at scale 1:1.

It is a major importance to remind that shear stress library (for a large range of discharge) is only assess throughout numerical calculation of friction velocity (T-3D) at scale 1:35 to 1:1 or by wall law (FLUENT) at scale 1:35. Even if values do not present discrepancy, it is crucial to perform some complementary investigations to address properly sediment related issues (morphodynamic simulations):

- To validate numerical method by comparison with a direct measure of shear stress (see paragraph V.) at scale 1:35 in gradually varied regime.
- To transpose methodology from scale 1:35 to 1:1 limiting uncertainties.

Finally, the comparison between erosion lab-tests and simulations results will lead to assess the erosion hazard of reservoir deposits. As a first approach, the diagnosis performed is based on the calculation and the spatialization of the relative deviation between the critical shear stress and the effective shear stress corresponding to a given flood event. Complementary investigations considering an approach based on a 3D hydro-sedimentary model will currently perform to improve this preliminary approach.

REFERENCES

[1] Kantoush, S. A. and Sumi, T., 2010. River morphology and sediment management strategies for sustainable reservoir in Japan and Europe Alps, Annuals of Disast. Prev. Res. Inst., Kyoto Univ., No. 53B

[2] Morris, G. L. and Fan, J., 1997. Reservoir Sedimentation Handbook: Design and Management of Dams, Reservoirs and Watersheds for Sustainable Use. New York: McGraw Hill.

[3] van Rijn, L.C., 1993. Principles of Sediment Transport in Rivers, Estuaries and Coastal Seas. Aqua Publications, 386 pp.

[4] Patel, V.C., 1965, Calibration of the Preston tube and limitations on its use in pressure gradients. Journal Fluids Mech. Vol 23 part I, pp 185-208.

Improving TELEMAC on a simple test case to simulate runoff and erosion generation

Florent Taccone,
Germain Antoine
and Nicole Goutal
Laboratoire National d'Hydraulique et Environnement, EDF R&D
Laboratoire d'Hydraulique Saint-Venant
6 Quai Watier 78400 Chatou France
Email: florent.taccone@gmail.com

Olivier Delestre
Laboratoire de Mathématiques J.A. Dieudonné
UMR 7351
École Polytech Nice-Sophia
Université de Nice-Sophia Antipolis
Parc Valrose 06108 Nice France

***Abstract*—This paper focuses on how to ensure the robustness of the resolution of Shallow Water Equations in the TELEMAC2D computation code in the case of rain induced runoff on steep slopes. To reproduce these conditions, a straight channel with a variable slope on which drops a constant rain is defined. With this test case, a comparison between the simulated discharge at the outlet and an analytical solution of the Shallow Water Equations for the rising part of the hydrograph and the plateau has been done. By stopping the rain in the middle of a simulation, numerical results and an analytical solution of the kinematic wave approximation were confronted during the emptying of the domain.**

Limitations of the numerical resolution are highlighted with the finite volume schemes. Improvements were made to better represent the rainfall-runoff responses, like another method of hydrostatic reconstruction [7] which has been implemented. Then, the model is extended to pollutant transfers and sediment transport in suspension. These results provide a strong basis for future application of modeling erosion at the watershed scale.

I. Introduction

The sediment transfers at the watershed scale involve several processes, because of the heterogeneity of the soil, but also the different flow regimes due to the complex topography of the field and the time and space variability of the meteorological conditions. In the mountainous regions, the filling of reservoirs is an important issue in terms of efficiency and environmental acceptability for producing hydro-electricity. Thus, the modelling of the sediment tranfers on highly erodible watershed is a key challenge from both economic and scientific points of view. A physically-based representation provides an explicit representation of the hydraulic and sedimentary variables, but needs several parameters and a fine discretization of the domain. The erosion processes being heavily reliant on the flow characteristics, we must have a robust and accurate representation of hydraulic dynamics. A simple test case has been defined in order to evaluate the different resolution methods of the Shallow Water equations with TELEMAC2D, in the particular case of steep slopes and shallow water depths.

One of the main difficulties is to have a numerical scheme able to represent correctly the hydraulic transfers, preserving the positivity of the water depths, dealing with the wet/dry interface and being well-balanced (in the sense of [13]) meaning preserving the hydrostatic balance of a lake at rest. Few schemes verifying these properties exist, and their accuracy still need to be evaluated in the case of rain induced runoff on steep slopes. Moreover, it is necessary to represent the suspension of tracers and sediments in the flow, from the hillslopes to the outlet of the watershed, with as little dispersion as possible in supercritical flow. In TELEMAC2D, several advection schemes have been recently implemented ([15] and [14]) to overcome this problem for river flow applications and need to be tested for runoff simulations. Subsequently, it is important to figure out the mesh and the hydraulic scheme effects on the erosion generation to anticipate the scaling effect for a real watershed application.

In this paper, a straight channel test case, with a variable slope, on which drops a steady rain is used, which represents what can be observed in a mountain watershed context. Different finite volume schemes are analyzed, and more particularly their bottom source term discretization. Then, the advection of passive tracer is tested in this situation to evaluate its efficiency. Finally, SISYPHE is used to represent the soil erosion on the test case and a study of the effect of the hydraulic scheme on rill generation has been realized.

II. Materials and Methods

In this work, the simulations have been performed with the V7P1R1 version of TELEMAC2D and SISYPHE.

A. Presentation of the test case

Following the work of [16], a test case on a straight channel of dimensions 4.04 X 0.115 m is created. On this domain, a steady rain, with an intensity of 25 mm/h, is applied during 100 s. The discharge at the outlet of this channel is observed. The duration of the simulation is 200 s, the first 100 seconds describing the rise of the hydrograph and the constant value and the last 100 seconds the emptying of the domain. The spatial discretization of the channel is a triangular mesh with a length of 1 cm. The choice of this test has been motivated by the fact that [9] gives analytical solutions for the discharge. To avoid effects of the upstream wall boundary, a 5 meters channel is created and the rain starts to fall 0.96 m away.

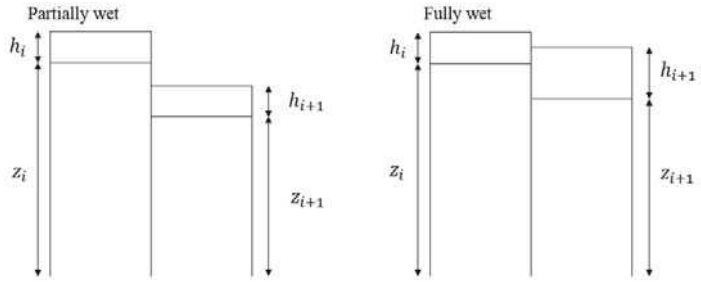

Fig. 1: Illustration of the partially wet and fully wet regimes at the interface of two cells

B. Overland flow simulation

To simulate rain induced runoff, TELEMAC2D solves the Shallow Water equations which are:

$$\frac{\partial U}{\partial t} + \frac{\partial F(U)}{\partial x} = S, \tag{1}$$

where $U = (h, hu)$, $F(U) = (hu, hu^2 + gh^2/2)$ and $S = (R, -gh(\partial_x z + S_f))$ with h the water height in m, u the flow velocity in m/s, g the gravity constant in m/s^2, R the rain intensity in m/s, z the bottom elevation in m and S_f the friction slope. For that, the following explicit finite volume scheme is used:

$$U_i^{t+1} = U_i^t - \frac{\Delta t}{\Delta x}(F_{i+1/2}^t - F_{i-1/2}^t) + \frac{\Delta t}{\Delta x} S_i, \tag{2}$$

where $F_{i+1/2}^t = F(U_{i+1/2+}, U_{i+1/2-})$ is the numerical flux at interface $i+1/2$ and $S_i = (R_i, s_{i+1/2-} + s_{i-1/2+})$ are the source terms. The friction slope is added to the scheme (2) by a semi-implicit treatment (see [12], [5] and [10]). It follows a Chézy's law where the coefficient is set to 30 m$^{1/2}$/s in this case.

Concerning the bottom source term discretization, one can use a hydrostatic reconstruction method and define the intermediate states $U_{i-1/2+} = (h_{i-1/2+}, h_{i-1/2+}u_i)$, $U_{i+1/2-} = (h_{i+1/2-}, h_{i+1/2-}u_i)$, $s_{i-1/2+}$ and $s_{i+1/2-}$. The classical hydrostatic reconstruction presented by Audusse *et al.* [1] gives:

$$\begin{aligned} h_{i-1/2+} &= \max(h_i + z_i - \max(z_{i-1}, z_i), 0), \\ s_{i-1/2+} &= \tfrac{g}{2}(h_i^2 - h_{i-1/2+}^2), \\ h_{i+1/2-} &= \max(h_i + z_i - \max(z_i, z_{i+1}), 0), \\ s_{i+1/2-} &= \tfrac{g}{2}(h_{i+1/2-}^2 - h_i^2), \end{aligned}$$

while a new reconstruction method introduced by Chen and Noelle [7] gives:

$$\begin{aligned} z_{i+1/2} &= \min(\max(z_i, z_{i+1}), \min(h_i + z_i, h_{i+1} + z_{i+1})) \\ h_{i-1/2+} &= \min(h_i + z_i - z_{i-1/2}, h_i), \\ s_{i-1/2+} &= \tfrac{g}{2}(h_i - h_{i-1/2+})(z_{i-1/2} - z_i), \\ h_{i+1/2-} &= \min(h_i + z_i - z_{i+1/2}, h_i), \\ s_{i+1/2-} &= \tfrac{g}{2}(h_i + h_{i+1/2-})(z_i - z_{i+1/2}). \end{aligned}$$

Based on the definition given by [7], a fully wet and a partially wet regime are distinguished at the interface of two cells. The figure 1 illustrates these regimes. The Audusse *et al.* [1] and Chen and Noelle's [7] hydrostatic reconstruction are computing exactly the same source term for the fully wet case. The Chen and Noelle's method modifies the source term in the partially wet case to better take into account the slope effect.

An alternative to the hydrostatic reconstruction, presented by Berthon and Foucher [3], consists in modifying the scheme (2) like:

$$U_i^{t+1} = U_i^t - \frac{\Delta t}{\Delta x}(X_{i+1/2}F_{i+1/2}^t - X_{i-1/2}F_{i-1/2}^t) + \frac{\Delta t}{\Delta x} S_i,$$

with $X_{i+1/2}^k = \begin{cases} \frac{h_i}{h_i+z_i} \text{ if } F_{i+1/2}^t > 0 \\ \frac{h_{i+1}}{h_{i+1}+z_{i+1}} \text{ elsewhere} \end{cases}$. The intermediate states become:

$$\begin{aligned} h_{i-1/2+} = h_{i+1/2-} &= h_i + z_i, \\ s_{i-1/2+} + s_{i+1/2-} &= \tfrac{g}{2} H_{i-1/2} H_{i+1/2} (X_{i+1/2} - X_{i-1/2}) \end{aligned}$$

with $H_{i+1/2}^k = \begin{cases} h_i + z_i \text{ if } F_{i+1/2}^t > 0 \\ h_{i+1} + z_{i+1} \text{ elsewhere} \end{cases}$.

The numerical fluxes are calculated with the HLLC method introduced by [23] and applied to the Shallow Water equations in [22].

C. Analytical solutions

[9] describes analytical solutions of the discharge at the outlet of the domain of the Shallow Water equations (1) for the rising part of the hydrograph and the constant value, and a kinematic wave approximation solution (3) for the complete problem. This approximation writes:

$$\frac{\partial h}{\partial t} + \frac{\partial hu}{\partial x} = P, \ \frac{\partial z}{\partial x} = -S_f \tag{3}$$

and the relative error between solutions of (1) and (3) is inferior to 1% for the rise of the hydrograph and the plateau for a slope superior to 1% on this test case. Using the exact solution of (1) for the 100 first seconds and the exact solution of (3) for the emptying of the domain, it is possible to compare the precision of the schemes.

D. Passive tracer and sediment transport

As described in [21], the suspended sediment transport is governed by the advection equation:

$$\frac{\partial hC}{\partial t} + \frac{\partial huC}{\partial x} = E - D, \tag{4}$$

with C the volumic concentration of sediment in the flow, E the erosion flux in m/s and D the deposition flux in m/s calculated with the classical Krone-Partheniades law with cohesive sediments. In each simulation, the bed is considered uniform, with one class of sediment. To simulate soil erosion with SISYPHE, the following parameters are chosen:

- Partheniades coefficient: 10^{-3} m/s,
- Critical erosion shear stress: 0.05 Pa,
- Critical deposition shear stress: 0.05 Pa,
- Sediment diameter: 40 μm,
- Skin friction coefficient: 1.

The passive tracers are simulated with the continuity equation (4) without source terms. To solve this equation, the LIPS

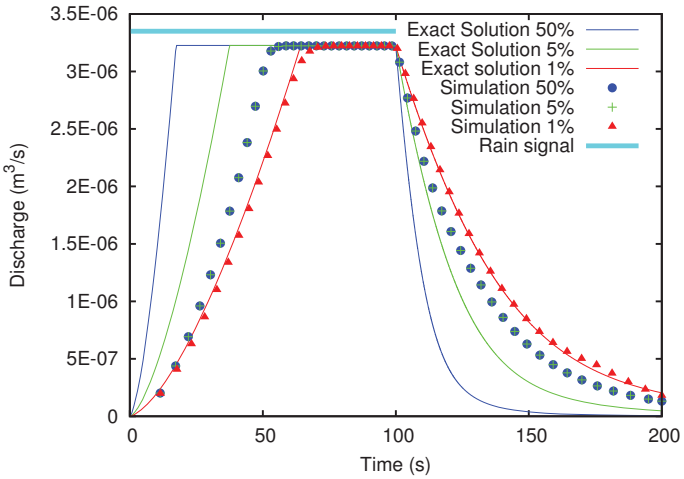

Fig. 2: Discharge (m^3/s) at the outlet of the domain during 200 s, comparison between simulation and analytical solution with the Audusse *et al.* reconstruction [1]

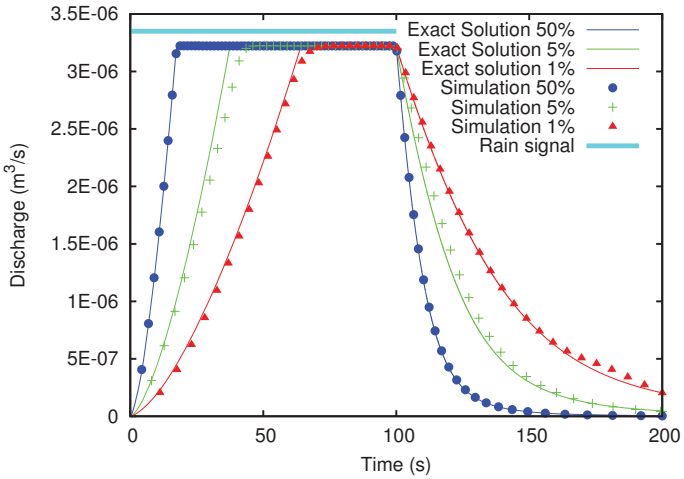

Fig. 3: Discharge (m^3/s) at the outlet of the domain during 200 s, comparison between simulation and analytical solution with the Chen and Noelle's reconstruction [7]

scheme has been used with three corrector steps (see [15]) as well as the ERIA scheme (see [14]), for their ability to deal with vacuum states.

III. Results

A. Hydraulic tranfers

The behaviour of the schemes are compared to the analitycal solution to compare their accuracy in the case of runoff with shallow water depths and steep slopes.

Figure 2 presents the discharge at the outlet with the classical hydrostatic reconstruction (Audusse *et al.* [1]). This scheme presents a limitation for steep slopes. Indeed, the results for the 5% and 50% slopes are identical. Moreover, for the 1% slope simulation, an irregularity is observed during the emptying of the domain after 160 s.

With the Chen and Noelle's [7] hydrostatic reconstruction, the discharges at the outlet are closer to the analitycal solutions. The figure 3 presents these results. This method corrects the slope limitation observed previously. However, there is a lag between the simulation results and the exact solution for the 5% slope and the irregularity at the end of the simulation for the 1% slope is more important.

The third scheme introduced by Berthon and Foucher [3] has been implemented in TELEMAC2D and tested. The figure 4 shows the results of the simulations with this scheme. This method is very efficient to solve the Shallow Water equations in this case. Nevertheless, this scheme has difficulties to treat the dry zones. Indeed, figure 5 shows aberrant velocities at the wet/dry interface with the Berthon and Foucher's scheme [3]. To limit that effect, the fluxes between wet and dry cells has been calculated with the Chen and Noelle's scheme, and this modification improves the treatment of vacuum states, as it is shown in figure 6. This modification improves the results on this test case but does not ensure a better equilibrium of the scheme in other configurations. The figure shows also that the boundary condition accelerates the flow significantly with

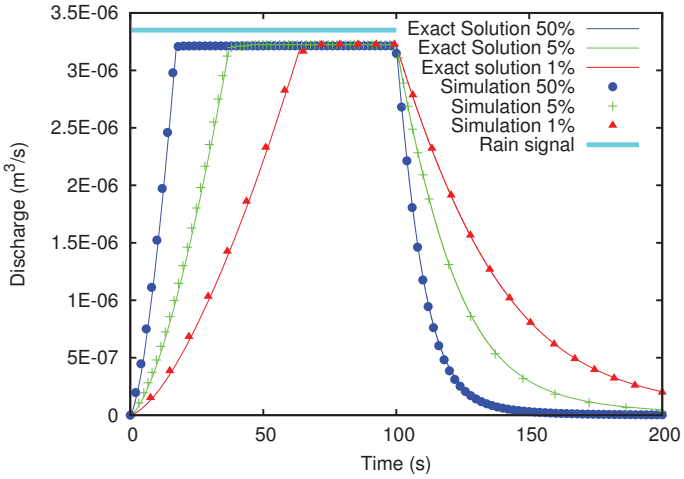

Fig. 4: Discharge (m^3/s) at the outlet of the domain during 200 s, comparison between simulation and analytical solution with the Berthon and Foucher's scheme [3]

the Berthon and Foucher's scheme [3] but it has been tested in every configuration that the downstream boundary does not impact the hydraulic results, shifting it several meters far from the discharge measurement, or creating a break in slope to accelerate the flow at the end of the channel.

To evaluate the precision of each scheme, table I shows the relative error of the computed discharges at the outlet compared with the analytical solution of the shallow water equation during the first 100 second of the simulations. The emptying of the domain is not taken into account because the exact solution of the kinematic wave system (3) is only an approximation of the Shallow water equations (1) solved numerically. The error is calculated by comparing the simulated value of the discharge q_s and the exact solution q_e at each second, with the relation:

$$Err = \frac{\Sigma_{i=1}^{100} \frac{|q_s - q_e|}{q_e}}{100}.$$

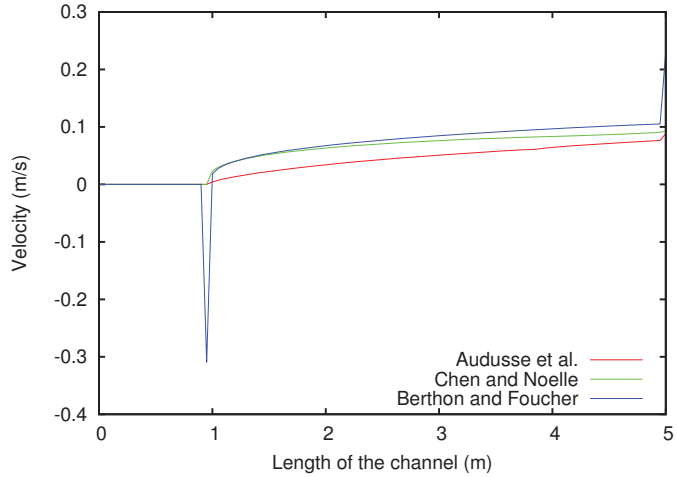

Fig. 5: Velocities (m/s) along the channel depending on the chosen scheme for the 5% slope simulation

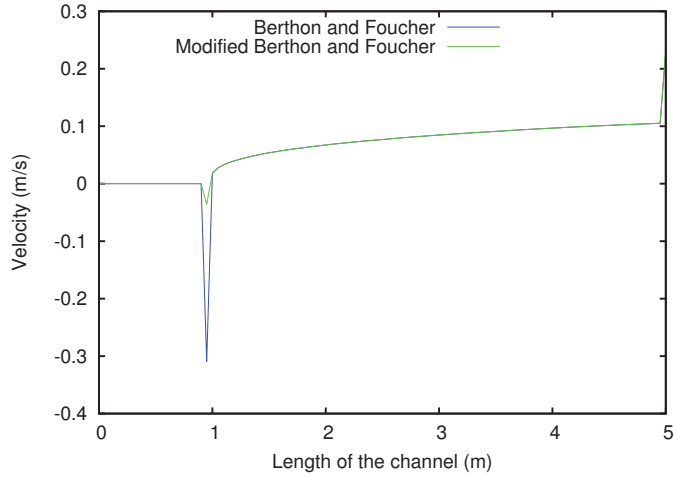

Fig. 6: Velocities (m/s) along the channel, effect of the correction on the Berthon and Foucher scheme for the 5% slope simulation

TABLE I: Relative error (%) of each scheme for the rise of the hydrograph and the constant value

Slope \ Scheme	Audusse *et al.*	Chen and Noelle	Berthon and Foucher
1%	7.97	8.86	5.88
5%	12.3	4.43	3.90
50%	24.7	1.02	2.71

The Berthon and Foucher's scheme [3] is the more efficient for the gentlest slopes (1% and 5%) while the Chen and Noelle's scheme [7] is more accurate for the steepest slope. Concerning the Audusse *et al.* scheme [1], it is more precise than the Chen and Noelle's scheme for the 1% slope, then, as it is shown in figure 2, for the 5% and 50% slopes, the results are far from the analytical solution.

Thus, we choose the Chen and Noelle's [7] hydrostatic reconstruction and the Berthon an Foucher's scheme [3] to test the tracers advection schemes and to couple the model with SISYPHE because of the slope limitation with the Audusse *et al.* [1] technique.

TABLE II: Concentration (g/l) of polluant for each scheme at one point at the outlet of the domain

Slope \ Scheme	LIPS [15]		ERIA [14]	
	Chen [7]	Berthon [3]	Chen [7]	Berthon [3]
1%	0.967	0.998	0.973	0.998
5%	0.970	0.999	0.970	0.999
50%	0.995	1.000	0.995	1.000

B. Polluant transfers

The objective here, is to ensure that these transport schemes can be used with the two new hydraulic finite volume schemes. A source term value of 1 g/l is fixed at one given point of the mesh, on the upstream part of the channel. The concentration at the central point of the outlet is measured. The table II gives the results of the concentration at the outlet for each scheme.

The results are similar, except for the 1% slope simulation where the ERIA scheme is more efficient. This scheme is chosen to solve the advection of the suspended sediment transport.

C. Erosion generation

1) Erosion without bottom modification: To simulate the erosion on the test case, we focus on the 5% and 50% slope because the maximal bed shear stress of the 1% simulation does not allow to have significant results. For every simulation, the erosion is homogeneous across the flow and is growing along the channel. Figure 7 shows the evolution of the bottom at the end of the simulations. On the 5% slope simulations, there is less erosion with the Chen and Noelle's scheme [7] than with the Berthon and Foucher's scheme [3], which is coherent with lag seen in figure 3. Concerning the 50% slopes, the erosion is similar for each scheme and the downstream boundary condition causes a deposition which is more important with the Berthon and Foucher's scheme [3]. Figure 8 shows the volumic concentration along the channel at the end of a 100 s simulation. We can observe that the concentration is lower for the Chen and Noelle's method [7] for the 5% slope which follows the results of the bottom evolution (figure 7). Concerning the 50% slope, the concentration profiles are similar. Some oscillations appear downstream in the Chen and Noelle's signal.

2) Erosion with topographical perturbation: Laboratory experiments ([2], [18]) have shown that rainfall in a straight channel could create a rill network due to erosion. This network depends on the spatial distribution and properties of the soil at the initial state. In our theoritical model, the soil is perfectly uniform at the initial state and the governing equations are solved to give exactly the same results along a cross section of the channel. To create a rill network, a perturbation of the soil at the initial state is introduced by adding to the topography a random number from a uniform law at each node of the mesh. The random number is drawn in

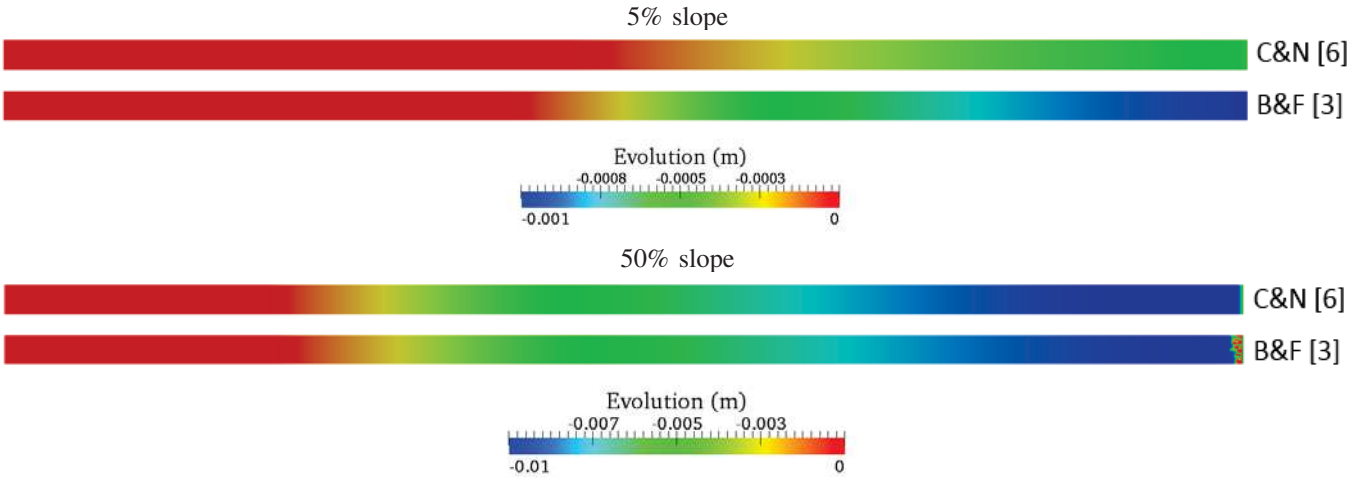

Fig. 7: Evolution of the bottom after 100 s of simulation with the two finite volume schemes and the 5% and 50% slopes

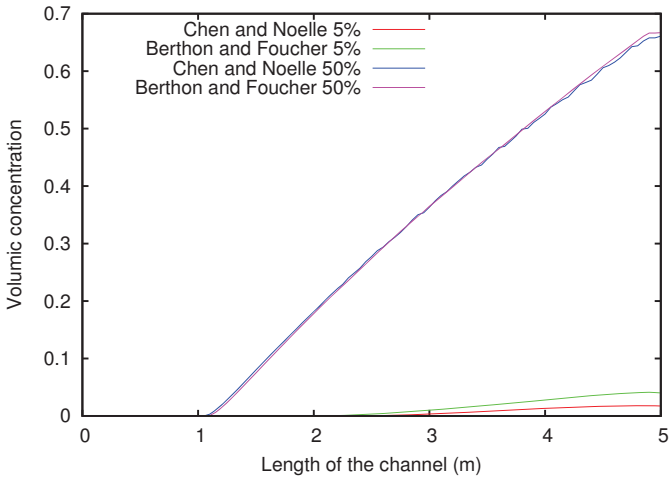

Fig. 8: Volumic concentration along the channel after 100 s of simulation with the two finite volume schemes and the 5% and 50% slopes

different intervals which characterize the size of the topographical perturbation. The sizes are 10^{-2} m, 10^{-3} m, 10^{-4} m and 10^{-5} m respectively defined by randomly drawing values from intervals of $[-10^{-2}; 10^{-2}]$, $[-10^{-3}; 10^{-3}]$, $[-10^{-4}; 10^{-4}]$ and $[-10^{-5}; 10^{-5}]$. Figure 9 illustrates the bottom elevation at the intial state for each size of the perturbation. For these simulations, we focus on the 5% slope case because the size of the distribution susceptible to generate rill erosion changes with the 50% slope.

Figure 10 presents the form of the erosion after 100 s of simulation depending on the range of the random number draw. For a 10^{-5} m and 10^{-4} m height of the perturbation, the bottom is smoothed whatever the hydraulic scheme, but the smoothing is more visible with the Berthon and Foucher's scheme [3], especially for the 10^{-4} m perturbation. For a 10^{-3} m size of the perturbation, a rill network is created, but the rills are wider with the Berthon and Foucher's scheme. For the higher height of the perturbation, we can see local erosion at certain points because the flow is blocked by the topographical pertubation and accumulates. For the Berthon and Foucher's scheme [3], local erosion is observed almost everywhere in the domain. This is due to the difficulty to treat the dry cells caused by the added topography. This highlights the difficulty of this scheme to handle wet/dry transition, even with the modification presented in III-A.

IV. Discussion

The hydrostatic reconstruction of Audusse *et al.* [1] can be a good choice for modelling hydraulic transfers over a watershed complex topography because of its properties. The positivity preserving and well-balanced properties, as well as its ability to deal with dry zones are crucial. The limitation of this technique, exhibited in figure 2, is a well-known problem. Indeed, [11] highlighted that for certain combinations of mesh size, slope and water height, the velocities are underestimated, in particular when $h < \Delta z$, with Δz the bottom difference between two neighboring points. This problem can be solved with a mesh refinement in a way to be always in the case $h > \Delta z$, but this is very expensive in term of computational time, especially with a view to model erosion on an entire watershed.

The development of the Chen and Noelle's [7] hydrostatic reconstruction method allows to overcome this problem. This technique consists of modifying the classical hydrostatic reconstruction when $h < \Delta z$, to take the full slope effect into account, while maintaining all the good properties of the scheme. Nevertheless, this modification causes problem when $\Delta z \approx h$ where the hydraulic values are not well calculated. For an application to a watershed case, this case is often oberved, for instance in the transition from plot runoff to river flow.

Analysis of the volumic concentration profiles confirms the diagnosis performed in the hydraulic part. Indeed, the 5% slope case is coherent with the underestimation of the velocities observed in figure 3. The computed shear stress being proportional to the square velocity, the difference between the concentration profile with the two schemes is even bigger

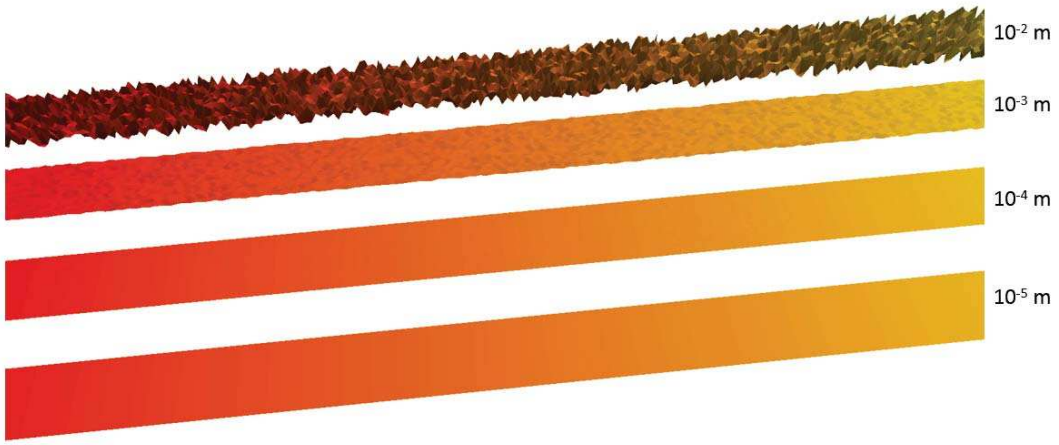

Fig. 9: 3D view of the initial bottom elevation in function of the range of the topographical perturbation

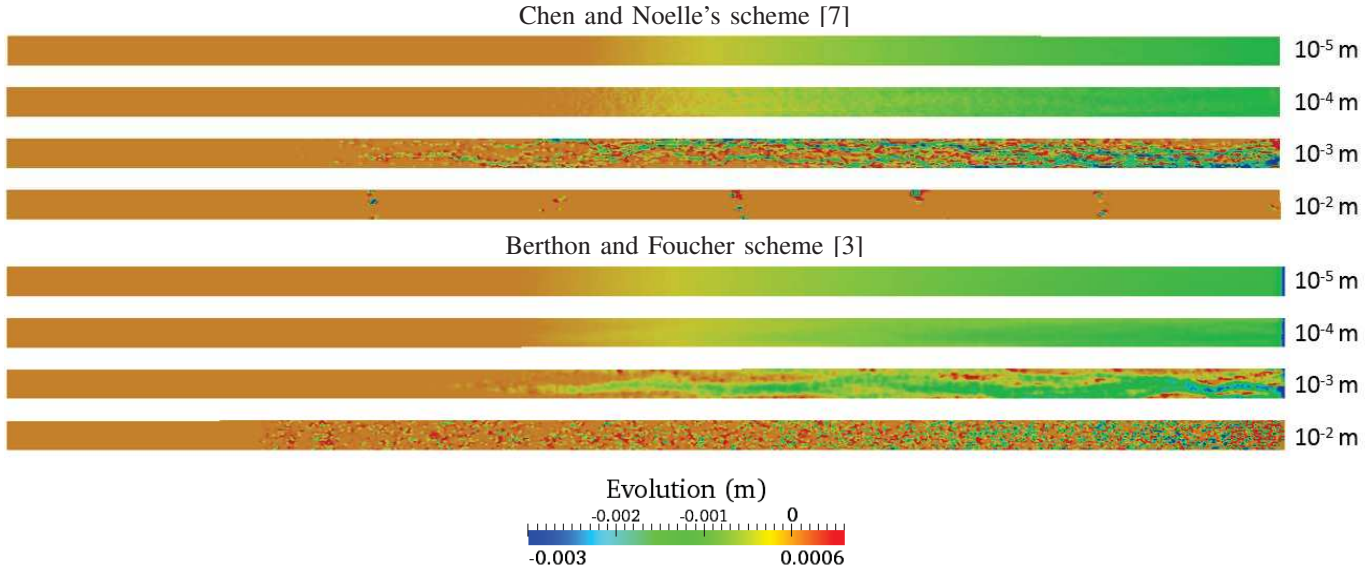

Fig. 10: Rills formation as a function of the range of the topographical perturbation, showing evolution of the bottom after 100 s of simulation

with a threshold law as the one used. Concerning the 50% slope simulation, the oscillation with the Chen and Noelle's technique [7] is due to the topographic difference created by the erosion. Indeed, the transport capacity of the flow is more important in this case so the bed evolution is faster and more susceptible to get close to the situation where $\Delta z = h$.

The Berthon and Foucher's scheme [3] presents issues at the wet/dry interface. These problems can be limited by using the Chen and Noelle's scheme [7] between a wet and a dry cell, but the equilibrium of the scheme is no more respected. In figure 10, for the highest magnitude of the topographical perturbation, these problems explain why the highest local erosion is simulated with this scheme. Its difficulty to deal with dry zones is an obstacle to its use for an application in watershed erosion. However, some treatment exists for this kind of problem (see [19]) but still needs to be adapted to this scheme.

V. Conclusion

The TELEMAC-SISYPHE hydrosedimentary computation code is adapted to river simulations. To extend the use to a watershed scale, a simple test case of runoff has been defined.

After highlighting the limits of the hydrostatic reconstruction present in the finite volume resolution for hydraulic computation (Audusse *et al.* [1]), two new schemes have been tested and have shown their efficiency in this test case (Chen and Noelle [7] and Berthon and Foucher [3]). The Chen and Noelle's hydrostatic reconstruction method is recommended as it is a good compromise between accuracy and robustness, has positivity preserving and well-balanced properties and is capable of handling the dry zones.

The advection schemes for passive tracer LIPS [15] and ERIA [14] give satisfactory results. When erosion is generated by SISYPHE on a smoothed bottom, the erosion is

homogeneous and the evolution of the bottom follows the hydraulic results. To generate rill erosion, a perturbation has been added to the bottom toopography. These configurations give very different results for these two schemes, and highlight the importance of the robustness of the Chen and Noelle's scheme.

As a perspective, there are still some ways to improve the code on this test case like adapt the treatment of the wet/dry interface with the Berthon and Foucher's [3] scheme or improve the Chen and Noelle's [7] method. Another scheme will be tested in future work: the Bouchut and Morales scheme [4] based on subsonic reconstruction. Then, these new methods will be confronted to real cases, thanks to data provided by the Draix-Bleone observatory [17]. The scale effects and the transition between hillslopes runoff and river flow will also be studied.

ACKNOWLEDGMENT

The authors would like to thank L. Staily for the help in this work.

REFERENCES

[1] E. Audusse, F. Bouchut, M.-O. Bristeau, R. Klein, and B. Perthame, "A fast stable well-balanced scheme with hydrostatic reconstruction for shallow water flows", *SIAM Journal on Scientific Computing*, vol. 25, no. 6, pp. 2050-2065, 2004.

[2] C. Berger, M. Schulze, D. Rieke-Zapp, and F. Schlunegger, "Rill development and soil erosion: a laboratory study of slope and rainfall intensity", *Earth Surface Processes and Landforms*, 2010.

[3] C. Berthon and F. Foucher, "Efficient well-balanced hydrostatic upwind schemes for Shallow-Water equations", *Journal of Computational Physics*, vol. 231, pp. 4993-5015, 2012.

[4] F. Bouchut and T. Morales, "A subsonic-well-balanced reconstruction scheme for shallow water flows", *SIAM Journal on Numerical Analysis*, vol. 48, pp. 1733-1758, 2010.

[5] M. O. Bristeau and B. Coussin, "Boundary conditions for the Shallow Water equations solved by kinetic schemes", INRIA, Technical Report 4282, 2001.

[6] N. Chahinian, "Comparison of infiltration models to simulate flood events at the field scale", *Journal of Hydrology*, vol. 306, pp. 191-214, 2005.

[7] G. Chen and S. Noelle, "A new hydrostatic reconstruction scheme based on subcell reconstructions", submitted to *SIAM Journal on Numerical Analysis*, 2015.

[8] N. Claude, "Interactions entre végétation, processus hydro-sédimentaires et morphodynamique des cours d'eau : état de l'art et principes de modélisation", *Note EDF LNHE ref. H-P73-2014-05213-FR*, 2015.

[9] O. Delestre, "Simulation du ruissellement deau de pluie sur des surfaces agricoles", Ph.D. dissertation, Université d'Orléans, 2010.

[10] O. Delestre and F. James, "Simulation of rainfall events and overland flow", *Proceedings of X International Conference Zaragoza-Pau on Applied Mathematics and Statistics, Jaca, Spain, september 2008, Monografas Matemticas Garca de Galdeano*, 2009.

[11] O. Delestre, S. Cordier, F. Darboux, and F. James, "A limitation of the hydrostatic reconstruction technique for shallow water equations", *Compte Rendu de l'Académie des Sciences, Série I*, vol. 350, pp. 677-681, 2012.

[12] F. R. Fiedler and J. A. Ramirez, "A numerical method for simulating discontinuous shallow flow over an infiltrating surface", *International Journal for Numerical Methods in Fluids*, vol. 32, pp. 219-240, 2000.

[13] J. M. Greenberg and A.-Y. Leroux, "A well-balanced scheme for the numerical processing of source terms in hyperbolic equations", *SIAM Journal on Numerical Analysis*, vol. 33, no. 1, pp. 1-16, 1996.

[14] J.-M. Hervouet, "Latest news on distributive schemes and dry zones: the ERIA scheme", in *Telemac-Mascaret User Conference*, 2016.

[15] J.-M. Hervouet, S. Pavan, and R. Ata, "Distributive advection schemes and dry zones, new solutions", in *Telemac-Mascaret User Conference*, 2015.

[16] G. Kirstetter, J. Hu, O. Delestre, F. Darboux, P.-Y. Lagre, S. Popinet, J. M. Fullana, and C. Josserand, "Modeling rain-driven overland flow: empirical versus analytical friction terms in the shallow water approximation", *Journal of Hydrology*, vol. 536, pp. 1-9, 2016.

[17] C. Le Bouteiller, S. Klotz, F. Libault, M. Estèves, "Observatoire hydrosdimentaire de montagne Draix-Blone", http://dx.doi.org/10.17180/OBS.DRAIX, Irstea, 2015.

[18] K. Michaelides, I. Ibraim, G. Nord, and M. Esteves, "Tracing sediment redistribution across a break in slope using rare earth elements", *Earth Surface Processes and Landforms*, vol. 35, pp. 575-587, 2010.

[19] V. Michel-Dansac, C. Berthon, S. Clain and F. Foucher, "A well-balanced scheme for the Shallow-Water equations with topography", *hal-01201825*, 2015.

[20] T. Takahashi, "Debris flow: Mechanics, Prediction and Countermeasures", Taylor & Francis, 2007.

[21] P. Tassi and C. Villaret, "Sisyphe v6.3 Users Manual", *Note EDF LNHE ref. H-P74-2012-02004-EN*, 2014.

[22] E. F. Toro, "Riemann Solvers and Numerical Methods for Fluid Dynamics", Springer, 2009.

[23] E. F. Toro, M. Spruce, and W. Speares, "Restoration of the contact surface in the HLL-Riemann solver", *Shock Waves*, vol. 4, pp. 25-34, 1994.

Cross-sectional variation of bed-load transport: Comparison of measurements and simulations

Rebekka Kopmann
Department of Hydraulic Engineering in Inland Waterways
Bundesanstalt für Wasserbau
Karlsruhe, Germany
rebekka.kopmann@baw.de

Lisa Walter, Roy Frings
Institute for Hydraulic Engineering and Water Resources Management
RWTH Aachen University
52056 Aachen, Germany

Abstract— **Bed-load transport in a gravel bed river does not run continuously either in time or in space. The variability was analysed by Frings and Vollmer [1] for the "Niederrhein" (Lower Rhine) using more than 10,000 bed-load samples. Even though the amount of data is extraordinary it is not always enough for statistical significance. Numerical modelling can help to close these gaps in the measurements.**

A 46.5 km long calibrated model (Rh-km 730 – 776.5) was used for further investigations. This reach includes 4 measurement points of the mentioned campaign at which the cross-sectional variation of the bed-load transport has been analysed. The numerical model was run over a period of 11.5 years (2000-2011) and the results have been compared to the measurements.

The model was validated by comparing the measured and simulated effective bed-load width and the centre of mass of bed-load transport. The agreement is satisfactory taking into account the uncertainties of measurements and numerical modelling. The comparisons prove that a cross-sectional variability can be reproduced by the numerical model, but with smoothing tendencies.

An artificial bed-load supply is simulated and compared to a reference run without bed-load supply. It could be found, that the coarse bed-load supply generally decreases the bed-load transport, which leads to a smaller effective bed-load width, but to a higher cross-sectional variation of bed-load transport. This investigation is a first step to determining the reasons for the measured high bed-load transport variation in the Lower Rhine.

I. INTRODUCTION

The analysis of the current status of inland Federal waterways and a forecast of its future status is one key task in the River Systems section of BAW. For that hydraulic-morphological investigations are done using morphodynamic numerical models simulating bed-load transport.

Bed-load transport in a gravel bed river does not run continuously, either in time or in space. Field survey measurements have shown these variations of bed-load transport. In the River Rhine more than 10,000 bed-load samples were analysed by Frings and Vollmer [1] in the period 1991-2010 for a 225 km long river reach called Lower Rhine. The Lower Rhine is a typical example of a single-channel, canalised river with bank protection, groynes and bank revetments. For an intense shipping traffic, bed load management is carried out containing dredging and disposal operations as well as artificial bed load supply [2]. Although the number of samples is enormous, the data resolution in time is not satifactory for all analysis cases and the statistical significance is not always given. Numerical modelling can help to close these gaps in the measurements.

With the measurement data no dependencies of discharge, bend radius or other influences for the cross-sectional variations could be found. It is assumed, that the number of samples are still not high enough for statistical investigations and / or that human influences (e.g. shipping, bed-load supply) dominate the variability. Using the high resolute data from the numerical simulation, a correlation between discharge and effective transport width could be found [3]. Further investigations are done to find causes for the cross-sectional variability of bed-load transport [3]. In particular, the influence of an artificial bed-load supply is shown in this paper.

In section II the measurements showing the cross-sectional variation of bed-load transport will be demonstrated. Section III presents the validation of the numerical model for investigations concerning cross-sectional variation of bed-load transport. In section IV the influence of bed-load supply to the variations are investigated. The paper is summarised in the conclusions.

II. CROSS-SECTIONAL VARIATION OF BED-LOAD TRANSPORT AT THE NIEDERRHEIN

The starting point for the presented investigation is the analysis from Frings and Vollmer [1] of more than 10,000 bed-load samples of River Rhine. These were conducted at the 225 km long river reach called "Niederrhein" (Lower Rhine) between the Rhenish Massif and the German-Dutch Border during the time period 1991-2010. Although the number of samples is enormous, the data resolution in time and space is not always high enough to get a statistical significance.

For a 46.5 km long part of the Lower Rhine (Rh-km 730 – 776.5) a numerical model already exists at BAW calibrated for the time period 2000 - 2011. This model was reused for this study. Four measurement sites from the analysis of Frings and Vollmer lay inside the numerical model: Düsseldorf V (Rh-km 749.5), Kaiserwerth (Rh-km 756), Gellep (Rh-km 762) and Krefeld (Rh-

km 768) (see Fig. 1). This stretch has a mean discharge of about 2300 m^3/s, a mean width of about 400 m and a mean slope of 0.17 ‰. The mean bed-load transport in a cross section in the years 2000-2011 is about 3.5 kg/s with a surface arithmetic mean grain size of about 15 mm. In this part an erosion tendency prevails, which is attenuated by bed-load supply.

To analyse the cross-sectional variability the cross sections of the four measurement sites are divided into 8-12 subsections (see Fig. 2), in which the bed-load transport was measured separately. Generally bed-load transport occurs between the *groyne head lines* (visualised by the blue lines nearest the groyne heads in Fig. 2). In the following it is called the potential bed-load width (BW_{pot}). This parameter differs along the flow length between 208 and 265 m with a mean value of 239 m. Usually the bed-load transport takes place only in a part of the potential bed-load width. The so called effective bed-load width (BW) is mostly smaller (narrower) than the BW_{pot} and varies considerably over time. With help of the measurements in the subsections the BW can be calculated as the sum of the subsection width, where bed-load transport occurred. The high variability of the cross-sectional bed-load transport becomes apparent as the effective bed-load width varies between 11 and 100% of the potential width. The mean BW value is 118 m.

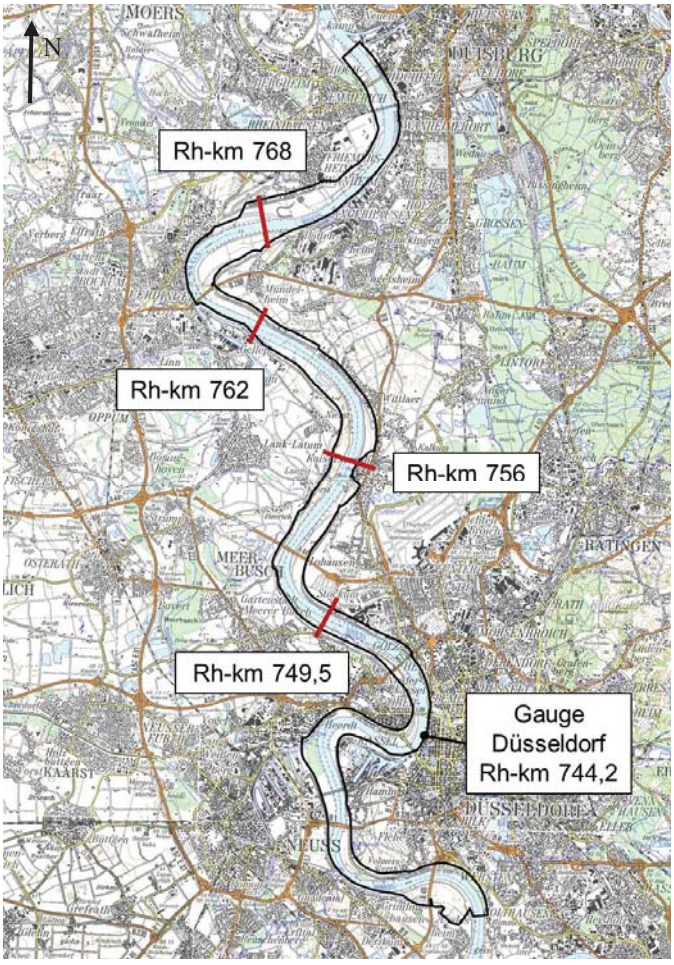

Figure 1 - Model area with measurement sites [3].

The centre of mass (COM) specifies the spatial mean of the cross-channel bed-load distribution and can be determined as the weighted arithmetic mean of the bed-load transport rates in the different subsections of a cross-section (see Fig. 3). Generally it was located close to the midstream with a slight tendency to the right banks. The averaged centre of mass is located at the standardised potential cross-section width of 0.07, but varies considerably between -0.54 and 0.73.

More information on the Rhine, its morphology and the human impact thereon can be found in [4] and [5].

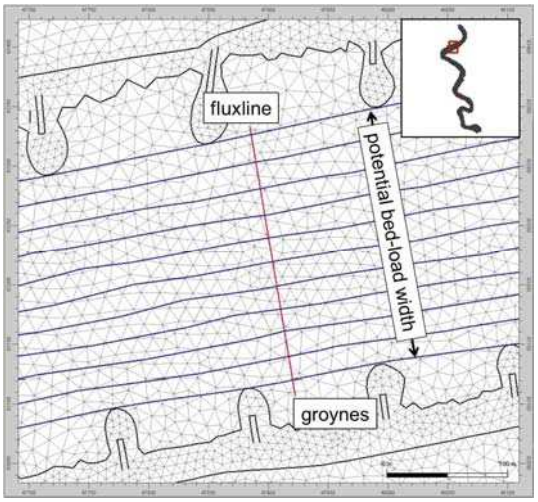

Figure 2 - Fluxline with 10 subsections for measurement of effective bed-load width.

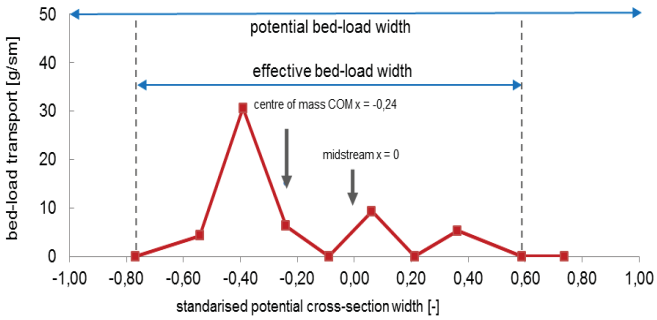

Figure 3 - Measured centre of mass of bed-load transport (COM) for gauge Düsseldorf Rh-km 749,5 on 25.03.2004

III. MODEL VALIDATION OF CROSS-SECTIONAL VARIATION

With an existing and already calibrated 46.5 km long TELEMAC2D-SISYPHE model V6P3 (opentelemac.org) with 190,000 nodes 11.5 years of the natural hydrograph 2000-2011 were simulated. On the parallel computer Bull BladeX (B520) at BAW the computing time is about 40 hours for this simulation period using 120 processors / subdomains.

The grid resolution with node distances between 5-50 m allows a proper reproduction of the groyne geometry as well as the analysis of the variability of the cross-sectional variation in the bed-load transport.

The details of the calibration are described by Backhaus et al [6]. Only the most important parameters of the hydrodynamic and morphodynamic modules TELEMAC2D [7] and SISYPHE [8] are listed here.

- Hydrodynamic time step: 4 s, morphological factor 4
- Nikuradse friction law, seven different friction zones
- Elder turbulence model
- Multi-grain (10 sediment classes), multi-layer model (5 layers, constant active layer thickness: 10 cm)
- Meyer-Peter and Müller transport formula, Karim, Holly, Yang hiding exposure formulation
- Koch and Flokstra and Talmon slope effect formulation

Before using the model for further investigations it must be shown, that the model is able to reproduce the measured bed-load transport and its variability. This validation was done by comparing the bed-load transport along the river stretch (Fig. 4) and representatively the distribution of the transport rate at some cross-sections (Fig. 5). Furthermore the mean values of the effective bed-load width and its variability (Fig. 6) were analysed.

Firstly the time averaged bed-load transport along the river stretch was compared (see Fig. 4). As the variability in time is quite high a reasonable number of measurements is needed for a significant calculation. This is the case only for four cross-sections, where the results of the numerical model match with the measurements very well.

Fig. 5 shows the distribution of the bed-load transport rate at cross-section Rh-km 749.5 for three different points in time. The quality of the reproduction of the numerical model ranges between near perfect and reasonable. A cross-sectional variability can be simulated with the numerical model, but is not as distinctive as in the measurements. Smoothing effects due to time and space discretisation or further numerical effects could be the reason. Furthermore the bathymetry was not measured at the same time with the bed-load transport measurements. Uncertainties due to divergent bed levels in the model should also take into account.

The time averaged effective bed-load width and the minimum and maximum values are compared between measurements and simulation in Fig. 6. The averaged values as well as the range between minimum and maximum agree well. But the differences between the highest and lowest time averaged values at the four cross-sections are higher for the measurements (e.g. measured difference of BW = 53 m, simulated = 16 m). Thus the spatial variability is slightly higher for the measurements. The temporal variability of the effective bed-load width can be expressed by the standard deviation of the effective bed-load width. It is again smaller for the simulations (27 – 38 m) than for the measurements (30 – 56 m).

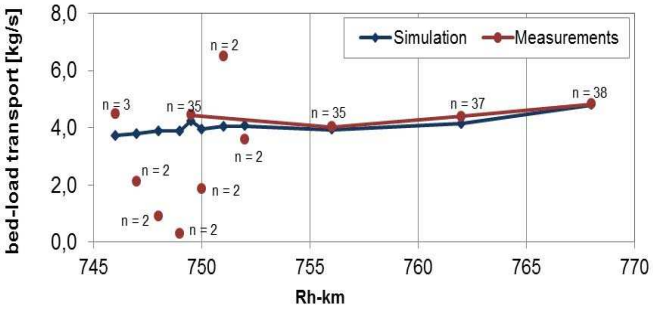

Figure 4 - Comparing the measured and simulated time averaged bed-load transport along the river stretch (n: number of measurements for the time averaging).

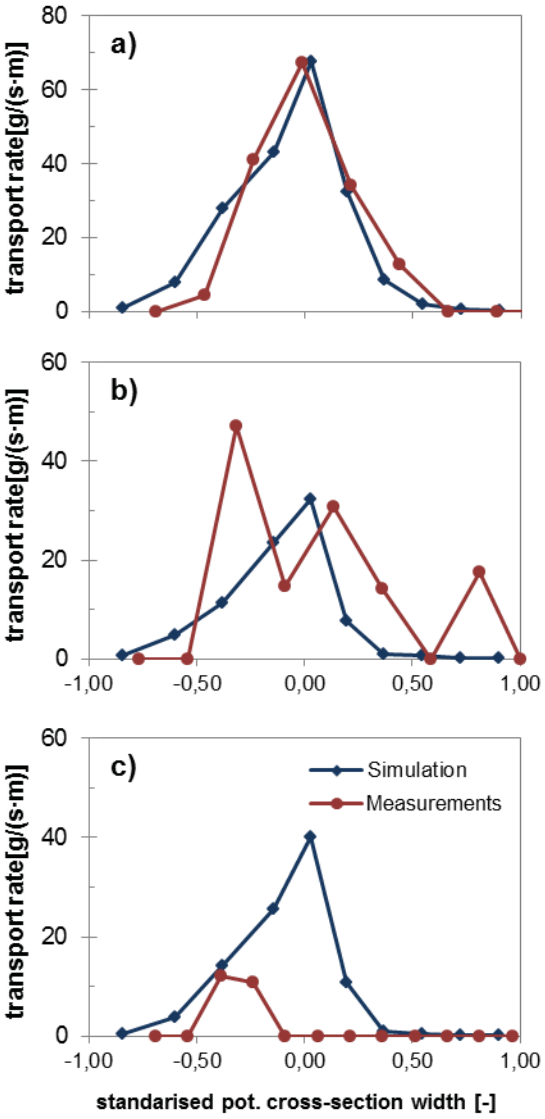

Figure 5 - Comparing the measured and simulated distribution of bed-load transport rate in the cross-section Rh-km 749.5 at a) 11.03.2008, b) 08.12.2005 and c) 23.11.2009.

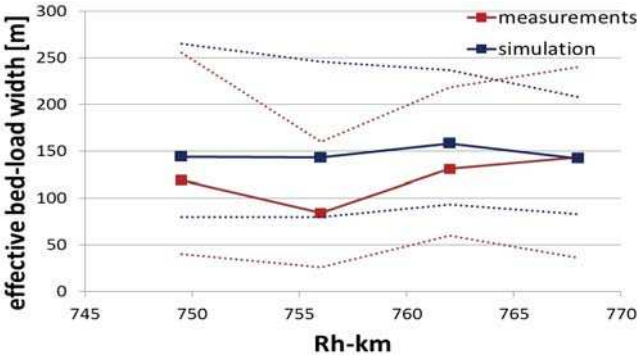

Figure 6 - Comparing the measured and simulated time averaged effective bed-load width and its minimum and maximum values.

The validation has proven that the model can be used to analyse the variability of bed-load transport in the cross-section. But smoothing tendencies of the numerical model must be taken into account for the interpretation.

IV. INFLUENCES ON CROSS-SECTIONAL VARIATIONS OF BED-LOAD TRANSPORT

The reasons for the high cross-sectional variability of bed-load transport in this river stretch are manifold. Natural influences like unsteady discharges, dune transport, turbulence effects, varying bend radii and sorting effects all affect this variability as well as artificial influences (human impacts) like navigation or bed-load management measures. Here only the influence of artificial bed-load supply is analysed. Further analysis can be found in [3].

The reference state (or baseline condition) used for the validation in section III does not take any dredging and disposal activities into account. To understand the influence of bed-load management measures only one artificial bed-load supply was simulated. Just above the first measurement gauge 640 m^3/d of sediment slightly coarser than the local bed material was supplied at an existing supply area (Rh-km 746.9 – 748) over the time period of about one year (01.06.2000 – 01.07.2001). This is twice as much material as supplied naturally to this area.

The influence of this measure is observed by the yearly averaged effective bed-load width (BW) (see Fig. 7). The BW is strongly correlated with the yearly averaged discharge (compare Fig. 7 with Fig. 8). The first change in the BW can obverved in 2003 at the first two measurement gauges 1.5 and 8 km below the supply area. At distances of 14 and 20 km downstream from the supply area the BW starts to differ from between 2005 or 2006 onwards. Using this data a very rough estimation of the bed-load transport velocity gives about 2 – 3 km/a. This corresponds with other estimations for the River Rhine in the range 2.5 – 5.5 km/a [9].

Interestingly, the bed-load supply leads generally to a smaller effective bed-load width. The strongest impact can be observed 8 km below the supply area. Only in the years 2006 and 2007 at Rh-km 768 does the BW increase due to the bed-load supply. So far there is no satisfactory explanation for this inconsistency. The general effect might be explained by a decreasing bed-load transport due to coarser bed-load material. Consequently the BW decreases as well as it is strongly correlated with the discharge and also with the bed-load discharge.

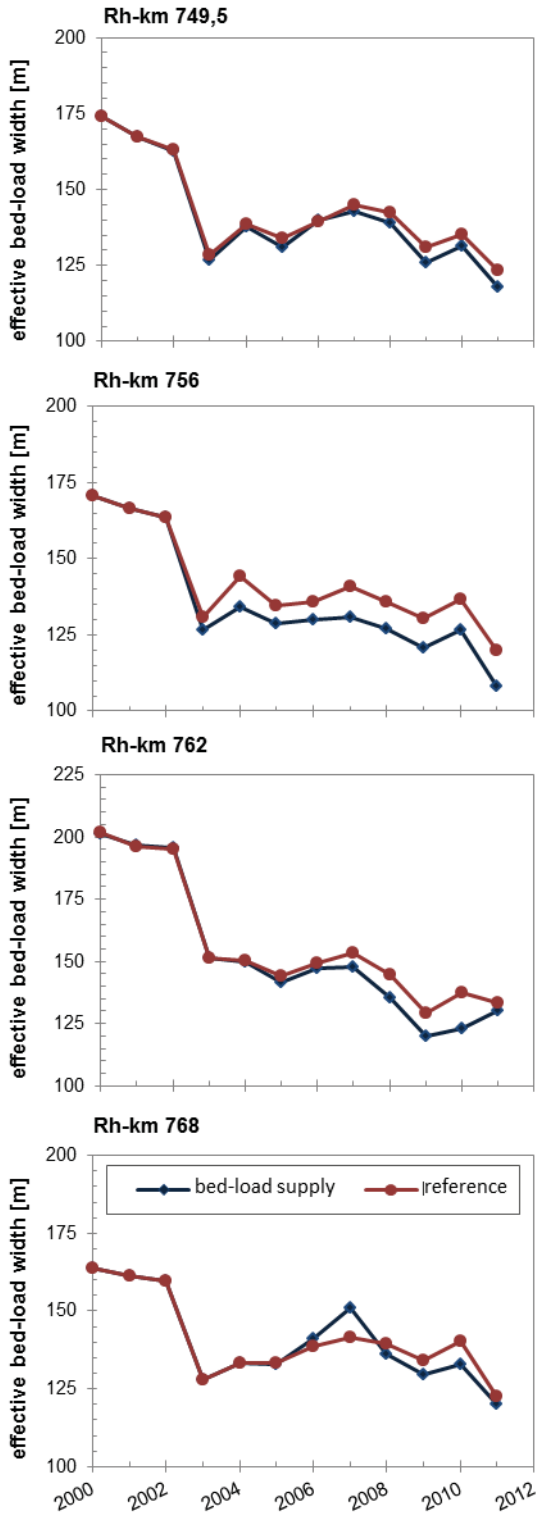

Figure 7 - Yearly averaged effective bed-load width for the four measurement sites with and without a single bed-load supply measure.

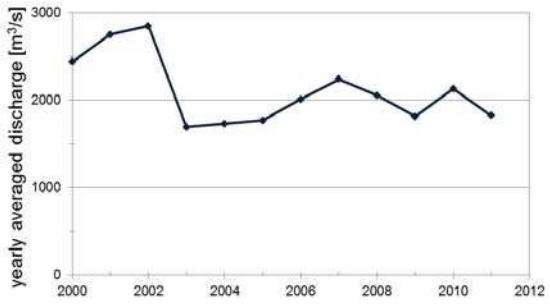

Figure 8 - Yearly averaged discharge.

Table 1 - Comparison of effective bed-load width (BW) and its standard deviation □BW Averaged for the given time period for the reference simulation and the simulation with bed-load supply

	Rh-km 749,5 2003-2011		**Rh-km 756 2003-2011**		**Rh-km 762 2005-2011**		**Rh-km 768 2006-2011**	
	BW m	σ_{BW} m	BW m	σ_{BW} m	BW m	σ_{BW} m	BW m	σ_{BW} m
Refer-ence	135	26	134	25	142	29	136	23
With bed-load supply	132	27	126	27	135	31	135	26

To demonstrate the cross-sectional variations of bed-load transport the standard deviation is used: The higher the standard deviation, the higher the variability. In Table I the effective bed-load widths and their standard deviations are calculated for chosen time periods. During these periods the BW are affected by the bed-load supply. For all monitored cross-sections the standard deviations are higher with bed-load supply although the effective bed-load widths are smaller. The increase of the standard deviation is 1 – 3 m, which is not negligible. Assuming a normal distribution of bed-load widths, 95 % of all simulated values lay inside the interval of four times the standard deviation (BW +/- 2 σ_{BW}). For example at Rh-km 768, without bed-load supply, the effective bed-load width (95 % of all values) varies between 90 – 182 m. The bed-load supply increases this interval to 83 – 187 m.

As shown in Fig. 7 the differences between the yearly averaged BW with and without bed-load supply vary over time and are therefore larger than the mean values given in table I. This is also true for the yearly averaged standard deviations. The bed-load supply leads to a maximum increase of 34% in the year 2007 at Rh-km 768 for the standard deviation.

The results show a significant indication that the bed-load supply intensifies the cross-sectional variation of bed-load transport. The influence of one year of bed-load supply can be seen for at least 9 years in the cross-sectional variations. The effect is probably negligible at the end of the simulation period. Further investigations with longer simulation periods and other bed-load management scenarios seem promising.

V. CONCLUSIONS

For a numerical hydro-morphodynamic model of a 46.5 km long stretch of the Lower Rhine the ability to simulate cross-sectional variability of bed-load transport was verified. This was done by comparing measured and simulated bed-load transport, effective bed-load width, its standard deviation and the distribution of bed-load transport along a cross-section. The results show that the average values and also the minimum and maximum values for simulation and measurements match very well. However, the simulation results are generally smoothed due to time and space discretisation and further numerical effects. This leads to smaller values of the standard deviation. Nevertheless the numerical model can be used to analyse the reasons for the cross-sectional variability of bed-load transport.

As an example, an investigation on the influence of bed-load supply to the cross-sectional variability of bed-load transport was presented. Further investigations can be found by Walter [3]. The chosen coarser bed-load supply leads generally to a lower bed-load transport which narrows the effective bed-load width, but intensifies the cross-sectional variability.

This investigation is a first step towards determining the reasons for the high bed-load transport variation measured in the Lower Rhine. The possibilities for different settings (scenarios) to examine natural or artificial influences simulated with the presented numerical model are huge. A better understanding of the complexity of the bed-load transport as well as the effectiveness of bed-load management measures are expected of these prospective studies.

REFERENCES

[1] Frings, R., Vollmer, S., "Cross channel variation of bed-load transport in rivers: measurement uncertainty and sampling guidelines," Sedimentology, submitted 2016.

[2] Schmidt, A., Backhaus, L., Heinzelmann, C. „Methoden zur Simulation morphodynamischer Prozesse in Bundeswasserstraßen," In Korrespondenz Wasserwirtschaft, 2014(7), Nr. 8, S. 456-461, 2014

[3] Walter, L., "Cross-channel variation of bed-load transport: a numerical sensitivity analysis with Telemac-2D / Sisyphe," Master thesis University of Aachen, 2016.

[4] Frings, R.M., Gehres, N., Promny, M., Middelkoop, M., Schüttrumpf, H. and Vollmer, S., "Today's sediment budget of the Rhine River channel, focusing on the Upper Rhine Graben and Rhenish Massif," Geomorphology, 204, 573-587, 2014 http://dx.doi.org/10.1016/j.geomorph.2013.08.035.

[5] Frings, R.M., Döring, R., Beckhausen, C., Schüttrumpf, H., and Vollmer, S., "Fluvial sediment budget of a modern, restrained river: The lower reach of the Rhine in Germany," Catena 122, 91-102, 2014

[6] Backhaus, L., Brudy-Zippelius, T., Wenka, T., & Riesterer, J., "Comparison of morphological predictions in the Lower Rhine River by means of 2-D and 3-D model and in situ measurements," Proceedings of River Flow , 2014

[7] Hervouet J.-M., " Hydrodynamics of Free Surface Flows, modelling with the finite,element method," J. Wiley & Sons Ltd, West Sussex, England, 340 pp., 2007

[8] Villaret, C., "Sisyphe user manual," EDF R&D internal report N° H-P73-2010-01219, 2010

[9] Promny, M., Frings, R., Gehres, N., Busch, N., Vollmer, S., Gölz, E., „Analyse und Bewertung der hydraulisch-morphologischen Situation zwischen Iffezheim und Mainz," BfG-Bericht 1702, Auftraggeber: Wasser- und Schifffahrtsdirektion Südwest, Koblenz, 2010

Numerical modelling of graded sediment transport based on the experiments of Wilcock and Crowe (2003)

Florian Cordier, Pablo Tassi
Nicolas Claude, Damien Pham van Bang
EDF R&D - LNHE - LHSV - CEREMA
6 Quai Watier, 78401 Chatou (France)
Email: (florian.cordier;pablo.tassi)@edf.fr

Alessandra Crosato
UNESCO-IHE
Westvest 7, 2611 AX Delft
The Netherlands

Stéphane Rodrigues
Ecole Polytechnique Universitaire de Tours
64 Avenue Jean Portalis, 37200 Tours (France)

***Abstract*—The current work focuses on the sediment transport of non cohesive graded sediment with the TELEMAC-MASCARET Modelling System. The 2D hydro-sedimentary numerical models are based on the experiments lead by Wilcock and Crowe [2003] ran in straight flumes where both water and sediment are recirculated, using a wide range of flows and grain sizes distributions (GSD). Motivations of this study lie on (*i*) the improvement of the transport rates estimation in the code with comparison to the classical formulation for bedload transport of MPM [1948] and (*ii*) the applicability of a graded sediment transport model to the numerical simulation of complex morphodynamic problems such as bar formation and propagation. Results show that the computed sediment fluxes are strongly sensitivite to the method of discretization of the GSD, and satisfactory transport rates can be obtained with a relevant discretization of the GSD.**

I. Introduction

Modelling the transport of mixtures of *non-cohesive* particles (also referred to as *graded sediment*) remains a challenge due to the difficulty to reproduce the non-linear interactions between grains of different shape and size. In the last decades, a variety of sediment transport models have been proposed [7], but most of them are based on experimental data and no general physics-based formula for sediment transport capacity exists, although some works linking phenomenon of turbulence to sediment mobilization are promising [9].

Two types of model have been proposed to estimate the sediment transport capacity of graded sediment : stochastic models and deterministic models. Stochastic models for mixed sediment are based on the computation of fractional mobility of sediment by using the concept of continuous-time Markov process (for more information, the reader is referred to [21], [26]). Stochastic models remained quite limited, as the model parameters (*e.g.* particles velocity) have to be determined from exhaustive field campaigns or experiments. Moreover, stochastics model have to be improved, such as taking into account the spatial and temporal variation of bed shear stress and sand content [26].

Deterministic models were first proposed to estimate the sediment transport capacity of *unisize* (also known as *uniform*) sediment [6], [7], [10]. Natural sand-gravel-bedded rivers often show a wide Grain Size Distribution (GSD), and application of classical bedload equations usually fails in reproducing relevant transport rates [17]. This failure occurs because of the strong interactions between fine and coarse grains, which play a major role on the sediment transport process [4], [5], [13]. This process is commonly refered to as the *hiding* or *hiding-exposure* effect, which is manifested by the nature of coarse grains to hide finer grains in their interstices. While the gravitational effects make the larger particles harder to move, the hiding effects tends to counterbalance this phenomenon by increasing coarse grain mobility and decreasing the mobility of fine grains. Simplest models proposed the calculation of a *hiding-exposure* coefficient for each size fraction of sediment (initially proposed in the seminal work of Einstein [5]), to be replaced in the classical sediment transport capacity formula for uniform sediment to estimate a Shields parameter and a *fractional transport rate* for each size fraction [14]. Today, those formulations are commonly used in numerical modelling of graded sediment processes [20].

However, neither of those classical transport formulations were based on data derived from beds of heterogeneous sediment, and there is no justification for assuming that either equation can simply be applied with the Shields parameter based on d_i (the grain size of the i^{th} class) multiplied by F_i (the volume fraction of the i^{th} class of sediment). The use of those classical approaches would be far more justifiable by using a representative grain size d (the median grain size or the geometric mean grain size). If a fractional transport procedure is to be used, it should be done with one of the formulations derived for that purpose [18] (and references therein). These more sophisticated models take account of the hiding effects of poorly-sorted sediment by calculating a fractional-based bed load transport based on a similarity analysis between the bed load transport rate of size fraction i denoted $q_{b,i}$ and with the skin friction relative to the same size fraction denoted τ_{ri} [3], [12], [16], [23]. The similarity hypothesis assumes that transport rates are determined by the same transport law for each fraction [3], [7].

In the framework of modelling alluvial bar formation, development and stabilization, it is of main interest to fairly estimate the sediment transport in natural rivers, since rivers commonly show a variability on the GSD [1] and bars evolution (*i.e.* armor formation and *break-up*) depend on fractional

transport rates estimation [11], [12], [15]. In other words, the simulation of bar dynamics often raises issues that can have an impact on the estimation of bar's characteristics such as their length, height, or temporality. Therefore, the authors proposed to implement and reproduce numerically the experiments of Wilcock and Crowe [23] (WC-2003) using a two dimensional fully-nonlinear physics based numerical model using the Telemac-Mascaret modelling system (TMS).

The model of Wilcock and Crowe [23] is interesting in the way that *i*) it is based on surface investigations and is particularly adapted for the prediction of transient conditions of bed armoring and scenarios of bed aggradation/degradation, *ii*) it considers the full size distribution of the bed surface (from finest sands to coarsest gravels), *iii*) it was calibrated using a total of 49 flume experiments with small-to-high water discharges and five different sediment mixtures and later modified and validated with 6239 values of Q_s, and *iv*) the hiding function has been designed to resolve discrepancies observed from previous experiments [12], [16] including the hiding exposure effect of sand content on gravel transport for weak to high values of sand content in the bulk mix.

Although the sophisticated formulas would be powerful tools as sediment transport estimators, it is yet not clear how to use it in the scope of numerical modelling. For example, previous numerical studies using the WC-2003 formula are based on the discretization of the GSD into only 2 size classes of bed material corresponding to sand and to gravel respectively [2], [22], whereas natural rivers usually show a continuous spectrum of grain sizes. Therefore, the numerical application of such models raises several problems in matter of GSD discretization: *i*) which method should be used to discretize the GSD? and *ii*) does the number of size classes of sediment plays an important role in the estimation of transport rates? The present paper aims to investigate these two points.

A description of the mathematical models (hydrodynamics and morphodynamics) and of the numerical treatment of physical processes is provided in Part II, together with the experimental data from WC-2003 used in this numerical study. In Part III, attention is given on the numerical modelling of graded sediment transport in the goal of reproducing the laboratory experiments of WC-2003. Results provided by the numerical models are analyzed and compared with experimental data in Part IV.

II. Materials and methods

A. Two-dimensional hydrodynamic model

The hydrodynamics solver Telemac-2D is internally coupled to the sediment transport and bed evolution module Sisyphe. The hydrodynamics module is based on the solution of shallow-water equations (SWE) obtained from several strong assumptions (hydrostatic pressure distribution, averaged vertical velocity, *etc.*), wherein the momentum diffusion coefficient is assumed equal to the turbulent viscosity, which is constant troughout the domain with $\nu_t = 10^{-6}$ m^2/s:

$$\begin{cases} \partial_t h + \vec{u}\cdot\vec{\nabla}(h) + h div(\vec{u}) = S_h \\ \partial_t u + \vec{u}\cdot\vec{\nabla}(u) = -g\partial_x z_s - S_{f,x} + h^{-1} div(h\nu_t\vec{\nabla}u) \\ \partial_t v + \vec{u}\cdot\vec{\nabla}(v) = -g\partial_y z_s - S_{f,y} + h^{-1} div(h\nu_t\vec{\nabla}v) \end{cases} \quad (1)$$

where $\partial_t = \partial/\partial_t$, g is the acceleration of gravity = 9.81 m.s^{-2}, h is the water depth [m], $z_s = z_b + h$ the free surface [m] (Fig.1) with z_b the elevation of the riverbed topography [m], $\vec{u} = (u, v)$ with $|\vec{u}|$ the module of $\vec{u}$, u (resp. v) the fluid velocity along the Cartesian x-axis (resp. y-axis) [m/s] and $S_{f,x}$ (resp. $S_{f,y}$) corresponds to the friction forces along the Cartesian x-axis (resp. y-axis). In this work, the friction coefficient is determined with the law of Strickler:

$$S_{f,i} = \frac{u_i|\vec{u}|}{K^2 h^{4/3}} \quad , \quad (2)$$

where K is the friction coefficient of Strickler and i is stands as the Einstein index.

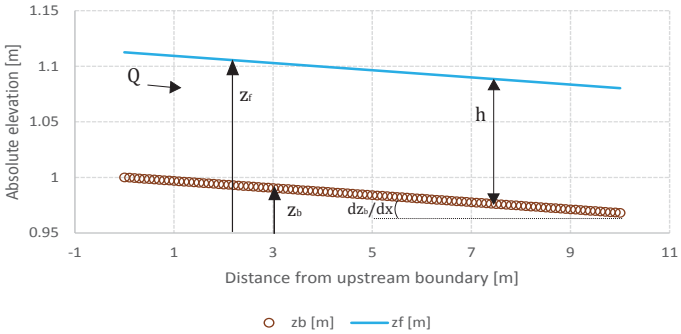

Fig. 1: Sketch illustrating the working-length of the experiments of WC-2003 and the main variables used in the SWE model.

B. Two-dimensional morphodynamics model

Graded sediment processes are successively modeled with the morphodynamic module by: *i*) discretizing the sediment mixture into sediment fractions, where the representative diameter of the i^{th} size class of sediment is user defined, *ii*) the application of a bedload transport capacity formula for each separate fraction and *iii*) using a mass conservation equation adapted for bedload transport for each fraction. The present model assumes a unique layer for the transport of sediment, and the recirculation of sediment was implemented to inject sediments exiting the downstream boundary through the upstream boundary. In this work, the equations to be solved are listed below:

a) Mass balance equation:

The riverbed evolution is computed from the Exner sediment mass balance equation:

$$\partial_t z_b + \frac{1}{\epsilon_0}\nabla\cdot q_b = 0 \quad , \quad (3)$$

where q_b is the volumetric bedload solid discharge per unit of width [m^2/s] and $\epsilon_0 = (1 - P_0)$ with $P_0 = 0.4$ the bed porosity.

The Exner equation can be generalized for graded sediment as [7]:

$$\partial_t z_b + \frac{1}{\epsilon_0}\nabla\cdot\sum_{i=1}^{N} q_{b,i} = 0 \quad , \quad (4)$$

where N is the number of size classes of sediment and $q_{b,i}$ corresponds to the fractional volumetric bedload solid discharge per unit of width of the i^{th} size class [m^2/s].

b) Estimation of sediment transport capacity:

The fractional transport rate $q_{b,i}$ is then estimated using two distinct bedload formulas: *i*) the formula of Meyer-Peter and Müller (MPM) [10] and *ii*) the formula of WC-2003 [23].

The formula of MPM [10] gives:

$$\frac{q_{b,i}}{\sqrt{g\Delta_s d_m^3}} = \alpha\Big(\theta - \theta_c\Big)^{\gamma}, \text{ with } \alpha = 8, \gamma = \frac{3}{2}, \text{ and } \theta_c = 0.047 \tag{5}$$

where d_m denotes the mean grain size diameter [m], θ the dimensionless Shields parameter and θ_c the dimensionless critical Shields parameter. The calibration of MPM formula on α and γ coefficients lead to other formulations, tested and verified for river applications [25].

The formula of WC-2003 is based on the estimation of the transport rate per unit of width for the i^{th} size fraction $q_{b,i}$ by the relation:

$$W_i^* = f(\tau/\tau_{ri}) = \frac{\Delta_s g q_{b,i}}{F_i {u_*}^3} \quad , \tag{6}$$

where W_i^* denotes the form of similarity collapse over fractional transport rate (also refered to as the dimensionless transport rate for the i^{th} class of sediment), τ [Pa] is the bed shear stress, τ_{ri} [Pa] the reference shear stress of the i^{th} size class (also refered to as the similarity parameter), F_i is the proportion of size i on the bed surface, $\Delta_s = \rho_s/\rho - 1$ is the relative submerged sediment density and u_* [m/s] the shear velocity. τ_{ri} is defined as the value of τ at which W_i^* is equal to a small reference value of 0.002 [7], [12]. The transport function is defined as follows:

$$W_i^* = \begin{cases} 0.002\Phi^{7.5} & \text{for } \Phi < 1.35 \\ 14\Big(1 - \dfrac{0.894}{\Phi^{0.5}}\Big)^{4.5} & \text{for } \Phi \geq 1.35 \end{cases} \quad , \tag{7}$$

where $\Phi = \dfrac{\tau}{\tau_{ri}}$ corresponds to the ratio between the fluid shear stress over the reference shear stress of size fraction i. The relationship between the variables and processes accounting for the transport of graded sediment are showed in Figure 2.

The definition of the hiding function was made in two steps. First, the authors introduced a hiding function analogous to that used in previous graded transport models [5] [16] [12] in the way that sediment transport rates are lowered for finer fractions (*i.e.* decrease of τ_{ri}) and increased for coarsest material (*i.e.* increase of τ_{ri}):

$$\frac{\tau_{ri}}{\tau_{rm}} = \left(\frac{D_i}{D_{sm}}\right)^b \quad \text{with} \quad b = \frac{0.67}{1 + \exp\left(1.5 - \dfrac{D_i}{D_{sm}}\right)} \quad , \tag{8}$$

where τ_{rm} is the reference shear stress of the mean size of bed surface, D_i is the grain size of fraction i and D_{sm} the mean grain size of bed surface. In this study, it is important to mention that d_m and D_{sm} are equivalent, as we use a single layer to model surface sediment transport. Secondly, the hiding function was modified to predict τ_{rm} in function of the dimensionless reference shear stress of mean size of bed surface ${\tau^*}_{rm}$:

$${\tau^*}_{rm} = \frac{\tau_{rm}}{(s-1)\rho g D_{sm}} \quad , \tag{9}$$

with ρ the water density. The dimensionless reference shear stress ${\tau^*}_{rm}$ was shown to decrease exponentially in function of the sand fraction at the bed surface denoted F_s [7] (wrongly mentionned as the percentage of sand in the original article of Wilcock and Crowe [23]):

$${\tau^*}_{rm} = 0.021 + 0.015\exp[-20F_s] \quad . \tag{10}$$

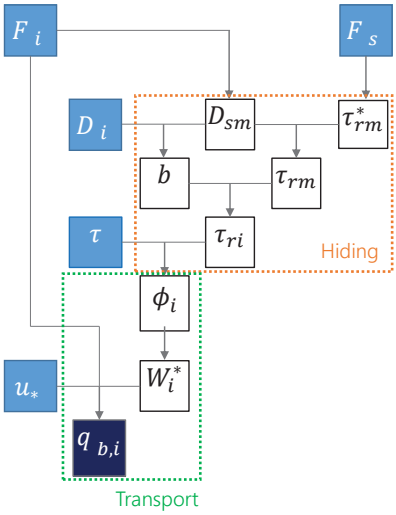

Fig. 2: Scheme of application of the mixed-size sediment transport model of WC-2003. Parameters in blue boxes are input parameters, those in white boxes are intermediary variables computed to estimate the transport rate of size fraction i in the black box.

In the module Sisyphe of TMS, the model was implemented in a new subroutine named `Wilcock_Crowe_bedload.f` which is called by `bedload_formula.f`. At each computational time step, the fraction of sand F_s is computed at each node in the subroutine `bedload_main.f` and transfered to several of its subroutines. The model requires information on the geometric mean grain size of the bed surface D_{sm} which is computed in the subroutine `mean_grain_size.f` (*cf.* Appendix A).

C. Wilcock and Crowe experiments

A brief description of the Wilcock and Crowe [23] experiments is given below. The experiments of WC-2003 were run in a laboratory tilting flume of 0.6 m wide and 8 m long working section, with a 1 m long upstream section dedicated to flow and morphodynamical adaptation. The flow depth was held in a narrow range for all flume runs with values between 0.09 m and 0.12 m, so that we can neglect the viscosity forces. Each experiment was run at least for 60 min to ensure the morphodynamic equilibrium and the data provided by WC-2003 are recorded from the final state of the experiments (*cf.* Tab.I).

The sediment transport model of WC-2003 was calibrated using five GSD by adding different amounts of sand to a gravel mixture. The sand ranged in size from 0.21 to 2.0 mm and the

gravel from 2.0 to 64 mm. For each single GSD, the fraction of sand F_s varied from 6.2% to 34.3%, which allows the representation of a wide range of natural gravel-bedded rivers. Sediment transport rates varied at least four orders of magnitude for each mixture, ranging from 1.8×10^{-5} kg m^{-1} s^{-1} to 1.2×10^{-1} kg m^{-1} s^{-1} [23]. The observations made by WC-2003 [23] assume that particles are subject mainly to bedload transport. The dataset includes hydraulics measurements (water depth, longitudinal flow velocity, discharge) and sedimentary records (transport rate, bulk and surface GSD). More details about the experimental set-up and methods of data recording is documented in Wilcock and McArdell [24].

Among the 49 experimental tests performed by WC-2003, 2 distinct cases (namely BOMC2 and BOMC4) are considered to carry out the numerical investigations presented later. Both laboratory experiments started with the same initial bed surface GSD composed of the bulk-mix denoted BOMC (Bed Of Many Colors, see Fig.3). Different input flowrates are injected in both experiments, resulting in a different final state equilibrium for the geometry (longitudinal slope), hydraulics (*i.e.* water depth, velocity, shear velocity, friction forces, *etc.*, see Tab.I) and sedimentary properties (*i.e.* transport rate, surface GSD, *etc.*, see Fig.3) between both systems.

Name	Q [m$^2/s$]	h [m]	-$\partial_x z_b$	u [m/s]	q_s [g/m/s]	Froude
BOMC2	0.067	0.112	0.0032	0.60	7.1	0.57
BOMC4	0.081	0.094	0.0077	0.90	157	0.90

TABLE I: Mean geometric, hydraulic and sedimentary variables recorded in the end of the experiments BOMC2 and BOMC4 of WC-2003.

The choice of reproducing numerically the laboratory experiments using the BOMC GSD was made in order to investigate the behavior of two distinct sediment transport capacity formulas, using extreme conditions of wide size distribution of sediments. Indeed, Fig.3 clearly shows the bimodality (close to trimodality) of the BOMC GSD. The comparison between BOMC2 and BOMC4 experiments allows the study of the system under the *partial* and *full* transport respectively.

III. Numerical modelling of graded sediment transport

The main caracteristics of the numerical models which have been developed to reproduce the two distincts scenarios of the experiments of WC-2003 (BOMC2 and BOMC4 respectively) are presented in this section. A description of the model geometry and the choice of boundary conditions is firstly given. Secondly, a step of calibration on bottom friction forces was necessary to achieve hydraulics uniform and permanent regimes. Finally, further details are presented on the set-up of the morphodynamic models.

The present study is intended to focus on the sediment transport capactity estimation. Other phenomenogical aspects such as riverbed evolution are not discussed here. As a consequence, the present numerical models are designed to start directly from the equilibrium conditions of WC-2003 experiments given in Tab.I.

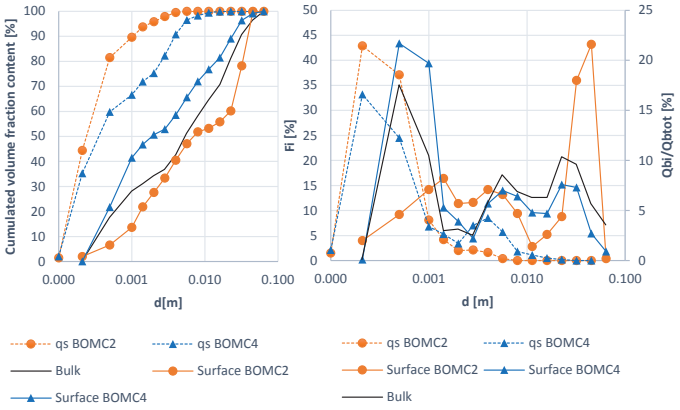

(a) (b)

Fig. 3: (a) GSD of the bulk, surface and transport for BOMC2 and BOMC4 experiments of WC-2003, (b) Frequency distribution of the surface granulometry and volume fraction of transport of each class of sediment.

A. Mesh and topography

The domain is represented by a computational mesh of 10 m long and 0.6m wide, composed of 4427 irregular triangles with an approximate size of 4 cm, so that the cross-sections are defined by approximately 18 nodes. The initial longitudinal slopes of BOMC2 and BOMC4 numerical experiments are given in Tab.I. Morphodynamics simulations are run using a constant computational time-step equal to 0.01 s. The strategy of model calibration is presented later in the paper.

B. Model boundary conditions

Numerical simulations are run under subcritical flow conditions (Tab.I). To achieve properly the uniform-permanent equlibrium state observed by WC-2003, the upstream boundary condition is defined as a constant discharge Q and the downstream boundary condition is imposed as a constant free surface profile (Fig.1). Friction forces due to the clear sidewalls [24] are neglected in the model. The hotstart generation (uniform steady flow) is reached after 100 s for both experiments.

The upstream boundary condition is set as a recirculating flux of sediment (*i.e.* outgoing sediments are reinjected upstream) generalized for graded sediment transport and the downstream boundary nodes are set as non-erodable (*i.e.* nodes elevation is fixed). Implementation of the recirculation of sediment required the modification of several Sisyphe subroutines (*cf.* Appendix B).

C. Model calibration

The calibration of the hydrodynamic model is performed on the basis of the modification of the roughness coefficient of Strickler (Eq.2). Sensibility analysis are firstly carried out using a small numerical time-step equal to $\Delta t = 0.005$ s with a Strickler coefficient in the range of [40-50] m$^{1/3}$/s. The arbitrary value of $\Delta t = 0.005$ s is chosen to achieve a CFL number equal in the order of 0.125. Results from calibration on water depths and longitudinal velocity are shown in Figure 4 and the absolute error plots suggest that a value

of $K = 45$ m$^{1/3}$/s yields satisfactory values of water depths and velocities, which remain less than 1% along the whole longitudinal profile.

The influence of the computational time-step is investigated to determine a good compromise between results quality and simulation time. Table II shows the absolute averaged error per node in water depth [m] using three higher values of Δt equal to 0.01, 0.02 and 0.05 s respectively, using $\Delta t = 0.005$ s as a reference. A time step equal to $\Delta t = 0.01$ s has been chosen for the numerical simulations reported here. Indeed, this value of time-step gives satisfactory results in matter of water depths compared to the reference time-step, whereas the value of $\Delta t = 0.2$ s gives values diverging from the reference with a value over 10%.

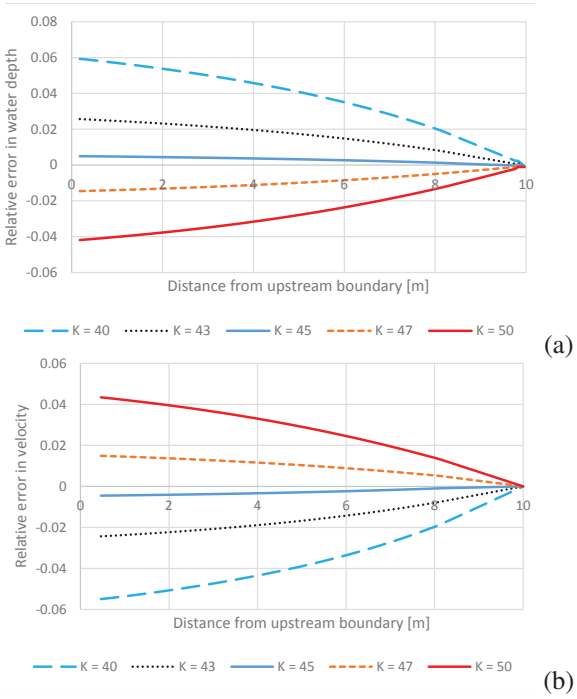

Fig. 4: Relative errors computed along the longitudinal profile for (a) the water depths and (b) the velocities, issued from variation of the Strickler friction coefficient.

Time step [s]	Error in water depth estimation [m]
0.01	$2.3{\cdot}10^{-8}$
0.02	$1.44{\cdot}10^{-3}$
0.05	0.115

TABLE II: Absolute averaged error per node in water depth [m] for different computational time-steps.

D. Morphodynamic parametrisation

As a single layer of transport is used in the current model, no GSD evolution of the riverbed is intended to be observed in the numerical experiments. Instead, the numerical models are implemented to run short-term simulations of 100 s, with the assumption that the morphodynamic equilibrium is already achieved from the beginning until the end of the computation. In the experiments of WC-2003, the bed does not present transverse slopes so that bed slopes effects acting sediment transport can be neglected as long as the formation of helical flows.

The discretization of the GSD into size classes of sediment is made in different ways, and the impact of such method of discretization is investigated in the following section:

- Fractional: The GSD is divided into N classes of sediment, where F_{i+1}=F_i $\forall i \in [1 : N-1]$.
- Diametral: The GSD is divided into N classes of sediment, where $D_{i+1} = D_i + A$ $\forall i \in [1 : N-1]$, where A is constant.
- Power-P-Diametral: The GSD is divided into N classes of sediment, where $D_{i+1} = D_i^P$ $\forall i \in [1 : N-1]$, where P is constant.

An example of GSD discretization using the three methods and different numbers of size classes is given in Figure 5. In this work, the following discretizations are considered: fractional for 2, 5 and 10 classes; diametral for 5 and 10 classes; and power-4 for 5 classes and power-2 for 10 classes.

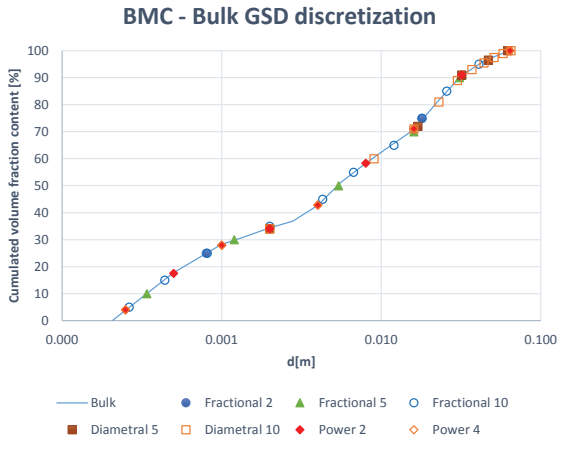

Fig. 5: Discretization of the BOMC GSD using the fractional, diametral and power methods.

IV. Analysis of results and comparison with experiments

Results from numerical investigations are presented hereinafter and are compared with laboratory data from WC-2003. Account is given on several aspects: *i*) the comparison between the MPM and the WC-2003 formulas, *ii*) the impact of GSD discretizing method on sediment transport modelling and *iii*) the influence of initial GSD in the simulations.

A. Comparison between MPM and WC-2003 formulas

The choice of the sediment transport capacity formula has a strong impact on the estimation of the bedload transport rate and fractional transport rates in the numerical models (Fig.6&7). While the formulation of MPM often shows discrepancies with laboratory data, the numerical application of the formulation of WC-2003 gives more satisfactory results (as the formuma was determined from the laboratory data)

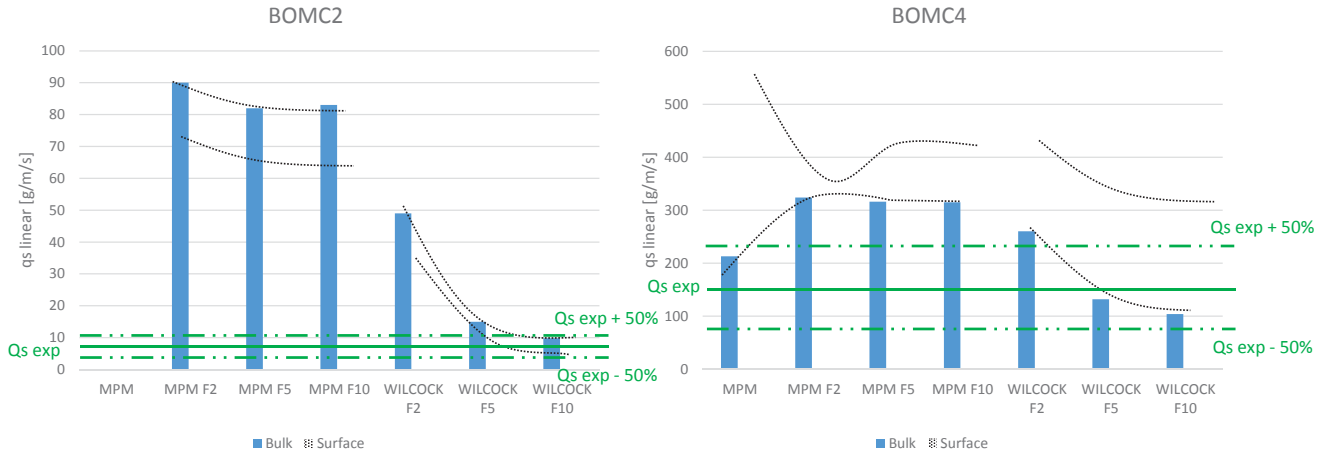

Fig. 6: Comparison between sediment transport rates [g/m/s] computed with MPM and WC-2003 formulas using the fractional discretization method. $Q_{s\ exp}$ corresponds to the flux rates measured in laboratory. F = Fractional discretization and the number stands for the number of size classes of sediment. Black dotted lines help to visualize the convergence.

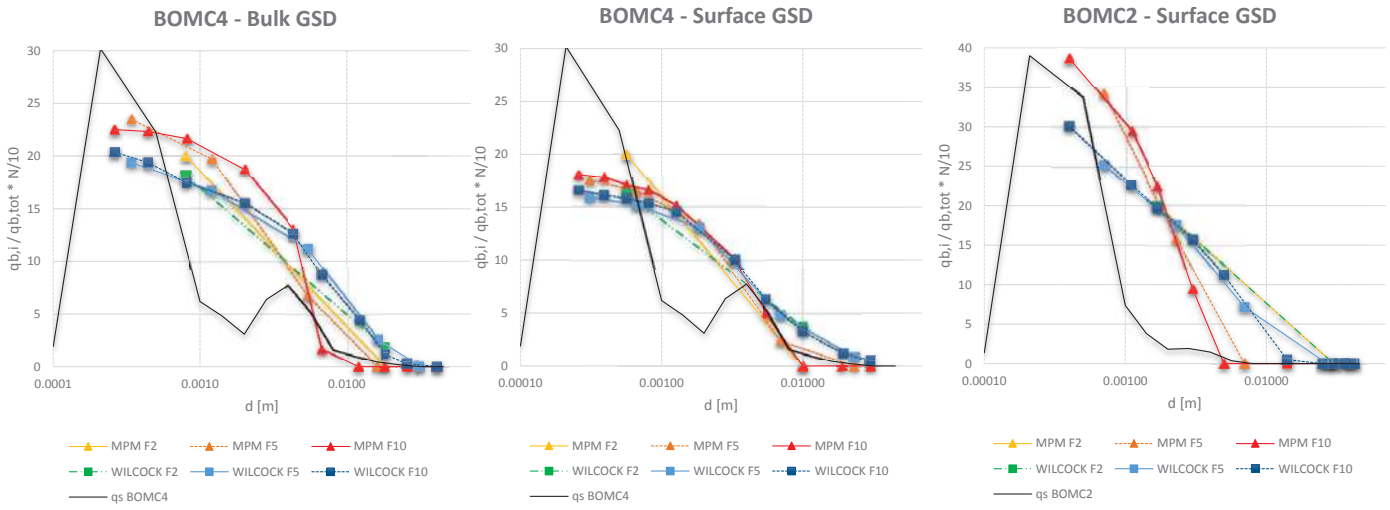

(a) (b) (c)

Fig. 7: Fractional transport rates of each sediment size-class divided by the number of classes, for BOMC4 experiment with (a) the bulk GSD and (b) surface GSD and the BOMC2 experiment with surface GSD (c).

and physical relevant results. Here, comparisons between bedload formulas are made by using the fractional discretization method, which gives the best results compared with the other discretizing methods (*cf.* IV-B). A convergence analysis on the number of discretizing sediment size classes has been lead to determine their impact on the transport of graded sediment. Convergence of the bedload transport rate (Fig.6) and of fractional transport rates (Fig.7) is observed in every case. It has to be noted that the formula of MPM converges relatively faster than the formula of WC-2003 (Fig.6).

Figure 6 clearly depicts the discrepancies between the sediment transport rates estimated by MPM and WC-2003. Under partial transport mode conditions (*i.e.* BOMC2 experiments), sediment fluxes computed by WC-2003 converge toward a value of 9.8 g.L.s^{-1} for the bulk GSD (*i.e.*) overestimation of 38%) and 5.8 g.L.s^{-1} for the surface GSD (*i.e.*) underestimation of 18%), that lies in the range of sediment fluxes measured in the experimental flume. Altough under total transport conditions (*i.e.* BOMC4 experiments) the bedload transport rate determined by the formula of WC-2003 differs from the measurements (Fig.6), the sediment transport model still computes realistic values with -34% of error for the bulk GSD and 102% for the surface GSD. This difference between laboratory measurements and numerical results can be explained by the experimental data-fitting of the WC-2003 formula. In the other hand, the formula of MPM generally tends to overestimate sediment transport when several size classes of sediment are used, whereas no general rule can be drawn when unisize sediment is used. The difference remains large considering different modes of transport, results provided by the MPM formula lie in a larger range of error of factor around [+50%;+200%] under partial transport conditions and [-100%;+1000%] under total transport conditions. Figure

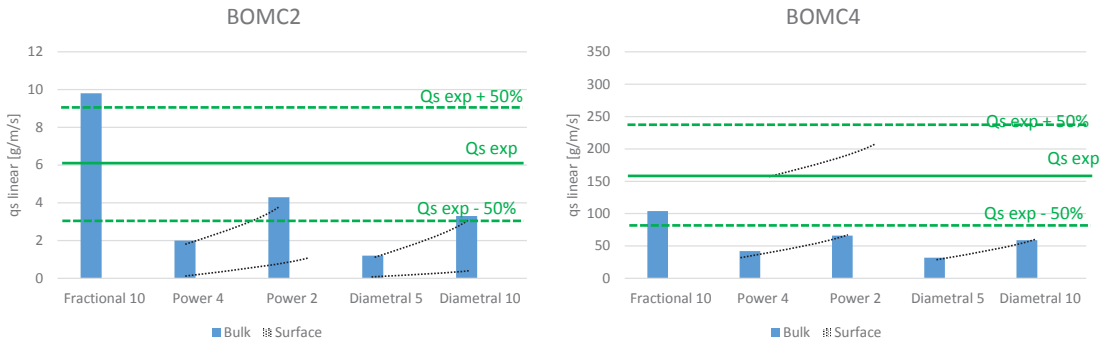

Fig. 8: Comparison between sediment transport rates [g/m/s] computed by the WC-2003 formula using different discretization methods (*cf* Fig.5) presented in IV-B.

7 highlights the differences in the fractional transport rates computed by both formulas. In every case, it is observed the general tendancy of monotonic sediment transport decrease with particle size increase, with the convergence toward a defined GSD shape with the increase of number of size classes. The hiding function of WC-2003 induces a counterbalance in the fractional transport rates, making them decrease for finer particles and increase for coarser ones, in comparison to values determined by the classical formulation of MPM.

While the unimodal shape of the fractional transport rate is reproduced for the BOMC2 experiment, the bimodal shape of sediment transport is not represented by the BOMC4 numerical models (Fig.7). According to the Figure 7, the formula of WC-2003 tends to smooth and skew the sediment transport, so that abrupt transitions conducting to bimodality of transport cannot be accurately represented in the models.

B. Comparison between GSD discretization methods

Natural rivers GSD commonly show a continuous sorting of sediment and a bimodal behavior. The representation of such density functions in the WC-2003 model requires the subdivision of the initial surface GSD into size classes of sediment. Different discretization methods can be used, and their impact on fractional sediment transport is not yet known. To test the impact of the GSD discretization method on fractional sediment transport estimation, several scenarios are proposed where three distinct methods are used (*cf.* III-D).

According to Figures 6&8, diametral and power discretization methods always give lower transport rates than methods based on the fractional discretization. This property can be explained among other things by the fact that the value of the mean diameter D_{sm} is strongly dependent to the chosen method of discretization. Indeed, Figure 9 shows the tendancy of D_{sm} underestimation for the fractional method and overestimation for the other ones, besides the fact that D_{sm} converges with the number of size classes increasing. Methods based on the power and diametral discretization show the same tendancy of total sediment transport increase with the number of discretizing size classes increasing. As a rule, the diametral discretization shows unsatisfactory results, with an error inferior to -50% on fluxes estimation, and a complete cessation of transport using the surface GSD. Altough the power-2-based method gives relatively acceptable values of

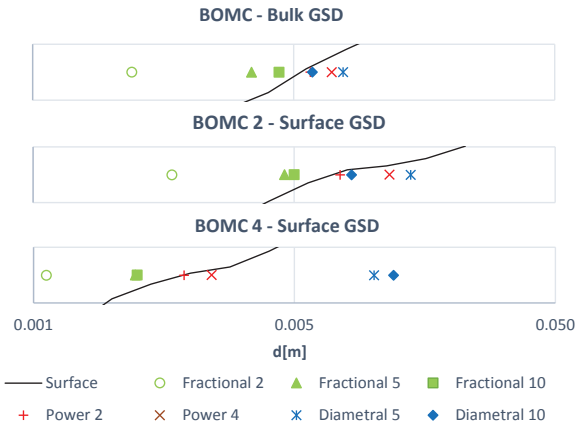

Fig. 9: Computed value of the mean diameter D_{sm} using different GSD discretization methods presented in IV-B.

transport rates (-63% of error for the bulk and +49% for the surface GSD) at full transport conditions (*i.e.* BOMC4 experiment), it tends to underpredict transport (-39% of error for the bulk and -83% for the surface GSD) at partial transport conditions (*i.e.* BOMC2 experiment).

To conclude, the current model needs an appropriate discretization of the GSD to be set-up, and that the fractional method seems to be appropriate to this model.

C. Influence of initial sediment composition

The choice of the surface GSD in the numerical model has a strong impact on the bedload transport rates and on fractional transport rates. Here, attention is given on the results obtained by the WC-2003 formula with *i*) a bed composed of the bulk GSD called BOMC and *ii*) a bed composed of the surface GSD sampled in the end of the experiments of WC-2003.

Firstly, it is obvious that different GSD provide different D_{sm} (Fig.7&9), which will have consequently an impact on the estimation of bedload transport (Eq.7).

Bedload fluxes computed here for 10 size classes of sediment under partial transport conditions (*i.e.* BOMC2) for the surface GSD are lower than the ones computed with the bulk

GSD of a factor equal to 3 (Fig.6). This tendancy is inverted under full transport conditions (*i.e.* BOMC4), where the total transport rate estimated from the surface GSD is stronger than the one produced by the bulk GSD, with a lower factor equal to 1.7.

Figure 7 highlights the differences in estimated fractional transport rates depending on the choice of the riverbed composition for the BOMC4 experiment. While the surface GSD gets finer than the bulk GSD at the end of the BOMC4 laboratory experiment (Fig.5), the comparison between transports rates given by the bulk GSD (Fig.7a) and the surface GSD (Fig.7b) show that a counterbalancing effect is applied to fractional transport rates. Indeed, the distribution of fractional transport rates tends to be finer by using the bulk GSD and coarser using the surface GSD.

V. Conclusion

Numerical investigations based on the experiments of WC-2003 constitute a first step for the modelling alluvial bars morphodynamics. Whereas most of engineering applications still rely on the use of classical sediment transport models (*i.e.* MPM) to model graded sediment processes, the present study outlines the importance of using adapted models such as the one proposed by Wilcock and Crowe [23]. The implementation of such sophisticated models is a necessary condition to improve the estimation of the fractional transport rates in natural rivers, thus a better simulation of bar armoring and armor break-up in the framework of bars modelling. Results from numerical modelling show that the formula of WC-2003 gives more relevant fractional and total transport rates compared to the ones given by the classical formula of MPM.

However, the numerical application of graded sediment transport models is not straightforward, as it shows in this case a lot of sensitivity to *i*) the method of GSD discretization and *ii*) the number of size classes of sediment. On the one hand, the method of fractional discretization shows more satisfactory results than the other methods presented in the paper. On the other hand, previous numerical studies implementing the formula of WC-2003 were conducted with only two size classes of sediments made of sand and gravel respectively [2], while the formula of transport was originally calibrated on 15 size classes of sediment. Moreover, in the configuration of the experiments, it is observed that D_{sm} may vary of several orders of magnitude depending on the number of size classes and that bedload transport rates become relevant starting from a number of 5 size classes of bed material.

This study also underlines the importance of the choice between the surface GSD and the bulk GSD for the modelling of alluvial bars dynamics. If the numerical model is designed to investigate long-term scenarios of bars dynamics starting from a flat bed, the initial surface GSD in the model should be the one of the bulk mix, and the model would require the definition of an active layer to take account of the vertical sorting processes allowing the surface GSD to change in time. If bars are already present as initial topographic conditions in the model, it would be more appropriate to dissociate the substrate and the active layer GSD together with planimetric variations of the GSD, which makes the process of model setting-up manifestly more difficult.

Altough the model of WC-2003 remains a satisfying estimator for the total transport rate, the models seems to be limited for the determination of fractional transport rates. The distribution of fractional transport rates tends to be smoothed out and no bimodality of transport is observed in contrast to the experimental runs. To complete this study, other experimental runs could be reproduced, including a different bulk GSD and greater number of sediment size classes. Further numerical models could be relaxed by including the definition of the active layer concept [8] in order to account for the temporal variation of the surface GSD. Another limitation is based on the fact that a wide GSD is associated to a decrease of bed porosity (which can be represented by the *Appolonian gasket* problem [19]), which require an appropriate formulation to be took into account.

Acknowledgment

We are grateful for the precious contribution of Pf. Wilcock for his online measurement data.

VII. References

[1] J. Bridge and R. Demicco, *Earth surface processes, landforms and sediment deposits*. Cambridge University Press, 2008.

[2] Y. Cui, "The unified gravel-sand (tugs) model: Simulating sediment transport and gravel/sand grain size distributions in gravel-bedded rivers," *Water resources research*, vol. 43, no. 10, pp. 1 – 16, 2007.

[3] M. de Linares and P. Belleudy, "Critical shear stress of bimodal sediment in sand-gravel rivers," *Journal of Hydraulic Engineering*, vol. 133, no. 5, pp. 555–559, 2007. [Online]. Available: http://dx.doi.org/10.1061/(ASCE)0733-9429(2007)133:5(555)

[4] I. Egiazaroff, "Calculation of nonuniform sediment concentrations," *Journal of the Hydraulics Division*, vol. 91, no. 4, pp. 225–247, 1965.

[5] H. A. Einstein, *The bed-load function for sediment transportation in open channel flows*. US Department of Agriculture, 1950, no. 1026.

[6] F. Engelund and E. Hansen, "A monograph on sediment transport in alluvial streams," Tekniskforlag Skelbrekgade 4 Copenhagen V, Denmark., Tech. Rep., 1967.

[7] M. H. Garcia, "Sedimentation engineering," *Processes, Measurements, Modeling, and Practice. ASCE Manuals and Reports on Engineering Practice*, vol. 110, pp. 1–1132, 2008.

[8] M. Hirano, "River bed degradation with armoring," Ph.D. dissertation, Japanese Society of Civil Engineering, 1971.

[9] C. Manes and M. Brocchini, "Local scour around structures and the phenomenology of turbulence," *Journal of Fluid Mechanics*, vol. 779, pp. 309–324, 2015.

[10] E. Meyer-Peter and R. Müller, "Formulas for bed-load transport," in *International Association for Hydraulic Structures Research*. IAHR, 1948.

[11] C. Orrú, A. Blom, and W. S. Uijttewaal, "Armor breakup and reformation in a degradational laboratory experiment," *Earth Surface Dynamics*, vol. 4, no. 2, p. 461, 2016.

[12] G. Parker, "Surface-based bedload transport relation for gravel rivers," *Journal of hydraulic research*, vol. 28, no. 4, pp. 417–436, 1990.

[13] G. Parker and P. C. Klingeman, "On why gravel bed streams are paved," *Water Resources Research*, vol. 18, no. 5, pp. 1409–1423, 1982. [Online]. Available: http://dx.doi.org/10.1029/WR018i005p01409

[14] G. Parker, P. C. Klingeman, and D. G. McLean, "Bedload and size distribution in paved gravel-bed streams," *Journal of the Hydraulics Division*, vol. 108, no. 4, pp. 544–571, 1982.

[15] D. M. Powell, A. Ockelford, S. P. Rice, J. K. Hillier, T. Nguyen, I. Reid, N. J. Tate, and D. Ackerley, "Structural properties of mobile armors formed at different flow strengths in gravel-bed rivers," *Journal of Geophysical Research: Earth Surface*, vol. 121, no. 8, pp. 1494–1515, 2016, 2015JF003794. [Online]. Available: http://dx.doi.org/10.1002/2015JF003794

[16] G. Proffitt and A. Sutherland, "Transport of non-uniform sediments," *Journal of Hydraulic Research*, vol. 21, no. 1, pp. 33–43, 1983.

[17] A. Recking, "A comparison between flume and field bed load transport data and consequences for surface-based bed load transport prediction," *Water Resources Research*, vol. 46, no. 3, pp. 1–16, 2010, w03518. [Online]. Available: http://dx.doi.org/10.1029/2009WR008007

[18] A. Recking, G. Piton, D. Vazquez-Tarrio, and G. Parker, "Quantifying the morphological print of bedload transport," *Earth Surface Processes and Landforms*, vol. n/a, pp. n/a – n/a, 2015.

[19] G. Schliecker and C. Kaiser, "Percolation on disordered mosaics," *Physica A: Statistical Mechanics and its Applications*, vol. 269, no. 24, pp. 189 – 200, 1999. [Online]. Available: http://www.sciencedirect.com/science/article/pii/S037843719900093X

[20] U. Singh, A. Crosato, S. Giri, and M. Hicks, "Sediment heterogeneity and discharge variability in the morphodynamic modeling of gravel-bed braided rivers," *Advances in Water Resources (under review)*, vol. n/a, pp. n/a–n/a, 2016.

[21] Z. Sun and J. Donahue, "Statistically derived bedload formula for any fraction of nonuniform sediment," *Journal of Hydraulic Engineering*, vol. 126, no. 2, pp. 105–111, 2000.

[22] G. T. Török, S. Baranya, and N. Rüther, "Three-dimensional numerical modeling of non-uniform sediment transport and bed armoring process," August 2012, department of Hydraulic and Water Resources Engineering, Budapest University of Technology and Economics.

[23] P. R. Wilcock and J. C. Crowe, "Surface-based transport model for mixed-size sediment," *Journal of Hydraulic Engineering*, vol. 129, no. 2, pp. 120–128, 2003.

[24] P. R. Wilcock and B. W. McArdell, "Surface-based fractional transport rates: Mobilization thresholds and partial transport of a sand-gravel sediment," *Water Resources Research*, vol. 29, no. 4, pp. 1297–1312, 1993.

[25] M. Wong and G. Parker, "Reanalysis and correction of bed-load relation of meyer-peter and müller using their own database," *Journal of Hydraulic Engineering*, vol. 132, no. 11, pp. 1159–1168, 2006.

[26] F.-C. Wu and K.-H. Yang, "A stochastic partial transport model for mixed-size sediment: Application to assessment of fractional mobility," *Water resources research*, vol. 40, no. 4, pp. 1–12, 2004.

APPENDIX A - MEAN DIAMETER CALCULATION

Originally, the definition of the average grain size D_{avg} [m] in Sisyphe was based on the simple weigthing average:

$$D_{avg} = \sum_{i=1}^{N} F_i D_i. \tag{11}$$

Where F_i and D_i [m] correspond to the volume fraction content and the diameter of the i size class respectively. In this work, the definition of D_{avg} is replaced by the mean surface diameter D_{sm} [m]. The calculation of D_{sm} was defined by a linear interpolation between size classes of sediments where fractions of sediment are respectively upper and lower 50% of cumulated material.

APPENDIX B - IMPLEMENTATION OF SEDIMENT RECIRCULATION IN SISYPHE

The implementation of sediment recirculation is made in two steps and generalized for transport of mixed-size sediment. Firstly, the variable of transport rate along the boundary nodes denoted `QBOR` is modified in `conlit.f` and `disimp.f` subroutines. As a result, volumes of entering sediments printed by `bilan_sisyphe.f` are equal to exiting volumes of sediments. Secondly, the value of the variable of transport rate in the whole domain `QSCL` which is originally computed with the bedload transport formula is replaced at upstream nodes by the value of the exiting volume of sediment.

Tridimensional numerical modelling of the suspended sediment transport dynamic in Loire River

Germain ANTOINE
EDF R&D, National Laboratory for Hydraulics and Environment
Saint-Venant Laboratory for Hydraulics
Chatou, France
Email: germain.antoine@edf.fr

***Abstract*—Several studies have been done with the objectives of quantifying and simulating sediment transport and morphodynamics of the Loire River, which is considered as one of the last wild sand bed rivers in Europe. However, few of these studies considered the suspended sediment load dynamics. In this study, a local reach of the Loire River is considered, with a complex geometrical configuration: the river reach is composed with two alternate bars in a bend, an adjacent channel is connected to the river by a lateral weir and the last cross section of the reach is defined by a large step. As the adjacent channel is used for electricity production, the work is focused on the deposition dynamics of suspended sediments coming from the Loire River to this channel.**

A field campaign was performed in 2015 during a flood event, in which measurements were made of both bathymetry and the 3D velocity field with an acoustic Doppler current profiler (aDcp). Based on these field data, a TELEMAC 3D model has been built for simulating flow and suspended sediment dynamics of this site. The hydrodynamic part of the model has been calibrated with the aDcp measurements, and three scenarios of discharge conditions in the Loire River have been defined. In order to represent properly the tridimensional flow patterns measured in the adjacent channel, specific values of wall friction coefficients have been calibrated. For the sediment part of the model, ten grain size classes have been simulated and the deposition patterns and volumes in the channel have been analysed. The comparison between numerical results and grain sizes measurements of deposits in the adjacent channel shows good agreements, and the study highlights the complex interactions and transfers from the Loire River in this configuration.

I. Introduction

Several studies have been done with the objectives of quantifying and simulating sediment transport and morphodynamics of the Loire River ([2], [7], [1]), which is considered as one of the last wild sand bed rivers in Europe. However, few of them considered the suspended sediment load dynamics. Two reasons are mainly reported to explain this lack of suspended sediment study: first the dataset for suspended sediment transport is poor. As the river is wide, with a complex morphology, it is difficult to assess properly suspended sediment fluxes in a river cross section. For the same reasons, the transport of the finer grain sized sediments is complex and could be strongly dominated by tridimensional motions of the flow, which means the use of a qualified 3D model.

In this study, a local reach of the Loire River is considered (Figure 1), with a complex geometrical configuration: the river reach is composed with two alternate bars in a bend, an adjacent channel is connected to the river by a lateral weir and the last cross section of the reach is defined by a large weir. As the adjacent channel is used for electricity production, the work is focused on the deposition dynamics of suspended sediments coming from the Loire River to this channel (Figure 2).

Fig. 1: General overview of the study site

Fig. 2: Deposits observed in the upstream part of the adjacent channel

A field campaign was performed in 2015 during a flood event in order to measure precisely the bathymetry of the river reach and the 3D velocity field using an aDcp. Based on these field data, a TELEMAC 3D model has been built for simulating both hydrodynamics and suspended sediment transport. As the adjacent channel is separated from the Loire River by a step significantly higher than the river bed level, bed load transport has not been considered.

The first part of this paper analyses the data obtained from the field campaign. The second part is about the methodology developed to calibrate the hydrodynamic part of the 3D model, and presents the different scenarios chosen for the numerical simulation. Finally, the third part shows the main results of the hydro-sedimentary model.

II. Field measurements

The field campaign has been performed in moderate flood-discharge conditions in March 2015, during a six-month return period flood. During the campaign, the discharge in Loire River was about 850 m^3/s. Both the bathymetric survey and aDcp measurements were done at the same time and with the same GPS system.

A. Bathymetry

The bathymetry measurements were collected using a multi-beam laser instrument. The bottom of the river reach is presented in Figure 3.

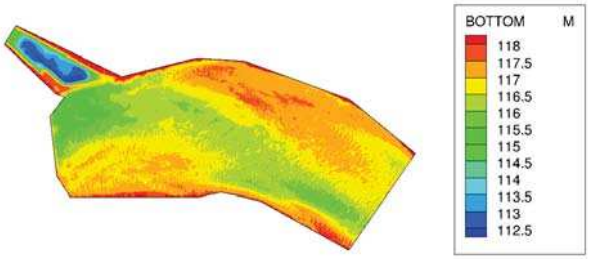

Fig. 3: Bathymetry of the study site

In Figure 3, two large bars can be observed along the reach. The first one, located on the right side, is about 400 meters long and begins at the upstream limit of the study site. The second one, located on the left side, is about 200 meters long and finishes in front of the large weir. On these two bars, it is possible to identify dunes about 70 centimeters high. Between the two bars, a deeper channel makes a straight connection between the left side of the domain entrance and the connection with the adjacent channel. The bottom of the upstream part of the adjacent channel is presented in Figure 4.

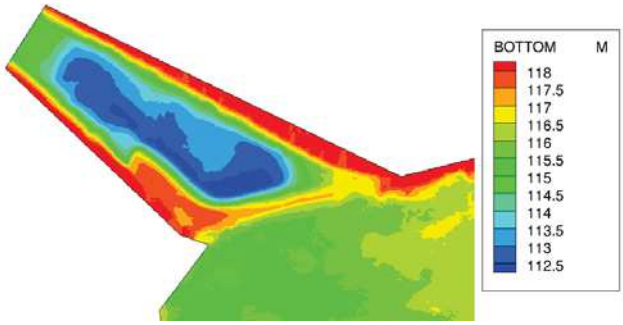

Fig. 4: Bathymetry of the adjacent channel

In the Figure 4, we can notice a significant deposit along the step separating the Loire River and the channel. This deposit propagates towards the downstream part of the channel along the left side. In the centre of the channel, measurements show a large and deep reservoir.

B. Flow velocities

The velocity field of the flow have been measured with a TELEDYN Rio Grande aDcp with a frequency of 600 kHz and with a vertical cell size defined at 25 cm. Along 17 cross profiles in the Loire River and eight profiles in the adjacent channel, five aDcp samples were taken. Along each cross section, these five measurements have been projected and averaged for every vertical and horizontal cells. The depth averaged values of these velocities measured along the profiles in the Loire River are presented in Figure 5, and the ones measured in the adjacent channel in Figure 6.

Fig. 5: Depth averaged velocities measured in the Loire River (in cm/s)

Fig. 6: Depth averaged velocities measured in the adjacent channel (in cm/s)

Figure 5 shows the effect of the complex bathymetry on the spatial distribution of the velocity. On the two bars, the flow velocity decreases with velocities around 1m/s or smaller, and the flow path is concentrated in the main channel between the twos bars. Especially, high velocities have been measured close to the connection with the adjacent channel, with a maximum value of 1.6 m/s.

The velocities measured in the connected channel are significantly smaller than the ones in the Loire river reach (Figure 6). The maximum measured value is about 0.35 m/s, and the aDcp measurement shows a very interesting 2D pattern. Indeed, a double loop of recirculating flow can be observed in this upstream part of the channel. The first loop, close to the river reach connection, rotates clockwise and is two times larger than the second one, counter-clockwise, which is located downstream.

Figure 7 shows a detailed example of spatial distribution of the measured velocities along a cross section in the Loire River, located close to the connection with the adjacent channel. In this figure, it is easy to see the significant magnitude of the transverse and vertical current (black arrows), and the complex distribution of the flow in three dimensions.

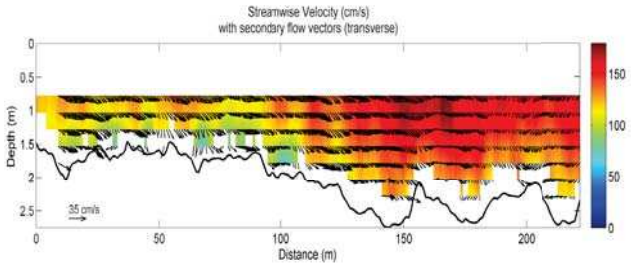

Fig. 7: Local values of flow velocity measured at the P10 cross section

Figure 8 shows another example of measured velocities in a cross section located in the adjacent channel, in the middle of the bigger loop. In this example, we can see that even if the observed velocity magnitudes are almost homogeneous vertically through the water column, the transverse velocities (black arrows) can be significant.

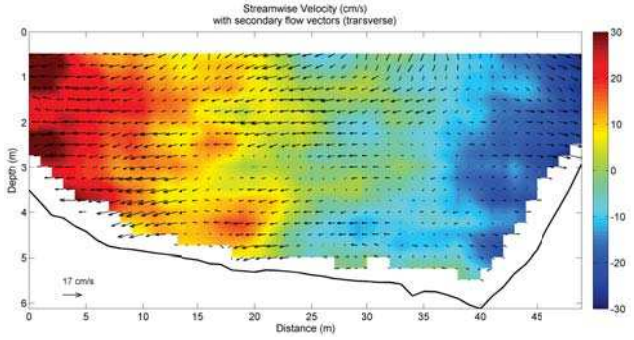

Fig. 8: Local values of flow velocity measured at the P21 cross section

III. Construction of the 3D model and calibration

A. Theoritical background

To simulate hydrodynamics and suspended sediment dynamics for this site, version 7.0 of TELEMAC 3D has been used [4]. The hydraulic part of the model solves a particular case of Navier-Stokes equations [3]. To represent the turbulent processes, several closure equations are available in TELEMAC 3D, as well as for bottom and wall friction source terms.

To simulate the suspended sediment transport dynamic, the hydraulic part of TELEMAC 3D is coupled with the advection dispersion equation, written as follow:

$$\frac{\partial C}{\partial t} + \frac{\partial UC}{\partial x} + \frac{\partial VC}{\partial y} + \frac{\partial}{\partial z}\left(WC - W_s C\right) = \frac{\partial}{\partial x}\left(\nu_t \frac{\partial C}{\partial x}\right) + \frac{\partial}{\partial y}\left(\nu_t \frac{\partial C}{\partial y}\right) + \frac{\partial}{\partial z}\left(\nu_t \frac{\partial C}{\partial z}\right) \quad (1)$$

where C is the suspended sediment concentration, (U, V, W) the three components of the flow velocity, W_s the settling velocity of suspended sediments, and ν_t the turbulent viscosity. The source terms representing the exchanges with the bed (erosion and deposition processes) are calculated as follows:

$$\left(\nu_t \frac{\partial C}{\partial z} + W_s C\right)_{z=Z_b} = F_D - F_E \quad (2)$$

with Z_b the bed level, F_D the deposition flux and F_E the erosion flux.

In this study, we focused on the non-cohesive suspended sediments. With this hypothesis, source terms for erosion and deposition processes are calculated as follow:

$$F_D - F_E = W_s(C_b - C_{eq}) \quad (3)$$

where C_b is the suspended sediment concentration calculated close to the river bed and C_{eq} the equilibrium concentration, calculated with the Zyserman and Fredsoe formula [8].

B. Construction of the 3D model and simulation scenarios

Across the whole domain, a homogeneous irregular mesh was defined, with $\Delta x = 1$ m. On the vertical axis, 10 horizontal plans were defined to discretize the 3D domain (4 128 192 elements).

Three boundary conditions were defined at the liquid boundaries of the domain. The upstream boundary condition is an imposed discharge value and the downstream boundary condition in the Loire River is defined by an imposed value of water level (given by the existing rating curve on the weir). The other downstream boundary condition is located at the end of the adjacent channel, with a imposed discharge value.

For calibrating the hydraulic part of the model, the discharge conditions in Loire $Q_{Measure}$ of the field campaign were chosen. After defining calibration parameters, two other discharge conditions of the Loire River were simulated: the annual mean discharge Q_{Module} and the two years return period flood $Q_{T=2years}$. The Table I shows the BC values for the three discharge conditions.

Scenario	$Q_{upstream}$ Loire (m^3/s)	$Q_{downstream}$ Channel (m^3/s)	$Z_{downstream}$ Loire (m NGF)
$Q_{Measure}$	850	-6.6	118.95
Q_{Module}	328	-6.6	118.11
$Q_{T=2years}$	1600	-6.6	120.02

TABLE I: Definition of the different boundary condition values

For the sediment part of the model, ten sediment classes were simulated separately. As an upstream condition, a fixed suspended sediment concentration of $C_{upstream} = 1$ g/l was defined, with a free fluxes outlet for the downstream boundary conditions. The diameter of these classes (from silt to fine sand) and the associated settling velocity values are presented in Table II.

For these 26 calculation scenarios, the simulation duration was 24 hours of physical time, starting from an initial state

Diameter (μm)	W_s (mm/s)	$Q_{Measure}$	Q_{Module}	$Q_{T=2years}$
40	1.44	C	C	C
63	3.57	C	C	C
100	9.00	C	C	C
150	17.14	C	C	C
200	23.79	C	C	C
300	37.77	C	C	C
400	52.43	C	C	C
600	83.23	C	NC	C
800	115.53	C	NC	C
1200	183.42	NC	NC	C

TABLE II: Sediment parameters for the different simulated scenarios (C: calculated, NC: non-claculated)

with a uniform water level. The steady state for hydraulic was obtained after one and a half hours of physical time. The simulations were performed on the EDF R&D cluster ATHOS, using 96 processors for each run. The spatial distributions of the velocity magnitude, the deposition patterns and volumes into the channel are analysed in the next section.

C. Hydrodynamic calibration

Figure 9 shows the velocity magnitudes simulated at steady state with a Strickler bottom coefficient of $K = 40$ m$^{1/3}$/s. Several values of K were tested, but the value $K = 40$ m$^{1/3}$/s gave the best results. Indeed, we can see that the spatial distribution of the velocities is well correlated to the measured values (Figure 5) : the velocities are smaller on the two alternate bars, and the highest velocities are located in the main bathymetry channel, close to the connection with the adjacent channel. Furthermore, the simulated values are very close to the measured ones.

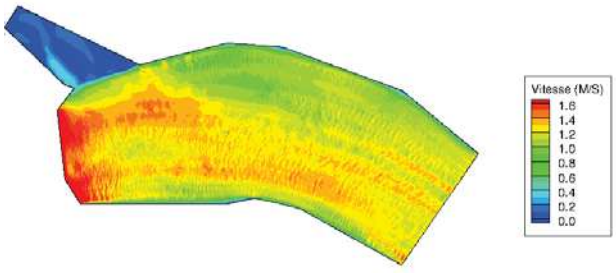

Fig. 9: Simulated depth averaged velocities over the whole domain

The depth averaged velocities were compared to the measured ones along several cross sections. Figure 10 shows an example of results along a river cross section, (total velocity magnitude in red, along X and Y axis components). We can see on this figure that the results are well correlated to the measured ones.

In order to represent properly the flow patterns measured into the adjacent channel, specific values of wall friction coefficients of the Nikuradse law [3] (from $k_{S\ Wall} = 0.01$ to 20 m) and several turbulence models were tested. A 2D geometrical reference of the flow pattern was defined (Figure 11) in order to compare the model output with the measurements. The best agreement was obtained with $k_{S\ Wall} = 5$ m and a $k-\epsilon$ model for both horizontal and vertical dimensions (Figure 12). In this

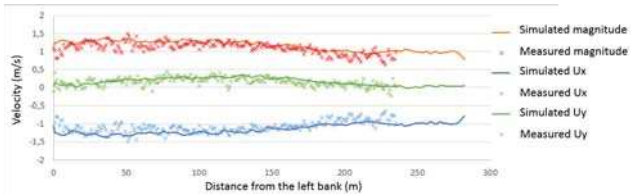

Fig. 10: Example of simulated depth averaged velocities along a cross section (continue lines). Comparison with measurements.

case, the choice of the turbulence model had a smaller effect on the simulation results than the $k_{S\ Wall}$ coefficient. A value of $k_{S\ Wall} = 5$ m could be considered as a non-physical value. However, Patzwahl et Güngör (2015) [6] used a similar values on the Elbe River ($k_{S\ Wall} = 7$ m), justifying this choice by the presence of sheet piling, not represented explicitly in the model.

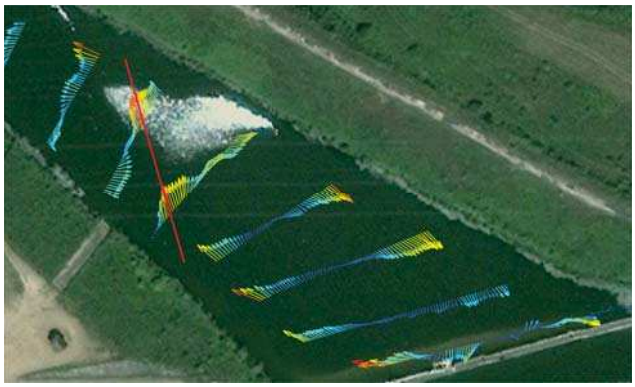

Fig. 11: Geometrical reference (red line)

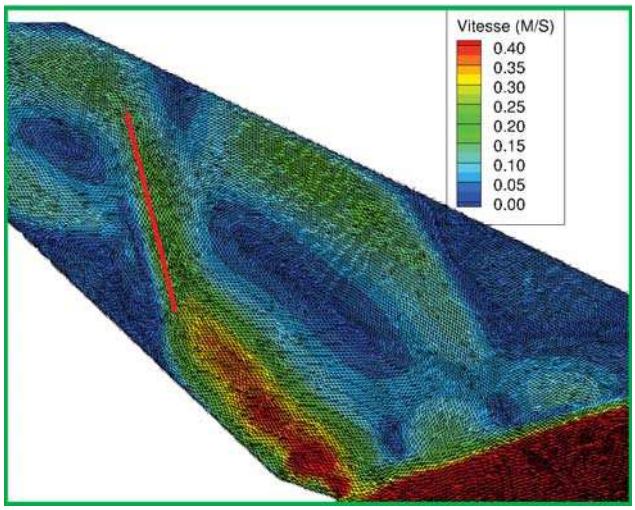

Fig. 12: Calibrated numerical results

IV. Results

A. Flow velocity in the adjacent channel

Depending on the discharge value in the Loire River reach, the flow pattern in the adjacent channel may significantly change. Figure 13 presents the spatial distribution of the calculated velocity magnitudes in the adjacent channel. In this figure, the flow patterns appear to be strongly affected by the changes in discharge conditions in the Loire River. For a discharge value $Q_{T=2years}$ in the Loire River, the double-recirculation pattern is accentuated, with higher velocity magnitudes along the pattern. In this case, the transfer between the river and the channel is accelerated. For Q_{Module}, the velocity magnitudes in the channel decrease and the transferred discharge is not high enough to keep producing the double-recirculation pattern: the simulated results show one small recirculation pattern at the entrance of the channel, with a significant part of the flow rate directed toward the downstream boundary condition.

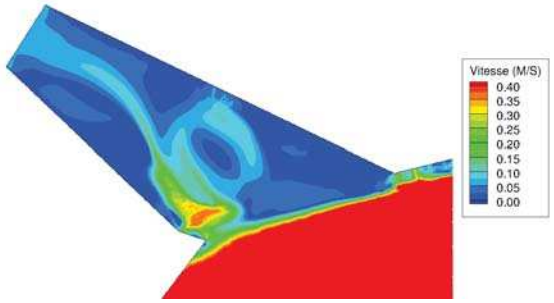

(a) Q_{Module}

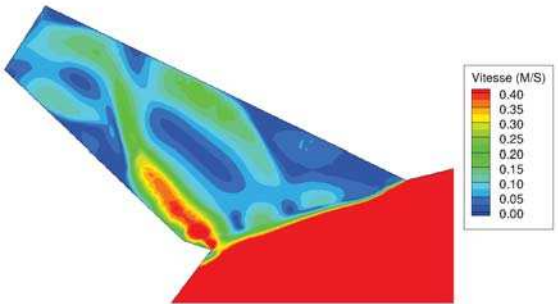

(b) $Q_{Measure}$

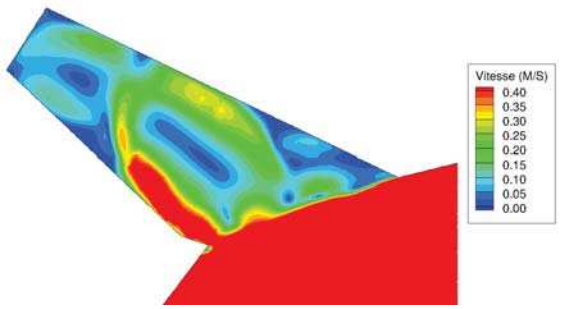

(c) $Q_{T=2years}$

Fig. 13: Simulated velocity magnitude in the adjacent channel for three discharge values in the Loire River

B. Suspended sediment concentration

As the top level of the step separating the adjacent channel from the Loire River is significantly higher than the Loire river bed, the spatial distribution of the suspended sediment concentration in the Loire River reach is of greatest importance for evaluating the sediment transfer to the channel. Depending on the settling velocity of the sediment class and the velocity magnitude in the Loire River, the suspended sediments may be transferred to the adjacent channel over the step.

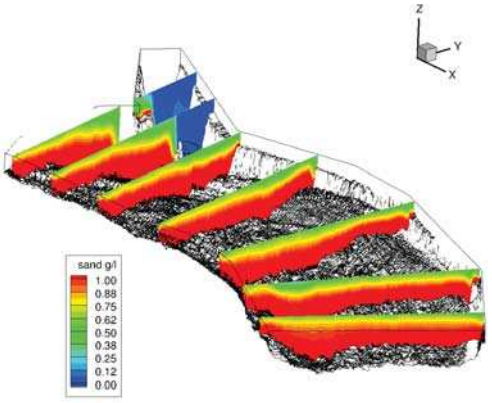

(a) $D = 100$ μm

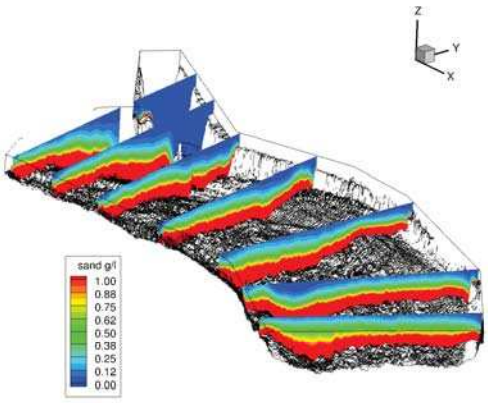

(b) $D = 300$ μm

Fig. 14: Suspended sediment concentration in the Loire River reach for two different sediment classes at $Q_{Measure}$

Figure 14 shows an example of the suspended sediment concentration distribution in the Loire River, in the $Q_{Measure}$ discharge condition and for the sediment classes $D = 100$ μm and $D = 300$ μm. These two figures show clearly that for one given discharge condition, the increase in settling velocity induces a decrease in the suspended sediment concentration transfer to the adjacent channel. For $D = 100$ μm, the suspended sediment concentration is well distributed in the cross sections of the Loire River and is transferred over the top of the adjacent step to the channel. For $D = 300$ μm, the suspended concentration increases with the water depth in any given cross section, so that only a fraction of the sediment fluxes is transferred to the channel.

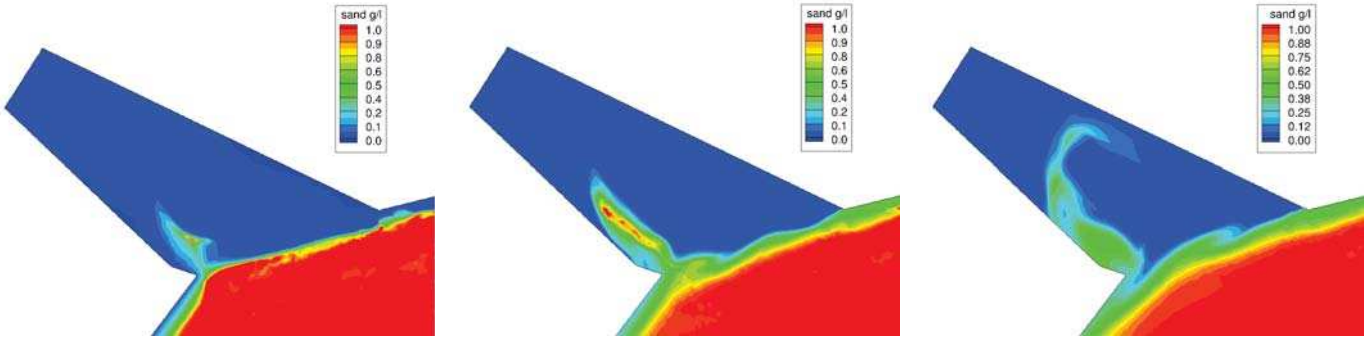

(a) Q_{Module} (b) $Q_{Measure}$ (c) $Q_{T=2years}$

Fig. 15: Spatial distribution of the depth averaged suspended sediment concentration in the adjacent channel for $D = 150$ μm

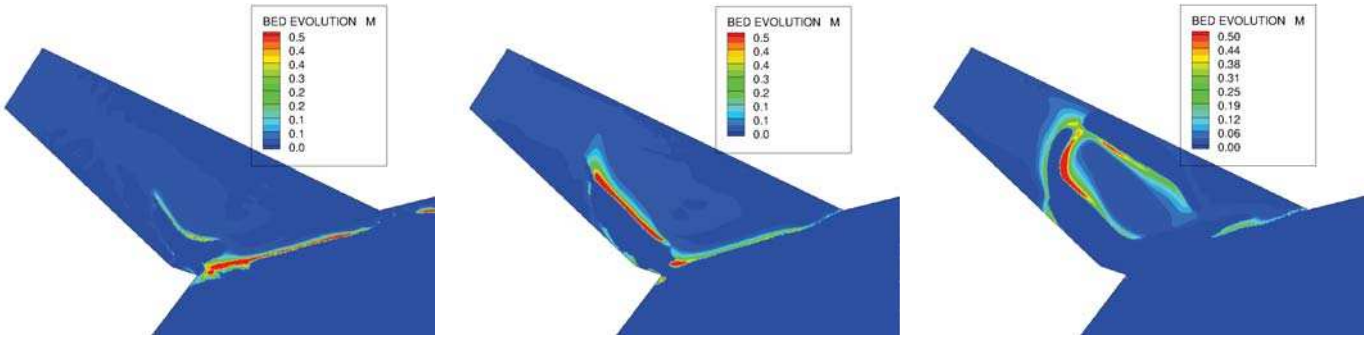

(a) Q_{Module} (b) $Q_{Measure}$ (c) $Q_{T=2years}$

Fig. 16: Spatial distribution of bed evolution in the adjacent channel for $D = 150$ μm at the end of the simulation

The Figure 15 shows the spatial distribution of depth averaged suspended sediment concentration in the adjacent channel, for $D = 150$ μm and the three simulated discharge conditions in the Loire River. These results illustrate the effect of the discharge conditions in the Loire River on the transfer of sediment fluxes to the adjacent channel, for a given sediment class. For Q_{Module} and $Q_{Measure}$, the main part of the suspended sediment flux is transported along the deposit on the left side of the channel. For $Q_{T=2years}$, the suspended sediment flux is transported along the double recirculation pattern to the deepest part of the channel, where it becomes diluted and dispersed.

C. Deposition dynamic in the adjacent channel

The rapid decrease of flow velocity in the adjacent channel increases the deposition probability of suspended sediments. Following the flow patterns observed in the channel, deposition will occur with different spatial distributions and volumes. For a given discharge in Loire River, a decrease of the sediment diameter allows the suspended sediments to be transported further to the downstream part of the adjacent channel and finally, to be dispersed and deposited. For a given sediment class, the increase of discharge condition in the Loire River will produce almost the same effect.

The Figure 16 shows the simulated bed evolution in the channel at the end of the simulation time, for the three tested discharge conditions of the Loire River and $D = 150$ μm. For Q_{Module}, deposition is mainly located on the step separating the Loire River and the channel, with a small deposit on the very upstream part of the left bank. With $Q_{Measure}$, the suspended sediments are transported and deposited further along the left bank deposit. At $Q_{T=2years}$ in the Loire River, the same sediment class propagates to the deepest part of the adjacent channel and is deposited in this zone following the flow pattern.

For each simulation, the sediment volume deposited in the adjacent channel at the end of the simulation has been estimated. These values are presented in Figure 17. This figure shows an interesting result: depending on the discharge value in the Loire River, the maximum value of sediment volume deposited in the channel corresponds to different values of sediment diameter.

For $Q_{T=2years}$, the deposited volume is maximal for $D = 150$ μm, instead of $D = 40$ μm for Q_{Module} and $D = 63$ μm for $Q_{Measure}$. This graph shows also that for a given discharge value in the Loire River, the maximal sediment diameter that can be transferred to the adjacent channel varies widely. As an example, sediment classes with diameters higher than $D = 150$ μm are mainly deposited outside of the channel for Q_{Module}. For $Q_{T=2years}$, the sediment class $D = 800$ μm is still transferred in small quantity to the channel.

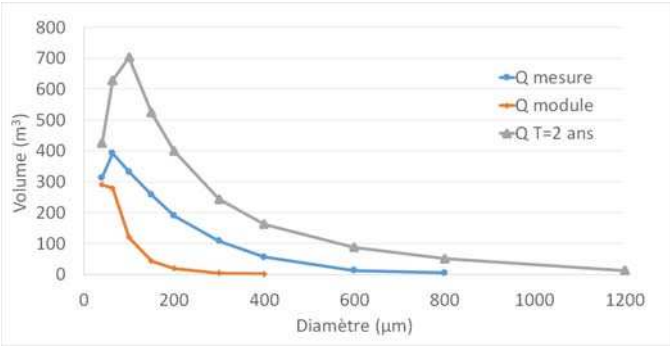

Fig. 17: Deposited volume (in m^3) of sediments in the adjacent channel as a function of sediment diameter

It is important to notice that these results concern absolute values of sediment volumes. However, the total incoming suspended sediment flux is different depending on the discharge condition in Loire River because the upstream suspended sediment concentration has been fixed at $C_{upstream} = 1$ g/l for each scenario. By normalizing the deposited sediment volume with the incoming suspended sediment volume:

$$V_{inlet} = \int_0^{T_{end}} C_{upstream} \times Q_{upstream} \mathrm{d}t \qquad (4)$$

it is possible to better understand the annual deposition dynamic in the channel. Indeed, the highest relative volume of deposited sediment is close to 3%, in the case of Q_{Module} and $D = 40$ μm. For diameters higher than $D = 300$ μm, the relative deposited volume becomes negligible. This results correlates very well with grain size measurements that have been done on deposit samples. These grain size measurements show that the grain size distribution depends on the location in the channel. On the left side deposit, the grain size distribution is mainly centred on one granular mode of $D = 60$ μm. But if we look at the deposits close to the channel step, the grain size distribution is composed with two principal modes: a first one centred on $D = 80$ μm, and a second one on $D = 300$ μm.

Thanks to these measurements and the numerical results, we can build a conceptual scenario of deposition dynamics during a period with successive hydrological events:

- during the usual discharge period, fine sediments ($D < 100$ μm) are transferred and dispersed to the adjacent channel. These fine sediments may come from upper sub-catchments, because for example of a local rain event or upstream dam operations;
- during floods, coarser sediments ($100 < D < 400$ μm) eroded from the sand-river bed are transported by suspension and deposited in the upstream part of the adjacent channel.

V. Discussion

Two points of this work have to be discussed. The first one is about the predictability of the hydrodynamic model. Indeed, the simulated recirculation flow patterns in the channel are significantly sensitive to the $k_{S\ Wall}$ parameter. As shown by Patzwahl and Güngör (2015) [6], this parameter could include several processes and physical configurations of the study site that are not represented explicitly in the model. As these elements vary depending on the water level, it is difficult to estimate the robustness of the numerical model in other discharge conditions. Furthermore, for high magnitude flood discharge values, the hydrodynamic feature of the study site may include flooded zones that are not represented in this work. In order to quantify and validate the robustness of this work, it could be interesting to perform other velocity measurements in the channel, for several discharge conditions.

The second point is about the bed load dynamic in the Loire River. This study has focused in great detail on the suspended sediment dynamics in one given configuration of the river bed. However, the bathymetry measurements have shown the presence of very mobile dunes on the Loire river bed. This observation is a sign of active bed load transport, even in case of moderate flood discharge conditions. This active bed load dynamic could greatly modify the bed configuration, and especially the position of alternate bars. Several studies ([2], [7], [5]) tried to estimate numerically or by field measurement this bar mobility, especially on the Loire River. This mobility could be accelerated or stopped by different anthropic or non-anthropic elements of the river bed, like a step for example. In this case, it could be interesting to know if the alternate bars configuration is stable (for example because of the step downstream the study site), or if it is dynamic with temporal cycles.

VI. Conclusion

In this study, a focus has been done on the suspended sediment dynamic in the Loire River. On a local river reach with an adjacent channel, a field campaign has shown that the flow velocities in the channel are strongly correlated to the discharge conditions in Loire River, and are structured with complex recirculation patterns. A TELEMAC 3D model has been calibrated to reproduce the measured velocities, with a good agreement. In order to reproduce the complex flow patterns in the channel, a specific value of $k_{S\ Wall}$ has been defined. Based on this calibration, three discharge scenarios and ten sediment classes have been simulated. The results show that the deposits observed in the adjacent channel are related to different upstream scenarios: the finer sediment classes ($D < 100$ μm) are transferred and deposited in the channel during low discharge conditions. During larger floods events with high suspended sediment concentrations, coarser sediment classes are deposited ($100 < D < 400$ μm) after being eroded from the sand river bed. This finding will be useful for river management, as well as for industrial activities. As a perspective, interesting work could be done in the future by using a multiclass sediment module in TELEMAC 3D.

REFERENCES

[1] B. Camenen, R. C. Grabowski, A. Latapie, A. Paquier, L. Solari, and S. Rodrigues, "On the estimation of the bed-material transport and budget along a river segment: application to the middle loire river, france," *Aquatic Sciences*, vol. 78, no. 1, pp. 71–81, 2016. [Online]. Available: http://dx.doi.org/10.1007/s00027-015-0442-3

[2] N. Claude, S. Rodrigues, V. Bustillo, J.-G. Brhret, P. Tassi, and P. Jug, "Interactions between flow structure and morphodynamic of bars in a channel expansion/contraction, loire river, france," *Water Resources Research*, vol. 50, no. 4, pp. 2850–2873, 2014. [Online]. Available: http://dx.doi.org/10.1002/2013WR015182

[3] J.-M. Hervouet, *Hydrodynamics of Free Surface Flows modelling with the finite element method.* Wiley, 2007.

[4] M. Jodeau and G. Antoine, "Telemac 3d and sediment transport : theoritical description - version 7.0. edf report." EDF R&D - LNHE, Tech. Rep., 2015.

[5] F. Mattia, D. Wang, J.-M. Hervouet, A. Leopardi, K. El kadi Abderrezzak, and P. Tassi, "Numerical simulations of bar formation and propagation in straight and curved channels," in *20th Telemac & Mascaret User Club*, 2013.

[6] R. Patzwahl and T. Güngör, "Horizontal flow field modelling in a channel mouth," in *22nd Telemac & Mascaret User Club*, 2015.

[7] S. Rodrigues, E. Mosselman, N. Claude, C. L. Wintenberger, and P. Juge, "Alternate bars in a sandy gravel bed river: generation, migration and interactions with superimposed dunes," *Earth Surface Processes and Landforms*, vol. 40, no. 5, pp. 610–628, 2015, eSP-13-0173.R2. [Online]. Available: http://dx.doi.org/10.1002/esp.3657

[8] J. Zyserman and J. Fredsoe, "Data analysis of bed concentration of suspended sediment," *Journal of Hydraulic Engineering*, vol. 120, no. 9, pp. 1021–1042, 1994.

Three-dimensional numerical modeling of sediment transport with TELEMAC-3D: validation of test cases

Jiawei Feng
Ecole Centrale de Nantes, France
jiawei.ecn@gmail.com

Magali Jodeau
EDF R&D LNHE, France
magali.jodeau@edf.fr

***Abstract*—The aim of this work is to validate specifically the proper calculation of TELEMAC-3D in numerical modeling of sediment transport. Generally, all the validation tests can be divided into two categories: (1) simulations with an analytical solution, existing exclusively in some special conditions (2) simulations deriving from physical experiments and in situ measurements with reliable initial, boundary and final conditions. Several validated cases are included in this paper and they will be included in the 8.0 release of TELEMAC, the first two belonging to the first category while the third belonging to the second. The first case is a simulation of a perfectly still settling basin containing water with an initial uniform sediment concentration. On the contrary, the second case is the development of suspend sediment transport at the upstream end of a channel with an initially clear flow. The third case simulates the turbidity currents in a flume with appointed flow conditions basing on a physical modelling of the LCH (Laboratory of Hydraulic Constructions) team of EPFL (Ecole Polytechnique Federale de Lausanne). Sensitivity analysis is performed for each case in order to optimize the numerical simulation, including horizontal and vertical mesh, physical (in particular the turbulence model) and numerical parameters. Calculations using TELEMAC-3D allow to reproduce the three-dimensional patterns of sediment transport correctly in general. Numerical results of each case are in agreement with the corresponding theoretical and practical considerations, demonstrating the powerful ability of TELEMAC-3D as a reliable tool to model sediment transport. Further research and practical applications can be performed using TELEMAC-3D.**

I. Introduction

Numerical morphodynamic models of increasing complexity are widely developed and used by both scientific and engineering communities over the past several decades so as to validate analytical solutions, in situ tests and furthermore predict complex applications of sediment transport. These models cover various topics in sediment transport, such as the natural or artificial bed evolution in rivers, estuaries and seas. A range of morphodynamic modeling systems like ECOMSed, Mike-21 and Delft-3D and ROMS generally include basic flow modules (from 1D to 3D), a wave propagation model and a sand transport model including suspended load and bed load. More detailed reviews can be found in other aricles like [1].

This open-source TELEMAC hydro-informatic system is adopted as our framework. Fundamental theories can be found in this key reference [2], covering the advanced topics in the application of the finite element method and the TELEMAC system as well. A thorough overview of morphodynamic modeling using the TELEMAC finite-elment system can be referred to [3], illustrating its ability to reproduce sediment transport patterns and resulting bed evolution in increasingly complex situations from small scale laboratory experiments to field scale river applications.

Considered as a raisonable tradeoff between simulation accuracy and calculation time, 2D depth-averaged modeling is thus extensively applied to medium-scale domains in the past decades. With the development of personal workstations and clusters, 3D modeling is being paid more and more attention at the moment and will turn into an inevitable trend in the future.

Concerning the sediment transport with TELEMAC system, multiple models can be utilized. Courlis, as one part of TELEMAC system, is available to model sediment transport in one dimension. For 2D modeling, the TELEMAC-2D hydrodynamic model is internally coupled to the 2D morphodynamic model SISYPHE. For 3D modeling, the suspended load is directly calculated by TELEMAC-3D, solving an additional 3D transport equation for the sediment concentration and computing the bed evolution. In most 1D or 2D models of depth-averaged sediment transport, the suspended sediment is assumed to be advected by the depth-velocity velocity. Taking into account the fact that the largest part of the sediment is transported near the bed, the depth-averaged velocity should be weighted by the verticle concentration profile. This inherent issue can be achieved by TELEMAC-3D, resulting in more precise simluations, whereas a correction factor needs to be introduced enabling results from 2D computation to approach 3D simulation result [4].

Validation tests play an important role in the development of code implementation. This paper begins by briefly describling the physical formulations used to model the sediment transport within TELEMAC-3D. It then presents three examples of validation studies that have been carried out using TELEMAC-3D. Unfortunately, the details of simulations may not be fully explained due to the space limitations.

II. Description of model formulations

A. Hydrodynamics

In this work the non-hydrostatic version is chosen and TELEMAC-3D solves the three-dimensional mass and momentum conservation equations [5]:

$$\begin{aligned}
\frac{\partial u}{\partial x}+\frac{\partial v}{\partial y}+\frac{\partial w}{\partial z}&=0\\
\frac{\partial u}{\partial t}+u\frac{\partial u}{\partial x}+v\frac{\partial u}{\partial y}+w\frac{\partial u}{\partial z}&=-\frac{1}{\rho}\frac{\partial p}{\partial x}+\nu\Delta(u)+F_x\\
\frac{\partial v}{\partial t}+u\frac{\partial v}{\partial x}+v\frac{\partial v}{\partial y}+w\frac{\partial v}{\partial z}&=-\frac{1}{\rho}\frac{\partial p}{\partial y}+\nu\Delta(v)+F_y\\
\frac{\partial w}{\partial t}+u\frac{\partial w}{\partial x}+v\frac{\partial w}{\partial y}+w\frac{\partial w}{\partial z}&=-\frac{1}{\rho}\frac{\partial p}{\partial z}+\nu\Delta(w)+F_z\\
p=p_{atm}+\rho g(Z_s-z)+\rho_0 g\int_z^{Z_s}\frac{\Delta\rho}{\rho_0}dz+p_d&
\end{aligned}\quad(1)$$

where u, v and w are the three-dimensional components of velocity; F_x, F_y are source terms and ν is the effective viscosity that needs to be computed by a turbulence model. The pressure is calculated in the last equation, where ρ_0 and $\Delta\rho$ are the reference density and the variation of density respectively and Z_s is the free surface elevation.

B. Sediment transport

1) Advection-dispersion equation for sediments: Here is the Cartesian coordinate form for the advection-dispersion equation in terms of seidments:

$$\frac{\partial c}{\partial t}+\frac{\partial uc}{\partial x}+\frac{\partial vc}{\partial y}+\frac{\partial wc}{\partial z}-\frac{\partial w_s c}{\partial z}=\frac{\partial \nu_t\frac{c}{x}}{\partial x}+\frac{\partial \nu_t\frac{c}{y}}{\partial y}+\frac{\partial \nu_t\frac{c}{z}}{\partial z}\quad(2)$$

where c denotes the sediment concentration; w_s is the sediment settling velocity and ν_t is the turbulent diffusivity coefficient.

2) Additional processes:

a) Hindered settling: Subroutine WCHIND models hindered concentration dependent settling velocity in TELEMAC-3D according to

$$W_C^{'}=W_C\times(1-\frac{C}{CGEL})^5\quad(3)$$

Here, $W_C^{'}$ is hindered concentration dependent settling velocity; W_C is sediment settling velocity; C is relative sediment concentration and CGEL is sediment concentration at which sediment forms a weak soil.

b) Flocculation: In TELEMAC-3D, two formulas are provided for taking flocculation into account.

On one hand, subtoutine WCTURB models the influence of turbulence on the settling velocity basing on the article of Van Leussen [6]. The formula for flocculation is

$$W_C^{'}=W_C\times\frac{1+A\times G}{1+B\times G^2}\quad(4)$$

where $W_C^{'}$ is settling velocity depending on flocculation and W_C is settling velocity of a particular sediment class in still water; Coefficient A controls the formation of flocs by turbulence while coefficient B controls the breaking of flocs by turbulence (Both A and B are empirical values for flocculation and breakup); the dissipation parameter $G=(\epsilon/\nu)^{1/2}$ is used to represent the turbulence intensity and can be computed with a $k-\epsilon$ model.

On the other hand, subroutine SOULSBYFLOC3D computes the fall velocity of mud flocs based on the Soulsby's formulation derived from Manning's floc database [7]. The description of the formula is rather long and thus is left out here. Complete expression of Soulsby's formula can be found in the aforementioned paper.

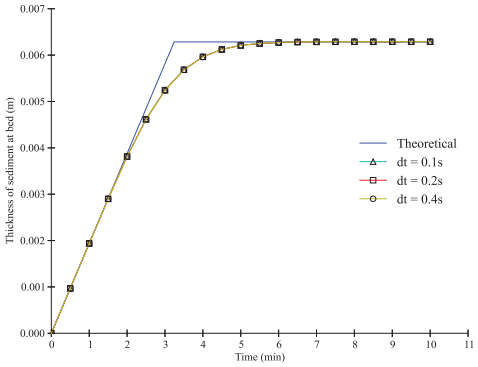

Fig. 1: Test of non-cohesive sediment

III. Validation tests

A. Settling basin

In the first case, we simulate a perfectly still settling basin containing water with an initial uniform sediment concentration. Theoretically, it takes a constant time period for a particle to fall from the water free surface to the bed, which equals the water depth divided by the sediment settling velocity.

a) Non-cohesive sediment: We assume that the initial sediment concentration is $2\,\mathrm{kg\,m^{-3}}$. The constant water depth is $5\,\mathrm{m}$ and the settling velocity of non-cohesive sediment equals $0.257\,\mathrm{m\,s^{-1}}$, hence all the sediment should fall to the bottom in $3.24\,\mathrm{min}$. Fig. 1 shows identical simulation results with different time steps.

b) Cohesive sediment: Formulae implemented in TELEMAC-3D for hindered settling and flocculation are tested as explained in section II-B2. And results are consistent with the theoretical solutions like those of non-cohesive sediment.

In order to verify that subroutine WCHIND is working well, 800 is assigned to CGEL and 40 is assigned to C (We assume that the initial sediment concentration is $50\,\mathrm{g\,L^{-1}}$ and threshold concentration for hindered velocity is $10\,\mathrm{g\,L^{-1}}$). Then result is compared between computer calculation and theoretical curve in fig. 2. The effect of hindered settling is well demonstrated.

While using Van Leussenformula, G is extremely small in this case. For this reason, variations of empirical coefficients A and B impact barely the final result. The curve is almost the same as that without taking flocculation into consideration in fig. 3.

At the last step of Soulsby formula, the mass-averaged settling velocity is calculated and compared with $0.2\,\mathrm{mm\,s^{-1}}$ and then the bigger one between them will be chosen. In this case, the shear velocity is very small and results in a very small mass-averaged settling velocity. Therefore, the final settling velocity is always $0.2\,\mathrm{mm\,s^{-1}}$. Fig. 4 proves our thought.

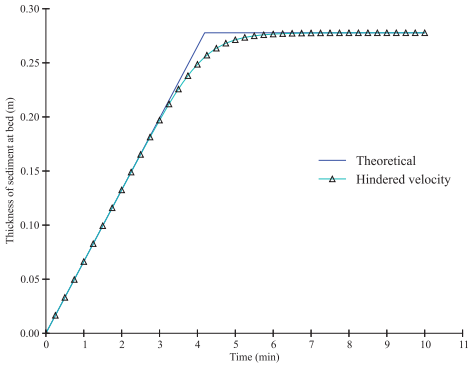

Fig. 2: Test of hindered velocity for cohesive sediment

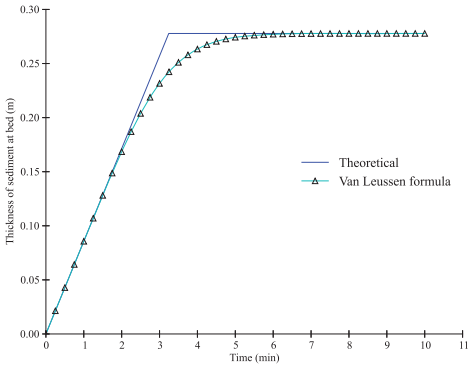

Fig. 3: Test of Van Leussen formula

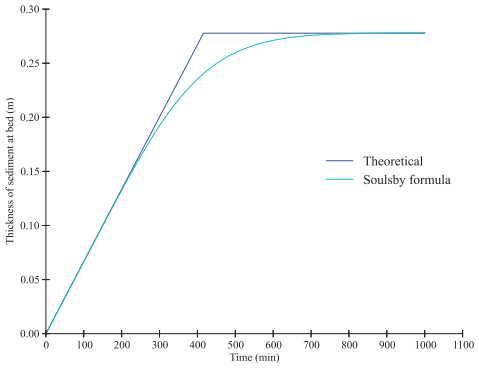

Fig. 4: Test of Soulsby formula

Further validations with respect to these two methods can be accomplished in the future cases, where the shear velocity plays a much more significant role.

c) Mixed sediment: In this situation, both non-cohesive and cohesive sediments exist simultaneously. The initial concentrations of non-cohesive and cohesive sediment are $2\,\mathrm{g\,L^{-1}}$ and $5\,\mathrm{g\,L^{-1}}$ respectively. The settling velocity of sand used in this test is $0.257\,\mathrm{m\,s^{-1}}$ while the settling velocity of mud is $0.0257\,\mathrm{m\,s^{-1}}$. There are three phases in total during the whole

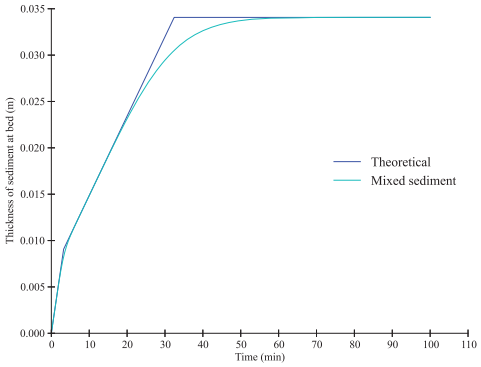

Fig. 5: Test of mixed sediment

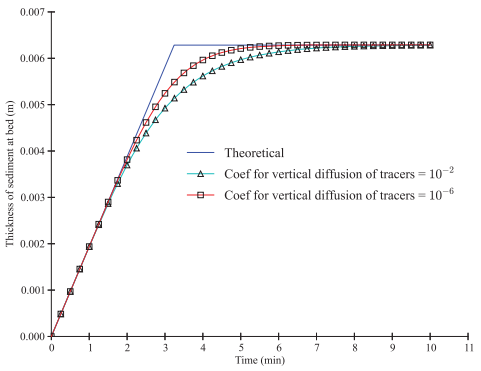

Fig. 6: Sensitivity tests of coefficient for vertical diffusion of tracers

process. In the first phase, both non-cohesive and cohesive sediments settle down simultaneously. In the second stage, all the non-cohesive sediment has already settled down and thus only cohesive sediment falls down to the bottom. In the last one, there is little sediment in the basin and almost all the sediment has reached the bottom of basin. Therefore, the bottom thickness remains nearly invariable.

Sensitivity tests show that the computed model result is sensitive to 'coefficient for vertical diffusion of tracers'. A better accordance between calculations and theorical results can be obtained with a smaller coefficient for vertical diffusion of tracers. On the contrary, time step (see fig. 1) and turbulence model won't have an impact on the simulation result. In all tests, mass balance is verified and the total quantity of sediment available in the flow does accumulate at the bed; continuity of sediment is preserved.

B. Suspended sediment transport development

This test case simulates the development of suspended sediment transport at the upstream end of a channel with an initially clear flow. Due to erosion of sediment from the bed, the suspended sediment transport rate increases with distance down the channel until equilibrium conditions are achieved even though the flow pattern is stationary. We as-

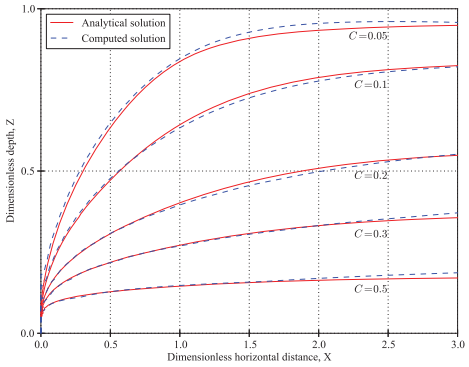

Fig. 7: Contours of equal sediment concentration along the longitudinal direction, ($A = 0.05, \lambda = 0.5$)

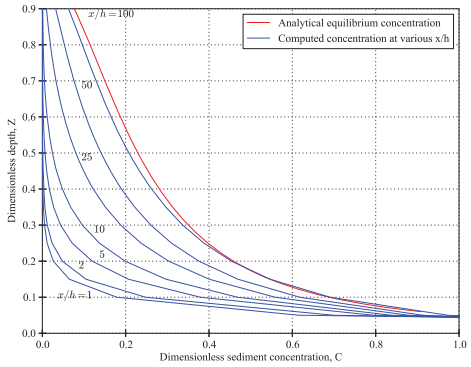

Fig. 8: Suspended sediment concentration profiles at various distances along a flume, ($A = 0.05, \lambda = 0.5$)

sume that there is no morphological change happening here and the longitudinal diffusion along the flume is neglected. In this condition, an analytical expression for the sediment concentration profiles was derived by Hjelmfelt and Lenau as a function of the distance down the channel [8]. Simulation results using TELEMAC-3D are compared with the theoretical analysis given by Hjelmfelt and Lenau. This test case has been used to validate Delft3D [9] previously. Some parameters here have been chosen identical as those in the validation case of Delft3D. The simulated flume is $120\,\mathrm{m}$ long and $10\,\mathrm{m}$ wide.

All variables of the following plots are nondimensionalized and these dimensionless variables are defined as follows:

$$\lambda = \frac{w_s}{\beta\kappa u_*},\ X = \frac{\beta\kappa u_* x}{\bar{U}h},$$
$$Z = \frac{z}{h},\ C = \frac{c}{c_a} \text{ and } A = \frac{a}{h}$$

where w_s is sediment settling velocity; β is the ratio of sediment diffusion to fluid diffusion; κ is Von Karman coefficient; u_* is the bed shear velocity; x is the longitudinal Cartesian coordinate; z is the vertical Cartesian coordinate; $\bar{U}$ is the depth-averaged GLM velocity components; h is the water depth; c is the mass sediment concentration; c_a is the mass sediment concentration at reference height and a is the height for suspended sediment concentration.

Fig. 7 shows that simulation results of TELEMAC-3D reproduce the analytical solution quite well, manifesting the adapatation of the suspended sediment concentration from an initially clear flow. Small differences for each contour do exist, but are considered to be negligeable, which is less than 5% as equilibrium conditions are approached toward the downstream end of the flume. Further investigation can be performed to reason the cause of this error, which is possibly caused by the computation scheme used in TELEMAC-3D. But parameters chosen at the moment render this test rather stable in a wide range of flow conditions and therefore it is considered to be an acceptable compromise..

Fig. 8 illustrates the gradual development of sediment concentration profile along the longitudinal direction of the flume, showing the progressive development of an equilibrium sediment concentration profile. It can be observed that the concentration profile develops step-by-step, and that equilibrium conditions have not been completely achieved even by a distance of $x/h = 100$. But we can assume reasonably that after passing through a longer distance, the sediment distribution can reach equilibrium condition. To prove this idea, another simulation is tested, where the length of the flume is changed to $1200\,\mathrm{m}$. Fig. 9 demonstrates suspended sediment concentration profile in the outlet of the 1200-m-long flume, which is in good accordance with the analytical solution Rouse profile.

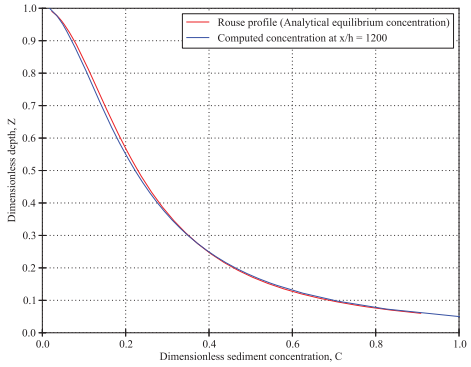

Fig. 9: Equilibrium sediment concentration profile computed $1200\,\mathrm{m}$ down a longer flume

As another check, it is quite useful to average C over the channel depth, i.e., to compute $C_{av} = \frac{1}{1-A}\int_A^1 C dZ$. C_{av} represents the average normalized concentration. The analytical solution with respect to C_{av} has been briefly given in [8] as well. Fig. 10 shows the longitudinal profile of the depth averaged suspended sediment concentration. Here the computed result is almost exactly same as the analytical solution of Hjelmfelt and Lenau.

Certain sensitivity tests were organized to observe whether some parameters have impacts on the final results. It should be pointed out that the reference height A is a crucial parameter from the standpoint of validation. The first plane above the bottom should be exclusively regarded as the reference plane, no matter the verticle mesh is equally distributed or not. Here

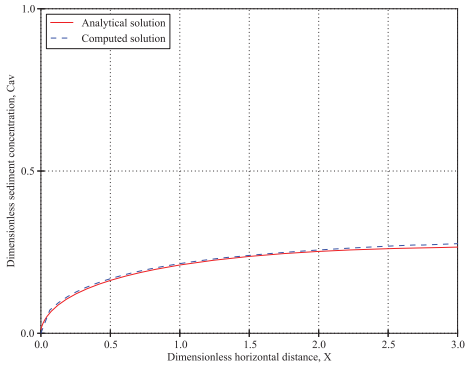

Fig. 10: Development of the depth-averaged suspended sediment concentration along a flume ($A = 0.05, \lambda = 0.5$)

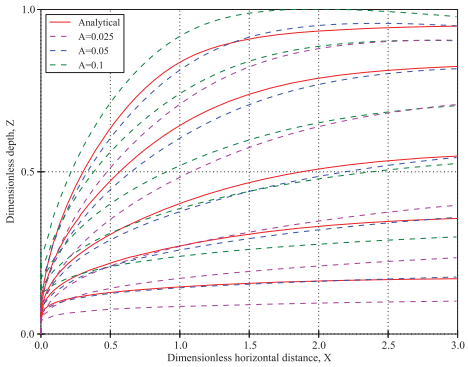

Fig. 11: Sensitivity analysis to reference height A

we anticipate 21 planes regularly spaced on the vertical. From Fig. 11, we can observe the sensible disparities among the dashed line when $A = 0.025$ or $A = 0.1$. The corresponding curves move upward if we augment the value of A. The reason lies in the relatively lower sediment concentration at higher elevations. We can approch the analytical solution while taking the first plane above the bottom as our reference plane, i.e. $A = 0.05$ here.

Several horizontal mesh resolutions were also examined. Considering that the flume width is $10\,\mathrm{m}$, mesh sizes of $1\,\mathrm{m}$, $2\,\mathrm{m}$ and $5\,\mathrm{m}$ were tested. It was proven that $2\,\mathrm{m}$ is the largest mesh size for the proper simulation of this case.

C. Turbidity currents

Turbidity currents are particle-laden gravity-driven underflows in which the particles are largely or wholly suspended by fluid turbulence [10]. The turbulence is typically generated by the forward motion of the current along the lower boundary of the domain, the motion being in turn driven by the action of gravity on the density difference between the particle-fluid mixture and the ambient fluid.

The objective of this case is to compare simulation results in TELEMAC-3D with experimental data obtained by Sabine

TABLE I: Dimensions of simulated device

Parameter	Dimension (m)
L	6.7
I	0.272
H	0.8
h	0.045
a	0.09
b	0.12

Chamoun during her PhD at LCH (EPFL). LCH team kindly made the data available for LNHE.

Experimental tests are carried out in an $8.55\,\mathrm{m}$ long, $0.272\,\mathrm{m}$ wide, and $1\,\mathrm{m}$ depth flume that can be tilted with a slope ranging from 0 to 5%. This flume is divided into three parts: the upstream part, also called the head tank ($0.8\,\mathrm{m} \times 0.272\,\mathrm{m} \times 1\,\mathrm{m}$), the main flume ($6.7\,\mathrm{m} \times 0.272\,\mathrm{m} \times 1\,\mathrm{m}$), and the downstream compartment ($1.05\,\mathrm{m} \times 0.272\,\mathrm{m} \times 1\,\mathrm{m}$). The head tank receives the water-sediment mixture from the mixing tank and is linked to the main flume by a sliding gate that, once opened, leads to the formation of the turbidity current inside the flume simulating a reservoir. Precise geometric dimensions are listed in tab. I, including sizes of inlet, outlet and the main flume. A sketch as fig. 12 is reproduced here as well so as to simplify the matching of corresponding dimensions. The parameter I and a, representing widths of the main flume and the outlet respectively, don't show up in fig. 12.

The whole experimental procedure is described as follows [11]. At the beginning of each test, the mixing tank is filled with water and a specific mass of fine powdery material (Thermoplastic Polyurethane in the case of the present study) is added until the desired concentration is obtained. Meanwhile, the main channel where the current will develop is filled with tap water up to a level of $80\,\mathrm{cm}$. Once ready, the mixture is pumped to the head tank, and returns to the mixing tank through a recirculation pipe. This recirculation lasts for a few minutes and helps in regulating the flow rate (around 1 l/s for all tests) through an electromagnetic flowmeter, insuring a good mixing and homogeneous concentrations between the two reservoirs. Before starting the test, the water level in the head tank and the main channel should be equal in order to avoid any head losses when the gate is opened and the turbidity current released. The concentration of the mixture is continuously measured using a turbidity probe placed in the head tank. Once the concentration measured reaches the desired value, the sliding gate separating the head tank from the main flume is opened and the turbidity current is released into the flume. Right at the entry of the flume, the current passes through a tranquilizer that reduces its initial turbulence scale and gives a nearly uniform horizontal distribution for the velocity field of the current. A clear water discharge is ejected through the diffusor placed right above the tranquilizer. The turbidity current then flows along the channel through a distance of 6.70 m and is monitored for the whole duration of the test. Once it reaches a location corresponding to the tested timing, the bottom outlet is opened with a specific discharge, controlled by the aforementioned valve and electromagnetic flowmeter placed downstream. The vented current reaches a basin where continuous concentration measurements

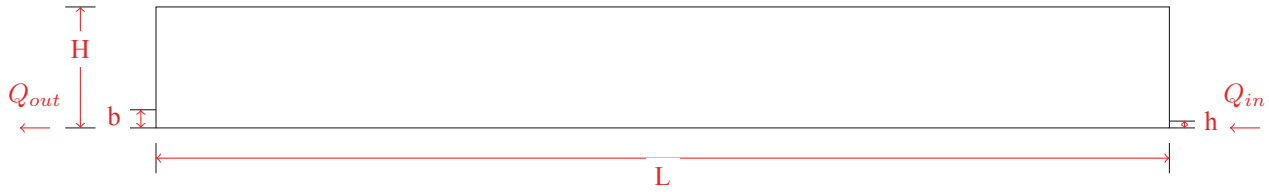

Fig. 12: Front view of the main flume

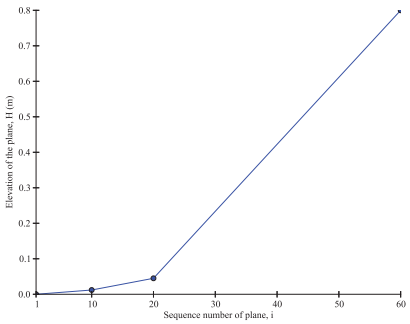

Fig. 13: Distribution of vertical cell sizes for turbidity current modelling.

TABLE II: Error analysis

Time (s)	PBIAS(%)	RMSE	RSR
51.39	17.902	0.000273	0.265
64.60	19.121	0.000365	0.265
78.00	16.895	0.000423	0.257
102.50	14.180	0.000596	0.297
133.26	10.374	0.000966	0.404
148.00	11.272	0.00114	0.438
160.89	8.573	0.00134	0.509

are achieved using a turbidity probe. Based on this, venting efficiencies are calculated for different scenarios.

Sensitivity tests indicate that the number of vertical levels should be sufficient enough to guarantee the proper simulation of turbidity currents. Thus the horizontal mesh size is equalling to $0.01\,\mathrm{m}$ and 60 irregularly spaced layers are in the vertical direction (Figure 13).

In fact, this case is very sensitive to the variation of sediment settling velocity. Besides Stokes' law, there are a number of formulae for the settling velocity of sediment particles. Benoît Camenen proposed a simple and general formula for the settling velocity of particles [12] in 2007 and a brief review can be found as well in the introduction part of this forementioned paper. Stokes' law gives a theoretical settling velocity of $1.5\,\mathrm{mm\,s^{-1}}$. According to Camenen's formula, we can obtain a settling velocity of $1.558\,\mathrm{mm\,s^{-1}}$. Here we have tested two other settling velocities, being equal to $1.3\,\mathrm{mm\,s^{-1}}$ and $1.7\,\mathrm{mm\,s^{-1}}$ respectively. Fig. 14 indicates that the computed result is quite sensitive to the settling velocity, proving that settling velocity is a crucial physical parameter in this numerical model. With a greater settling velocity, more sediment will settle down in a closer place to the inlet and less sediment can cover a rather long distance in the flume. This phenomena corresponds with our common sense. We can note that differences in the simulation results exist but seem not very obvious whether Stokes' law or Camenen's formula is chosen.

Different methods used for evaluation of numreical models have been proposed, they are represented by a number of evaluation indicators. Among these indicators, RMSE, RSR and PBIAS are calculated for the sake of assessment in this case. Here we only consider the settling velocity given by Stokes' law. Table II indicates that values of RMSE and RSR increase with respect to the time while values of PBIAS decrease with time. It can be considered that good agreement is achieved between measurements and simulations. Values of PBIAS at different moments are no more than 20. Generally speaking, values of RSR are smaller than 0.5. Judging from criterias in [13], both criterias of model evaluation are met, demonstrating a very good performance of our numerical modelling.

Although the simulation results fit the experimental data well, modifications could be made in order to improve the accuracy of the numerical models. In the earlier discussions, constant settling velocities are taken into account. But in the reality, sediment particles will not have this velocity from the very beginning. They should go through a process of flocculation. In order to solve this deficiency, the model could be improve with the use of settling velocity measurements.

Fig. 15 demonstrates features of turbidity currents during midel simulations. Beneath, screeenshots (See Figure 16) are taken from the recorded video so as to compare them qualitatively with the simulation results.

IV. Conclusion-Future work

TELEMAC-3D has already been validated across a great number of processes and their interactions. The 'tip of the iceberg' can be easily accessed in the directory of TELEMAC-3D examples. The validation tests shown in this paper have demonstrated the ability of TELEMAC-3D to model the following processes: (1) sediment settling, (2) suspended sediment transport and (3) turbidity currents. On the basis of this paper, further research will focus on the definition of benchmarks, the combinations and interactions of processes as well as more applications in the prototype-scale and real-life situations.

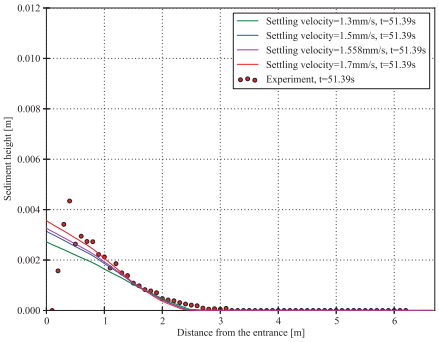

(a) t = 51.39 s

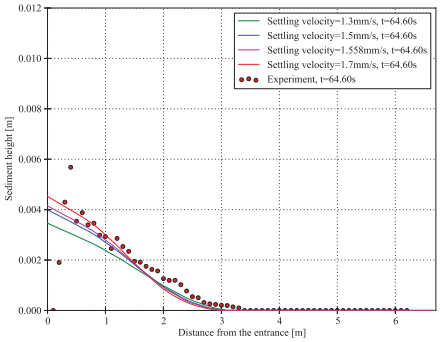

(b) t = 64.60 s

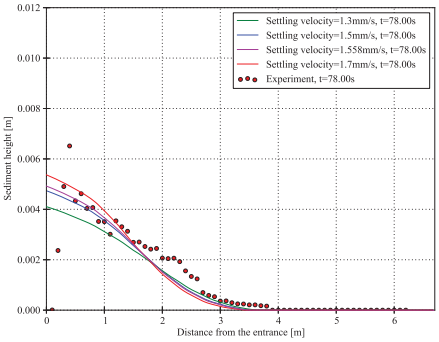

(c) t = 78.00 s

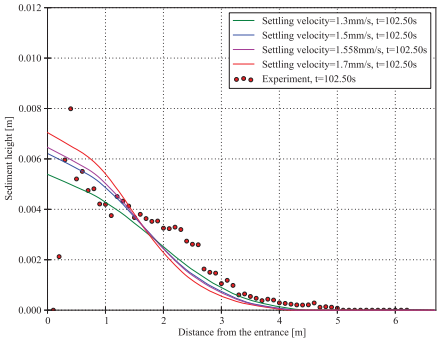

(d) t = 102.50 s

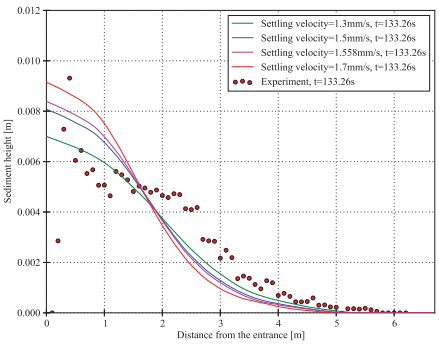

(e) t = 133.26 s

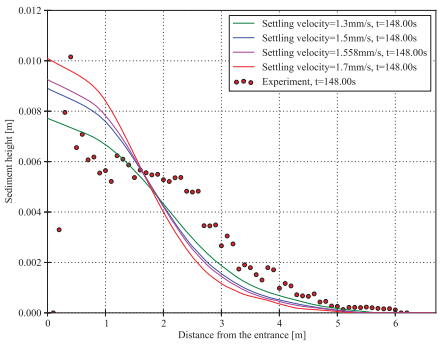

(f) t = 148.00 s

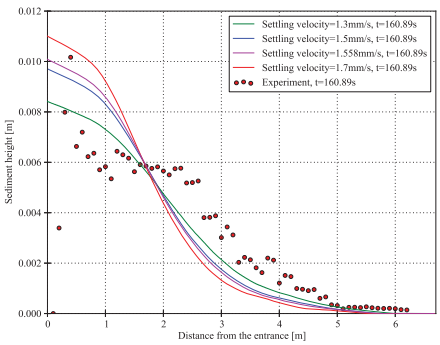

(g) t = 160.89 s

Fig. 14: Sensitivity analysis of settling velocity

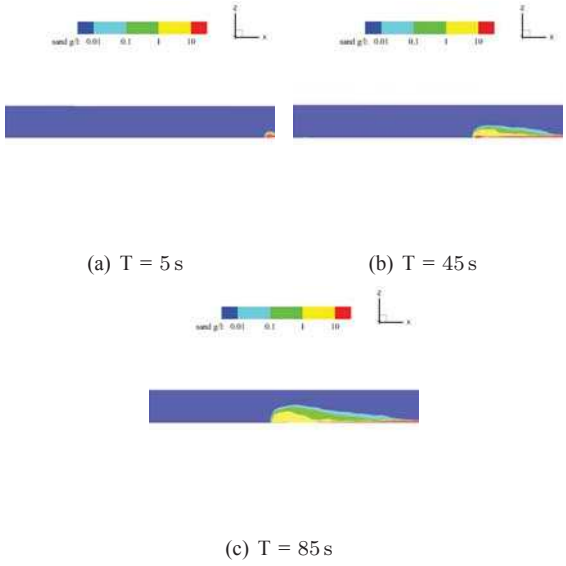

(a) T = 5 s (b) T = 45 s

(c) T = 85 s

Fig. 15: Different stages of simulated avancing turbidity currents, front view (2D)

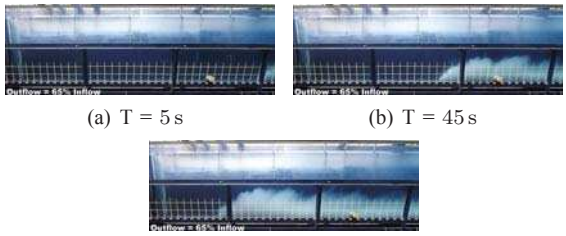

(a) T = 5 s (b) T = 45 s

(c) T = 85 s

Fig. 16: Different stages of experimental avancing turbidity currents, front view (2D)

Acknowledgment

The authors would like to thank Sabine Chamoun for providing the experimental data of the third test. Gratitudes are as well extended towards Giles Lesser for his kind help in the second validation case.

References

[1] Athanasios (Thanos) N Papanicolaou, Mohamed Elhakeem, George Krallis, Shwet Prakash, and John Edinger. Sediment transport modeling review—current and future developments. *Journal of Hydraulic Engineering*, 134(1):1–14, 2008.

[2] Jean-Michel Hervouet. *Hydrodynamics of free surface flows: modelling with the finite element method*. John Wiley & Sons, 2007.

[3] Catherine Villaret, Jean-Michel Hervouet, Rebekka Kopmann, Uwe Merkel, and Alan G Davies. Morphodynamic modeling using the telemac finite-element system. *Computers & Geosciences*, 53:105–113, 2013.

[4] N Huybrechts, C Villaret, and JM Hervouet. Comparison between 2d and 3d modelling of sediment transport: application to the dune evolution. In *River Flow*, 2010.

[5] OPERATING MANUAL. Telemac modelling system. 2016.

[6] W. van Leussen. *Estuarine macroflocs and their role in fine-grained sediment transport: Macrovlokken en hun bijdrage aan de slibtransporten in Estuaria*. Universiteit Utrecht, Faculteit Aardwetenschappen, 1994.

[7] RL Soulsby, AJ Manning, J Spearman, and RJS Whitehouse. Settling velocity and mass settling flux of flocculated estuarine sediments. *Marine Geology*, 339:1–12, 2013.

[8] A t Hjelmfelt and Charles Walter Lenau. Nonequilibrium transport of suspended sediment. In *Journal of the Hydraulics Division: Proceedings of the American Society of Civil Engineers*, number HY7, 1970.

[9] GR Lesser, JA Roelvink, JATM Van Kester, and GS Stelling. Development and validation of a three-dimensional morphological model. *Coastal engineering*, 51(8):883–915, 2004.

[10] Eckart Meiburg and Ben Kneller. Turbidity currents and their deposits. *Annual Review of Fluid Mechanics*, 42:135–156, 2010.

[11] Sabine Chamoun. Experimental set-up. Technical report. Personal communication.

[12] Benoît Camenen. Simple and general formula for the settling velocity of particles. *Journal of Hydraulic Engineering*, 133(2):229–233, 2007.

[13] Daniel N Moriasi, Jeffrey G Arnold, Michael W Van Liew, Ronald L Bingner, R Daren Harmel, and Tamie L Veith. Model evaluation guidelines for systematic quantification of accuracy in watershed simulations. *Transactions of the ASABE*, 50(3):885–900, 2007.

Morphological modelling in reservoirs: the experience of Artelia

Matthieu de Linares, Olivier Cazaillet, Julien Schaguene and Adlane Rebaï
Artelia Eau & Environnement
Echirolles, France
matthieu.delinares@arteliagroup.com

***Abstract*— This paper displays an overview of the work done by ARTELIA in recent years on numerical modelling of sediment transport in reservoirs using the TELEMAC system. The goal of the paper is thus to show the present possibilities of the software as well as new developments that further improve it.**

I. INTRODUCTION

The studies presented cover different kinds of questions (from the impact of dam erasing to the impact of dam building), and different kinds of sediment and transport processes, from fine mud transported in suspension to coarse sand transported by bedload. They thus involve different software. When sand transport is the main mechanism, SISYPHE is used, coupled with TELEMAC 2D or 3D. In the case of mostly fine sediment transport, TELEMAC 3D is used. In some cases, both types of transport processes must be taken into account at the same time. Developments on TELEMAC 3D have been implemented in order to be able to compute mixed sediment transport with fine (clay, silt) and coarse sediment (here sand) at the same time. The results of these developments applied to compute sediment deposition over years in two reservoirs in Africa are presented.

Some of the studies presented have had access to detailed datasets that enable a proper calibration. In some other cases, calibration is not possible. This is the case when studying the erasing of an old dam, or when studying the impact of a dam that has yet to be built.

II. EXAMPLE OF STUDIES

A. *Study of the flushing of the inlet channel of Inga powerplant*

Inga power plant, on the Congo River, cannot run to its full power, in part because of the sand deposits in the inlet channel.

A TELEMAC 2D - SISYPHE numerical model (with total transport formula) has first been calibrated using observed sediment deposition upstream of the dam (see Fig. 1 and 2 below). It has then been used to estimate the efficiency of the proposed works.

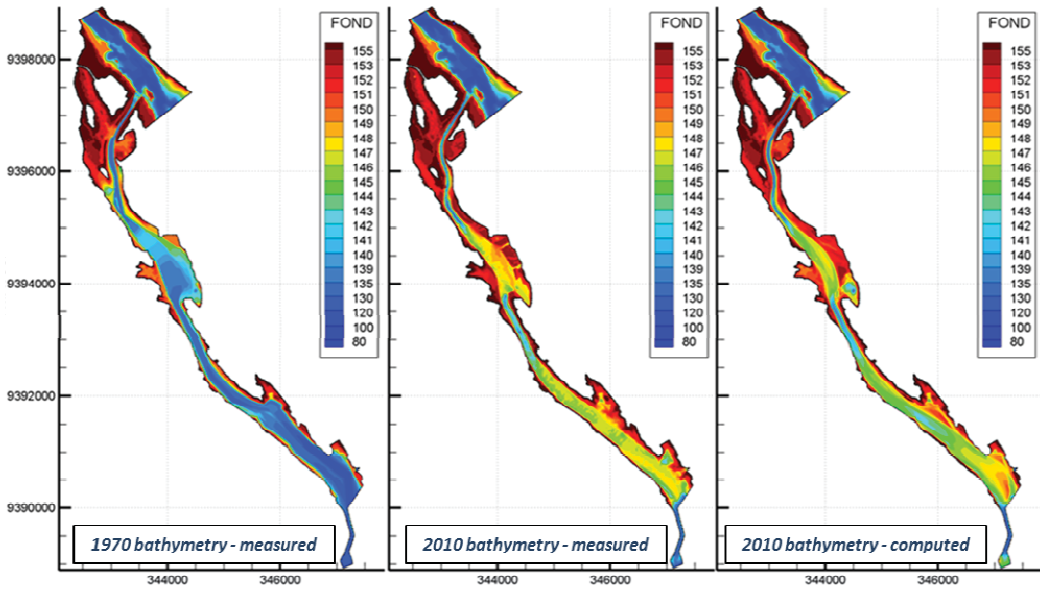

Figure 1. Inga – measured and computed bed evolution

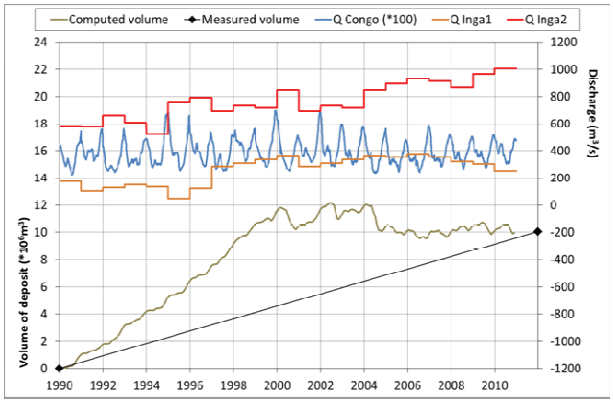

Figure 2. Inga – Evolution of the volume of deposit in the inlet channel

B. *Hydrosedimentary study of the Longefan basin*

A three-dimensional numerical model has been set-up to compute flow and sediment transport in the Longefan reservoir, a silt trap for the hydro-electric facilities diverting the Arc River (French Alps). The sediment in the basin was silt. Erodability parameters for the sediment are based on laboratory characterization in a flume. Flow measurements have shown that a complex circulation can develop in this reservoir. The model has been successful to simulate the measured flow circulation as well as the measured sediment transfer through the reservoir. Deposition patterns in the reservoir were also well reproduced (see Fig. 3 and 4). The model has then been used to help prepare flushings, and to study the impact of the deposits in the reservoir on the siltation capacity of the reservoir.

The work on this study is presented in more details in [1].

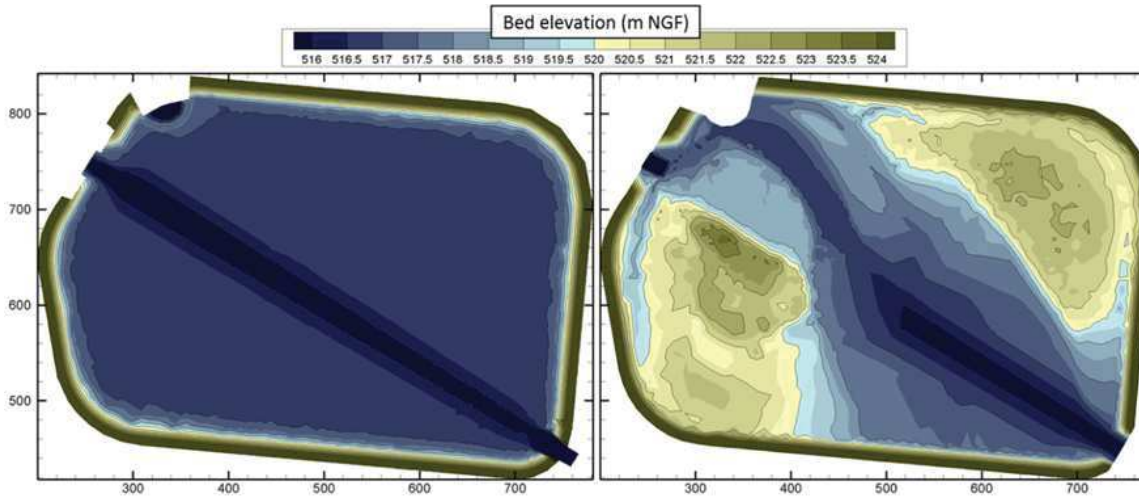

Figure 3. Longefan – Model bathymetry : initial state and with sediment deposits

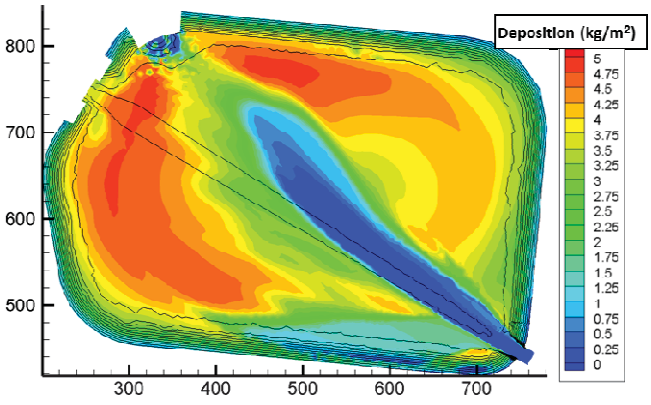

Figure 4. Longefan – Example of model results

C. *Preliminary studies for the lowering of the Boutet dam*

The town of Châtres-sur-Cher initiated a feasibility study to define a new layout for the Boutet dam on the Cher, both to restore the free circulation of migratory fish but also to ensure sedimentary continuity.

Numerical modelling (TELEMAC 2D coupled with SISYPHE) was carried out by ARTELIA in order to study the impact of two scenarios (partial and total removal of the dam) on the current patterns, on sediment transport and morphology. The new equilibrium profiles of the river following the work modifications have been calculated. Fig. 5 below presents the computed bathymetry at the site of the dam for different studied configurations.

The use of the multiclass formulation enables to have at the same time sand deposits in the middle of the reservoir and fine sediment deposits on the banks.

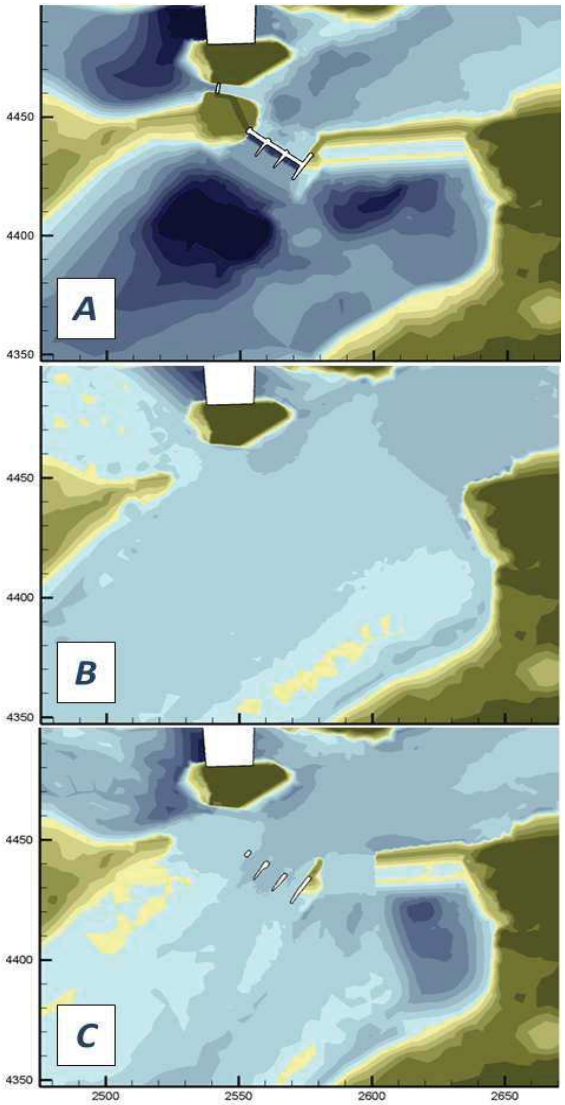

Figure 5. Boutet – A : initial bathymetry, B : computed equilibrium bathymetry for total erasing of the dam, C : computed equilibrium bathymetry for partial erasing of the dam.

III. NEW DEVELOPMENTS FOR MULTICLASS COMPUTATIONS

D. *Description of the multiclass (sand – fine sediment) modelling.*

New developments have been implemented in TELEMAC 3D v7p0 in order to compute transport of one class of sand (through total transport) and two classes of fine sediment (through suspension). For that purpose, the 'MIXED SEDIMENT' mode available in TELEMAC 3D has been adapted. In particular, a bed model has been developed, in order to properly manage the evolution of the mass of the different sediment classes in the bed, and to take into account the composition of the sediment bed to compute erosion fluxes.

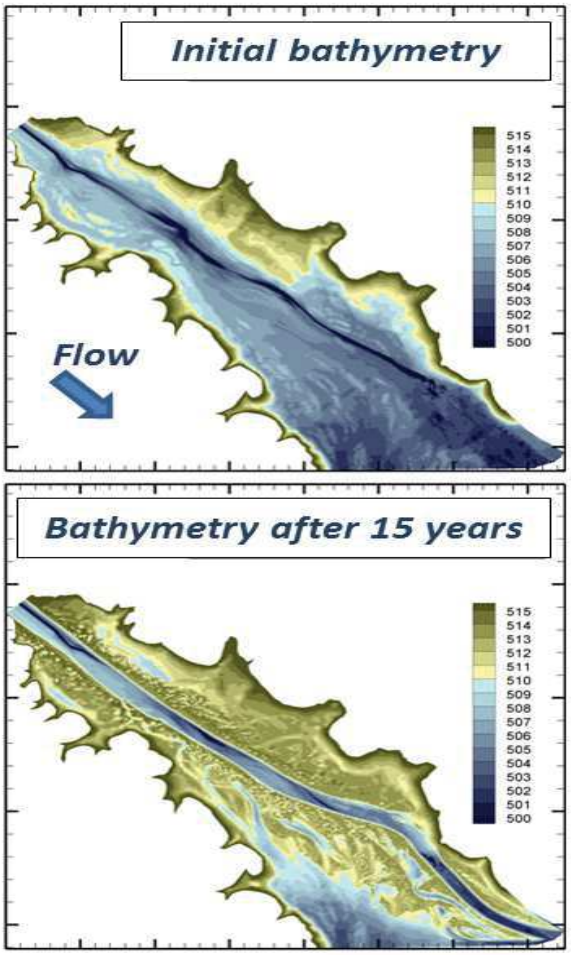

Figure 6. Computation of bathymetric evolution after the building of a dam on an African dam

For sand, Soulsby-Van Rijn formula (see [2]) is used to compute total load transport. For the two fine sediment classes, erosion fluxes are computed through Partheniades law (see [3]).

E. Application for a project of a dam on an African river (confidential)

For a dam project in Africa, ARTELIA was requested to carry a numerical study aimed at determining the medium-term sediment deposits in the reservoir and in particular upstream of the inlet channel, and checking the effectiveness of bottom outlet works to flush out deposited sediments. An example of model results is presented in Fig. 6.

F. Application on Kapichira reservoir

Kapichira reservoir, on the Shire river in Malawi, has experienced significant deposition since its building in 2001. Field data have been collected from the site, including bathymetry survey data, suspended sediment samples and bed sediment samples (granulometric analysis of these shows that the deposits consist in both sand and fine sediment). This has enabled the set up and calibration of a numerical model which is able to reproduce the sediment deposits in the reservoir since the building of the dam. An example of results of this calibration is presented in Fig. 7.

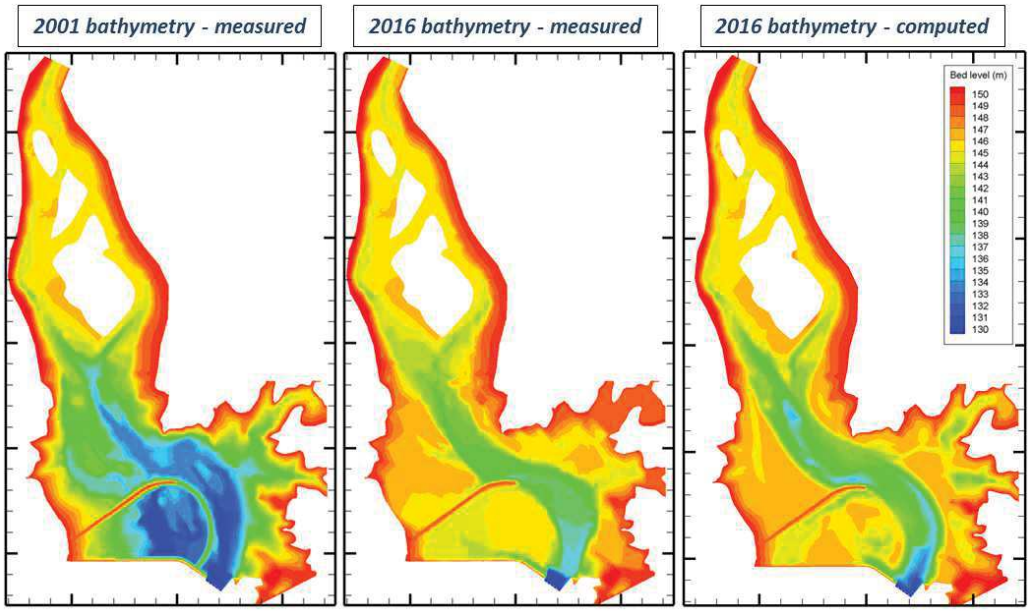

Figure 7. Kapichira _ comparison of computed and measured bed evolution

G. Possible improvements

The formulation for multiclass transport used here is very simple, as the different classes do not interact. A more complex formulation for sand-mud transport like the one presented in [4] and already adapted in TELEMAC 3D for an estuarine model (see [5]) could be used. Furthermore, a more general model should allow for any number of fine sediment classes and sand classes.

Another possible improvement would be to implement a more refined bed model, able to store the information on successive layers of deposit. Fine sediment consolidation should also be taken into account within this bed model.

IV. CONCLUSION

The examples presented here show that TELEMAC is a powerful tool for studied sediment transport and morphological evolution in reservoirs, for a wide range of processes and configurations.

Proper calibration of the model is not always possible. More experience is needed on well-documented cases to improve confidence in the model on such cases where calibration is not possible.

A proper data set for calibration should include bathymetric evolution, suspended sediment, and bed granulometry. Ideally, laboratory measurements on the sediment found on site should also be performed to help define fall velocity, the parameters of the erosion law and the parameters of the bed model (most notably consolidation).

Multiclass computations are needed in some cases. At the present time the Telemac system is still limited in this regard. Some improvements have been presented here.

The formulation for the transport of multiclass sediment needs lots of inputs and parameters, it is thus necessary, in order to use them adequately, to dispose of a detailed data set.

References

[1] de Linares M., Laperrousaz E. "A numerical model to help a sustainable management of sediments at Longefan reservoir (France)", Symposium of the International Commission on Large Dams (ICOLD), Seattle, 12-16 August 2013

[2] Soulsby R., 1997, Dynamics of Marine Sands, Thomas Telford

[3] Partheniades, E., (1965). Erosion and Deposition of Cohesive Soils. J Hydraulics Division 91:105-139

[4] Le Hir Pierre, Cayocca Florence, Waeles Benoit (2011). Dynamics of sand and mud mixtures: a multiprocess-based modelling strategy. Continental Shelf Research, 31(10), S135-S149

[5] De Linares, M., Walther, R., Schaguene, J., Cayrol, C. and Hamm, L. “Development of an hydro-sedimentary 3D model with sand-mud mixture - Calibration and validation on 6 years evolution in the Seine Estuary” 13th International Conference on Cohesive Sediment Transport Processes (INTERCOH), Leuven, 7-11 Septembre 2015

Modelling mud in 3D for the Blyth Estuary, Suffolk (UK).

Michiel A.F. Knaapen[(1)], Thomas Benson[(2)]
Coasts and Estuaries Group
HR Wallingford
Wallingford, United Kingdom
m.knaapen@hrwallingford.com [(1)]
t.benson@hrwallingford.com [(2)]

Willeke van de Wardt
Department of Civil Engineering & Management
University of Twente
Enschede, the Netherlands
w.vandewardt@student.utwente.nl

***Abstract*— The modelled sediment transport in the Blyth Estuary is compared to measurements from a field campaign carried out by University College London in 2002. The results show the importance of spatially and temporally varying critical shear stress for erosion. 3D effects were found to be relatively unimportant when compared to a SUBIEF-2D model.**

I. INTRODUCTION

The Blyth estuary in Suffolk, is a generally well-mixed estuary, with a tidal prism of about 2.6 x 106 m^3 [1]. Longitudinal salinity profiles typically show depth-mean salinities in the range 30.7 to 33.9‰, although mid-ebb salinities as low as 26.3‰ have been recorded within the middle estuary after very heavy rainfall [2]. Fluvial inflow is minimal: 90% of mean monthly fresh water flows is less than 0.9 m^3s^{-1} , which is approximately 1.5% of the gross ebb transport [2].

In the past, land reclamation turned the Blyth estuary into a tidal river. After natural failure of a seawall, some reclaimed land was returned to the natural dynamics of the tides and grassland turned into tidal flats. Contrary to expectations, it still remains a tidal flat. Reference [1] reported saltmarsh elevational gain of about 4 mm yr^{-1}, but the sediment import volumes from the North Sea are significantly lower.

Large-scale suspended mud transport in the southern North Sea has been well studied. The offshore suspended sediment concentration (SSC) is low (typically <10 mg/l) but increases in the winter. Concentrations in estuarine and coastal waters are much higher. Several areas also show elevated SSC, including a zone between Great Yarmouth and Lowestoft in which average concentrations exceed 65 mg/l [3]. There is some association between elevated SSC and high spring tidal currents in this zone

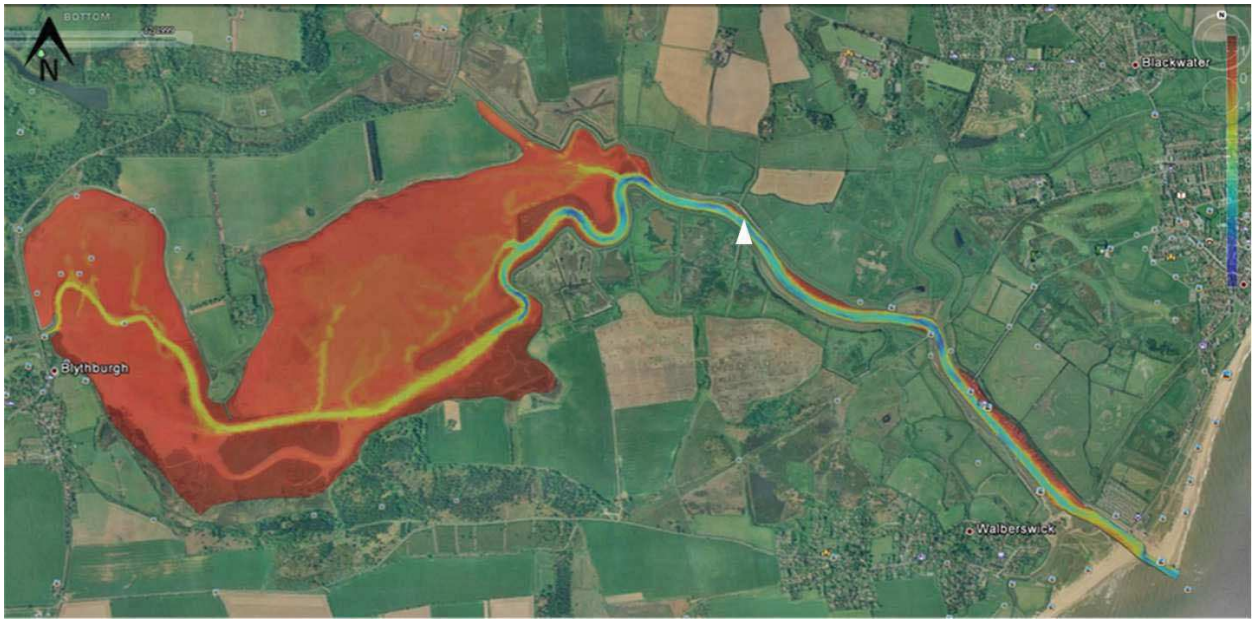

Figure 1 Bathymetry and topography of the Blyth Estuary

The estuarine bed is muddy, with little saltmarsh vegetation, and the sediment transport is dominated by mud transport. The sediment in the entrance channel consists mainly out of sand and some gravel [1].

The estuary mouth is very narrow (**Error! Reference source not found.**), restricting the influence of wave action from offshore. This shape makes the Blyth interesting for model validation. During floods, suspended sediment concentrations are determined largely by the concentration entering from the North Sea. During ebbs, most of the suspended sediment originates from the tidal flats in the wide basin. This difference helps to identify suitable values for parameterisation of erosion and deposition from measurements of suspended solids.

Previous work was carried out over a decade ago to simulate the sediment transport mechanisms in the estuary using the now redundant SUBIEF-2D [2,4]. The aim of the present study is to evaluate whether the use of a modern fully coupled TELEMAC-3D model can improve the accuracy of the model.

II. FIELD MEASUREMENTS

Field data were collected by the Coastal & Estuarine Research Unit (University College London) for a spring tide and for a neap tide in 2001. The data for the spring tide were collected on 19-20th of October and the data for the neap tide were collected on the 26-27th of September [4]. The field campaign measured flows and suspended sediment concentrations through the water depth at one location in the narrow entrance seawards of the tidal flats. This location is indicated by the white triangle in **Error! Reference source not found.**, just east of the point where the estuary widens.

There, the tide has a range of about 2.5 m during springs and about 1.5 m during neaps. The measured depth averaged current speeds reached almost 1.2 m/s during spring tide and about 0.9 m/s during neap tide. Depth averaged suspended sediment concentrations reached approximately 150 mg/l.

The collected dataset also contains data about the suspended sediment concentrations. The SSC is dominated by mud, with floc sizes varying between 25 and 300 µm [4].

III. MODELLING

The Blyth is modelled using TELEMAC3D, with 7 sigma layers. The seabed is modelled with 2 layers and a single mud fraction. The model is driven by measured tidal water levels at the open water boundary. The model is calibrated against measured data for the spring tide and afterwards validated against measured data of the neap tide. After that the sediment transport as calibrated and validated against the measured SSC.

About 80 simulations were run with varying values for critical shear stresses for erosion and deposition, erosion rate constant, with and without flocculation and a range of friction coefficients, including spatially varying bed friction and the critical erosion rate. The final model settings are given here.

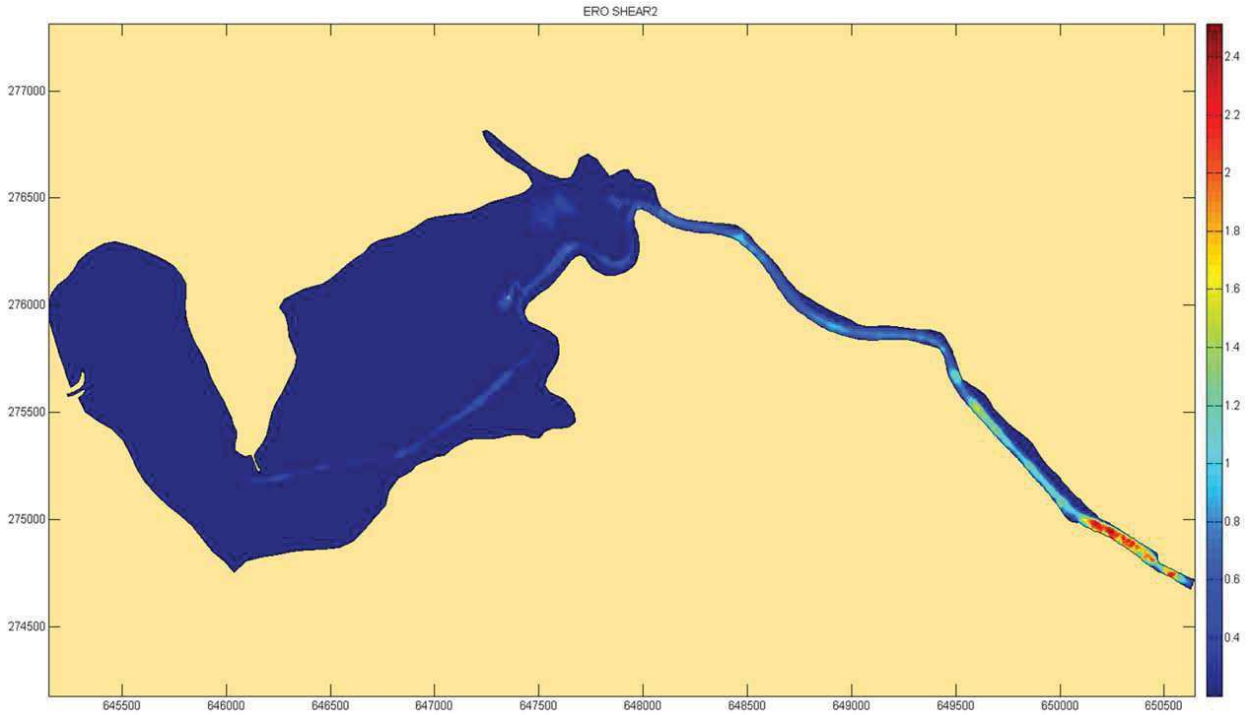

Figure 2 Spatial variation of the critical shear stress for erosion

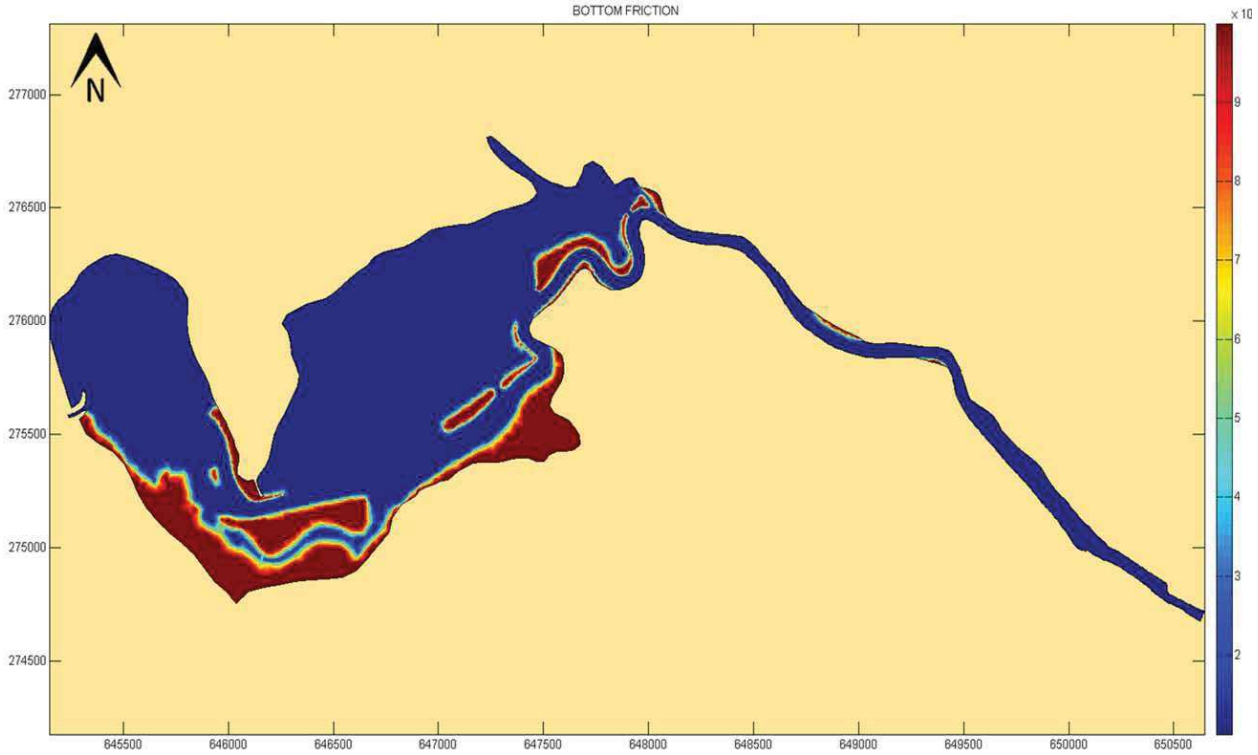

Figure 3 Nikuradse roughness length varies of the model domain

At the offshore boundary, the sediment concentration was varied linearly with the discharge volume. The maximum concentrations were set at 100 mg/l.

The bed friction is parameterised with the Nikuradse friction, with a friction coefficient varying between 0.1 m for the salt marsh locations and 0.001 on the deeper, mud covered parts (**Error! Reference source not found.**).

The resuspension of cohesive sediment is modelled using the Partheniades formulation, with the erosion coefficient set at 8e-5 $kgm^{-2}s^{-1}$. with the critical erosion stress varying over the domain. As the bed material in the channel is coarse during spring tide periods, the critical erosion stress is varied from 0.2 $kgm^{-2}s^{-1}$ on the flats to 2.51 $kgm^{-2}s^{-1}$ near the estuary mouth.

In the period before peak neap tide, mud settles in the channels, and the flats are more compacted. Therefore, the critical erosion stress is varied from 0.4 $kgm^{-2}s^{-1}$ on the flats to 0.8 $kgm^{-2}s^{-1}$ in the channels.

During the period before peak spring tide all mud is removed from the channel bed, leaving a bed dominated by gravel (near the North Sea to the west of the domain) and sand (**Error! Reference source not found.**). Assuming that during slack tides some sediment does settle on the bed, the sediment thickness in the channels is set to 0.2 m.

The flocculation is modelled using the formulation of Soulsby [5]. In contrast, the existing 2D modelling used a flocculation model that based on in situ measurements [4].

IV. FLOW RESULTS

Figure 4 show the comparison between the simulated current speed for the calibration period (spring tide) and the measured current speed. The model values have been extracted at several locations as there is some uncertainty in the exact location of the survey location.

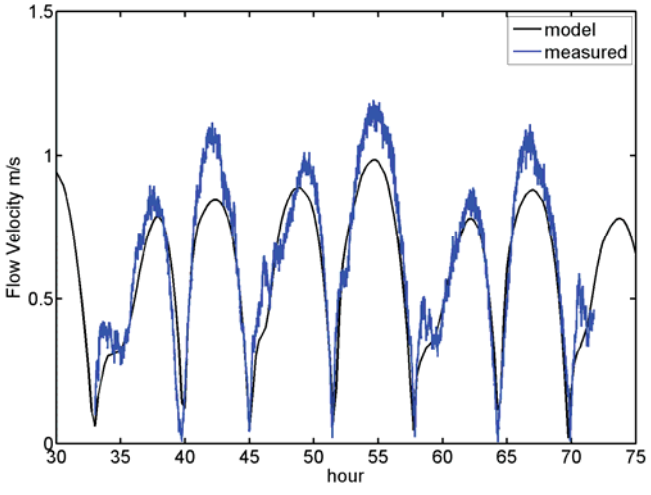

Figure 4 Measured (blue) and modelled current speed (black) during the flood tide. The time is denoted in hours since the start of the model run.

The model slightly under predicts the peak current speed. As the model is driven by tidal constituencies at the seaward boundary, this under-prediction might be caused by additional surge levels at the entrance of the estuary.

The differences for the modelled current speed during the validation period (neaps) is very similar Figure 5. The peak current speed are still underestimated, but otherwise, the model fits the data quite well.

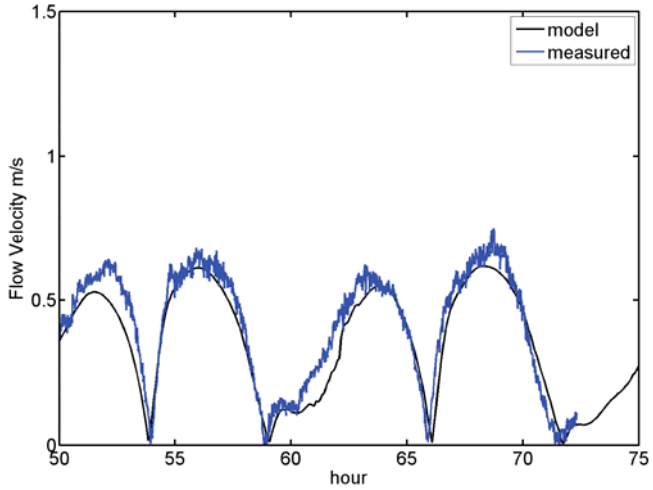

Figure 5 Measured (blue) and modelled current speed (black) during the neap tide. The time is denoted in hours since the start of the model run.

V. SEDIMENT RESULTS

Figure 6 and Figure 7 show the comparison between the simulated sediment concentrations and the measured concentrations. The peak SSC during spring tide is about 1.5 times the peak SSC during neap tide.

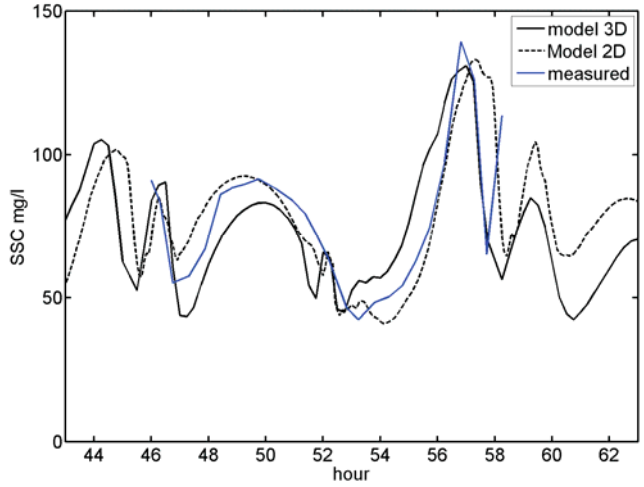

Figure 6 Comparison between modelled SSC in 2D (dashed) and 3D (solid) and measured SSC for the spring tide. The time is denoted in hours since the start of the model run.

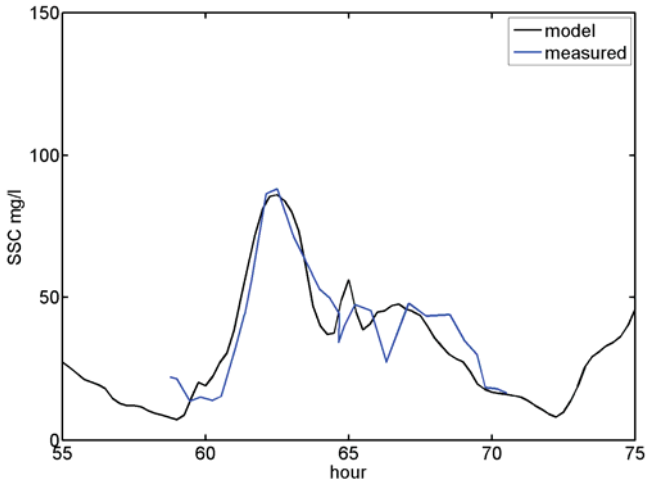

Figure 7 Comparison between modelled SSC in 2D (dashed) and 3D (solid) and measured SSC for the neap tide. The time is denoted in hours since the start of the model run.

The range of concentrations is similar to that reported for inshore waters [3]. Spring-neap variation is also evident in the ebb flood asymmetry of the residual transports. During spring tide, the SSC are largest during the ebb, giving a nett export of sediment (Figure 6). During the neap tide the SSC are higher during flood (Figure 7). Now the import of sediment during the flood exceeds the export during the ebb, giving a nett import of sediment.

VI. MODEL TESTING

The model results are tested using three different quantifications: the bias, identifying offsets in the mean value as in either under or over predictions; the root-mean-square error and the Brier Skill Score (BSS) [6] which provides a value of how well the model predicts the changes in the measured data. The BSS is 1 for a perfect fit, 0 when the model predicts no change from the mean value when the data shows otherwise and negative values when the modelled change is reverse to the measured changes. The resulting values for the three error values are given in Table 1. As there was an issue with the boundary conditions of the 2D runs for the neap tide, these runs have been excluded from the comparison table.

Table 1 Error statistics for the modelled suspended sediment transport rate.

	Spring		Neap	
	2D	3D	2D	3D
Bias (mg/l)	-0.4	-2.2	-	0.08
RMSE (mg/l)	17.3	18.1	-	9.5
BSS (-)	0.54	0.49	-	0.81

During the springs the 3D results are not as good as the 2D results. The bias is marginally higher with the model under predicting the SSC by 2.2 mg/l. the RMSE are comparable, with 18 mg/l for the 3D model, compared to 17 mg/l for the 2D model. The BSS values are poor, close to 0.5, with the 2D model doing marginally better.

In the 3D model, the biggest source of error is the inaccurate phasing of the increasing concentrations during the ebb phase. Furthermore, the peak concentrations during the flood are under predicted. In the 2D model, the phasing of the concentrations during the flood is the biggest source of error.

The statistics for the neap period are much better. The bias is less than 0.1 mg/l, the RMSE down to 10 mg/l and the Brier Skill Score is up to 0.81. The model reproduces the neap tide sediment dynamics quite well.

VII. Discussion

There is very little difference in the results of the 2D model and the 3D model, apart from the incorrectly calibrated 2D model for the neap tide. For the spring tide, the 2D results even are marginally better. Apparently, the 2D version provides an accurate representation of the essential processes. The lack of salinity differences in the Blythe and the relatively low sediment concentrations, results and a flow that is very uniform over the vertical and acts as a quasi 2D flow. The results suggest that the sediment suspension and deposition are represented well enough in the 2D version of TELEMAC.

During the spring flood, the 3D model under predicts the SSC values. This indicates that the sediment suspension in the channel is restricted too much. In the 2D model, the peak concentrations during the spring flood are reproduced better, but the peak is reached earlier than the measurements show. This implies that improvements are needed in the resuspension of the models.

The cause of the differences in the phasing of the peak concentrations is currently not known, but it is likely to be related to the differences in spatial parameterisation of bed friction and also the use of different flocculation models.

Another difference between the models, that could explain the difference in the predicted SSC's, are the bed friction formulation, Nikuradse for the present model, while the previous 2D model used the Manning roughness formulation.

In addition, the original SUBIEF-2D model solver suffered from some mass conservation problems over intertidal areas. This latter is far less an issue in TELEMAC3D.

The 2D model re-suspends sediment too much when the water column is under saturated. This element is better reproduced by the 3D model.

In the calibration process of the 3D model, first the critical shear stress for erosion was increased, which had little effect. By next reducing the sediment layer thickness to 0.0m, the sediment supply was reduced significantly. For the majority of the period, this was very beneficial to the modelling results. For the Spring flood, however, this lead to an under prediction of the SSC. Possibly more focus on the downstream channel sediment budget may improve the results for this period.

The modelled SSC peak during spring ebb precedes the measured values. Sediment is eroded too rapidly from the tidal flats in the middle of the estuary. The peak values however, a predicted quite accurately. This indicates that more effort should be spend on the sediment resuspension on the flats. This is hampered by the lack of measured data for this area. of particle size which might explain at least some of the differences in the results from each model.

The modelling was done in two parts, to provide a calibration and a validation period. However, it has proven to be critical to vary the critical erosion stresses and thickness of the active layer over time and space. This means that the validation phase required additional tuning, which is not purpose of a model validation. To avoid this issue, a much longer model run is required. This increases the complexity of the model, and will likely require additional measured data. In particular it will require information on the consolidation processes, which are not available at present.

VIII. Future work

One of the key differences is the use of the flocculation model. The difference in the flocculation models, which affects the resuspension and deposition of the sediments , might explain the model discrepancies in the phasing of the peak concentrations. This will be the main topic for further work on the Blythe sediment transport modelling.

IX. Conclusions

The sediment transport in the Blythe estuary has been modelled using TELEMAC3D. The results are compared with results of TELEMAC2D and with measurements of the current speed and suspended sediment concentrations (SSC). The predicted SSC from both TELEMAC2D and TELEMAC3D agree reasonably well with the measured value.

As there is limited difference between the 2D and 3D results, the sediment transport processes are shown to be 2 dimensional. There is no stratification in the Blythe and the sediment concentrations are too low to cause any density effects.

The largest source of error is the timing of the resuspension during spring ebbs. This can only be remediated with additional information on the sediment dynamics on the flats, which was not available for this project.

References

[1] J. R. French, H. Burningham, and T. Benson, "Tidal and Meteorological Forcing of Suspended Sediment Flux in a Muddy Mesotidal Estuary," Estuaries and Coasts, vol 31 (189), pp. 843-859, 2008.

[2] J.R. French, T. Benson, and H. Burningham, "Morphodynamics and sediment flux in the Blyth estuary, Suffolk, UK: conceptual modelling and high resolution monitoring", in Morphodynamics and sedimentary evolution of estuaries, D.M. Fitzgerald and J. Knight Eds. Springer-Verlag, New York, 2005, pp. 143-171.

[3] HR Wallingford, Southern North Sea Sediment Transport Study, Phase 2. HR Wallingford Report, EX-4526, Wallingford, 2002.

[4] T.D. Benson, In Situ Particle Size Instrumentation for Improved Parameterisation and Validation of Estuarine Sediment Transport Models, PhD. Tesis, University College London, 2004.

[5] R. Soulsby, A.J. Manning, J. Spearman, R.J.S. Whitehouse, "Settling velocity and mass settling flux of flocculated estuarine sediments, " Marine Geology, vol 339, pp 1-12, 2013.

[6] J. Sutherland, A. Peet, and R. Soulsby, "Evaluating the performance of morphological models", Coastal Engineering, vol 51(8-9), pp. 971-939, 2004.

TELEMAC-3D and Seamounts

Alan Cooper and Jeremy Spearman
HR Wallingford Ltd
Wallingford, OX10 0BA, UK
Corresponding author: A J Cooper
a.cooper@hrwallingford.com

***Abstract*—TELEMAC-3D has been used to make schematic solutions of flow in the ocean at a seamount. It is found that there is a possibility of trapping of water above the seamount. However in monitoring the seamount to observe such features it is necessary to include current measurements at very small height above the seamount surface. Such area of trapping can contribute to the formation of metal-rich crusts on the seamount surface which form a valuable resource for metals increasingly in demand for "green" technology.**

I. INTRODUCTION

Minerals are essential for economic development, the functioning of society and maintaining our quality of life. The consumption of most raw materials has increased steadily since World War II, and demand is expected to continue to grow in response to the burgeoning global population and economic growth, especially in Brazil, Russia, India and China (BRIC) and other emerging economies.

We are also using a greater variety of metals than ever before. New technologies such as those required for modern communication and computing and to produce clean renewable, low-carbon energy require considerable quantities of many metals.

In the light of these trends, there is increasing global concern over the long-term availability of secure and adequate supplies of the minerals and metals needed by society. Of particular concern are 'critical' raw materials (E-tech elements), so called because of their growing economic importance and essential contribution to emerging 'green' technologies, yet which have a high risk of a shortage of supply.

The following E-tech elements are considered to be of highest priority for research: cobalt, tellurium, selenium, neodymium, indium, gallium and the heavy rare earth elements. Some of these E-tech elements are highly concentrated in seafloor deposits (ferromanganese nodules and crusts), which constitute the most important marine metal resource for future exploration and exploitation.

For example, the greatest levels of enrichment of Tellurium are found in seafloor Fe-Mn crusts encrusting some underwater mountains (seamounts). Tellurium is a key component in the production of thin film solar cells, yet it is prone to security of supply concerns because of projected increased demand resulting from the widespread deployment of photovoltaic technologies, low recycling rates and its production as a by-product from copper refining.

Figure 1 - Low-carbon technologies requiring rare-earth metals

II. FORMATION OF DEPOSITS

As a result, it is vital to assess alternative sources of supply of tellurium and the other E-tech elements, the largest source of which is held as seafloor mineral deposits. Our research programme aims to improve understanding of E-tech element concentration in seafloor mineral deposits, which are considered the largest, yet least explored, source of E-tech elements globally.

Ferromanganese oxide deposits (Fe-Mn deposits) deposits are known to be highly variable in both thickness and composition. Yet there is surprisingly little information about what controls this. What information exists is sparse and spread across different ocean basins. Despite this it is known that local conditions may allow deposits (e.g. crust) to form in one area yet, a few tens of kilometres away, to be absent.

Our research will focus on two key aspects:

- The formation of the deposits, and reducing the impacts resulting from their exploitation.
- Reducing the impacts resulting from their exploitation.

Detailed studies (on the scale of individual seamounts) could enable us to better understand the environmental conditions forming these crusts such as local hydrography, biological productivity, turbulence, past changes in water mass and upwelling, and changes in the oxygen minimum zone.

What is the magnitude of the topography effect and can it be predicted?

Seamounts generate upwelling and turbulence of cold, oxygenated and nutrient-rich water that enhance nutrient supply and bioproductivity and which interacts with the shallower, Mn-rich, oxygen minimum zone (OMZ) water masses causing Mn oxidation, precipitation and drawdown of ionic metals dissolved in the water column.

At the seamount-scale, the basement morphology will have an effect on upwelling and mixing - hence influencing the thickness of Fe-Mn deposits and their composition, especially on the outer rim or upper flanks of the seamount.

This task will determine the present hydrochemical and physical conditions at the site of deposition of the Fe-Mn deposits. The specific objectives are to estimate spatial (three-dimensional) patterns of the ocean circulation, water mass composition and chlorophyll content, and to numerically model the deep ocean circulation and its spatial variability.

Knowns:

- Role of oxygen minimum zone (OMZ) in the precipitation of iron and manganese oxides.
- OMZ sustained by high biological surface water productivity. Maintains high concentrations of dissolved Mn and Fe.
- Interface between OMZ and oxygenated deep-water oxidises dissolved Fe and Mn which precipitate as oxihydroxide particles that settle through the water column.
- General role of large-scale seafloor bathymetry on FeMn crusts.
- Seamounts that intercept the OMZ also cause local upwelling that enhances mixing and precipitation of Fe and Mn oxyhydroxides. They also enhance local surface productivity.

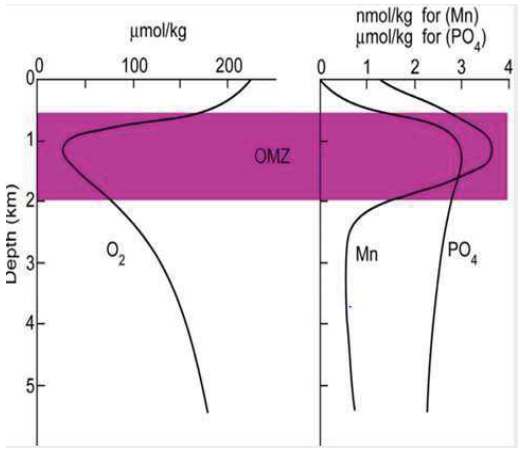

Figure 2 - Formation of deposits

BUT: of over 33,000 seamounts globally, less than 500 have been visited and only a few hundred Fe Mn crust samples studied in total.

We will also address how to minimise the environmental impacts of mineral exploitation.

III. SEAMOUNTS

Seamounts are undersea mountains in deep water (typically 4000m). They are an important part of the marine environment as they contain ecosystems and geology that differ from those of both the deep sea and the shallow sea.

The top of a seamount may be at any level but often is about 1000m below the sea surface resulting in the local ocean current passing across the seamount above its peak in the top few hundred metres of the water column.

Seamounts are of particular interest in the current climate of pressure on resources of rare earth minerals because the Fe-Mn crusts which form on seamounts are particularly rich in metals which are essential for low-carbon technology.

Seamounts represent a unique flow regime within ocean systems - according to G I Taylor it would be expected that in a uniform flow with constant density there would appear a "Taylor column" above the seamount where the water would be trapped (in a frame of reference rotating with the earth).

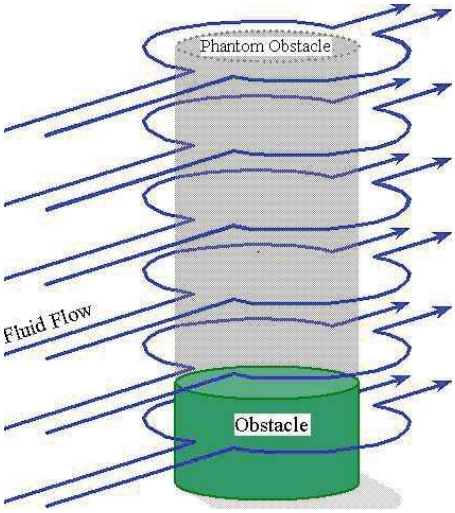

Figure 3 - A Taylor column

i.e. there is a "phantom" obstacle.

This trapping of water above the seamount may account for the exceptional environments experienced on top of seamounts, including the presence in the crusts of manganese and other metals. One of the goals of the research is to identify to what extent this theoretical idea is repeated in real seamount systems.

The present study has taken a particular seamount to study, the Tropic Seamount, which is located at 23o 52.80'N 20o 42.60'W close to the Tropic of Cancer off the west coast of Africa. It is located within the southwest flowing Canary Current which occupies approximately the top 500m of the water column down from the surface. The peak of the seamount is at about 1000m below the surface so the ocean current does not extend down as far as the top of the seamount but is able to flow past above the peak comparatively unaffected.

This seamount will be the subject of a substantial monitoring exercise in November/December 2016 carried out by NERC, NOC Southampton.

Prior to this monitoring, and as a first step, we have investigated the ability of TELEMAC to reproduce the classical Taylor Column behaviour.

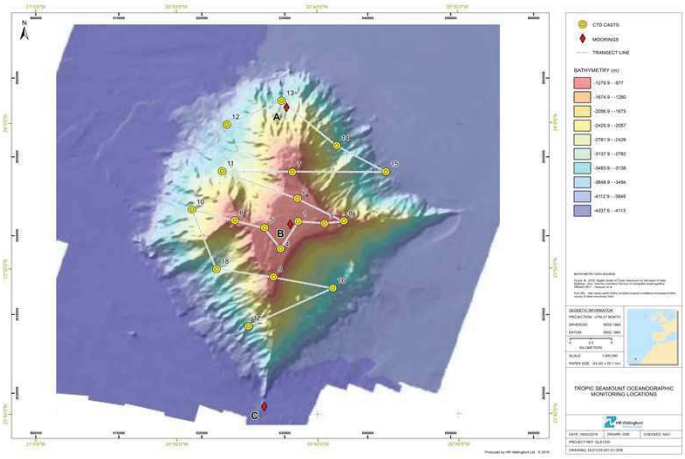

Figure 4 - Tropic Seamount

IV. MONITORING EXERCISE

Hydrographic interaction with the seamount, and especially the disturbance of the flow field around it will be examined by deploying three moorings, spaced ~50km from the centre of the seamount, and deployed for ~40 days. Each mooring will comprise recording current meters and micro-CTDs located at three different positions above the bottom (~1000, 2000 and 3000m water depths).

In addition, hydrographic grids will be occupied using CTD- and lowered ADCP profiling plus vessel-mounted 75 kHz ADCP profiling to measure instantaneous currents throughout the water column as well as suspended sediment and chlorophyll. A similar approach will be adopted for the RGR and VC by our UPS partners, except that the temporal variability of near-bottom currents will be observed over a period of 3 years and will include conjugated Acoustic Doppler Current Profilers (ADCP) - Sediment Trap Moorings in two distinct hydrodynamical locations.

Instruments to be used

- ADCP current profiler (upward looking)
- 5 single point CMs/DVs
- Vessel mounted ADCP
- Moorings will be at two levels:

Through depth profiling will be at 18 locations and include

- Current speed and direction (downward-looking ADCP)
- Salinity, temperature and depth (CTD probe)
- Turbidity (OBS)
- Water samples (Rosette sampler)
- Profiling rig altitude (Altimeter)

Table 1 - Instrumentation

Mooring	Location	Approx. Water Depth (m)	Height Above Sea Bed (m) - lower instrument	Parameters required - lower instrument	Height Above Sea Bed (m) Upper	Parameters required - upper instrument
A	Seamount Slope	3000	1000	UVW, salinity, temperature	2000	UVW, salinity, temperature.
B	Seamount Surface	1000	8	UVW, salinity, temperature (Profiler U/L)	900	UVW, salinity, temperature
C	Abyssal Plain	4300	1000	UVW, salinity, temperature	3300	UVW, salinity, temperature

Vessel mounted ADCP will drive between the CTD profiling stations. A complete route will be a steaming distance of 115km taking just under 7 hours.

V. SCHEMATIC MODELLING

Schematic simulations have been made in TELEMAC with a flat bottomed channel and an analytical shaped circular seamount in the middle of it.

The current has been modelled with boundary conditions for uniform flow across the channel and analytical formulae for the current speed and density distribution through the water depth. When flow is initiated the current increases from zero to a steady state flow.

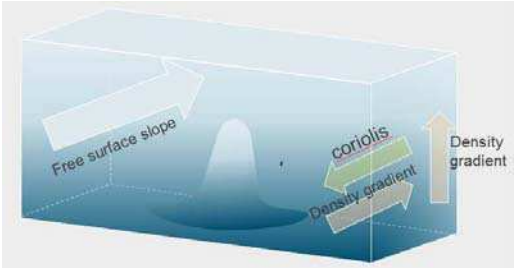

Figure 5 - Model set-up for geostrophic flow

The resulting flows show an area of low current above the seamount and below the ocean current above as expected (Figure 6). This feature is like a very short Taylor column.

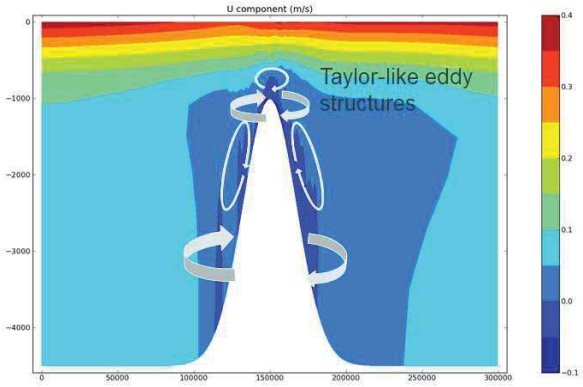

Figure 6 - Longitudinal cross-section through a theoretical seamount showing the predicted current speed (U component, m/s)

A horizontal plane through the middle of the seamount shows that the horizontal current has a clockwise circulation as seen from above, above the slope of the seamount (Figure 7). This area of low current in this simulation extends about 200m above the peak. Near the peak the current speed is slow (Figure 6) but even in the area around the peak the flow takes on a largely circular form and this current can trap materials and if they are heavier than water they may fall to the bed and become a permanent feature of the seamount.

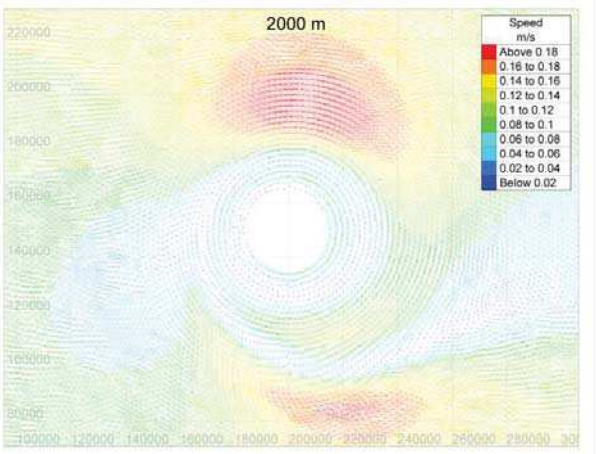

Figure 7 - Horizontal slice through a theoretical seamount showing the predicted current velocity 2000m the below water surface

The area of low current above the peak of the seamount can be seen to cause the current speed contours to "dome" (Figure 6), although the tracer contours are mostly unaffected (Figure 8).

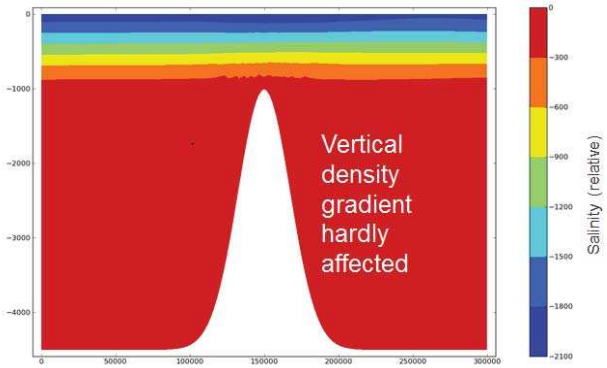

Figure 8 - Model density longitudinal profile through the seamount

The conclusion of the modelling is that the area of trapped fluid above the seamount may be very thin (only 20-200m top to bottom) so observations need to extend very near to the top of the seamount. Figure 9 shows near bed flows around Tropic Seamount subjected to the same imposed current and at different contour levels it can be seen that the current follows the contours indicating that the material just above the seamount is trapped.

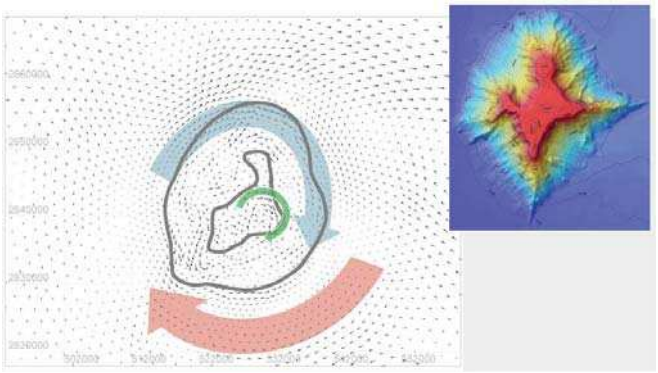

Figure 9 - Currents above the bed – example of Tropic Seamount

VI. CONCLUSIONS

The aim of the study is to obtain 4D maps of the water mass distribution, currents and their variability above the study sites. The resolution of the hydrographic grids and moorings are designed to capture the velocity fields around the sites of interest at the scales of 10's of kilometres.

So far the schematic modelling shows the possibility of entrapping of material in the water just above the seamount. However the layer of entrapped water is bounded above by the ocean current and it may be a very thin layer so that monitoring of currents at the seamount needs to measure currents within a few metres of the seamount.

Development of a dynamic riparian vegetation model in TELEMAC-2D

Baptiste Clement, Nicolas Claude, Germain Antoine & Marion Duclercq
EDF R&D National Laboratory for Hydraulics and Environment (LNHE)
Chatou, France
nicolas-n.claude@edf.fr

Abstract— **Issues associated to the development of riparian vegetation in rivers become more and more considered by scientists and managers. Bio-hydro-morphodynamic numerical models can provide a significant help to better understand the complex interactions between plants and hydrogeomorphic processes, and can become helpful tools for streams management. It is in this context that a dynamic riparian vegetation model, based on the works of Van Oorschot *et al.* [2016] has been implemented in TELEMAC-2D. This model simulates colonization by seed dispersal, growth and mortality of plants of Salix type. Three mortalities were considered: uprooting, flooding and desiccation. The influence of vegetation on hydrodynamics is modelled by a drag force. The implementation of the ecological mechanisms has been tested and verified on a simple case. In the future, the present dynamic vegetation model can be improved by considering interactions between sedimentary processes and plants, by improving parameterization of ecological mechanisms and by modelling of multiple species.**

I. INTRODUCTION

Riparian vegetation is a common feature of rivers. In these hydrosystems, plants and hydrogeomorphic processes are strongly interconnected. Vegetation affect hydrodynamic by deflecting and reducing the flows [1], [2], [3], [4]. This influence is related to plants characteristics such as the density, stem diameter and height, and flexibility [5], [6], [7]. The impact of vegetation on flows also modifies the sediment transport. Thus, presence of plants tends to decrease sediment transport capacity, and causes deposition of particles [8], [9], [10]. The flow deflecting can also contribute to erode the bed close to patches [11], [12]. Furthermore, vegetation influences banks evolution by reinforcing soil cohesion thanks to the biomechanic action of roots and through addition of organic materials [13], [14]. Plants can also destabilize banks by modifying water circulation in the soil and causing mass failure [15]. At a larger scale, vegetation encourages the aggradation of alluvial bars [16] and secondary channels [17], and affects the river planform [18], [19].

In return, hydrology and morphodynamic processes affect also the vegetation dynamic. Riparian plants have adopted specific traits to survive to high disturbances encountered in streams, namely flooding, scour, burial and high flow velocities [20]. For example, riparian species use both sexual and asexual reproduction to optimize their recruitment in rivers, i.e. to colonize a maximum of wet and bare substrates [21]. In these systems, plants have also adapted their timing and period of seed dispersal to flow regime [22]. After germination, seedlings grow very fast in order to produce large dense roots systems to reduce the risks of uprooting [20]. The biomass development above riverbed is also very quick and leads to flexible stems to decrease their drag and their flow resistance [23].

Interactions between plants and hydrogeomorphic processes evolve with the age of vegetation [21]. During their early stage, plants have low effect on flow and sediment transport. However, during this phase, hydrogeomorphic disturbances strongly affect vegetation development. When plants get older, this relationship becomes more balance. Thereafter, with an adult population, the relationship is reversed and more unidirectionnal with plants affecting more the hydrogeomorphic processes than the opposite [16]. Thus, to simulate long-term evolution of a vegetated river, a model representing plants by only one age (without growth and mortality) seems not reliable [24]. For long-term morphodynamic prediction of rivers, it is necessary to take into account links between plants and hydrogeomophic processes, and to consider the evolution of these interactions as a function of the vegetation dynamic. Practically, this corresponds to couple a physic-based morphodynamic model to an ecological model which reproduces seed dispersal, colonization, growth and mortality of plants. Based on this assessment, [24] have recently proposed a sophisticated bio-morphodynamic model to study in details interactions between vegetation and morphodynamic of a meandering river.

The objective of our project is to couple a vegetation model to the TELEMAC-MASCARET system to provide in future an operational tool for river managers. To this end, a work was previously initiated to model the effect of vegetation on hydrodynamic [25]. This paper presents the second step which has consisted in implementing a dynamic riparian vegetation model based on the works of [24]. Note that a dynamic aquatic plant model was also implemented previously by [26]. The ecological model developed in this study simulates recruitment, colonization, growth and mortality of riparian plants. Thus, in a first part, we recall

briefly how the effect of plants on hydrodynamic is modelled in TELEMAC-2D. In a second part, the dynamic ecological model is detailed. In a third part, the implementation of the ecological model is verified. Finally, a conclusion and some outlooks are proposed.

II. MODELLING THE EFFECT OF VEGETATION ON HYDRODYNAMIC

In this study, the hydrodynamic simulations were performed with TELEMAC-2D which solves the depth-averaged shallow-water equations with the finite element method. The effect of vegetation on flow is modelled by adding a drag force (*Fd*) in the momentum equations.

Drag force has been calculated from the following relation [7]:

$$\overrightarrow{F_d} = -\frac{1}{2} C_d \rho \alpha_v A * \min(h_v, h) * \left|\overrightarrow{U_v}\right| * \overrightarrow{U_v} \quad (1)$$

Where C_d is the drag coefficient, ρ is water density, α_v is a shape factor equals to 1 for a rigid cylinder, $A = m * D$ is the projected area of stems in the flow direction (with m the number of stems per m² and D the stems diameter), h_v and h are the plant height and the water depth, respectively, and $\overrightarrow{U_v}$ is the vector of flow velocity acting on the vegetation.

If $h_v \geq h$ (emerged vegetation), $\overrightarrow{U_v} = \vec{U}$, the depth averaged velocity. If not $h_v < h$ (submerged vegetation):

$$\overrightarrow{U_v} = \eta_v \vec{U} \left(\frac{h_v}{h}\right)^{1/2} \; with \; \eta_v = \frac{1 - D\sqrt{m}}{1 - \frac{h_v}{h} D\sqrt{m}} \quad (2)$$

Thus, to estimate the drag force induced by vegetation, the diameter, height and density of the considered plants should be known.

III. DESCRIPTION OF THE DYNAMIC RIPARIAN VEGETATION MODEL

A dynamic riparian vegetation model, based on the works of [24], has been implemented in TELEMAC-2D in order to simulate the establishment, the growth and the decay of plants in a river (Figure 1). The plants modelled have characteristics corresponding to Salix species.

Vegetation is defined in each node of the mesh by an occupation matrix:

$$Occ = \left(s_{i,j}\right)_{\substack{0 \leq i \leq a_{max} \\ 0 \leq j \leq t_{run}}} \quad (3)$$

Where $s_{i,j} \in [0,1]$ is the cover fraction related to the vegetation of age *i* during the year *j* of simulation. a_{max} is the maximum age of the plant (here *Salix* plants have a life expectancy of 60 years) and t_{run} the number of full years in the simulation. The initial vegetation cover is set up by defining the first column of the occupation matrix.

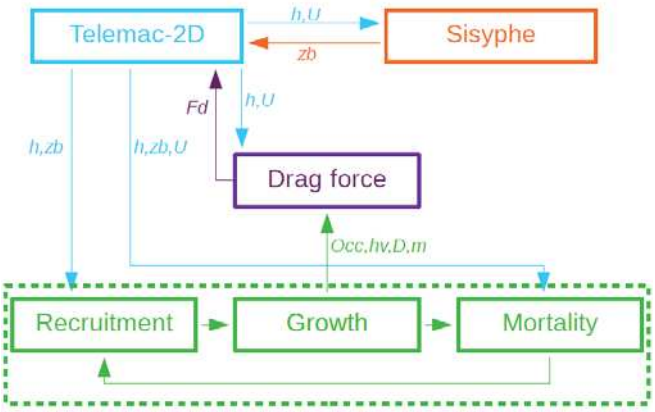

Figure 1. Diagram of coupling between TELEMAC-2D and the ecological model (shown by green dotted line).

A. Evolution of the occupation

Characteristics of vegetation (cover fraction, diameter, height, density) are updated once in a year after the window dispersal (see part III.B). The following equation gives the relationship between cover fraction of a vegetation at the year *j+1*, cover fraction at the year *j*, mortality at the year *j* ($\alpha_{i,j}$) and the initial fraction ($s_{i-j,0}$ or $s_{0,j-i}$):

$$\forall \, i \geq 1 :$$
$$s_{i+1,j+1} = \max(s_{i,j} - \alpha_{i,j} * s_{i-j,0} \, ; \, 0) \; si \; i \geq j \quad (4a)$$

$$or \; s_{i+1,j+1} = \max(s_{i,j} - \alpha_{i,j} * s_{0,j-i} \, ; \, 0) \; si \; i < j \quad (4b)$$

At each (ecological) time step, the fraction of age *i+1* equals the fraction of age *i* a year before, minus the fraction freed by mortality. We distinguish the case where vegetation existed at the initial state ($i \geq j$), from the case where vegetation developed during simulation ($i < j$).

B. Recruitment

Riparian species have complex reproduction mechanisms adapted to hydrogeomorphic disturbances [20]. In the present model, we simplify these processes by only representing the sexual reproduction. The period of seed dispersal called window dispersal (WD) corresponds to the time when flow decreases in rivers (here it is supposed to be the month of June for *Salix* type). During this period, seeds are carried on by the river flow and the wind. Seeds germinate when they are deposited on a bare and wet substrate.

We assume that areas of germination at the year *j* are those submerged during WD ($h_{max}(t \in WD_j) > 0$) and emerged at the end of WD ($h\left(t = end\ of\ WD_j\right) = 0$). Thus, we are sure that seeds have been deposited on a wet substrate and that they have not been carried away by a water level rise.

When colonization takes place, the cover fraction of vegetation at age 0, $s_{o,j}$. is set up at 0.8 [24] when there is no plants at all. When plants occupy partially the bed, empty spaces are filled by a vegetation at age 0 [24]: $s_{o,j} = 1 - \sum_{i=1}^{a_{max}} s_{i,j}$.

C. Growth

Growth of plant height (h_v), root length (r), and stem diameter (D) were implemented as logarithmic functions (Figure 2) with the following formula [Van Oorschot et al. 2015]:

$$G = F_V * \log(i+1) \quad \forall i \geq 1 \qquad (5)$$

Where G is the size ($G = h_v\ ou\ r\ ou\ D$), F_V is the vegetation type dependent logarithmic growth factor and i is the vegetation age in years. The values of parameters are given in Table I.

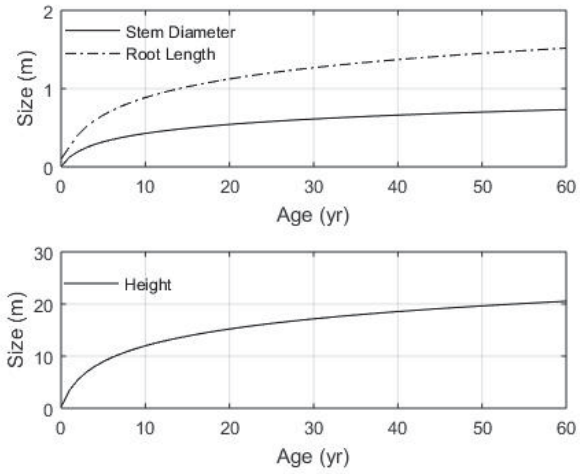

Figure 2. Growth curves of the *Salix* Type.

TABLE I. Vegetation growth parameter [24].

Parameters	Unit	Type	Reference
Vegetation type	-	*Salix*	
Maximum age	an	60	Braatne *et al.* (1996) [27]
Initial root length	m	0.1	Canadell *et al.* (1996) [28]
Initial shoot length	m	0.25	Van Velzen *et al.* (2003) [29]
Initial stem diameter	m	0.002	Van Velzen *et al.* (2003) [29]
Fv root	-	0.85	Canadell *et al.* (1996) [28]
Fv shoot	-	11.5	Kleyer *et al.* (2008) [30]
Fv diameter	-	0.41	Van Velzen *et al.* (2003) [29]
Timing of seed dispersal	month	June	Kleyer *et al.* (2008) [30]

D. Mortality

Plants start to die as soon as they are flooded or their roots are above the water table for 15 successive days or more [24]. Vegetation can also be uprooted from the substrate when the flow velocity is too high. The modelling of these processes is detailed in the following paragraphs. Plants can also die if they are buried by sediments or if a scour height gets higher than the length of roots. However, these two mechanisms are not yet implemented.

Total mortality of an age i at the year j of simulation, $\alpha_{i,j}$, corresponds to the sum of the mortality by flooding $a_{i,j}$, by desiccation $b_{i,j}$ and by uprooting $c_{i,j}$.

$$\alpha_{i,j} = \min(a_{i,j} + b_{i,j} + c_{i,j}, 1) \qquad (6)$$

The three mortalities are calculated using a threshold function Γ, applied to a variable called morphodynamic pressure related to the mortality considered [24]. The function is schematized below on the figure 3.

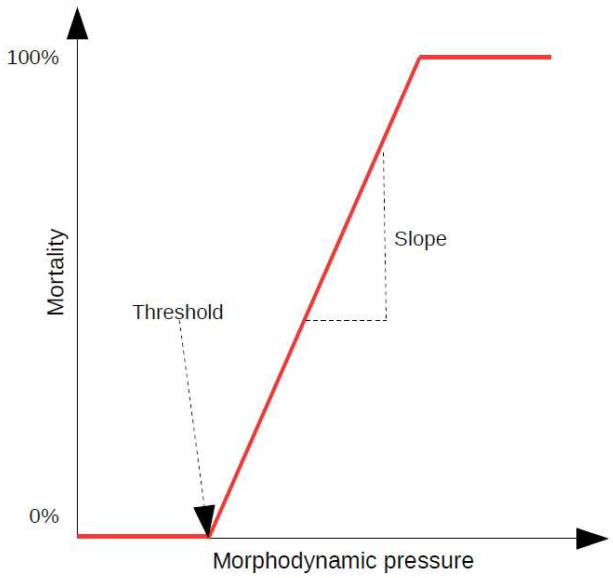

Figure 3. Form of mortality functions.

When the morphodynamic pressure overtakes a threshold value, mortality increases linearly until 100%. Function's parameters (threshold and slope) are characteristics of the mortality and the Life Stage (LS) of the vegetation considered. All values are displayed in Table II.

For mortality by flooding $a_{i,j}$, we compute $n_{sub,j}$ the number of days included in a period of 15 or more successive days of flood (days where water depth is not zero). Then $a_{i,j}$ is calculated by applying the appropriate Γ function:

$$a_{i,j} = \Gamma_{flood,LSk}(n_{sub,j}) \quad \forall i \geq 0, et\ i \in LSk \qquad (7)$$

Where *LSk* is the Life Stage in which belongs the age i.

TABLE II. Parameters of morality [24].

		Life stages *Salix* type				Reference
Parameter	**Unit**	**LS1**	**LS2**	**LS3**	**LS4**	
Number of years in LS	an	0	1-9	10-49	50-60	Van Velzen *et al.* (2003) [29]
Number of stems	stems/m²	25	15	0.16	0.16	Van Velzen *et al.* (2003) [29]
Desiccation threshold	days	25	190	240	365	Geerling *et al.* (2006) [31]
Desiccation slope	%/day	0.024	0.005	0.005	∞	Geerling *et al.* (2006) [31]
Flooding threshold	days	70	260	310	365	Geerling *et al.* (2006) [31]
Flooding slope	%/day	0.024	0.005	0.005	∞	Geerling *et al.* (2006) [31]
Flow velocity threshold	m/s	0.55	7.0	12.0	6.0	Geerling *et al.* (2006) [31]
Flow velocity slope	%/m.s^{-1}	2.4	0.5	0.5	0.5	Geerling *et al.* (2006) [31]

Likewise, mortality by desiccation $b_{i,j}$ is calculated by counting $n_{des,i,j}$, the number of drought day included in a period of drought longer than or equal to 15 days. A day is defined as dry when the roots do not reach the water table. We assume that the water table and the free surface have the same elevation i.e.:

$$z_b - r(i) > SL \tag{8}$$

Where z_b is the bed elevation, r is the root length and SL is the free surface elevation. Note that during drought conditions, there is no water in some areas covered by plants. To verify if roots reach the water table, we need to obtain a SL value on these dry nodes (see Eq. 8). For that purpose, we have partitioned the domain into several zones. In each zone, a reference point has been identified such as it is always under water. To verify if a non-submerged node is in dry condition or not (as defined above), we use the SL value calculated by TELEMAC-2D on its reference node.

Then $b_{i,j}$ is calculated as follows:

$$b_{i,j} = \Gamma_{desic,LSk}\left(n_{des,i,j}\right) \ \forall i \geq 0, i \in LSk \tag{9}$$

Mortality by uprooting $c_{i,j}$, is calculated by applying $U_{max,j}$, the highest flow velocity on the year j to the function Γ:

$$c_{i,j} = \Gamma_{uprooting,LSk}\left(U_{max,j}\right) \ \forall i \geq 0, i \in LSk \tag{10}$$

IV. VALIDATION OF IMPLEMENTATIONS

In this part, we present the results of a simulation carried out to check that the processes and equations presented above were correctly implemented into TELEMAC-2D.

A. Presentation of the model

The model represents a straight rectangular canal of 76.5 m long and 1 m large. The bathymetry, inspired from the experiments of [32], has been defined in order to have a bed slope of 0.05% with a low part (channel) and high part (bar) (Figure 4). The mesh is composed of more than 32000 nodes, spaced in average of 5 cm. Boundary conditions are a water discharge at the inlet and free surface elevation at the outlet of the channel.

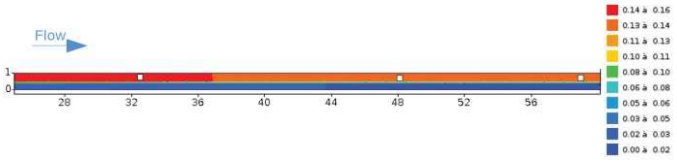

Figure 4. Bed elevation (m) in the model. From left to right, the 3 white squares indicate nodes n°15896, n°21803 and n°25928.

B. Hydrograph

A simplified hydrograph has been imposed at the inlet boundary to test the processes implemented in the ecological model (Figure 5 and Table III). The hydrograph is composed of four discharges: one flow to submerge the bar (Q = 0.04 m^3/s), one flow with an emerged bar (Q = 0.02 m^3/s), one flow corresponding to a drought situation, when roots do not reach the free surface (Q = 0.015 m^3/s) and one flow to reach high velocities in order to uproot young vegetation from the bar (Q = 0.1 m^3/s). Roots length has been fixed to 2 cm for all the life stages to simplify the test. Five years were simulated to observe the vegetation evolve 5 times. The implementation of an ecological process is tested each year of the simulation (Table III). To reduce computation time, 3 seconds in the model represent a day in real life.

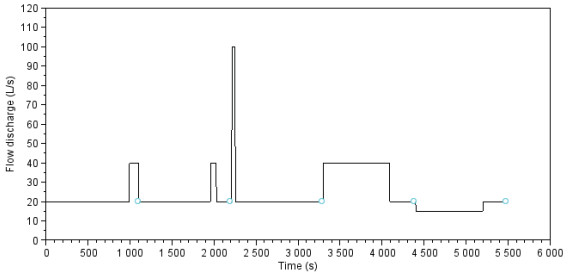

Figure 5. Hydrograph used for the test. Transitions between each ecological time steps (each years) are marked by blue circles.

TABLE III. Test program.

Year	Date of the end of year (s)	Processes tested
1	1095	Recruitment failure
2	2190	Recruitment
3	3285	Uprooting
4	4380	Flooding
5	5475	Desiccation

C. *Validation of the processes implementation in the ecological model*

Figure 6 shows the cover fractions of vegetation that germinates on the bar (0 years old - LS1) for each year of the simulation. Figure 7 presents each year the sum of cover fractions of vegetation that are 1 to 9 years old (LS2)

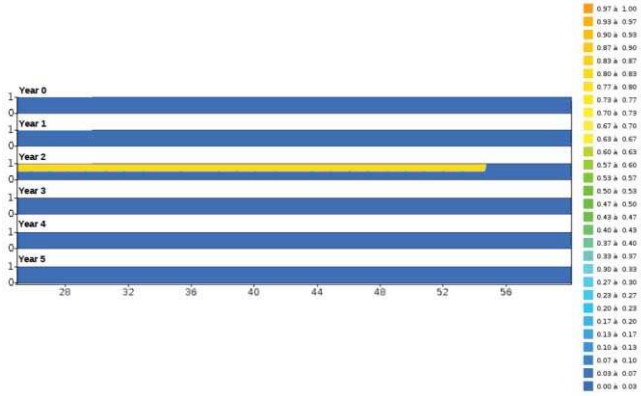

Figure 6. Cover fraction for the LS1.

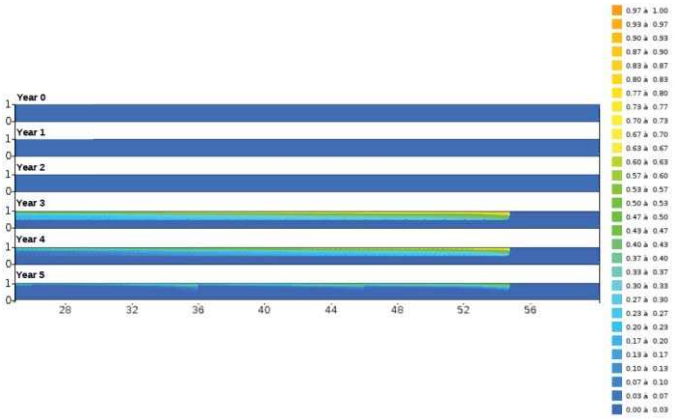

Figure 7. Cover fraction for the LS2.

1) *Year 1: Recruitment failure*

There is no vegetation at initial state (year 0 in Figures 6 and 7). The hydrograph of the first year is composed of a flood that starts during the window dispersal (WD) and finishes after this period. So, the bar is still submerged on the 1st of July at the end of the WD (Figure 8). As no bare and wet substrate is available to allow a plant recruitment, no vegetation appears during year 1 (LS1 is empty, see Figure 6).

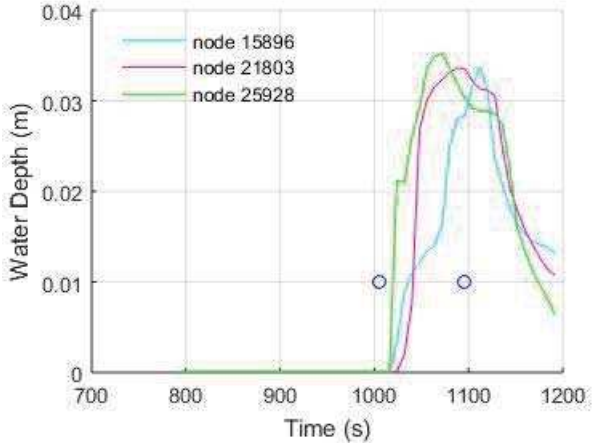

Figure 8. Water depth on 3 nodes located on the bar at the end of year 1. Blue circles mark the beginning and the end of the window dispersal. See Figure 4 for the location of the 3 nodes.

2) *Year 2: Recruitment*

During the second year of the simulation, a flood begins before the window dispersal and finishes before the 1st of July. With this hydrology, a large part of the bar becomes emerged during the WD (see nodes 15896 and 21803 on Figure 9) and then is colonized by plants (Figure 6, year 2). The cover fraction related to new vegetation is 0.8. We also see in the downstream part of the bar that plants do not colonize the substrates which are not submerged during the WD (see node 25928 on Figure 9, and Figure 6).

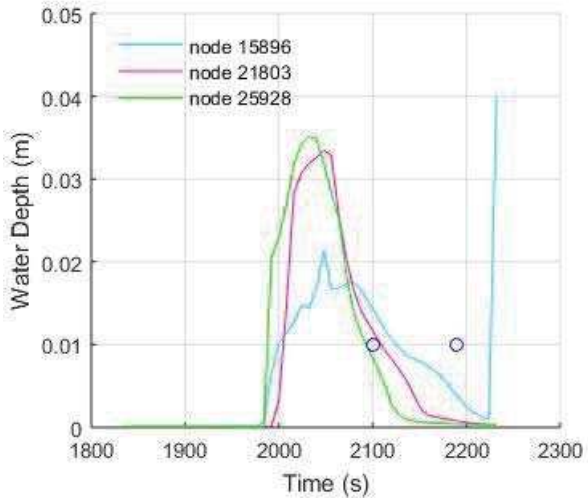

Figure 9. Water depth on 3 nodes located on the bar at the end of year 2. Blue circles mark the beginning and the end of the WD. See Figure 4 for the location of the 3 nodes.

3) *Year 3: Uprooting*

Vegetation established at the end of the second year is now 1 year old (LS2, Figure 7). The third year of simulation is marked by a large flood with maximal velocities (U_{max}) sufficiently high on the bar (Figure 10) to allow locally the uprooting of some plants (i.e. U_{max} higher than 0.55m/s, see Table II). This explains why the spatial distribution of the cover fraction of LS2 is similar to the spatial distribution of U_{max}.

To check the calculation of mortality by uprooting, a comparison of the results of the simulation on one node with a handmade calculation using equations given part III is performed. For that purpose, node n°21803 is considered. TELEMAC graphic outputs give 0.79 m/s, a fraction of 0.8 at year 2 and a fraction of 0.33 at year 3. According to Figure 3 and Table II, mortality by uprooting reaches a value of 2.4*(0.79-0.55) = 0.58. We find the same occupation at the year 3 than the implemented model since thanks to Eq 4: 0.8-0.58*0.8 = 0.33.

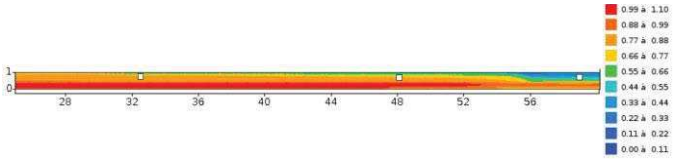

Figure 10. U_{max} (m/s) during year 3. From left to right, the 3 white squares indicate nodes n°15896, n°21803 and n°25928.

4) *Year 4: Flooding*

During the year 4, a very long flood has been simulated. The bar is flooded almost uniformly more than 260 days (Figure 11), which overcomes the mortality threshold by flooding for LS2 (Table II). It leads to a slight decrease of the cover fraction of vegetation on the bar (Figure 7, year 4).

To verify the calculation performed by the code, we use the node n°21803 which has been flooded 283 days (Figure 11) and presents a new fraction of 0.24 at year 4 (Figure 7). According to Figure 3 and Table II the mortality by flooding is estimated manually to 0.005*(283-260) = 0.115. Then, the new fraction is deduced: 0.33-0.8*0.115 = 0.23. The result of the handmade calculation is equal to the result of the simulation.

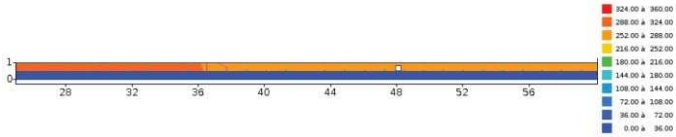

Figure 11. . Number of flooded days (N_{sub}) during year 4. Node n°21803 is indicated by a white square.

5) *Year 5: Drought*

The fifth year of simulation presents a long period of low flow. For these flow conditions, the roots are not connected to the water table. The dry period is longer than the mortality threshold by drought for LS2 (Table II). Thus, a part of the plants dies by desiccation during this year (Figure 7, year 5). At the end, vegetation is still present close to the left bank and across the bar with a regular spacing (Figure 7). This spatial distribution is partly due to the domain partitioning method used to estimate the water table elevation (part III.D). The method to reproduce vegetation mortality by desiccation will be improved in the future.

To check the calculation, we perform a handmade calculation of the mortality by drought on the node n°21803. This area has been in drought conditions 258 days during year 5 (Figure 12). At the end of this year, the fraction is null on the node. According to Figure 3 and Table II the mortality by drought can be estimated to 0.005*(258-190) = 0.34. The new fraction is then 0.23-0.8*0.34 < 0. Since a fraction cannot be negative, the result is rounded to 0. Thus, the handmade calculation and the simulation give the same result.

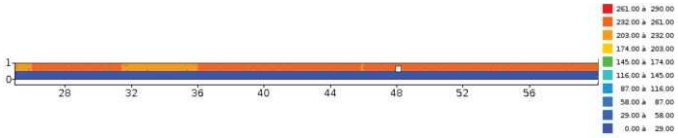

Figure 12. Number of drought days (N_{des}) during year 5. Node n°21803 is indicated by a white square.

V. CONCLUSIONS AND OUTLOOKS

Issues associated to the development of riparian vegetation in rivers become more and more considered by scientists and managers. Bio-hydro-morphodynamic numerical models can provide a significant help to better understand the complex interactions between plants and hydrogeomorphic processes, and can become helpful tools for streams management.

A dynamic riparian vegetation model, based on the works of [24] has been implemented in TELEMAC-2D. This model simulates colonization by seed dispersal, growth and mortality of plants of Salix type. Three mortalities were considered: uprooting, flooding and desiccation. The implementation of these mechanisms has been tested and verified on a simple case.

This work constitutes a first step toward a more complete and realistic bio-hydro-morphodynamic model. Several outlooks can be listed, among others:

- To model interactions between vegetation and sedimentary processes since these relationships control significantly the evolution of rivers [16]. A preliminary work would consist in modelling the plants death by burial and scour.
- To optimize the parameterization of ecological processes (growth and mortality curves) by calibrating the parameters from field or laboratory measurements.
- To complete the model in order to simulate the dynamic of multiple species (poplars, invasive or protected species…), their interactions and the feedbacks of plant communities on the flow and sediment transport.

Furthermore, a first application is ongoing on a 3 km long reach of the Isère River (Figure 13). The objective is to better understand the effect of flow regulation on plants development. For this purpose, a TELEMAC-2D model is coupled to the ecological model described in this paper and two hydrographs are simulated: one corresponding to natural flows and one representing regulated flows. For instance, Figure 14 shows, as preliminary result, the evolution of the recruitment areas during 3 years for a regulated hydrology. Thereafter, a comparison of the 2 simulations will be carried out to characterize qualitatively the influence of the water management on vegetation dynamic.

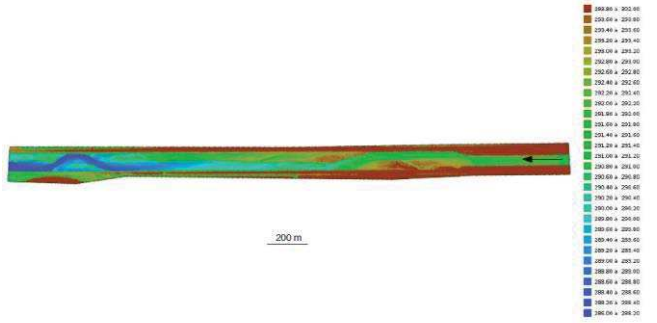

Figure 13. Bathymetry of the study reach represented in the TELEMAC-2D model. The black arrow indicates the flow direction.

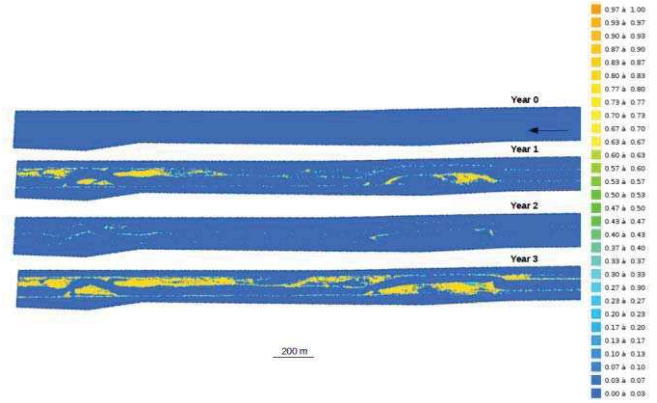

Figure 14. Fraction of area colonized by seedlings.

REFERENCES

[1] W. L. Cowan, "Estimating hydraulic roughness coefficients", Agricultural Engineering, 37(7), 473-475, 1956.

[2] D. Liu, P. Diplas, J. Fairbanks, and C. Hodges, "An experimental study of flow through rigid vegetation", *Journal of Geophysical Research: Earth Surface*, 113(F4), 2008.

[3] L. Zong, and H. Nepf, "Spatial distribution of deposition within a patch of vegetation", *Water Resources Research*, 47(3), 2011.

[4] H. Nepf, "Hydrodynamics of vegetated channels", *Journal of Hydraulic Research*, 50(3), 262-279, 2012.

[5] S. Petryk and G. Bosmajian, Analysis of flow through vegetation, *Journal of the Hydraulics Division*, *101*(7), 871-884, 1975.

[6] M. Baptist, V. Babovic, J. Rodríguez Uthurburu, M. Keijzer, R. Uittenbogaard, A. Mynett and A. Verwey, "On inducing equations for vegetation resistance", *Journal of Hydraulic Research*, *45*(4), 435-450, 2007.

[7] W. Wu, F. D. Shields, S. J. Bennett and S. S. Wang, "A depth-averaged two-dimensional model for flow, sediment transport, and bed topography in curved channels with riparian vegetation", *Water Resources Research*, *41*(3), 2005.

[8] F. López and M. García, "Open-channel flow through simulated vegetation: Suspended sediment transport modeling", *Water resources research*, *34*(9), 2341-2352, 1998.

[9] T. Tsujimoto, "Fluvial processes in streams with vegetation", *Journal of hydraulic research*, *37*(6), 789-803, 1999.

[10] E. M. Follett and H. M. Nepf, "Sediment patterns near a model patch of reedy emergent vegetation", *Geomorphology*, *179*, 141-151, 2012.

[11] T. Bouma,, L. Van Duren, S. Temmerman, T. Claverie, A. Blanco-Garcia, T. Ysebaert and P. Herman, "Spatial flow and sedimentation patterns within patches of epibenthic structures: Combining field, flume and modelling experiments", *Continental Shelf Research*, *27*(8), 1020-1045, 2007.

[12] S. Temmerman, T. Bouma, J. Van de Koppel, D. Van der Wal, M. De Vries and P. Herman, "Vegetation causes channel erosion in a tidal landscape", *Geology*, *35*(7), 631-634, 2007.

[13] M. J. Van de Wiel and S. E. Darby, "A new model to analyse the impact of woody riparian vegetation on the geotechnical stability of riverbanks", *Earth Surface Processes and Landforms*, *32*(14), 2185-2198, 2007.

[14] N. Pollen-Bankhead and A. Simon, "Enhanced application of root-reinforcement algorithms for bank-stability modeling", *Earth Surface Processes and Landforms*, *34*(4), 471-480, 2009.

[15] M. Rinaldi and N. Casagli, "Stability of streambanks formed in partially saturated soils and effects of negative pore water pressures: the Sieve River (Italy)", 1999.

[16] A. Gurnell, "Plants as river system engineers", *Earth Surface Processes and Landforms*, *39*(1), 4-25, 2014.

[17] S. Rodrigues, J.-G. Bréhéret, J. J. Macaire, S. Greulich and M. Villar, "In channel woody vegetation controls on sedimentary processes and the sedimentary record within alluvial environments: a modern example of an anabranch of the River Loire, France", *Sedimentology*, *54*(1), 223-242, doi:10.1111/j.1365-3091.2006.00832.x, 2007.

[18] M. Tal and C. Paola, "Effects of vegetation on channel morphodynamics: results and insights from laboratory experiments", *Earth Surface Processes and Landforms*, *35*(9), 1014-1028, 2010.

[19] W. M. Van Dijk, R. Teske, W. I. van de Lageweg and M. G. Kleinhans, "Effects of vegetation distribution on experimental river channel dynamics", *Water Resources Research*, 49(11), 7558-7574, 2013.

[20] S. Karrenberg, P. J. Edwards and J. Kollmann, "The life history of Salicaceae living in the active zone of floodplains", *Freshwater Biology*, *47*(4), 733-748, 2002.

[21] D. Corenblit, E. Tabacchi, J. Steiger and A. M. Gurnell, "Reciprocal interactions and adjustments between fluvial landforms and vegetation dynamics in river corridors: a review of complementary approaches", *Earth-Science Reviews*, *84*(1), 56-86, 2007.

[22] J. M. Mahoney and S. B. Rood, "Streamflow requirements for cottonwood seedling recruitment-an integrative model", *Wetlands*, *18*(4), 634-645, 1998.

[23] F. Siniscalchi and V. Nikora, "Dynamic reconfiguration of aquatic plants and its interrelations with upstream turbulence and drag forces", *Journal of Hydraulic Research*, *51*(1), 46-55, 2013.

[24] M. van Oorschot, M. G. Kleinhans and H. Middelkoop, "Distinct patterns of interaction between vegetation and morphodynamics", *Earth Surface Processes and Landforms*, 2016.

[25] N. Claude, G. Antoine, R. Yassine, V. Verschoren, C. Schwarz, S. Temmerman and C. Jourdain, "Numerical simulations of flow around vegetation with TELEMAC-2D: application on laboratory xperiments and on the Isere river (France)", *Proceeding of XXII TELEMAC-MASCARET User Conference*, Daresbury (UK), October, 2015.

[26] V. Verschoren, C. Schwarz, J. Schoelynck, K. Buis, G. Antoine, N. Claude, P. Meire and S. Temmerman, "Implementing plant growth of flexibele aquatic", *Proceeding of XXII TELEMAC-MASCARET User Conference*, Daresbury (UK), October, 2015.

[27] vegetation into a hydrodynamic model (Telemac2D)

[28] J. Braatne, S. Rood and P. Heilman, "Life history, ecology and conservation of riparian cottonwoods in north America". In: Stettler, R., Bradshaw, G., Heilman, P., Hinckley, T. (Eds.), Life history, ecology, and conservation of riparian cottonwoods in North America. NRC Research Press, Ottawa, Ch. 3, pp. 57–85, 1996.

[29] J. Canadell, R. B. Jackson, J. B. Ehleringer, H. A. Mooney, O.E. Sala and E.D. Schulze, "Maximum rooting depth of vegetation types at the global scale". *Ecologia* 108 (4), 583–595, 1996.

[30] E. Van Velzen, P. Jesse, P. Cornelissen and H. Coops. "Stromingsweerstand vegetatie in uiterwaarden. Deel 2 achtergronddocument versie 1" (Dutch). Tech. rep., RIZ, Arnhem, 2003.

[31] M. Kleyer, Bekker, R., Knevel, I., Bakker, J., Thompson, K., Sonnenschein, M., Poschlod, P., van Groenendael, J., Klimes, L., Klimesova, J., Klotz, S., Rusch, G., Hermy, M., Adriaens, D., Boedeltje,

G., Bossuyt, B., Dannemann, A., Endels, P., Götzenberger, L., Hodgson, J., Jackel, A.-K., Kühn, I., Kunzmann, D., Ozinga, W., Römermann, C., Stadler, M., Schlegelmilch, J., Steendam, H., Tackenberg, O., Wilmann, B., Cornelissen, J., Eriksson, O., Garnier, E., Peco, B, "The LEDA Traitbase: a database of life-history traits of the Northwest European flora", *Journal of Ecology* 96 (6), 1266–1274, 2008.

[32] G. Geerling, A. Ragas, R. Leuven, J. van Den Berg, M. Breedveld, D. Liefhebber and A. Smits, "Succession and rejuvenation in floodplains along the river Allier (France)". *Hydrobiologia* 565 (1), 71–86, 2006.

[33] E. Pasche and G. Rouve, "Overbank flow with vegetatively roughened flood plains", *Journal of Hydraulic Engineering*, *111*(9), 1262-1278, 1985.

Putting fish in the tank: An Agent Based Model with flow interaction

Thomas Benson[1], Kate Rossington[1], Rick Bruintjes[1,2]
[1] HR Wallingford, Howbery Park, Wallingford, OX10 8BA, UK
[2] Biosciences, College of Life and Environmental Sciences, University of Exeter, Exeter, EX4 4QD, UK

t.benson@hrwallingford.com

***Abstract*— An Agent Based Model (ABM) coded in Matlab is described in which fish (or other marine creatures) are introduced into the 3D underwater flow domain modelled by TELEMAC. The released fish individuals are preassigned a set of physiological characteristics and behavioural traits and are then free to swim and interact with each other in the flow field environment. The model is particularly designed to model potential impacts on marine organisms due to anthropogenic induced stresses, such as caused by underwater noise and/or interaction with power station intakes or hydro-power turbines. A description of the algorithms is given followed by an example of how the ABM can be used to assess the potential stress exerted on fish populations due to underwater noise generated from pile driving during construction of a hypothetical offshore windfarm. Future developments of the model will also be described.**

I. INTRODUCTION

Since the 1970's, the growth of micro-processing power has led to the development of ecological models that consider a population from the point of view of the individuals instead of the more classical top-down empirical models based on demographics [7]. Such models are known as Agent Based Models (ABM) or Individual Based Models (IBM).

A well-known example of an ABM is called *Boids*, which was developed in 1987 by Reynolds [13] to simulate the flocking behaviour of birds. This model demonstrated how a few simple rules (refer to Section II.A) could produce realistic emergent patterns of flock-like behaviour. The qualitative realism of this approach meant it has been used in Hollywood movies such as Tim Burton's film Batman Returns (1992).

Whereas the classical top-down modelling approach is useful for assessing observed trends in populations, the ABM approach, whereby a set of individuals each with its own set of prescribed behaviours and responses with no overarching rules on the population, has potential to make predictions into the future [7]. Combined with an increase in the requirement for ecological assessments as part of Environmental Impact Assessments (EIA), ABM models like *Boids* offer potential in simulating impacts on species populations in response to shocks to the environment, be they anthropogenic or natural in origin.

Recent research at HR Wallingford has investigated how the ABM approach could be used to assist in the assessment of the impacts of underwater sound on fish in the marine environment [15]. In the marine industry, regulators and decision makers have become more aware of the importance of underwater sound and its potential impact on animals. For example, underwater sound has been shown to have detrimental impacts on fish physiology by increasing blood cortisol (stress hormone) levels [21], increase heart rate [6] and inducing temporary hearing loss [18] [2] [20]. On a behavioural level, sound exposure in fishes can reduce anti-predator responses [3] [19], change swimming patterns [8] [9] and alter group behaviour [4]. Additionally, the impacts of sound exposure can be more severe in individuals of low body condition [12].

Guidelines now outline how much sound emitted during marine construction works is acceptable, what the potential effects are and how it can be monitored and mitigated [1] [14]. This has resulted in the requirement for studies of the impact of underwater sound on organisms that can be used for EIAs as regulators require better data on the impacts in order to properly assess potential effects.

This paper describes an ABM model developed at HR Wallingford called *HydroBoids*. The model algorithms will be described followed by a description of case study where data on fish behavioural in response to pile driving noise were collected and used to parameterise the model. Initial results from the model will also be presented.

II. MODEL DESCRIPTION

In *HydroBoids*, numerous fish individuals (or other mobile marine creatures) are represented as moving Lagrangian points in a three dimensional underwater space which are carried (advected) by the Eulerian hydrodynamic flows calculated by the TELEMAC modelling system [10]. A flow result file must first be generated using TELEMAC which can be either time varying or steady state and either 2- or 3-dimensional.

The fish are placed into the model domain defined by the TELEMAC geometry file within defined polygon regions and with a given initial horizontal and vertical separation, thus defining the total number of fish in the calculation. Each placed fish is assigned characteristics or traits that are both *physiological* (e.g. swim speed) and also *behavioural* (e.g. schooling).

The fishes physiological characteristics are applied across the population as normally distributed values about a mean with a specified standard deviation. The ability to model this type of inter-population variability is an important reason why the ABM approach is useful for modelling ecological impacts

since not all the individuals will respond in the same way or be affected to the same degree [1].

A. Swimming and flow interaction

The main physiological characteristic is the fish swim speed which is assigned to each individual in the population from a normal distribution of speeds (i.e. some fish can swim faster than others as would be the case in reality). Each modelled species is also assigned a maximum acceleration to prevent an individual from changing speed and direction too abruptly given its mass and momentum.

If the swim speed for a particular species is set to zero, these individuals are effectively Lagrangian drifters that are advected purely by the flow. Turbulence can also be applied using a random walk model with constant viscosity in the horizontal direction and a mixing length formula in the vertical direction, which effectively turns the simulation into a classical Lagrangian dispersion model.

The fish move in 3D underwater space, therefore in general those individuals near to the bed will be subjected to slower flows than those near the surface. If a 2D model result is used then the vertical flow profile is assumed to be logarithmic and hence the fish near the bed will be advected less than those in the surface waters. If a 3D hydrodynamic file is used then the flows are interpolated directly at the fishes 3D location.

As shown in Figure 1, fish that are assigned a swim speed in the model move under their own propulsion in addition to the flow advection according to a *correlated random walk* (CRW) algorithm [5] [22]. A CRW is a pattern of movement where the direction of the fish at the current time step is dependent on the direction at the previous time step. A directional error term, or *directedness*, is added at each time interval chosen randomly from a normal distribution with a predefined standard deviation. Assuming no other influences on movement, if the directedness term is zero, the correlated random walk is simply a straight line and if the directedness term is maximum (180°) then the correlated random walk is a conventional uncorrelated random walk [22]. The directness parameter has both a horizontal (azimuth) and a vertical (elevation) value, the latter usually being smaller since fish tend to move in the horizontal plane more frequently.

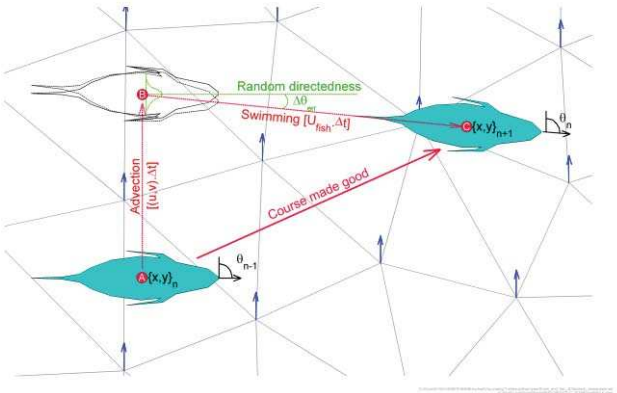

Figure 1: Schematic of 2D fish movement using a correlated random walk and advection by hydrodynamic flows (indicated as blue vectors on at triangular mesh nodes)

Thus to define a new fish position at each step in a correlated random walk one only needs 1) the present fish position, 2) its previous direction, 3) the angular error in the present direction (directedness), and 4) the swim speed, or distance travelled, during each step [22].

Correlated random walks are a good analogy to animal movements because the angular error at each step can represent a variety of unknown external influences on the ability of an animal to continue a course on a particular bearing. Examples of such influences are rough terrain, complex and chaotic small scale water movements, inaccuracy of any navigation method being used, or any other dispersion or displacement made at a smaller scale than explicitly modelled.

After the new position of each fish has been calculated the model checks that this position is valid (i.e. within the model domain and not on dry land). If not, the fish maintains its position from the previous time step and rotates its direction 90 degrees to the left or right (chosen randomly).

B. Behavioural traits

Behavioural traits are also assigned to the fish depending on particular characteristics of that species, which may include the following:

- Schooling
- Migration
- Predator-prey interaction and scavenging
- Response to external stimuli

Each of these behavioural traits is described below.

1) Schooling

HydroBoids uses the *Boids* method of Reynolds [13] to simulate schooling behaviour. Three simple rules are prescribed to all the individuals in the model to control schooling behaviour as shown diagrammatically in Figure 2. These rules are:

1. *Collision avoidance* (or *separation):* Avoid contact with neighbours and obstacles
2. *Velocity matching* (or *alignment):* Match the general speed and direction of neighbours
3. *Flock centring* (or *cohesion*): Steer towards the centre of surrounding neighbours

A modification of the original method is to include a *probability of schooling* (refer also to Section C) which introduces some randomness into the schooling behaviour to take into account unknown causes of variability that are not modelled, effectively allowing the school to become less rigid in pattern. Setting the probability of schooling to a value of one returns the schooling algorithm to the classical *Boids* approach, whereas a value of zero effectively turns of schooling behaviour.

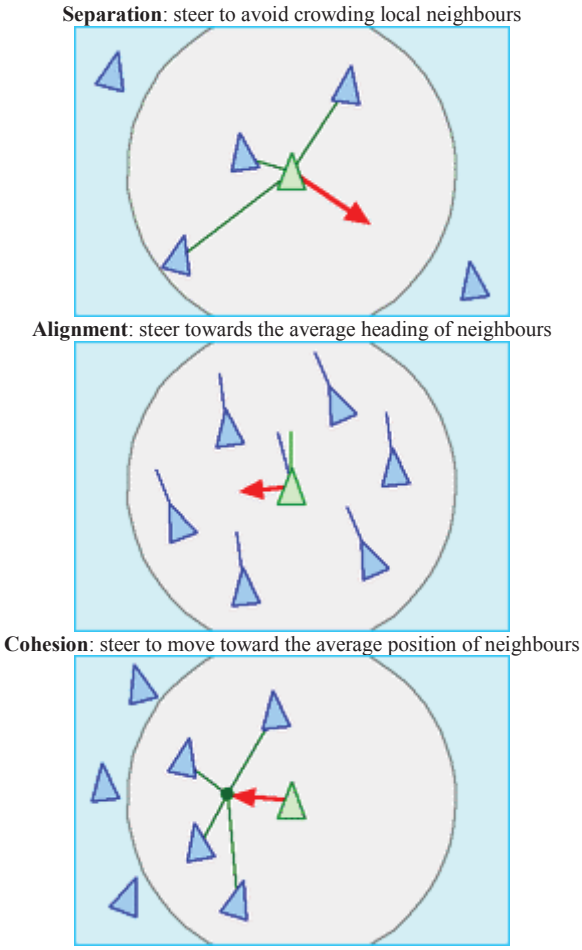

Figure 2: The three rules of the *Boids* method of schooling behaviour (adapted from http://www.red3d.com/cwr/boids)

2) *Migration*

The instinctive behaviour of a some fish species to travel from their current location to a predetermined distant location, such as annual spawning grounds, is included in a simplistic way by defining one or more waypoints which the individuals are explicitly programmed to head towards. The justification for using such a heuristic method is that, for many species or situations, the exact method or behavioural cue that the individuals use to find their way along a migration path is not known to science. All that is known is that the animals somehow find their way to the same location year after year. Therefore the migration path is explicitly defined as shown in Figure 3 which shows migration of fish up the Mersey Estuary, with the tidal flow modelled using TELEMAC-2D. Of course if a behavioural cue is identified for any given species then this can be readily modified in the code.

As with schooling, a *probability of navigation* is applied which means each fish species has a user specified probability (between 0 and 1) which is tested for each fish at each model time interval to decide whether it steers towards the next waypoint or not. A probability of navigation value of one means that the probability will always be met and hence the fish will immediately change their heading for the next waypoint. A probability of zero completely turns off migration behaviour. Fractional values between zero and one mean that some of the fish population will be chosen at random to change direction towards the next waypoint. For example, a probability of 0.25 means that, on average, 25% of the fish population will be chosen to navigate. When selected, the fish also have their speeds returned to normal (if not already so) which means that any other previous fleeing response to a stimulus or predator is reset. The fish that are not chosen carry on with their correlated random walk or may be selected to perform another behavioural activity (e.g. schooling).

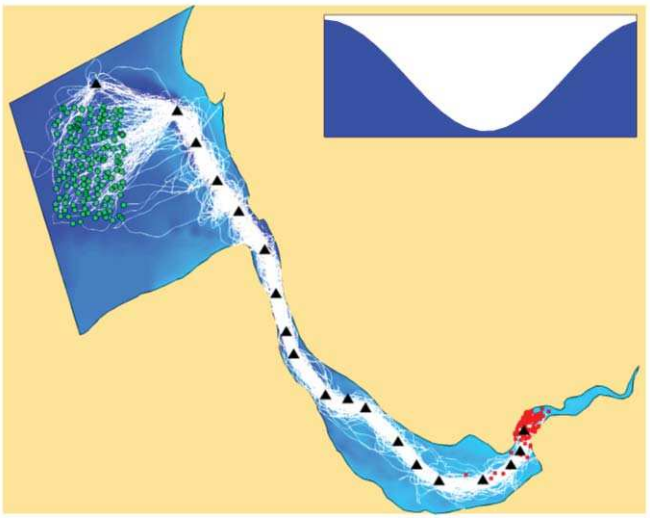

Figure 3: Example of modelled tracks (white lines) of fish navigating up the River Mersey (UK) using the waypoint method during a single tide modelled by TELEMAC2D. The fish start and end positions are represented by green circles and red squares respectively.

3) *Predator-prey interaction and scavenging*

If more than one species is introduced into the model flow domain simultaneously, it is possible to assign predator-prey interactions between them. For each species, a list of prey species is prescribed, with the list empty for those that do not predate. If the predator species comes into a specified target range of one or more of its prey (synonymous with the sensitivity of the eyesight of the predator) then it swims towards the closest individual at a defined *chase speed*. This is shown schematically in Figure 4. If the predator then reaches a distance closer than a second threshold range it is assumed that it cannot see the prey anymore and so carries on moving according to a correlated random walk. Similarly, the prey are assigned a range at which they can detect predators. If a predator is within that range they swim directly away from the predator at their own predefined chase speed. Once a chase has finished, i.e. when the prey has either been eaten or escaped, the individuals carry on at chase speed until they are selected to navigate when their speed is reset to normal.

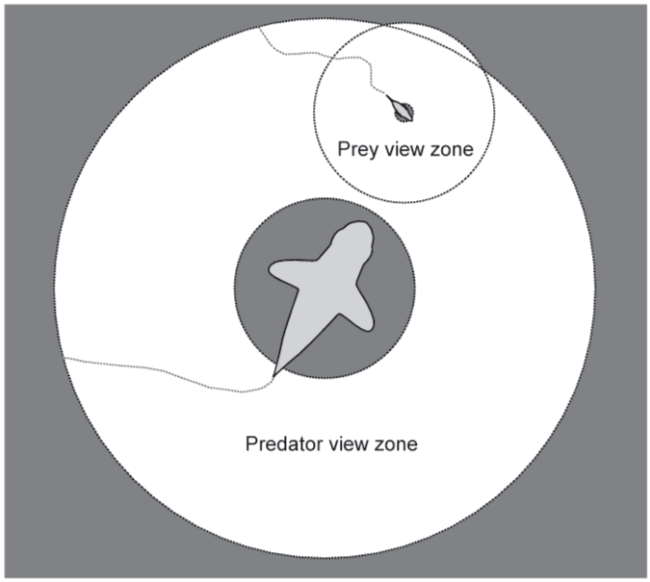

Figure 4: Predator-prey zones of detection. Dark grey zones are out of view. In this example the predator shark in the centre has detected its prey, but the prey is unaware of the danger.

Feeding of fish that do not predate on other modelled fish species (for example those that feed on phytoplankton) can be parameterised using a *probability of feeding*. In this case, the selected fish change speed randomly to a fraction of their average swim speed (chosen randomly) to simulate scavenging behaviour.

4) Response to external stimuli

The individuals within the model can be programed to respond to a stimulus such as underwater sound or a pollutant tracer. The stimulus field is input directly from the TELEMAC hydrodynamic file as a variable and can be a time varying field or constant.

Upon exposure to a stimulus above a specified certain threshold, the swim direction of the fish is changed to be either directly towards or away from the source (e.g. a pile driver emitting noise) or, alternatively, up or down the gradient of the stimulus field (e.g. a pollutant tracer). For example a fish may respond to a sound level above 140 decibels and swim directly away from the noise source. Another example is shown in Figure 5 where fish have been assigned a thermophilic response to a thermal plume modelled in TELEMAC-3D. The fish therefore swim up the temperature gradient towards the plume discharge and against the flow. The direction of each fish is further modified as they move due to the correlated random walk.

As well as changing direction, each fish affected by a particular stimulus is assigned a new swimming speed selected randomly from a normal distribution of fleeing speeds as a multiple of its usual speed. Swimming speed reverts to the fish's usual swimming speed the next time it is selected to navigate, which again is decided each time interval based on the *probability of navigation* (see Section 2).

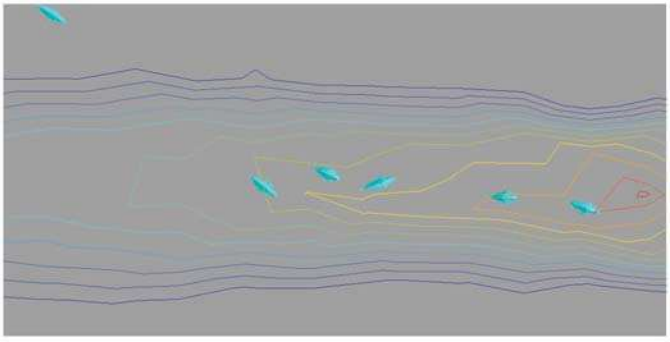

Figure 5: Fish parameterised with a thermophilic response to a modelled thermal plume discharge in TELEMAC-3D (indicated with coloured contours).

C. Probability and decision making

A fundamental problem with any ABM is how to implement and validate a numerical method for decision making in animals. For example, will a fish decide to navigate towards a spawning ground in preference to staying with the school? The basis of such choices will ultimately depend on which is the best in terms of increasing the *fitness* of the individual animal in question [1]. Data on this problem is both difficult to obtain and the number of decisions that require parameterising can be many. Keeping the number of decisions to a minimum is therefore important, although too few will make the simulation unrealistic.

In *HydroBoids*, decisions are parameterised heuristically using weighted probabilities. Probabilities (i.e. fractional values between zero and one) are set by the user for each of the behavioural traits, i.e. navigation, schooling, feeding and responding to a stimulus. These probabilities are specified in such a way so that they add up to less than or equal to one. At the beginning of each time step, an imaginary dice (i.e. a random number generator) is rolled for each fish to determine which activity it will perform during the time step. If none of the activities are chosen, then the fish carries on with a correlated random walk.

This process is modified if the fish individual finds itself in a situation involving high risk such as a dangerously high stimulus above a specified threshold (e.g. a loud underwater noise level) or in the presence of a predator that is within a specified range. In such instances the fish is assumed to be in *panic mode* and the probability is ignored and the individual responds regardless.

III. MODEL APPLICATION

The model has been developed as part of ongoing research at HR Wallingford in collaboration with the University of Exeter. Calibration of fish behavioural characteristics and stimulus thresholds is an important area in which data are currently lacking. To address this, experiments have been carried out in a former ship building dock (dimensions 90 x 18 x ~2m deep) in which electronically tagged fish were subjected to intermittent pile driving noise over a six day period (Bruintjes et al, in prep.). A brief summary of the experiment is given here.

Trials were performed over 6 days, during which pile driving was carried out twice daily for two hours, with a one hour pause between the two periods. A ~1.6 kJ pile driver hammer was used to strike a 7.5 m long 0.17 m diameter pile at a strike rate of 10 strikes per minute. Equal numbers of tests were performed with the pile located at each end of the dock (see Figure 6). The southwest end of the dock was shallower, with a depth of approximately 1.7 m as opposed to 2.6 m at the opposite end. At the deeper end there was also a deeper area near the original entrance to the dock which was cordoned off with a net so fish could not enter it. In each trial the movements of between 14 to 24 (~18 on average) acoustically tagged cod were measured. The batches of cod were reused for 3 piling periods, to give a total of 71 cod tested.

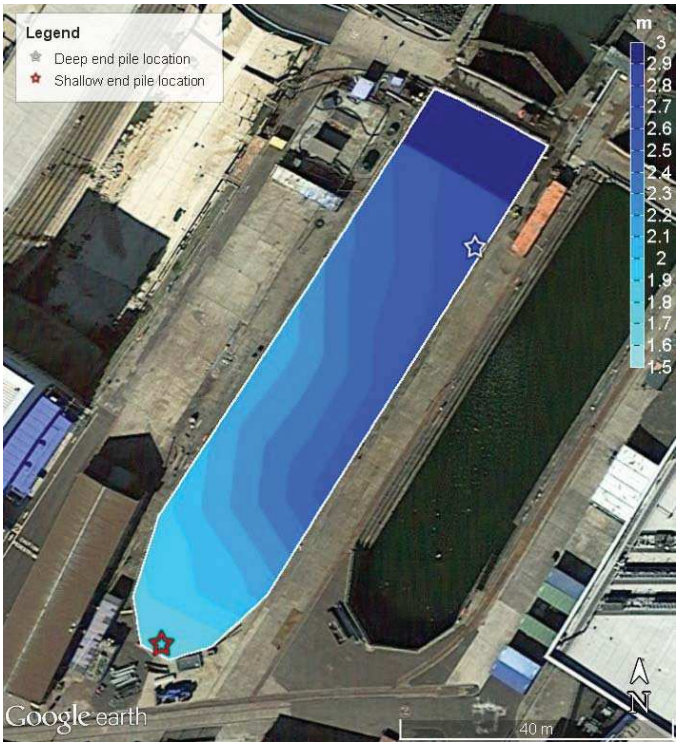

Figure 6: The ship building dock in which fish tag measurements were made (Blyth, UK) with water depth contours drawn. The pile driving was carried out at the two marked locations.

During the experiments to sound field was also measured throughout the dock at 27 locations using a hydrophone. The RMS sound pressure fields for the deep and shallow end pile locations are shown in Figure 7.

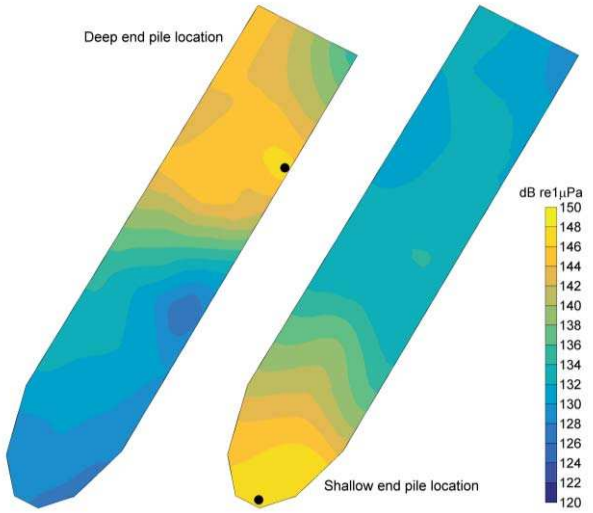

Figure 7: RMS sound pressure measured during pile driving at the deep and shallow end pile locations

The average fish positions for each of the experiments are shown in Figure 8 and Figure 9 for the deep and shallow end pile driver location scenarios respectively. Also plotted on these graphs (in grey) are the results from the *HydroBoids* model. The model was run ten times for each pile location scenario and the standard deviation of all the results are plotted as error bars. Parameters for the model setup are summarised in Table 1. As can be seen, the measured distances of the fish from the piles are largely contained within the standard error of the modelled distances which suggests that the model is capturing the variability in the data.

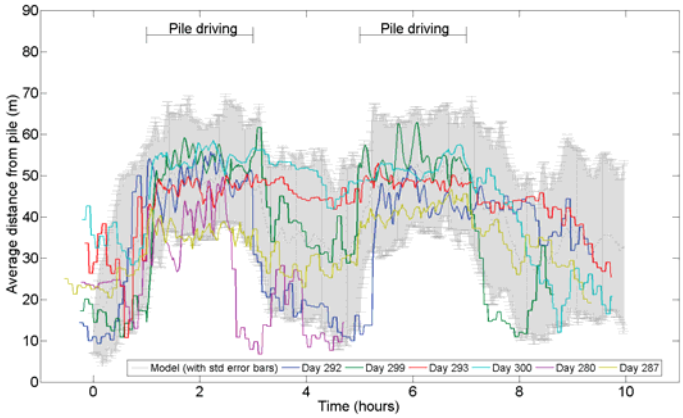

Figure 8: Measured (coloured lines) and modelled (grey error bars) distances of fish from the pile during piling at the deep end of the dock. Periods of pile driving are indicated.

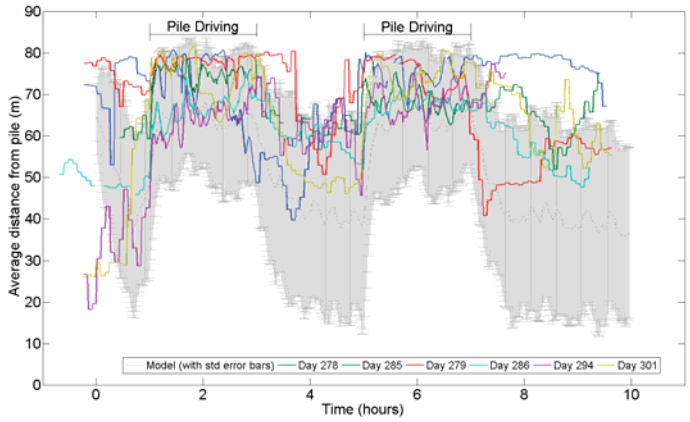

Figure 9: Measured (coloured lines) and modelled (grey error bars) distances of fish from pile during piling at the shallow end of the dock. Periods of pile driving are indicated.

Interestingly, the model appears to give better comparison for the deep end pile location. It appears that the fish prefer to stay in deeper water after they have experienced the piling sound and therefore do not return as quickly as in the model. This possibly indicates that they have a memory of the previous piling event. Another finding was that the model fit improves if a low *probability of responding* to the stimulus of just 5% is used. So it appears that the fish take time to decide whether to move away from the noise. These are both interesting findings and will be investigated further in a future paper.

Parameter	*Value*
Swim speed range (normal)	0.2 to 0.3 m/s
Maximum acceleration	0.5 m/s^2
Fish time step	2.5 s
Number of fish per run	24
Directedness (horizontal and vertical)	3º & 0.1º
Probability of navigation	5%
Probability of schooling	50%
School separation (min/max)	0.2 - 0.5m
Probability of feeding	5%
Sound threshold of potential response	135 dB re1µPa (+/-3dB)
Probability of responding to stimulus	5%
Swim speed multiplier during stimulus	2.5
Stimulus response action	Flee directly from source

Table 1 – Summary of *HydroBoids* model parameters

IV. Future Work

HydroBoids is an ABM that has been around for several years but has recently undergone significant development. Recently the model has been used in a collaboration between HR Wallingford and the Zoological Society of London to locate the spawning grounds for Smelt in the Thames estuary [17]. Currently, another collaboration with Nottingham and Southampton Universities is underway to use the *HydroBoids* model to investigate the interaction of eels with hydro-power turbines and fish passes on an EPSRC funded project titled *Vaccinating the Nexus* [16]. New algorithms associated with avoidance behaviour of eels and other species will be incorporated into the model code during this collaboration.

The model is presently coded in Matlab. This enables changes to be made to the software relatively easily and results can be visualised *on-the-fly* which allows for rapid development with good quality control. In the future when the software has become less developmental, the code could be translated in Fortran and incorporated in the TELEMAC suite. This would be preferential since the code would be more computationally efficient and would potentially enable two way coupling of interactions between fish and the hydrodynamics and/or tracers such as to simulate the depletion of algal food supply.

V. Conclusions

Here an Agent Based Model has been described which has potential to assist in the EIA process for marine construction works to assess potential impacts on fish populations (or other marine wildlife). Early results show that the model can offer useful insights into population dynamics and is easily adapted to a wide range of scenarios. The coupling of the flows with TELEMAC is a novel improvement to standard ABM models which generally do not consider the flow field.

References

[1] Ainslie, M. et al. (2009) Assessment of natural and anthropogenic sound sources and acoustic propagation in the North Sea. TNO Defensie en Veiligheid, Den Haag.

[2] Amoser, S. & Ladich, F. (2003) Diversity in sound-induced temporary hearing loss in otophysine fishes. Journal of the Acoustical Society of America, 113, 2170-2179.

[3] Bruintjes, R. et al. (2016) Rapid recovery following short-term acoustic disturbance in two fish species. Royal Society Open Science, 3, 150686.

[4] Bruintjes, R. & Radford, A.N. (2013) Context-dependent impacts of anthropogenic sound on individual and social behaviour in a cooperatively breeding fish. Animal Behaviour, 85, 1343-1349.

[5] Codling, E.A. et al. (2008) Random walk models in biology. Journal of the Royal Society Interface, 5, 813 - 824.

[6] Graham, A.L. & Cooke, S.J. (2008) The effects of sound disturbance from various recreational boating activities common to inland waters on the cardiac physiology of a freshwater fish, the largemouth bass (Micropterus salmoides). Aquatic Conservation-Marine and Freshwater Ecosystems, 18, 1315-1324.

[7] Grimm, V., Railsback, S. F., 2005. Individual-Based Modeling and Ecology. University Press, Princeton.

[8] Hawkins, A.D. et al. (2014) Responses of free-living coastal pelagic fish to impulsive sounds. Journal of the Acoustical Society of America, 135, 3101-3116.

[9] Neo, Y.Y. et al. (2015) Impulsive sounds change European seabass swimming patterns: Influence of pulse repetition interval. Marine Pollution Bulletin, 97, 111-117.

[10] http://www.opentelemac.org

[11] Popper, A.N. et al. (2014) Sound exposure guidelines for fishes and sea turtles: A technical report prepared by ANSI-Accredited Standards Committee S3/SC1 and registered with ANSI pp. 75.

[12] Purser, J. et al. (2016) Condition-dependent physiological and behavioural responses to anthropogenic sound. Physiology & Behavior, 155, 157-161.

[13] Reynolds, C. W. (1987), Flocks, herds, and schools: A distributed behavioral model, Computer Graphics, 21(4):25-34.

[14] Robinson, S.P. et al. (2014) Good practice guide for underwater sound measurement. National Measurement Office, Marine Scotland, The Crown Estate.

[15] Rossington, K. et al. (2013) Eco-hydro-acoustic modeling and its use as an EIA tool. Marine Pollution Bulletin, 75, 235-243.

[16] http://nexus.soton.ac.uk/vaccinating-the-nexus

[17] https://www.zsl.org/conservation/smelt-osmerus-eperlanus

[18] Scholik, A.R. & Yan, H.Y. (2002) Effects of sound on auditory sensitivity of fishes. Bioacoustics, 12, 186-188.

[19] Simpson, S.D. et al. (2016) Anthropogenic sound increases mortality by predation. Nature Communications, 7.

[20] Smith, M.E. et al. (2004a) Acoustical stress and hearing sensitivity in fishes: does the linear threshold shift hypothesis hold water? Journal of Experimental Biology, 207, 3591-3602.

[21] Smith, M.E. et al. (2004b) Sound-induced stress response and hearing loss in goldfish (Carassius auratus). Journal of Experimental Biology, 207, 427-435.

[22] Willis, J. (2011) Modelling swimming aquatic animals in hydrodynamic models. Ecological Modelling, 222, 3869-3887.

Modelling the dispersion of the caesium-137 in the coastal waters of Fukushima using Telemac-3D

Vito Bacchi*
Saint-Venant Laboratory for Hydraulics
6 quai Watier – Chatou, France
vito.bacchi@irsn.fr
*now at the Institut de Radioprotection et de Sûreté Nucléaire (IRSN)

Pablo Tassi
EDF R&D and
Saint-Venant Laboratory for Hydraulics
pablo.tassi@edf.fr

Agnès Leroy
EDF R&D and
Saint-Venant Laboratory for Hydraulics
agnes.leroy@edf.fr

***Abstract*—The objective of this work is to present the implementation, verification and validation of a three-dimensional model capable to reproduce the propagation of the caesium-137 radionuclide in coastal waters and its interaction with suspended sediments, in the framework of the open-source TELEMAC-MASCARET modelling system. The mathematical model is based on the non-conservative transport of radionuclides, where the interaction with the particulate matter is considered. The resulting numerical model is verified by comparisons between numerical and analytical solutions of selected test cases. Finally, the model is validated with the Fukushima Dai-ichi case by comparing numerical results with field measurements of radionuclides concentration in the Japan Sea.**

I. Introduction

On March 11, 2011, a devastating earthquake of magnitude 9.0 and a tsunami struck the Tohoku area, Japan, causing major damage to the cooling systems of reactors in the Fukushima Dai-ichi Nuclear Power Plant (NPP), operated by Tokyo Electric Power Company (TEPCO). In order to cool the reactor cores and the spent fuel in storage pools, large amounts of seawater and freshwater were used. A significant part of this radioactivity-contaminated water was discharged into the Pacific Ocean close to the power plant. In addition, between March 12 and 15 2011, several hydrogen explosions resulted in the release of significant radioactivity into the atmosphere, some of which was deposited onto the sea surface over a wide area of the Pacific Ocean. Consequently, high concentrations of iodine (^{131}I), strontium ($^{90}S_r$) and caesium-137 ($^{137}C_s$) were found in seawater and seabed sediments along the coastline of Fukushima Prefecture [25]. Moreover, radionuclides were detected in marine debris caught near Fukushima Prefecture [7]. The human and non-human populations of the nearby regions were exposed temporarily or permanently to the substances, either by external irradiation or by ingesting plants growing in the local area.

A significant number of modelling studies on the dispersion of radionuclides released from Fukushima into the Pacific Ocean have been recently published in the scientific literature. Recently, in the framework of the MODARIA project, supported by the International Atomic Energy Agency (IAEA), different models were applied to the accidental releases and discharges from Fukushima Dai-ichi NPP accident. A brief description of these models is given below. The reader is referred Periáñez et al. [19] for a detailed description of these models.

The model developed by IMMSP/KIOST (Institute of Mathematical Machine and System Problems, Ukraine, with the Korea Institute of Ocean Science and Technology, Republic of Korea) for radionuclide transport proposes two approaches: Eulerian and Lagrangian, and water circulation and sediment transport are obtained from the hydrodynamic SELFE model [22], [29]. The oceanic dispersion model named LORAS (Lagrangian Oceanic Radiological Assessment System) has been developed by Korea Atomic Energy Research Institute (KAERI) to evaluate the transport characteristics of the radionuclides released into the sea for a nuclear accident [13]. A particle random-walk model (SEA-GEARN) has been used by the Japan Atomic Energy Agency (JAEA) to simulate radionuclide transport in the Pacific Ocean. This model is based on the three-dimensional advection/diffusion dispersion equations. The SisBAHIA model [1] was developed by the Instituto de Engenheria Nuclear in Brazil and solves the transport of contaminants with the Eulerian and Lagrangian approaches. Finally, the USEV model, developed by the University of Sevilla (Spain), is based on the three-dimensional advection/diffusion dispersion equations. For these models, water circulation has been obtained from JCOPE2 hydrodynamic model [17], [18].

The numerical experiments of the MODARIA project were carried-out for a perfectly conservative radionuclide (Exercises 1 and 2) and for $^{137}C_s$, including water/sediment interactions (Exercises 2, 3 4a and 4b), using different hydrodynamic forcings and numerical and physical parameters (Exercises 1 and 4b). The model outputs were also compared with TEPCO measurements of radioactivity in water and sediments [25]. As a conclusion, it was found that the main reason of discrepancies between the model results was due to the differences between the numerical schemes and parameterizations used among these models.

The common point of all these models is the size of the computational domain (35°N–38.5°N, 140.5°E–144°E, covering approximately 670 km long and 620 km wide) and the need of employing a realistic reproduction of oceanic conditions such as ocean current, temperature, salinity, and sea surface height (SSH) for performing accurate numerical simulations on the oceanic dispersion of radionuclides. In general, these models use the hydrodynamics obtained with general circulation models based on data assimilation techniques (NCOM, JCOPE2) or variation method, as for the JAEA model which uses the three-dimensional variational (3D-VAR) data assimilation system [28], Meteorological Research Institute (MRI) Multivariate Ocean Variational Estimation (MOVE)

with the eddy-resolving ocean general circulation model, MRI Community Ocean Model (`www.mri.com`; [27]) at the Japan Meteorological Agency (JMA), which makes it possible to adjust the numerical results with field observations.

It can be considered that these models should be useful and powerful tools in post-emergency situations, when the estimation of future contamination of water, sediments and biota rely on data from analogous periods of previous years [21], or for the assessment of the long-term consequences of the accident, including transfers of radionuclides to sediments and biota, as well as evaluating the potential role of sediments as a source of contamination once radionuclide concentrations in seawater have decreased [15]. However, a model should be capable of providing quick-responses to emergency situations [21]. Rapid responses can be achieved using meteorological data or tide conditions from operational numerical models in order to accurately predict the radioactivity transport. In this case, the accuracy of the model could be improved by a refined spatial discretization and the model extension could be limited to the coastal area in the vicinity of the NPP.

In this context, the objective of this study is to develop a three-dimensional (3D) numerical tool able to reproduce the dispersion of radionuclides in coastal waters in an emergency situation such as the Fukushima Dai-ichi NPP accident. With this aim, the developed model has been forced only with data available immediately after (or during) the accident, as the weather conditions (wind, pressure, temperature) and/or the harmonic components of tides, and the model domain was limited to the coastal area near Fukushima and refined in the coastal area nearby the NPP.

The model was developed within the open source TELEMAC-MASCARET system, which is an integrated modelling tool for use in the field of free-surface flows. The various simulation modules use efficient algorithms based on the finite-element or finite volume methods. Space discretization is performed with unstructured triangular elements, which means that it can be locally refined in particular areas of interest. The mathematical model for radionuclides transport was built based on previous studies on non-conservative radionuclides [11], [16], where the interactions with the particulate matter has been considered. To account for these processes, a module that solves three-phase interaction has been implemented and described in the next section. This newly developed module was coupled with the 3D Reynolds-Averaged Navier-Stokes hydrodynamics module TELEMAC-3D of the TELEMAC-MASCARET system. Details on the 3D hydrodynamics model can be consulted in [5] and are not presented hereafter.

II. Radionuclides transport model

A. Conceptual Model

The radionuclides transport model is based on previous studies on non-conservative radionuclides propagation in sea waters, e.g. [11], [14], [16]. In particular, the model implemented in this work is a three phase's model with the following characteristics: (*i*) dissolved phase consists of radionuclides that are dissolved and adsorbed onto fine particles without settling velocity (diameter < 0.8 mm is preferred, according to Kobayashi et al. [9]), (*ii*) the large particle matter (LPM) phase consists of radionuclides that are adsorbed with the LPM which has settling velocity, (*iii*) active bottom sediment phase consists of radionuclides that are adsorbed with the LPM which deposit on the seabed, and the particle re-suspends according to the bottom velocity. For sediments, it is assumed that the LPM is an aggregate which has a single radius and density and the movement of each particle is characterized by velocity, diffusivity and settling velocity of the particle itself. For these conditions, a conceptual scheme describing the interaction between phases and the ionic exchanges is showed in Figure 1, where radionuclides uptake/release processes between water and sediments are formulated in terms of kinetic transfer coefficients k_1 and k_2. A detailed description of this formulation can be found in [16], [17].

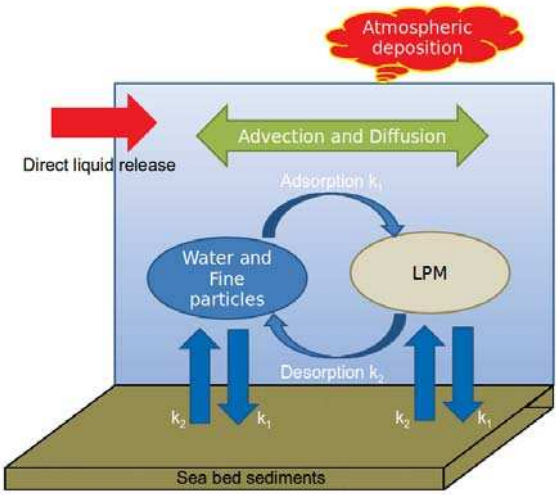

Fig. 1: Conceptual sketch describing the interaction between the three phases model and the ionic exchanges. The kinetic model considers that exchanges of radionuclides between water and sediments are governed by a first-order reversible reaction, being k_1 and k_2 the forward and backward rates, respectively.

B. Governing Equations

The radionuclide transport model describes the water-sediment sorption processes. It includes the advection-diffusion equations for dissolved C_s^w and adsorbed by suspended sediment C_p^w radioactivity in the water column, and the equations for concentration of the dissolved C_s^b and adsorbed C_p^b radioactivity in the bottom deposits, expressed in [Bq/l], [Bq/m^3] or [kg/m^3]. The transport of radionuclides dissolved (or absorbed by sediments) in water can be written as a classic advection-diffusion equation, by considering as an additional source term the exchange between the solid and the dissolved phases:

$$\frac{\partial C_s^w}{\partial t} + \frac{\partial U C_s^w}{\partial x} + \frac{\partial V C_s^w}{\partial y} + \frac{\partial W C_s^w}{\partial z} = \frac{\partial}{\partial x}\left(\nu_h \frac{\partial C_s^w}{\partial x}\right) + \frac{\partial}{\partial y}\left(\nu_h \frac{\partial C_s^w}{\partial y}\right) + \frac{\partial}{\partial z}\left(\nu_v \frac{\partial C_s^w}{\partial z}\right) - \lambda C_s^w - a_{1,2}^w (S_d^w K_d^w C_s^w - C_p^w) + P_s^w \quad (1)$$

$$\frac{\partial C_p^w}{\partial t} + \frac{\partial U C_p^w}{\partial x} + \frac{\partial V C_p^w}{\partial y} + \frac{\partial (W - w_s) C_p^w}{\partial z} = \frac{\partial}{\partial x}\left(\nu_h \frac{\partial C_p^w}{\partial x}\right) + \frac{\partial}{\partial y}\left(\nu_h \frac{\partial C_p^w}{\partial y}\right) + \frac{\partial}{\partial z}\left(\nu_v \frac{\partial C_p^w}{\partial z}\right) - \lambda C_p^w - a_{1,2}^w (S_d^w K_d^w C_s^w - C_p^w) + P_p^w \quad (2)$$

where U, V, W [m/s] are the velocity field components along the $x, y, z-$directions, respectively, ν_h and ν_v [m^2/s] are respectively the horizontal and vertical diffusion coefficient for radionuclides, λ [s^{-1}] is the radionuclide decay constant, P_s^w and P_p^w are the input of the dissolved radionuclides from the source point and the input of the radionuclides which adsorbed to the LPM from the source point [kg/m^{2}s], respectively, S_d^w [kg/m^3] or [g/l] is the sediment concentration and w_s [m/s] is the sediment settling velocity. Above, the distribution coefficients K_d^w and K_d^b [m^3/kg] are defined under steady hydraulic conditions as:

$$S_d^w K_d^w = \lim_{t\to\infty}\left(\frac{C_p^w}{C_s^w}\right), \quad \frac{S_d^b}{\epsilon} K_d^b = \lim_{t\to\infty}\left(\frac{C_p^b}{C_s^b}\right) \quad (3)$$

with ϵ [-] the bed porosity.

In Equations (1–2), the radionuclides are treated as passive tracer, and the exchanges between the different phases are described by diffusion, sorption, and sedimentation-resuspension processes. The adsorption and desorption of radionuclides between liquid and solid phases are described by the radionuclide exchange rates $a_{1,2}^w$ [day^{-1}] and $a_{1,2}^b$ [year^{-1}], usually considered as constants for practical applications [11]. The variation of the dissolved ($m_s^b = C_s^b Z_b$) and adsorbed ($m_p^b = C_p^b Z_b$) mass of radioactivity in the bottom deposits can be written as follows:

$$\frac{\partial m_s^b}{\partial t} = \frac{F_{dif}}{Z_b}\left(C_s^w - \frac{C_s^b}{\epsilon}\right) - \lambda m_s^b - a_{1,2}^b \left(\frac{S_d^b}{\epsilon} K_d^b C_s^b - C_p^b\right) Z_b \quad (4)$$

$$\frac{\partial m_p^b}{\partial t} = \left(\frac{C_p^w D}{S_d^w} - \frac{C_s^b E}{S_d^b}\right) - \lambda m_p^b - a_{1,2}^b \left(\frac{S_d^b}{\epsilon} K_d^b C_s^b - C_p^b\right) Z_b \quad (5)$$

Above, F_{dif} [m^2/s] is the diffusion coefficient describing the exchange between the bed and the water at the bottom and Z_b [m] is the thickness of the bottom layer.

C. Boundary conditions

The boundary condition for C_s^w and S_d^w at the free surface Z_s is a no-flux condition, expressed as:

$$\left(\nu_v \frac{\partial S_d^w}{\partial z} + w_s S_d^w\right)_{z=Z_s} = 0, \quad \left(\nu_v \frac{\partial C_s^w}{\partial z} + w_s C_s^w\right)_{z=Z_s} = 0 \quad (6)$$

where Z_s is the z-coordinate of the free surface. The boundary condition for C_s^w, C_p^w and S_d^w at the bed describes the exchange of radionuclides and of sediments with the bed. The fluxes into the bottom are induced by the diffusion of radioactivity (desorption) between the bed sediments and water, and the flux of radioactivity associated to the depositional and erosional rates, as follows:

$$\begin{aligned} \nu_v \frac{\partial C_s^w}{\partial z} &= \frac{F_{dif}}{Z_b}\left(C_s^w - \frac{C_s^b}{\epsilon}\right), \\ \nu_v \frac{\partial C_p^w}{\partial z} + (W - w_s) C_p^w &= \frac{C_p^w}{S_d^w} D - \frac{C_p^b}{S_d^b} E, \\ \left(\nu_v \frac{\partial S_d^w}{\partial z} + w_s S_d^w\right)_{z=Z_s} &= D - E. \end{aligned} \quad (7)$$

For cohesive sediments, the deposition rate equation is described by the empirical Krone law [4]:

$$D = \begin{cases} w_s S_d^w (1 - \tau/\tau_{cd}) & \text{if } \tau < \tau_{cd} \\ 0 & \text{otherwise} \end{cases}$$

where τ_{cd} [N/m^2] is the deposition critical bed shear stress, w_s [m/s] the mud settling velocity near the bed and τ [N/m^2] is the bed shear stress. The erosion rate follows the empirical Partheniades law [4]:

$$E = \begin{cases} M(\tau/\tau_{ce} - 1) & \text{if } \tau > \tau_{ce} \\ 0 & \text{otherwise} \end{cases}$$

where τ_{ce} [N/m^2] is the erosion critical shear stress of the mud layer and M the Partheniades coefficient (kg/sm^2). For a single layer bed with a concentration S_d^b [kg/m^3], the mass conservation equation for the bed evolution is given by:

$$S_d^b \frac{\partial Z_b}{\partial t} = D - E. \quad (8)$$

III. Model verification

In this section, the capability of the model at reproducing the advection and dispersion of radionuclides and its interactions is assessed by comparisons between numerical and analytical solutions.

A. Kinematic exchange of radioactivity between water and suspended sediment in a basin

The objective of this test case is to assess the ability of the model to reproduce the kinematic exchange of radioactivity between suspended sediments and water. A square basin $\Omega = [5\times5]$ [m^2] with constant water depth $h = 2$ [m] is considered, zero flow velocity $\vec{U} = (U, V, W) = (0, 0, 0)$ [ms^{-1}] and solid boundaries. The initial distribution of the dissolved $C_{s,0}^w = C_s^w(t = 0)$ and adsorbed by sediments $C_{p,0}^w = C_p^w(t = 0)$ radioactivity is uniform and equal to 10.0 [Bq/l] and the value of the diffusion coefficient of the tracers $K = 10$ [m^{2}s^{-1}]. The decay constant $\lambda = 0.00001$ [s^{-1}] and the radionuclide exchange rate $a_{1,2} = 0.000001$ [day^{-1}]. For these conditions, Equations (1–2) simplify into:

$$\frac{\partial C_s^w}{\partial t} + \lambda C_s^w = a_{1,2}^w C_p^w, \quad \frac{\partial C_p^w}{\partial t} + \lambda C_p^w = -a_{1,2}^w C_p^w \quad (9)$$

Analytical solutions of Equations (9) are:

$$C_s^w(t) = (C_{s,0}^w + C_{p,0}^w) \exp^{-\lambda t} + C_p^w(t), \quad (10)$$

$$C_p^w(t) = C_{p,0}^w \exp^{-(\lambda + a_{1,2}^w)t} \quad (11)$$

For this test case we use an unstructured mesh and a time step of 10 [s]. Figure 2 shows the good agreement between the numerical and the analytical results for both the dissolved and adsorbed radioactivity.

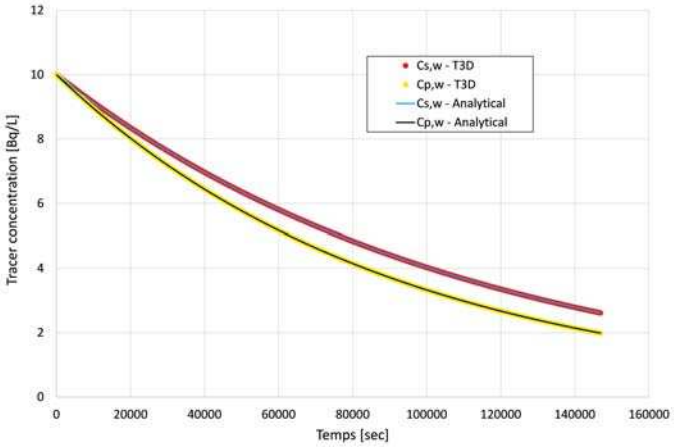

Fig. 2: Comparison between the numerical results and the analytical solution for the kinematic exchange of radioactivity between water and suspended sediment in a basin, see section III-A.

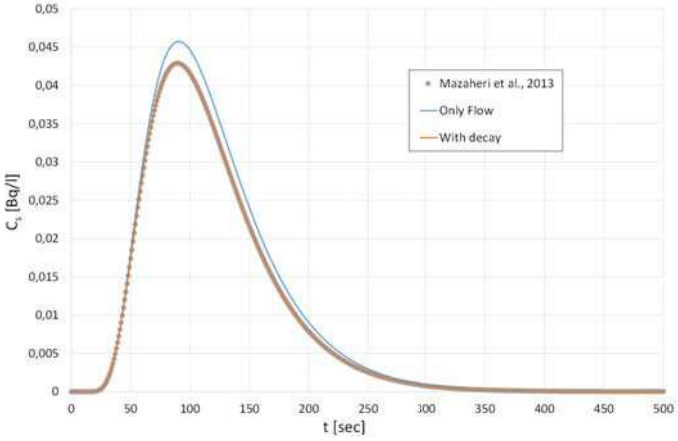

Fig. 3: Time evolution of the tracer decay in a permanent flow field test, see section III-B.

B. Tracer decay in a permanent flow field

The purpose of this test case is to assess the ability of the numerical model to reproduce the physical behavior of radionuclides dissolved in water, when transported by an uniform flow field in a rectangular domain $\Omega = [1 \times 500]$ [m^2] with initial constant water depth $h = 1.0$ [m] and flow velocity $\vec{U} = (U, V, W) = (0, 0, 0)$ [ms^{-1}]. At boundaries $x = 0$ and $x = 500$ m, a constant water discharge $Q(0, t) = 1.0$ [m^{3}s^{-1}] and water depth $h(500, t) = 1.0$ [m] were imposed, respectively. No friction is considered at the bottom of the channel. At $t = 0$ [s], an initial triangular distribution of the dissolved radioactivity is considered between $x = 95$ [m] and $x = 105$ [m], with a peak value equal to 1.0 Bq/l at $x = 100$ [m]. At the inflow and outflow boundaries, a constant zero radioactivity and a Neumann-like boundary condition are imposed, respectively. An unstructured mesh with typical element size equal to 0.5 [m] and time step of 0.5 [s] was used. The decay constant $\lambda = 0.0007$ [s^{-1}]. For a uniform and unidirectional flow field, the analytical solution of the tracer transport equation is reported in detail in [12]. In Figure 3, numerical results show that the temporal variation of the tracer concentration at the middle of the channel (orange line) is accentuated by the radioactivity decay, in comparison with a reference situation without decay (blue line). This result confirms that the simulated behavior of the dissolved radioactivity is physically based and in agreement with the analytical solution.

IV. Application to the Fukushima Dai-ichi accident

A. Model construction

This study covers the oceanic coastal area nearby the Fukushima Dai-ichi NPP: 36.5°N–38.5°N, 140.6°E–143.4°E (covering an extension of c. 300 km to 300 km), see Figure 4). The computational domain was discretized with 62,451 triangular elements, followed by extruding each triangle along the vertical direction into linear prismatic columns spanning the water column from the bottom to the free-surface. Each column is composed of a fixed number of prismatic elements, that number being chosen during the simulation set-up. The horizontal mesh size varied from 200 [m], near to the Fukushima Dai-ichi NPP to 10 [km] off-shore, depending on the resolution of the bathymetrical data (derived from the Japan Oceanographic Data Center) and the water depth. The vertical resolution of the layered mesh is 5 layers, resulting in elements with a height of the order of 50 [m] in the coastal area of the NPP and the computational time step was equal to 10 [s]. The simulations were performed for a total time of 90 days (from the March 1st 2011 to May 30th 2011). The model was initialised and forced at the oceanic boundary with tides (surface elevation and the currents). The tides are provided as complex amplitudes of earth-relative sea-surface elevation for eight primary ($M2$, $S2$, $N2$, $K2$, $K1$, $O1$, $P1$, $Q1$), two long period (Mf, Mm) and three non-linear harmonic constituents ($M4$, $MS4$, $MN4$), computed with the methodology reported in [2], [3]. The tidal constituents were extracted from the Oregon State University Tidal Prediction Software (OTPS/TPXO). These data are available on line (`http://volkov.oce.orst.edu/tides/OhS.html`). Current velocity and water surface elevation values were used to initialise the model the March 1st 2011. At initial time, the dissolved radionuclides concentration was set to zero. On the free surface, the model was also forced by wind and atmospheric parameters computed from the European Centre for Medium-Range Weather Forecasts (ECMWF) model.

B. Source terms

The amount of $^{137}C_s$ released directly into the ocean was given by [19]. According to Kobayashi et al. [10], this quantities correspond to the data of $^{137}C_s$ released directly into the ocean from the Fukushima Dai-ichi NPP. Four releases points were defined in the mesh along the coast between the northern discharge channel and the southern discharge channel of the Fukushima Dai-ichi NPP and it was assumed that the direct release into the ocean started on March 26th, see Figure 5. Discharges were assumed to continue until June 30. The blue line in Figure 5 shows the temporal variation of the released amount of $^{137}C_s$ used in the numerical simulations. These data were estimated based on the concentrations of radionuclides at the northern and southern discharge channels

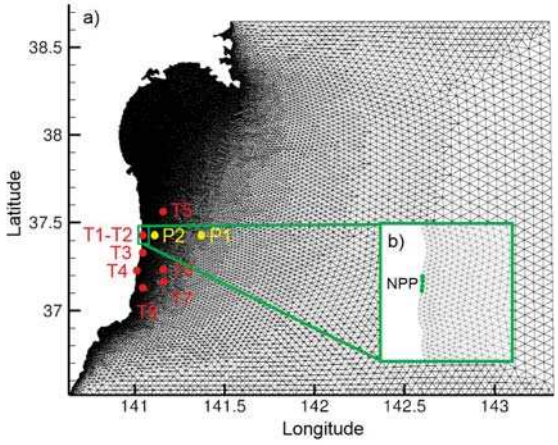

Fig. 4: a) Computational grid and sampling points where calculated $^{137}C_s$ concentrations in surface water have been compared with measurements. Points $P1$ and $P2$ are issued from the MODARIA project Exercice 1; b) grid points employed for reproducing the NPP (in green).

of the Fukushima Dai-ichi NPP, which were monitored almost twice a day. This source term estimation led to a total $^{137}C_s$ release of 3.5 PBq from March 26th to June 30.

In [19], the authors used the ensemble average values of wet deposition of $^{137}C_s$ on the free surface issued from two atmospheric dispersion models. These models were developed by KAERI [23], [24] and JAEA [26]. Both are particle tracking dispersion models and permit to model the dispersion of radionuclides released to the atmosphere and evaluate the subsequent deposition on the sea surface. In this work, this dataset was projected onto the computational domain. An example of wet deposition in the proximity of the NPP is reported in 5.

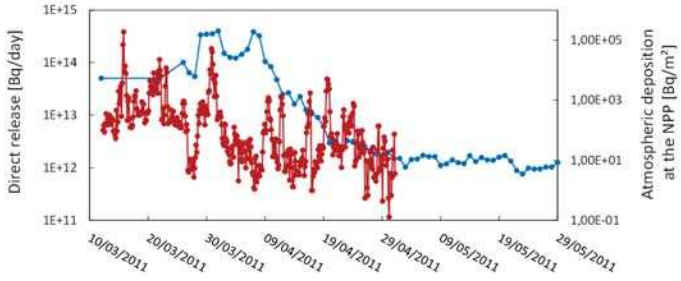

Fig. 5: Source term of caesium $^{137}C_s$ used in the numerical simulations, see section IV-B.

C. Numerical results

In this section, numerical simulations were performed from March 1st to June 1st 2011. Time series of calculated $^{137}C_s$ concentrations obtained with TELEMAC-3D were first compared to the measured concentrations obtained by TEPCO (T1 to T8, red points in Figure 4). These measurements were reported in regular press releases [25]. As showed in Figure 6, TELEMAC-3D reproduces well the concentration values at the measurements points. Particularly, nearby the NPP (points T1 to T4), good agreement between numerical results and observations is found from March 28th, two days after the beginning of the direct release into the ocean. As observed in Figure 6, numerical results match well the measurements captured in the offshore zone, both in the south zone (points T6 to T8) and in the north zone (point T5) of the Fukushima Dai-ichi NPP. For these points, there is no evidence that the numerical results are improved starting from March 26. Conversely, the model is able to correctly reproduce the order of magnitude of the measured concentration of $^{137}C_s$ during the simulation period. The model is therefore able to reproduce the propagation and diffusion of the released $^{137}C_s$ in the vicinity of the NPP.

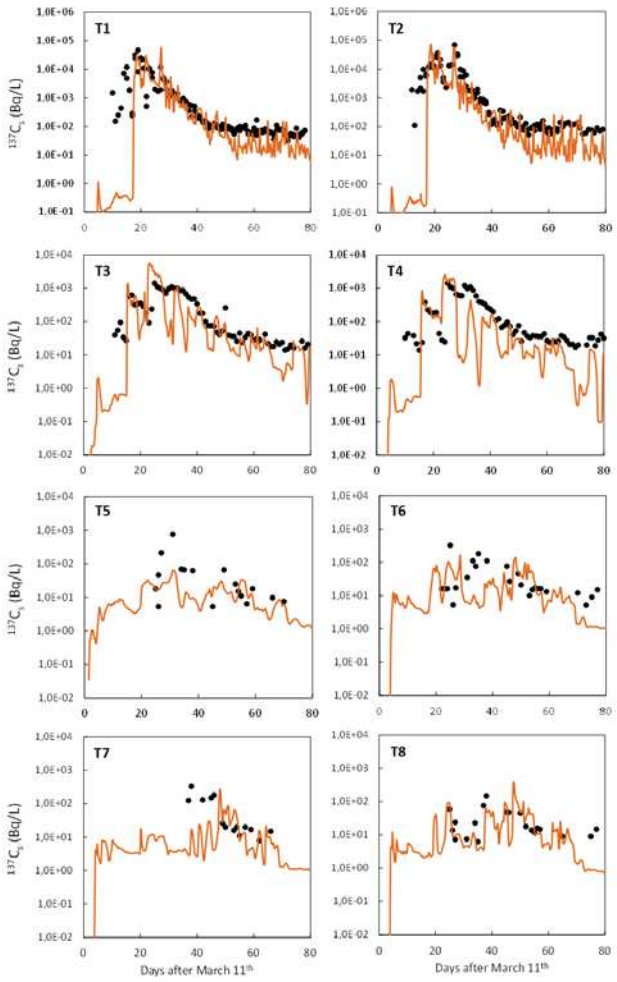

Fig. 6: Comparison between computed and measured $^{137}C_s$ concentration on the water surface, collected by TEPCO [25].

Maps of calculated $^{137}C_s$ distributions in surface water are presented in Figure 7. Corresponding maps obtained from interpolation of measurements are shown in Inomata et al. [6]. The calculated distributions, corresponding to the concentrations of the dissolved fraction of $^{137}C_s$ reflect the water circulation performed by the model. We observe that our model tend to produce an elongated patch in the North-South direction (Figures 7a-c) and, later, leading to offshore transport of radionuclides (Figures 7d-f). An accumulation of radionuclides is also observed along-shore and especially in the coastal zone of the numerical model, indicating that the main current direction is from South to North and, in a second time,

toward the North/East direction.

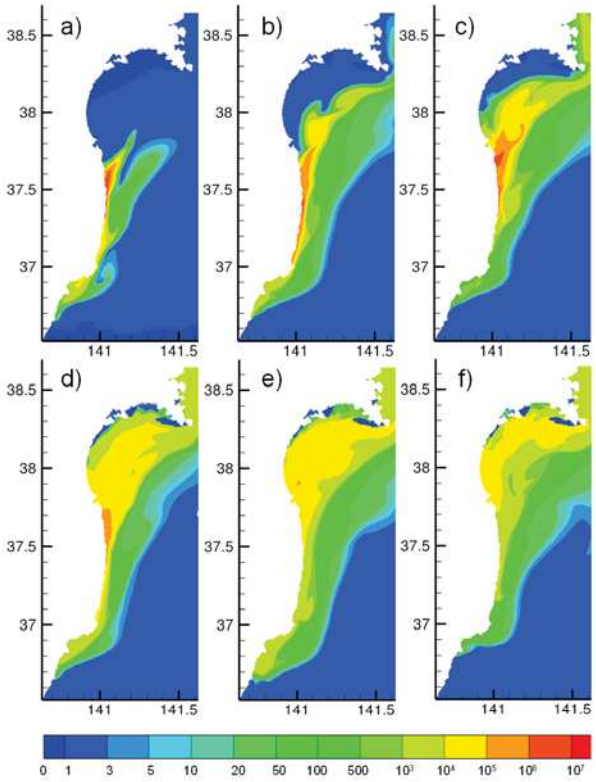

Fig. 7: Numerical results of the $^{137}C_s$ distribution on the water surface: a) April 1, b) April 6, c) April 11, d) April 21, e) May 1 and f) May 11, 2011.

Numerical results at coastal scale obtained with TELEMAC-3D are slightly different from the general path of an isotropic dispersion of radionuclides around the Fukushima Dai-ichi NPP reported by Inomata et al. [6]. Many reasons can explain these discrepancies. Firstly, the measured path has to be attributed to the small number of measurements and different sampling times used to produce these maps by an optimal interpolation method. Secondly, large scale models have showed the presence of a large anticyclonic eddy south of Fukushima, which plays a central role in the transport of radionuclides and which can affect the hydrodynamics near the coastal area around Fukushima, see [8]. Given the intensity and variability of currents in this area, as well as the presence of unsteady eddies due to current convergence here, small differences in the hydrodynamics can produce different dispersion patterns [19], [21].

V. Conclusions

The main objectives of this work were (*i*) to present the implementation, verification and validation of a three-dimensional model able reproducing the propagation of $^{137}C_s$ radionuclide in coastal waters and its interaction with suspended sediments, in the framework of the open-source TELEMAC-MASCARET modelling system and (*ii*) to evaluate the performances of the validated mode in an emergency situation as the Fukushima Dai-ichi NPP accident.

The mathematical model was based on the non-conservative transport of radionuclides, where the interaction with the particulate matter is considered, see e.g. [11], [14], [16]. This process was accounted for by solving a three-phase interaction problem, where the transfer of radionuclides from the liquid (water) to the solid phase (sediments) is governed by kinetic transfer coefficients. The resulting numerical model was first verified by comparisons between numerical and analytical solutions of selected test cases. We observed that the agreement between the analytical and numerical solution was satisfying for the performed tests, showing that the spatial and temporal distribution of the tracer concentration was well reproduced by the model. Moreover, both the kinematic exchanges of radionuclides between water and sediments and the radioactive decay were well reproduced.

The validation of the model with the Fukushima Dai-ichi case was realized by comparing numerical results with field measurements of radionuclides concentration in the Japan Sea (TEPCO measurements performed after the accident of 2011). The numerical results show that the model is able to reproduce the propagation and diffusion of the released $^{137}C_s$ in the vicinity of the NPP. Therefore, numerical results obtained with a small scale model with a simple forcing are consistent, at a coastal-scale, with models which employed general circulation model based on data assimilation techniques or variation method for hydrodynamics, see e.g. [20]. As a consequence, this kind of model could be employed in an emergency situation, when the dissolved radioactivity is considered.

Acknowledgments

This study was supported by the French ANR-Amorad project and performed through a collaboration between the Electricité de France (EDF) and the Saint-Venant Hydraulics Laboratory. The authors are very grateful to Prof. R. Periáñez, for suggestions and for kindly providing data from the MODARIA project. The present work benefited from the input of Mrs. Yoann Audouin and Davide Boscia, who provided valuable technical assistance. The authors wish to thank Dr. Françoise Siclet for her advice during the early steps of the research summarised here.

References

[1] Cunha, C.L.N., Rosman, P.C.C., 2005. *A semi-implicit finite element model for natural water bodies*. Water Res. 39, 2034e2047.

[2] Egbert, G. D., Bennet, A., F., Foreman, M. G. G., 1994. *TOPEX/POSEIDON tides estimated using a global inverse model*. Journal of Geophysical Research. Vol. 99, Issue C12.

[3] Egbert, G. D., Erofeeva, S. Y., 2002. *Efficient Inverse Modeling of Barotropic Ocean Tides*. Journal of Atmospheric and Ocean Technology. Vol. 19. pp. 183-204.

[4] García, M. (2008) Sediment Transport and Morphodynamics. Chapter 2 of *Sedimentation Engineering: Processes, Measurements, Modeling, and Practice* pp. 21-163. doi: 10.1061/9780784408148.ch02

[5] Hervouet, J-.M., 2007. *Hydrodynamics of Free Surface Flows: Modelling with the Finite Element Method*. ISBN: 978-0-470-03558-0, 360 pp.

[6] Inomata, Y., Aoyama, M., Tsubono, T., Tsumune, D., Hirose, K., 2016. *Spatial and temporal distributions of 134Cs and 137Cs derived from the TEPCO Fukushima Daiichi Nuclear Power Plant accident in the North Pacific Ocean by using optimal interpolation analysis*. Environ. Sci. Process. Impacts 18, 126136.

[7] Kawamura, H., Kobayashi, T. and Furuno, A., In, T., Ishikawa, Y., Nakayama, T., Shima, S. and Awaji, T. 2011. *Preliminary numerical experiments on oceanic dispersion of 131-I and 137-Cs discharged into the ocean because of the Fukushima Daiichi nuclear power plant disaster*. J. Nucl. Sci. Technol., 48: 13491356.

[8] Kawamura, H., Kobayashi, T., Furuno, A., Usui, N., Kamachi, M., 2014. *Numerical simulation on the long-term variation of radioactive cesium concentration in the North Pacific due to the Fukushima disaster*. J. Environ. Radioact. 136, 64-75.

[9] Kobayashi, T., Otosaka, S., Togawa, O., and Hayashi, K.: *Development of a non-conservative radionuclides dispersion model in the ocean and its application to surface cesium-137 dispersion in the Irish Sea*, J. Nucl. Sci. Technol., 44, 238247, 2007.

[10] Kobayashi, T., Nagai, H., Chino, M., and Kawamura, H.: *Source term estimation of atmospheric release due to the Fukushima Daiichi Nuclear Power Plant accident by atmospheric and oceanic dispersion simulations*, J. Nucl. Sci. Technol., 50, 255 264, 2013.

[11] Margvelashvily, N., Maderich, V., Yuschenko, S., Zheleznyak, M., 2000. *3-D numerical modelling of mud and radionuclide transport in the Chernobyl Cooling Pond and Dnieper–Boog Estuary*. Fine Sediments Dynamics in the Marine Environnement Proceedings of INTERCOH-2000. Ed. J.C. Winterwerp and C. Kranenburg, Elsevier, p. 595-610.

[12] Mazaheri, M., Samani, J.M., Samani, M.V., 2013. *Analytical Solution to One-dimensional Advection-diffusion Equation with Several Point Sources through Arbitrary Time-dependent Emission Rate Patterns*. J. Agr. Sci. Tech., 15: 1231-1245.

[13] Min, B.I., Periáñez, R., In-Gyu, Kim, Kyung-Suk, Suh, 2013. *Marine dispersion assessment of 137Cs released from the fukushima nuclear accident*. Mar. Pollut. Bull. 72, 22e33.

[14] Periáñez, R., 1998. *A three dimensional $r-$coordinate model to simulate the dispersion of radionuclides in the marine environment*. Ecological Modelling 114, 5970.

[15] Periáñez, R., 2003. *Redissolution and long-term transport of radionuclides released from a contaminated sediment: a numerical modelling study*. Estuar. Coast. Shelf Sci. 56, 514.

[16] Periáñez, R. 2005. Modelling the dispersion of radio nuclides in the marine environment: An introduction. Springer, Berlin, ISBN: 3-540-24875-7.

[17] Periáñez, R., Suh, K.S. and Min, B.I. 2012. *Local scale marine modelling of Fukushima releases. Assessment of water and sediment contamination and sensitivity to water circulation description*. Mar. Pollut. Bull., 64(11): 23332339.

[18] Periáñez, R., Suh, Kyung-Suk, Min, Byung-Il, 2013. *Should we measure plutonium concentrations in marine sediments near Fukushima?* J. Radioanal. Nucl. Chem. 298, 635e638.

[19] Periáñez, R., Brovchenko, I., Duffa, C., Jung, K-T., Kobayashi, T., Lamego, F., Maderich, V., Min, B-I., Nies, H., Osvath, I., Psaltaki, M., Suh, K.S., 2015. *A new comparison of marine dispersion model performances for Fukushima Dai-ichi releases in the frame of IAEA MODARIA program*. J. Environ. Radioactivity, 150: 247-269.

[20] Periáñez, R., Suh, K.S. and Min, B.I. 2015. *Numerical Modeling as a Tool for Managing Nuclear Accidents: The Fukushima Daiichi Case*. Energy Vol. 4: Nuclear Science.

[21] Periáñez, R., Bezhenar, R., Brovchenko, I., Duffa, C., Iosjpe, M., Jung, K-T., Kobayashi, T., Lamego, F., Maderich, V., Min, B-I., Nies, H., Osvath, I., Outola, I., Suh, K.S., de With, G. 2016. *Modelling of marine radionuclide dispersion in IAEA MODARIA program: Lessons learnt from the Baltic Sea and Fukushima scenarios*. Science of the Total Environment, In press.

[22] Roland, A., Zhang, Y.J., Wang, H.V., Meng, Y., Teng, Y.C., Maderich, V., Brovchenko, I., Dutour-Sikiric, M., Zanke, U., 2012. *A fully coupled 3D wave-current interaction model on unstructured grids*. J. Geophys. Res. 117, 1e18.

[23] Suh, K.S., Jeong, H.J., Kim, E.H., Hwang, W.T., Han, M.H., 2006. *Verification of the Lagrangian particle model using the ETEX experiment*. Ann. Nucl. Energy 33, 1159e1163.

[24] Suh, K.S., Han, M.H., Jung, S.H., Lee, C.W., 2009. *Numerical simulation for a dispersion of a pollutant using Chernobyl data*. Math. Comput. Model. 49, 337e343.

[25] TEPCO (Tokyo Electricity Power Corporation). 2011. Available at: `http://www.tepco.co.jp/en/`.

[26] Terada, H., Katata, G., Chino, M., Nagai, H., 2012. *Atmospheric discharge and dispersion of radionuclides during the Fukushima Dai-ichi Nuclear Power Plant accident. Part II: verification of the source term and analysis of regional-scale atmospheric dispersion*. J. Environ. Radioact. 112, 141e154.

[27] Tsujino, H., Motoi, T., Ishikawa, I., Hirabata, M., Nakano, H., Yamanaka, G., Yasuda, T., Ishizaki, H., 2010. Reference Manual for the Meteorological Research Institute Community Ocean Model (MRI.COM) Version 3. Technical Reports of the MRI. 59. Meteorological Research Institute, Tsukuba, Japan.

[28] Usui, N., Ishizaki, S., Fujii, Y., Tsujino, H., Yasuda, T., Kamachi, M., 2006. *Meteorological Research Institute multivariate ocean variational estimation (MOVE) system: some early results*. Adv. Space Res. 37, 806e822.

[29] Zhang, Y., Battista, A.M., 2008. *SELFE: a semi-implicit Eulerian-Lagrangian finite-element model for cross-scale ocean circulation*. Ocean. Model. 21 (3e4), 71e96.

Development of a Large-Eddy-Simulation approach for free surface complex flows.

Adrien Bourgoin,
Sylvain Guillou,
and Jerome Thiebot.
LUSAC,
60 rue Max Pol Fouchet
50130 Cherbourg-Octeville
Email: adrien-externe.bourgoin@edf.fr

Riadh Ata
and Sofiane Benhamadouche
LNHE/MFEE, EDF R&D,
6 quai Watier,
78400 Chatou
Email: riadh.ata@edf.fr

***Abstract*—For the purpose of improving turbulent process modelling of environmental flows, a LES approach is being developed in TELEMAC-3D [3]. Although still not widely used, LES is increasingly applied for this kind of flows, thanks to the computational resources growth. RANS modelling, such as the one using the standard $k-\epsilon$ model, remains favourable for numerical modelling of natural flows, and is by the way the only procedure currently available in the code for turbulence modelling. Nevertheless, in many cases, this approach cannot provide efficiently enough the intended data, such as the turbulence induced by the bathymetry. The present study is thus dedicated to the development of the model TELEMAC-LES. The different stages involved the implementation of several LES subgrid scale models, such as the standard and the dynamic Smagorinsky [13], [1], [8], and several numerical tools and tests for performing a LES. For example, the turbulent inlet boundary condition is achieved by a Synthetic Eddy Method [4] which produces a fluctuating and coherent boundary condition in order to perform the validation cases. Moreover, as TELEMAC-3D uses prismatic meshes that can be strongly anisotropic, the turbulence model has to be modified, by introducing two filter length scales instead of one. An important part of the developments has been achieved. The chosen validation cases, a flow over periodic hills [9] and in an open channel [6], reveal lots of issues related to this kind of models (numerical scheme order, mesh quality, mesh anisotropy, CPU time, boundary conditions, periodicity,...).**

I. Introduction

In environmental flows over complex geometry, understanding turbulence is essential for studying other processes, such as sediment transport or heat transfers. A RANS (Reynolds Averaged Navier-Stokes) treatment can be used in TELEMAC-3D [3], that aims to model an averaged turbulent flow, by using for example the famous $k-\epsilon$ model. Although this kind of modelling is mostly used for natural flows, it is sometimes not accurate enough for providing specific information. The improvement of computation ressources nowadays permits using Large-Eddy-Simulation for modelling environmental flows. This approach enables simulating the random aspect of turbulence, which plays an important role in transport phenomena. The method consists in introducing a subgrid model, which models the smallest motion scales, whereas the other ones are directly simulated by the Navier-Stokes equations.

It also requires additional processing, particularly for the boundary conditions treatment. For example, contrary to RANS model, some velocity fluctuations have to be introduced in the computation domain. Morevoer, near solid boundaries, wall models are regularly used for avoiding a considerable mesh refinement.

In this paper, several developments already done or being done in TELEMAC-3D are described. They are tested using a validation test case [2] representing an open channel flow at a low Reyolds number.

II. Methods

A. Subgrid models

The main idea of Large-Eddy Simulation (LES) is to divide the energy spectrum in two parts, by using a numerical filter. The first part correponds to the smallest scales named subgrid scales, which are modelled ; and the second part is the biggest scales which are directly solved with the Navier-Stokes equations. This operation introduces a new unknow tensor, called subgrid tensor and yields each variable expanded into large-scale and subgrid parts. For its treatment, there are two main approaches, which are the functional and the structural modeling [12]. This first idea is to estimate the effect of this term, and the second one is to reproduce it directly. In order to develop a LES approach in TELEMAC-3D, the selected subgrid models are the standard Smagorinsky [13], its dynamic extension [8] and the WALE model [11]. Indeed, these schemes are the most used in the litterature, and can be used for many configurations of flows with a reasonable computation cost.

1) Smagorinsky model: The Smagorinky model [13] is a subgrid model and can be referred as a functionnal model. It aims to introduce a subgrid viscosity ν_T for modeling the energy transfer processus of the subgrid scales, by using quantities emanating from the resolved scales, with the formulation:

$$\nu_T = (C_s\bar{\Delta})^2|\bar{S}| \tag{1}$$

where C_s is the Smagorinsky constant, $\bar{S}$ is the filtered rate-of-strain tensor and $\bar{\Delta}$ is the filter width. This last viscosity is

linked in practice to the grid size.Then this quantity is added to the molecular viscosity and is involved in the diffusion step of the Navier-Stokes solving. However this subgrid model is based on a homogeneous and isotropic turbulence assumption, so it requires some adaptations to apply it to complex configurations. For example in channel flows modelling, the Smagorinsky constant has to be reduced near the walls, by introducing a damping function [16] or by using the dynamic formulation of this constant [1], [8]. This latter approach consists in evaluating the Smagorinsky constant by using powers of the rate of strain tensor, together with a larger implicit filter, of width $\tilde{\Delta}$. Its expression is:

$$C_s^2 = \frac{< L_{ij} M_{ij} >}{< M_{ij} M_{ij} >} \tag{2}$$

where $< . >$ represents a space averaging introduced for the stability of the model and:

$$\left\{ \begin{array}{lcl} L_{ij} & = & \widetilde{\bar{u}_i \bar{u}_j} - \tilde{\bar{u}}_i \tilde{\bar{u}}_j \\ M_{ij} & = & 2\left(\bar{\Delta}^2 (|\widetilde{\bar{S}}|\widetilde{\bar{S}}_{ij} - \tilde{\Delta}^2 |\tilde{\bar{S}}|\tilde{\bar{S}}_{ij}\right) \end{array} \right. \tag{3}$$

where $\bar{S}_{ij}$ is the rate-of-strain tensor for the resolved scale defined by:

$$\bar{S}_{ij} = \frac{1}{2}\left(\frac{\partial \bar{u}_i}{\partial x_j} + \frac{\partial \bar{u}_j}{\partial x_i}\right) \tag{4}$$

Due to the prismatic meshes used with TELEMAC-3D, two filter widths have been defined in order to adjust the scheme to the anisotropic grid. Indeed, TELEMAC uses a vertical and a horizontal viscosities, that depend also respectively on a vertical length scale $\bar{\Delta}_v$ and a horizontal one $\bar{\Delta}_h$. However the explicit filter is defined by a unique length scale.

2) WALE model: The WALE (Wall Adapting Local Eddy) subgrid model [11] is another extension of the Smagorinsky model. It aims also to model a subgrid viscosity by using the square of the velocity gradient tensor, in order to obtain a better near wall behavior. The subgrid viscosity is estimated with:

$$\nu_T = \Delta_s^2 \frac{(S_{ij}^d S_{ij}^d)^{3/2}}{(\bar{S}_{ij}\bar{S}_{ij})^{5/2} + (S_{ij}^d S_{ij}^d)^{5/4}} \tag{5}$$

where S_{ij}^d is

$$S_{ij}^d = \frac{(\bar{g}_{ij}^2 + \bar{g}_{ji}^2)}{2} - \delta_{ij}\frac{\bar{g}_{kk}}{3} \tag{6}$$

and

$$\bar{g}_{ij} = \frac{\partial \bar{u}_i}{\partial x_j} \tag{7}$$

The length scale Δ_s involves an other constant, it is assumed to be $\Delta_s = C_w V^{1/3}$ with $C_w = 0.325$.

B. Boundary conditions

1) Synthetic Eddy Method (SEM): In order to solve the partial differential equations in a finite domain, initial and boundary conditions have to be specified. This section exhibits the methods developed for determining suitable conditions for Large-Eddy simulation computations. The inflow has a strong influence on hydrodynamics. Indeed, free surface flows are dominated by the advection phenomena. So the imposed values of the velocity and the pressure have to be as realistic as possible. The most popular approach is to prescribe Dirichlet boundary condition over the inlet area, but it assumes which requires knowing the velocity fluctuations. To overcome this problem, an idea is to generate a synthetic turbulence at the inlet plane [4]. This method consists in introducing a virtual box around the inlet, where artificial eddies will be created. Its dimensions are defined by:

$$\left\{ \begin{array}{lcl} x_{j,min} & = & \min\limits_{x \in S, i \in 1,2,3} (x_j - \sigma_{ij}(x)) \\ x_{j,max} & = & \max\limits_{x \in S, i \in 1,2,3} (x_j + \sigma_{ij}(x)) \\ \Delta x_j & = & x_{j,max} - x_{j,min} \end{array} \right. \tag{8}$$

where σ_{ij} is the length scale for the ith velocity components in the jth direction, given by:

$$\sigma_{ij} = \max(\frac{k^{3/2}}{\epsilon}, \bar{\Delta}) \tag{9}$$

Then the velocity fluctuations are generated with the action of N synthetic eddies placed randomly in the virtual box.

$$u_i' = \frac{1}{\sqrt{N}} \sum_{k=1}^{N} c_i^k f_{\sigma_{ij}}(\boldsymbol{x} - \boldsymbol{x}^k) \tag{10}$$

where the function f is defined by:

$$f_{\sigma_{ij}}(\boldsymbol{x} - \boldsymbol{x}^k) = \prod_{j=1}^{3} \sqrt{\Delta x_j} \sqrt{\frac{3}{2\sigma_{ij}}} \left(1 - \frac{|x_j - x_j^k|}{\sigma_{ij}}\right) \tag{11}$$

and c_i^k is an amplitude, written as:

$$c_i^k = a_{ij} \epsilon_j^k \tag{12}$$

with $\epsilon_j^k \in \{-1, 1\}$ and a_{ij} is the Cholesky decomposition of the Reynolds stress tensor R_{ij}:

$$\begin{pmatrix} \sqrt{R_{11}} & 0 & 0 \\ R_{21}/a_{11} & \sqrt{R_{22} - a_{21}^2} & 0 \\ R_{31}/a_{11} & (R_{32} - a_{21}a_{31})/a_{22} & \sqrt{R_{33} - a_{31}^2 - a_{32}^2} \end{pmatrix} \tag{13}$$

As the Reynolds stress tensor is unknown, it is assumed here that its extra diagonal components are assumed to be null and the others are evaluated with $R_{ii} = (2/3)k^+ u_\tau^2$. The introduced synthetic turbulence is also isotropic. The turbulent kinetic energy is evaluated by assuming that:

$$k^+ = 0.07(y^+)^2 \exp\left(\frac{-y^+}{8}\right) + \frac{4.5\left(1 - \exp\left(\frac{-y^+}{20}\right)\right)}{1 + \frac{4y^+}{Re_\tau}} \tag{14}$$

where Re_τ is the Reynolds number based on the friction velocity and $y^+ = \frac{y u_\tau}{\nu}$.

Then, at each time step, the synthetic eddies are transported in the box by a mean flow that is evaluated by the Reichard law:

$$U^+ = 2.5 log(1 + \kappa y^+) + 7.8\left(1 - e^{-\frac{y^+}{11}} - \frac{y^+ e^{-0.33 y^+}}{11}\right) \tag{15}$$

Of course, after a certain time, the eddy will leave the virtual box. Then, they will be replicated randomly at the inlet. The synthetic eddy method allows to get a fully developed turbulence quickly, by assuming the presence of an infinite domain upstream of the computation domain.

2) Recycling: A second approach for providing the inflow boundary condition is the pseudo-periodicity, named also recylcing. This method aims to use the velocities got at a specific position $x = x_R$ (often the outlet), by introducing it at the inlet. The classical method is to prescribe for each component i of the velocity:

$$u_i(0, x, y, z, t) = u_i(x_R, y, z, t - \Delta t) \quad (16)$$

This method gives good results and is less expensive than synthetic turbulence. However, as explained in [15], it introduces a spurious perdiocity in the streamwise direction, which is obviously unphysical and this artificial frequency can be responsible for instabilities if it corresponds to an acoustic mode. Moreover, in a wall bounded flow, the boundary layer is slightly thicker at the outlet than at the inlet. In [14], a spanwise shift of the turbulent boundary layer is added to the velocity profile prescribed at the inlet. Indeed, if δ_0 and δ_R are respectively the boundary layer thickness at the position $x = 0$ and $x = x_R$, the inflow condition is:

$$u_i(x_0, y, z, t) = u_i(x_R, y\delta_R/\delta_0, z + \Delta z, t - \Delta t) \quad (17)$$

where Δz is the spanwise shift introduced for avoiding complete periodicity, and $t - \Delta t$ corresponds to the previous time.

III. Results

The above mentioned points have been implemented with the trunk version of TELEMAC-3D. The non-hydrostatic version is used and the advection scheme is the MURD scheme [3]. with the predictor-corrector second-order in time option. By using a implicited theta schemes as well, it allows to get closer to a second-order, that is required for performing an efficient LES. Friction laws are set up at the bottom and at the lateral boundaries.
However, the choice of a wall model is still in discussion. For these first results, the inlet boundary condition is the synthetic eddy method. The recycling is not used yet, and the subgrid model is the standard Smagorinsky model with a Van Driest damping function [16].

A. Presentation of the test case

The developments are first used with the reference from [2]. This case is a DNS of fully developed turbulent channel flow at the Reynolds number of $Re = 2340$, that has been selected in order to minimise the effect of subgrid models. Indeed, at the beginning, the global behavior of TELEMAC is examined in terms of turbulence. This case is a free surface shallow water flow in a rectangular channel of dimensions $[4\pi\delta, 3\pi\delta/2, \delta]$. The grid used has $64 \times 48 \times 65$ points. The normal stress profiles are compared to the experiments of Komori [5].

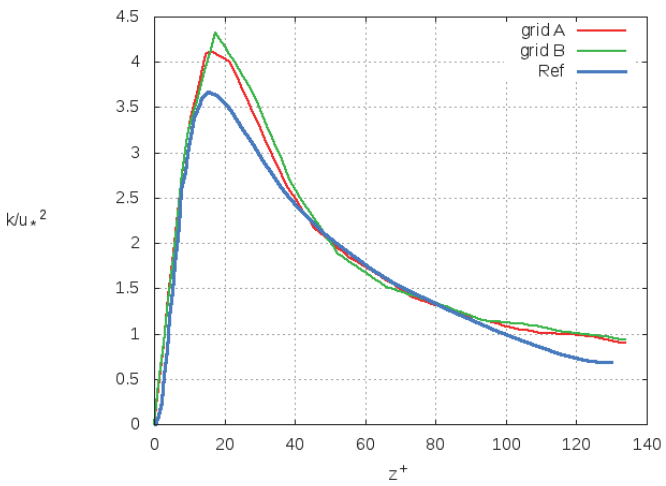

Fig. 1: Turbulent kinetic energy introduced by the SEM at the inlet plane along the centered vertical axis, from the simulations A and B and the results from [5].

In the simulations performed with TELEMAC, this case is reproduced by using two grids which settings are shown in the table I, and based on the water depth $\delta = 1/\pi$. These grids involve a polynomial distribution of the planes, in order to be refined at the boundary layer. For characterizing the friction, a Stricker law is prescribed with a value of $St = 71$, in order to get a Reynolds based on the friction velocity of about $Re_\tau = 134$.

B. Validation of the SEM

The SEM is used for synthetizing velocity fluctuations at the inlet plane, that are also transported with advection. In order to define the distrubution of these fluctuations, the Reynolds stress tensor has to be prescribed. The graphs 2, 3 and 4 show the dimensionless Reynolds stresses for each grid, as well as the turbulent kinetic energy in figure 1.

C. Steady flow

As for the synthetic eddy method, the RMS velocity components are compared to experimental data [10], and the mean streamwise flow to a theoretical log law [7].

IV. Discussion

According to figures 2, 3 and 4, the fluctuations of velocity introduced by the synthetic eddy method are closed to the prescribed profiles, given by the analytical turbulent kinetic energy formulation. This expression also gives very accurate results, shown in figure 1, for the turbulent kinetic energy compared to those from the experiments from [5]. Indeed,

Run	$\Delta x = \Delta y$	$\Delta x^+ = \Delta y^+$	Δz^+_{min}	Δz^+_{max}
A	0.02	8.4	3.6	7.9
B	0.05	21.1	6.7	13.2

TABLE I: Mesh properties

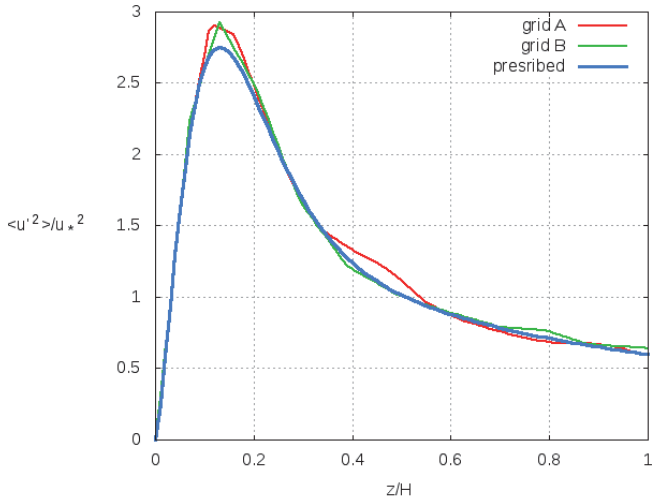

Fig. 2: Streamwise dimensionless component of fluctuacting velocity profile at the inlet plane along the centered vertical axis, from the simulations A and B et the profile prescribed in the SEM.

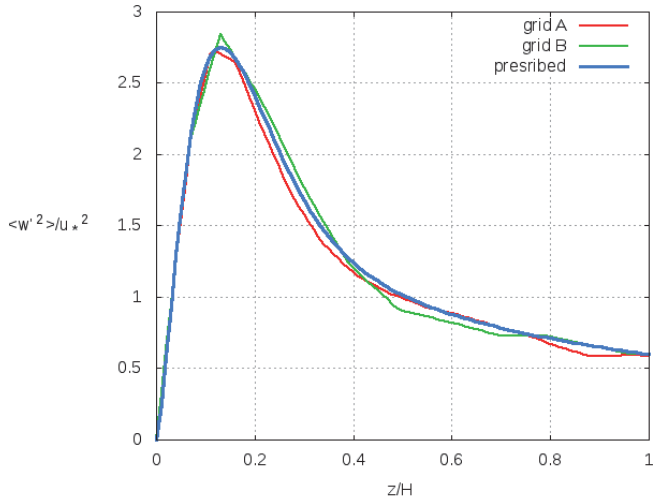

Fig. 4: Vertical dimensionless component of RMS velocity profile at the inlet plane along the centered vertical axis, from the simulations A and B et the profile prescribed in the SEM..

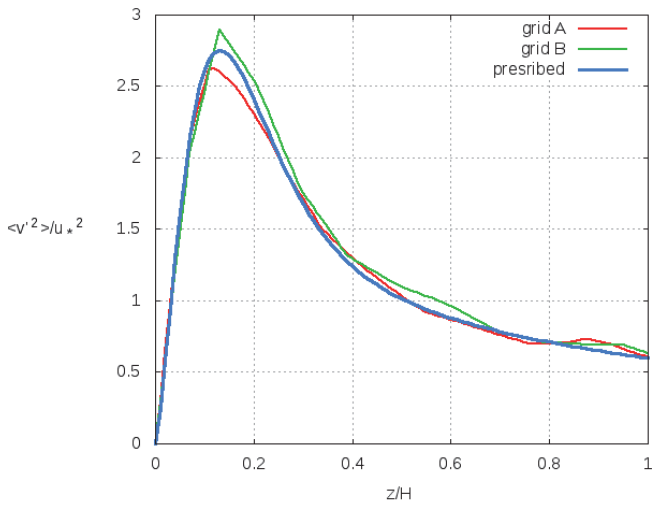

Fig. 3: Spanwise dimensionless component of RMS velocity profile at the inlet plane along the centered vertical axis, from the simulations A and B et the profile prescribed in the SEM.

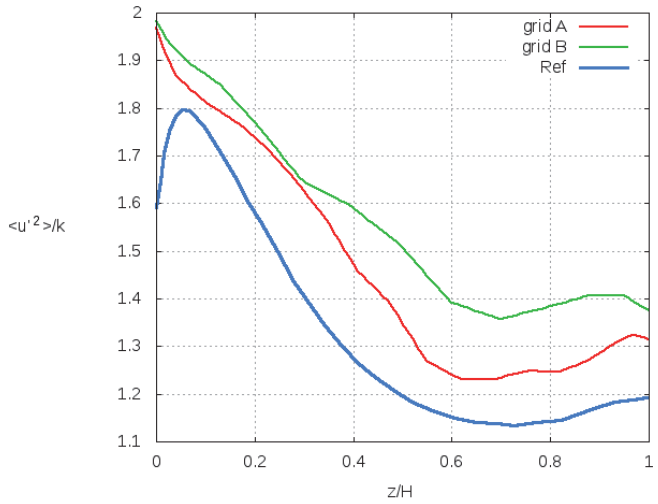

Fig. 5: Streamwise dimensionless component of RMS velocity profile in the middle of the channel along the centered vertical axis, from the simulations A and B and the results from [5].

the prescribed profile of turbulent kinetic energy is consistent with the experimental amplitude and peak at the boundary layer. Even if the turbulence is assumed to be isotropic at the inlet, it is not at all the case for this open channel flow, the anisotropic behavior is recovered very quickly in the channel. As shown in figures 5, 6 and 7, that describe the Reynolds stresses components along the centered vertical line of the computation domain, the global distribution of the fluctuations are reproduced, excepted at the bottom. Indeed, particulary for the streamwise and the spanwise velocities, the variations in the boundary layer are not well modelled, due to the friction treatment.

Furthermore, in figure 8, that is the turbulent kinetic energy profile along the vertical axis, the amplitude of the velocity fluctuations descreases sharply with the fluid progression, particularly for the coarse mesh. At this low Reynolds number, this loss of energy is quite alarming, because the subgrid model has a negligible effect in this case. This dissipation of the kinetic energy is sufficient for yielding the turbulence almost vanished by using pseudo-periodicity instead of SEM. Moreover, this loss of energy seems to be highly dependent on the way of transport of the synthetic eddies in the virtual box. Further investigations will be carried out to quantify the numercal dissipation rate in TELEMAC-3D and to check the effect of the friction treatment on these turbulent fluctuations.

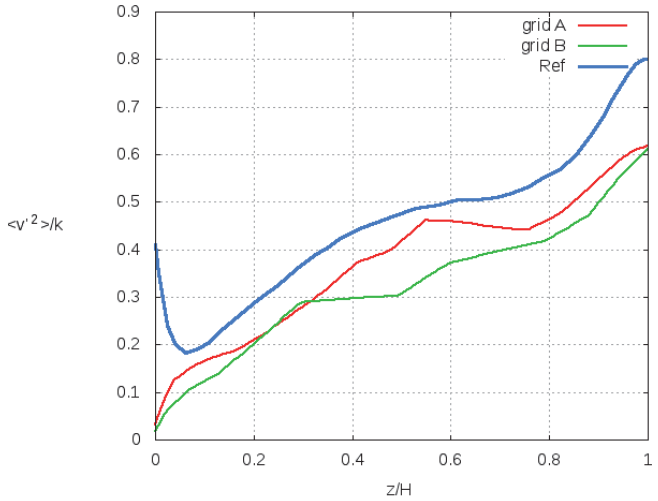

Fig. 6: Spanwise dimensionless component of RMS velocity profile in the middle of the channel along the centered vertical axis, from the simulations A and B and the results from [5].

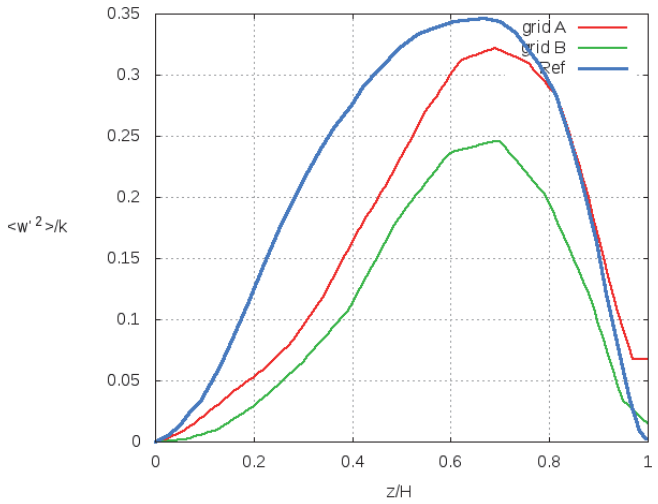

Fig. 7: Vertical dimensionless component of RMS velocity profile in the middle of the channel along the centered vertical axis, from the simulations A and B and the results from [5].

V. Conclusion

A Large-Eddy-Simulation (LES) approach is developed in TELEMAC-3D. After carrying out a state of the art of LES methods in hydraulics, two subgrid models are selected to be implemented. Since this kind of simulation requires specific boundary conditions, the Synthetic Eddy Method (SEM) is used at the inlet boundary for generating velocity fluctuations, and a wall model is being discussed.

The first developments allow us to get preliminary results. The SEM is a good alternative to a precursor simulation, since it can introduce accurately velocity fluctuations following a prescribed Reynolds stress tensor with a low computation cost.

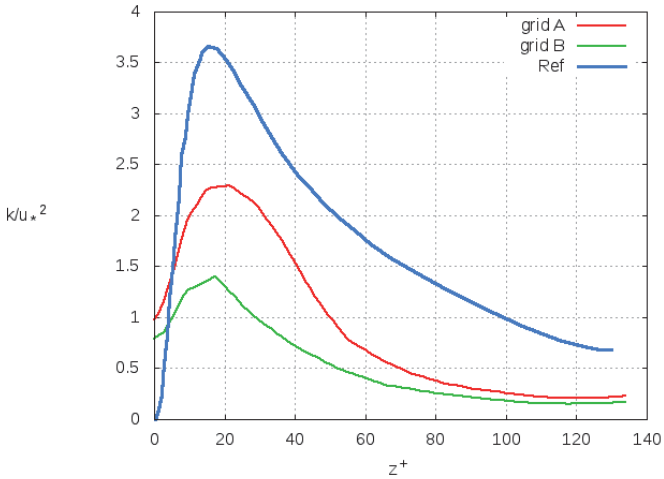

Fig. 8: Turbulent kinetic energy profile in the middle of the channel along the centered vertical axis, from the simulations A and B and the results from [5].

So, by defining a simple analytical turbulence kinetic energy profile, it quickly leads to a fully developed turbulence flow.

The global behavior of our turbulence indicators are satisfactory but the first results show that the turbulent kinetic energy decreases faster than expected with the flow progression. Indeed, a wide part of turbulence intensity introduced by the SEM is lost from the very start of the fluid progression.

References

[1] Massimo Germano, Ugo Piomelli, Parviz Moin, and William H Cabot. A dynamic subgrid-scale eddy viscosity model. *Physics of Fluids A: Fluid Dynamics (1989-1993)*, 3(7):1760–1765, 1991.

[2] RA Handler, TF Swean, RI Leighton, and JD Swearingen. Length scales and the energy balance for turbulence near a free surface. *AIAA journal*, 31(11):1998–2007, 1993.

[3] Jean-Michel Hervouet. *Hydrodynamics of free surface flows: modelling with the finite element method*. John Wiley & Sons, 2007.

[4] Nicolas Jarrin, Sofiane Benhamadouche, Dominique Laurence, and Robert Prosser. A synthetic-eddy-method for generating inflow conditions for large-eddy simulations. *International Journal of Heat and Fluid Flow*, 27(4):585–593, 2006.

[5] Satoru Komori, Hiromasa Ueda, Fumimaru Ogino, and Tokuro Mizushina. Turbulence structure in stably stratified open-channel flow. *Journal of Fluid Mechanics*, 130:13–26, 1983.

[6] Arthur G Kravchenko, Parviz Moin, and Karim Shariff. B-spline method and zonal grids for simulations of complex turbulent flows. *Journal of Computational Physics*, 151(2):757–789, 1999.

[7] CW Li and JH Wang. Large eddy simulation of free surface shallow-water flow. *International journal for numerical methods in fluids*, 34(1):31–46, 2000.

[8] Douglas K Lilly. A proposed modification of the germano subgrid-scale closure method. *Physics of Fluids A: Fluid Dynamics (1989-1993)*, 4(3):633–635, 1992.

[9] C Mellen, J Fröhlich, and W Rodi. Large-eddy simulation of the flow over periodic hills. *16th IMACS world congress*, 2000.

[10] Iehisa Nezu, Hiroji Nakagawa, and Gerhard H Jirka. Turbulence in open-channel flows. *Journal of Hydraulic Engineering*, 120(10):1235–1237, 1994.

[11] Franck Nicoud and Frédéric Ducros. Subgrid-scale stress modelling based on the square of the velocity gradient tensor. *Flow, turbulence and Combustion*, 62(3):183–200, 1999.
[12] Pierre Sagaut. *Large eddy simulation for incompressible flows: an introduction*. Springer Science & Business Media, 2006.
[13] Joseph Smagorinsky. General circulation experiments with the primitive equations: I. the basic experiment*. *Monthly weather review*, 91(3):99–164, 1963.
[14] PR Spalart, M Strelets, and A Travin. Direct numerical simulation of large-eddy-break-up devices in a boundary layer. *International Journal of Heat and Fluid Flow*, 27(5):902–910, 2006.
[15] A Spille-Kohoff and Hans-J Kaltenbach. Generation of turbulent inflow data with a prescribed shear-stress profile. Technical report, DTIC Document, 2001.
[16] Edward R Van Driest. Turbulent boundary layer in compressible fluids. *Journal of spacecraft and rockets*, 40(6):1012–1028, 2003.

A new framework for convergence studies in TELEMAC-2D

Agnès Leroy
LNHE, EDF R&D, Chatou, France
and Saint-Venant Laboratory for hydraulics,
Ecole des Ponts, CEREMA, EDF R&D, UPE, Chatou, France
Email: agnes.leroy@edf.fr

Sébastien Boyaval
Saint-Venant Laboratory for hydraulics,
Ecole des Ponts, CEREMA, EDF R&D, UPE, Chatou, France

***Abstract*—With the aim of increasing the accuracy of the TELEMAC suite, an important amount of time has been or will be spent on convergence studies. The aim of this work is to provide a framework for these studies in TELEMAC-2D. The main two advantages of this framework are: *i*) to provide an automatic way to perform such studies, the mesh refinement and error computation being handled by TELEMAC-2D and *ii*) to avoid introducing errors during the post-processing step. The user will only have to activate the convergence study option and to specify a number of refinement levels for the study, directly in the steering file. Besides, the user will only have to provide a coarse mesh of the case, the mesh refinement being handled by TELEMAC-2D. At this stage of development, the convergence studies can only be performed using linear elements. A convergence study on a schematic test-case with an analytical solution, involving only diffusion, was performed. A first order convergence was obtained regarding the tracer.**

I. Introduction

Performing convergence studies is a key task when assessing the reliability of a code aiming at discretising a continuous field (*e.g.* a PDE solution). Being able to automatically perform mesh convergence tests is thus an important feature for a code, both for the users and the developers. Indeed, in many studies the effect of mesh refinement is looked at[1], which is often time-consuming. It is also the main way to assess the quality of new developments, like new advection schemes [2], new finite elements basis, etc. For now we only consider cases for which an analytical solution can be found: the present work does not apply to engineering studies yet.

In this paper a framework for automatic convergence studies is introduced for TELEMAC-2D, only involving nested meshes. The aim is to enable the user to launch a convergence study, setting the number of refinements (called herein NLEVELS) to be performed on the provided mesh in the steering file, and letting TELEMAC-2D manage the successive mesh refinements, runs and error computations. The subroutine HOMERE_TELEMAC2D will manage this process.

The computed errors are the L_1, L_2 and L_∞ errors. For example for a tracer T defined on a domain Ω, let V be the domain volume, T^{num} the numerical solution, T^{ref} the reference solution and T_0 a mean value of T. We only consider time-independant solutions – for unsteady cases a time-average of the solution should be done. These errors are then defined as:

$$L_1(T) = \frac{1}{V}\sqrt{\int_\Omega |T^{num} - T^{ref}|\, d\Omega} \tag{1}$$

$$L_2(T) = \frac{1}{V}\sqrt{\int_\Omega \left(\frac{T^{num} - T^{ref}}{T_0}\right)^2 d\Omega} \tag{2}$$

$$L_\infty(T) = \max_\Omega |T^{num} - T^{ref}| \tag{3}$$

It was chosen to use a family of computation meshes nested in a single finer mesh where the reference solution is known, as a Finite Element field (for which we know a good/exact quadrature formula). The numerical solution is reconstructed on the finest mesh for each error calculation in order to ensure that the discretisation error is the same for each L_1 or L_2 error calculation. In this way the error calculation in itself does not affect the convergence rate. For now, this has only been implemented with linear elements.

To make this easier, STBTEL was modified in order to provide a correspondence array between the elements of the fine mesh and each coarser mesh. The construction of the finest mesh and of the correspondence array is done in HOMERE_TELEMAC2D, before the simulations. There will thus be two different meshes in the simulation: one only serves to compute the errors (it is the finest one) and the other only serves to run the simulations. Both are built from the coarse mesh provided by the user.

TELEMAC-2D is then called NLEVELS times from inside a FOR loop. The first simulation is run on the mesh provided by the user, and for each finer simulation the mesh is overwritten. At each iteration the error between the numerical solution and an analytical solution (to be provided by the user) is calculated and printed. The mesh is refined before calling TELEMAC-2D again. The complete process is summarised in the Figure 1.

The notations used in this paper are the ones of [1] and correspond to the Fortran variables in TELEMAC.

In the sections below, the new keywords introduced in TELEMAC-2D are described, followed by the new arrays allocation and the mesh refinement process. The fourth section describes the error calculation. The last section describes the results obtained on a schematic test-case using this new framework in TELEMAC-2D.

[1] when the discretisation relies on a mesh (as opposed to spectral discretisations).

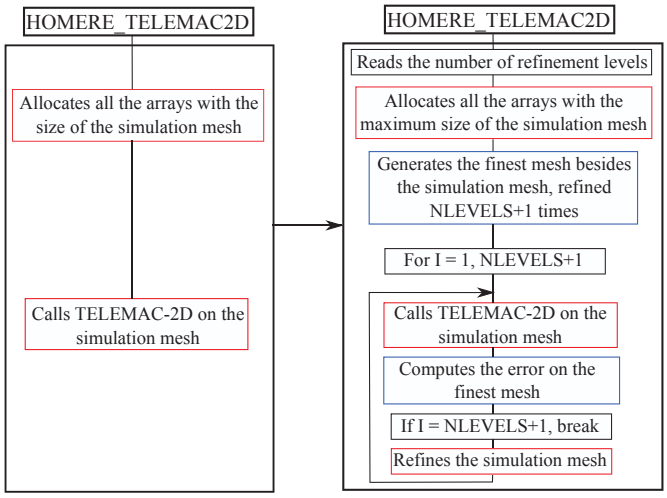

Figure 1: Structure of the new framework for convergence studies in TELEMAC-2D (right), compared to the classical one (left). The red boxes indicate the operations done on the simulation mesh, while the blue boxes indicate the operations done on the finest mesh built for the error computation.

II. Proposed developments

A. New keywords

The new keywords CONVERGENCE STUDY (ETUDE DE CONVERGENCE in French) and REFINEMENT LEVELS (NIVEAUX DE RAFFINEMENT in French) were added to the TELEMAC-2D dictionary. The first one is a boolean indicating if the user wants to perform a convergence study. The second one is an integer that allows the user to specify the number of refinement levels: for example, setting its value to 4 will trigger 5 TELEMAC-2D simulations with the finest mesh refined 4 times, while the error will be computed on the original mesh refined 5 times.

B. New array sizes

All the array sizes and the mesh size for the simulations have to be large enough to perform the finest run without memory leakage. Everything was implemented so as not to affect classical single simulations. As in the TELEMAC system, we denote here the number of elements in the mesh by NELEM, the number of nodes in the mesh by NPOIN, the number of boundary points by NPTFR and the number of segments (for a given type of element) by NBSEGEL. We also denote the number of refinements asked by the user by NLEVELS. The following changes then have to be done:

- NELMAX, the maximum number of elements in the mesh, becomes NELEM $\times$ 4^{NLEVELS}
- NBSEGEL, the number of segments of a given type of element, becomes NBSEGEL $\times$ 2^{NLEVELS}
- NPMAX, the maximum number of points in the mesh, becomes NPOIN $\times$ 7^{NLEVELS} (this is a majoration)
- NPTFRX, the maximum number of boundary points, becomes NPTFR $\times$ 7^{NLEVELS}

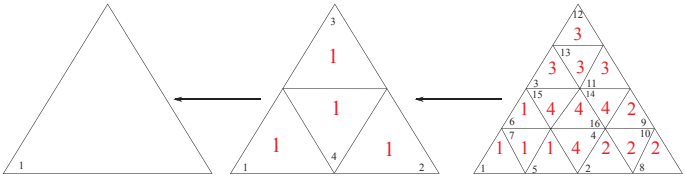

Figure 2: Sketch of the construction of the correspondence array, starting from one tringle (left) and refining twice. The black numbers are the elements indices while the red numbers are the correspondence array values.

- arrays of size NELEM are now allocated with the size NELEM $\times$ 4^{NLEVELS}
- arrays of size NPOIN are now allocated with the size NPOIN $\times$ 7^{NLEVELS}
- arrays of size NPTFR are now allocated with the size NPTFR $\times$ 7^{NLEVELS}

These modifications occur in the subroutines ALMESH, BIEF_ALLVEC, BIEF_ALLMAT, BIEF_NBSEGEL and BIEF_ALLVEC_IN_BLOCK. They now all take a new optional argument that gives the number of refinement levels in the convergence study.

Note that these changes correspond to piecewise "P1" linear elements, but changing elements would imply further modifications in the code. This has not been done yet.

C. Mesh refinement using STBTEL

The strategy chosen here to perform convergence studies is to make TELEMAC-2D call a dedicated subroutine of STBTEL to refine the mesh. A new subroutine was thus created in STBTEL, called REFINE_MESH. It refines a mesh N times by successive divisions of all the triangle elements by four. N is given as a mandatory argument to the subroutine. It calls the subroutine DIVISE on the mesh N times, and then calls the subroutines VERIFI, VOISIN, RANBO and RENUM, like what STBTEL usually does.

When building the finest mesh, REFINE_MESH is called once with N = NLEVELS. The correspondence array then has to be built so an optional argument is passed to REFINE_MESH:

- CORRESP – this new correspondence array of size NELMAX $\times$ NLEVELS can be filled during the refinement process to store the index of the elements of the coarser mesh to which the elements of the finer mesh belonged. This array is built in the subroutine DIVISE.

Considering an initial mesh composed of only one triangle and two refinement levels, the construction of the correspondence array is illustrated in Figure 2. In that array, each line corresponds to all the elements of one level N and stores the values of the elements indices to which they belonged on the previous mesh (at level $N-1$).

Considering an arbitrary number of refinements NLEVELS = N, the correspondence array thus has the

following structure:

$$C = \begin{pmatrix} 1 & 1 & 1 & 1 & & & & & & & & & & \\ 1 & 2 & 3 & 4 & 1 & 1 & 1 & 2 & 2 & 2 & ... & 4^2 & 4^2 & 4^2 \\ \vdots & & & & & & & & & & & & & \\ 1 & 2 & ... & 4^N & 1 & 1 & 1 & ... & 4^{N+1} & 4^{N+1} & 4^{N+1} & & & \end{pmatrix} \quad (4)$$

On the other hand, when refining the simulation mesh once before a new simulation, REFINE_MESH is called with $N = 1$. The correspondence array is not built in this case, but other actions have to be performed, involving other optional arguments:

- LIHBOR, LIUBOR, LIVBOR, HBOR, CHBOR, (of size NPTFRMAX), UBOR, VBOR (of size NPTFRMAX $\times$ 2), LITBOR, TBOR, ATBOR, BTBOR (bief object) – they all store information relative to the boundaries (in the same order): the type of boundary conditions on H, U, V, the water height, the friction coefficient, the values of the velocities or flow rates, the type of boundary conditions on the tracers, the values of the tracers and the coefficients for heat fluxes. They have to be filled based on the values of the surrounding boundary points for all the new points on the boundary.
- ZF and H (bief objects) – store the values of the bottom elevation and of the water depth on the 2D mesh. They need to be filled for all the new points in the mesh (H then contains the initial water depth).
- TEXP, TTILD, TN (bief objects) – store the explicit, implicit source terms for the tracers and the value of the tracers at the former time-step. Their dimension needs to be updated at each mesh refinement.

D. Error calculation

For each TELEMAC-2D simulation, the L_1, L_2 and L_∞ errors are computed. For now, only errors compared to an analytical solution can be calculated. This is done in a new subroutine of TELEMAC-2D called ERROR_COMPUTATION. First, the numerical solution is reconstructed on the finest mesh. This is done in a loop on all the elements of the finest mesh. The index of the element of the simulation mesh to which that fine element belongs is found thanks to the correpsondence array. Then, a linear interpolation is done to reconstruct the value of the field (a tracer for example) on each point of the fine element. Let I be a point of the fine mesh, located inside the element JELEM of the coarser mesh. The vertices of JELEM are denoted by J1, J2, J3. Their coordinates are denoted by X_{J1}, X_{J2}, X_{J3} and Y_{J1}, Y_{J2}, Y_{J3}. The same notation is used for the coordinates of the point I. The value of a tracer T at the point I, T_{I}, is given by:

$$T_{\text{I}} = A \times T_{\text{J1}} + B \times T_{\text{J2}} + C \times T_{\text{J3}} \quad (5)$$

with:

$$A = \frac{|(X_{\text{I}} - X_{\text{J2}})(Y_{\text{J3}} - Y_{\text{J2}}) - (X_{\text{J3}} - X_{\text{J2}})(Y_{\text{I}} - Y_{\text{J2}})|}{|(X_{\text{J2}} - X_{\text{J1}})(Y_{\text{J3}} - Y_{\text{J1}}) - (X_{\text{J3}} - X_{\text{J1}})(Y_{\text{J2}} - Y_{\text{J1}})|} \quad (6)$$

$$B = \frac{|(X_{\text{I}} - X_{\text{J1}})(Y_{\text{J3}} - Y_{\text{J1}}) - (X_{\text{J3}} - X_{\text{J1}})(Y_{\text{I}} - Y_{\text{J1}})|}{|(X_{\text{J2}} - X_{\text{J1}})(Y_{\text{J3}} - Y_{\text{J1}}) - (X_{\text{J3}} - X_{\text{J1}})(Y_{\text{J2}} - Y_{\text{J1}})|} \quad (7)$$

$$C = \frac{|(X_{\text{I}} - X_{\text{J1}})(Y_{\text{J2}} - Y_{\text{J1}}) - (X_{\text{J2}} - X_{\text{J1}})(Y_{\text{I}} - Y_{\text{J1}})|}{|(X_{\text{J2}} - X_{\text{J1}})(Y_{\text{J3}} - Y_{\text{J1}}) - (X_{\text{J3}} - X_{\text{J1}})(Y_{\text{J2}} - Y_{\text{J1}})|} \quad (8)$$

This is a linear reconstruction of the numerical solution on the finest mesh. To reconstruct a solution using quasi-bubble or quadratic elements, the formulation above would be modified: the degrees of freedom of the mesh are not the same for the different types of elements.

The reference solution T^{ref} on the finest mesh must be provided by the user in the subroutine ERROR_COMPUTATION through an analytical expression.

The errors defined by the equations (1), (2) and (3) in the continuous framework are then calculated through:

$$L_1(T) = \frac{1}{\text{NPOIN}} \sum_{\text{I}=1}^{\text{NPOIN}} \left| T_{\text{I}} - T_{\text{I}}^{ref} \right| \quad (9)$$

$$L_2(T) = \frac{1}{\text{NPOIN}} \sqrt{\sum_{\text{I}=1}^{\text{NPOIN}} \left(T_{\text{I}} - T_{\text{I}}^{ref} \right)^2} \quad (10)$$

$$L_\infty(T) = \max_{I=1,\text{NPOIN}} \left| T_{\text{I}} - T_{\text{I}}^{ref} \right| \quad (11)$$

For each discretisation, they are dumped, together with the number of mesh points, in a file called ERRORS.DAT in the results directory.

III. TEST ON A SCHEMATIC CASE

To test this framework for convergence studies, a schematic case with an analytical solution was designed. It only involves the diffusion of a tracer so that the convergence study measures the error done on the resolution of the time-discretised tracer equation:

$$\frac{T^{n+1} - T^n}{\Delta t} = -K \nabla^2 T^{n+1} \quad (12)$$

where K is the coefficient of diffusion for the tracer and Δt is the time-step size

The case consists of a square basin of side $L = 200m$. The water height is constant and equal to $2m$ and the velocity is equal to zero. The tracer is initialised through:

$$T = \left(1 - \frac{2K}{\Delta t} \left(\frac{2\pi}{L} \right)^2 \right) \sin\left(\frac{2\pi}{L} x \right) \sin\left(\frac{2\pi}{L} y \right) \quad (13)$$

K is taken equal to $1ms^{-2}$ and Δt equal to $1s$. The solver accuracy for the tracer diffusion was set to 10^{-10}. The advection and diffusion of velocities were deactivated in the steering file. The simulation is done for 1 iteration and we compare the numerical solution for the tracer to the analytical solution after one time-step:

$$T = \sin\left(\frac{2\pi}{L} x \right) \sin\left(\frac{2\pi}{L} y \right) \quad (14)$$

Three refinement levels were asked for in the convergence study, yielding four TELEMAC-2D simulations. The mesh for each simulation and the mesh for the error calculation are

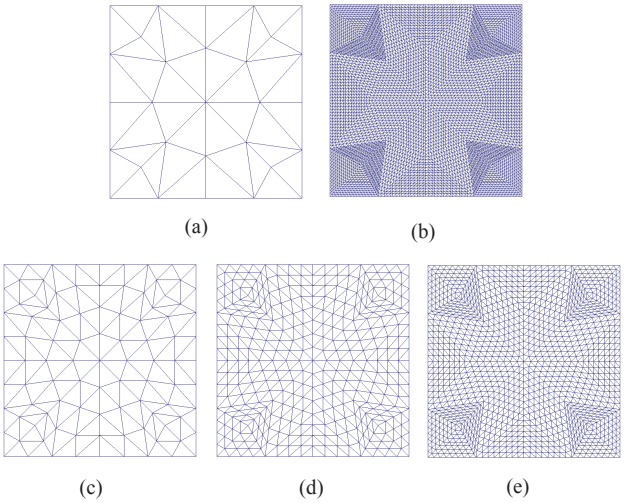

Figure 3: Test on a schematic case: view of the meshes for each simulation – (a) initial mesh, (c), (d), (e) successive refinements and of the mesh for the error calculation (b).

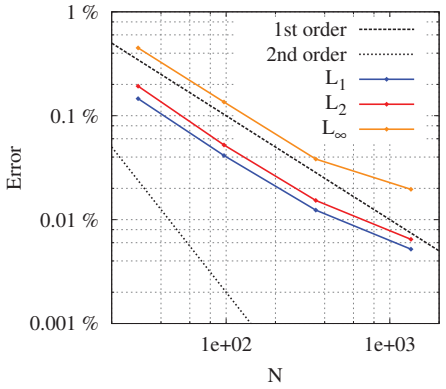

Figure 4: Test on a schematic case: results of the convergence study with three refinement levels.

shown in the Figure 3. The initial mesh contains 40 elements.

The total time spent for the four successive runs is of $4s$ on one processor (only the diffusion matrix inversion for the tracer is performed, on one time-step). Figure 4 shows the results of the convergence study, regarding the L_1, L_2 and L_∞ errors. For the three of them, a first order convergence is obtained. For the simulation on the finest mesh, the error is slightly higher than expected, probably due to the worsened aspect ratio of the triangles after three refinements.

IV. Conclusion and future work

In this paper a framework for convergence studies is proposed. It has the advantage of making everything automatic for the user. It also makes sure that no additional error is introduced when computing the L_1, L_2 and L_∞ errors. However, the drawback is that the simulations are launched one after the other on the computer, whereas launching them at the same time on different processors would increase the performance. This may be possible using the TELEMAC-2D API but has not been investigated yet.

Some improvements can be done to the present formulation: it could be extended to more types of finite elements, and also it could be extended to do convergence studies on real cases, using a reference numerical solution on a very fine mesh to compute the errors.

References

[1] LNHE, EDF R&D, *Guide to programming in the Telemac system version 6.0*, 2010.

[2] S. Pavan, "Nouveaux schémas de convection pour les écoulements à surface libre," Ph.D. dissertation, Université Paris-Est, 2016.

Sensitivity analysis and uncertainty quantification in 2D morphodynamic models using a newly implemented API for TELEMAC2D/SISYPHE

R. S. Mouradi[1,2], Y. Audouin [2], C. Goeury [2], N. Claude [2], P. Tassi [2,3] and K. El kadi Abderrezzak [2,3]
[1]École Nationale Supérieure d'Électronique, Informatique, Télécommunications, Mathématiques et Mécanique, France (ENSEIRB-MATMECA)
[2]EDF R&D National Laboratory for Hydraulics and Environment (LNHE)
[3]Saint-Venant Laboratory for Hydraulics
Chatou, France
Email: remsophia.mouradi@gmail.com

***Abstract*—In this study, the modules TELEMAC-2D and SISYPHE of the Telemac-Mascaret Modelling System (TMS) have been used in combination with the OpenTURNS library (www.openturns.org) to perform an uncertainty quantification analysis of two-dimensional morphodynamic problems. OpenTURNS is a scientific library usable as a Python module dedicated to uncertainties treatment.**

A recently implemented API (Application Program Interface) allowed the communication between OpenTURNS and TELEMAC-2D/SISYPHE, and therefore the efficient implementation of Monte-Carlo like algorithms. In this problem, each uncertain sedimentological parameter, e.g. inlet mean diameter, Shields parameter, etc. has been associated to a statistical distribution, defined with OpenTURNS. A number of TELEMAC-2D/SISYPHE simulations has been proposed regarding the predefined random entries in order to guarantee the convergence of the Monte Carlo-like algorithms.

This work allowed the implementation of uncertainty quantification analysis of computationally intensive morphodynamic simulations in the TMS. Thanks to the access to computer resources and optimized software, we were able to perform the uncertainty quantification analysis with a large set of variables, and therefore push the study further with the correlations effects analysis.

Keywords: Uncertainty quantification, Morphodynamic modelling, API, Monte-Carlo like algorithms, Sensitivity analysis

I. Introduction

Morphodynamic simulations have been increasingly used in the last few decades to model the bed evolution in rivers, coasts and estuaries. In this context, most of the equations are empirical and the parameters involved in the calculations are generally poorly defined in literature. The impact of the uncertainties related to those parameters remains unknown.

In order to quantify the impact of inputs uncertainties on simulations results, an uncertainty study is conducted. Ranking the variables in terms of influence allows to orientate the investigations when performing measurements or calibrating parameters for the simulations. In this study, the uncertainty quantification is applied to SISYPHE [16], a sediments transport module, coupled with TELEMAC2D [15] for hydrodynamics, that integrate the TELEMAC-MASCARET modelling system.

The Monte Carlo method is used to propagate the uncertainties through SISYPHE. This approach requires random generation of several configurations of inputs, using their probability distributions. Successive deterministic model simulations are then submitted to generate a set of responses that correspond to the set of inputs.

In order to have total control over the simulation's parameters and therefore conduct an efficient uncertainty study, an API (Application Program Interface) is developed for SISYPHE. This interface, when coupled with TELEMAC2D's available API, makes running hundreds of cases simultaneously possible through a cluster, taking total benefit from the available processors. Running an optimal number of cases guarantees the statistics convergence.

Finally, The pre-processing of uncertain data, as well as the post-processing of the results, are done using the OpenTURNS uncertainty library [2].

This paper is organized as follows: a description of the context and general goals, followed by the present study objectives are given. Section III deals with the API's implementation and coupling with TELEMAC2D. Section V discusses the uncertainty quantification steps and alternates theory and results for each of these. In this section, a sensitivity analysis followed by an uncertainty propagation are investigated. Correlations between variables are also studied using copulas and an ANCOVA (ANalysis of COVAriance) sensitivity analysis is applied. In the last section, conclusions and perspectives are drawn.

II. Context and goals

This study is set out in the context of EDF numerical tools development. EDF's R&D National Laboratory for Hydraulics and Environment department (LNHE) uses the TELEMAC-MASCARET system to simulate complex hydro-environmental phenomenons (such as dam breaks and flooding risks) in order to anticipate the risks related to electrical production.

TELEMAC-MASCARET results are therefore expected to produce highly reliable results. However, a great number of parameters used in these studies, specifically in morphodynamic simulations, can be set by the user and are uncertain. In order to determine the uncertain parameters impact on the system's result, an uncertainty quantification study is necessary.

In this context, an uncertainty quantification study is conducted in the morphodynamic simulation module SISYPHE. To make this study possible, an API (Application Program Interface) is implemented and coupled to TELEMAC2D, to guarantee the inter-operability with SISYPHE.

III. API'S DEVELOPMENT

The work here focused on the implementation of SISYPHE's API and its coupling to TELEMAC2D's already available API via FORTRAN modules. The API's main goal is to have control on a simulation while running a case. For example, it must allow the user to stop the simulation at any time step, retrieve some variables values and change them if necessary. SISYPHE's API is contained in the source folder of the TMS, as shown in Figure 1, and can therefore call all SISYPHE's subroutines to conduct morphodynamic simulations.

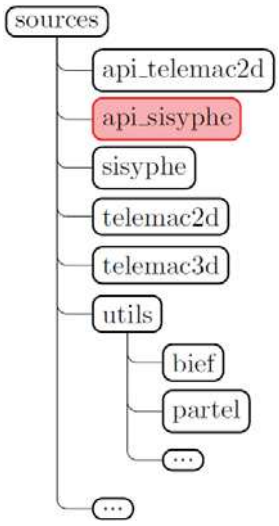

Fig. 1: Extract of TELEMAC-MASCARET sources folders

In order to make this possible, a FORTRAN structure called instance was developed in the API. It contains a list of variables declared as pointers (memory addresses [8]) that are pointing to SISYPHE's variables. This gives direct access to the physical memory of variables, and allows therefore to retrieve their values, and modify them. Furthermore, modifications have been made in SISYPHE's main subroutines to make morphodynamic cases execution possible time step by time step. Finally, parallel runs have also been treated.

In addition to this, to make running coupled cases via the API possible, a communication interface is developed in FORTRAN. This interface contains communication subroutines that send TELEMAC2D's variables to SISYPHE and vice-versa. It also contains subroutines that manage coupled cases and take into consideration the coupling period.

A number of modifications in TELEMAC2D and SISYPHE sources were necessary. These modifications, along with the API and the coupling developments, were validated using three different compilers (NAG, IFORT, GFORTRAN), on classical SISYPHE cases and coupled TELEMAC2D-SISYPHE cases, available in the system.

IV. UNCERTAINTY TREATMENT LIBRARY OPENTURNS

OpenTURNS (Open source initiative to Treat Uncertainties, Risks'N Statistics) [2] is an open source C++ Library for uncertainty treatment used through python scripts. It is co-developed since 2005 by EADS IW, EDF R&D and PHIMECA Engineering. Various statistical methods are implemented in this library and allow to follow the uncertainty study steps [1] represented in Figure 2.

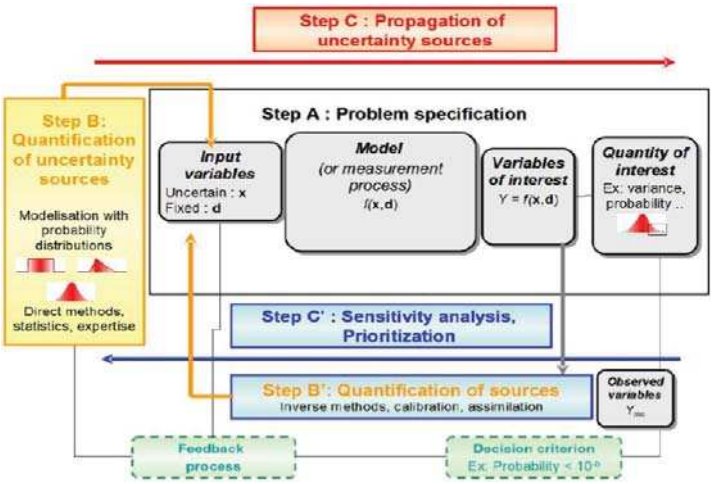

Fig. 2: Steps for an uncertainty study

V. UNCERTAINTY QUANTIFICATION

A. Problem specification

1) Hydrodynamic model: The hydrodynamic phenomenons in two-dimensional fields for free-surface and shallow water flows are modelled using the Saint-Venant equations, which are an integrated form of Navier Stokes 2D equations [9]. Saint-Venant equations are the following:

$$\begin{cases} \dfrac{\partial h}{\partial t} + \nabla \cdot (hu) = 0 \\ \dfrac{\partial u}{\partial t} + u\dfrac{\partial u}{\partial x} + v\dfrac{\partial u}{\partial y} = -g\dfrac{\partial Z_s}{\partial x} + F_x + \dfrac{1}{h}\nabla \cdot (h\nu_t \nabla u) \\ \dfrac{\partial v}{\partial t} + u\dfrac{\partial v}{\partial x} + v\dfrac{\partial v}{\partial y} = -g\dfrac{\partial Z_s}{\partial y} + F_y + \dfrac{1}{h}\nabla \cdot (h\nu_t \nabla v) \end{cases} \quad (1)$$

Where u and v are the velocity components, h the water depth, Z_s the free surface elevation, F_x and F_y are source terms (for example the friction) and ν_t the eddy viscosity.

2) Morphodynamic model: The main goal of a morphodynamic simulation is to predict the bed evolution of a given domain considering the flow conditions. Two types of sediment transport exist [6]:

- **Bed-load** : sediments are transported without losing contact with the bed. Their speed is therefore lower than the flow velocity.
- **Suspension** : corresponds to sediment transport in the absence of direct contact with the bottom. Sediments are here transported with a speed equal to the velocity of the flow.

In this study, only bed-load uncertain parameters are investigated. The main equation for this phenomenon is Exner's equation 2, that calculates the evolution of the bottom elevation Z_f.

$$(1-\lambda)\frac{\partial Z_f}{\partial t} + \nabla \cdot \overrightarrow{q_b} = 0 \tag{2}$$

Where λ is the porosity of the sediment, $\nabla\cdot$ the divergence operator and $\overrightarrow{q_b} = q_b \times (\cos\alpha_t \overrightarrow{e_x} + \sin\alpha_t \overrightarrow{e_y})$, α_t being the angle between the flow direction and the sediment transport direction and q_b the bed-load transport rate per width.

The transport rate q_b can be calculated using several empirical formulas. In this study, we focus on Meyer-Peter and Müller formula [13], as written below:

$$\frac{q_b}{\sqrt{g(s-1)d^3}} = \alpha_{MPM}(\theta - \theta_c)^{3/2} \tag{3}$$

- α_{MPM} being a transport coefficient specified by the user;
- d the sediments mean diameter;
- $s = \rho_s/\rho_f$ the relative density, where ρ_s is the sediments density and ρ_f the fluid density;
- θ and θ_c resp. the Shields number and its critical value indicating the movement's threshold.

The Shields number θ is the dimensionless shear stress τ calculated as in equation 4. The threshold θ_c is given as a parameter of the simulation by the user.

$$\theta = \frac{\tau}{g(\rho_s - \rho)d} \tag{4}$$

3) Summary of the uncertain parameters: The porosity λ, the mean diameter d, the Shields critical parameter θ_c and five other parameters, described in [16], are considered as uncertain for the current study. A summary of these variables and their definitions are given in Table I Section V-B.

4) Study cases: The uncertainty quantification is conducted for two distinct cases.

Experimental case - Channel : The channel case is a numerical reproduction of Ashida and Michiue's experiment [18] in which the erosion downstream of a dam is studied. The case, illustrated in Figure 3, is modelled in 2D with boundary conditions on flow discharge (Red boundary in Figure 3 - $Q = 0.0314\ m^2 \cdot s^{-1}$) and imposed water depth (Blue boundary in Figure 3 - $H = 0.06\ m$), as well as walls on the remaining boundaries. The channel has a $20\ m$ length, $0.8\ m$ width and $0.2\ m$ slope. An experimental duration of 10 hours is simulated using a time step $\Delta t = 0.1\ s$ within 1 minute of sequential TELEMAC2D/SISYPHE calculations on an Intel-Xeon(R) 3.40GHz core.

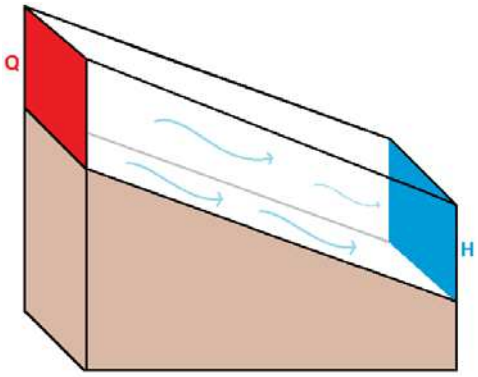

Fig. 3: Ashida et Michiue channel experiment representation

Real case - Bifurcation : A real case of a bifurcation between the Colastiné river in Argentina and a channel access to the Santa Fe harbour is also studied [14], as illustrated in Figure 4. For this case, a flow discharge $Q_1 = 2416.42\ m^2 \cdot s^{-1}$ and two water depths $H_1 = 13.053\ m$ and $H_2 = 13\ m$ are set as boundary conditions. A real duration of 10 days is simulated, with a time step of $\Delta t = 20\ s$, within 1 hour of sequential calculations on an Intel-Xeon(R) 3.40GHz core.

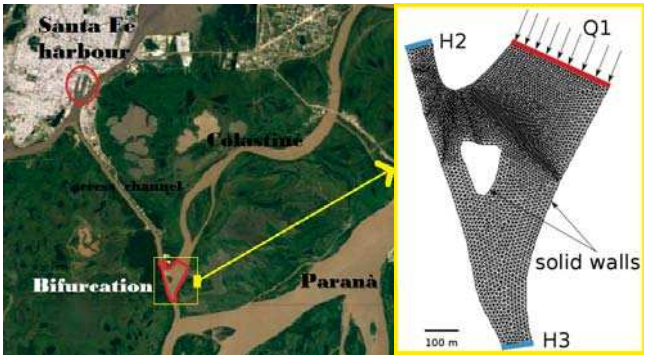

(a) (b)

Fig. 4: Study domain satellite image (a) and mesh (b)

B. Uncertainty sources quantification

The goal here is to define variation intervals and probability density functions (PDF) for each uncertain parameters. We remind that, for a random variable X defined on an interval $[a, b]$, a PDF $f(x)$ is defined as follows :

$$\mathbb{P}(X \in [a,b]) = \int_a^b f(x)dx \tag{5}$$

For all the variables from 2 to 8 defined in Table I, variation intervals were found in literature, without further information about their probabilities. Consequently, using the principle of maximum entropy [3], uniform probability density functions are chosen for those variables.

For the experimental channel case, only one mean diameter measure is available and is subject to measurements errors. The errors interval is considered as a variation interval and a uniform PDF is applied for the mean diameter on its measurement interval. For the real bifurcation case, several samples of sediments are extracted in different sections of

the river. Different values of the mean diameter are possible. In order to take all of them into consideration, a PDF that corresponds to the sample is selected and validated via the QQ-Plot method [2].

The summarized variables and their probability density functions are presented in Table I.

Variable	Definition	PDF
d	Sediments mean diameter	Log-Normal(Field Data) / Uniform(Measure errors)
α_{MPM}	Meyer-Peter and Müller transport coefficient	Uniform[5,15]
θ_c	Shields critical parameter	Uniform[0.03,0.06]
λ	Porosity	Uniform[0.25,0.4]
α_S	Skin friction coefficient	Uniform[1.0,6.6]
Φ_S	Angle of repose of the sediments (Slope effect on transport direction)	Uniform[30,80]
β_2	Deviation parameter (Slope effect on transport amplitude)	Uniform[0.1,5.0]
α_c	Secondary currents coefficient	Uniform[0.75,1.0]

TABLE I: Uncertain parameters and their PDFs

C. Sensitivity analysis

1) Monte-Carlo Sampling and statistical estimations: The Monte Carlo method requires random generation of input variables from their probability distributions. The resulted sampling of a given size N is a $N \times V$ matrix, V being the number of uncertain parameters. Each row of the matrix $x^i = (x_1, ..., x_V)^i$ represents a possible configuration for the coupled hydro-morphodynamic simulation. Corresponding realizations of the output are generated by successive deterministic simulations with each configuration of the inputs. Statistical estimators of the response $Y = (Y_1, ..., Y_N) = (M(x^i))_{i\in\{1,...,N\}}$ can therefore be computed from the output as follows :

Mean : $$E[Y] = \mu_Y = \frac{1}{N}\sum_{i=1}^{N} M(x^i) \tag{6}$$

Variance : $$Var(Y) = \frac{1}{N-1}\sum_{i=1}^{N}[M(x^i) - \mu_Y]^2 \tag{7}$$

Standard deviation : $$\sigma_Y = \sqrt{Var(Y)} \tag{8}$$

These statistical moments are useful for both the uncertainty sensitivity analysis and uncertainty propagation.

The convergence order of the Monte-Carlo sampling method is given by the Central Limit Theorem [7] as $\mathcal{O}\left(\frac{1}{\sqrt{N}}\right)$. The estimated statistics are also random quantities and are impacted by estimation uncertainties. Confidence intervals on estimators should therefore be calculated. The non-parametric "bootstrap" method provides information about the statistics uncertainties given few hypothesis [11]. Let $x = (x_1, ..., x_N)$ denote a sample of N independent and identically distributed realizations according to a probability density function $f(x)$. The statistical moment $\theta = T(F)$ (mean, variance, etc.), is estimated by $\hat{\theta} = T(\hat{F})$, where $\hat{F}$ is the empirical cumulative density function that gives equal probability $\frac{1}{N}$ to each observed value x_i defined by :

$$\hat{F}(x) = \frac{1}{d}\sum_{i=1}^{N} 1_{x_i \le x} \tag{9}$$

The idea of the non-parametric bootstrap is to simulate data from the empirical cumulative density function. Given that $\hat{F}$ is build upon equal probability for the observations $(x_1, ..., x_N)$, a sample of same size N from $\hat{F}$ would simply be a selection from $(x_1, ..., x_N)$ with repeated values. A number of B samples are generated following this strategy, and estimators properties can therefore be deduced as shown in Figure 5.

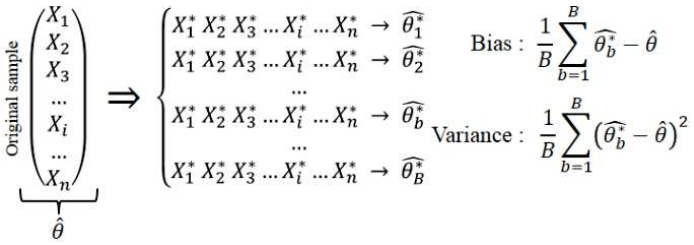

Fig. 5: Bootstrap algorithm [11]

The confidence interval I_θ is then estimated as follows :

$$I_\theta = [0.025 - q_{\widehat{\theta}_b}, 0.975 - q_{\widehat{\theta}_b}] \tag{10}$$

Where $\alpha - q_X$ is the α-quantile of a variable X defined as :

$$\mathbb{P}(X \le q_X(\alpha)) = \alpha \quad \forall\alpha \in [0, 1] \tag{11}$$

2) Analysis of variance: The main goal of a sensitivity analysis is to rank the uncertain parameters according to their influence. In order to do so, a definition of ranking indices is necessary. The indices used here are called Sobol Indices [10].

The definition of Sobol Indices is a result of the ANOVA (Analysis Of VAriance) variance decomposition. In fact, given a set of V **independent** uncertain parameters $X = (X_1, ..., X_V)$, the variance of a response $Y = M(X)$ can be calculated, using the total variance theorem [4], as follows [10]:

$$Var[Y] = \sum_{i=1}^{V}\mathcal{V}_i(Y) + \sum_{i<j}\mathcal{V}_{ij}(Y) + ... + \mathcal{V}_{12..V}(Y) \tag{12}$$

Where $\mathcal{V}_i(Y) = Var[E(Y|X_i)]$ and $\mathcal{V}_{ij}(Y) = Var[E(Y|X_iX_j)] - \mathcal{V}_i(Y) - \mathcal{V}_j(Y)$, etc.
$E(Y|X_i)$ is Y's conditional expectation with the condition that X_i remains constant.

One can therefore calculate first order sensitivity indices that estimate the influence of a variable X_i without its interactions with other variables:

$$S_i = \frac{\mathcal{V}_i(Y)}{Var[Y]} = \frac{Var(E[Y|X_i])}{Var[Y]} \tag{13}$$

And total indices that estimate the global influence of a variable (including interactions):

$$S_{Ti} = S_i + \sum_{j\neq i} S_{ij} + \sum_{j\neq i, k\neq i, j<k} S_{ijk} + ... = 1 - \frac{\mathcal{V}_{-i}(Y)}{Var[Y]} \tag{14}$$

$\mathcal{V}_{-i}(Y)$ being conditional expectations variances that do not involve X_i.

There are two ways to estimate the Sobol indices defined in equations 13 and 14 :

SALTELLI method [7]: Step 1: Two independent samples A and B of size N are generated for the V uncertain variables. For example, sample A can be written as follows:

$$A = \begin{pmatrix} x_1^{A,1} & x_2^{A,1} & ... & x_V^{A,1} \\ x_1^{A,2} & x_2^{A,2} & ... & x_V^{A,2} \\ \vdots & \vdots & \ddots & \vdots \\ x_1^{A,N} & x_2^{A,N} & ... & x_V^{A,N} \end{pmatrix} \quad (15)$$

A new sample C is created using columns of B except for column i that is replaced with data from A:

$$C = \begin{pmatrix} x_1^{B,1} & ... & x_i^{A,1} & ... & x_V^{B,1} \\ x_1^{B,2} & ... & x_i^{A,2} & ... & x_V^{B,2} \\ \vdots & & \vdots & & \vdots \\ x_1^{B,N} & ... & x_i^{A,N} & ... & x_V^{B,N} \end{pmatrix} \quad (16)$$

Simulations using the samples A, B and C result with :

$$\begin{cases} y_k^A = M((x_1^{A,k}, ..., x_V^{A,k})) & k = \{1, N\} \\ y_k^B = M((x_1^{B,k}, ..., x_V^{B,k})) & k = \{1, N\} \\ y_k^C = M((x_1^{C,k}, ..., x_V^{C,k})) & k = \{1, N\} \end{cases} \quad (17)$$

Which can be used to estimate Sobol indices as follows:

$$S_i = \frac{\frac{1}{N}\sum_{k=1}^{N} y_k^A y_k^C - (\mu_{Y^A})^2}{\sigma_{Y^A}^2} \quad (18)$$

$$S_{Ti} = 1 - \frac{\frac{1}{N}\sum_{k=1}^{N} y_k^B y_k^C - (\mu_{Y^B})^2}{\sigma_{Y^B}^2} \quad (19)$$

Overall, for a given sample size N, $(V+2) \times N$ simulations are necessary to estimate the first order and total Sobol indices for each variable X_i.

Polynomial chaos method (PCE): The models response can be approached by an analytical function :

$$M(X) = M_0 + \sum_{i=1}^{V} M_i(X_i) + \sum_{1 \le i < j \le V} M_{i,j}(X_i, X_j) + \quad ... \quad + M_{1,...,V}(X_1, ..., X_V) \quad (20)$$

$M_i(X_i)$ represents the variable X_i's contribution to the result of the simulation. The variance can therefore be calculated as follows [4]:

$$Var[Y] = \sum_{u \subseteq \{1,...,V\}} [Var[M_u(X_u)] + \sum_{v \subseteq \{1,...,V\}, v \cap u = \emptyset} Cov\left[M_v(X_v), M_u(X_u)\right]] \quad (21)$$

In this particular case of independent variables, the covariance term $Cov\left[M_v(X_v), M_u(X_u)\right]$ vanishes, and the decomposition becomes then equal to ANOVA. Sobol indices can therefore be estimated as:

$$S_i = \frac{Var\left[M_i(X_i)\right]}{Var[Y]} \quad (22)$$

$$S_{Ti} = \frac{\sum_{u \subseteq \{1,...,V\}, i \in u} Var\left[M_u(X_u)\right]}{Var[Y]} \quad (23)$$

The contributions $M_i(X_i)$ can be calculated by estimating the models response using a polynomial chaos expansion, which can, in a simplified way, be written as:

$$M(X) = \sum_{|\alpha| \le P} a_\alpha \Psi_\alpha(X) \quad (24)$$

Where $\{\Psi_\alpha, \alpha \in \mathbb{N}^V\}$ is a multivariate polynomial basis and a_α adequate coefficients for the estimation of the model's response, that can be determined using projection methods [4].

The X_i-univariate polynomials shares are the exact contribution of X_i to the polynomial expansion, and are therefore an estimation of $M_i(X_i)$.

3) Results:

Channel's results: For a sample of size $N = 30000$, a number of $(2+8)\times 30000$ simulations are necessary to estimate Sobol indices via a SALTELLI method. Up to 500 cores are used to launch the simulations, for a calculation time of 20 hours overall. The observed variances of Z_f in m^2 and some interest points (1, 86 and 150) are given in Figure 6.

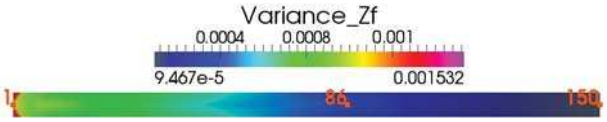

Fig. 6: Channel case - Z_f variances implied by 8 uncertain parameters

First order and total Sobol indices are therefore calculated using the SALTELLI method, and their confidence intervals estimated via Bootstrap. The results are given for the point 86 in Figure 7. Similar results are observed for the other interest points.

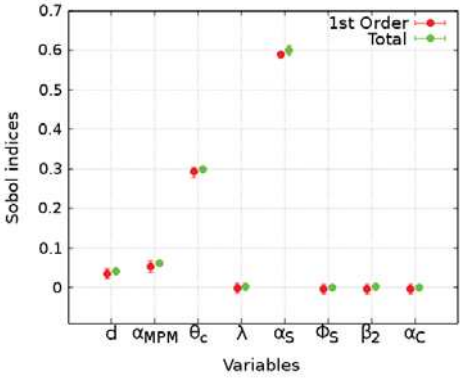

Fig. 7: Channel case - Sobol indices for Point 86

The skin rugosity coefficient α_S is by far the most influencing variable, followed by θ_c the Shields critical parameter. The influence of other variables can be considered negligible.

The SALTELLI method and the PCE method for the estimation of Sobol indices are compared in the interest points for the same sample size $N = 30000$, as shown in Figure 8.

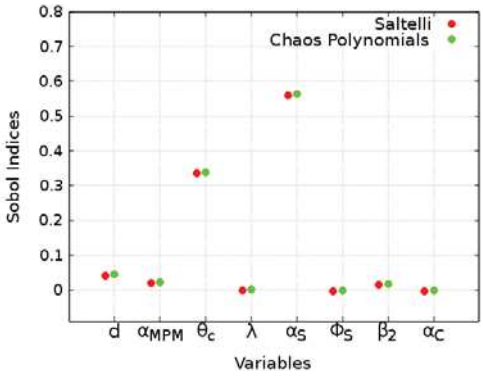

Fig. 8: Channel case - Comparison of Sobol indices calculation using SALTELLI and PCE methods for Point 1

Both methods give equal estimations of Sobol indices for $N = 30000$. Given that the PCE method needs a total of N runs to estimate Sobol indices, which is 10 times less than the cost of SALTELLI method, it will be used from now on.

Bifurcation's results: For the bifurcation application, a sample of size $N = 12800$ is used . An overall 19 hours of simulation using 800 cores is necessary. The observed variances are given in Figure 9.

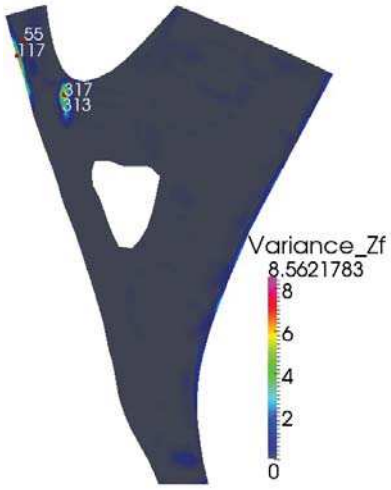

Fig. 9: Bifurcation - Variances of Z_f

Sobol indices are estimated in interest points like 317 (Figure 9) using the PCE method, as shown in Figure 10.

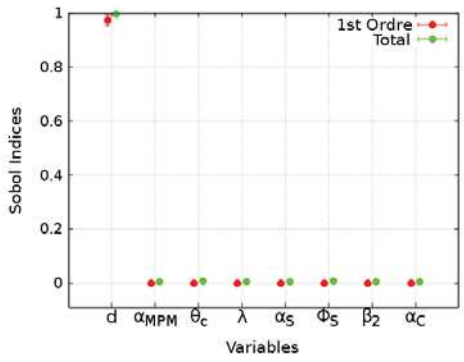

Fig. 10: Bifurcation - Sobol indices for point 317

For this case, the observed variances seem to result only from the diameters uncertainty. All the other uncertain variables seem to be none influencing.

D. Uncertainty propagation

In this section, the impact of the parameters uncertainty on the model's response will be investigated using statistics defined in section V-C1, like the mean and the variance.

1) Channel's results: The sensitivity analysis has shown a great difference between the observed results for an experimental and a real case. In fact, for a real case, the mean diameter of sediments seems to be the only influencing parameter, while it is nearly meaningless for an experimental case. In order to investigate the influence of the sediment diameter, a new set of $N = 30000$ uncertainty runs is launched, considering as an only uncertain parameter the mean diameter (other parameters are constant). The observed statistics (mean in m and variance in m^2) are given in Figure 11.

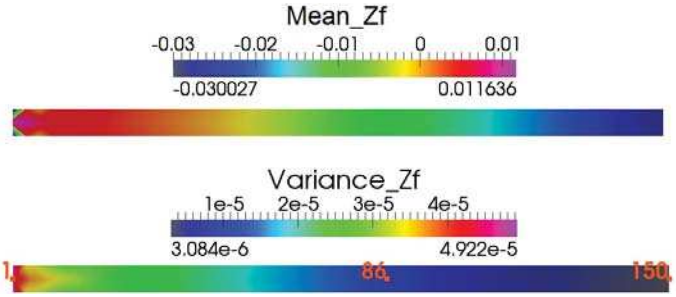

Fig. 11: Channel case - Statistics of Z_f for $N = 30000$

Uncertainties seem to be more important in the upstream direction, which corresponds to a higher erosion upstream and therefore bigger chances of bottom variations. This could also be confirmed through comparing the statistical mean of the final bottom elevations to a deterministic result with the statistical mean of sediment diameters on the channel's center line, as shown in Figure 12. The statistical mean of final bottom elevation is closer to the final deterministic result in the downstream direction.

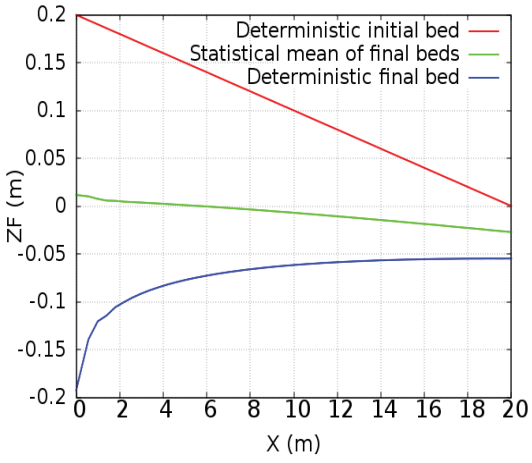

Fig. 12: Evolution of the bottom in the channel's center line

To quantify the uncertainty propagation, a statistical number called variation coefficient is defined in equation 25.

$$c_v(Z_f) = \left| \frac{\sqrt{Var(Z_f)}}{\mu(Z_f)} \right| = \left| \frac{\sigma(Z_f)}{\mu(Z_f)} \right| \quad (25)$$

Variation coefficients c_v are evaluated in interest points with high and low variances (points 86 and 150 in Figure 11), and their convergence investigated with the Bootstrap method, as shown in Figures 13 and 14.

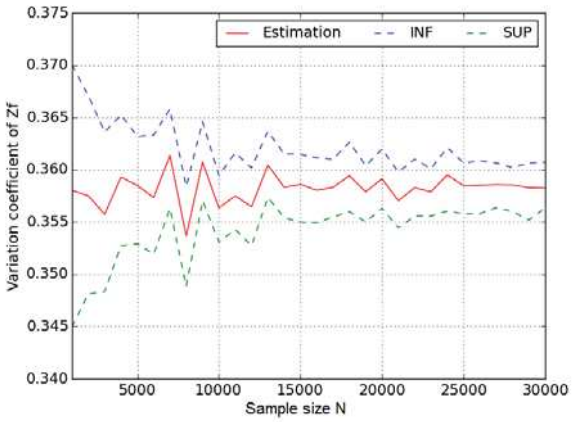

Fig. 13: Variation coefficient for point 86

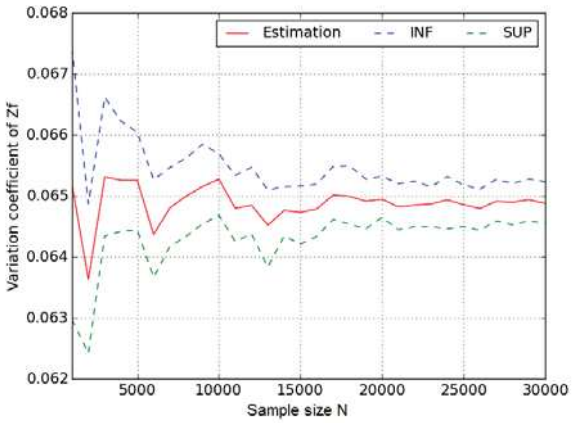

Fig. 14: Variation coefficient for point 150

In comparison with a variation coefficient of $c_v = 0.07$ for the diameter's sample, the uncertainty seems to be highly propagated in some interest points as point 86. This in fact confirms that even if the diameter seems to be none influencing while conducting the sensitivity analysis, its uncertainty is still propagated. In other interest points like 150, the variation coefficient of the output is lower than that of the input. In both cases (low and high c_v) the results have converged at about $N = 16000$. The confidence interval (INF and SUP in Figures 13 and 14) for $c_v = 0.36$ is ± 0.005 and for $c_v = 0.06$ is ± 0.001. The convergence of the statistical estimations and the narrow confidence intervals indicate that our calculations can be trusted for the chosen size $N = 30000$.

2) Bifurcation's results: For the Bifurcation case, there is no need to investigate the diameter as an only uncertain parameter, as it is influencing the result at about 100%. The same calculations as in sensitivity analysis have been exploited to estimate the statistics in Figure 15.

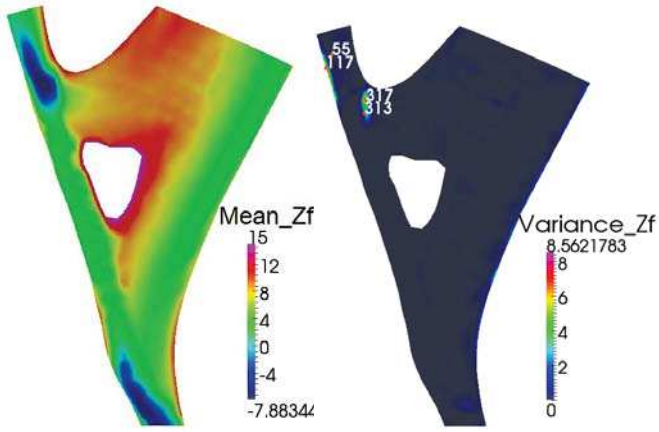

Fig. 15: Bifurcation - Statistics for Z_f - N = 12800

The highest variances seem to be concentrated in specific areas (for example, interest points 317 and 313 in Figure 15). This could be interpreted as the result of higher movements in this areas, which is demonstrated in Figure 16, where the initial and final bottom elevations have been shown for point 317 with a diameter of $d = 0.149mm$. This diameter corresponds to the minimum value of the studied sample. For the maximum value, no bed evolution has been observed.

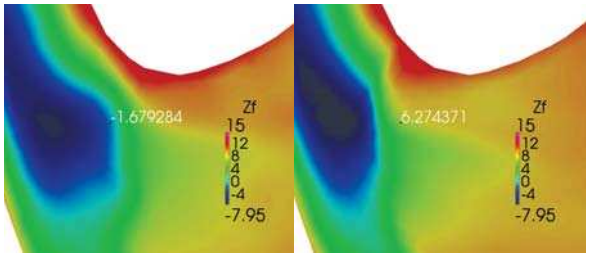

(a) (b)

Fig. 16: Z_f in point 317 for d=$0.149mm$ - First (a) and last iteration (b)

This difference of movement is explained by the threshold defined by the Shields parameter, which most certainly doesn't allow the maximum diameters sediments to be transported. For $d = 0.149mm$, a sedimentation area around point 317 is observed, which is confirmed by the bottom elevation values, going from $Z_f = -1.68m$ in the beginning of simulation to $Z_f = 6.27m$ at the end.

Nevertheless, interpreting the variances using its minimum-maximum scale can give a false idea about where variances shall appear. In fact, one can interpret that there are no other variances areas than close to points 317 and 313, which is not true and can be proved with rescaling the variances as shown in Figure 17.

Furthermore, the variation coefficients c_v have also been estimated for this case in low and high variance points and their convergence studied. The same conclusions can be drawn.

Fig. 17: Bifurcation - reduced scale of variations for Z_f

For a variation coefficient of the diameter being $c_v = 0.42$, uncertainty is more or less propagated in different points. For example, in point 317 (Figure 18), $c_v = 1.879$ which corresponds to a high uncertainty propagation. For point 55 (Figure 19), $c_v = 0.137$ which is far less than the variation coefficient of the diameter's sample and corresponds to an uncertainty that is not propagated.

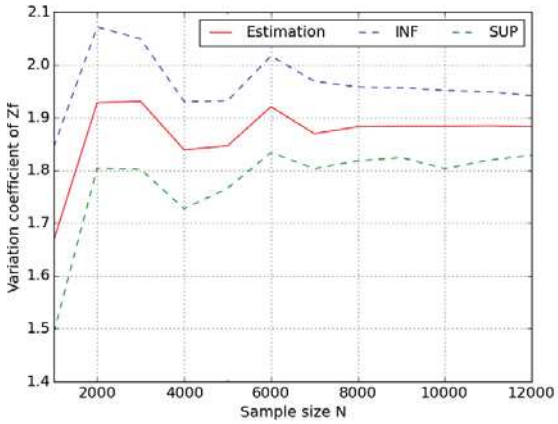

Fig. 18: Bifurcation -Variation coefficient point 317

The variation coefficients converge at about $N = 8000$ for both cases, which signifies that the results of this study can be

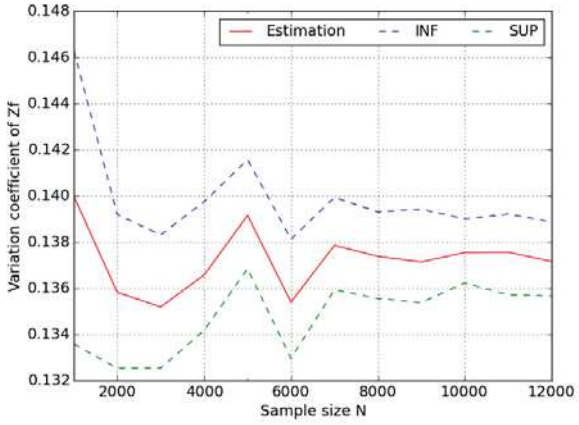

Fig. 19: Bifurcation -Variation coefficient point 55

trusted as $N = 12800$. Furthermore, the confidence intervals are ± 0.1 for $c_v = 1.879$ and ± 0.002 for $c_v = 0.137$ and are tightening with the increasing sample size.

E. Correlations impact

Several physical relationships can exist between the considered uncertain parameters. These correlations between the variables can impact the uncertainty study, given that the parameters are no longer sampled independently. In order to model the correlations, copulas are introduced in section V-E1. For the sensitivity study, the ANOVA method can no longer be used, because of the independent parameters hypothesis it implies. A new method called ANCOVA (ANalysis of COVAriance) is introduced in section V-E2. The uncertainty study is conducted with the correlations consideration on the channel's case. In fact, given that the only influencing parameter in the Bifurcation is the diameter, it has been concluded that the correlation study for this case would be useless.

1) Copulas for correlations modelling: A copula is a function that defines a dependency structure between a set of variables [5]. In fact, it links the multivariate probability density function of random set of variables $(X_1, ..., X_V)$ to their univariate probability density functions.

A copula is a V-dimensional function C defined on $[0,1]^V$ that verifies:

- $\forall u \in [0,1]^V \ \forall i \in [|1:V|]$, if $u_i = 0$ then $C(u) = 0$
- $\forall i \in [|1:V|]$ and $u_i \in [0,1]$, $C(1, ..., 1, u_i, 1, ..., 1) = u_i$
- $\forall u, v \in [0,1]^V$ verifying $\forall i \in [|1:V|] \quad u_i \leq v_i$ then $V_C([u,v]) \geq 0$

Where $V_C([u,v])$ is the C-volume of the space $[u_1, v_1] \otimes \ldots \otimes [u_V, v_V]$ defined as follows :

$$V_C([u,v]) = \Delta_{u_V}^{v_V} ... \Delta_{u_1}^{v_1} C(\mathbf{w})$$

$\Delta_{u_i}^{v_i}$ being the i^{th} finite differential:

$$\begin{aligned}\Delta_{u_i}^{v_i} C(\mathbf{w}) = &C(w_1, ...w_i, v_i, w_{i+1}, ..., w_V) \\ &-C(w_1, ...w_i, u_i, w_{i+1}, ..., w_V)\end{aligned}$$

The Sklar theorem [5] allows to define a relation between the multivariate PDF f_X of the set $X = (X_1, ..., X_V)$ and the univariate probability density functions f_i of X_i as follows :

$$f_X(x_1, ..., x_V) = c(F_1(x_1), ..., F_V(x_V)) \times \prod_{i=1}^{V} f_i(x_i) \quad (26)$$

Where F_i are the univariate cumulative distribution functions of X_i associated to the probability density functions f_i. On the other hand, c is the probability density function of the copula C defined as follows:

$$\forall \mathbf{u} \in [0,1]^V \quad c(u_1, ..., u_V) = \frac{\partial^V C}{\partial u_1 ... \partial u_V}(u_1, ..., u_V) \quad (27)$$

In this study, a classical Gaussian copula is used [2]. It requires the calculation of a correlation Matrix using Spearman

indices [2] from the relationships between variables. The relationships modelled here are the following:

- The empirical relation between the Meyer-Peter and Müller coefficient and the Shields number, that was introduced by Wiberg and Smith [17] as follows:

$$\alpha_{MPM} = 9.64 \times \theta^{0.166} \tag{28}$$

  Which implies a correlation between α_{MPM}, α_S and d.

- The relationship between the Shields critical parameter and the dimensionless sediments diameter [16].

- The modified Komura porosity formula [19]:

$$\lambda = 0.13 + \frac{0.21}{(d + 0.002)^{0.21}} \tag{29}$$

- The following relationship between the deviation parameter and the sediments diameter [12]:

$$\beta_2 = 9 \left(\frac{d}{H} \right)^{0.3} \tag{30}$$

2) Analysis of covariance: For dependent variables, it is possible to calculate the variance with the ANCOVA decomposition as follows:

$$Var[Y] = \sum_{u \subseteq \{1,\dots,V\}} [Var[M_u(X_u)] + \sum_{v \subseteq \{1,\dots,V\}, v \cap u = \emptyset} Cov\left[M_v(X_v), M_u(X_u)\right]] \tag{31}$$

New sensitivity indices can be defined as:

$$\begin{cases} S_i^U = \dfrac{Var\left[M_i(X_i)\right]}{Var[Y]} \\ S_i^C = \dfrac{Cov\left[M_i(X_i), \sum_{v \subseteq \{1,\dots,V\}, v \cap \{i\} = \emptyset} M_v(X_v)\right]}{Var[Y]} \\ S_i = S_i^U + S_i^C = \dfrac{Cov\left[M_i(X_i), Y\right]}{Var[Y]} \end{cases} \tag{32}$$

Where S_i is the total influence of the variable X_i, S_i^U the uncorrelated part of influence and S_i^C the correlated part.

ANCOVA indices can be negative because of the covariance term. In order to interpret the signification of negative indices, their absolute values are compared. In fact, if $|S_i^C|$ has a high value, this means that S_i^U is close to S_i, which signifies that correlations of the variable X_i have weak influence on the result. Inversely, if it has a high value, this means that correlations of X_i have great impact on the simulation's result.

Lastly, as show in section V-C2, the terms $M_i(X_i)$ can be estimated via the polynomial chaos expansion. However, in order to guarantee the orthogonality of the polynomial chaos basis, it is necessary to estimate the coefficients of the expansion using uncorrelated entries X. The M_i terms are estimated afterwards using the correlated values of the entries.

3) Results: The ANCOVA indices are compared to the Sobol (ANOVA) ones in order to quantify the impact of correlations on the sensitivity analysis, as shown in Figure 20.

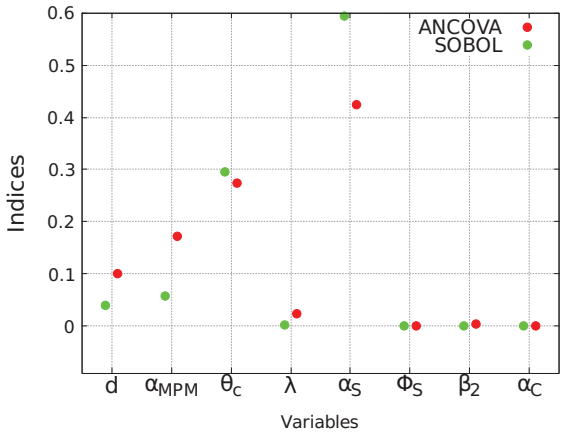

Fig. 20: Sensitivity indices for point 86

In this case, the global order of influence doesn't change. The gap between the variables in terms of influence is reduced, for example between the variables α_{MPM} and θ_C. Furthermore, some of the variables that seemed to be of weak influence at first are now considerably influencing, for example α_{MPM}. Other variables for which no correlation was considered didn't change their sensitivity indices (eg. α_C). In order to estimate the part of the correlations influence in the total ANCOVA influence, the comparative Figure 21 is drawn.

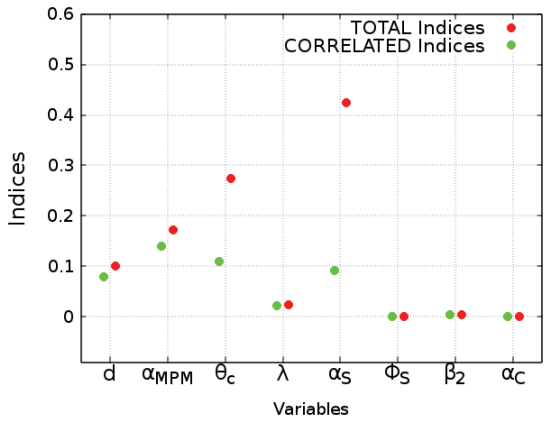

Fig. 21: ANCOVA Indices Vs correlated ANCOVA indices

It can be observed that variables for which the sensitivity indices have considerably increased (d and α_{MPM}) owe all their new influence to the correlations.

Other variables that were initially influencing also have part of their influence that is due to the correlations (θ_C and α_S).

Furthermore, the variances with independent uncertain parameters and correlated uncertain parameters are compared as shown in Figure 22.

It is clearly noticed that variances considerably increase when adding correlations in this case. It can be explained by observing the new variation interval of α_{MPM} for example.

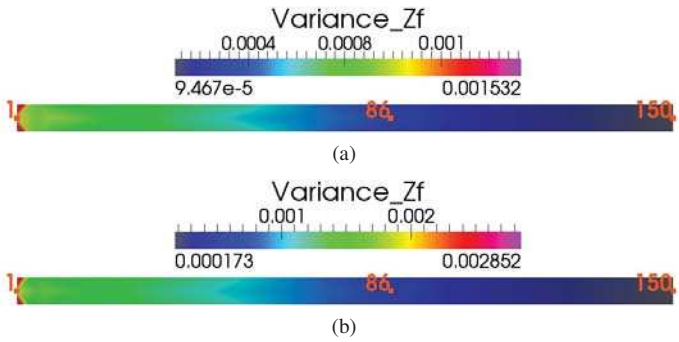

Fig. 22: Uncertainty propagation without (a) and with (b) correlations for the channel's case

In fact, the transport coefficient of the Meyer-Peter and Müller formula initially varies between the values 5 and 15. When correlations are added, α_{MPM} varies between 9.5 and 11, which implies that we statistically observe more movement (erosion) as compared to cases with no correlations.

VI. Conclusion and perspectives

In this study, an uncertainty quantification of a morphodynamic problem has been proposed.

In a sensitivity analysis step, differences were observed between a real case and an experimental case. In fact, for the real bifurcation case, the diameter was the only influencing parameter, which is not the same for the channel.

In order to analyse the influence of sediments diameter on the model's response, an uncertainty propagation study was conducted, considering as an only uncertain parameter the sediments diameter. This study has shown that the diameter has highly propagated uncertainties where there is movement. In fact, high variances were observed in maximum erosion points for the channel, and in a deposition zone for the bifurcation.

Finally, correlations were added and increased the variances significantly. An ANCOVA method was implemented in order to conduct a sensitivity analysis. The gap between the variables' influences decreased and variables that seemed first none-influencing (sediments diameter and transport coefficient of the Meyer-Peter and Müller formula) became of considerable influence when adding correlations.

This study can be generalized to other applications, such as the use of different sediment transport formulas, the study of suspended sediment transport or the influence of different physical phenomenons, for example waves (TOMAWAC module in the TELEMAC-MASCARET system).

References

[1] A. PASANISI, M. COUPLET and A.H DUTFOY LEBRUN, "Guide méthodologique pour le Traitement des Incertitudes," *Note EDF-MRI, reference H-T57-2013-02207-FR*, 2013.

[2] Airbus-EDF-IMACS-Phimeca, "Reference Guide - OpenTurns 1.7," 2016.

[3] B. SUDRET, "Uncertainty propagation and sensitivity analysis in mechanical models. Contributions to structural reliability and stochastic spectral methods," *Accreditation to supervise research report*, 2007.

[4] Y. CANIOU, "Global sensitivity analysis for nested and multiscale modelling. PhD thesis. Blaise Pascal University Clermont II France," 2012.

[5] G. CHASTAING, "Indices de Sobol généralisés pour variables dépendantes," 2010.

[6] M. GARCIA, "Sedimentation engineering : processes, measurments, modeling, and practice ASCE," 2008.

[7] C. GOEURY and N. GOUTAL, "Analyse de sensibilité et propagation d'incertitude dans les modèles numériques : Application à l'hydraulique," 2014.

[8] H. DELOUIS and P. CORDE, "Cours Fortran 95 - IDRIS," 2007.

[9] J. HERVOUET, "Hydrodynamics of free surface flows, Wileys," 2007.

[10] B. IOSS, "Revue sur l'analyse de sensibilité globale de modèles numériques," 2010.

[11] M. KADIRI-OTTMANI, "Traitement statistique d'un échantillon," *Technical report of CEA*, 2002.

[12] M. VAN ORMONDT, C. BRIERE, D.J.R. WALSTRA, L.C. VAN RIJN and A.M. TALMON, "FThe effects of bed slope and wave skewness on sediment transport and morphology," 2006.

[13] E. MEYER-PETER and R. MÜLLER, "Formulas for Bed-Load Transport," 2004.

[14] P. TASSI, M.I. MORELL and C.A VIONNER, "Flow pattern at a river diffluence at the alluvia system of the Paraná River," *Journal of Applied Water Engineering and Research*, 2014.

[15] R. ATA, C. GOEURY, P. LANG, J. DESOMBRE, J.M. HERVOUET, "TELEMAC MODELLING SYSTEM - Release 7.0 - USER MANUAL," 2014.

[16] P. TASSI and C. VILLARET, "SISYPHE USER'S MANUAL - Release 6.3 - USER MANUAL," 2014.

[17] P. WIBERG and J. SMITH, "Model for calculating bed load transport of sediment," *Journal of Hydraylic Engineering*, 1989.

[18] W. WU, "Depth-averaged two-dimensional numerical modeling of unsteady flow and uniform sediment transport in open channels," *Journal of Hydraylic Engineering*, 2004.

[19] W. WU and S. WANG, "Formulas for sediment porosity and settling velocity," *Journal of Hydraylic Engineering*, 2006.

The depth-averaged Mixing Length turbulence model for Telemac-2D

Clemens Dorfmann, Gerald Zenz
Institute of Hydraulic Engineering and Water Resources Management
Graz University of Technology
Stremayrgasse 10/II, 8010 Graz, Austria
clemens.dorfmann@tugraz.at

***Abstract*—In this paper the depth-averaged Mixing Length turbulence model and its implementation in Telemac-2D is presented. The new turbulence model is verified and validated by means of a laboratory experiment concerning the flow around a spur-dyke. The experiment is well suitable for testing the Mixing Length model since in the region of a groyne-like structure significant horizontal flow velocity gradients with possible recirculation flows prevail, which in turn have an influence on the turbulence production, the computed turbulent eddy viscosity and the resulting velocity distribution. Additionally to these laboratory measurements, the implemented Mixing Length model is compared to the depth-averaged *k-ε* turbulence model. The validation reveals the correct implementation of the turbulence model and its applicability for open channel flow computations.**

I. Motivation

In flows with high transverse velocity gradients, e.g. flows around structures, strong recirculation flows or flows in reservoirs, the influence of the horizontal velocity gradients on the turbulence production can be significant. In such cases the transverse shear may be the dominant turbulence generation mechanism in contrast to e.g. straight river applications where usually most of the river turbulence is generated by bed friction. Hence the main idea is to combine the depth-averaged parabolic eddy viscosity model with the Prandtl's mixing length theory for the horizontal in order to account for both the vertical and horizontal turbulence production. The resulting depth-averaged Mixing Length turbulence model forms a zero-equation turbulence model, which, as per this definition, doesn't account for any transport processes.

The main characteristic of the Mixing Length model implemented in Telemac-2D is that it accounts for the physical influence of the local horizontal velocity gradients on the turbulent eddy viscosity to be computed. The model yields or tends to the parabolic eddy viscosity model if the horizontal depth-averaged velocity gradients vanish or if the turbulence is mainly produced by bed friction, respectively.

II. Eddy Viscosity Concept In Telemac-2D

Telemac-2D solves the depth-averaged Saint-Venant equations in two dimensions (www.opentelemac.org). The turbulent diffusion by means of the depth-averaged Reynolds stresses appearing in the depth-averaged momentum equations are determined by the Boussinesq's eddy viscosity assumption [1]. This hypothesis assumes that, in analogy to the viscous stresses in laminar flows, the turbulent stresses are proportional to the mean velocity gradients or in other words, the momentum transfer caused by turbulent eddies can be modelled with an eddy viscosity. The turbulent eddy viscosity ν_t is not a fluid property but strongly depends on the local state of turbulence and may vary largely in time and space. The role of the turbulence model is to determine the turbulent viscosity ν_t and its spatial and time dependent distribution in a model domain.

III. The Depth-Averaged Mixing Length Model

In the depth-averaged Mixing Length model the total turbulent viscosity ν_t is split in a vertical component ν_t^V and a horizontal component ν_t^H [2]:

$$\nu_t = \sqrt{(\nu_t^V)^2 + (\nu_t^H)^2} \tag{1}$$

A. Calculation of the vertical eddy viscosity

The vertical eddy viscosity ν_t^V is computed by means of the depth-averaged parabolic eddy viscosity model in which the vertical viscosity is generated by bed friction. This model implies a perfect balance between hydrostatic pressure gradient and vertical shear stress. With the assumption of two-dimensional flow and a logarithmic velocity profile along the water depth the vertical eddy viscosity follows a parabolic profile along the depth. Starting with the Prandtl's Mixing Length hypothesis the eddy viscosity along the water depth $\nu_{t,z}$ is related to the mean velocity gradient and the mixing length:

$$\nu_{t,z} = l_m^2 \left|\frac{\partial u}{\partial z}\right| \tag{2}$$

where u is the mean flow velocity, z is the vertical coordinate and l_m is the mixing length. Assuming a logarithmic velocity profile the vertical velocity gradient is:

$$\frac{\partial u}{\partial z} = \frac{U^*}{\kappa z} \tag{3}$$

where U^* is the shear velocity and κ is the von Kármán constant equal to 0.4.

The mixing length distribution $l_m(z)$ along the water depth is given by [3]:

$$l_m(z) = \kappa z \sqrt{1 - \frac{z}{h}} \quad (4)$$

where h is the water depth.

Substituting (3) and (4) into (2) and integrating (2) over the water depth the depth-averaged vertical eddy viscosity ν_t^V is obtained as:

$$\nu_t^V = \frac{1}{h}\kappa U^* \int_0^h z\left(1 - \frac{z}{h}\right) dz = \frac{1}{6}\kappa U^* h = \alpha_t\, U^* h \quad (5)$$

The basic assumption of the depth-averaged parabolic eddy viscosity model is that in open channel flow the turbulence is mainly generated by bed friction in that the depth mean turbulent viscosity is correlated with the shear velocity U^* and the water depth h. The theoretical proportionality constant $\kappa/6 = \alpha_t$ in (5) is valid only for infinitely wide channels and doesn't account for anisotropic structures of turbulence in horizontal and vertical directions as well as for the transversal or longitudinal dispersion. So for most of the 2D depth-averaged applications this constant can be considered as too low. Elder [4] and later Fischer et al. [5] developed, based on the equation and experiments in laboratory channels and natural streams, dispersion equations for the transport of substances in natural streams and determined higher values for the proportionality constant α_t. Fischer et al. [5] propose that for transverse turbulent dispersion α_t is about 0.15 in laboratory channels and 0.6 in irregular natural streams with weak meanders. Wu et al. [6] compare five depth-averaged turbulence models in the simulation of flows around a spur-dyke, in a sudden-expanded flume and in two natural rivers. They apply values for α_t in from 0.6 to 1.0. Vionnet et al. [7] in turn, use in their numerical models values in the range of $\kappa/6$ to 0.3. Jia and Wang [8] employ in their 2D depth-averaged numerical model the coefficient $\alpha_t = A \cdot \kappa/6$ with A as calibration parameter for which they recommend values in the range of 1 to 10. Steffler and Blackburn [9] in the River2D model for α_t use a default value of 0.5 and indicate values from 0.2 to 1.0 as a reasonable range. As it can be seen from these elaborations the proportionality coefficient α_t has to be considered as a calibration coefficient. For the implementation in Telemac-2D the theoretical constant in (5) has been replaced by a selectable empirical calibration coefficient α_t (with $\alpha_t = 1/6\,\kappa \approx 0.067$ as default value).

B. Calculation of the horizontal eddy viscosity

The horizontal eddy viscosity ν_t^H is computed according to the Prandtl's mixing length theory by means of the depth-averaged horizontal mixing length l_m and the horizontal mean strain-rate tensor S_{ij}:

$$\nu_t^H = l_m^2 \sqrt{2 S_{ij} S_{ij}} \quad (6)$$

The horizontal mean strain-rate tensor S_{ij}

$$S_{ij} = \frac{1}{2}\left(\frac{\partial U_i}{\partial x_j} + \frac{\partial U_j}{\partial x_i}\right) \quad (7)$$

is computed by means of the depth-averaged velocity derivatives, written in Cartesian coordinates:

$$2 S_{ij} S_{ij} = 2\left(\frac{\partial U}{\partial x}\right)^2 + 2\left(\frac{\partial V}{\partial y}\right)^2 + \left(\frac{\partial U}{\partial y} + \frac{\partial V}{\partial x}\right)^2 \quad (8)$$

The depth-averaged mixing length l_m is calculated by integrating equation (4) over the water depth:

$$l_m = \frac{1}{h}\kappa \int_0^h z \sqrt{1 - \frac{z}{h}}\, dz = \frac{4}{15}\kappa h \quad (9)$$

Inserting (8) and (9) into (6) yields the horizontal turbulent viscosity ν_t^H due to horizontal shear:

$$\nu_t^H = \left(\frac{4}{15}\kappa h\right)^2 \sqrt{2\left(\frac{\partial U}{\partial x}\right)^2 + 2\left(\frac{\partial V}{\partial y}\right)^2 + \left(\frac{\partial U}{\partial y} + \frac{\partial V}{\partial x}\right)^2} \quad (10)$$

In (9) it is assumed that the mixing length l_m depends on the water depth h which restricts the size of the turbulent eddies. However the assumption l_m as a function of the water depth can lead to an underestimation of ν_t^H since l_m may be larger than the water depth [2]. The dependence of the mixing length l_m on the water depth can be seen as a weakness of the Mixing Length model. Hence for the implementation in Telemac-2D the theoretical constant $4/15\ \kappa$ in (10) has been replaced by a selectable empirical calibration coefficient C_l (with $C_l = 4/15\ \kappa \approx 0.107$ as default value).

The literature research regarding the use of the horizontal Mixing Length model and the related choice of the C_l coefficient in typical open channel flow simulations has not given that many results. Wu et al. [6] in the before mentioned four case studies for C_l use values from 0.16 to 0.48. Steffler and Blackburn [9] recommend a C_l coefficient of 0.1 as a typical value which corresponds to the theoretical coefficient. However they point out that depending on the type of flow the factor C_l may be adjusted. Stansby [10] validated a three-dimensional numerical model against the experimental data for shallow wakes of a conical island. He proposed a two-mixing-length, eddy-viscosity turbulence model with a vertical mixing length of classical Prandtl form and a horizontal mixing length. Stansby estimated the vertical mixing length l_v to be equal to $0.09h$ assuming a boundary layer thickness of $\delta = 0.2h$. He assumed the horizontal mixing length l_h to be a multiple β of the vertical mixing length l_v. Stansby tested this formulation for the replication of either eddy formation or stable wake. He reports good

predictions when using a β value equal to 6 which yields a horizontal mixing length l_m of about half the water depth with $C_l \approx 0.5$. Stansby in [11] reduced the 3D approach to the depth-averaged form and investigated the same case by means of a 2D depth-averaged numerical model. By using β equal to 6 the prediction of stable wakes was poor. However, when vortex shedding was prominent, the 2D and 3D model wake structures were similar. Chini and Stansby in [12] implemented the two-mixing-length eddy-viscosity turbulence model into the 3D numerical model Telemac-3D. They tested the model against two datasets. The first case was the flow around a conical island with associated wake patterns. The second case was the tidal flow around a headland. Based on Stansby's findings [10] a ratio of $\beta = 6$ between the horizontal mixing length and the vertical mixing length was applied. In both the case studies Telemac-3D combined with the two mixing length eddy viscosity model could replicate the experimental results. Apparently the approach proposed by Chini and Stansby [12] didn't find the way into an official release of Telemac-3D.

IV. The Depth-Averaged Mixing Length Model In Telemac-2D

The combination of the parabolic eddy viscosity model (5) and the horizontal Mixing Length model (10) yields finally the depth-averaged Mixing Length model implemented in Telemac-2D in which the eddy viscosity coefficient is composed of three components: a constant, a bed shear generated term and a transverse shear generated term:

$$\nu_t = \nu_{t,c} + \sqrt{(\alpha_t U^* h)^2 + \left[(C_l h)^2 \sqrt{2S_{ij}S_{ij}}\right]^2} \qquad (11)$$

where $\nu_{t,c}$ is the constant eddy viscosity coefficient (keyword: velocity diffusivity) with the default value in Telemac-2D of 1.E-6 m²/s.

Near the wall the damping effect of the wall on the turbulence may be important and thus the relation for the mixing length in (9) could produce too high turbulent viscosities in the wall region. For the mesh nodes near the wall instead of using the water depth as the length scale the distance from the nodes to the wall $dist_{wall}$ should be used. Two different approaches have been tested for the near-wall treatment, namely the method by Jia and Wang [8] and the method by Cea et al. [2]. Both the approaches compute almost identical turbulent viscosity values at the wall boundary nodes. Therefore as limiter for the mixing length $l_{m,w}$ at the wall boundary nodes the simpler method by Cea et al. has been kept:

$$l_{m,w} = min\, C_l(h,\, dist_{wall}) \qquad (12)$$

The Mixing Length model is activated in the steering file by the keyword TURBULENCE MODEL = 5. The calibration coefficients α_t and C_l may be changed in the subroutine mixlength.f.

V. Numerical Validation: Flow Around A Spur-dyke

The turbulence model implemented in Telemac-2D is verified and validated by means of a laboratory experiment concerning the simulation of the flow around a spur-dyke [13]. Rajaratnam and Nwachukwu [13] measured the flow velocities around a spur-dyke in a laboratory flume. The experiment is well suitable for testing the Mixing Length model since in the region of a groyne-like structure significant horizontal flow velocity gradients with possible recirculation flows prevail, which in turn have an influence on the turbulence production, the computed turbulent eddy viscosity and the resulting velocity distribution.

In the validation process it is not intended to perform a sensitivity analysis by varying some physical and numerical parameters with the objective of matching the experimental results. Additionally to the measurements, also the numerical results of the simulation with the depth-averaged k-ε turbulence model are compared. This laboratory experiment has been used as comparative test also by other depth-averaged numerical models like the CCHED2D model [8] and the Coastal Modeling System CMS [14].

A. Experimental setup

The experiments were conducted in a straight tilting rectangular flume with the dimensions: 37 m long, 0.91 m wide and 0.76 m deep. The test reach was located in the downstream half of the flume. Rajaratnam and Nwachukwu carried out 13 different experiments by varying the length or the shape of the spur-dyke, the water depth and the bed roughness. For the validation conducted here the experimental run A1 is used.

In experimental run A1 the spur-dyke was made by a 3 mm thin and 0.152 m long aluminium plate projecting perpendicular to the vertical side wall. The flow discharge was 0.0453 m³/s and the approach flow depth was 0.189 m. The flume bed and sides were hydraulically smooth. The flume was inclined to establish uniform flow conditions.

Rajaratnam and Nwachukwu measured the velocity profiles along four cross sections in the locations x/b = 2, 4, 6 and 8, with x starting at the spur-dyke station and b the spur-dyke length (0.152 m). The flow velocities were measured at two vertical levels z/h=0.03 and z/h=0.85. In the experiment the reattachment length of the eddy zone downstream of the spur-dyke was found to be approximately 12b.

B. Numerical setup

The computational domain covers 10 m of the flume length. A horizontal flume bed is assumed. The mesh consists of 8780 nodes and 17020 triangular elements with maximal edge lengths of 0.08 m. In the region of the spur-dyke and in the recirculation zone behind the structure a higher mesh resolution with minimal edge lengths of about 0.015 m is used. The spur-dyke is placed 4 m downstream of the inlet and perpendicular to the right wall.

Accordingly to the experiment at the upstream boundary an inflow discharge of 0.0453 m/³s and at the outflow boundary a constant flow depth of 0.189 m are specified. The

Strickler roughness coefficient is set to be equal to 90 $m^{1/3}/s$ for the whole domain. For the side walls a fully slip condition is applied. As advection scheme for the flow velocity the explicit MURD scheme is used. In the simulation with the k-ε turbulence model the method of characteristics is used for the advective transport of the turbulent kinetic energy k and the turbulent dissipation ε. In the case of the Mixing Length model the default values for α_t and C_l equal to 0.067 and 0.107, respectively, are applied. A simulation time step of 0.02 seconds is used and the simulation is run until a steady state flow field is reached.

C. Numerical results

The evaluation of the depth-averaged Mixing Length model is shown in Fig. 1 by means of the computed turbulent eddy viscosity ν_t. From a verification point of view the model doesn't produce any unphysical low or high spikes and the spatial distribution is reasonable. Near the spur-dyke where higher velocity gradients prevail the eddy viscosity is accordingly higher than in the surrounding area. Clearly visible is the operation of the limiter for the mixing length l_m in that the eddy viscosity is reduced near the side walls of the flume and the spur-dyke. The comparison with the k-ε turbulence model (Fig. 1) shows that both turbulence models in terms of the computed eddy viscosity behave quite differently. The Mixing Length model gives higher turbulent diffusion near the head of the spur dyke whereas the k-ε model gives much higher eddy viscosity values downstream of the spur dyke.

The numerical results in terms of velocity distribution and the location of the four cross sections are shown in Fig. 2. Both the turbulence models are able to produce the backward-flow region behind the groyne. The Mixing Length model computes a larger recirculation zone downstream of the spur-dyke compared to the k-ε model. In comparison to the measured reattachment length the Mixing Length model (deployed with the standard parameters) slightly overpredicts while the k-ε model underpredicts the recirculation length. In the other regions upstream and downstream of the spur-dyke both the turbulence models produce very similar velocity distributions, which confirms also the correct implementation of the depth-averaged Mixing Length model in Telemac-2D.

For the comparison of the measured velocity profiles with the Telemac-2D results the data measured at level z/h=0.85 are used. Fig. 3 shows the measured and the simulated velocities in x-direction in the four cross sections. The measured data reveal significant negative velocities near the wall and the maximum positive velocities arising just outside the shear layer in all the cross sections. In the main flow region the velocity distribution is almost uniform. Compared to the measurements both the turbulence models provide good predictions of the velocity distributions in the four cross sections. However the Mixing Length model performs better, especially in the cross sections x=6b and x=8b, where the k-ε model largely underpredicts the magnitude of the negative velocities near the wall. It also computes too low flow velocities in the main flow region where the Mixing Length model gives good results. For the quantitative assessment Table 1 lists the root-mean-square error (RMSE) between the measured and the simulated velocities in the four cross sections. The RMSE values show the almost similar performance of both the turbulence models in cross section x=2b. With increasing distance from the spur-dyke x=2b, 4b and 8b the RMSE indicates a considerably higher agreement between the Mixing Length model and the measurements.

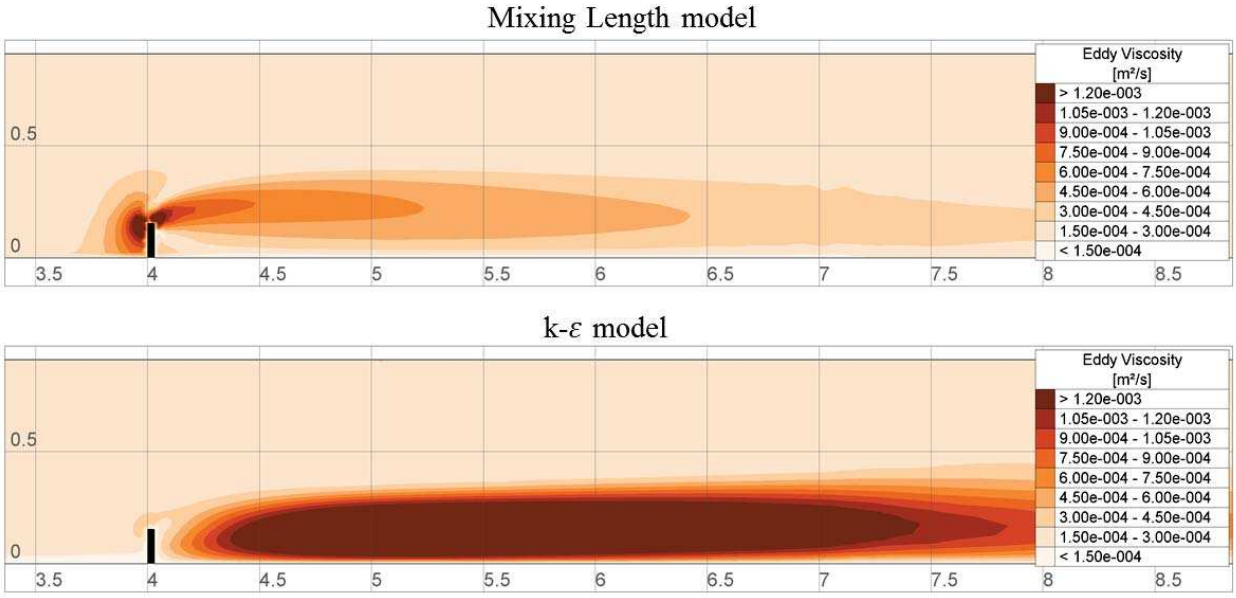

Figure 1. Plan view, computed turbulent eddy viscosities by the Mixing Length model and the k- ε model

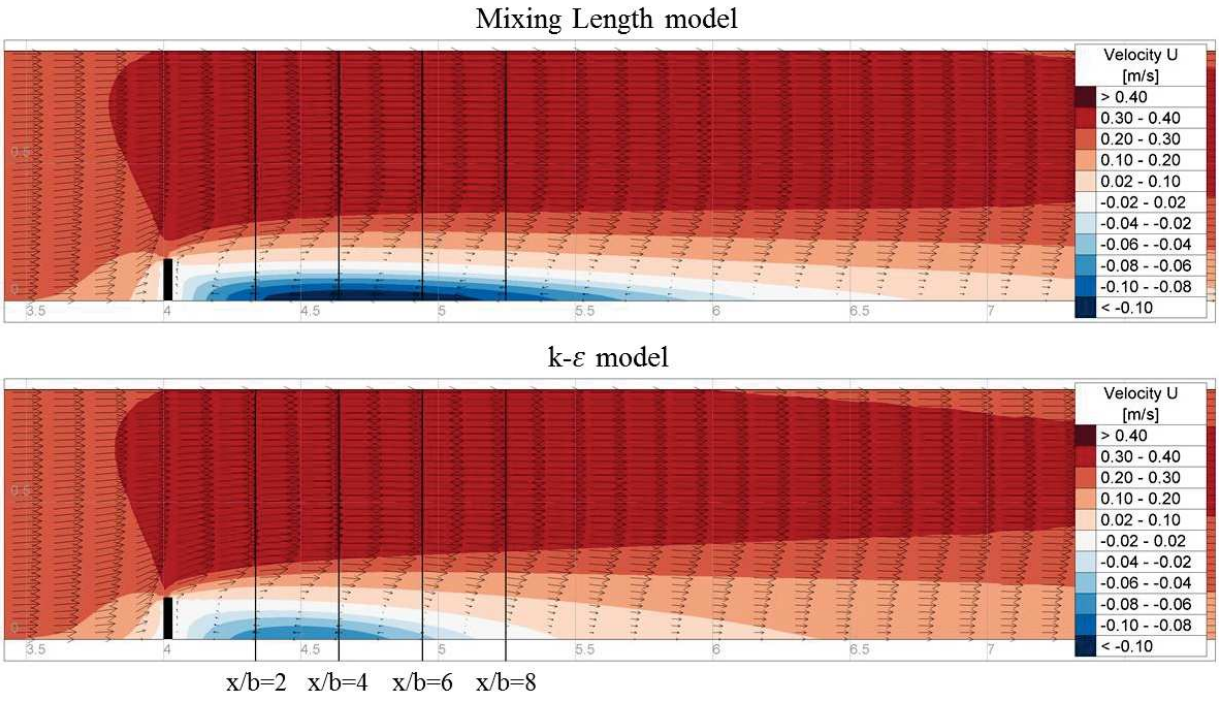

Figure 2. Plan view, computed flow velocities by the Mixing Length model and the k- ε model

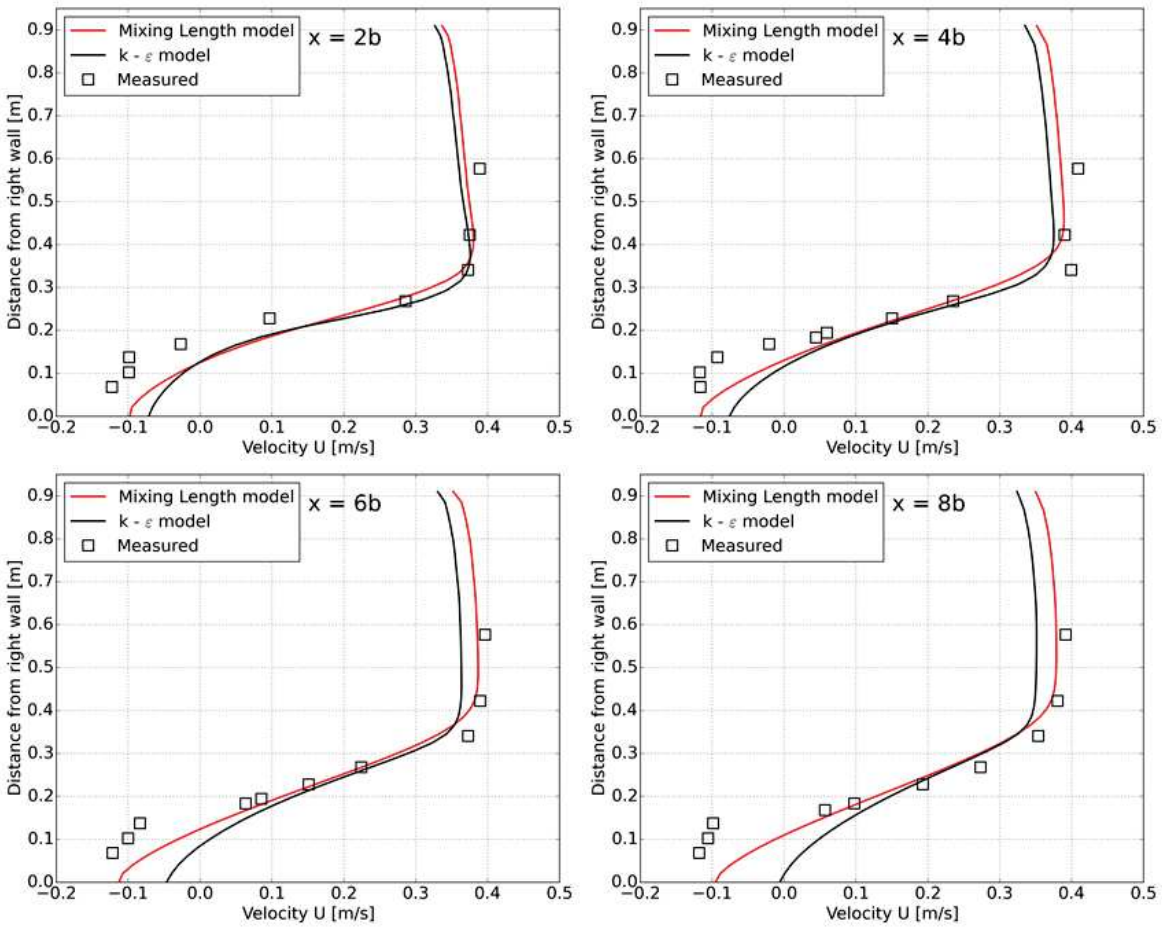

Figure 3. Comparison of the measured and calculated flow velocities in the cross sections x/b = 2, 4, 6 and 8

TABLE I. RMSE VALUES FOR THE K-ε MODEL AND THE MIXING LENGTH MODEL IN ´THE CROSS SECTIONS X/B = 2, 4, 6 AND 8

RMSE [m/s] Velocity U	**x = 2b**	**x = 4b**	**x = 6b**	**x = 8b**
***k*-ε model**	0.0687	0.0644	0.0710	0.0929
Mixing Length model	0.0658	0.0539	0.0470	0.0609

VI. CONCLUSION

This paper describes the depth-averaged Mixing Length turbulence model and its implementation into the open source 2D depth-averaged numerical model Telemac-2D. The zero-equation turbulence model combines the depth-averaged parabolic eddy viscosity model with the Prandtl's mixing length theory for the horizontal in order to account for both the vertical and horizontal turbulence production. The computed eddy viscosity is composed of three components, namely a constant, a bed shear generated term and a transverse shear generated term. Hence the main characteristic is that the turbulence model accounts for the physical influence of the local horizontal velocity gradients on the turbulent eddy viscosity to be computed. The model yields or tends to the parabolic eddy viscosity model if the horizontal depth-averaged velocity gradients vanish or if the turbulence is mainly produced by bed friction, respectively.

The depth-averaged Mixing Length model is verified and validated by means of a laboratory experiment concerning the flow around a spur-dyke and the comparison with the two-equation k-ε turbulence model. The validation reveals the correct implementation of the turbulence model and its applicability for open channel flow computations.

The Mixing Length model can be a viable alternative to the zero-equation turbulence models already available in Telemac-2D especially in cases where the transverse shear might be the dominant turbulence generation mechanism like in flows around structures or flows in reservoirs. The computations using the Mixing Length model are around 20% faster than with the k-ε model. However it should be remembered that the Mixing Length turbulence model, unlike the k-ε model, doesn't account for transport processes of turbulent quantities. In its depth-averaged form the proposed model, like the k-ε model, doesn't account for dispersive transport due to vertical non-uniformities of the mean flow velocities when using the theoretical coefficients emerging from the integration. Therefore depending on the type of flow these coefficients may be seen as tuning coefficients.

REFERENCES

[1] Hervouet J.-M., 2007. Hydrodynamics of Free Surface Flows: modelling with the finite element method. Wiley

[2] Cea L., Puertas J. and Vázquez-Cendón M.E., 2007. Depth Averaged Modelling of Turbulent Shallow Water Flow with Wet-Dry Fronts. Archives of Computational Methods in Engineering, 14, 303-341

[3] Nezu I. and Nakagawa H., 1993. Turbulence in Open-Channel Flows. IAHR Monograph, Rotterdam, The Netherlands

[4] Elder J.W., 1959. The dispersion of marked fluid in turbulent shear flow. Journal of Fluid Mechanics, 5(4), 544-560

[5] Fischer H.B., List J.E., Koh R.C.Y., Imberger J., Brooks N.H., 1979. Mixing in Inland and Coastal Waters. Academic Press, San Diego

[6] Wu W., Wang P. and Chiba N., 2004. Comparison of Five Depth-Averaged 2-D Turbulence Models for River Flows. Archives of Hydro-Engineering and Environmental Mechanics, 51, 183-200

[7] Vionnet C.A., Tassi P.A. and Martin Vide J.P., 2004. Estimates of flow resistance and eddy viscosity coefficients for 2D modelling on vegetated floodplains. Hydrological Processes, 18, 2907-2926

[8] Jia Y. and Wang S.S.Y., 1999. Numerical model for channel flow and morphological change studies. Journal of Hydraulic Engineering (ASCE), 125, 924-933

[9] Steffler P. and Blackburn J., 2002. River2D - User Manual, University Of Alberta

[10] Stansby P.K., 2003. A mixing-length model for shallow turbulent wakes. Journal of Fluid Mechanics, 495, 369–384

[11] Stansby P.K., 2006. Limitations of Depth-Averaged Modeling for Shallow Wakes. Journal of Hydraulic Engineering (ASCE), 132, 737-740

[12] Chini N. and Stansby P.K., 2014. MODELLING THE FLOW AROUND AN ISLAND AND A HEADLAND: APPLICATION OF A TWO MIXING LENGTH MODEL WITH TELEMAC3D. 34th Coastal Engineering Proceedings

[13] Rajaratnam N. and Nwachukwu B., 1983. Flow near groin-like structures. Journal of Hydraulic Engineering (ASCE), 109, 463-480

[14] US Army Corps of Engineers, 2011. Verification and Validation of the Coastal Modeling System, Report 3, U.S. Army Engineer Research and Development Center

Sensitivity Studies in the context of a complex 3D river model application using TELEMAC-3D

Constantin Schweiger

Institute for Hydraulic Engineering and Water Resources Management
(RWTH Aachen University)
Aachen, Germany

Sven Wurms, Rebekka Kopmann

Federal Waterways Engineering and Research Institute (BAW)
Karlsruhe, Germany

***Abstract*—Within the scope of Master Thesis a 3D-hydrodynamic-numerical model was built for a geometrical complex river section of the Middle Rhine using TELEMAC-3D. Besides the setup, calibration and validation of the model several sensitivity studies were conducted e.g. the influence of different models for turbulence and pressure. As the resilience of a visual comparison of the cross-sectional distribution of flow velocity is limited when there is a high similarity between different results, a quantitative evaluation method has been developed. It considers the sum of squared differences between measured and simulated results. The application of this method showed that in the case of a geometrical complex river section the use of the k-epsilon-model leads to better results than the combination of mixing length and Smagorinsky model. In areas with abrupt precipices, the non-hydrostatic model calculates more realistic flow patterns in the form of vertical eddies whereas the use of the hydrostatic pressure assumption leads to unrealistic streamlines that run parallel to the precipice and riverbed.**

I. INTRODUCTION

The model area contains the Middle Rhine between Oberwesel and St. Goar (Rhine-km 548.5 – 556.5). Within this river stretch several geometrical complex characteristics are located. Fig. 1 shows the model at Rhine-km 551.0. It is characterized by a 90° bend with a partly overflowing gravel bank and a sediment deposition in the fairway at the inner bend (*Jungferngrund*) as well as a big rock at the outer bend (*Tauber Werth*). The latter is problematic for the inland waterway transport as ships which drive upstream tend to drift to the centre of the fairway due to a transverse flow. Another critical area is the rocky deep channel.

An already existing Telemac-2D model of a larger stretch of the Rhine (Rhine-km 483.5 – 557.0) was assumed to not compute satisfying results for the section considered in this work. Thus, the setup of a TELEMAC-3D model was necessary.

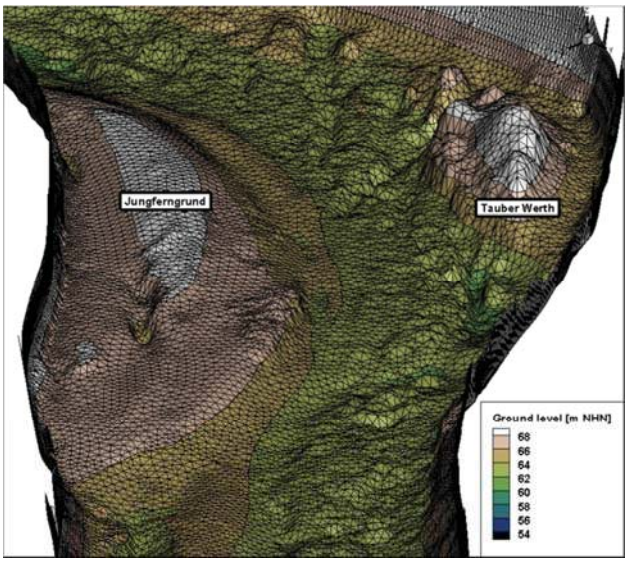

Figure 1 - Area of the Jungferngrund (Rhine-km 551.0) with the gravel bank at the inner and the rock at the outer bend (perspective: upstream)

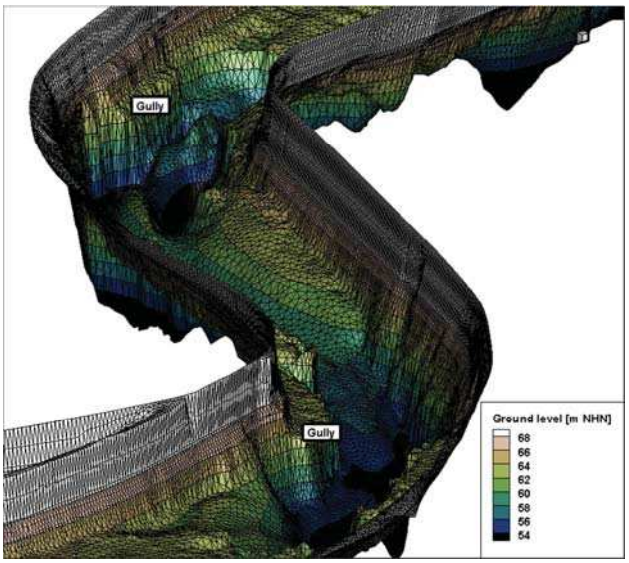

Figure 2 - Area of the deep channel (Rhine-km 552.0 – 554.5) with maximum depth of 12 m below the surrounding riverbed (perspective: upstream)

The computational grid from the existing TELEMAC-2D model was built on the basis of a digital terrain model (DTM) with a resolution of 0.5 x 0.5 m [1]. From that the computational grid for the relevant model area between Rhine-km 548.5 and 556.5 was generated.

II. MODEL SETUP

A. Relevant Model Parameters

The 3D model was built on the basis of the existing 2D model. Due to the smaller model extent, the computational grid was shorten. The result was an unstructured grid consisting of 92,000 nodes with a mean node distance of 5 meters. For the vertical discretization 10 equally spaced sigma-layers were chosen. This seems reasonable as vertical flow separations both near the surface and near the riverbed were expected due to the heterogeneous geometry. For the same reason, the non-hydrostatic model for pressure was selected. In this case, the TELEMAC-Code solves the Navier-Stokes (NS) equations for all three velocity components (*U*, *V* and *W*) [2]. On the contrary, only *U* and *V* are calculated with the NS equations using the hydrostatic pressure assumption. Afterwards, the vertical velocity component W is obtained from the 3D-continuity equation and *U* and *V* are being unchanged [3]. For turbulence modelling, the k-epsilon model was selected. With time steps around 1 s the solver could not reach convergence for the diffusion of k-epsilon. Thus, a smaller time step of 0.1 s was necessary. As a steady state was reached after 4 h, the total simulation time was set to 5 h (180,000 time steps).

Regarding the boundary conditions (BC) a discharge was set at the inflow and an associated water level at the outflow. To reduce the simulation time, a previous computation file was used. It was generated on the basis of an earlier conducted simulation with constant viscosities. Additionally, a turbulent kinetic energy *k* profile, which was assumed at the inflow boundary, guaranteed a fully developed turbulent flow regime in the area of investigation starting at Rhine-km 550.5.

For the study measurements of the water level along the river stretch and measurements of the flow velocity at defined cross sections using an *Acoustic Doppler Current Profiler* (ADCP) were available. Furthermore, a database with discharges obtained from measured water levels along the Rhine served as a data basis. For calibration a low water discharge of Q1 = 907 m³/s and a discharge of Q2 = 2025 m³/s, both at the gauging station Kaub, were used. The latter is in the order of the effective discharge in terms of the annual sediment load. With a mean water discharge of Q3 = 1610 m³/s the model was validated. The model area and the 18 cross sections are illustrated in (Fig. 3). An overview of the relevant model parameters is given in Table 1.

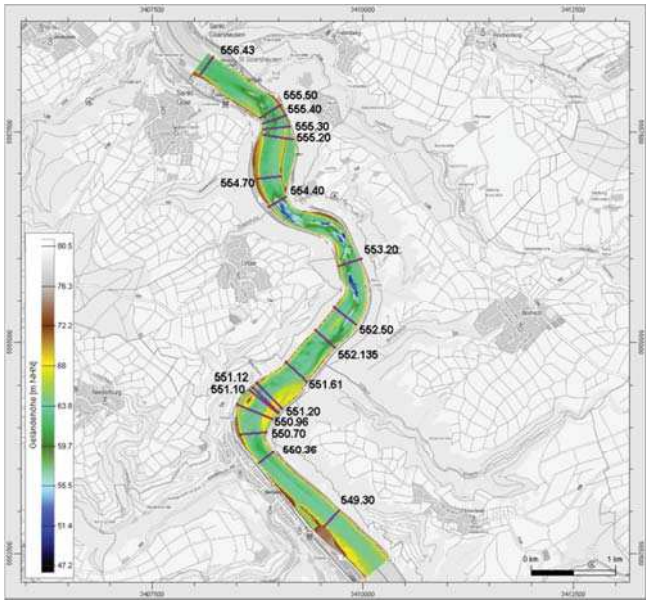

Figure 3 - Model area (Rhine-km 548.5 – 556.5) and cross sections where ADCP measurements were conducted

Table 1. Model preferences

Parameter	Value
number of nodes mean horizontal node distance	92,000 5 m
boundary conditions - inlet - outlet	 Q1 = 907 m³/s (Cal1); Q2 = 2025 m³/s (Cal2) H1 = 65.70 m; H2 = 67.58 m
vertical discretization	10 equidistant sigma layers
time discretization - time step - number of time steps	 0.1 s 180,000
friction data	skin friction and form roughness (Nikuradse friction law)
turbulence model	k-epsilon (horizontal & vertical)
equations	Navier-Stokes equation with non-hydrostatic model

For the Nikuradse friction law the equivalent roughness coefficient corresponds to the sum of the skin friction of the sediment and the form roughness of the river bed. The skin friction varies between the d_{50} and the d_{90} of the grain size distribution. The form roughness is obtained from the standard deviation of the bed level. From high-resolution measurements of the bed level the standard deviation was computed for each node considering all measurements inside the node patch weighted by distance. The benefit of

this method is the consideration of local heterogeneities of the bottom which are smaller than the resolution of the mesh. As the river stretch is characterized by a highly heterogeneous bedrock, the use of spatially differentiated roughness coefficients is required.

B. Calibration and Validation

The model was calibrated by gradually adapting the roughness coefficients to match the measured event-related water levels Hereby it was possible to calibrate the model for both calibration discharges with just one friction data set. The differences between the simulated and measured water levels along the river stretch are within a range of ± 5 cm which corresponds with accuracy of the measured data except some outliers. In terms of validation a similar accuracy could be reached except for the region between Rhine-km 554.0 and 555.5 (Fig. 4). Inaccuracies of measurements could be a possible explanation: Typically, measured water levels of different discharges are parallel shifted. This is not true for the validation discharge in the section with the big differences

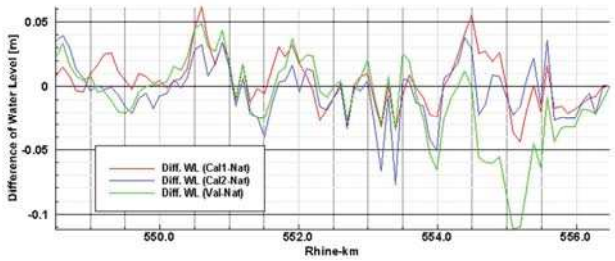

Figure 4 - Differences between simulated and measured water levels along the river stretch for the calibration and validation discharges

III. QUANTITATIVE EVALUATION METHOD

The analyses of the cross-sectional distribution of flow velocities is a suitable method to compare either measured data with the results of a simulation or results of different simulations among each other. A common way is a visual comparison of the velocity fields. The resilience of this approach is limited as soon as there is a high similarity between the different results or in the case of a heterogeneous distribution of flow velocities. This circumstance led to the development of a quantitative evaluation method which is able to locate areas with a high/low agreement. In the following, the relevant steps for the comparison of measured and simulated data at a cross section are described (see also [4]).

1. Extraction of the simulation data using the discrete points of the measurement (Fig. 5). Projection on a 100 x 100 raster so that the cross sections of the measurement and the simulation match exactly in position.

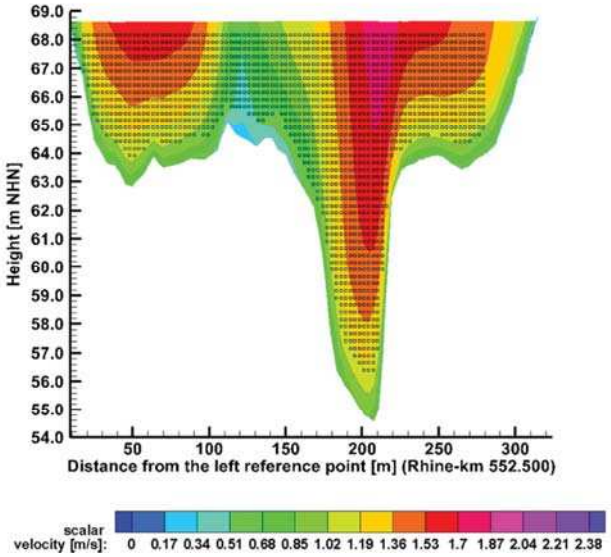

Figure 5 - Extraction of the simulation data

2. Calculating the squared differences between the measured and calculated flow velocities of the congruent area.

$$\Delta^2 = \left(v_{i,Mes} - v_{i,Sim}\right)^2$$

3. Dividing each cross section into a constant number of fields (here 54). Calculation of the mean flow velocity of the measured data individually for each field as well as the sum of the squared differences. The latter is normalized by the individual sum of discrete points within each field (Fig. 6)

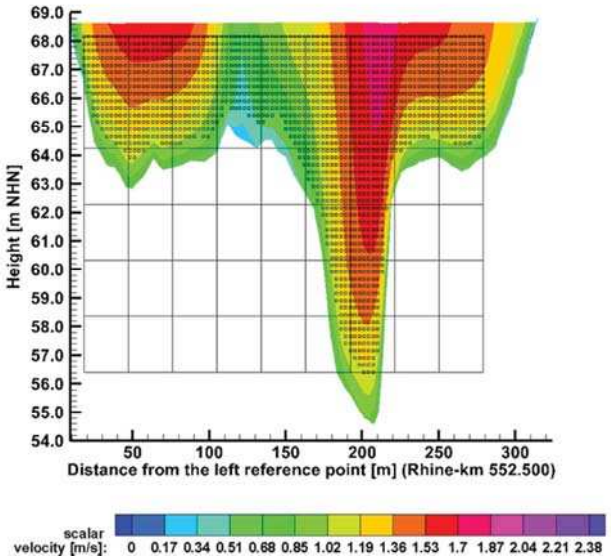

Figure 6 - Extraction of the simulation data

4. Classification of rating categories in each field: According to the accuracy of an ADCP measurement of 4 % for single values and higher flow velocities [5], the first category is equivalent to a deviation of 4 % of the calculated mean flow velocity of the measured data

Figure 7 - Rating categories and corresponding colouring

5. Comparison of the sum of squared differences with the rating categories and assignment of the corresponding colouring (Fig. 8).

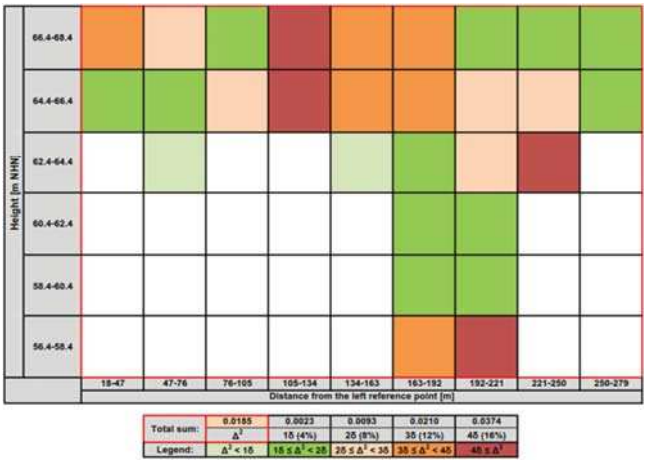

Figure 8 - Final result of the quantitative evaluation method for Rh-km 552.5

Using this method, areas with a low or a high agreement with the measured data are coloured in orange/red or green respectively. The *total sum* of the squared differences enables the comparison of different simulation results for one cross section (Fig. 8, bottom). In terms of interpretation, the following aspects have to be considered

- Each cross section is always divided into (here) 54 fields. Thus, the number of discrete points per field as well as its dimensions varies with the dimensions of the cross section.
- As the measured data is extrapolated in the area of the riverside, the result of the quantitative evaluation method should not be over-interpreted near the riverside.
- The squared differences are calculated in the case the measured and the simulated velocities are not zero. As soon as there is one discrete point within a field unequal to zero, the results will be compared. Thus, the result of the quantitative evaluation method in a field located at the edge can be based on a low amount of discrete points.
- The rating values (δ) differ from cross section to cross section due to the varying mean flow velocity. Thus, different simulation results can only be compared for the same cross section. For the same reason, the total sums of the squared differences of different simulations are only comparable for the same cross sections

IV. SENSITIVITY STUDIES

Within the scope of the sensitivity studies the influences of several parameters on the flow field were investigated. For comparing the results, representative cross sections along the model stretch were selected. Among others, the following parameters were considered in the sensitivity study:

- Horizontal discretization: refinement of the mesh
- Turbulence model: combination of mixing length model & Smagorinsky model
- Equations: hydrostatic pressure assumption

A. Calibration and Validation

To investigate the influence of the discretization, the existing grid was horizontally refined resulting in a mean node distance of 2.5 m. The refinement leads to a significant increase of the simulation time by a factor of 3.3 (from about 7 h to about 23 h). Nevertheless, the refinement shows its benefit of a more detailed flow pattern in areas of shear zones e.g. in the location of the deep channel.

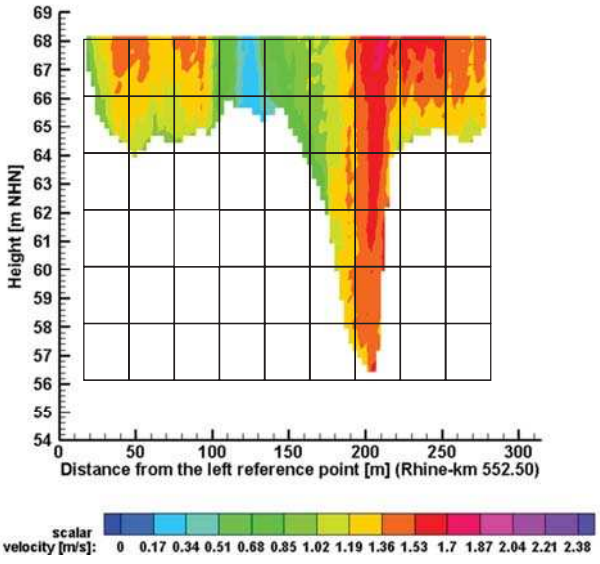

Figure 9 - Cross-sectional distribution of flow velocity of the ADCP measurement at Rhine-km 552.5

Fig. 9 shows the measured cross-sectional distribution of flow velocities at Rhine-km 552.5. Upstream of this cross section there is a large rock located in the centre of the river. It leads to a separation of the flow and therefore to a shear zone in the area of the confluence at Rhine-km 552.5, 125 m from the left reference point (Fig. 9).

The same cross section is extracted from both of the simulation results using the reference grid and the refined grid (Fig. 10). Concerning the shear zone, the visual comparison of the two figures is practicable and shows that the refinement results in a higher agreement with the measurement regarding the flow velocities.

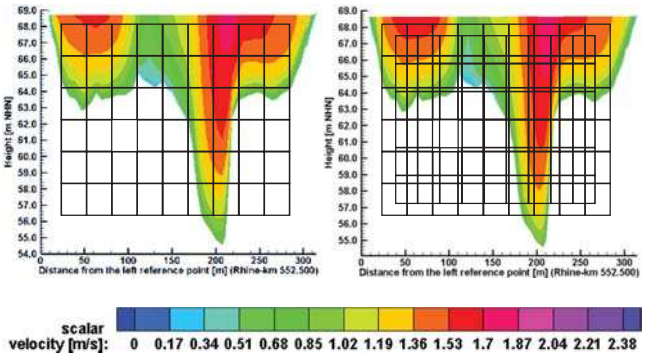

Figure 10 - Cross-sectional distribution of flow velocity using the reference grid (left) ant the refined grid (right) at Rh-km 552.5

However, a visual comparison of the different distributions of flow velocities is not reliable for the main part of the cross section. Thus, the quantitative evaluation method is used. The results are given in Fig. 11 and Fig. 12

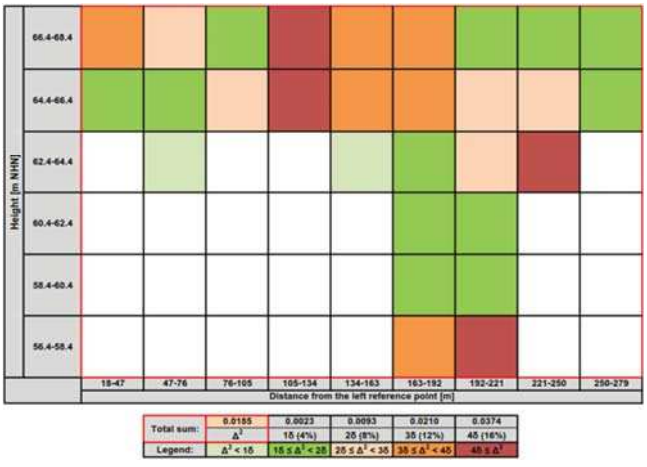

Figure 11 - Quantitative evaluation method for the simulation using the reference grid at Rhine-km 552.5 with a total sum of 0.0185

Figure 12 - Quantitative evaluation method for the simulation using the refined grid at Rhine-km 552.5 with a total sum of 0.0038

The quantitative evaluation method shows clearly that the refinement results in a better computation of the flow velocities. Especially in the area of the shear zone (76 to 134 m ftl) as well as in the area of the maximum flow velocities near the surface (163 to 250 m ftl) the simulation matches better with the measured data. The total sum (Δ^2) proofs the better result due to the refinement as Δ^2 decreases from 0.0185 to 0.0038.

On the contrary, the application of the quantitative evaluation method at Rhine-km 551.12 (downstream of the *Tauber Werth*) shows that the refinement of the grid only leads to slightly better agreement with the measured flow velocities. The reference simulation has a total sum of 0.0273 (Fig. 13). Due to the refinement, the total sum is decreased to 0.0161 (Fig. 14).

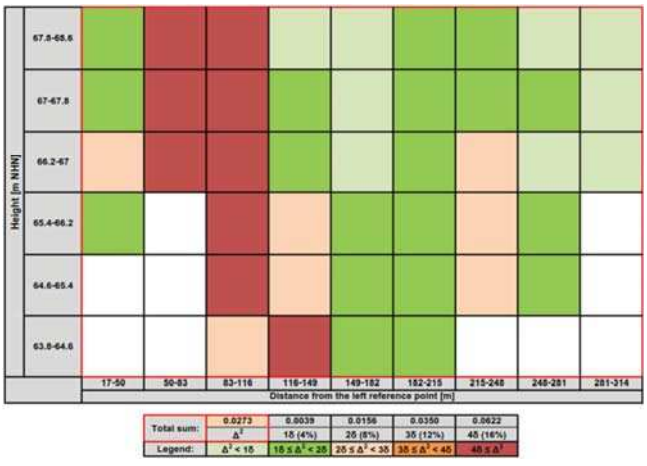

Figure 13 - Quantitative evaluation method for the simulation using the reference grid at Rhine-km 551.12 with a total sum of 0.0273

Figure 14 - Quantitative evaluation method for the simulation using the refined grid at Rh-km 551.12 with a total sum of 0.0161

As the refinement of the entire grid leads to an increase of the simulation time by a factor of 3, only the local refinement of the grid is useful ue to less computational effort on the one hand and better results in areas of interest on the other hand.

B. *Turbulence Model*

Concerning turbulence modelling, the influence of the mixing length model by Nezu and Nakagawa for vertical direction in combination with the Smagorinsky model for horizontal direction was investigated. The k-epsilon model describes the transport of kinetic turbulence and dissipation with two differential equations.

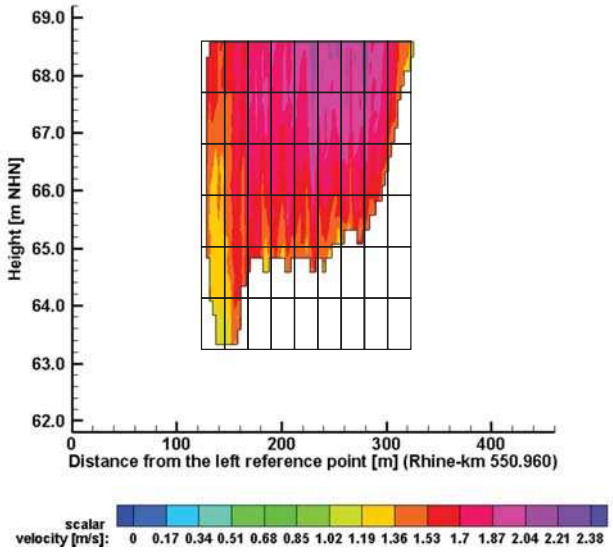

Figure 15 - Cross-sectional distribution of flow velocity of the ADCP measurement at Rh-km 550.96. The black mesh indicates the area where the quantitative evaluation method is applied

The mixing length model and the Smagorinsky model are only algebraic models and need therefore less computation time. The differences between the turbulence models are most distinctive in zones of highly turbulent flow. For further information, see [2].

To enable a reliable comparison of the velocity distribution, the model was recalibrated using the mixing length model to have an almost equal water level compared to the simulation using the k-epsilon model.

The calibration showed that the mixing length model is more sensitive to the roughness coefficients. In addition, the use of the mixing length model enables a time step of 1 s which leads to a significant reduction of the simulation time to 18 min (factor 24).

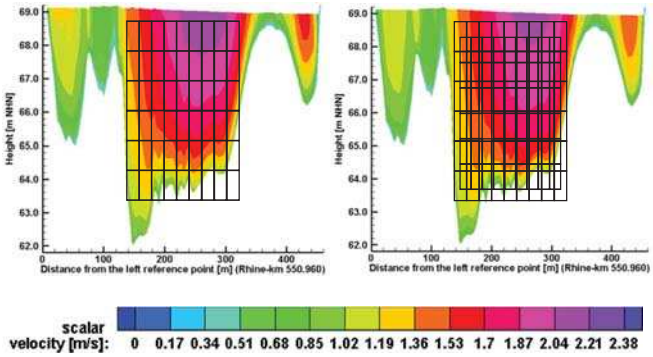

Figure 16 - Cross-sectional distribution of flow velocities using the k-epsilon model (left) and the mixing length model (right)

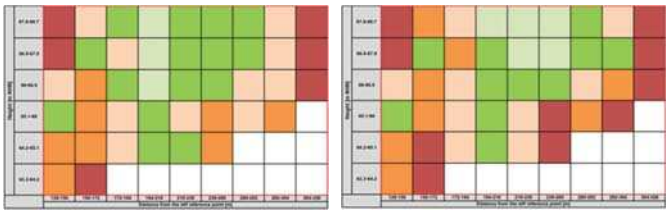

Figure 17 - Quantitative evaluation method for the simulation using the k-epsilon model (left) (total sum of 0.0334) and the mixing length model (right) (total sum of 0.0406) at Rhine-km 550.96

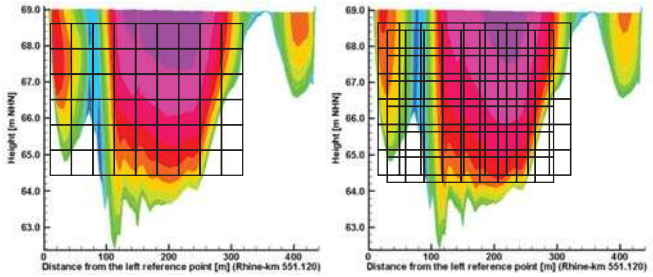

Figure 18 - Cross-sectional distribution of flow velocity using the k-epsilon model (left) ant the mixing length model (right) as well as the area of investigation at Rhine-km 551.12

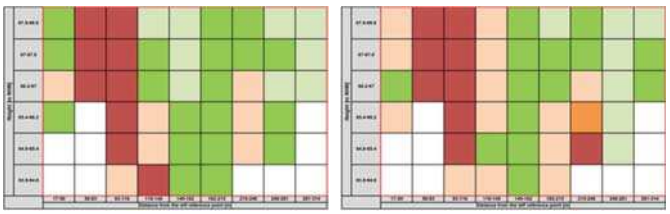

Figure 19 - Quantitative evaluation method for the simulation using the k-epsilon model (left) (total sum of 0.0273) and the mixing length model (right) (total sum of 0.0289) at Rhine-km 551.12

The comparisons of the distribution of flow velocities at different cross sections show that the k-epsilon model is more qualified for the river section considered in this work. Although the use of the mixing length model enables a time step of 1 s and, hence, reduces the simulation time significantly, the use of the k-epsilon model is sensible due to the heterogeneous geometry resulting in a highly turbulent flow pattern. This is justifiable as the k-epsilon model leads to a higher agreement with the measured data which is proofed by the quantitative evaluation method.

C. Pressure Assumption

Using the hydrostatic pressure assumption, the vertical velocity component *W* is obtained from the 3D-continuity equation. As the vertical velocity component has a significant influence on the current in the presence of a heterogeneous geometry, differences between the two pressure models must occur in structural complex river sections. At first, the resulting water levels are compared (Fig. 20).

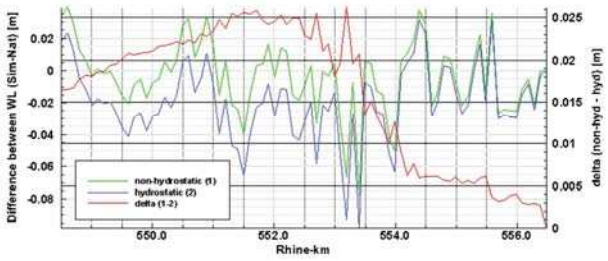

Figure 20 - Differences between simulated and measured water level as well as their difference

The differences between the water levels of the two pressure models vary between 0 and 2.5 cm. Especially in the area of the gully the hydrostatic mode leads to a lower water level. This indicates the presence of highly turbulent flow processes that cannot be computed with the hydrostatic pressure assumption in detail. As this special river section is characterized by the presence of abrupt precipices, a further investigation is conducted. In this context, a longitudinal section in the area of the deep channel (approximately Rh-km 553.5) is investigated as shown in Fig. 21.

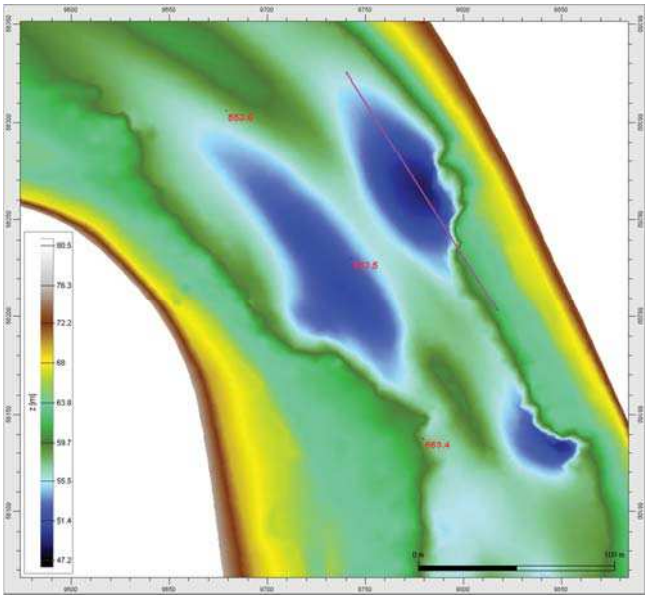

Figure 21 - Resulting 2D-streamlines using the hydrostatic (left) and the non-hydrostatic (right) pressure assumption

The bottom drops from about 62 m NHN to less than 50 m NHN on a distance of 20 m in flow direction. To detect differences between the two pressure models, vertical 2D slices are extracted from both of the simulations and streamlines are visualized afterwards (Fig. 22).

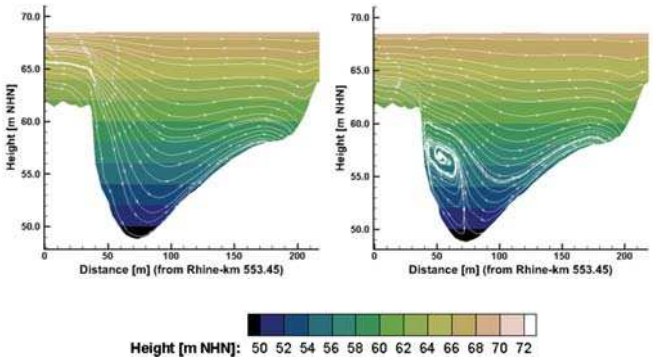

Figure 22 - Area of investigation at Rhine-km 553.5

The use of the hydrostatic pressure assumption results in implausible streamlines that run parallel to the precipice and the riverbed (Fig. 22, left). The non-hydrostatic pressure mode leads to a more realistic flow pattern. Due to the abrupt precipice, a vertical flow separation in the form of an eddy is computed (Fig. 22, right) as expected. In addition, the difference concerning the simulation time is marginal as the non-hydrostatic mode requires 7 h 15 min and the hydrostatic pressure assumption 7 h. Thus, the use of the former is advisable in the presence of a highly heterogeneous geometry.

V. CONCLUSIONS

Due to the heterogeneous bed of the river stretch between Rhine-km 548.5 and 556.5, a 3D-hydrodynamic-numerical modal was built to examine the resilience of an existing 2D model of the river stretch. The model was successfully calibrated and validated within the range of the low water discharge and the effective discharge by successively adapting the friction coefficients. The differences between the measured and the simulated water levels rage between the measurement accuracy of ± 5 cm. In Addition, there is a high agreement between the measured and the simulated distributions of flow velocities. In the context of sensitivity studies, a quantitative evaluation method was developed as the reliability of a visual comparison of the distribution of flow velocities is limited as soon as there is a high similarity between the results of different simulations. Applying this method to the results of the sensitivity studies shows that the refinement of the grid in areas of interest is useful due to the better computation of special flow characteristics e.g. in the presence of shear zones. As the refinement of the entire model leads to an increase of the simulation time by a factor of 3, only a local refinement of the grid is advisable.

In terms of turbulence modelling, the use of the k-epsilon model results in a higher agreement with the measured data compared to the use of the mixing length model. The quantitative evaluation method proofs that the k-epsilon model results in a better calculation of the flow pattern at the representative cross sections at Rhine-km 550.96, halfway of the 90°-bend, and at Rhine-km 551.12, downstream of the Tauber Werth. However, the use of the mixing length model leads to adequate results so that this model is applicable in case of river sections with a more homogenous riverbed.

The use of the non-hydrostatic pressure mode has no significant influence on the simulation time and is sensible as soon as there are abrupt precipices. One example is the area of the deep channel where a vertical flow separation in the form of an eddy is computed. The hydrostatic pressure assumption results in implausible streamlines that run parallel to the precipice and riverbed. Besides, the simulated water level is up to 2.5 cm lower than the measured water level. The maximum difference occurs in the area of the deep channel which is characterized by a highly turbulent flow regime. Therefore, the presence of vertical flow processes with a significant influence of the vertical velocity component W is plausible and, hence, requires the calculation of W with the NS-equation.

REFERENCES

[1] German Federal Institute of Hydrology (BfG), “Erstellung eines Digitalen Geländemodells der Gewässersohle des Mittelrheins.“, German Federal Institute of Hydrology (BfG), Koblenz, 2012.

[2] Hervouet J.-M., “ Hydrodynamics of Free Surface Flows, modelling with the finite,element method”, J. Wiley & Sons Ltd, West Sussex, England, 133 pp., 2007.

[3] Hervouet J.-M., “Solving non-hydrostatic Navier-Stokes equations with a free surface”, Laboratoire National d’Hydraulique et Environment (LNHE), France, 2003.

[4] Schweiger, C., “Setup and calibration of a numerical 3D flow model for sensitivity studies at the River Rhine between Oberwesel and St. Goar”, Master Thesis at Institute of Hydraulic Engineering and Water Resources Management, RWTH Aachen University, Aachen, Germany, 2016.

[5] Morgenschweis, G., “Hydrometrie. Theorie und Praxis der Durchflussmessung in offenen Gerinnen“, Springer, Berlin, Germany, 40 pp., 2010

2D and 3D numerical study of the Montevideo Bay hydrodynamics and fine sediment dynamics

Pablo Santoro
Instituto de Mecánica de los Fluidos
e Ingeniería Ambiental
Universidad de la República
Montevideo, Uruguay
Email: psantoro@fing.edu.uy

Mónica Fossati
Instituto de Mecánica de los Fluidos
e Ingeniería Ambiental
Universidad de la República
Montevideo, Uruguay
Email: mfossati@fing.edu.uy

Pablo Tassi
Saint Venant Laboratory for Hydraulics
EDF R&D
Chatou, France
Email: pablo.tassi@edf.fr

Nicolas Huybrechts
Roberval Laboratory, LHN (UTC)
CEREMA
Compiègne, France
Email: nicolas.huybrechts@cerema.fr

Damien Pham Van Bang
Saint Venant Laboratory for Hydraulics
CEREMA
Chatou, France
Email: damien.pham-van-bang@cerema.fr

Ismael Piedra-Cueva
Instituto de Mecánica de los Fluidos
e Ingeniería Ambiental
Universidad de la República
Montevideo, Uruguay
Email: ismaelp@fing.edu.uy

***Abstract*—This work has two main objectives, firstly the effect of the consolidation process on the bed evolution and fine sediment dynamics of the Río de la Plata estuary are explored. Secondly, the implementation of a high resolution 3D wave-current-sediment transport model to simulate the flow field and sediment transport processes of the Río de la Plata estuary and more specifically at Montevideo Bay area. We used a previously implemented 2D wave-current-sediment transport model. The consolidation model was calibrated by settling column experiments results, and good agreement was found between measured vertical bed density profiles in the Montevideo Bay area and the model results. Regarding the second objective, it is presented here the main characteristics of the 3D model implementation and a sensitivity analysis to different hydrodynamics and sediment transport parameters. In particular it is analysed the model response under different erosion-deposition paradigms.**

I. Introduction

Montevideo Bay hosts the main port of Uruguay along with a large industrial development. Nowadays there are many maritime engineering projects in the area, including the construction of new breakwaters, land reclamation for container terminals, navigation channels deepening, etc. All these projects need a reliable characterization of the hydrodynamics in the area and also for some of them the sediment dynamics. Numerical modelling is a powerful tool in that sense, not only for the design of these projects but also to assess their impact on the whole area.

A two-dimensional depth-averaged circulation, wave, sediment transport and bed evolution model was successfully implemented for the Río de la Plata focusing on the Montevideo coastal area [22]. Based on the open source TELEMAC-MASCARET Modeling System (TMS), it was possible to address the simulation of both the tidal and wave hydrodynamics, fine sediment transport and bed evolution with a single code. Using a single mesh for all the modules (TELEMAC2D-TOMAWAC-SISYPHE), and taking advantage of its non-structured nature, it was possible to provide high-resolution results in areas of complex geometries. The model was calibrated and validated using data of sea surface elevation (SSE), currents, waves, and suspended sediment concentration (SSC) in several stations. The obtained results show good agreement with the measured data, representing satisfactorily the main features of the Río de la Plata dynamics [22]. In this work we use this two-dimensional model to explore the effect of the mud consolidation process on the model results.

Even though good results were obtained with the 2D model regarding the hydrodynamic and fine sediment dynamics in the Río de la Plata, a three-dimensional approach allows to represent in more detail the sediment transport and stratification processes in this estuarine environment. The previous experience generated during the implementation of the 2D model paved the way for the three dimensional modules implementation. In this article we briefly describe the main characteristics of the modules set up and then present results from different sensitivity analysis with the circulation and sediment transport modules.

II. Study Area

The Río de la Plata is located on the east coast of South America. Its axis runs from NW to SE and is approximately 280 km long. Its surface area is approximately 35,000 km^2, and its width varies from 20 km at the innermost part to approximately 220 km at its mouth (Figure 1a). The river communicates freely with the ocean and experiences seasonal freshwater discharge from its two major tributaries (the Paraná and Uruguay rivers), with annual average discharge of approximately 16,000 m^3/s and 6,000 m^3/s, respectively. Two main regions can be identified based on the morphology and dynamics of the Río de la Plata. A shallow area located along the Punta Piedras-Montevideo line separates the inner region from the outer region. The inner region has a fluvial regime, with no stratification or preferential flow direction. In the outer region, the increase in river width generates complex flow patterns. This outer region is formed by brackish waters of

variable salinity that are influenced by the tides, the winds, and the contribution of fresh water from the river basin.

The tidal regime is dominated by the M2 component, followed by the O1 component which is responsible for the diurnal inequality. The tidal amplitude is greater along the Argentinean coast (order of 1 m), while it is about 0.4 m along the Uruguayan coast. The meteorological tide (storm surge events) is of great importance being of the same order of magnitude as the astronomical tide [23]. Currents at the estuary are controlled by the oceanic tide. Although the amplitude of the tides is small, the very large estuary mouth generates a tidal prism that can dominate the flow regime despite the significant discharge received from the tributaries.

The outer Río de la Plata and the adjacent continental shelf are covered with sands, while silty clays, clayey silts and silts, are confined to the upper and the middle portions of the estuary. The suspended sediment load is mainly carried by the Paraná river in amounts up to 160 million tons/year of fine sand, silt, and clay. Fine sands mostly settle in the innermost part of the Río de la Plata and are responsible for the Paraná Delta Front progradation [13]. Fluvial fine cohesive sediments are further advected to the inner part of the estuary.

Montevideo Bay covers an area of approximately 12 km^2 and is part of the Río de la Plata (Figure 1c). The water depth reaches 5 m in the outer part of the bay and between 1 m and 1.5 m in the inner area. The navigation channels are approximately 11 m deep. The bay receives two urban streams, Pantanoso and Miguelete. Water circulation in the bay mainly occurs due to the sea level variations along the bay mouth and due to shear induced by the outer flow and the local winds.

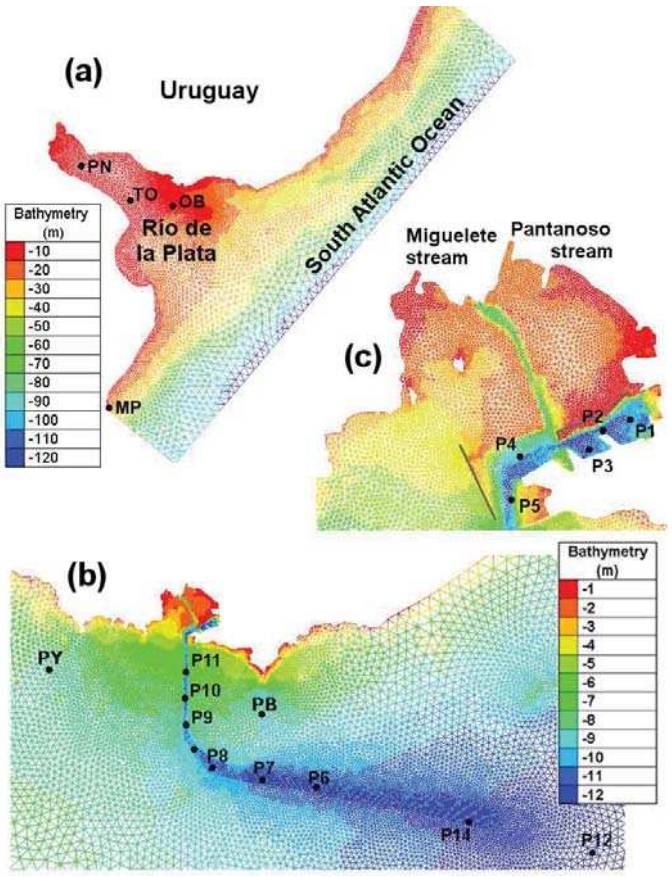

Fig. 1: (a) Río de la Plata unstructured mesh, (b) detail of Montevideo coastal area, (c) Montevideo Bay detail.

III. 2D HYDRODYNAMIC AND SEDIMENT TRANSPORT MODELLING: INFLUENCE OF THE CONSOLIDATION PROCESS

A consolidation model was chosen among the available options in the sediment transport model. The model was calibrated against settling column experiment results. A set of simulations was performed in order to initialize the bed and explore the impact of different erosion parameters configurations on the results. Finally a two years simulation including the consolidation process was performed and the results are compared against the ones obtained without considering this process.

A. Consolidation multilayer algorithm

Three different consolidation models are implemented in SISYPHE [26] [29]: multi-layer empirical algorithm, multi-layer iso-pycnal Gibson's model and vertical grid Gibson's model. We decided to use the second one as it has more physical meaning than the first one, and is less expensive from the computational point of view and more stable than the third one [29].

The consolidating muddy bed is discretized in layers of increasing concentrations, these concentrations being constant and imposed by the user. The determination of mass fluxes between consecutive layers is based on the Gibson's theory. This 1DV sedimentation-consolidation "multi-layer" model is based on an original technique to solve the Gibson equation, developed in [27]. Like in the previous model the concentration of different layers are fixed, the associated thicknesses are directly linked to the amount of sediment that they contain. The mass balance in layer i is:

$$\frac{M_i(t+\Delta t) - M_i(t)}{\Delta t} = F_i(t) - F_{i+1}(t) \tag{1}$$

where M_i is the mass of sediment in layer i, Δt the model time step, and F_i the sediment flux from the layer i to layer $i+1$.

As the model assumes the concentration of each layer to be constant over time, only the masses and thicknesses of these layers vary. The mass balance can be written in terms of the thicknesses of layers $Ep_i(t)$ (Figure 2) as follows:

$$Ep_i(t+\Delta t) = Ep_i(t) + \frac{(F_i(t) - F_{i-1}(t))\,\Delta t}{C_i} \tag{2}$$

As explained in [27] the sediment flux $F_i(t)$ can be written as:

$$F_i(t) = \frac{(V_{s,i}(t) - V_{s,i-1}(t))C_{i-1}C_i}{C_{i-1} - C_i} \tag{3}$$

where $V_{s,i}$ is the falling velocity of the layer i, defined as:

$$V_{s,i}(C_i) = \begin{cases} k(C_i)C_i\left(\frac{1}{\rho_s} - \frac{1}{\rho_f}\right), & if \quad C_i \leq C_{gel} \\ k(C_i)C_i\left(\frac{1}{\rho_s} - \frac{1}{\rho_f}\right) & \\ +k(C_i)\frac{\sigma'(C_{i-1}) - \sigma'(C_i)}{\frac{1}{2}(Ep_{i-1}(t) + Ep_i(t))}, & \text{otherwise} \end{cases} \tag{4}$$

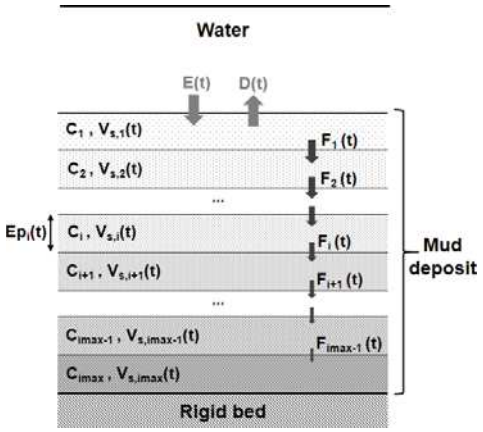

Fig. 2: Schematic vertical view of multilayer bed.

where ρ_s is the sediment density, k is the permeability, σ' is the effective stress, and C_{gel} the transition concentration between sedimentation and consolidation schemes [2]. There is not a standard methodology in the literature to determine the empirical functions for both permeability and effective stress, some alternatives are mentioned in this section.

For the determination of the closure equations for permeability and effective stress, most of study reported some fitting exercise on settling curve, i.e. the position of supernatant/suspension interface. They considered mostly the least square technique for the adjustment to experimental results. In this study we modified the module SISYPHE (subroutine `TASSEMENT_2.f`) in order to include the following closure equations as proposed in [27] and [28] :

$$k = \begin{cases} K_1 \left(\frac{C_i}{\rho_s} - 1\right)^{K_2}, & if \quad C_i \leq C_0 \\ K_3 \left(\frac{C_i}{\rho_s} - 1\right)^{K_4}, & if \quad C_i > C_0 \end{cases} \tag{5}$$

$$\sigma' = B_1 \left(B_2 - \frac{\rho_s}{C_i}\right)^{B_3} \quad if \quad C_i > C_0 \tag{6}$$

where K_1,K_2,K_3,K_4 and B_1,B_2,B_3 are constants to be determined during the calibration procedure.

B. Consolidation model calibration

The coefficients K_i and B_i in the closure equations for the permeability and effective stress (5 and 6) were determined by try and error comparing visually the experimental settling curve obtained in laboratory experiments. Several settling column experiments were carried out at the IMFIA (during FREPLATA-IFREMER Project founded by the French Fund for the Global Environment) using sediment samples from different zones of the estuary [4]. This simple laboratory 1D vertical (1DV) test is usually used to analyse the sedimentation and self-weight consolidation characteristics under motionless conditions [14], [24], [20]. The tests were focused on the influence of mud composition, initial concentration and salinity on the self-weight consolidation process. The experimental facilities consist of three 2 m height and 0.088 m diameter Plexiglas columns with measuring tapes in order to manually record the interfaces evolution. Each column was filled with a mixture of cohesive sediment and water and then the clear-muddy water interface and the bed-muddy water interface positions were registered over an extended time period. The main results were in good agreement with results available in the literature [14], [20].

In a later project [17] additional settling column experiments were made using mud samples taken in the Montevideo Bay area. Five settling column experiments were performed, considering different experiments durations and initial heights. At the end of some of these experiments the mud density was determined at three locations of the mud deposit. These locations are not precisely specified and were defined as "top of the deposit", "middle of the deposit" and "bottom of the deposit". In order to calibrate the closure equations for the permeability and effective stress we utilized the longest experiment. The mud used for this experiment had the following sediment size composition: 8% colloids, 39% clay, 52% silt and 1% fine sand. The initial concentration of the mixture of cohesive sediment and water was 93.2g/l, the initial mixture height was 0.987m and the experiment last 101 days. Unfortunately no density measurements were made at the end of this experiment, however we compare the model results against density measurements at the end of two shorter experiments (7 and 22 days duration).

In order to reproduce the settling column experiments a square domain of 1m x 1m with elements of 0.35m size was constructed, this does not has an effect on the results as we are looking at a 1DV process. The time step is 60 seconds and the simulations length 365 days. The bed was discretized using 20 layers with the following concentrations (g/l) from top to bottom: 100.; 120.; 140.; 160.; 180.; 200.; 220.; 240.; 260.; 280.; 300.; 325.; 350.; 375.; 400; 425.; 450.; 475.; 500.; 550.

The coefficients K_i and B_i were determined by try and error taking as reference values the ones presented by [27], the model showed to be very sensitive to all the parameters. Satisfactory results were obtained choosing the following values:

K_1=235 ; K_2=3.3 ; K_3=50 ; K_4=8 and C_0=150g/l

B_1=2.2.10^{-8} kg/m/s2 ; B_2=27 ; B_3=7.9

Figure 3 shows a comparison of the observed and simulated water-mud interface evolution for the longest experiment, the model is able to reproduce satisfactorily the experimental results. Figure 4 shows a comparison of concentrations values measured at the end of the shorter experiments, and the vertical concentration profiles obtained with the model at the same times. The measured concentration values have been located in approximate vertical positions representative of the "top of the deposit", "middle of the deposit" and "bottom of the deposit". As it can be seen the model give acceptable results when compared against observed concentration values.

C. Influence on the sediment transport and bed evolution

1) Bed initialisation and sensitivity to erosion parameters: A set of simulations was performed with two objectives: to initialize the bed and to explore different erosion parameters configurations. The bed is discretized using 20 layers with the concentration already presented in the consolidation model calibration. It is initialized with an initial thickness of 0.10m for layers 1 to 19, and 0.20m for layer 20 over the whole

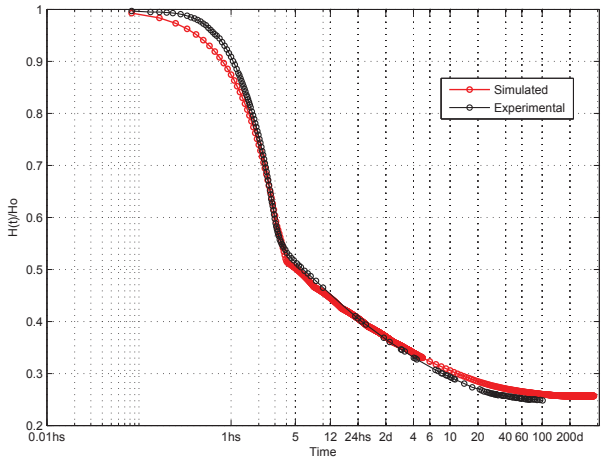

Fig. 3: Comparison of simulated and observed water-deposit interface evolution in the settling column experiment.

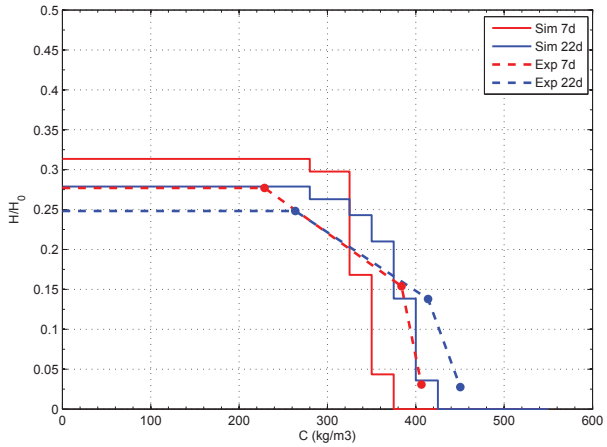

Fig. 4: Comparison of simulated vertical concentration profiles at 7 days (red) and 22 days (blue), against measured concentration values (dots with respective colours).

domain . Starting from this initial condition the period January 2009 to August 2010 (20 months) was simulated using realistic forcings. The consolidation of the initial bed generates a significant drop in the total bed height. In order to avoid modifications in the hydrodynamics due to this unrealistic drop of the bottom, the "STATIONARY MODE" keyword available in SISYPHE was utilized. That means TELEMAC2D does not receive any bottom elevation update during the simulation.

Three simulations were made increasing the complexity of the model in terms of the erosion parameters configuration. In the first simulation all the layers have the same parameter values (critical shear stress for erosion τ_{ce} and Partheniades coefficient M). The second one has different critical shear stress for erosion for each layer. The third one has both different critical shear stress for erosion and Partheniades constant for each layer.

The erosion parameters (τ_{ce} and M) relationship with the sediment concentration depends on the sediment and environment characteristics. Without any specific information for the Río de la Plata, and in order to explore the sensitivity of the model to these parametrisations, reasonable formulations presented in the bibliography from other study cases were used

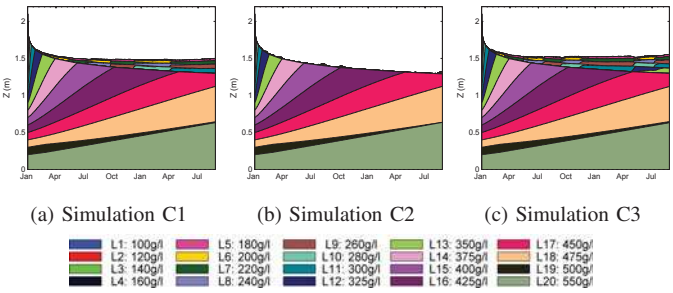

(a) Simulation C1 (b) Simulation C2 (c) Simulation C3

Fig. 5: Simulated temporal evolution of vertical bed concentration profile at Punta Brava during January 2009 - September 2010.

for this analysis. The constants in these formulations were modified in order to obtain critical shear stress for erosion of layer and Partheniades parameter values similar to those obtained during the sediment transport model calibration without the consolidation process [22] for concentrations around 350 g/l.

The parameters employed in simulation C1 are the ones which have been selected during the calibration of SISYPHE without consolidation. Then for the simulations C2 and C3 the critical shear stress depends on the layer concentration as follows:

$$\tau_{ce}^{i} = 10^{-6} C_i^2 \tag{7}$$

where C_i is the layer i concentration (kg/m^3), and $\tau_{c,e}^{i}$ the critical shear stress for erosion of layer i (Pa). This potential relationship between the critical shear stress for erosion and the concentration has been widely used with the exponent varying between 0.9 and 2.5 [12], [31].

For simulation C3 the selected relation between the Partheniades parameter and the layer concentration is [21]:

$$M^{i} = 10^{-13} C_i^3 \tag{8}$$

It is remarked again that the relationships among the erosion parameters and bed characteristics are strongly site-specific. Here reference relationships from biblography were considered in order to explore the effect of the consolidation process on the model results.

Figure 5 shows the temporal evolution of the vertical concentration profile at PB station (see Figure 1b) during the twenty simulated months for simulations C1, C2 and C3. Each layer, and its concentration, is identifiable by its colour. In all the simulations it is clearly appreciable the evolution of the initial bed sediment, which at the end of the simulation reaches a concentration of 450 g/l (L17) on its top layer and shows a decrease in its total height of approximately 0.7 m. Simulations C1 and C2 results show a "new" deposit of sediment over the initial one. The lower concentration of this deposit is close to 180 g/l while at the end of the 20 simulated months its maximum concentration reaches 300 - 350 g/l. On the other hand simulation C2 results do not show this new deposit, only few short episodes with net deposition are identifiable but the fresh deposit is quickly eroded.

Figure 6 shows examples of the SSC at several stations (see Figure 1) during 2009 and 2010. It is worth noting that in terms of the suspended sediment dynamics simulation C1

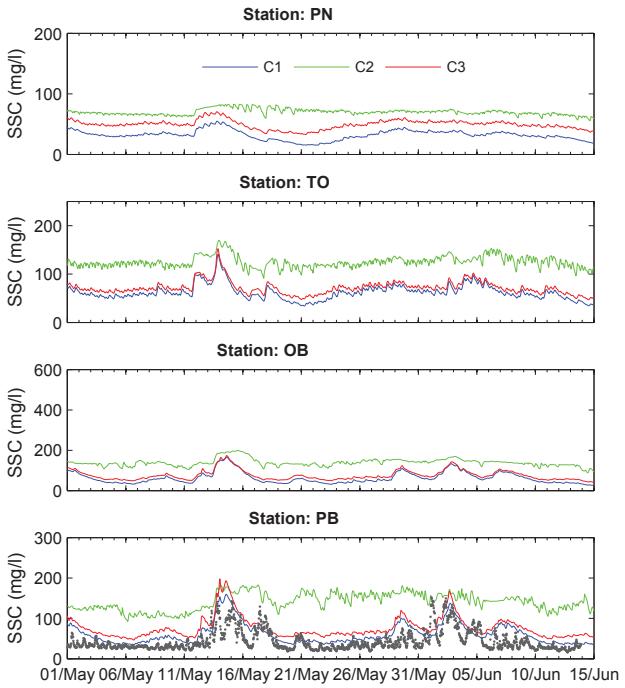

Fig. 6: SSC time series during May-June 2009 obtained with the different consolidation simulations.

produce the same results as the simulation without consolidation. Simulation C2 results shows that a lot of sediment is eroded and remains in suspension quasi permanently. This behaviour is coherent with the low value of critical shear stress for erosion of the low concentration layers. Because of that, in general the net flux is erosive in most of the estuary. Simulation C3 results show slightly higher values of SSC compared to simulation C1 results, but a very similar behaviour. In most of the estuary the top layer shows a concentration of 160 - 180 mg/l, the erosion parameters are much smaller than those obtained in the calibration without consolidation.

Based on this results it was decided to select the configuration of simulation C3 to make a longer simulation, not affected by the initial conditions of the bed, and see the impact on the bed evolution results.

2) Effect on the bottom evolution: Taking as initial condition the bed obtained at the end of simulation C3, it was made a two years long simulation using realistic forcings (2009-2010). The sediment transport model set up is the same utilized in simulation C3.

Figure 7 shows the bottom evolution during the second year of simulation with and without considering the consolidation process. In general terms there is not a significant change in the patterns of erosion and deposition zones. Lower values of accretion are obtained considering the consolidation process. In the inner-intermediate zone of the estuary areas where few changes in the bed elevation are observed without considering the consolidation process, then show a small decrease in the bed elevation.

As part of a project to study the nautical depth in the Montevideo Bay area [17], vertical bed density profiles in the navigation channels were measured using an instrument

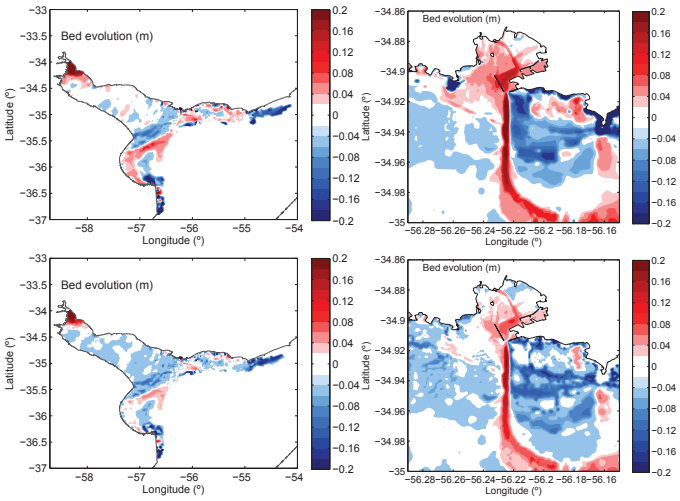

Fig. 7: Bottom evolution during the second year of simulation (2010) without consolidation (upper pannel) and considering it (lower pannel).

based on the tuning fork technology [7]. Figure 8 shows a comparison between the simulated and measured vertical mud concentration profiles at several points inside the bay and along the navigation channel (see Figure 1b,c). In general there is a very good agreement between the model results and the measurements. Stations P1 to P4 are located in the harbour area inside the bay, the model represents well the concentration in the upper layer as well as the profile shape, and slightly overestimates the higher concentration values for depths greater than 0,5 m approximately. In the stations located on the access channel the model results reasonable good. In the outter stations (P12 to P14) located at the beginning of the access channel the model is able to reproduce a higher increase of the mud concentration with the depth inside the bed.

IV. 3D HYDRODYNAMIC AND SEDIMENT TRANSPORT MODELLING

A. Domain and computational mesh

The modelled domain and horizontal mesh are the same that were utilized for the 2D model. It includes the Rio de la Plata and its maritime front zone approximately until the 200 m depth on the continental shelf (Figure 1a). The main freshwater inflows are included, rivers Paraná and Uruguay at the north-west boundary. The mesh elements size ranges from approximately twelve kilometres at the oceanic boundary to ten meters in the vicinity of the Montevideo Bay, it has 30059 nodes and 58594 elements. Figure 1b and c show the mesh at Montevideo Bay zone and includes its bathymetry. It can be seen the navigation channel which gives access to Montevideo's harbour and the harbour basins and internal channels in the bay.

1) Circulation module: The hydrodynamic module TELEMAC 3D was implemented for the selected domain taking into account the fluvial discharges of Paraná and Uruguay rivers, tides at the oceanic boundary (astronomical and meteorological from a regional model), and wind and sea level pressure from ERA-Interim ReAnalysis. The subroutines `BORD3D.f` and `METEO.f` were modified in order to impose oceanic and meteorological boundary conditions with

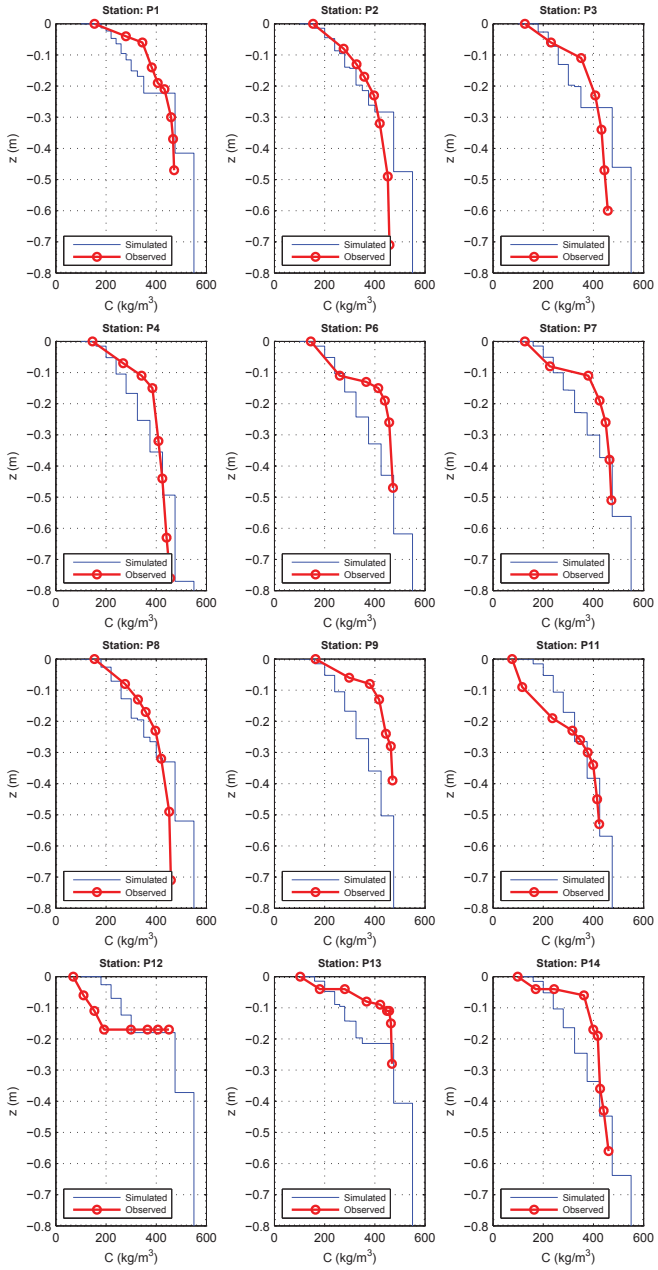

Fig. 8: Comparison of observed vertical mud density profiles and simulation results at the end of a two years simulation.

temporal and spatial variability. The daily flow information of the Paraná and Uruguay rivers was provided by the Argentinian National Water Institute. Relevant tidal waves, both astronomical and meteorological, are imposed at the oceanic open boundary. Sea surface elevation values provided by a regional tidal model [11] are prescribed at oceanic boundary nodes. On the free surface, wind and sea level pressure forcings are considered. For the wind surface stress ($\overrightarrow{\tau}_{wind}$) an aerodynamic bulk formula is employed (9). The wind drag coefficient was selected as a calibration parameter.

$$\overrightarrow{\tau}_{wind} = \frac{\rho_{air}}{\rho_{water}} a_w \mathbf{U_w} \|\mathbf{U_w}\| = C_d \mathbf{U_w} \|\mathbf{U_w}\| \qquad (9)$$

where C_d is the wind drag coefficient, $\mathbf{U_w} = (U_w, V_w)$ the components along the x and y directions of wind veolcity 10m above the water, and ρ_{water} and ρ_{air} the water and air densities respectively. The wind drag coefficient can be set as constant value or as a function of the wind velocity using the formulation proposed by [3]:

$$a_w = \begin{cases} 0.565 \times 10^{-3} & \text{if} \quad \|\mathbf{U_w}\| \leq 5\text{m/s} \\ (-0.12 + 0.137\|\mathbf{U_w}\|) \times 10^{-3} & \\ \text{if} \quad 5\text{m/s} \leq \|\mathbf{U_w}\| \leq 19.22\text{m/s} & \\ 2.513 \times 10^{-3} & \text{if} \quad \|\mathbf{U_w}\| \geq 19.22\text{m/s} \end{cases} \qquad (10)$$

where $\|\mathbf{U_w}\|$ is the wind velocity module.

Both the salinity and suspended fine sediment were considered in the simulations and modelled as active tracers. The turbulence is modelled using the $k-\varepsilon$ model.

Regarding the bottom friction computation, several tests were performed using the Nikuradse formulation for turbulent rough bed conditions [18] and the Reichardt equation for hydraulically smooth conditions [19]. For this study case the results showed a small impact of the bottom roughness on the hydrodynamic variables, SSE and currents. The sensitivity analyses presented here were made using the Nikuradse bottom friction formulation for hydraulically rough conditions with k_s=0.1mm.

2) Wave module: The third generation spectral wave model TOMAWAC is forced with 10m wind from the European Centre of Medium Weather Forecast ERA-Interim Reanalysis. At the oceanic boundary the model is forced by wave statistics from a regional model [1]. A Jonswap spectrum is constructed at each boundary node based on the significant wave height, peak period, mean direction, and directional spread given by the regional model with a temporal resolution of 3 hours. The model was configured to takes into account the following processes: white capping, bottom friction, depth breaking, and quadruplets interactions.

3) Sediment transport module: As well as for the bi-dimensional model only one sediment class is considered, which is defined as cohesive. The bed is assumed to be uniform over the domain, however areas where non-cohesive sediments are predominant were set as non-erodables. In order to compute the erosion and deposition fluxes the classical Krone and Partheniades laws were applied [9], [16]. The parameters to be defined are the settling velocity, the Partheniades coefficient, and both the critical shear stress for deposition and erosion. The consolidation process was not taken into account in the three-dimensional model.

The set of subroutines dealing with sediment transport processes in TELEMAC3D, called SEDI3D [10], treats the settling velocity as a constant value, however it is greatly influenced by the flocculation process. The major factors that control this process are the suspended sediment concentration (SSC), the turbulence and the shear stress [32]. In this study the code was modified (subroutine `VITCHU.f`) in order to make the settling velocity dependent on the SSC based on the following relationship [5], [6], [15], [30]:

$$W_s = W_s^0 \left(\frac{C}{C_0} \right)^m \qquad (11)$$

being C the suspended sediment concentration, W_s^0 a reference settling velocity corresponding to the depth-averaged suspended sediment concentration C_0, and m is a coefficient

between 0.5 and 3.5 [30]. Without any experimental estimation for the Río de la Plata, after testing different values for the coefficient m it is taken to be equal 1.

The boundary and initial conditions are as well the same utilized for the 2D model. The SSC imposed at the boundaries is zero except for the two sections corresponding to Uruguay and Paraná Rivers. At Paraná Las Palmas boundary the imposed SSC is 47 mg/L, while at Uruguay and Paraná Guazú boundary it is 154 mg/L.

For the sensitivity analysis the initial condition was a null value of SSC for the whole domain. At the erodable area the bed is composed of cohesive sediment with a concentration of 450 g/l, there is no limitation on the available sediment to be eroded.

4) Coupled Circulation, Wave and Sediment transport: The three dimensional module TELEMAC 3D, including the sediment transport library SEDI3D can be run internally coupled with the wave module TOMAWAC. The exchange information among the different modules take place at a user defined coupling period. The circulation module TELEMAC 3D is the leading code and calls TOMAWAC. Only depth averaged information is exchanged between the circulation and wave modules.

As the wave module increases the computation time considerably, in the same way it was made for the bi-dimensional model [22] an alternative coupling procedure is proposed in order to save computational time. In this case it was decided to use the wave model results obtained with previous simulations of the 2D morphodynamic model TELEMAC2D-TOMAWAC-SISYPE. The corresponding subroutines of SEDI3D (`CLSEDI.f`) were modified in order to read the wave parameters from the results file of these previous simulations. The wave induced bottom shear stress, which is essential for the sediment transport library, was computed using the Swart formulation [25] based on the significant wave hegiht and peak period provided by TOMAWAC and using a Nikuradse equivalent bottom roughnes k_s=0.1mm.

The total bottom shear stress is computed by a vectorial addition between the currents and waves bottom stress, considering the currents direction and the mean wave propagation direction.

$$\tau_{cw} = \sqrt{\tau_c^2 + 2\tau_c\tau_w \left|\cos\varphi\right| + \tau_w^2} \qquad (12)$$

where τ_c is the currents induced bottom shear stress, τ_w is the wave induced bottom shear stress, and φ the angle between the currents direction and the mean wave propagation direction.

B. Sensitivity analysis

In this section it is analysed the sensitivity of the model results to the wind drag coefficient, and also to the sediment transport model parameters. The later is divided in two based on the sediment exchange paradigm, exclusive versus simultaneous erosion-deposition paradigms [8]. These two approaches are very different, and so it is the behaviour of the model results. For each paradigm it is analysed the sensitivity to the settling velocity (W_s), the Partheniades coefficient (M), and both the critical shear stress for deposition and erosion (τ_{cd}, τ_{ce}).

It was performed a sensitivity analysis to the number of vertical layers (not shown here), in which we used 10, 16, 20, 30 sigma levels equally spaced along the vertical. Even though increasing the number of vertical layers provides a higher vertical resolution, the simulations became more expensive form a computational point of view. For example, if we take as a reference the computation time required to complete the simulation with 9 layers, then the computation time taken by the simulation with 15 layers was approximately 20% higher, the simulation with 20 layers approximately 55% higher and with 30 layers 360% higher. From the sensitivity analysis we conclude that the number of vertical layers does not have an appreciable effect on the sea surface elevation behaviour. Minor differences can be observed in the currents and salinity results. Using more than 16 layers gave very similar results. Taken into account this it was decide to use 16 sigma levels.

1) Wind drag coefficient influence: Five simulations were made in order to evaluate the influence of the wind drag coefficient on the model results. The considered C_d values are presented in Tabel I, the first simulation is called "Ref" as it is the reference value utilized in the bi-dimensional model. For the last simulation (CD4) the wind drag coefficient is computed using the formulation presented in (10).

TABLE I: Sensitivity simulations to the wind drag coefficient.

Simulation	Ref	CD1	CD2	CD3	CD4
C_d	3×10^{-6}	2×10^{-6}	4×10^{-6}	5×10^{-6}	Variable

Figure 9 shows the sea surface elevation series at the station MP, PB and PN during August 2010. As it can be seen the wind drag coefficient has an appreciable influence on the results specially during storm surge events (e.g. 14th August). There are differences between the SSE obtained with simulations CD1 and CD3 (lowest and highest C_d respectively) which exceed 1m.

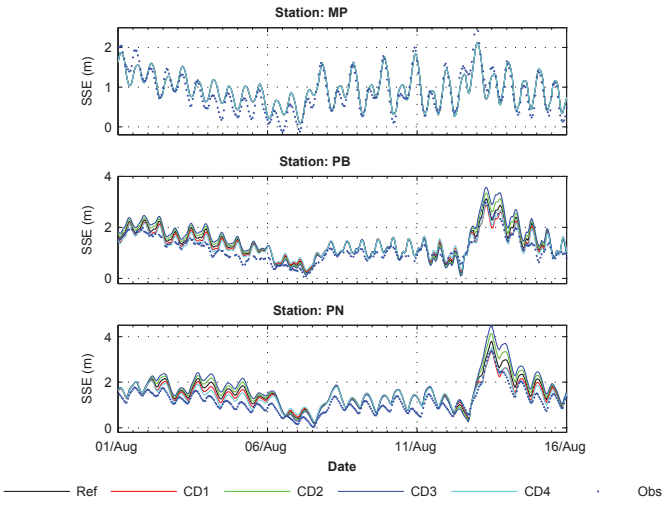

Fig. 9: SSE elevation series during August 2010.

Figure 10 shows a comparison among the measured and simulated current intensity and direction at the station OB. Three bins are shown, being the bin 2 the closest to the bottom. The model results where vertically interpolated to the estimated bin height of the ADCP. The influence of the wind drag coefficient is noticeable both on the currents intensity and directions.

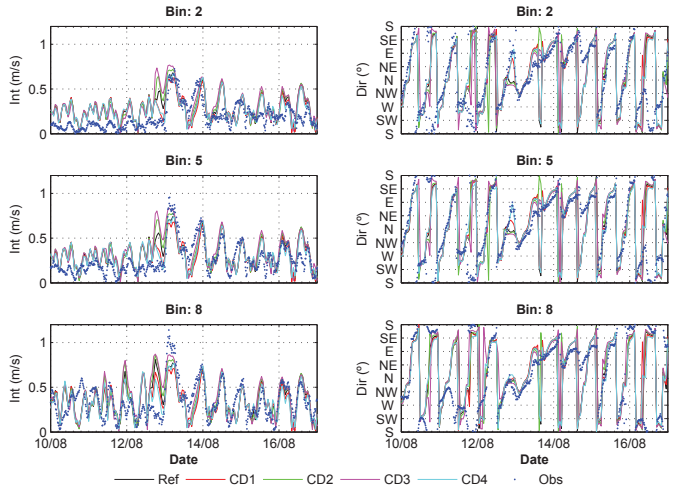

Fig. 10: Currents series at OB during August 2010.

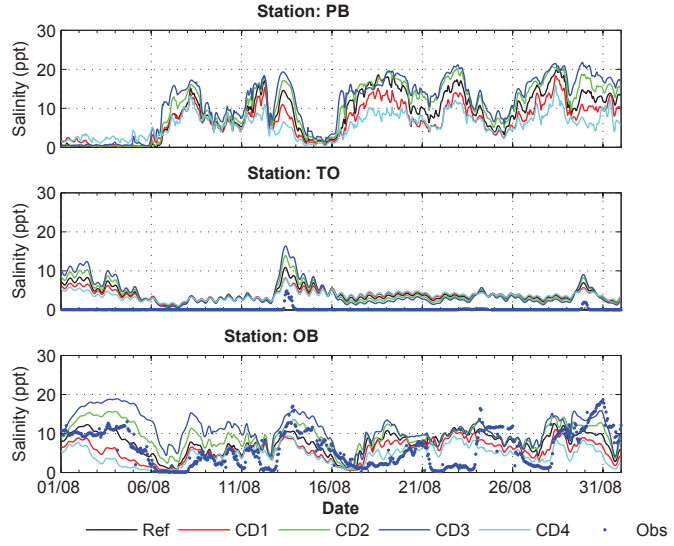

Fig. 11: Salinity series at PB, TO and OB during August 2010.

Figure 11 shows the salinity time series at the station PB, TO and OB during August 2010 obtained with the different model configurations in the mid water column (layer 5). At the last two stations observed data were also included. The influence of the wind drag coefficient on the salinity field is important. The model results shows the ability of the model to capture the main characteristics of the salinity front mobility.

2) Erosion-deposition paradigms:

a) Exclusive erosion-deposition paradigm: Table III shows the parameters for the nine simulations performed using this erosion-deposition paradigm. In order to facilitate the comparison of the results among the different simulations are grouped first taking into account the value of the Partheniades coefficient (M), three values were tested: 3×10^{-7}, 1×10^{-6} and 3×10^{-6} kg/m^2/s. Then for each of these values different critical shear stress for deposition and erosion (τ_{cd}, τ_{ce}) were tested: 0.10, 0.15 and 0.20 Pa. Finally for the last subset of simulations also different values of W_s^0 were considered (being the reference concentration C_0 in (11) equal to 0.1g/l).

Figure 12 shows the SSC series at the bottom and surface layers at the stations PN,PB, TO and OB during August 2010.

TABLE II: Exclusive erosion-depostion (EED) simulation set parameters.

	$W_s^0(mm/s)$	$\tau_{ce}(Pa)$	$\tau_{cd}(Pa)$	$M(kg/m^2/s)$
EED 1	0.1	0.20	0.20	3×10^{-7}
EED 2	0.1	0.10	0.10	3×10^{-7}
EED 3	0.1	0.20	0.20	1×10^{-6}
EED 4	0.1	0.15	0.15	1×10^{-6}
EED 5	0.1	0.10	0.10	1×10^{-6}
EED 6	0.1	0.20	0.20	3×10^{-6}
EED 7	0.1	0.15	0.15	3×10^{-6}
EED 8	0.5	0.20	0.20	3×10^{-6}
EED 9	0.02	0.20	0.20	3×10^{-6}

As it can be seen the effect of the Partheniades coefficient M on the results is very strong. By comparing for example the simulations EED1, EED3 and EED6 we can see that increasing M increase the base SSC value and also magnitude of the storm resuspension event. It has a dramatic impact on the maximum SSC values at the bottom layer during the storm events, note that for the higher values of M SSC up to near 200g/l are reached at PB station. As expected the effect of critical shear stress for deposition and erosion (τ_{cd}, τ_{ce}) is also important, decreasing the threshold value increases the base SSC values and of course the magnitude of the storm resuspension events.

In the last subset of simulations two simulations with different settling velocities were included. As it can be seen in Figure 12 with $W_s^0 = 0.1$mm/s after the storm resuspension events it takes several days to return to the base SSC values. If we decrease the W_s^0 value the sediment remains in suspension for a longer time, increasing the base SSC values associated to the tidal forcing and also extending the time required to go back to normal conditions after the storm events. As it can be seen if we use $W_s^0 = 0.1$mm/s it takes weeks for the SSC to decrease after the storm events. On the other hand, increasing W_s^0 up to 0.5 mm/s effectively decreases the time required to go back to normal conditions after the storm events, but also strongly decrease the base SSC values. If we look at the impact on the bottom SSC values, higher settling velocity values leads to higher bottom SSC values and vice versa. On one hand a higher settling velocity value implies that the sediment will settle faster so it is expected to have higher bottom SSC values, on the other hand it also implies that the deposition flux will be higher which tends to decrease the bottom the SSC values. As observed in 12 it seems that the first effect prevails, so decreasing the settling velocity increase the base SSC values and decrease the maximum bottom SSC values.

Figure 13 shows the bottom evolution during the period July-August 2010 at the station P10 (see Figure 1b) located in the S-N section of the access channel to the Montevideo Bay, and the value of the maximum SSC during the simulated period. Based on the dredging activities a rough estimation of the siltation rates in the navigation channel at station P10 is between 0.20-0.30 m after two months. Increasing M increases the siltation rate at the navigation channel, however it also increases the maximum SSC value up to concentration far too high. It is interesting to note the effect of the settling velocity on the navigation channel siltation rate. Comparing simulations EED6, EED8 and EED9 we can see that even though the lowest settling velocity (EED9) shows higher base SSC values

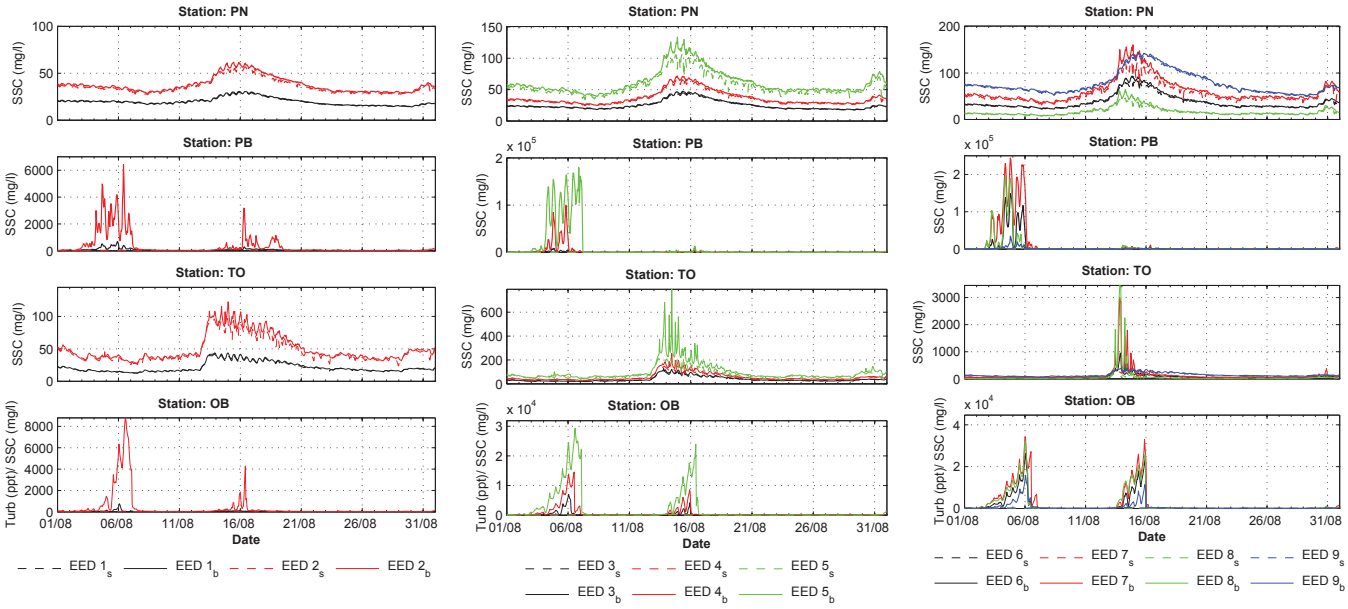

Fig. 12: Bottom and surface SSC series during August 2010 for the EED paradigm simulations.

the siltation rate is lower. A higher value of settling velocity leads to higher SSC near the bottom and higher deposition flux inside the navigation channel. Furthermore it can be seen that the high siltation rates obtained for simulations EED 5 to EED 8 take place due to very high concentrated sediment suspensions moving near the bottom which are captured by the navigation channel due to its geometry and favourable conditions for sediment deposition.

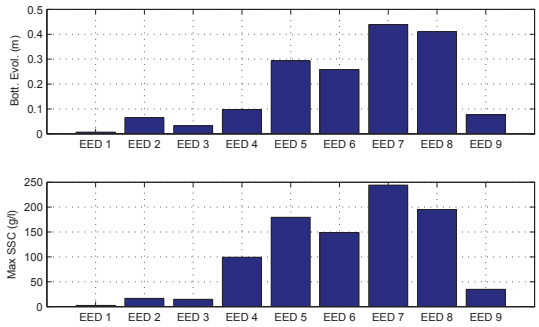

Fig. 13: Bottom evolution at station P10 and maximum SSC during the period July-August 2010 for the EED paradigm simulations.

In summary, the influence of M on the SSC results is very important, and depends on the selected τ_c. In many of these simulations the maximum bottom SSC are far to high, and actually out of the hypothesis of the model. Suspensions with concentrations higher than 80 g/l can be considered as low density fluid mud [12] and can not be modelled as a Newtonian fluid and so the model results are conceptually wrong. Even playing with the three parameters it is very difficult to find a set fulfilling the general characteristics of the suspended sediment dynamics in the whole estuary under this paradigm. The rate of SSC decreasing after the storm events showed to be mainly controlled by the W_s value. High values of settling velocity are needed in order to reproduce the observed behaviour after storm events, however this leads to lower values of SSC during calm conditions specially at the inner zone of the estuary. The way to increase the base SSC would be to decrease the critical shear stress for erosion or increase the Partheniades coefficient, however this will leads to higher maximum bottom SSC which are out of the hypothesis of the present model.

b) Simultaneous erosion-deposition paradigm: Table III shows the parameters utilized for the six simulations performed using the simultaneous erosion-deposition paradigm. In the first three simulations (SED 1 to SED 3) the Partheniades coefficient is increased leaving the other parameters unchanged, the tested values are: 3×10^{-6}, $1.\times10^{-5}$ and 3×10^{-5}. In the following simulations SED 4 the effect of increasing the reference settling velocity W_s^0 from 0.1 mm/s up to 0.5 mm/s is tested. Simulation SED 5 has a higher critical shear stress for erosion threshold (0.15 Pa) compared to simulation SED 4 (0.1Pa). Finally simulation SED 6 is not directly comparable to any of the previous simulations, it has the lowest settling velocity and a low Partheniades coefficient value.

TABLE III: Simultaneous erosion-depostion (SED) simulation set parameters.

	$W_s^0(mm/s)$	$\tau_{ce}(Pa)$	$M(kg/m^2/s)$
SED 1	0.1	0.10	3×10^{-6}
SED 2	0.1	0.10	1×10^{-5}
SED 3	0.1	0.10	3×10^{-5}
SED 4	0.5	0.10	3×10^{-5}
SED 5	0.5	0.15	3×10^{-5}
SED 6	0.05	0.10	5×10^{-6}

Figure 14 shows the SSC series at the bottom and surface layers at the stations PN, PB, TO and OB during August 2010. It can be seen that increasing the Partheniades coefficient increases the base SSC value, the SSC during the storm events and also amplifies a signal with semi diurnal frequency clearly related to the astronomical tide. Simulation SED 4 has a settling velocity five times higher compared to simulation SED 3. As it can be seen the effect is to decrease strongly the base SSC value and the maximum SSC during the storm events, the signal with tidal frequency is still clearly noticeable in station like PN and TO. Simulation SED 5 results are similar to those

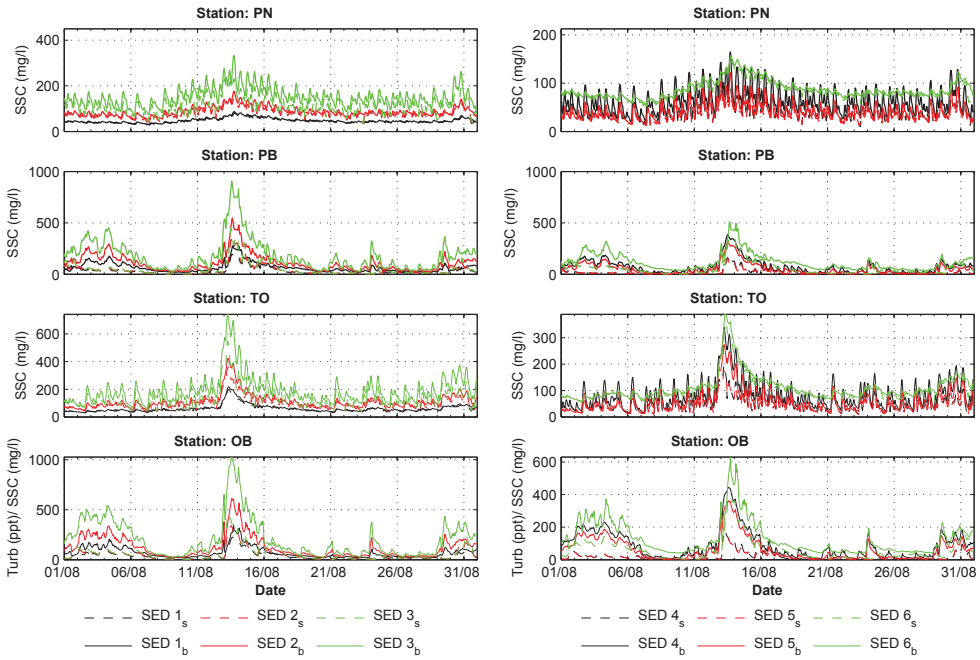

Fig. 14: Surface and bottom water SSC series during July-August 2010 for the SED paradigm simulations.

obtained with simulation SED 4, being the only difference between them an increase of the erosion threshold from 0.1Pa to 0.15 Pa. The differences are more noticeable at the inner stations, being as expected the SSC values slightly lower in the simulation SED 5. Finally about the simulation SED 6 results, it is first interesting to note their similitude to those obtained with the simulation SED 2. Moreover, the base SSC value is similar between them and also the maximum SSC during storm events, however the signal with tidal frequency is much smaller in simulation SED 6 results. Simulation SED 6 has a lower settling velocity and a lower Partheniades coefficient, both approximately half of the values utilized in simulation SED 2.

Figure 15 shows the bottom evolution during the period July-August 2010 at the station P10, and the value of the maximum SSC during the simulated period. In the first three simulations, increasing M increases the siltation rate the navigation channel as well as it also increases the maximum SSC value. In this case the maximum SSC values are still under the hypothesis of the present model.

The effect of the settling velocity on the navigation channel siltation rate is the opposite to the one obtained with the EED paradigm. As we can see comparing simulations SED 3 and SED 4 results, a higher settling velocity (SED 4) shows both lower SSC values and siltation rate in the navigation channel. Under this paradigm deposition occurs continuously, a higher settling velocity leads to lower SSC near the bottom. Taking into account the settling velocity formulation presented in 11, the deposition flux has the following expression:

$$D = W_s \times C = \frac{W_s^0}{C_0} \times C^2 \qquad (13)$$

So even though increasing W_s^0 tends to increase D, the lower SSC values near the bottom have the opposite effect which seems to prevail.

Finally even though simulations SED 6 and SED 2 results have similar SSC values, the navigation channel siltation obtained with simulation SED 6 is lower. This is in fact reasonable taking into account the deposition flux expression (13), as similar SSC values are obtained in both simulations with a lower settling velocity value in simulation SED 6.

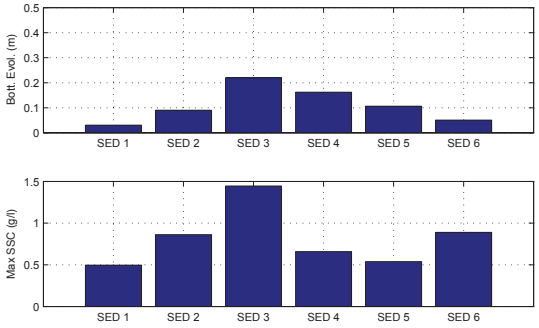

Fig. 15: Bottom evolution at station P10 and maximum SSC during the period July-August 2010 for the SED paradigm simulations.

V. Discussion and Conclusion

The influence of the consolidation process on the sediment transport module was explored modifying a multi-layer isopycnal Gibson's model available in SISYPHE. The closure equations for the permeability and effective stress were calibrated based on settling column experiments, the model results were very sensitive to the calibration parameters. Good agreement was found between measured vertical density profiles and the model results. Including the consolidation model allowed us to have spatial variability on the erosion parameters. In zones where erosion is dominant the top layer, exposed to the hydrodynamic action, has higher sediment concentration and so a higher critical shear stress for erosion. The simulated suspended sediment dynamics behaviour in the Montevideo

Bay area does not show significant differences compared to the results without consolidation. A possible explanation is that in contrast with other estuaries, at the Río de la Plata only a few centimetres of the bed are eroded (maximum SSC in general do not exceed 1g/l) even during the storm events. So in our simulations with the 2D model the bed-water column sediment exchange usually is not enough to involve more than one layer of the bed.

A three dimensional hydrodynamic and sediment transport model was successfully implemented for the study area. A sensitivity analysis to the wind drag coefficient showed that it has a significant impact on the model results. It has a noticeable impact on the SSE specially during the storm surge events. The effect on the currents and salinity distribution is linked and also influenced by the vertical mixing. Higher C_d values leads to a location of the salinity front further inside the estuary and less vertical stratification. The results obtained with the variable wind drag coefficient are closer to those obtained with the lower C_d values.

We have evaluated the effect of the erosion-deposition parameters on the model results under two different erosion-deposition paradigms. As it was shown with the exclusive erosion-deposition paradigm high values of settling velocity are needed in order to reproduce observed SSC behaviour after the storm events. This leads to low base values for the SSC in calm conditions, which can be compensated by increasing the Partheniades coefficient or decreasing the critical shear stress for erosion threshold. All these actions tends to increase the bottom SSC, which already was far too high in all the tested configurations. This was in fact the main problem found with this paradigm, the maximum bottom SSC during storm events are out of the hypothesis of the present model. Increasing the critical shear stress threshold for deposition would help to decrease the high bottom SSC values, however it implies also increasing the critical shear stress for erosion which will not allows us to represent the base SSC values in calm conditions. So it was not possible to find a combination of parameters representing properly the general dynamics of the suspended sediment dynamics of the estuary keeping the SSC values under the range of applicability of the present model.

On the other hand with the simultaneous erosion-deposition paradigm it was much easier to find several set of parameters capturing some of the main characteristics of the fine sediment dynamics in the estuary. The Partheniades coefficient showed to have an interesting effect on the SSC signal related to the astronomical tide. As it was shown different combinations of parameters can give similar SSC results (SED 2 versus SED 6 simulations), having however different results on the navigation channel siltation. The effect of the settling velocity on the navigation channel siltation rate is the opposite to the one obtained with the EED paradigm, increasing the settling velocity leads to lower siltation rates.

Based on this sensitivity analysis the simultaneous erosion-deposition paradigm will be adopted for future works. The exclusive erosion-deposition paradigm seems to be an interesting option to consider if the model is extended to include a description of the fluid mud behaviour, as well as the consolidation process.

ACKNOWLEDGMENT

This work was conducted within the Uruguayan - French cooperation project ECOS-Sud U014U01.

REFERENCES

[1] R. Alonso, "Evaluación del potencial undimotriz de Uruguay," Master's thesis, Universidad de la República, Uruguay, Dec. 2012.

[2] B. Camenen and D. Pham van Bang, "Modelling the settling of suspended sediments for concentrations close to the gelling concentration," *Continental Shelf Research*, vol. 31, no. 10, pp. S106–S116, Jul. 2011. [Online]. Available: http://linkinghub.elsevier.com/retrieve/pii/S0278434310002219

[3] R. Flather, "Results from surge prediction model of the north-west european continental shelf for april, november and december 1973." Institute of Oceanography (UK), Report 24, 1976.

[4] M. Fossati and I. Piedra-Cueva, "Self-weight consolidation tests of the río de la plata sediments," in *INTERCOH 2015 13th International Conference on Cohesive Sediment Transport Processes: 7-11 September 2015 Leuven, Belgium : book of abstracts*. Flanders Marine Institute, 2015.

[5] G. Franz, L. Pinto, I. Ascione, M. Mateus, R. Fernandes, P. Leitão, and R. Neves, "Modelling of cohesive sediment dynamics in tidal estuarine systems: Case study of Tagus estuary, Portugal," *Estuarine, Coastal and Shelf Science*, vol. 151, pp. 34–44, Dec. 2014. [Online]. Available: http://www.sciencedirect.com/science/article/pii/S0272771414002698

[6] O. Gourgue, W. Baeyens, M. Chen, A. de Brauwere, B. de Brye, E. Deleersnijder, M. Elskens, and V. Legat, "A depth-averaged two-dimensional sediment transport model for environmental studies in the Scheldt Estuary and tidal river network," *Journal of Marine Systems*, vol. 128, pp. 27–39, Dec. 2013. [Online]. Available: http://linkinghub.elsevier.com/retrieve/pii/S0924796313000833

[7] V. Groposo, R. L. Mosquera, F. Pedocchi, S. B. Vinzón, and M. Gallo, "Mud Density Prospection Using a Tuning Fork," *Journal of Waterway, Port, Coastal, and Ocean Engineering*, vol. 141, no. 5, p. 04014047, 2015. [Online]. Available: http://ascelibrary.org/doi/10.1061/%28ASCE%29WW.1943-5460.0000289

[8] H. Ha and J.-Y. Maa, "Evaluation of two conflicting paradigms for cohesive sediment deposition," *Marine Geology*, vol. 265, no. 3-4, pp. 120–129, Sep. 2009. [Online]. Available: http://linkinghub.elsevier.com/retrieve/pii/S0025322709001765

[9] R. Krone, "Flume studies of the transport of sediment in estuarial shoaling processes." Hydraulic Engineering Laboratory and Sanitary Engineering Research Laboratory. University of California, Berkeley., Tech. Rep., 1962.

[10] C. LeNormant, "Description of sedi3d, the sediment library of telemac-3d release 2.2." EDF R$D LNHE, Tech. Rep., 2002.

[11] C. Martínez, J. Silva, E. Dufrechou, P. Santoro, M. Fossati, P. Ezzatti, and I. Piedra-Cueva, "Towards a 3d hydrodynamics numerical modeling system for long term simulations of the río de la plata," in *36th IAHR World Congress*, 2015.

[12] A. J. Mehta, *An introduction to hydraulics of fine sediment transport*, ser. Advanced series on ocean engineering. New Jersey: World Scientific, 2014, no. volume 38.

[13] A. Menéndez and A. Sarubbi, "A model to predict the paraná deltafront advancement," in *Workshop on Morphodynamic Processes inLarge Lowland Rivers*, 2007.

[14] C. Migniot, "Tassement et rhéologie des vases. Première partie," *La Houille Blanche*, no. 1, pp. 11–29, Feb. 1989. [Online]. Available: http://www.shf-lhb.org/10.1051/lhb/1989001

[15] J. Nicholson and B. A. O'Connor, "Cohesive Sediment Transport Model," *Journal of Hydraulic Engineering*, vol. 112, no. 7, pp. 621–640, Jul. 1986. [Online]. Available: http://ascelibrary.org/doi/10.1061/%28ASCE%290733-9429%281986%29112%3A7%28621%29

[16] E. Partheniades, "A study of erosion and deposition of cohesive soils in salt water." Ph.D. dissertation, University of California, Berkeley, 1962.

[17] F. Pedocchi, V. Groposo, R. Mosquera, and I. Piedra-Cueva, "Estudio de la profunidad náutica del puerto de montevideo." IMFIA - Facultad de Ingeniería - Universidad de la República, Report, 2012.

[18] S. B. Pope, *Turbulent flows*. Cambridge ; New York: Cambridge University Press, 2000.

[19] H. Reichardt, "Vollständige Darstellung der turbulenten Geschwindigkeitsverteilung in glatten Leitungen," *ZAMM - Zeitschrift für Angewandte Mathematik und Mechanik*, vol. 31, no. 7, pp. 208–219, 1951. [Online]. Available: http://doi.wiley.com/10.1002/zamm.19510310704

[20] H. Samadi-Boroujeni, M. Fathi-Moghaddam, M. Shafaie-Bajestan, and H. M. Vali-Samani, "Chapter 13 Modelling of sedimentation and self-weight consolidation of cohesive sediments," in *Proceedings in Marine Science*. Elsevier, 2008, vol. 9, pp. 165–191. [Online]. Available: http://linkinghub.elsevier.com/retrieve/pii/S1568269208800150

[21] L. P. Sanford and J. P.-Y. Maa, "A unified erosion formulation for fine sediments," *Marine Geology*, vol. 179, no. 1-2, pp. 9–23, 2001. [Online]. Available: http://linkinghub.elsevier.com/retrieve/pii/S0025322701002018

[22] P. Santoro, M. Fossati, P. Tassi, N. Huybrechts, D. Pham Van Bang, M. Benoit, and I. Piedra-Cueva, "Hydrodynamic and fine sediment transport numerical modelling, application to the río de la plata and montevideo bay," in *Proceedings of the XXIIth Telemac-Mascaret User Club*, 2015, pp. 119–126.

[23] P. E. Santoro, M. Fossati, and I. Piedra-Cueva, "Study of the meteorological tide in the río de la plata," *Continental Shelf Research*, vol. 60, pp. 51–63, 2013. [Online]. Available: http://linkinghub.elsevier.com/retrieve/pii/S0278434313001180

[24] G. C. Sills and K. Been, "Self-weight consolidation of soft soils: an experimental and theoretical study," *Géotechnique*, vol. 31, no. 4, pp. 519–535, Jan. 1981. [Online]. Available: http://www.icevirtuallibrary.com/content/article/10.1680/geot.1981.31.4.519

[25] D. Swart, *Offshore sediment transport and equilibrium beach profiles*, ser. Publications // Delft Hydraulics Laboratory. W.D. Meinema B.V., 1974. [Online]. Available: https://books.google.fr/books?id=qYYNAQAAIAAJ

[26] P. Tassi and C. Villaret, *Sisyphe v6.3 User's Manual*, 1st ed., EDF R&D, 6 quai Watier - 78401 CHATOU, 1 2014.

[27] J. Thiebot, S. Guillou, and J.-C. Brun-Cottan, "An optimisation method for determining permeability and effective stress relationships of consolidating cohesive sediment deposits," *Continental Shelf Research*, vol. 31, no. 10, pp. S117–S123, Jul. 2011. [Online]. Available: http://linkinghub.elsevier.com/retrieve/pii/S0278434310003675

[28] Thiebot, J., "Numerical modelling of the processes which govern the formation and the degradation of muddy massifs - application to the rance estuary and to the sèvre niortaise river banks," Ph.D. dissertation, Agro Paris Tech, Mar. 2008.

[29] L. A. Van, "Modélisation du transport des sédiments mixtes sable-vase et application à la morphodynamique de l?estuaire de la gironde," Ph.D. dissertation, Universite PARIS-EST, 2012.

[30] W. van Leussen, "The variability of settling velocities of suspended fine-grained sediment in the Ems estuary," *Journal of Sea Research*, vol. 41, no. 1-2, pp. 109–118, Mar. 1999. [Online]. Available: http://linkinghub.elsevier.com/retrieve/pii/S138511019800046X

[31] R. Whitehouse, Ed., *Dynamics of estuarine muds: a manual for practical applications*. London: Telford, 2000.

[32] J. Winterwerp, "On the flocculation and settling velocity of estuarine mud," *Continental Shelf Research*, vol. 22, no. 9, pp. 1339–1360, Jun. 2002. [Online]. Available: http://linkinghub.elsevier.com/retrieve/pii/S0278434302000109

Wave library: A strategy for reducing computation times in coastal sediment transport studies

Pat Prodanovic, PhD., P.Eng.
Hydrotechnical Engineer
Riggs Engineering Ltd.
205-1240 Commissioner's Road West
London, Ontario, Canada N6K 1C7
Email: pprodanovic@riggsengineering.com

***Abstract*—The intent of this paper is to present a methodology that is capable of significantly reducing computation times in coastal sediment transport studies by decoupling wave propagation calculations from three way coupling. The proposed methodology takes a wave hindcast at an offshore model boundary and completes standard wave propagation computations for a large number of combinations of water levels, wave heights, wave periods and wave directions using the procedure called task farming (carrying out large number of simple/routine simulations). After completion of the wave library, wave transformation results are saved in a master file where each record represents results for a particular water level, offshore wave height, wave period and wave direction. At the last step in the proposed methodology, hydrodynamic and sediment transport modules are dynamically linked and wave data is simply read from the master wave library file rather than computed each time step. The methodology ensures wave radiation stresses are passed to the hydrodynamic model, and wave heights and periods are passed to the sediment transport module for proper representation of coastal processes. By decoupling wave propagation from three way coupling and replacing it with results from a wave transformation library significantly reduces computational burden while still capturing relevant physics. However, the decoupled procedure is applicable only in situations where bed evolution is not significant enough to alter wave propagation characteristics, and where currents do not significantly influence wave propagation. An example of a study carried out using the above procedure is summarized in the paper.**

I. Introduction

The main intent of this paper is to develop a strategy to reduce the computational burden associated with coastal studies that require use of the long term wave climate. An example of such a study is a coastal sediment transport study that seeks to quantify morphologic changes to the sea bed over a time horizon that ranges in the order of years. Coastal morphological studies, usually part of larger scope environmental assessments, may look to identify how new or modified structures (piers, wharves, groynes, breakwaters, etc.) alter coastal processes and potentially disrupt the balance in the littoral transport that presently exists at a given area. Environmental assessment studies typically look into quantifying such impacts, and are a prerequisite to regulatory permits for construction of new (or modifications to existing) structures.

The Telemac suite of numerical models provides a set of tools for carrying out coastal sediment transport or morphological studies. Coastal studies of this nature can be simulated using the procedure that is known as three way coupling. Such a procedure links hydrodynamics (Telemac-2D or Telemac-3D), wave transformation and propagation (Tomawac), and sediment transport (Sisyphe) modules in a dynamic feedback manner. Each module influences and is influenced by the other during the course of the simulation, thus capturing relevant physical processes at play in the coastal environment. Three way coupling works as follows: water levels and currents from the hydrodynamic module are passed to the wave module, and influence wave propagation. At the same time wave radiation stresses computed by the wave module produce wave induced currents which are then passed back to the hydrodynamic module. Coastal sediment transport calculations are influenced by both hydrodynamics and wave forcing, and have the effect of changing the sea bed in response to the forcing given. The updated sea bed is then fed back to hydrodynamic and wave modules, repeating the process again.

To be of practical value coastal sediment transport and morphologic studies require results from simulations of many years. Meaningful multi year simulations involving coastal sediment transport are extremely computationally expensive, and require use of large number of computational cores to keep simulation times reasonable. Due to heavy computational burden, three way coupling on today's personal computers is simply not practical. One strategy strategy to reduce the computational burden is to decouple wave propagation from the three-way coupling procedure.

Decoupling wave propagation from three way coupling could be achieved by setting up a standalone wave hindcast simulation, saving the results at a specified time step, and then reading the wave results in a coupled hydrodynamics/sediment transport model. This strategy has the potential to reduce the computational burden compared to three way coupling, but is still computationally expensive. A proper wave hindcast (for use in sediment transport modelling) requires coupling of both hydrodynamics and wave propagation in order to get the physics of the problem correct (especially the influence of water levels on wave propagation). Such a strategy was previously used in [1]. But the above strategy is rather cumbersome as it requires the user to simulate hydrodynamics/wave propagation first, followed by hydrodynamics/sediment transport second (with wave results read at specified time step) for the entire simulation period of interest. Essentially, the user has to carry out two separate simulations. Regardless of it cumbersomeness, this strategy certainly works in reducing

the computation burden compared to similar simulations using three way coupling.

An alternate strategy to above is one that carries out a large number of stationary wave propagation simulations on a nearshore grid for different combinations of water level, offshore wave height, period and directions. Such simulations are carried out using only the wave propagation module (as the water level is given as a parameter in the stationary calculations). A script is then set up to execute the large number (of rather simple) wave propagation simulations, and store its results for further use. Then, coupled hydrodynamics/sediment transport simulations are set up to read (at a set time step specified) wave results from the library file. Reading the wave library results allows the user to significantly speed up the simulations, while ensuring proper representation of relevant physics within the model.

To the best knowledge of the author, implementation and execution details of wave libraries for use in morphologic simulations or other studies are rare. One example is found in a coastal sediment transport study [2]. In their study the authors determine a wave climate at a site by setting up a wave transformation model with a total of 891 simulations to represent relevant combinations of wave height, directions and period. The results of their wave transformation simulations are such "that an offshore time series of waves can be transferred to any point by interpolation between the results from the simulations", [2], Chapter 2. The wave library results were then used to transform an offshore time series of wave data to a nearshore node for used in a harbour development study.

Another example of a wave library is given in [3], where the authors describe carrying out 1920 nearshore transformation simulations. "Then, when requiring wave data for long term sediment transport simulations, the wave library is used to interpolate the nearshore analysis to the hydrodynamic model grid. This way waves are not simulated during sediment transport computations, which saves (computation) time", [3], p. 144.

The benefits of using the wave transformation library are certainly promising. The only challenge lies in its creation. This paper attempts to advance this shortcoming, and offer a methodology (along side with complete source code) that will assist users in creating wave libraries for use in their projects. Note that even though the focus of this paper are coastal morphological studies, wave libraries could certainly be a useful tool for other coastal studies (i.e., establishing a wave climate for use in engineering design).

The rest of the paper presents is organized as follows: Section II will present the relevant details on how to set up and simulate a wave transformation library. The descriptions will include detailed steps needed to develop a wave library for use in various projects. An example of the wave transformation library that was developed as part of a harbour improvement project in Port Stanley, Ontario, Canada will be provided in Section III. Concluding remarks are given in Section IV.

II. Wave transformation library

A wave transformation library (or a wave library for short) is a methodology that simulates large number of combinations of scenarios using a spectral wave model. Wave library allows the user to pre-compute a large number of simulations representing all possible combination of relevant forcings, and store its results for future use. A key benefit of a wave library lies in not having to repeat same wave simulations over and over again (as would be the case in completing a proper wave hindcast). On very fine nearshore grids (required for resolving hydrodynamics and sediment transport processes) proper wave hindcast simulations are very costly, and consist of large portion of the overall computational burden.

Two different types of the wave transformation libraries are envisioned, namely i) those having a computation domain with classical offshore boundaries (where waves propagate from outside), and ii) those with enclosed or semi-enclosed domains (i.e., where wind driven waves dominate).

Wave libraries for enclosed or semi-enclosed domains (where wave are generated internally and not propagated from outside) can also be used. In such cases the library is set to simulate all relevant combinations of water level, wind speed and direction. By knowing a time series of wind speed and direction, along with a time series of water level, the user can obtain a time series of any simulated wave parameter (like wave height, period, direction, etc.) after completing the wave library simulations. Examples of use of wave libraries in enclosed or semi-enclosed domains include marina planning studies, detailed design of structures (i.e., floating breakwaters), etc.

The focus of this paper, however, is on development and construction of the wave transformation libraries for use in traditional coastal projects using open offshore boundaries. In these cases waves are externally generated and propagate to the area of interest.

A. Steps in constructing a wave library

The general steps used to construct a wave transformation library are sketched out below:

1) Obtain long term historic records of water levels at the site of interest (typically a water level gauge at an existing harbour).
2) Obtain long term historic records of offshore wave conditions (either a wave buoy or a wave hindcast node). Long term wave records are typically available from local agencies.
3) Create a model mesh for hydrodynamic (and morphodynamic) simulations. This step includes developing a detailed mesh to resolve the physics of the problem under investigations.
4) Create a model mesh for nearshore wave transformations. Similarly to above, wave transformation simulations may require a mesh with larger boundaries than the hydrodynamic mesh (required to extend to the hindcast node or the wave buoy).
5) Determine relevant combinations of water level, offshore wave height, period and directions for use in nearshore wave transformations. In this step, the user selects discretization of the water level to use in the library. Also directional statistics of the time series

wave data are inspected, which aid in ultimately selecting and narrowing down the combinations of wave height, period and directions to use in the wave library simulations.

6) Set up a base case wave model satisfying the stationary propagation assumption, including all necessary files. At the offshore model boundary, an assumption has to be made on parameterization of wave energy entering the domain (JONSWAP, TMA spectrum, etc.).

7) Set up a script for simulation of previously identified combinations of nearshore wave transformations. Depending on the discretization used, the number of simulation can be in the order of several thousand.

8) Simulate the combinations of wave transformation simulations, and save its results.

9) After simulations are complete, merge results from all nearshore wave transformations into a master wave library file. Each record in the master wave library file corresponds to a wave transformation results for a known water level, offshore wave height, period and direction.

10) Select a time period to carry out morphologic simulations from the historic record. Then, extract a time series of water level, offshore wave height, period and direction for the desired time period. This time series will be used to extract records from the master wave library. Depending on the project requirements, the selected time period is typically measured in years.

11) Extract from the master wave library file one record per desired time step in the simulations. Records from the master wave library file are selected to correspond to water levels and offshore wave height, period and directions from extracted time series from step 10. Extraction ensures that each time step in the simulated time in the coupled hydrodynamic and sediment transport simulations is linked to a wave conditions that would result at that particular time. This extracted file is referred to as the master wave library time series file.

12) If hydrodynamic and wave transformation meshes are different, transpose the master wave library time series file from the nearshore grid (see step 4) to the hydrodynamic grid (see step 3).

13) Lastly, set up a coupling between hydrodynamics and sediment transport simulations, and simply read the master wave library time series file during the course of the simulations. For example, if the results are stored on the hourly time step, read the wave data each hour in the coupled model. Ensure wave radiation stresses are passed to the hydrodynamic model, and wave height, period and direction are passed to the sediment transport model.

B. Limitations of the wave library in morphologic studies

In using the wave library as sketched out above, the user has to ensure the methodology is valid to the problem at hand. For example, offshore wave data referred to in Step 2 must be located such that stationary wave propagation to the site of interest apply and are valid. Offshore nodes at hindcast sites typically meet this requirement, but should always be checked and verified by the user.

The user must be made aware that decoupling waves from three way coupling simulations neglects a number of physical processes in order to save computation time. First, influence of currents on the generation and propagation of waves is neglected, as hydrodynamics and wave propagation processes are intentionally decoupled. Second, influence of morphologic changes (raising and lowering of the sea bed produced by the sediment transport module) are not communicated to the wave or hydrodynamic modules.

It must be left up to the user to ensure the effect of current on wave propagation is minor (or otherwise acceptable), and that morphologic changes to the sea bed during the coarse of the simulations do not influence wave propagation in a drastic way. If it can be demonstrated that above limitation are acceptable, simulations using the wave library can be safely used.

Of course, the ultimate way of verifying the validity of the wave library approach for a particular site for which morphodynamic simulations are carried out involves setting up i) three way coupling with hydrodynamics, wave propagation and sediment transport, and ii) decoupling wave propagation from three way coupling and replacing it with results from the wave transformation library. If comparisons between the results yield acceptably similar results, the wave library approach can be deemed valid.

C. Wave library for the Telemac modelling system

The above methodology has been implemented for use in the Telemac modelling system via the Python programming language. All of the code was written so that it works under both Python 2 and Python 3. The code was developed to aid the user in the process of constructing a wave library for a domain having open boundaries. (Minor modification to the code would allow development of the wave library for enclosed or semi-enclosed domains.) The code is packaged under the PPUTILS project on GitHub:

`https://github.com/pprodano/pputils`

Guidance in using the source code is provided next, with brief explanations. As all of the code is publicly available the interested user is encouraged to look at the source code for additional detail if necessary.

To start the construction of the wave library, steps 1 and 2 are required first, and simply involve gathering historical time series data. Next, the methodology includes developing a hydrodynamic model mesh (step 3) and wave library model mesh (step 4). Tools in PPUTILS can be used to a construct a digital terrain model and a model mesh, and then interpolate the terrain model over the model mesh (see reference [4]) thus allowing the user to complete the entire modelling project using nothing but open source tools.

Different meshes for the hydrodynamics and wave propagation may be required as the wave propagation mesh may

need to cover an area larger in extent (governed by the location of the hindcast node or the wave buoy). As in all numerical modelling projects the mesh has to be constructed to properly resolve the shoreline/bathymetry for the area of interest, yet must be kept as small as possible to limit computational burden. The mesh that may be sufficient for wave propagation may not suffice for hydrodynamics and/or sediment transport. There is a utility in PPUTILS that will transpose simulated results from one mesh onto another. More on this will be provided later.

Step 5 in the above methodology involves the assembly of relevant wave propagation scenarios. As a first step, the user has to inspect the time series record of water level [WL], and decide the range and discretization of the water levels to be used in the library. For example, if water levels vary between -1.0 and +1.0 m chart datum, the user may decide to discretize this range by 0.2 m, and have a vector of water levels as follows: [1.0, -0.8, -0.6, ..., 0.8, 1.0]. Such a discretization means that the wave library will be based on 11 different water levels.

In order to derive the wave combinations to be used in the wave library, the user is required to obtain directional statistics on the historic time series wave data. Directional statistics are typically published by the same agencies that supply the wave data. After inspecting directional statistics, the user will then be in a position to decide which combination of wave parameters occur often enough to be included in the library. As a rule of thumb if a wave condition occurs more than 50 hours in the record, that wave condition should be included in the library. The user is required to derive tuples of offshore wave height [Hm0], wave period [Tp], and direction [Dir]. All relevant tuples of the form [Hm0, Tp, Dir] are required to be determined, and saved in a file. Discretization of the wave direction of 22.5 degrees is usually sufficient, but not all combinations need be included in the library. For example, if the shoreline is oriented in the east west direction and located on the northern limit of the domain, then offshore waves approaching from the north-west, north, and north-east need not be included in the library.

To determine the wave library combinations, each value of the discretized water level is to be combined to each offshore wave conditions tupple. The user is ultimately required to produce a comma delimited file with the following headings: [id, WL, Hm0, Tp, Dir], where id is the identifier of the particular scenario, and rest of the variables are defined above.

Step 6 requires the user to set up a base case stationary simulation in Tomawac. The Tomawac steering file has to have the following keywords: `2D RESULTS FILE`, `INITIAL STILL WATER LEVEL`, `BOUNDARY SIGNIFICANT WAVE HEIGHT`, `BOUNDARY PEAK FREQUENCY`, and `BOUNDARY MAIN DIRECTION 1`. The output variables from the base case Tomawac model can include any one of the available variables, but should, at a minimum, include `WAVE HEIGHT HM0`, `PEAK PERIOD TMD`, `MEAN DIRECTION`, `FORCE X`, and `FORCE Y`.

After having the stationary base case wave model, and the scenarios of combinations, the user is required to run the `mkscenarios.py` script (step 7). Inputs to the `mkscenarios.py` are the base case Tomawac file, and the wave library scenarios comma separated file with the following headings: [id, WL, Hm0, Tp, Dir]. Upon execution, the script creates number of files equalling the number of scenarios, as well as a script named `run_scenarios.sh` that executes the simulations in Tomawac (i.e., step 8). The above process is referred to as task farming, where Tomawac is required to compute a large number of rather straightforward wave propagation calculations.

After all of the wave library computations are completed, the master wave library file is constructed by extracting from each Tomawac result file the output variables for each particular scenario. Creation of the master wave library file (step 9) is completed by running the `mkwavelibfile.py` script, which creates the master wave library file. The `mkwavelibfile.py` script uses a custom written module called `selafin_io_pp.py` that reads and writes SELAFIN format in pure Python. Each record in the master library file contains all of Tomawac's output variables for each scenario in the library.

Step 10 simply requires the user to extract out of the historic time series a subset of time for which the morphologic simulations are to be carried out. The offshore time series file is to contain, time, water level, wave height, period and direction in a comma separated file.

Next, step 11 requires reconstruction of the 2d wave hindcast for the selected time period of interest. The script `mkwavelibts.py` takes in the master wave library life and an offshore time series ascii file of the simulation time series, and creates a SELAFIN result file. This result file is created by extracting from the wave library a record that most closely resembles the record in the time series offshore data correspond to the desired time step. The selection algorithm calculates a multi-dimensional distance metric based on the sum of square root difference of each of the four parameters (WL, Hm0, Tp, Dir) between the hindcast and the library values. The record in the library (for any point in simulated time) is then selected as one having the smallest distance.

All of the above steps are carried using results stored on the wave model mesh. The hydrodynamic and sediment transport calculations may be made on a different mesh. The script in PPUTILS called `transp.py` takes a SELAFIN result file on one mesh, and transposes it to another mesh, thus completing step 12.

The final step in the methodology (step 13) includes setting up the coupling between hydrodynamics and sediment transport, where the wave data is simply read from a file, rather than being computed at each time step. To complete the coupling (assumed to take place between Telemac-2d and Sisyphe) and capture the relevant physics requires modifying the following subroutines: i) `prosou.f`, to add wave generated currents to hydrodynamics, and ii) `condim_sisyphe.f`, to read wave height, period and direction in Sisyphe. Of course, transport formulas in Sisyphe have to be selected that are specifically formulated to deal with influence of waves.

III. Application of a wave library

This section presents the application of the wave library to an existing harbour sedimentation study. The example

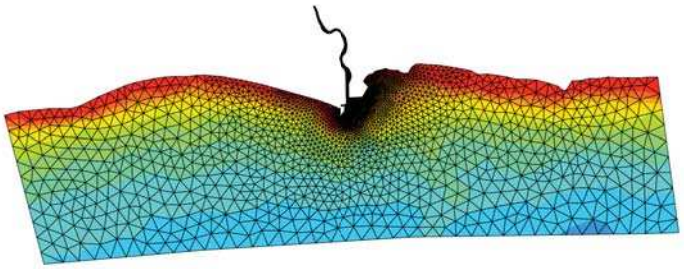

Fig. 1: Hydrodynamic/morphodynamic model mesh

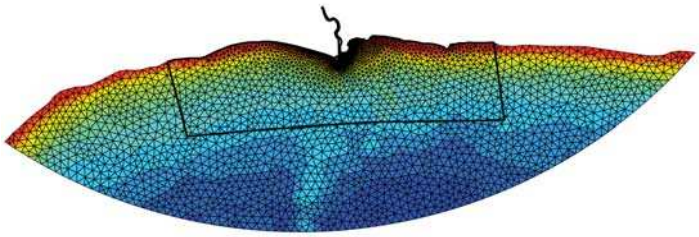

Fig. 2: Wave transformation model mesh

presented will illustrate how the methodology in Section II was used to derive a wave library for use in nearshore sediment transport modeling.

A. Port Stanley Harbour improvements, Ontario Canada

After acquiring the harbour from the federal government, the local municipality has undertaken a variety of infrastructure improvements at Port Stanley, Ontario, Canada. Located on the north shores of Lake Erie, Port Stanley harbour was originally developed in the late 1800's to facilitate marine transport of aggregate, coal, grain and other goods on the Great Lakes waterways.

Recently Port Stanley's west breakwater had been rehabilitated and dredging had taken place to remove sediments deposited by Kettle Creek. Further, the material removed during recent dredging activities were placed in a new disposal cell constructed adjacent to the west breakwater. The disposal cell has been designed to serve two purposes: i) house dredge material, and ii) create valuable recreation lands adjacent to the town's busy beach.

B. Development of the wave library for Port Stanley

To facilitate recent development at the harbour a wave library for the nearshore area of Port Stanley was developed. Historic time series water level data is obtained from the gauge set at the harbour. The gauge includes hourly water levels from 1960-present. Time series data for offshore wave conditions are obtained from an existing US Army Corps of Engineers wave hindcast. The hindcast node closest to Port Stanley was used to extract offshore wave height, period and direction for the period 1979-2014.

The PPUTILS toolkit was used to develop a model mesh for the hydrodynamic and sediment transport model, extending from the harbour to approximately the -12 m depth contour, approximately 4 km offshore (see Figure 1). Similarly, PPUTILS was used to develop a mesh for the wave transformation calculations (see Figure 2). The wave module mesh extended to the hindcast node (to approximately the -18 m contour, and covers a much larger area than the hydrodynamics.

The scenarios for the wave library are developed following processing of the time series data. The water levels in the library were discretized in a 0.15 m step, ranging from 0.0 to 1.5 m above chart datum. Similarly, directional statistics from the offshore wave (supplied by the US Army Corps of Engineers as part of the wave hindcast) was used to develop wave scenarios. Wave height was discretized in 0.5 m increments, ranging from 0.3 to 4.5 m. Wave period was discretized in 1 sec increments, ranging from 1 to 9 sec. Wave directions was discretized by the 22.5 deg bands, resulting in 16 cases for wave directions. A total number of combinations used in the wave library computations totaled 2,222. The scenarios executed capture all possible combinations of wave conditions relevant to the study of coastal sediment transport at Port Stanley.

In the Tomawac wave library simulations, the JONSWAP spectrum was used to parameterize the wave energy entering the boundaries in the model. Rest of the steps outlined in Section II were carried out, and ultimately created a reconstructed wave result file (in SELAFIN format, on the same mesh as the hydrodynamic/sediment transport model) for use in future simulations. A coupling between Telemac-2d for hydrodynamics, and Sisyphe for coastal sediment transport was then set up. Subroutine `prosou.f` was modified to read the wave induced force from the reconstructed wave file and capture the effect of wave generated currents. Likewise, `condim_sisyphe.f` soubroutine from Sisyphe was modified to read the wave height, period and direction, and capture wave induced effects on sediment transport.

C. Reality check of the wave library

A simple way of checking the appropriateness of the discretization applied in the wave library is to compare the offshore time series from the hindcast against the reconstructed time series produced by the library. If the two time series reasonably match, the discretization appears to be valid. This is the only conclusion that could be made from this comparison. Figure 3 shows the comparison for water levels, offshore wave height, period and direction from the Port Stanley case. From the results shown it can be concluded that the discretization generally appears to be appropriate for the domain. Note some hysteresis on the wave library water levels is evident, and is a direct result of i) discretization of the water levels used, ii) procedure used to select a particular record from the wave library for a given point in time, and iii) the range in historic lake levels. For the Port Stanley case such a small water level fluctuation makes rather minor differences in wave propagation calculations, and the hysteresis noted is deemed to be of no relevance. However, an improvement in the procedure used to select the particular record from the wave library (in `mkwavelibts.py`) should be investigated.

A more data intensive approach in checking the validity of the constructed wave library would be to compare results with actual wave data. If historic records of offshore and nearshore wave buoy data exist, the wave library approach could be used to transform the offshore wave data to the nearshore. Then,

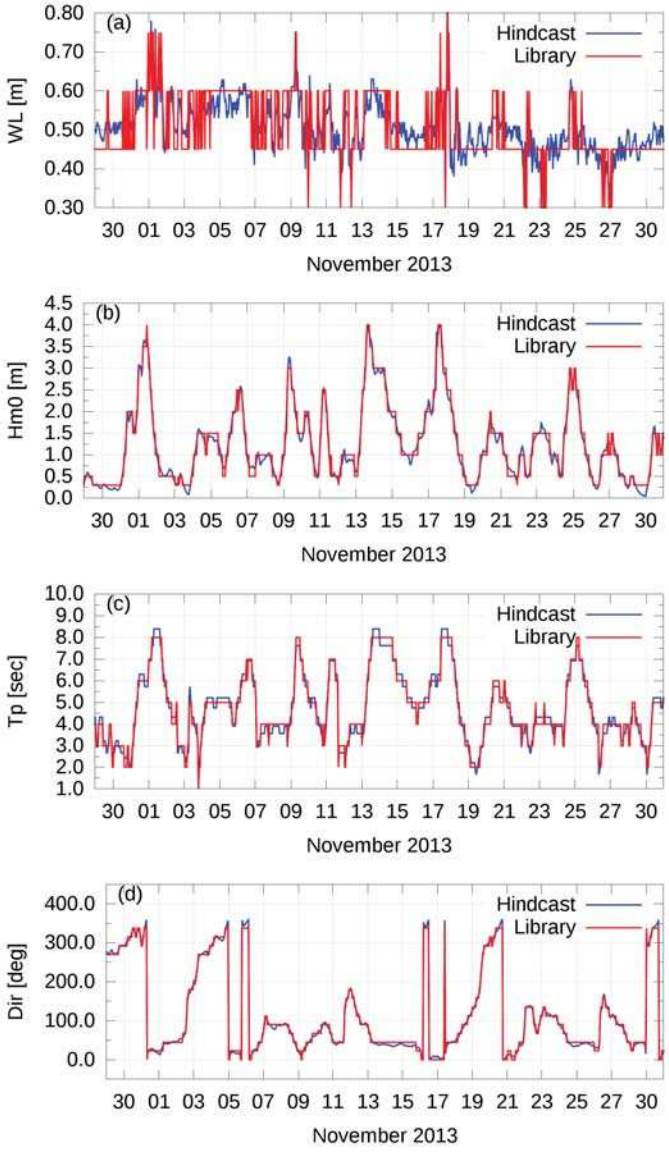

Fig. 3: Wave transformation model mesh

the nearshore wave data reconstructed from the wave library could be compared to the observed wave, and appropriate conclusions could be drawn. Unfortunately, such data does not exist for the Port Stanley example, but may be explored in the future.

The final way of justifying the appropriateness of the wave library (and the methodology proposed in this paper) would be to compare sediment transport simulation results from a) three way coupling (where wave data is calculated every time step), and b) two way coupling (where wave data is reconstructed from the wave library and simply read during the simulations). Such computations are presently work in progress for the Port Stanley study, and will be reported once they become available.

D. Reduction in computational times

The task farming process that simulated the 2,222 Tomawac simulations is one that required approximately 24 hours of simulation time on a quad core personal desktop computer. As the wave computations are a simple task farming process, it is relatively easy to employ a number of different personal computers in carrying out a portion of the overall task (i.e., computer A simulates cases 1-500, computer B simulates cases 501-1000, etc). The only requirement is that each computer has the Telemac modelling system installed. The processing time of the simulation results are estimated to take not more than 2-3 hours, provided the user understand the procedure outlined in the paper.

The reduction of the computational times between i) three way coupling, and ii) two way coupling with wave library are striking. On a quad core desktop computer three way coupled simulations for 273 days of simulation for the Port Stanley domain would take approximately 12 days of calculations going at 100% CPU load. (This estimate was obtained by scaling three way coupled calculation simulating a storm lasting four days.) In the comparisons, two way coupling calculations with inputs from the wave library last approximately 1.5 hours for a 273 day simulation. The reduction in the computational burden (from 12 days to 1.5 hours) implies that coastal sediment transport calculation could be carried out using ordinary desktop computers, and need not rely on expensive computer clusters.

IV. Conclusions and Recommendations

This paper presents a methodology with the aim to drastically reduce computation time associated with coastal sediment transport studies by decoupling wave propagation from three way coupling. A methodology was outlined in the paper that allows a user to set up a wave transformation library for a domain, and then simply read the wave results in two way coupled simulation rather than using computationally expensive three way coupling. The methodology allows for wave induced currents to be added to the hydrodynamics, and wave forcing to be linked to the sediment transport calculations. However, the two way coupling procedure neglects some physics (currents do not influence wave propagation, and evolution of the sea bed have no influence on hydrodynamics or wave propagation). It is left up to the user to determine the impact of the neglected physics, and determine whether two way coupled simulations can be justified.

Reduction in simulation times from traditional three way coupling is significant, and allows a user to carry multi year coastal sediment transport simulations using ordinary desktop computers.

References

[1] P. Santoro and et al., "Hydrodynamic and fine sediment transport numerical modelling, application to the Rio de la Plata and Montevideo Bay" *XXII TELEMAC-MASCARET User Conference*, Daresbury Laboratory, UK, pp. 119-126, 2015.

[2] B. Elfrink and I. Brøker and G. Viggósson, "Bakkafjara sediment transport and morphology study, Report prepared by DHI Water and Environment, Hørsholm, Denmark, 2006.

[3] R. Walther, C. Cayrol, and L. Hamm, "Evaluation of an offshore disposal site in then Loire estuary through field monitoring and 3D numerical modelling," *XXI TELEMAC-MASCARET User Conference*, Grenoble, France, pp. 141-151, 2014.

[4] P. Prodanovic, "QGIS as a pre- and post-processor for TELEMAC: mesh generation and output visualization" *XXII TELEMAC-MASCARET User Conference*, Daresbury Laboratory, UK, pp. 119-126, 2015.

Statistical synthetic boundary conditions for a large 3D model, Scaldis, to reduce computation time

Maximova, T. [1], Smolders, S. [1], Vanlede, J.[1]
[1]Flanders Hydraulics Research
Berchemlei 115, 2140 Antwerp- Borgerhout, Belgium
tatiana.maximova@mow.vlaanderen.be

***Abstract*—This paper describes a methodology of using statistical synthetic boundary conditions which represent water level frequencies for a full year in a shorter period to reduce the computation cost for a large 3D model of the Scheldt estuary, Scaldis. For ecotope mapping water level frequencies of a full year are necessary to create the maps. The model is run for a shorter period which is statistically representative for the entire year.**

I. INTRODUCTION

In the framework of the projects "Integral Plan for the Upper Sea Scheldt" and "Agenda for the Future", an integrated plan is developed, in which navigability, safety and nature are combined. Currently, the capacity of the Upper Sea Scheldt is not sufficient and it hinders traffic flows. The river is classified as class IV route upstream Baasrode (located 113 km from the mouth). In the future it is desired to classify the entire Upper Sea Scheldt as a navigational route of Va class. It is important that the design of the enlargement leads to a multifunctional Scheldt with assets for navigability, a sustainable natural system and guarantees for protection against flooding [1].

An integrated model for the Scheldt estuary is developed in the TELEMAC 3D software. The Scaldis model, a new unstructured high resolution model of the tidal Scheldt is developed for the entire estuary, but with special attention to the upstream parts. The upstream part is represented in the model grid in high resolution resulting in a large extra number of computational nodes.

The model is developed and calibrated for 2013. Afterwards, it is adapted for the year 2050 to analyse the effects of several scenarios on the hydrodynamics, sediment transport and ecology. The expected (until 2050) changes in the bathymetry are implemented in the model. More flood control areas (FCA) with controlled reduced tide (CRT) are active in the model (accordingly to the Sigma plan) [2].The de-embanked areas, FCA's and CRT's got an update of their average bed level to account for sedimentation in these zones. Sea level rise and increasing or decreasing tidal amplitude are taken into account in different scenarios for 2050.

For the ecotope mapping it is necessary to calculate water level frequencies based on a full year. However, it is very costly to run the 3D Scaldis model for such a long period. To limit the calculation time, a different approach is used. The model is run for a shorter period which is statistically representative for the entire year.

This paper describes methodology used for the scenario analysis for the year 2050 with the statistical synthetic boundary conditions (water levels downstream and discharges upstream).

II. THE NUMERICAL MODEL

A. *Calibrated model for 2013*

The TELEMAC model developed in the framework of this project covers a large part of the North Sea, the entire Scheldt estuary and the Eastern Scheldt. Upstream, the model extends to the limits of the tidal intrusion (Figure 1).

The use of an unstructured grid allows to combine a large model extent with a high resolution upstream. The grid resolution varies from 500 m at the offshore boundaries to 7-9 m in the Upper Sea Scheldt.

The model grid consists of 459,692 nodes in 2D mesh and 873,419 elements. In the 3D model we use 5 levels totalling 2,298,460 of nodes with the following distribution of sigma layers : 0D, 0.12D, 0.30D, 0.60D, 1D.

Wind and salinity are included in the model. The most recent available bathymetry is used. The downstream model boundary is located in the North sea. Scaldis is nested in the regional ZUNO model of the southern North Sea. The time series of the water level calculated in ZUNO are defined at the downstream boundary of Scaldis (after correction of the harmonic components) [3, 4]. The upstream boundary is located at the tidal border. There are 8 upstream boundaries with prescribed discharge and free tracer.

Figure 1. Model domain

The model is calibrated for 2013 by comparison of the modeled and measured water levels, discharges and velocities [3]. Afterwards it is adapted for the year 2050 by implementation of the expected changes [5].

B. Model adaptation for 2050

For the analysis of different scenarios in 2050 several changes were implemented in the model.

The model bathymetry for the reference scenario is updated accordingly to the Sustainable Management Plan. This plan focusses on maintaining the fairway with respect for the tidal nature. The designed bathymetry takes into account the needs for navigation and the characteristics of the river. The impact on the tidal nature is limited to specific areas. The hydrodynamic and morphological processes can develop to the extent that the safety and tidal nature are not endangered. The Sustainable Management Plan aims to optimize the existing management efforts for navigation and protection of the river banks [6].

The bathymetry of different alternatives was provided by a project partner (IMDC). It was developed based on the requirements for accessibility for ships of a certain class, shipping simulations and design rules for navigational channels. The shape of the river channel is different in some alternatives due to the changes of river width, bends, sills, etc. The model grid had to be adapted so that it can be used for the calculation of the scenarios with different bathymetries. An example of the changes implemented in the model grid is shown in Figure 2. Bathymetry of two different alternatives for the same location is presented in Figure 3 and Figure 4.

The new grid has 472,400 nodes in 2D and 898,372 elements. This is 12,708 nodes more than the grid of Scaldis 2013 (in 2D). In 3D (5 levels) the new model grid has 2,362,000 nodes in total.

More flood control areas are implemented in the model. An estimation is made about the increase in bed level of the FCA's with CRT and the de-embankments by the year 2050 [5]. An example of FCA/CRT area is given in Figure 5.

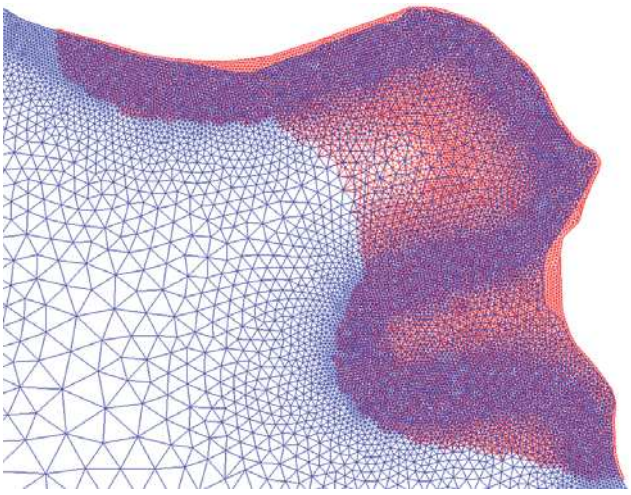

Figure 2. Changes in the model grid near the bend of Kramp in the Upper Sea Scheldt (blue colour: grid 2013, red colour: grid 2050)

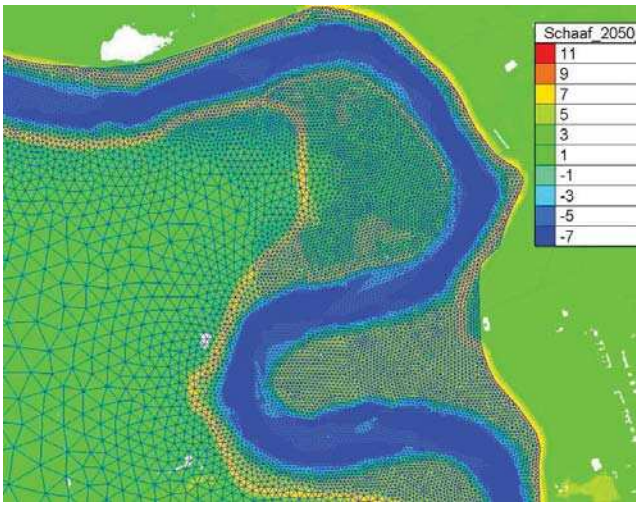

Figure 3. Bathymetry (mTAW) of Schaaf scenario at the bend of Kramp (the adapted grid at the background)

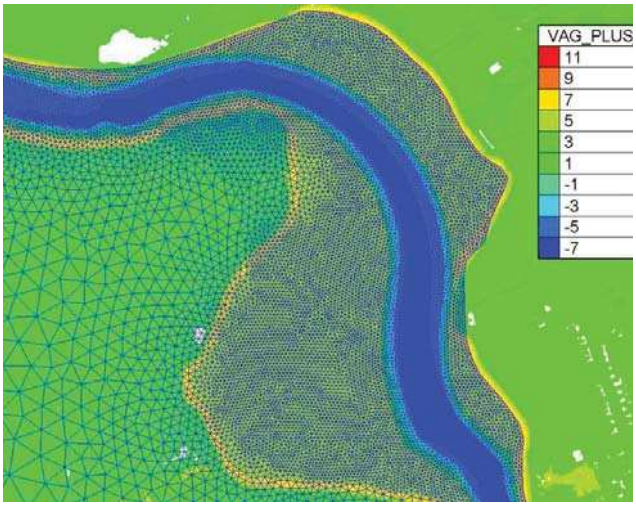

Figure 4. Bathymetry(mTAW) of VaG scenario at the bend of Kramp (the adapted grid at the background)

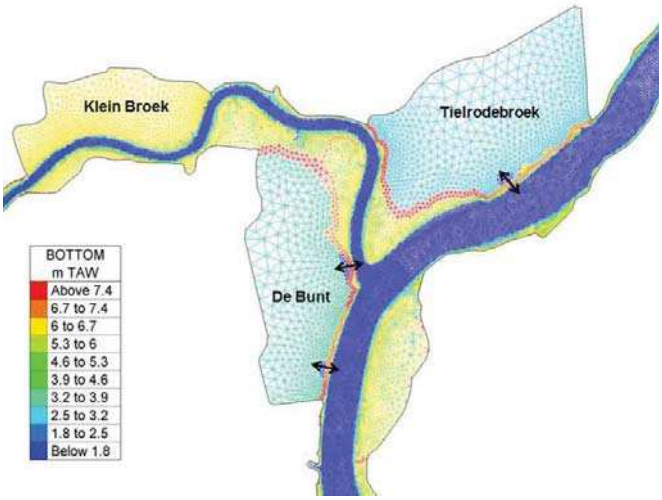

Figure 5. FCA/CRT Tielrodebroek, FCA/CRT De Bunt and the de-embankment of Klein Broek [5]

All these areas were already included in the mesh of the Scaldis model for 2013. In the model representing 2050 culverts connecting FCA's and CRT's are activated. The bathymetry of the flood control areas is updated.

III. METHODOLOGY

A. Introduction

The model will be used to evaluate the effects of different alternatives (specified morphology of the Scheldt river in a specific state and at a specific time), under different scenarios (a range of boundary conditions to take into account sea level rise, increasing or decreasing tidal amplitude, high or low discharge).

There are four different alternatives and four scenarios in 2050. This results in 16 simulations. For the ecotope mapping it is necessary to calculate water level frequencies based on a full year. However, it is very costly to run the 3D Scaldis model for such a long period. It takes about 37 hours to simulate 20 days using 180 processors plus it takes several hours to assemble the output files. 2D Selafin file has size of 30 Gb and 3D file is 128 Gb (run of 20 days). It was found that 180 processors is an optimal number for running this model [5]. The use of a larger number of processors does not decrease the simulation time (Figure 6).

In the framework of this project it would be impossible to run the model for the entire year for 16 scenarios. Therefore, it was necessary to find a different approach for the calculation of 1 year model output.

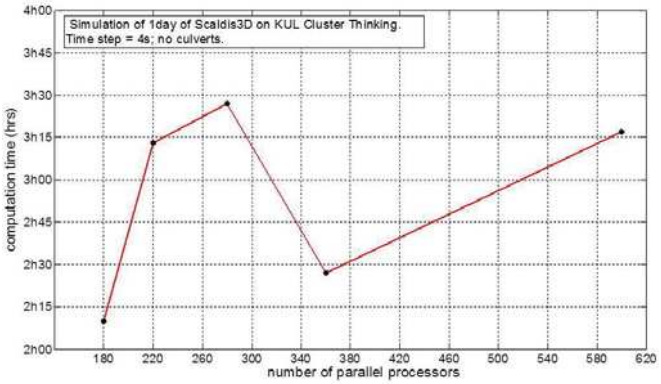

Figure 6. TELEMAC 3D Scaldis model performance on KUL Cluster Thinking on different number of parallel processors [5]

B. Statistical synthetic boundary conditions

Instead of running the model for the entire year two shorter periods with synthetic boundary conditions are simulated.

A period of 3 months is simulated with a synthetic discharge boundary containing events with a return period equal to or smaller than 1/6 year. The downstream boundary is a harmonic boundary without storm surge. In these 3 months a May – June period is represented and also a summer period. This run is the 'normal discharge' scenario. It is representative for the entire year if it is repeated 4 times.

Also the 'events discharge' scenario is simulated. It is a run of about two weeks with a discharge time series that contains 3 discharge events with return periods of 1 year, 1/2 year and 1/3 year. The downstream boundary of this run contains a storm surge period additional to the harmonic signal [1].

The downstream and upstream synthetic boundary conditions are calculated by IMDC. The methodology is described in detail in [7]. The surge is determined based on measurements from 1980 to 2010 at Vlissingen. The independent extreme events are found from the time series by the POT selection. Using these POT values, the empirical surge corresponding to T1, T1/2 and T1/3 was defined. The 30 largest surge events are then used to find the normalized profiles of surge (scaled from 0 to 1) [7]. The time series of the storm surge are found by combination of the normalized profiles and empirical values (Figure 7).

The discharge time series for the 'normal' and 'events discharge' scenarios were calculated by IMDC with the help of 1D hydrodynamic models of the Scheldt basin and its tidal tributaries [7]. The input of these models consists of precipitation time series as determined by the hydrological models. To find the time series representative for the year 2050 the precipitation and evaporation data are perturbed to the year 2050 with the perturbation tool of KULeuven [8]. Long term simulations are performed with the hydrodynamic models for the period 1982 to 2010. Independent events are selected from the time series by the POT selection. The average discharges during all May – June periods are used as a threshold. Based on these POT values the statistical parameters are calculated for the set up of the representative upstream discharges. The normalized profiles are found by normalization (scaling from 0 and 1) of all the time profiles of the biggest yearly May – June events and by calculation of the average profile. The final time series are made by combination of the statistical parameters and normalized profiles.

The 'normal discharge' and 'events discharge' scenarios are simulated for 2013 and for different combinations of alternatives and scenarios in 2050. The water level distribution in specific points, required for the ecotope mapping, is obtained by adding the 4 times 'normal' and 1 time 'events' scenarios.

C. Available data

I. Water levels

The following time series of water levels are available for Vlissingen:

- Storm surge (5 days) for the return periods T1, T1/2 and T1/3;
- Harmonic tide for 3 months for 2013 and 2050 calculated with the overall ZUNO model (a correction of the harmonic components is done);
- Harmonic tide for a short period with an upstream storm for 2013 and 2050.

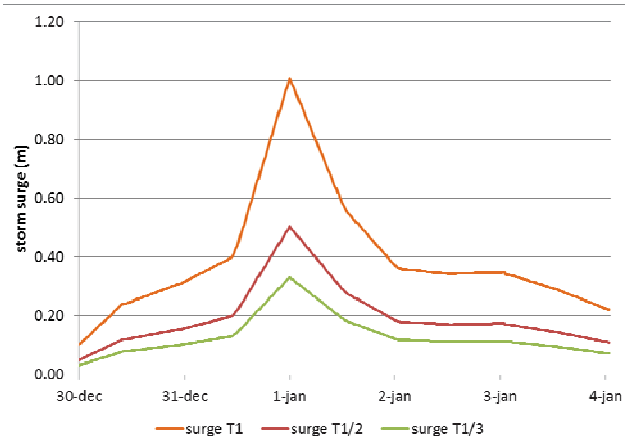

Figure 7. Storm surge at Vlissingen

The downstream boundary of the Scaldis model is located in the North sea. Therefore, the tide in Vlissingen will not be used directly for the calculations. Instead, the storm surge at Vlissingen (Figure 7) will be combined with a harmonic model boundary condition (in the North sea) obtained from a harmonic ZUNO run.

II. Discharges

The following time series of discharge are available for Rupel, Dender (tributaries of the Scheldt) and Scheldt (Leie-Bovenschelde):

- 3 months with representative May – June month and summer month for 2013 and 2050 (Figure 8);
- 7 days with storm events for the return period T1 for 2013 and 2050 (Figure 9);
- 7 days with storm events for the return period T1/2 for 2013 and 2050 (Figure 10).

IV. SCENARIOS

A. Normal discharge scenario

Downstream boundary of the 'normal discharge' scenario is a harmonic boundary without storm surge. Upstream boundary is a synthetic discharge boundary containing events with a return period equal to or smaller than 1/6 year.

The simulation period is 3 months.

3 months time series of the harmonic tide without storm surge is used as the downstream boundary condition. 3 months discharge time series are used as the upstream boundary conditions.

The maximum discharge of Dender (the second peak in the time series (Figure 8)) is expected 15 hours after the maximum high water at Vlissingen (IMDC, pers. comm.). The maximum high water is selected based on the analysis of 1 year harmonic time series for 2013 and 2050 respectively. The resulting combination of water level and discharge is presented in Figure 11 for the year 2050. A similar analysis was done for 2013.

Different spring-neap cycles are observed during the selected 3 months. Therefore, some of these tides represent average astronomical tide.

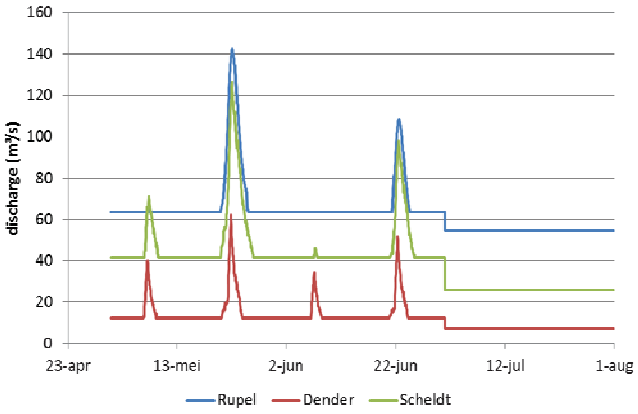

Figure 8. Synthetic discharge time series for 3 months for 2050

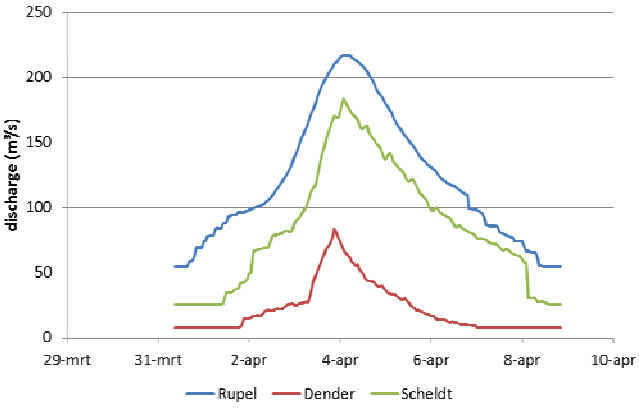

Figure 9. Discharge with return period T1 for 2050

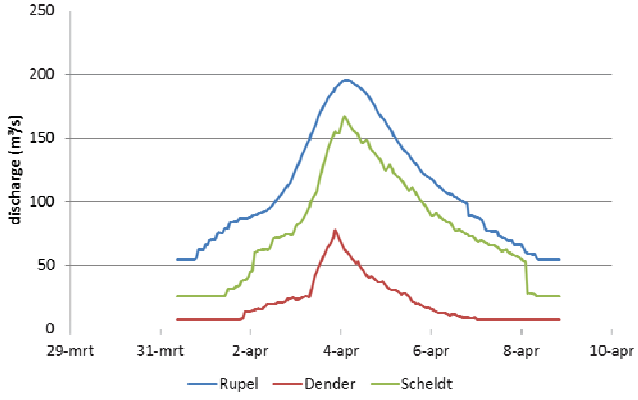

Figure 10. Discharge with return period T1/2 for 2050

The selected periods for the analysis are:

- from 01/08/2013 22:20 to 01/11/2013 21:20 for the current state run;
- from 12/08/2050 22:00 to 12/11/2050 21:00 for the run for 2050. Three days will be added to these periods for the spin up of the model.

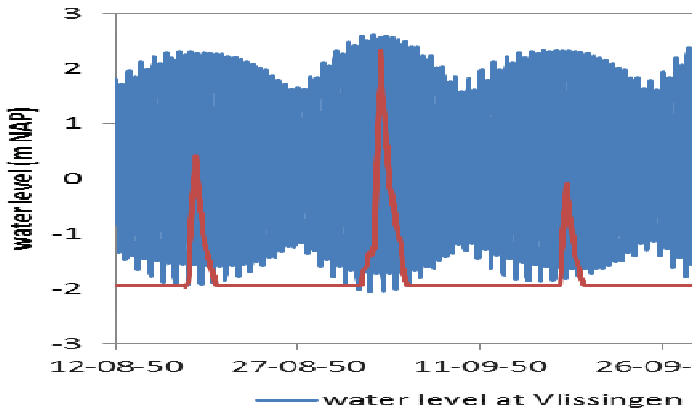

Figure 11. Combination of the time series for 2050 (for 'normal discharge' scenario)

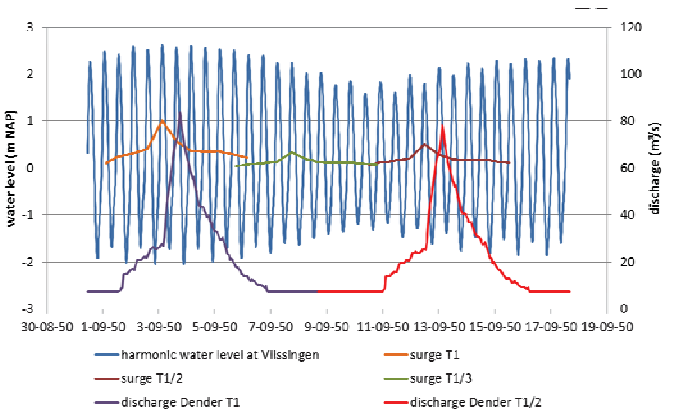

Figure 12. Combination of the time series for 2050 (for 'events discharge' scenario)

B. *Events discharge scenario*

The downstream boundary is a harmonic signal plus a storm surge signal. The typical storm surge was determined in a statistical way in [7] and is presented in Figure 7.

The upstream boundary is a discharge time series that contain 2 discharge events with return periods of 1 year and 1/2 year.

The simulation period is 2 weeks (or a few days longer depending on the combination of the boundary conditions upstream and downstream).

I. *Downstream boundary condition*

The water level at Vlissingen calculated in the harmonic ZUNO run is analyzed for the entire year 2013 (and 2050) and the maximum high water is found.

The peak of each storm surge (T1, T1/2, T1/3) should coincide with high water (conservative approach). The time series of the T1 surge is shifted so that the peak of T1 surge coincides with the highest high water at Vlissingen (23/08/2013 03:20 for the current state run, 03/09/2050 3:00 for 2050 run). The same surge time series are used for 2013 and 2050.

The time series of the surges with return periods T1/3 and T1/2 are made to coincide with high waters too. The surges are combined so that there are about 4.5 days between their peaks (Figure 12). To decrease the simulation period we let surges overlap for a limited time. When they overlap, the highest surge is taken for the calculation. The surge signal will be added to the harmonic water levels to get the downstream boundary condition of the Telemac model.

II. *Upstream boundary condition*

In total 14 days of discharge time series are available (7 days for T1 and 7 days for T1/2 return periods).

The maximum discharge at Dender is observed 15 hours after the maximum surge at Vlissingen. The peak of discharge T1 is therefore put 15 hours after the peak of surge T1; the peak of discharge T1/2 is put 15 hours after the peak of surge T1/2.

When no data are available (between discharges T1 and T1/2) a constant average discharge is used upstream. To decrease the simulation period we put the surge T1/3 between surges T1 and T1/2 (Figure 12).

If the downstream and upstream boundary conditions are combined in the way described above the following periods should be included in the analysis:

- from 20/08/2013 22:20 to 06/09/2013 12:20;
- from 31/08/2050 11:00 to 17/09/2050 16:00.

Three days will be added to these periods for the spin up of the model.

C. *Tidal range scenarios*

The model will be used to evaluate the effect of an increased and reduced tidal amplitude near Schelle and further upstream in the Upper Sea Scheldt. The increase and decrease of the amplitude will be enforced by changing the roughness in the Western Scheldt. By changing the roughness, the tidal propagation will be influenced, without simulating specific measures in the downstream parts of the estuary (e.g. creating additional flooding areas, deepening, etc.) [1].

Tidal range scenarios A+, A0 and A- will be modeled. In these scenarios the tidal amplitude at Schelle is 5.70, 5.40 and 5.00 m respectively (Table 1).

A necessary change of the bed roughness in the Western Scheldt is found by the sensitivity analysis. First, a modeled tide with a tidal amplitude of 5.40 m at Schelle was found in the calibrated model run. Afterwards a constant change of the roughness field of the Western Scheldt was applied (the area is shown in Figure 13). Different values of the roughness correction were tested (Figure 14).

When the bed roughness is decreased by 0.00426 $m^{-1/3}s$, the tidal amplitude at Schelle increases and becomes about 5.70 m. The increase of the roughness field by 0.00554 $m^{-1/3}s$ results in the tidal amplitude of about 5 m at Schelle.

TABLE I. TIDAL RANGE SCENARIOS

Scenario	Tidal amplitude at Schelle (m)
A+	5.70
A0	5.40 (current tidal range)
A-	5.00

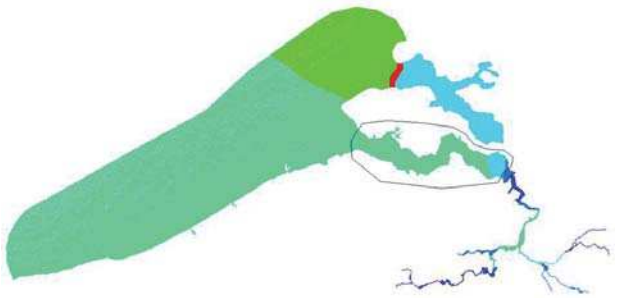

Figure 13. Bed roughness field of the Scaldis model (the polygon indicates the area where the bed roughness is adapted)

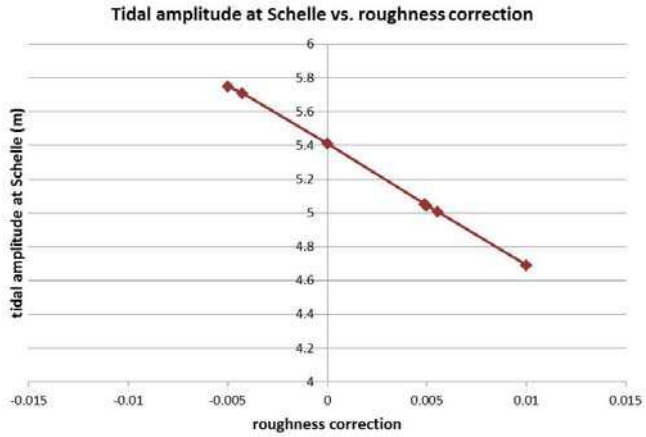

Figure 14. Plot of the tidal amplitude at Schelle vs. roughness correction

D. Sea level rise scenarios

The sea level rise scenarios in this study are based on the KNMI climate scenarios for the Netherlands [1]. The following runs will be modeled for 2050:

- the "low" scenario (CL, +15 cm in 2050);

- the "high" scenario (CH, +40 cm in 2050).

The downstream boundary conditions for year 2050 will be increased with these values.

The tidal range scenario A+ will be combined with the sea level rise CH. The tidal range scenario A- will be combined with the sea level rise CL. More information about the scenarios is given in [1].

V. CONCLUSIONS

This paper describes methodology used for the scenario analysis for the year 2050 with the statistical synthetic boundary conditions.

The model is developed and calibrated for 2013 in the TELEMAC 3D software. Afterwards, it is adapted for the year 2050 to analyse the effects of several scenarios on the hydrodynamics, sediment transport and ecology. The expected (until 2050) changes in the bathymetry are implemented in the model.

For the ecotope mapping it is necessary to calculate water level frequencies based on a full year. To limit the calculation time, two shorter periods ('normal discharge' (QN) and 'events discharge' (QE) runs) with synthetic boundary conditions are simulated instead of running the model for the entire year.

The output of the QN and QE runs is combined to produce the time series for each point for a period 4*QN + QE (which represents one year). These time series are used to calculate percentiles of water levels, tidal amplitudes, maximum and average flood and ebb velocities, bed shear stress, etc., which will be used for the ecological analysis.

REFERENCES

[1] IMDC/INBO/UA/WL (2015). Modelling instruments for Integrated Plan Upper Sea Scheldt. I/NO/11448/14.165/DDP

[2] Smolders S., Leroy A., Teles M.J., Maximova T., Vanlede J., (2016). Culverts modelling in TELEMAC-2D and TELEMAC-3D. Proceedings of the 23rd TELEMAC-MASCARET User Conference, 11-13 October 2016. Paris, France

[3] Smolders, S.; Maximova, T.; Vanlede, J.; Verwaest, T.; Mostaert, F. (2015). Integraal Plan Bovenzeeschelde: Subreport 1 – 3D Hydrodynamisch model Zeeschelde en Westerschelde. WL Rapporten, 13_131. Flanders Hydraulics Research: Antwerp, Belgium

[4] Vanlede, J.; Smolders, S.; Maximova, T.; Teles, M. J. (2015). The unstructured Scaldis model: a new 3D high resolution model for hydrodynamics and sediment transport in the tidal Scheldt. Proceedings of the 36th IAHR World Congress. 28 June – 3 July, The Hague, the Netherlands

[5] Smolders, S.; Maximova, T.; Vandenbruwaene, W.; Vanlede, J.; Verwaest, T.; Mostaert, F. (2016). Integraal Plan Bovenzeeschelde: Deelrapport 5 – Scaldis 2050. WL Rapporten, 13_131. Flanders Hydraulics Research: Antwerp, Belgium

[6] IMDC (2015a). Duurzaam Beheerplan Boven-Zeeschelde. Duurzame bathymetrie. I/RA/11448/14.240/JFA/

[7] IMDC (2015b). Bepalen van randvoorwaarden voor de referentiesituatie (2050) m.b.t. debiet en waterstand. I/NO/11448/15.128/TFR/

[8] Ntegeka V., Willems P., (2009) CCI-HYDR Perturbation Tool: a climate change tool for generating perturbed timeseries for the Belgian climate, Manual version January 2009, K.U.Leuven – Hydraulics Section & Royal Meteorological Institute of Belgium

Latest news on distributive advection schemes and dry zones: the ERIA scheme

Jean-Michel Hervouet
Laboratoire National d'Hydraulique et Environnement, Electricité de France
6 Quai Watier, 78400 Chatou, France
Email: jmhervouet@free.fr

***Abstract*—This paper is a continuation of "Distributive advection schemes and dry zones, new solutions", published in 2015, and "Ongoing research on advection schemes", published in 2014 in this series of proceedings (References [12] and [13]). The 2015 publication described an adaptation of distributive schemes called the LIPS scheme (Locally Implicit Psi Scheme). The use of a local implicitation coped with dry zones. The drawback was a number of linear systems to solve. We present here another solution inspired from the iterative process of the NERD scheme (Reference [8]). The new method loops on triangles while the NERD scheme looped on segments. The rotating cone test shows that the new method is better than the LIPS scheme, much less sensitive to the Courant number, and faster since it does not solve linear systems. A test case is presented, with bridge piers and an island treated as a dry zone. It shows the ability of the method in such situations: the maximum principle is strictly obeyed and mass conservation is obtained at machine accuracy.**

I. Introduction

Mass conservation, maximum principle and stability on dry zones are now fairly well handled in the Telemac system (see the Telemac release notes from 2007 to 2013 given in references, which can be found on the website www.opentelemac.org). Consequently minimising the numerical diffusion has now become the new cutting edge where progresses improve the quality of studies. For example the release of pollutants in rivers, the stability of stratifications, and the numerical simulation of non-linear waves are highly dependent on the quality of advection schemes, on their space and time orders.

In the 2014 Telemac User Club several improvements were presented (References [12]). In finite volumes the HLLC scheme (Reference [6]), with first and second order, was implemented. In finite elements, the classical N and PSI distributive schemes could be improved by adding the derivative in time in the upwinding process. It was done in a predictor-corrector procedure, after a publication by Mario Ricchiuto (Reference [11]). The predictor gives an approximation of the derivative in time of the tracer, which is then used in the corrector step.

Three test cases were presented: a pollutant plume in a steady state river, the transport of a stain, and the rotating cone. The height of the cone after one rotation, which should theoretically be 1, was 0.21 for the classical PSI scheme, 0.47 for the HLLC second order scheme, and 0.53 for the new predictor-corrector PSI scheme.

In 2015 a new criterion for proving monotony was coined, which allowed to perform as many correction steps as wanted, with a predictor which is just maintained within a given range and is not even subjected to mass conservation (Reference [13]). With 4 extra correction steps the rotating cone dramatically grows from 0.53 to 0.75. A second order in time version of the predictor-corrector was also developed, in accordance with References [1] and [11].

Then, to cope with dry zones, a locally implicit predictor-corrector scheme was designed, with high implicitation only in the dry zones. This new scheme allows to choose an arbitrary time-step, and the rotating cone height after one rotation raised to 0.79. This scheme was called LIPS (Locally Implicit Psi Scheme).

In 2016 the stability criterion was changed in the LIPS scheme, raising the cone height after one rotation to 0.84. However the drawback of the LIPS scheme is that a number (at least one) of linear systems must be solved. More recently a new scheme was designed, that combines the idea of the NERD scheme and all the ideas developed during Sara Pavan's PhD (Reference [14]). This new scheme is called ERIA, acronym of **E**lement by element **R**esidual distributive **I**terative **A**dvection scheme). *Eria* is also a genus of asiatic orchids. The NERD scheme was a succession of iterations on all the segments.The new scheme is a succession of iterations on all the triangles, advection being solved locally with the new predictor-corrector and corrections already presented. The advantage is that a PSI scheme can be applied locally, while with the NERD scheme only the N scheme could be used. The ERIA scheme appears to be better and faster than LIPS, and less sensitive to Courant number. It requires no solution of linear system. The cone height after one rotation is 0.46 without correction and 0.75 with 4 corrections, with a symmetry seemingly better preserved than previous schemes. If tuned with sub-iterations, the cone heigth can even be higher than 0.86.

We shall now give detailed explanations on the new ERIA scheme and show the first results.

II. The ERIA scheme

The NERD scheme is based on fluxes between points given by the N scheme. As the NERD scheme basically works on isolated segments, there is no way to use the PSI scheme concept, which involves *a minima* three points. We show here

the possibility of a triangle-based iterative scheme. It consists in treating independently every triangle with its own local fluxes, the quantities of water and tracers carried by points being shared between triangles according to rules that will be detailed. The local fluxes are limited to ensure the positivity of the water mass locally carried by the points. This is done by provisionnally reducing the local fluxes. The part of the initial fluxes which is left-over is kept for the next iteration. The iterations are stopped exactly like in the NERD scheme, when all the fluxes have been transfered, or when a maximum of iterations is reached.

After one iteration the quantities carried by points are assembled, so that a new depth and a new value of tracer can be computed. This keeps the positivity of depth and the monotony of tracers if it has been ensured locally on every triangle. Hereafter we thus only study the problem on a single triangle, with limited fluxes that will not cause negative depths and will ensure stability. Boundaries and sources are treated before (if bringing water) and after (if removing water) the transfer of internal fluxes, exactly like with the NERD scheme, and so are not taken into account here.

A. Predictor step

In the predictor step at element level, we will have initial quantities of water dedicated to every point, denoted $volp(i)$ ("vol" for volume and "p" for predictor). Classical distributive schemes choose simply:

$$volp(i) = \frac{S_T\ h_i^n}{3} \tag{1}$$

where S_T is the area of the triangle and h_i^n is the initial depth of point i, so that the sum of all volumes locally given to point i is the total quantity of water carried by this point, i.e. $S_i\ h_i^n$, where S_i is the integral of the test function of i, also the area associated to this point. We keep this constraint here but the distribution is different. When dealing with an element we want to get final local volumes denoted $V_{i\ local}^{n+1}$ such that:

$$V_{i\ local}^{n+1} = volp(i) - \Delta t \sum_{j\ in\ t} \overline{\Phi}_{ij} \geq 0 \tag{2}$$

where $volp(i)$ is our initial volume that remains to be defined. The fluxes $\overline{\Phi}_{ij}$ are the local fluxes Φ_{ij} (from i to j) given by the N scheme, but limited in a way that will also be defined later. The bar thus means "limited". The notation $\sum_{j\ in\ t}$ means a sum on the two other points of the triangle t that contains i. This can also be written in terms of depth, but if we start from the initial depths and if we transfer all the fluxes of one element it will give a local depth $h_{i\,local}^{n+1}$ that may be different, for the same point, in another element. Namely we have:

$$V_{i\ local}^{n+1} = \frac{S_T\ h_{i\ local}^{n+1}}{3} = \frac{S_T\ h_i^n}{3} - \Delta t \sum_{j\ in\ t} \overline{\Phi}_{ij} \geq 0 \tag{3}$$

The initial volumes $volp(i)$ are chosen following an offer and demand principle, so as to minimise the further reduction of fluxes. Let us first imagine that a classical local volume $S_T h_i^n/3$ has been *a priori* given to point i in a triangle. Sometimes this local volume will not be large enough to keep the depth positive (without reducing the fluxes). Sometimes it will be largely enough, e.g. points that will receive water in the triangle could even be given no initial volume. Namely when point i in an element is such that:

$$\frac{S_T\ h_i^n}{3} - \Delta t \sum_{j\ in\ t} \max(\Phi_{ij}, 0) \geq 0 \tag{4}$$

it can give this positive quantity to its *alter ego* in other elements and keep a positive final local depth $h_{i\ local}^{n+1}$. On the contrary in elements where i is such that:

$$\frac{S_T\ h_i^n}{3} - \Delta t \sum_{j\ in\ t} \max(\Phi_{ij}, 0) < 0 \tag{5}$$

it is in need of the opposite of this negative quantity. We can thus compute a total demand $td(i)$ and a total offer $to(i)$ for every point, by summing on all the neighbouring elements, introducing the notation $\sum_{t\ni i}$ meaning a sum on all triangles t containing a point i:

$$to(i) = \sum_{t\ni i} \max\left(\frac{S_T\ h_i^n}{3} - \Delta t \sum_{j\ in\ t} \max(\Phi_{ij}, 0), 0\right)$$

$$= \sum_{t\ni i} \max\left(\frac{S_T\ h_{i\,local}^{n+1}}{3} + \Delta t \sum_{j\ in\ t} \min(\Phi_{ij}, 0), 0\right) \tag{6}$$

$$td(i) = -\sum_{t\ni i} \min\left(\frac{S_T\ h_i^n}{3} - \Delta t \sum_{j\ in\ t} \max(\Phi_{ij}, 0), 0\right)$$

$$= -\sum_{t\ni i} \min\left(\frac{S_T\ h_{i\,local}^{n+1}}{3} + \Delta t \sum_{j\ in\ t} \min(\Phi_{ij}, 0), 0\right) \tag{7}$$

We can then choose for each occurence of i the initial volume that it will get, reasoned as a correction of the *a priori* initial value $S_T\ h_i^n/3$:

In elements where i is "donnor":

$$volp(i) = \frac{S_T\ h_i^n}{3}$$

$$- \left(\frac{S_T\ h_i^n}{3} - \Delta t \sum_{j\ in\ t} \max(\Phi_{ij}, 0)\right) * \frac{td(i)}{\max(td(i), to(i))} \tag{8}$$

In elements where i is "receiver":

$$volp(i) = \frac{S_T\ h_i^n}{3}$$

$$-\left(\frac{S_T\ h_i^n}{3}-\Delta t\sum_{j\ in\ t}\max(\Phi_{ij},0)\right)*\frac{to(i)}{\max(td(i),to(i))} \tag{9}$$

The formulas ensure that all that is given is received. If demand exceeds offer, all donnors will give what they have to give and it will be shared between receivers, if offer exceeds demand, all receivers will get what they need and the donnors will give only what is necessary.

We have thus optimally distributed the water between triangles, but this is not enough to avoid negative depths and this is why we now limit the fluxes. We now want that the limited fluxes are such that:

$$volp(i)-\Delta t\sum_{j\ in\ t}\max(\overline{\Phi}_{ij},0)\geq 0 \tag{10}$$

So we define $\beta(i)$ such that, if:

$$\Delta t\sum_{j\ in\ t}\max(\Phi_{ij},0)>volp(i) \tag{11}$$

we have:

$$\beta(i)=\frac{volp(i)}{\Delta t\sum_{j\ in\ t}\max(\Phi_{ij},0)} \tag{12}$$

and for all fluxes that leave point i:

$$\overline{\Phi}_{ij}=\min(\beta(i),\beta(j))\Phi_{ij} \tag{13}$$

A key point in the procedure is the fact that the fluxes Φ_{ij} are N or PSI fluxes. It means that in a triangle one of them at least is 0, and that the two others are either converging to a single point (1-target case) or leaving a single point (2-target case). All fluxes leaving a point have thus the same sign, so reducing them independently will reduce the total flux leaving the point. *It would not be the case with fluxes of different signs*. In the case of N or PSI fluxes it is easy also to understand that in $\min(\beta(i),\beta(j))$ one of the β will be equal to 1 if Φ_{ij} is not 0 (because a point only gives or only receives, and a point that receives water has $\beta=1$), so our reduction is the minimum that can be done. Choosing a constant reduction within a triangle would slow down a lot the process, with situations where a dry point could be able to stop the flux between the two other possibly wet points.

Compared to the other distributive schemes, here the new volume $volp(i)$ replaces $S_T\ h_i^n/3$ in the formulas, e.g. the predictor will locally become:

$$\frac{S_T\ h_{i\ local}^{n+1}}{3}C_{i\ local}^{n+1}=volp(i)C_i^n$$

$$-\Delta t\sum_{j\ in\ t}\min(\overline{\Phi}_{ij},0)C_j^n-\Delta t\sum_{j\ in\ t}\max(\overline{\Phi}_{ij},0)C_i^n \tag{14}$$

where C_i^n is the original concentration of tracer for point i, $C_{i\ local}^{n+1}$ is the final local concentration of the same point (i.e.obtained without communicating with other elements), and $h_{i\ local}^{n+1}$ is the final local depth of point i, defined by Equation 3.

The predictor equation can be rearranged in the form:

$$\frac{S_T\ h_{i\ local}^{n+1}}{3}C_{i\ local}^{n+1}=\frac{S_T\ h_{i\ local}^{n+1}}{3}C_i^n$$

$$-\Delta t\sum_{j\ in\ t}\min(\overline{\Phi}_{ij},0)\left(C_j^n-C_i^n\right) \tag{15}$$

To get the real equation actually solved at predictor level, we still need to add the PSI reduction, denoted with a backward arrow. It is applied to the right-hand side, so that we now write:

$$\frac{S_T\ h_{i\ local}^{n+1}}{3}\left(C_{i\ local}^{n+1}-C_i^n\right)=$$

$$-\Delta t\overleftarrow{\sum_{j\ in\ t}\min(\overline{\Phi}_{ij},0)\left(C_j^n-C_i^n\right)} \tag{16}$$

We briefly recall here what is the PSI non linear reduction: if a_1, a_2 and a_3 are the quantities to be reduced, corresponding to points 1, 2 and 3 in a triangle. We define the total contribution in the triangle as:

$$a_{tot}=a_1+a_2+a_3 \tag{17}$$

The three original contributions are then modified by multiplication factors, with the effect that the sum is unchanged (thus keeping the mass conservation) and that all contributions have the sign of the total. For example if $a_{tot}>0$ this is obtained by replacing:

$$a_1\text{ with }\frac{\max(a_1,0)\ a_{tot}}{\max(a_1,0)+\max(a_2,0)+\max(a_3,0)}$$

$$a_2\text{ with }\frac{\max(a_2,0)\ a_{tot}}{\max(a_1,0)+\max(a_2,0)+\max(a_3,0)} \tag{18}$$

$$a_3\text{ with }\frac{\max(a_3,0)\ a_{tot}}{\max(a_1,0)+\max(a_2,0)+\max(a_3,0)}$$

Similar formulas with function $\min$ are used when $a_{tot}<0$. With triangles there exists a simpler equivalent consisting of reduced fluxes Φ_{ij}^{psi} (see e.g. Reference [3]), but it works only with original N fluxes, not when derivatives in time are added, and moreover the formulas given here easily extend to other elements.

Equation 14 shows that monotony is given by the positivity of the coefficient of C_i^n, which is $volp(i)-\Delta t\sum_{j\ in\ t}\max(\overline{\Phi}_{ij},0)$, or $S_T\ h_{i\ local}^{n+1}/3$, and it is exactly the condition 10 that we have secured with the reduction of fluxes. This is also valid for Equation 16 where, compared to Equation 14, the negative component in the coefficient of C_i^n is reduced. It appears thus that the local positivity of volumes is the only condition to stabilise a PSI scheme. Merging all

local values, by weigh-averaging all occurences of a point in its different triangles, will give a final mass conservative and monotone result.

As we have limited the fluxes, we must do a book-keeping of all fluxes that still must be transfered, and try to transfer them in successive iterations. At the end of an iteration k, the fluxes that have not been transfered, thus being kept for iteration $k+1$, are denoted Φ_{ij}^{k+1}, they are:

$$\Phi_{ij}^{k+1} = \Phi_{ij}^{k} - \overline{\Phi}_{ij}^{k} = (1 - \min(\beta(i), \beta(j)))\, \Phi_{ij}^{k} \qquad (19)$$

Iterations are stopped when all the remaining fluxes are 0, or small enough, or after a maximum number of iterations. This will cause no problem if the fluxes finally transfered are the same than the fluxes transfered for computing the new depths with the continuity equation, what we have called the "positive-depths" algorithm. However this algorithm was so far based on a "segment by segment" transfer which is compatible with the NERD scheme (and is in fact its main idea). If we want the ERIA scheme to be fully compatible with the algorithm doing the correction of depths to get positive values, we must then change this algorithm and organise "triangle by triangle" transfers of water, as described above. This raises no additional difficulty, except that this new algorithm had to be implemened and offered as a new option for the treatment of negative depths (namely option 3, the NERD scheme requiring option 2). NERD and ERIA are thus incompatible.

A first very promising result is that testing what has just been said, by running only the predictor step without further correction, the rotating cone height after 1 rotation is already 0.4603. This is to be compared with the 0.21 of the PSI scheme and the 0.39 of the NERD scheme.

B. Corrector step

We now consider that the predictor step has given us, on a given triangle, local values of the predictor, which we denote $C^*_{i\,local}$. When assembled, these local values will give another monotone value $C^*_{i\,global}$. To facilitate the explanations we first study a basic solution that will be monotone but with high numerical diffusion. We shall then present a more complicated version with a very low numerical diffusion. The key difference between them is the value considered for computing the derivative in time.

1) Basic solution: We take here the local value of the depth for the derivative in time introduced in the corrector right-hand side, i.e. the value obtained after a local transfer of fluxes, without considering the other triangles. We thus write the corrector in the form:

$$\frac{S_T\ h_{i\ local}^{n+1}}{3} C_{i\ local}^{n+1} = \frac{S_T\ h_{i\,local}^{n+1}}{3}(C_i^* - C_i^n)$$

$$+\frac{S_T\ h_i^n}{3} C_i^n - \Delta t \sum_{j\ in\ t} \overline{\Phi}_{ij} C_i^n \qquad (20)$$

$$\overleftarrow{+\frac{S_T\ h_{i\,local}^{n+1}}{3}(C_i^n - C_i^*) + \Delta t \sum_{j\ in\ t} \min(\overline{\Phi}_{ij}, 0)\left(C_i^n - C_j^n\right)}$$

It is nothing else than a PSI scheme with in the right-hand side the estimated derivative first added (immediately after the sign $=$), then removed in PSI reduced form (first term under the backward arrow). It simplifies into:

$$\frac{S_T\ h_{i\ local}^{n+1}}{3} C_{i\ local}^{n+1} = \frac{S_T\ h_{i\,local}^{n+1}}{3} C_i^*$$

$$\overleftarrow{+\frac{S_T\ h_{i\,local}^{n+1}}{3}(C_i^n - C_i^*) + \Delta t \sum_{j\ in\ t} \min(\overline{\Phi}_{ij}, 0)\left(C_i^n - C_j^n\right)} \qquad (21)$$

The monotony condition can be enforced locally by imposing that the coeffcient of C_i^n is positive:

$$\frac{S_T\ h_{i\,local}^{n+1}}{3} + \Delta t \sum_{j\ in\ t} \min(\overline{\Phi}_{ij}, 0) \geq 0 \qquad (22)$$

This is, if we look at our definition of $h_{i\,local}^{n+1}$, strictly equivalent to Condition 10. We have thus derived a viable scheme, but unfortunately its numerical diffusion is too high, probably because the local depth is too far from the actual final depth, so upwinding is not well done locally. The results with the rotating cone are the following:

TABLE I: basic solution, effect of corrections on numerical diffusion.

corrections	0	1	2	3	4	5
cone height	0.46	0.30	0.32	0.33	0.34	0.34

The performance is downgraded by the corrections, this is thus very disappointing.

2) A better solution: In the previous solution, instead of choosing a local volume $S_T\ h_{i\,local}^{n+1}/3$, we would prefer taking $S_T\ h_i^{n+1}/3$, i.e. choosing a volume corresponding to the real final depth of point i, but this would lead to monotony problems (this is well exemplified by the rotating cone test case which crashes). What freedom do we have to choose the local volumes? Actually, any kind of volume $volc(i)$ (c added for "corrector") would not spoil mass conservation as soon as we have:

$$\sum_{t\ \ni\ i} volc(i) = S_i\ h_i^{n+1} \qquad (23)$$

at the condition that we write the corrector as:

$$volc(i)\left(C_{i\ local}^{n+1} - C_i^*\right) =$$

$$\overleftarrow{volc(i)(C_i^n - C_i^*) + \Delta t \sum_{j\ in\ t} \min(\overline{\Phi}_{ij}, 0)\left(C_i^n - C_j^n\right)} \qquad (24)$$

i.e. that we use also $volc(i)$ for the derivative in time in the right-hand side. As a matter of fact the sum over all triangles around i will then give:

$$S_i\ h_i^{n+1}C_i^{n+1} = S_i\ h_i^{n+1}C_i^* +$$

$$\sum_{t\ \ni\ i} \overleftarrow{volc(i)(C_i^n - C_i^*) + \Delta t \sum_{j\ in\ t} \min(\overline{\Phi}_{ij}, 0)\left(C_i^n - C_j^n\right)} \tag{25}$$

where we see that $volc(i)$ just replaces the classical $S_T\ h_i^{n+1}/3$ in the right-hand side. Only the distribution of volumes locally reduced has an influence on the global result. At this level it is interesting to look at the proof of monotony of our previous explicit predictor-corrector, if we exclude sources and boundary terms. It was:

$$S_i h_i^{n+1}C_i^{n+1} = S_i h_i^{n+1}C_i^*\ +$$

$$f_i S_i h_i^{n+1}\left(C_i^n - C_i^*\right) + \Delta t \sum_j \mu_j \min(\Phi_{ij}, 0)\left(C_i^n - C_j^n\right) \tag{26}$$

f_i and μ_j being coefficients in the range [0,1], due to the PSI reduction in various triangles. We have here a very similar problem, but with a fundamental advantage on our side: at element level the PSI reduction represented by the backward arrow would give $f_i = \mu_j$, which fortunately avoids a stricter stability condition. The only problem is, as usual, the positivity of the coefficient of C_i^n, which is locally, before reduction:

$$volc(i) + \Delta t \sum_{j\ in\ t} \min(\overline{\Phi}_{ij}, 0) \tag{27}$$

The PSI reduction, which is actually a multiplication by a number in the range [0,1], will not change the sign. We thus only need to ensure that:

$$volc(i) + \Delta t \sum_{j\ in\ t} \min(\overline{\Phi}_{ij}, 0) \geq 0 \tag{28}$$

Condition 28 is close to Condition 10. A striking remark is that the classical predictor-corrector approach would have introduced here a combination of both conditions in the form:

$$volc(i) - \Delta t \sum_{j\ in\ t} \max(\overline{\Phi}_{ij}, 0) + \Delta t \sum_{j\ in\ t} \min(\overline{\Phi}_{ij}, 0) \geq 0 \tag{29}$$

It is also:

$$volc(i) - \Delta t \sum_{j\ in\ t} abs(\overline{\Phi}_{ij}) \geq 0 \tag{30}$$

We are here less restrictive and it will bring a better behaviour of the scheme for high Courant numbers. We have seen that choosing $volc(i) = S_T\ h_{i\,local}^{n+1}/3$ for the derivative in time leads to monotony but behaves poorly. We would like to have instead $volc(i) = S_T\ h_i^{n+1}/3$ but it is potentially unstable. Can we mix both solutions? We can again organise exchanges between triangles. When $h_{i\,local}^{n+1} < h_i^{n+1}$ the point i needs an extra volume $S_T\ \left(h_i^{n+1} - h_{i\,local}^{n+1}\right)/3$ to get the correct derivative in time, without spoiling the local monotony. When $h_{i\,local}^{n+1} > h_i^{n+1}$ this is not so obvious, we can only, to avoid negative volumes, go down to a minimum value $h_{i\ \min}^{n+1}$ such that:

$$\frac{S_T\ h_{i\ \min}^{n+1}}{3} = -\Delta t \sum_{j\ in\ t} \min(\overline{\Phi}_{ij}, 0) \tag{31}$$

That is to say we can only give a volume $S_T\ \left(h_{i\,local}^{n+1} - h_{i\ \min}^{n+1}\right)/3$. We have thus for every point again a total offer and a total demand, but with different definition, thus denoted $toc(i)$ and $tdc(i)$ (again c added for "corrector"). If the total offer $toc(i)$ exceeds the total demand $tdc(i)$ we can revert to choosing $S_T\ h_i^{n+1}/3$ everywhere. If not we can share the available extra quantity. The strategy is summarised by using for every point the volume $volc(i)$:

$$volc(i) = \frac{S_T\ h_{i\,local}^{n+1}}{3}$$

$$+\frac{S_T\ \max\left(h_i^{n+1} - h_{i\,local}^{n+1}, 0\right)}{3}\frac{\min(toc(i), tdc(i))}{tdc(i)} \tag{32}$$

The total demand is:

$$tdc(i) = \sum_{T\ \ni i}\ \max\left(\frac{S_T h_i^{n+1}}{3} - \frac{S_T h_{i\,local}^{n+1}}{3}, 0\right) \tag{33}$$

The total offer is:

$$toc(i) = \sum_{T\ \ni i} \frac{S_T\left(h_{i\,local}^{n+1} - h_{i\ \min}^{n+1}\right)}{3}$$

$$= \sum_{T\ \ni i}\left[\frac{S_T h_{i\,local}^{n+1}}{3} + \Delta t \sum_{j\ in\ t} \min(\overline{\Phi}_{ij}, 0)\right] \geq 0 \tag{34}$$

This solution leads to the following results with the rotating cone:

TABLE II: final solution, effect of corrections on numerical diffusion.

corrections	0	1	2	3	4	5
cone height	0.460	0.698	0.738	0.748	0.752	0.753

The shape of the cone is well preserved (see Figure 1). We have a regular convergence, tested up to 12 corrections, where we have a height of 0.756.

Using the PSI fluxes or the N fluxes in the computation of the offer $to(i)$ in the predictor step does not make any difference, so it is simpler to keep the N fluxes.

By construction, the scheme is sensitive to the time step (like NERD and LIPS, but unlike other distributive schemes

which organise their own time stepping). Table III compares NERD, ERIA and LIPS at various time steps on the rotating cone test. DT is the basic time step that does a rotation in 32 steps. It is not a convergence study, since the mesh size is unchanged, we only test here the effect of the Courant number. The error given is the square of the Euclidian norm of the difference between the original cone and its value after one rotation. This parameter is interesting, though difficult to interpret because it mixes two kinds of errors: the amplitude error and the phase error. All the tests are done with a fixed number of 5 corrections. The table shows however that NERD and ERIA are at their best with larger Courant numbers.

TABLE III: effect of time step on numerical diffusion and error.

time step	DT	DT/2	D/4	DT/6
NERD cone height	0.39	0.34	0.29	0.23
NERD error	10.05	11.47	13.68	16.94
ERIA cone height	0.75	0.78	0.80	0.86
ERIA error	1.01	1.08	2.34	4.50
LIPS cone height	0.10	0.15	0.32	0.64
LIPS error	26.64	23.31	15.18	5.16

time step	DT/7	DT/8	DT/16	DT/32
NERD cone height	0.21	0.21	0.18	0.17
NERD error	17.82	18.41	20.06	2.72
ERIA cone height	0.87	0.85	0.81	0.74
ERIA error	4.75	4.03	1.76	1.31
LIPS cone height	0.76	0.82	0.82	0.74
LIPS error	4.22	4.70	2.31	1.36

The surprise is that the ERIA scheme is amazingly not very sensitive to the Courant number. There is however an optimum, with an impressive maximum height of 0.87, which corresponds to a Courant number of about 1, though the shape should also be discussed and compared, as it is not better (see Figure 2), and paradoxically coincides with the worst error. Figure 1 corresponds to DT, the fist column in the table. This large time step gives for ERIA, as for NERD, the minimum error. In the same conditions LIPS gives a poor cone height of 0.10 and the maximum error. The reason is that for high Courant numbers the LIPS scheme reacts by increasing implicitation, and the implicit part of LIPS is done without PSI reduction, as this would introduce non-linearity in the (otherwise linear) system. The two other schemes are on the contrary always explicit, at the cost of a few successive iterations to transmit all the fluxes.

III. A TEST CASE WITH DRY ZONES

The test case of a flow around bridge piers, in the Telemac-2D portfolio of examples, has been chosen, but the bottom has been modified so that a part of the domain is dry, thus forming an island. To achieve this, a disc of radius 4 m has been carved out around the point of coordinates (6,0), by setting the bottom elevation at 5 m instead of 0. In Figures 3 and 4 the tracer on

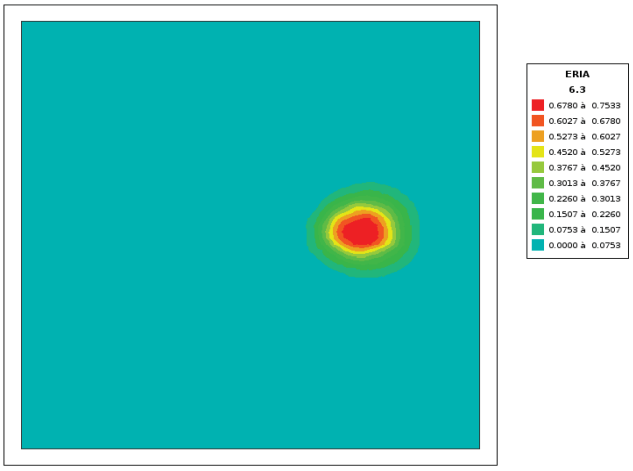

Fig. 1. Rotating cone test. Cone after one rotation, with ERIA scheme, 5 corrections. One rotation in 32 steps (DT).

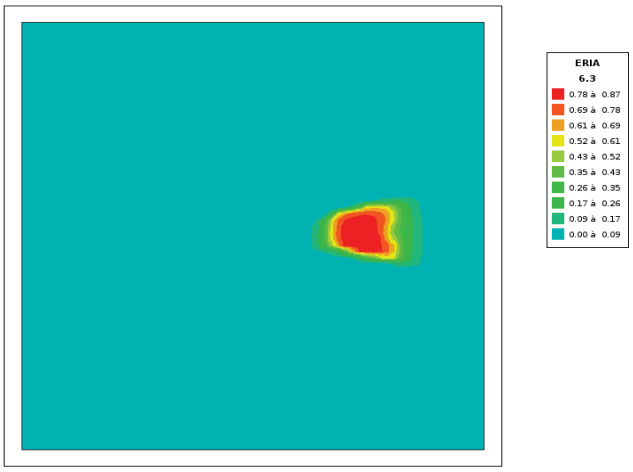

Fig. 2. Rotating cone test. Cone after one rotation, with ERIA scheme, 5 corrections. One rotation in 224 steps (DT/7).

the island has been artificially set to 0 after the computation, to visualise the island. Otherwise the values are between 1 and 2, according to the initial and boundary conditions. The island contour is uneven due to the mesh roughness. Being a steady state, this case is not really meant for the predictor-corrector approach since the derivative in time is about 0, but we show the ability to cope with dry areas. With no correction the new ERIA scheme appears again to perform better than LIPS, as regards the numerical diffusion (see the extent of the yellow level, which represents values between 1.6 and 1.7). With smaller time steps they tend to give closer results (not shown here). The loss of mass at the end of the 200 steps of 0.4 s is 0.45 10^{-12} for ERIA and 0.1 10^{-8} for LIPS (tracers without unit). It is due to the fact that ERIA only depends on machine accuracy while LIPS depends on its solver accuracy. The Malpasset dam break test case has also been tested and behaves correctly.

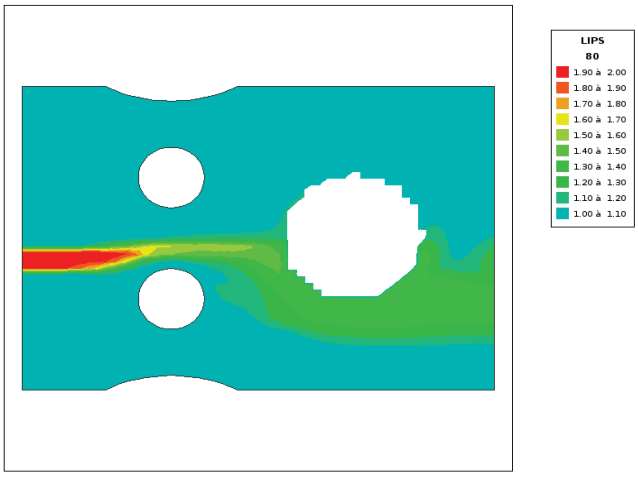

Fig. 3. Bridge pier test case with an island. Tracer with LIPS.

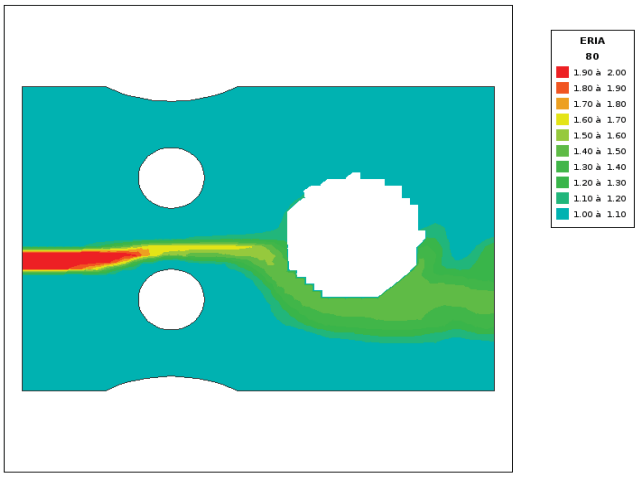

Fig. 4. Bridge pier test case with an island. Tracer with ERIA.

IV. Conclusion

The ERIA scheme takes advantage of two recent progresses done in the field of distributive advection schemes, namely:

- The predictor-corrector approach, with iterations on corrections if necessary.
- The idea of the NERD scheme applied to triangles, to get an unconditional stability.

Moreover a new system of distribution of masses between elements, done in a different way at predictor and corrector levels, relaxes the stability condition.

The scheme has the following properties:

- Mass conservation
- Monotony
- Low numerical diffusion
- Ability to cope with dry zones
- Unconditional stability
- No linear system to solve

The low numerical diffusion is obtained by the optimised distribution of available water when splitting the mesh into isolated triangles for doing an iteration of the scheme. This was the case also, in a lesser extent, with the NERD scheme. This idea could actually as well be applied to the other distributive schemes.

In the rotating cone test case the height of the cone after one rotation can now be more than 4 times higher than what we get with the classical PSI scheme. There is no extra problem with domain decomposition parallelism. The sensitivity to the Courant number has been much reduced, compared to the LIPS scheme.

Is there still room for improvement? Why not? We know that the weak form of the method of characteristics still gives far better results on the rotating cone test (but fails to be monotone and is not mass conservative, and so is discarded for most applications). There is a number of technical weaknesses or problems of the new scheme that could be examined and are as many hints of possible improvements:

- The "upwind" of the derivative in time, which is considered the breakthrough that triggered the initial progress of all distributive schemes, is actually not really an upwind, just a PSI non linear limitation. A real upwind spoils so far the stability proof and remains an open problem. This is the case of all predictor-corrector distributive schemes.
- The ERIA scheme is only a first order scheme. The theory of a second order form remains to be done, and attempts to do so were to no avail so far. The difficulty, as always, is the proof of stability. It is probable that a second order form would require a stricter stability condition, thus more limitation of the fluxes, thus more iterations.
- The extension to 3D will probably raise technical problems. We have heavily used in the derivation the fact that the N scheme leads only to a 1-target and a 2-target case. It is certainly not the case with prisms.
- The need to tune parameters such as the number of corrections. It would be better to have an automatic adaptation.

Anyway, a lot of interesting progresses have been done recently in the field of distributive schemes, bringing a new advantage to unstructured meshes. These low-diffusion schemes offer a lot of new possibilities to explore.

References

[1] ABGRALL R., MEZINE M.: Construction of second order accurate monotone and stable residual distribution schemes for unsteady flow problems. Journal of Computational Physics. 188:16-55. 2003.
[2] HERVOUET J.-M., PHAM C.-T.: Telemac version 5.7, release notes. Telemac-2D and Telemac-3D. 2007.
[3] HERVOUET J.-M.: Hydrodynamics of free surface flows, modelling with the finite element method. Wiley & sons. 2007.
[4] HERVOUET J.-M., RAZAFINDRAKOTO E., VILLARET C.: Telemac version 5.8, release notes. Telemac-2D, Telemac-3D and Sisyphe. 2008.
[5] HERVOUET J.-M.: Telemac version 5.9, release notes. Bief, Telemac-2D, Telemac-3D and Sisyphe. 2009.
[6] TORO E.F.: Riemann Solvers and Numerical Methods for Fluid Dynamics. Springer, 2009.
[7] HERVOUET J.-M.: Telemac version 6.0, release notes. Telemac-2D and Telemac-3D. 2010.
[8] HERVOUET J.-M., RAZAFINDRAKOTO E., VILLARET C.: Dealing with dry zones in free surface flows: a new class of advection schemes. Proceedings of the AIRH congress, Brisbane, June 2011.

[9] ATA R., HERVOUET J.-M.: Telemac version 6.2, release notes. Telemac-2D, Telemac-3D. 2012.
[10] HERVOUET J.-M., PAVAN S.: Telemac version 6.3, release notes. Telemac-2D, Telemac-3D. 2013.
[11] RICCHIUTO M.: An explicit residual based approach for shallow water flows. Inria Research Report n°8350, Project-Team Bacchus, September 2013.
[12] HERVOUET J.-M., PAVAN S., ATA R.: Ongoing research on advection schemes. Proceedings of the 21^{st} Telemac User Club, Artelia,Grenoble, France, 15-17 October 2014.
[13] HERVOUET J.-M., PAVAN S., ATA R.: Distributive advection schemes and dry zones, new solutions. Proceedings of the 22^{nd} Telemac User Club, STFC Daresbury, UK, 13-16 October 2015.
[14] PAVAN S.: New advection schemes for free surface flows. Thèse présentée pour l'obtention du grade de docteur de l'Université Paris-Est. 15 February 2016.

Comparison of 2 D and 3 D model for the Lower Rhine part from Xanten to Emmerich

Marie Brunel
Federal Waterways Engineering
and Research Institute (BAW)
76227 Karlsruhe, Germany
marie.brunel@baw.de

Dr. Regina Patzwahl
Federal Waterways Engineering
and Research Institute (BAW)
76227 Karlsruhe, Germany
regina.patzwahl@baw.de

Abstract— **Nowadays, at the Federal Waterways Engineering and Research Institute (BAW) the standard hydro-numerical river model is a two dimensional, depth-averaged model with relatively high horizontal resolution with one unique parameter set being valid over the whole discharge range from low waters to floods. However, in order to reduce the model dimensionality (3D to 2D) a few factors need to be taken into account to offset the information loss. In our approach using Nikuradse roughness law the required singular, consistent set of parameters can be only achieved when one uses the horizontal eddy viscosity coefficient computed by the *Elder* approach. The computed viscosity coefficients can get very high and lead to unwanted consequences. In this context, it is often suggested to switch to a vertically coarse discretised 3D-model which can be almost as computationally efficient as a 2D-model but which is closer to the physics and more credible when it comes to the mathematical basis of the numerical model. In this study we do the recommended step and have a look at the consequences from the modeller's point of view. We investigate issues as computational costs, additional efforts to the modeller, calibration properties, velocity distributions and assess the advantages and disadvantages.**

I. INTRODUTION

Nowadays, at the Federal Waterways Engineering and Research Institute (BAW) the standard hydro-numerical river model is a two dimensional, depth-averaged model with relatively high horizontal resolution. It is due to the fact that this sort of model provides a good balance between simulation time and quality of results. However, in order to reduce the model dimensionality (3D to 2D) a few factors need to be taken into account to compensate for the information loss. First of all, 2D-models cannot compute neither vertical secondary flows and turbulence nor correct velocity distribution in the entrance and the exit of a bend. Significantly, the dispersion of the vertical velocity profile needs to be taken into account. This becomes an important issue when the model is to be calibrated over a whole discharge range from low water levels to floods and for in-stationary flow conditions as in morphological and flood scenario applications. Furthermore, in trained rivers - such as the German waterways - the hydraulic impact of 3D-structures like groynes and parallel dams need to be adequately represented with a single consistent set of parameters. The whole discharge spectrum has to be taken into account where the flow conditions in context of the regulation structures change with rising water levels: from emerged obstacles to barely submerged sills, showing critical flow over their crest, to thoroughly submerged sills which can be treated as additional form roughness to the flow. These flow conditions lead to increased backwater as do the momentum dispersion of the vertical velocity profile and vertical turbulence. The 2D-model parameterises these vertically induced losses by horizontal losses. Experience shows that in our standard modelling approach using Nikuradse roughness law the required singular, consistent set of parameters can be only achieved when one uses the horizontal eddy viscosity coefficient computed by the *Elder* approach which combines turbulent losses and the effect of momentum dispersion. The computed viscosity coefficients can get very high and in certain combinations of geometrical and flow conditions can then lead to distorted or wrong velocity cross sections. Moreover, advanced horizontal turbulence modelling becomes awkward.

In this context, it is often suggested to switch to a vertically coarse discretised 3D-model which can be almost as computationally efficient as a 2D-model but which is closer to the physics and more credible when it comes to the mathematical basis of the numerical model. Using the Telemac suite allows a straightforward switch from 2D to 3D using the same mesh and adding vertical layering.

Over the years, at BAW numerous 3D river models and flume investigations also with other solvers, e.g. [1,2], were set-up and successfully used in project work. One drawback of these models is the computational effort which is needed, even more so as river models get longer (> 25 km) and the need for high resolution grows.

In this study we make the recommended step and have a look at the consequences from the modeller's point of view. We will stay simple in the way the 3D-model is set-up and look at computational cost, practical issues such as calibration efforts and for differences in the results.

II. MODEL DESCRIPTION

A. *The 2D reference model*

We have chosen a 24 km long stretch of River Rhine as study case. The 2D-Telemac [3] model is located between

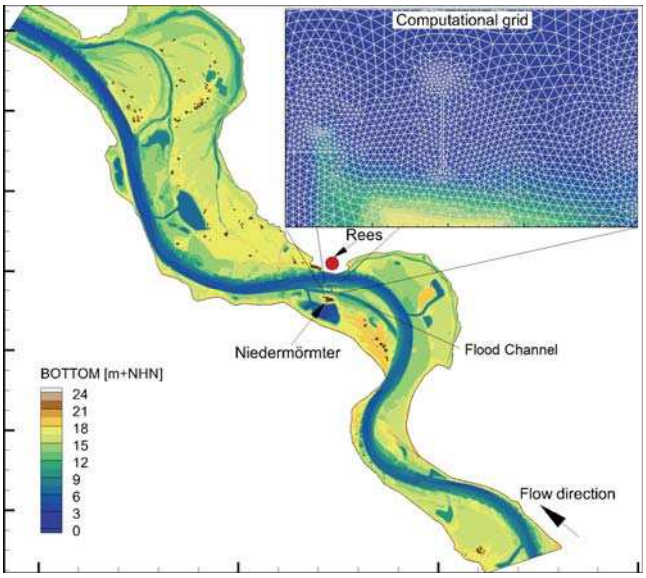

Fig. 1: Bottom elevation of the model area and grid structure

Xanten (Rhine kilometre (Rh-km) 825) and Emmerich (Rh-km 849) in North Rhine-Westphalia, close to the Netherlands border. This river section contains groynes, bends, flood channel and many retention areas. The flood channel was built between 2010 and 2015 and it is located in a bend upstream Rees (Rh-km 834 – 838). It contains an opening that allows ferry boat service between Rees and the village of Niedermörmter.

The main channel is discretised with a mean resolution of 5 m in summing up to a total of 1.4 million elements. The grid was divided in different areas according to its land uses characteristics (river, groynes, arable land …) and its size. Thus, the distribution of Nikuradse roughness coefficient k_s was realised in the model via 781 different zones.

TABLE I. NUMERICAL PARAMETERS OF THE 2D-TELEMAC MODEL

No. total of elements	***Min./Max edge length [m]***
1.4 Mio	0,44/38,21
Turbulence Model	***Roughness Model***
Elder	Nikuradse
Type of advection	***Time step [s]***
14;5	1.0
Telemac Version	***Parallel Processes***
V6p3	80

The model was calibrated by matching computed results to water level references by adjusting Nikuradse roughness coefficient k_s. For calibration it is suitable to define identity numbers for each roughness type and define the k_s-values in an external table. Having the most important impact on the water level elevation, the k_s-values of the river bed as well as the values for the scour fillings occurring in the two up-stream bends were modified from the lowest to the biggest discharge in order to fit as best possible to the water level measurements. For the rest of the roughness patches standard values were chosen (see Table III). All of the main parameters are reported in Table I. We have used 10 different water level measurements which were taken between 2009 and 2015 and are all listed in Table II.

Some of the water level references are somewhat outdated as they were taken before the flood channel was opened in 2015 (Q = 1031 m³/s, Q = 2274 m³/s and Q = 5469 m³/s). In order to finally validate the friction model the flood channel was closed in the mesh and these three discharge scenarios were simulated both with the current model and the modified model with the closed flood channel.

TABLE II. DISCHARGES USED FOR THE 2D-MODEL SIMULATION

Discharges [m³/s]			
Low water			
1031*	1108	1526	1706
Mean water			
1920	2009	2274*	3053
Flooding			
4673	5469*		
*: discharges used for 3D-simulations			

The distribution of the most important k_s-values over the model domain after calibration is given in Table III.

TABLE III. K_S VALUES FOR THE MODEL AREA

Zone type	***k_s [m]***	***Zone type***	***k_s [m]***
River bed	0.02 -0.06	Arable land	0.35
Scour filling	0.025 – 0.15	Field	0.15
Bank	0.03	Wood	0.4
Groynes	0.5	Water body	0.05
Other areas	0.1		

B. *Extension to 3D*

The 3D-Telemac [4] model uses the same horizontal base mesh as the 2D-Telemac model described above. As the aim of the study is to evaluate vertically coarse 3D-modelling and not setting up a full 3D-modell, sigma layering with non-uniform discretisation with three and five vertical levels respectively was defined. All relevant numerical parameters are given in Table IV. For this 3D-model, the aim was to simulate three representative discharges (e.g. emerged and submerged groynes) for this stretch of Rhine River.

TABLE IV. NUMERICAL PARAMETERS OF THE 3D-TELEMAC MODEL

No. total of elements	***Min./Max edge length [m]***
1.4 Mio x 3 or 5 respectively	0,44/38,21
Turbulence Model	***Roughness Model***
k-epsilon, mixing-length	Nikuradse
Type of advection	***Time step [s]***
14,5	2.0
Telemac Version	***Parallel Processes***
v7p1, hydrostatic	140

A re-calibration of the 3D-model was needed and done with the same water level references as used for the 2D-model. Technically, in a 3D-model, k_s is a boundary condition. The chosen way of defining the k_s-values via IDs and tables is not available for the 3D-model. So, in order to keep things simple for calibration, a uniform distribution of k_s was chosen. A k_s-value of 0.04 m for the bottom was found to give reasonable results and can be regarded as an averaged

value of the k_s-distribution along the river bed defined in the 2D-model.

III. INVESTIGATIONS

Within the scope of the study, several parameters were chosen and modified in order to compare the 2D- and 3D-simulations. We have focused on the vertical and horizontal turbulence model and the number of layers. Six scenarios were analysed (Table V). Due to time limitations, other vertical discretisation methods were not studied. Both models are operated with stationary boundary conditions.

TABLE V. 3D-SCENARIOS

Turbulence model	K-epsilon Isotropic
	mixing length (vertical) + Smagoringsky (horizontal)
	mixing length (vertical) + constant viscosity (horizontal) of 0.01 m²/s
Number of layers	3 log. distributed
	5 log. distributed

We will focus on the additional effort for the modeller for setting up a 3D-model, have a look at the computational costs, we will look at the models' behaviour with increasing discharge in respect to computed water levels and look at the velocity distribution.

IV. RESULTS

A. *Additional effort for modeller for setting up a 3D-model*

Although Telemac-2D and Telemac-3D are relatively similar, the adjustment of the different parameters, data management, modeller adaptation to a 3D-model and simulation is an additional effort for modeller.

Furthermore, the 3D-result management is quite difficult: first because of the amount of data and second because a pre-treatment of the results is needed before any practical usage. E.g. the 3D-result file needs to be sliced before analysing the vertical distribution of the defined and/or computed parameters is possible. An adequate and efficient processing system is needed (e.g. Postel).

B. *Computational Cost*

Regarding the computational cost, we can consider two different aspects for comparison: the computational time for a given duration of simulation (here, we took 10 000 time steps) or until the stationary state of the flow was reached. Even though on average the 2D simulation time is quantitatively less important than for 3D simulations, the difference of duration to reach the steady state is not significant. Table VIII offers a comparison of the computational time. The 2D-model is about 3.75 times faster than the "cheapest" 3D-model with three layers and the *mixing-length* model combined with constant horizontal viscosity. Adding the *Smagorinsky* turbulence model for horizontal turbulence adds little to the computational effort. As well known, the *k-epsilon* model costs much more computational effort: it is 8.5 times slower than the 2D-model, operated with Elder.

TABLE VI. COMPARISON OF THE COMPUTATIONAL TIME AND STATIONARY REGIME ATTAIN TIME

	Computational time for 10 000 seconds of simulation [min] per processing unit			**Time to attain stationary regime [min]**		
2D-model	2,18			19,76		
3 layers	***Q1031***	***Q2274***	***Q5469***	***Q1031***	***Q2274***	***Q5469***
k-epsilon	17,47	17,18	18,51	127,53	77,31	155,48
mixing length, Smagorinsky	9,03	9,47	11,1	67,73	52,09	69,57
mixing length, constant viscosity	8,21	8,51	11,15	63,22	26,38	99,24
5 layers	***Q1031***	***Q2274***	***Q5469***	***Q1031***	***Q2274***	***Q5469***
k-epsilonc	34,35	36,27	37,33	250,76	123,32	332,24
mixing length,Smagorinsky	15,43	16,38	18,34	115,73	98,28	152,22
mixing length, constant viscosity	13,48	14,59	17,17	103,80	72,95	169,98

C. *Calibration over discharge spectrum with one parameter set*

As already claimed in the introduction, the standard numerical two-dimensional river model set-up at BAW is supposed to use one single set of parameters over the whole discharge and flow condition spectrum. This also holds for the 3D-simulations. In order to stay comparable within the model variations, the k_s-value of 0.04 m was not changed. The restriction to one parameter set for all discharges has caused some problems in the recalibration of water-levels. In the case of the low and mean water discharges, the differences between the model and the 2D reference are small, even with the simpler k_s-distribution used in 3D. Fig. 2 shows the water level differences between simulation and measurements for all three discharges. In order to compare with ease, we will stay in large scale and globality. But it is evident that local modification of k_s-coefficients is required for better results and calibration. For low and mean flow, the result for the 3D-model especially with *k-epsilon* and 3 layers are slightly better or comparable to the 2D reference. *k-epsilon* with 5 layers and the model operated with *mixing-length* and *Smagorinsky* model give good results too. The results for the combination of *mixing-length* and constant viscosity model with 5 layers for low water (Fig. 2, above) show water levels too high compared to the reference water levels. The chosen horizontal viscosity of 0.01 m²/s is obviously too high. The computed water levels for Q = 2274 m³/s (Fig. 2, middle) are on average above the 2D reference water level with a peak at Rh-km 835 of 0.13 m. Lowest water levels are computed by the model operated with *k-epsilon* and 5 layers. For the flood event (Fig. 2, bottom) all water levels computed by the 3D-models strongly underestimate the water level of the 2D-simulation (0.25 m) and reference water level (0.35 m).

Partially these differences (~0.05 m) result from the absence of the flood channel during the measurements. The rest is due to numerical reasons and cannot be improved easily. From experience it is known that models run with *k-epsilon* model usually are little sensitive to changes of k_s-values [3]. So in order to raise the computed water level by 0.30 m a very large k_s-value would be needed and would

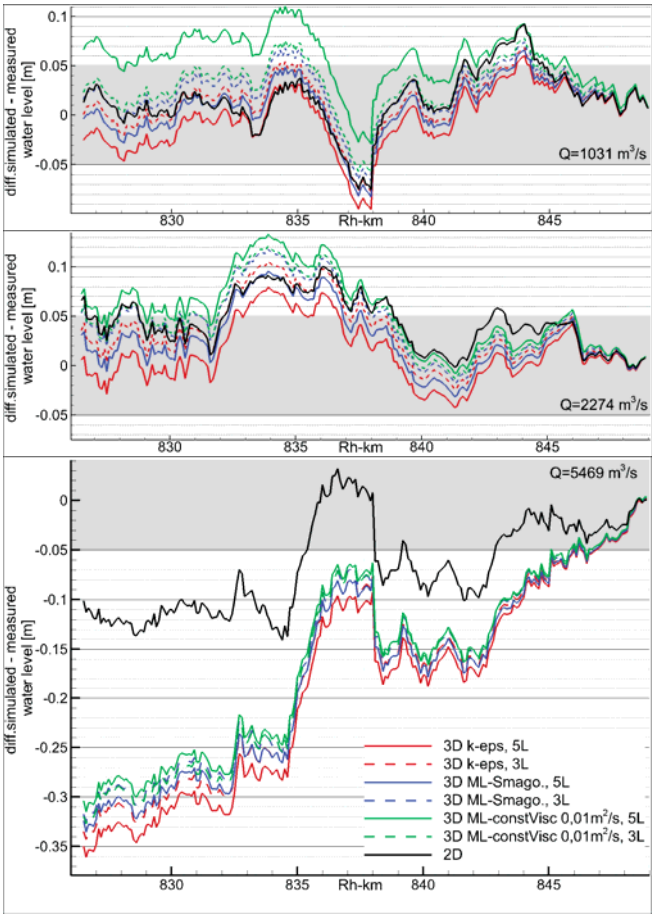

Fig. 2: Water level difference between simulated and reference water level for all of the 2D and 3D simulations

certainly lead to a massive overestimation of the water levels for the other two discharges.

Models operating with *mixing-length* models usually are more sensitive to this parameter but increasing the k_s-values would also lead to an overestimation of the water levels for the other two discharges.

D. *Lateral Velocity distribution*

In order to look for differences in the lateral velocity distribution of the models we extracted several cross-sections from the result files (2D-depth-averaged for the 3D-computations). Fig. 3 shows the scalar velocity in the cross section Rh-km 832.2 for the 3 discharges simulated with 3 layers. It allows comparisons between the different turbulence models in 3D-simulation with the 2D-model. Some differences can be notified on the outer part of the right bank and the river between 3D and 2D. The three turbulence models calculate relatively similar velocities except in the critical locations previously listed. Disparities come to 0.15 m/s at the left bank and 0.05 m/s in the bend.

Fig. 4 offers a comparison between the 2D-model, and the *Smagorinsky* turbulence model with different numbers of layers, 3 and 5. The selected cross section at Rh-km 838.1 is located at the exit of the flood channel. The contrasts between 3 and 5 layers are not significant. In fact, the maximum difference between the two models is 0.01 m/s in right and left bank and the river bend. Nevertheless, we can

notice a significant difference between 2D and 3D. First of all, the peak of velocity in the bend is shifted by 50 m for Q = 1031 m³/s (Fig. 4 a) and 100 m for Q = 5469 m³/s (Fig. 4 c). Moreover, in the channel exit we can observe a variation of 0.1 to 0.3 m/s between the 2D and 3D simulations.

E. *Velocity distribution in the entrance and exit of bends*

In theory the lateral and longitudinal velocity distribution in the entrance and exit of bends of depth-averaged 2D-models differs from that of 3D-models. Especially at the exit of the bend, where secondary flow is still fully developed it takes some distance before the water body has switched back to an "undisturbed" flow condition. Such a difference in distribution of velocities can be significant when it comes to the morphological and nautical assessment of river regulation measures.

In the simulations described here no such effect was clearly visible. There are differences but they are small and cannot clearly be associated with this effect. Investigations at BAW [5] on this matter showed little influence on the results of transport modelling.

F. *Velocity distribution in the vertical*

When secondary flow occurs, the flow direction in the upper parts of the water body differs from that of the lower part. For transport, the bottom near flow direction is the determining one. To see this effect it is enough to run simulations with three layers. The effect is visible in both the computationally cheaper *mixing-length* approach as well the *k-epsilon* model.

V. Discussion

To calibrate a river model with only one unique parameter set for a large range of discharges means a harsh restriction to the representation of the physics and the modelling. In doing so, one can get along in 2D, using the Elder approach, which combines turbulent losses and the effect of momentum dispersion. All vertical losses are transferred to the horizontal level, so, one often gets a good result with an approach, that is nonphysical in this respect. A roughness predictor like the van-Rijn predictor [6] can help in getting correct water levels for very high discharges as it adds roughness to account for the bed form hysteresis but can bear disadvantages e.g. when it comes to investigating future river training measures.

In 3D river models, the increasing losses which occur with increasing discharge and which lead to backwater effects can mostly be produced by the turbulence models. This investigation showed that for parts of these losses cannot be taken account for by the turbulence models used. Again roughness predictors like the van-Rijn predictor [6] might help as they increase roughness with increasing discharges but very often, 3D river models are rather insensitive to higher roughness coefficients, even more so with high discharges. From other investigations [1] we learned that switching to the non-hydrostatic version can also

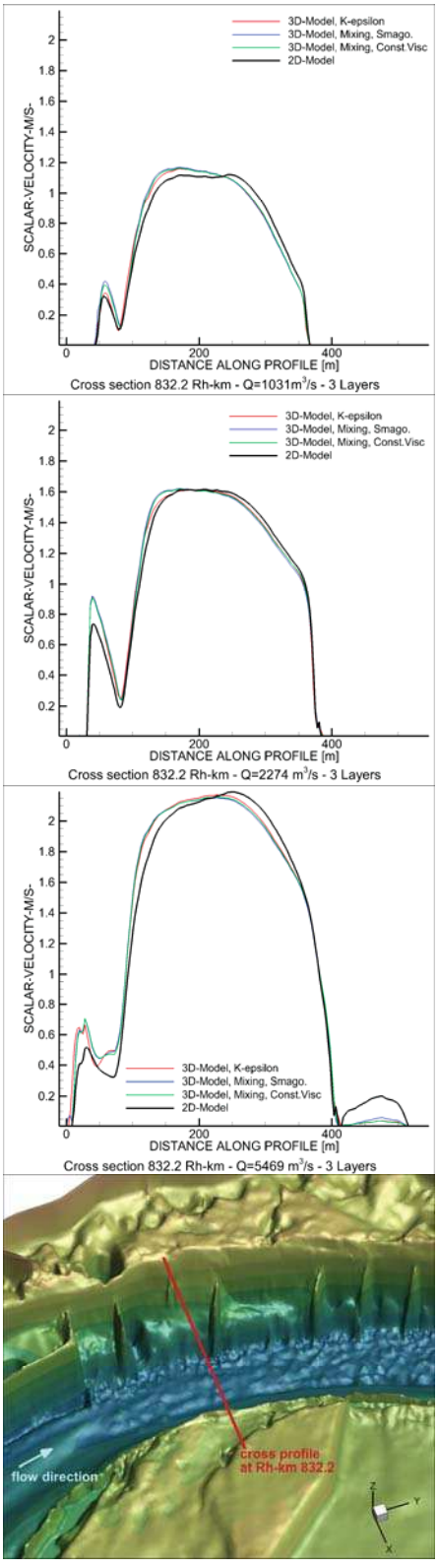

Fig. 3: Comparison of the computed scalar velocity along the cross section Rh-km 832.2 for low flow (a) mean flow (b) high flow (c) for the 3D simulation (3 layers, different turbulence models) with the 2D simulation. A global view of the cross section geometry is offered in plot d)

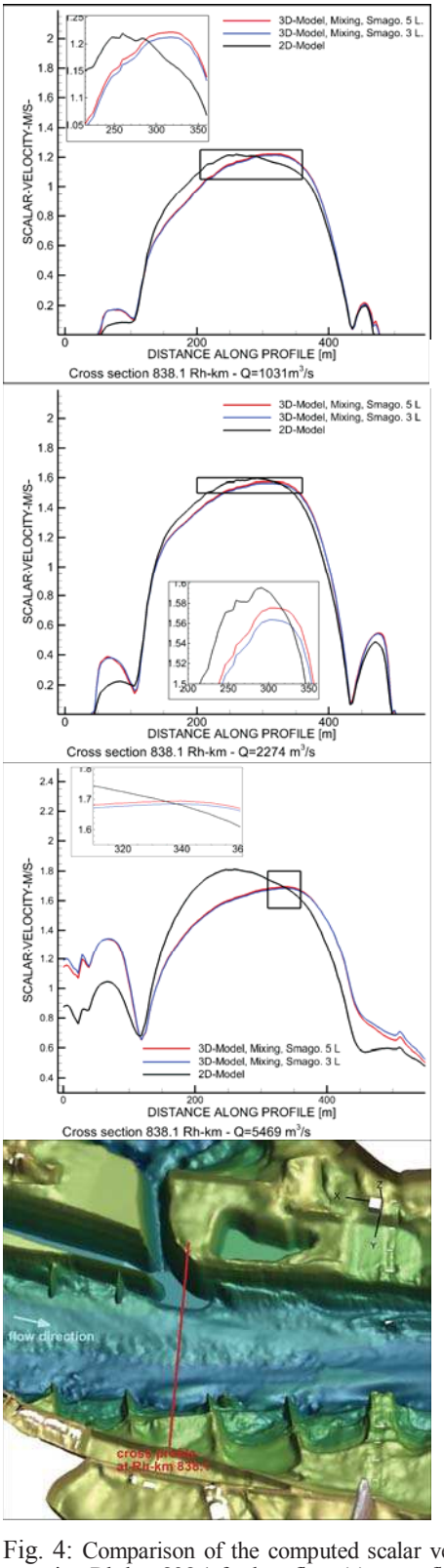

Fig. 4: Comparison of the computed scalar velocity along the cross section Rh-km 838.1 for low flow (a) mean flow (b) high flow (c) for the 3D simulation (*Smagorinsky* model, 3 and 5 layers) with the 2D. A global view of the cross section geometry with the exit of the flood channel is offered in plot d)

lead to increased losses with increased discharges. If it also works for very high discharges is still to be tested.

It is well known, that 3D-modelling increases the computational time in relation to 2D-modelling depending on the turbulence model and number of layers (in this study at least 3.75 times more computational effort). On the other hand it allows obtaining less artificial results. This type of data is then useful for instance in the study of bed load transport, as several horizontal layers allow vertical variability of the velocity vector.

VI. CONCLUSION

The aim of this work was to explore if a vertically coarse discretised 3D river model can be a substitute for a 2D-model which's "only" fault is its simplified model physics. The investigation confirmed that even the 3D model with its turbulence models as they are, cannot *per se* fulfil the demand for a river model which can be operated with one set of parameters over the whole discharge range. There seems to be need for investigating formulations for river energy loss modelling valid over the whole discharge range in order to simplify the modellers life.

ACKNOWLEDGEMENT

The authors thank all colleagues who were willing to support this work with advice and discussion, namely Rebekka Kopmann and Jacek Jankowski for reading and discussing the manuscript.

REFERENCES

[1] Baron, M. and R. Patzwahl (2013), Influence of numerical schemes in representing flow over and around groynes, Proceedings to the 20th Telemac-Mascaret User Conference.J.

[2] Patzwahl, R., Jankowski, J. and Lege, T., Very high resolution numerical modelling for inland waterway design. In: Proceedings of RiverFlow2008, IAHR, Izmir, Turkey

[3] J-M. Hervouet (2007), Hydrodynamics of the free surface flows: modelling with the finite element method. Chichester: Wiley, Formerly CP

[4] www.opentelemac.org, TELEMAC-3D manual.

[5] Riesterer, J., Grafmüller, T. and T. Wenka (2013), Comparison of hydraulic and morphological predictions of Telemac-3D/Sisyphe and SSIIM in curved laboratory channels, Proceedings to the 20th Telemac-Mascaret User Conference.

[6] L.C. van Rijn (1984), Sediment Transport, Part III: Bed forms and alluvial roughness, J. Hydr. Engrg., ASCE, 110(12), 1733-1754.

Implementation of a new Layer-Subroutine for fractional sediment transport in SISYPHE

Markus Reisenbüchler
Chair of Hydraulic Engineering and Water Resources Management
Technical University of Munich
Arcisstr. 21, 80333 Munich, Germany
markus.reisenbuechler@tum.de

Minh Duc Bui
Chair of Hydraulic Engineering and Water Resources Management
Technical University of Munich
Arcisstr. 21, 80333 Munich, Germany
bui@tum.de

Peter Rutschmann
Chair of Hydraulic Engineering and Water Resources Management
Technical University of Munich
Arcisstr. 21, 80333 Munich, Germany
peter.rutschmann@tum.de

***Abstract*—One of the most critical issues in the modelling of graded sediment transport is the vertical discretization of the bed into different layers and their interaction, particularly between the active layer and active stratum. By applying the TELEMAC - SISYPHE system to study the influence of an open stone ramp on flood events of a river stretch in Germany we had often faced challenges related to unphysical simulation and numerical instability. To improve the sediment transport module SISYPHE concerning this matter, some parts of the FAST computer code (developed by KIT and TUM) are adapted into the TELEMAC environment. The present paper shows the fundamentals of a new layer subroutine and modifications required for the SISYPHE environment. Special treatments for nonerodible grid points are also presented. The calculated results of the developed model are compared with laboratory measurements conducted by Günter (1971) to analyse the behaviour of new implementation.**

I. INTRODUCTION

Modelling of graded sediment transport is quite a challenging task. The mixing of different soil layers with different sediment classes below the surface is not trivial. The module SISYPHE, part of the TELEMAC-MASCARET modelling environment, includes an algorithm for this task - the *layer.f*-subroutine. Applying this code to a fractionized sediment model some instabilities and errors are observed. Therefore, at the Chair of Hydraulic Research and Water Resources Management, Technical University of Munich (TUM) is a new version for SISYPHE implemented. The main idea is to adapt the *layer.f* and related subroutines based on the FAST computer code, which has been developed at the Institute for Hydromechanics, University of Karlsruhe, Germany (KIT) and TUM. As usual for graded sediment transport models a so called size-fraction method is used, in which the bed is divided into different layers and size-fractions, each characterised by a certain diameter and volumetric percentage of occurrence in the river bed. The effect of fractional sediment transport leads to an exchange of grains between the layers, and so a grain sorting process can be approached. A special treatment of nonerodible parts within a calculation domain comes up during the code development. Nonerodible regions, like concrete walls, bridge piers or large stone settings are typical structures in river engineering cases. In the present paper the structure for vertical layer discretization, fractional grain exchange within layers and nonerodible treatment is presented. Almost all variables in the new version remain the same as ones used before in the SISYPHE source code. The new approach is validated by modelling two of the well documented laboratory experiments performed in 1971 by Günter at the Laboratory of Hydraulics, Hydrology and Glaciology, Eidgenössischen Technischen Hochschule (ETH) Zürich, Switzerland [2]. Finally, brief remarks of the model application for a real case study are also given.

II. SISYPHE

A. Background and theoretical aspects

The existing and the new codes are both based on the so-called size-fraction method, where bed material is divided into a certain number of grain classes, which are different in size and percentage of occurrence. Furthermore, the bed is discretised in vertical direction into several layers. The first one is the active layer, which is directly exposed to the flow. Below this one are several subsurface layers, which are only in exchange with the surrounding layers. Due to evolution of the river bed, the thickness of the layers changes as well as the available percentages of each grain-class in each layer [4].

The bed-level change due to a fraction i is calculated from a mass-balance (1):

$$(1\text{-}p)\frac{\partial Z_{b,i}}{\partial t}+\nabla\overrightarrow{Q_{b,i}}=0 \qquad (1)$$

using p = porosity of the bed material; and $\overrightarrow{Q_{b,i}}$ = fractional bed load flux, determined by an empirical transport function. The total bed deformation is then determined in the following equation:

$$\frac{\partial Z_b}{\partial t}=\sum_{i=1}^{NSICLA}\frac{\partial Z_{b,i}}{\partial t} \qquad (2)$$

using NSICLA = number of all size classes [1].

B. River bed representation in the numerical model

In the TELEMAC-MASCARET modelling environment the calculation domain is represented by a grid consisting of nodes connected to unstructured triangular elements. To

perform a simulation it is necessary to provide initial conditions all over the domain for each node. For the morphologic simulation information about the bottom (e.g. the river bed level ZF and the rigid bed elevation ZR, with ZF ≥ ZR) is necessary. Furthermore, the initial composition of the river bed has to be specified by the number of vertical soil layers NOMBLAY, the number of grain size classes NSICLA, the availability of each class i within the layer k $AVAIL_{k,i,}$ and the thickness of each layer ES_k [4].

III. NEW IMPLEMENTATION

By applying the SISYPHE modelling environment from version v6p3 to a large, complex real river application in Germany some errors and numerical problems arouse. A common error message after several time steps was "Error in layer" and the simulation stopped. Using the newer release version v7p0 it was not even possible to start the simulations. From the User-Forum of TELEMAC it seems that many users face these problems. In order to solve this issue, the layer concept from FAST was adapted and integrated into SISYPHE. In the following parts, another treatment of the interaction of the layers to each other and of a nonerodible part is presented. Furthermore, the existing bedload formula after Hunziker [3] is modified and the transport function after Wu [5] is implemented in *qsform.f* subroutine. The new code was initially developed for the version v6p3r2 of the TELEMAC-SISYPHE system, but it is also integrated in the newer releases.

C. Treatment of nonerodible nodes

Modelling nonerodible parts in a calculation domain is a quite common task in river engineering problems. The river bed is commonly very thick until bedrock is reached, however, in some locations (e.g. stone ramps, concrete walls at embankment structures or at weirs, etc.) the river bed is nonmovable. In numerical models, a node is classified as nonerodible when the thickness of its layers is zero $ES_k = 0$. However, it should be noted, that during the simulation period deposition can occur at these places and the deposited materials can be eroded depending on the local hydromorphological conditions. This process should be considered in the numerical model. Furthermore, the condition

$$\sum_{i=1}^{NSICLA} AVAIL_{k,i} = 1 \qquad (3)$$

has to be fulfilled in any case, to avoid mass inconsistencies and division by zero.

The new developed code includes an additional size class in addition to the actual available ones to represent nonerodible structures. So that a high stability, consistency and flexibility of the model could be achieved. This additional size class is independent per se from the defined bed grain sizes, as the transport rate of this additional class is defined to be zero and it is excluded from most of the internal calculations. This additional grain class occurs only at nonerodible layers. Following equations can be formulated for any layer k:

$$\text{if } ES_k = 0 \text{ then } \begin{cases} AVAIL_{k,NSICLA} = 1 \\ \sum_{i=1}^{NSICLA-1} AVAIL_{k,i} = 0 \end{cases} \qquad (4)$$

Equation (4) states that in case of a layer with zero thickness, its material contains up to 100 % of the additional grain class. Vice versa in case of erodible layers the additional grain class does not occur. This is formulated in (5), which claims that in this case the sum of residual grain classes must be 100 %.

$$\text{if } ES_k > 0 \text{ then } \begin{cases} AVAIL_{k,NSICLA} = 0 \\ \sum_{i=1}^{NSICLA-1} AVAIL_{k,i} = 1 \end{cases} \qquad (5)$$

From physical point of view this additional grain class can be compared to a large boulder which cannot be moved by the flow, which is quite close to reality. The implementation of this treatment requires modification in some relevant subroutines showed in the following list:

- *bedload_formula.f*
- *bedload_hunz_meyer.f*
- *bedload_main.f*
- *init_avai.f*
- *init_compo.f*
- *init_sediment.f*
- *init_transport.f*
- *layer.f*
- *mean_grain_size.f*
- *qsform.f*
- *tob_sisyphe.f*

In fact, the subroutine *noerod.f* to define the rigid bed is not needed anymore, as this function is now fully integrated into *init_compo.f*. In case of using the bed roughness predictor, suitable values for Nikuradse grain roughness k_s must be specified, since SISYHPEs bed roughness predictor options might not work proper on nonerodible nodes.

D. River bed decomposition

In the SISYPHE system, the river bed is decomposed into vertical layers, initially in the *init-compo.f* and *init_avai.f* subroutines and during the simulation in the *layer.f* subroutine. It is important to note that the initially defined number of layers at each node NOMBLAY remains the same during the calculation. Furthermore, for each layer a maximum possible thickness has to be defined. In case of the first layer, the active layer, this is named ELAY0, which can be either constant or depending on the diameter of the material in the active layer. The second layer, the active stratum thickness is named ESTRAT0 and must be also defined. The last layer has no thickness limit. Otherwise, it could happen that in case of high deposition the defined number of layers are not capable to represent the total sediment thickness. Vice versa it is not possible that a layer can get a negative value. It is determined as follows:

$$ZF - ZR = \sum_{k=1}^{NOMBLAY} ES_k \qquad (6)$$

The river bed elevation ZF is determined in a geometry file, which includes the information BOTTOM. The rigid bed level can be defined either constant or varying for each node depending on the river structures. Here an algorithm is implemented to read the information ZR from the same file. This function works the same as for BOTTOM or BOTTOM FRICTION and is therefore not explained here further.

The new layer treatment considers the following three different options, depending on the defined number of layers:

- One layer case
- Two layer case
- Multilayer case

In case of only one layer (NOMBLAY = 1) the total available thickness is equal to the thickness of the active layer after:

$$ES_{NOMBLAY} = ZF - ZR \quad (7)$$

A two layer case (NOMBLAY = 2) includes an active layer with a maximum defined thickness and one residual layer below, as shown in (8).

$$ES_1 = \min(ELAY0; ZF - ZR) \quad (8)$$

$$ES_{NOMBLAY} = ZF - ZR - ES_1$$

The following lines describe the code sequence for decomposition of a multilayer case (NOMBLAY ≥ 3):

$$ES_1 = \min(ELAY0; ZF - ZR) \quad (9)$$

$$ES_2 = \min(ESTRAT0; ZF - ZR - ES_1)$$

….

$$ES_k = \min\left(ESTRAT0; ZF - ZR - \sum_{k=1}^{k-1} ES_k\right)$$

$$ES_{NOMBLAY} = ZF - ZR - \sum_{k=1}^{NOMBLAY-1} ES_k$$

After that, the available percentages of each class i in each layer k has to be defined ($AVAIL_{k,i}$). This can be done explicitly for each layer in *init_compo.f*. Via mass balance the volumetric amount of sediment VOL in the domain is calculated using (10).

$$VOL = \sum_{k=1}^{NOMBLAY} ES_k * \sum_{i=1}^{NSICLA} AVAIL_{k,i} \quad (10)$$

In fig. 1 the discretization of the river bed surface and the nonerodible level is schematized for an exemplary case with maximum five layers at three nodes. Node one is initially nonerodible and so the bottom surface is equal to the nonerodible level (ZF=ZR) and all layer thicknesses are zero. At node two the nonerodible level is lower than the surface and the difference is distributed to into layers, starting from the top. Layer one to four attains their maximum defined thickness and the last one reaches to the rigid bed. The third nodes rigid bed is at a medium height and only four layers are necessary to distribute the river bed. The thickness of layer 5 is zero.

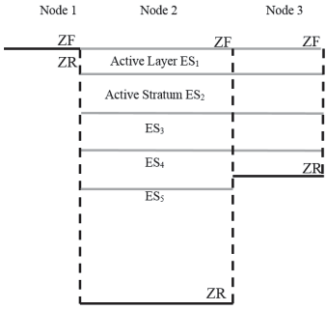

Figure 1. Scheme of vertical river bed discretization at three different nodes.

E. Vertical layer interaction

Based on the initial discretised bed, the model calculates the interaction of layers to each other and to the flow. The key concept is the existence of an active layer, where the flow picks up the transportable sediment and receives the grains that the flow is unable to transport [1].

For erosion of the river bed the temporal change of the volumetric percentage of a fraction i in the active layer is calculated considering the taken material from the flow and the available material in the stratum below. This is done via a mass balance, given in (11).

$$\frac{\partial AVAIL_{1,i}}{\partial t} * ES_1 = \frac{\partial Z_{b,i}}{\partial t} - \frac{\partial Z_b}{\partial t} * AVAIL_{2,i} \quad (11)$$

using $\frac{\partial AVAIL_{1,i}}{\partial t}$ = change of fraction i in the active layer, ES_1 = active layer thickness; $\frac{\partial Z_{b,i}}{\partial t}$ = bed level change of fraction i; $\frac{\partial Z_b}{\partial t}$ = total bed level change; $AVAIL_{2,i}$= available percentage of fraction i in the active stratum layer. The active stratum is capable of an exchange with the stratum below, balanced in (12). If the layer below is nonerodible or the maximum number of layer is reached, no interaction will take place.

$$\frac{\partial AVAIL_{k,i}}{\partial t} * ES_k = \frac{\partial Z_b}{\partial t} * (AVAIL_{k,i} - AVAIL_{\min(NOMBLAY,k+1),i}) \quad (12)$$

For deposition case, the material enters the top element, so no relation with lower layers has to be considered here, see (13).

$$\frac{\partial AVAIL_{1,i}}{\partial t} * ES_1 = \frac{\partial Z_{b,i}}{\partial t} - \frac{\partial Z_b}{\partial t} * AVAIL_{1,i} \quad (13)$$

Due to the deposition the active stratum gets some upward directed movement and material is in exchange with the layer above, the same for other substrate layers:

$$\frac{\partial AVAIL_{k,i}}{\partial t} * ES_k = \frac{\partial Z_b}{\partial t} * (AVAIL_{k-1,i} - AVAIL_{k,i}) \quad (14)$$

After updating the available percentages of each fraction in each layer, the thickness of each layer is new distributed according to the procedure shown in part *D* (see (7) – (9)). Finally via a counter check mass balance is ensured and the total amount of sediment within this time step is reached.

F. Empirical transport functions

The transport function after Hunziker has been developed in 1995 using the data conducted by Günter. This equation is already implemented in SISYPHE. However, the hiding function has to be adapted for the additional grain class treatment and the code is rewritten to solve the equations within one loop over all grid nodes. The basic of this transport function is the concept of equal incipient motion for all sediments. Sediment transport starts only if the dimensionless shear stress of the flow is higher than the dimensionless threshold. The determining parameters are here the critical shields parameter θ_c and a relation between the mean grain diameter of the surface layer d_m and subsurface layer d_{mo}. The critical shear stress is then modified according to the following equation.

$$\theta_{cm}=\theta_c*\left(\frac{d_{mo}}{d_m}\right)^{0.33} \quad (15)$$

According to the Günter experiments a hiding/exposure function is evaluated and parametrized in order to describe which sediments are more or less exposed to the flow. The sediment discharge after Hunziker is given in (16).

$$Q_{b,i}=\sqrt{(s-1)*g*d_m^3}*AVAIL_{1,i}*5*(\varphi_i(\mu*\theta_{dm}-\theta_{cm}))^{3/2} \quad (16)$$

using s = relative density, g = gravity, d_m = mean diameter of the surface layer, φ_i = hiding factor, μ = parameter for skin friction correction, θ_{dm} = dimensionless shear stress parameter depending on the mean diameter and flow condition, θ_{cm} = modified critical shields parameter considering mean diameters of surface and subsurface layers [4].

The empirical transport function after Wu assumes that the probability of a grain to be exposed to the flow is depending on the diameter of the grain and the surrounding grains as well as the availability. Including a correlation parameter m = 0.6, which can be used in the calibration, the hiding and exposure function is formulated in (17) with

$$\theta_{cm}=\theta_c*\left(\frac{p_{e,i}}{p_{h,i}}\right)^m \quad (17)$$

using the critical shields parameter θ_c and the probability of exposure $p_{e,i}$ and hiding $p_{h,i}$ of a grain i at the surface layer. The transported bedload discharge is given as

$$Q_{b,i}=\sqrt{(s-1)*g*d_i^3}*AVAIL_{1,i}*0.0053*\left(\mu*\theta_{d_i}/\theta_{cm}-1\right)^{2.2} \quad (18)$$

using θ_{d_i} = dimensionless shear stress parameter depending on the diameter of each grain and flow condition, θ_{cm} = modified critical shields parameter including the hiding factor. For more details and full description of the formulas after Wu see [3].

IV. Calculation results

G. Günter experiment – grain sorting

The new developed subroutines are validated by modelling the laboratory experiments conducted by Günter in 1971 at the ETH Zürich. The experiments were performed in a 40 metres long and 1 meter wide rectangular channel. Sediment mixtures of a certain defined composition were installed in this channel according to a defined slope. Running the experiment with constant flow conditions after around 40 days, erosion leads to a development of new slopes and armoured layers by wash out of fine materials [2].

It was decided to recalculate the laboratory experiments with the bed load transport formula after Hunziker and Wu. For the validation two experiments were numerically modelled, experiment #3 and #9. The initial river bed composition in case #3 according to Günter is close to a typical river bed composition in an alpine river bed. The second case #9 is rather unnatural, with high amount of fine and coarse grains and less intermediate ones [3]. For each test case are the determining parameters given, in table I hydrodynamic quantities and in table II the morphodynamic ones.

The numerical mesh consist of around 900 elements with an average edge length of 33 centimetres. This mesh allows with an average time step of 0.5 seconds the simulation of 40 days in an acceptable duration. The boundary conditions for the hydrodynamic part are constant discharge at the inlet and fixed water level at the outlet, 1 centimetre lower than estimated water depth at the end of the experiment h_G. River bed roughness is defined after Nikuradse with a temporal bed roughness predictor, depending linearly on the ratio between skin friction and mean dimeter of the active layer, with $k_s = \alpha d_m$ [4]. The ratio coefficient α is used for calibration.

Morphological boundary conditions are defined as free, so that no material enters the domain and the river bed can evolve without constraints. The river bed is discretised into three layers, with a constant active layer thickness of three times the initial d_{90}. Active stratum is defined to be three times the active layer. Shields parameter θ_c and the hiding-factor of Wu transport function are assumed to be most influencing the result and are used in the calibration, too.

Table I. Boundary and final flow conditions

Case	Q_{in}	I_0	h_G	I_G
[/]	*[l/s]*	*[‰]*	*[cm]*	*[‰]*
#3	56.0	2.50	9.91	2.327
#9	39.4	4.00	6.87	4.176

Table II. Initial sediment composition

size class i	1	2	3	4	5	6
$d_{m,i}$ [cm]	0.051	0.151	0.255	0.360	0.465	0.560
#3-Initial	0.359	0.208	0.119	0.175	0.067	0.072
#9-Initial	0.336	0.117	0.099	0.139	0.129	0.180

The simulations were performed using the existing codes, named “old”, insofar as it was possible, and the new developed codes, named “new”. The calibration parameters are adjusted in order to get good results in all versions with the same parameter set for each test case. The simulations are analysed regarding to grainsize distribution in the surface layer, water depth and river bed inclination. All values of the domain are considered and averaged. Table III shows the defined parameters and results together with the corresponding bed load functions and different versions of the program. The development of the grainsize distribution in the surface layer is shown in fig. 2 to fig. 5 separately for each experiment and bed load function. Important is, that with the “old” codes of SISYPHE no simulation could be performed using version v7p1, as in all cases the simulation stops after a few time steps with “Error in layer”. Using the new code structures the crashes does not occur, but the gained results are unrealistic, which points to a deeper error in the source code of the program. However, this error seems to be corrected in the newest unreleased version of TELEMAC, the trunk-version, and more realistic results are gained for old and new layer treatment. This topic was also discussed in the TELEMAC-MASCARET user forum.

TABLE III. RESULTS OF THE SIMULATIONS

		#3				#9			
		Hunziker		*Wu*		*Hunziker*		*Wu*	
α		2.5		2.5		2.0		2.0	
θ_c		0.044		0.044		0.047		0.047	
m		/		0.7		/		0.7	
		h_G [cm]	I_G [‰]	h_G [cm]	I_G [‰]	h_G [cm]	I_G [‰]	h_G [cm]	I_G [‰]
v6p3	*old*	10.42	1.8	9.87	2.5	6.75	3.9	6.75	3.9
	new	9.99	2.2	9.97	2.5	6.75	3.9	6.81	4.2
v7p1	*old*	/	/	/	/	/	/	/	/
	new	10.51	1.6	11.45	1.0	7.01	3.1	7.63	2.3
trunk	*old*	10.11	1.8	9.87	2.5	6.74	3.9	6.82	4.1
	new	9.98	2.4	10.0	2.4	6.75	3.9	6.82	4.1

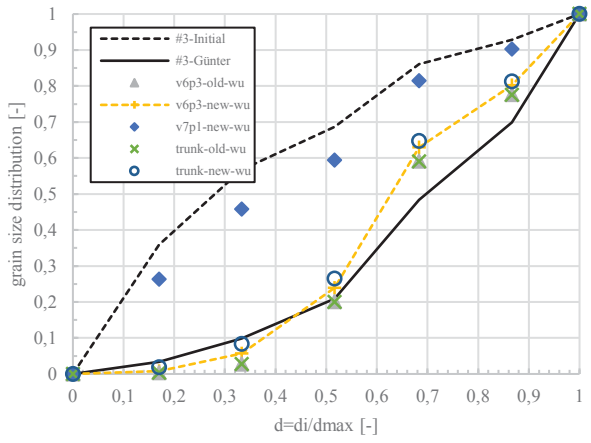

Figure 2. Case #3 - grain size distribution using Wu’s function

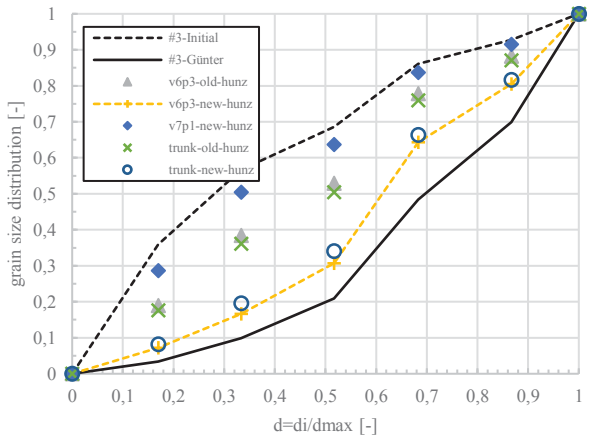

Figure 3. Case #3 – grainsize distribution using Hunziker’s function

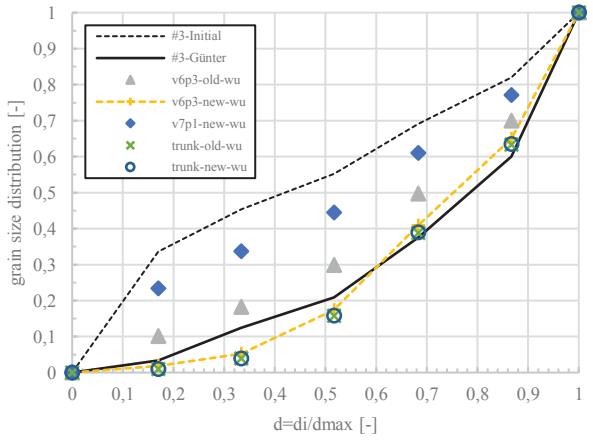

Figure 4. Case#9 – grainsize distribution using Wu’s function

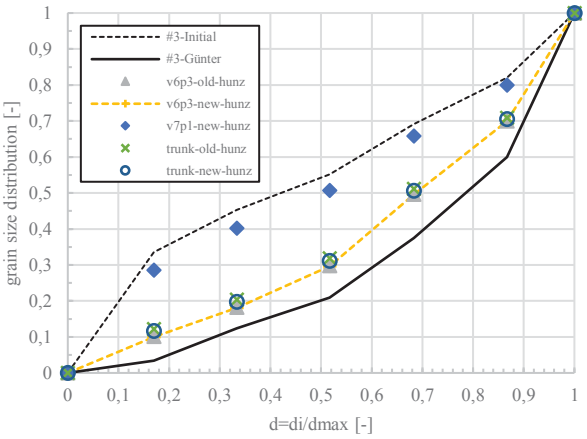

Figure 5. Case#9 – grainsize distribution using Hunziker’s function

The bed load function after Wu shows very good agreement with the measurements conducted by Günter for test case #3 and #9 (fig. 2 and fig. 4). The water depths are

close to the measurements with an absolute difference lower than 1 millimetre and the inclination has an absolute maximum deviation of 0.2 per mille. However, the discrepancy between old and new layer treatment is rather small and in both cases the armouring of the river bed is well represented. The small differences are a result that the Wu bedload function takes the diameter of the subsurface layer not directly into account. In the Wu's formula only the available percentage of a grain in the surface layer is considered. The Hunziker's function (abbr. hunz) instead uses the diameter of the substrate layer directly to modify the critical shields parameter, see (15). Therefore, the exchange between layers gets more important. In fig. 3 the differences of the grain sorting process are more significantly visible. With the new layer treatment a better sorting is achieved for test case #3 applying version v6p3 and the unpublished trunk version. Also the water depth and bed slope are more accurate simulated with the new codes. For simulation test case #9 only slightly better results are gained with the new layer treatment compared to the existing codes (fig. 5).

The new layer treatment allows to simulate the Günter experiments with a numerical model with high accuracy. But it must be considered that also the existing codes can be used to simulate the experiment, in most cases. However, when the calculation domain contains nonerodible nodes, the existing codes shows their weaknesses. With the new layer treatment this problem can be solved, as it can be seen the following part.

H. River case – nonerodible treatment

The functionality of the new treatment for nonerodible areas is now tested by the application to the real case, where the problems arises first by applying the original SISYPHE codes. The test case is a three kilometres long river stretch with floodplain in the southern part of Germany, which includes an open stone ramp to limit the erosion in this region. Furthermore, in the river stretch exists a ground sill below a bridge to prevent scour. The ramp, the ground sill and the floodplain with embankment dams are initially classified as nonerodible. The domain consist of around 130'000 nodes and 250'000 elements, which does not allow a manual identification of nonerodible nodes via node number.

Applying the new subroutines for nonerodible areas and layer treatment, this river stretch is finally analysed by a quite accurate and stable hydromorphological model. The simulations are also performed successfully on a server in parallel mode. In fig. 6, a longitudinal section along the river channel is given, with flow from left to right. From the initial river bed (black line) with the fixed parts at the ramp rkm 4.6 and the ground sill at rkm 2.975 the simulation of a flood event over six days leads to significant bed level change. The model is able to simulate the observed water levels along the domain in a very good manner and the shape of the flooded area is close to the expected one. The initial nonerodible ramp is after the flood event covered with sediments, which is a problem for the maintenance. The ground sill keeps the river bed upstream of it on a similar level, but downstream of the ground sill large erosion is observed due to the weir operating during the flood event at the outflow boundary.

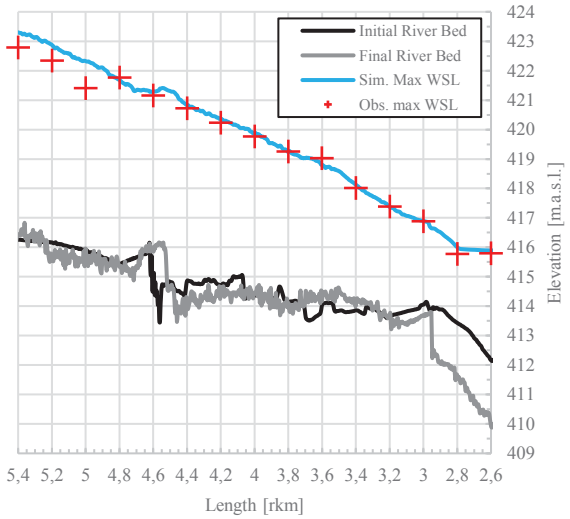

Figure 6. Longitudinal section of the river case for initial (back line) and final (grey line) river bed and for simulated (blue line) and observed (red crosses) water surface levels.

With the developed model several scenarios and modifications were analysed to increase the flood safety for the surrounding cities. By a modification at the ramp and the ground sill the water levels of a 100-year flood could be halved to a maximum height of 1 m at the floodplains, which offers in combination with a flood protection dam a feasible protections system.

V. CONCLUSION

The modelling environment TELEMAC-MASCARET is a powerful tool to analyse river engineering issues. The problem of numerical errors regarding fractional sediment transport leads to the implementation of an alternate treatment of grain sorting processes and nonerodible structures on the river bed. The newly developed code increases the stability and flexibility of the TELEMAC-SISYPHE system. The code was validated by the numerical modelling of laboratory test cases. The measurements of the bed armouring, flow depth and final river bed slope were accurately represented. The final adaption to a real case study shows the model capacity for long river stretches with complex bed structures. This model provides a promising tool to analyse the impact of sediment transport during a flood event in fluvial rivers.

REFERENCES

[1] M. D. Bui, P. Rutschmann, "Numerical modelling of non-equilibrium graded sediment transport in a curved open channel", Computers & Geosciences 36: pp. 792-800, 2010

[2] A. Günter, "Die kritische mittlere Sohlenschubspannung bei Geschiebemischungen unter Berücksichtigung der Deckschichtbildung und der turbulenzbedingten Sohlenschubspannungsschwankungen", VAW Reports 3, ETH Zürich, 1971

[3] R. Hunziker, "Fraktionsweiser Geschiebetransport", VAW Reports 138, ETH Zürich, 1995

[4] P. Tassi, C. Villaret, "Sisyphe v6.3 User's Manual", EDF R&D, 2014

[5] W. Wu, "Computational river dynamics", Taylor & Francis Group, London, 2007

Towards the simulation of submerged bottom structures with vertical walls using Telemac-3D

Pengze Wang
EDF R&D LNHE / Polytech Nice-Sophia / Mines ParisTech
6 quai Watier, 78401 Chatou, France

Antoine Joly & Agnès Leroy
EDF R&D LNHE / LHSV (Ecole des Ponts, CEREMA, EDF R&D, UPE)
6 quai Watier, 78401 Chatou, France
Email: antoine.joly@edf.fr

***Abstract*—In the Telemac-Mascaret community, there is an increasing need for Telemac-3D to handle unstructured 3D meshes. One of the main target applications is the simulation of submerged structures in the flow. With this aim in view, a first step is to modify the code so that it can account for vertical structures on the bed. This is done while maintaining the advantages of the layered 3D meshes currently used in Telemac-3D, since a full destructuration would imply more complex neighbour searches, data access and would require major changes in the algorithms. The proposed approach will be presented in this article, including a description of the necessary developments, comparisons of CPU time before and after the changes, and a qualitative test case.**

I. Introduction

Telemac-3D is quite a powerful tool for 3D environmental simulations. One of its strengths lays in the data structure within the code: the 3D meshes are built as a layering of one 2D mesh. This makes the data access and neighbour search efficient, and simplifies the resolution of the 3D Navier–Stokes equations. However, it comes with drawbacks since Telemac-3D is then unable to handle submerged bodies and bathymetries presenting vertical sections.

The aim of this work is to allow Telemac-3D to model submerged structures with vertical walls and a flat top when they lie on the bed; for example steps or submerged cylinders. A simplified representation of the kind of problems considered here is provided in Figure 1.

The chosen methodology is to keep the main geometrical advantage of Telemac-3D, namely the layered elements. This data structure makes the memory access efficient and facilitates all the operations that need to be performed along the vertical axis (such as the integration along the depth). This means that in the proposed formulation, the mesh for these problems will still be defined from an extrusion of a two-dimensional mesh. However, in the mesh some nodes and element faces will represent the sides of a vertical structure and all the nodes and elements inside that structure will be ignored.

The following modifications to Telemac-3D are thus proposed:

- all the loops shall be modified in order to account for a variable number of nodes or elements along the vertical axis;
- a new geometrical file will be read to define the elements and nodes belonging to a vertical structure;
- the boundary conditions on the sides of the vertical structures will be added to the boundary conditions file;
- wall boundary conditions will be imposed on the sides and top of the vertical structures;
- a new variable for the visualisation of these vertical structures will be added to the output.

Each of these modifications will be described in detail in section II. Comparisons of CPU time before and after the modifications will be shown for a test-case that does not involve vertical structures in section III. Finally, an illustration of the kind of problems that the code can handle after the modifications will be shown in section IV.

Finally, it should be noted that the work presented here is still in progress, and is not ready to be integrated into an official release of Telemac-3D yet.

II. Proposed developments

A. Modification of the three-dimensional loops

The first design choice was to have a variable number of planes per node or element in the 2D mesh. To do so, the bed plane number is made variable, and loops through the mesh points or elements start from its value. Figure 2 shows a sketch of the definition of the bed nodes and elements. In this way, all the arrays are still stored with the same structure as before. For example, an array stored at the nodes of a mesh with a number of 2D points NPOIN2 and containing NPLAN planes is stored as a succession of memory blocks of size NPOIN2, each corresponding to a plane of the 3D mesh, NPLAN times. The loops through the mesh points or elements will only jump a few positions in the arrays, so as not to access anything inside the vertical structures. This approach should only have a minimal influence on cases without vertical structures (see the section III for the numerical tests).

The bed nodes will be named `STARTPP` and the bed elements `STARTPE` in the code. For example, a loop over all the nodes of the mesh is now written as:

```
DO IPOIN2=1,NPOIN2 !Loop on all 2D nodes
  !Loop on all planes in the domain
  DO IPLAN=STARTPP(IPOIN2),NPLAN
    !Index of the 3D node
    IPOIN3=(IPLAN-1)*NPOIN2+IPOIN2
    <...>
  ENDDO
ENDDO
```

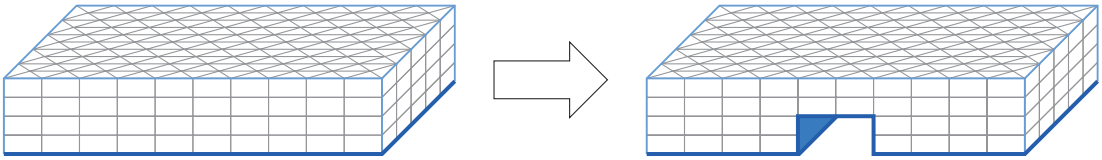

(a) Classic layered mesh in Telemac-3D (b) Mesh with a vertical structure

Fig. 1: Illustration of a problem with a vertical structure.

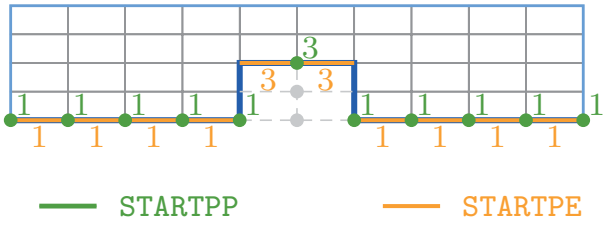

Fig. 2: Sketch of the bed plane number definition for the nodes (STARTPP) and elements (STARTPE), when modelling vertical structures. The grey circles represent the ignored nodes whereas the dashed line represents the ignored elements.

B. New formatted data file for the vertical structures

Currently, Telemac-3D can only read a two-dimensional mesh, which is then extruded along the vertical to form the three-dimensional mesh. To limit the modifications to the code, and to keep the possibility for the user to define the vertical discretisation, this has been kept. The vertical structures will be defined in a new formatted data file, where the height of each structure will be defined as well as the list of points and elements of the 2D mesh lying inside each structure. This implies that in the two-dimensional mesh provided to Telemac-3D, the sides of the vertical structures must correspond to triangle edges and the inside of the vertical structures must be meshed An example of such a mesh can be found in figure 3.

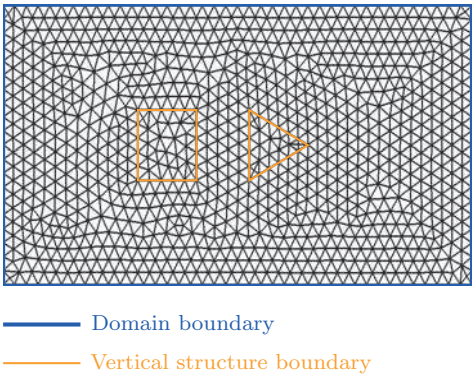

Fig. 3: Two-dimensional mesh for a test case involving two vertical structures. The meshed boundaries of the vertical structures are highlighted in orange.

The vertical structures file is referenced in the steering file using the following keywords:

```
/-----------------------------------------------------/
/                OPTIONS FOR VERTICAL STRUCTURES
/-----------------------------------------------------/
VERTICAL STRUCTURES ON THE BED = YES
FILE FOR VERTICAL STRUCTURES = <File name>
```

This file then needs to follow the following format for each vertical structure:

```
<NFR> <NPOIN_VST> <NELEM_VST> <ZVST>
<List of the boundary nodes>
<List of all the nodes inside and on the boundary>
<List of all the elements inside>
```

Where NFR is the number of nodes on the boundary of the vertical structure, NPOIN_VST is the number of points along the boundary and inside the vertical structure, NELEM_VST is the number of elements inside the vertical structure and ZVST is the z-coordinate of the top of the step. This file can be easily defined using Salome_Hydro, see Wang [1] for the complete methodology.

Furthermore, it should be noted that the plane of the mesh closest to the value ZVST will be moved to this value and it will be fixed.

C. Defininition of the vertical structures' side boundary conditions

The side boundary conditions of the vertical structures will be added to the original boundary conditions file. This has only been tested for meshes in MED format and their corresponding boundary condition files. As a reminder, the BOUNDARY CONDITIONS FILE for a mesh in MED format is structured as follows:

```
<Number of boundaries>
<Boundary type> <name of group in mesh>
...
```

Adding the boundary nodes of the vertical structures to the boundary nodes of the domain is not trivial as this means that some of the boundary nodes are now inside the two-dimensional domain. This is an issue, since in the Bief the detection of the boundary segments is done by checking if the triangles' faces are missing a neighbour. Such process does not work when boundary segments are located inside the mesh. Therefore, the algorithm for the boundary segments detection must be modified, as well as for the detection of boundary triangles. The existing formulation for boundary segments detection was kept, but an additional check was

added: segments are also detected as belonging to the boundary when they belong to a triangle lying in a vertical structure. The triangles that are connected to these segments, but that are outside of a vertical structure, are then added to the list of boundary elements.

Finally, the neighbouring list IFABOR of each element in three-dimension had to be updated. Indeed, a neighbour search through the face of an element whose neighbour lies within a vertical structure should yield either a liquid or solid boundary condition instead of the index of the element, so that the latter is ignored.

D. Imposition of the vertical structures' side boundary conditions

On vertical structures, the imposition of boundary conditions must only be done from the bed to the top of the structure. The loops along the three-dimensional boundary nodes or elements must then start from the first plane and stop at the plane colinear to the top of the vertical structure. To do so, a new variable ENDCLI was defined. Figure 4 shows the values ENDCLI takes on classical boundaries and on vertical structures.

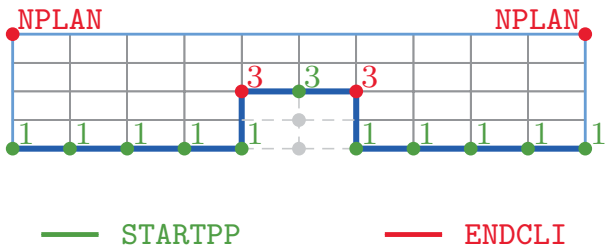

Fig. 4: Sketch of the starting and ending plane number for lateral boundary nodes of vertical structures (STARTPP and ENDCLI respectively). The grey circles represent the ignored nodes whereas the dashed line the ignored elements.

Therefore, loops along the boundaries are now written as:

```
DO IPTFR2=1,NPTFR2 !Loop on boundary nodes
  IPOIN2=NBOR2(IPTFR2)
  !Loop on boundary planes
  DO IPLAN=STARTPP(IPOIN2),ENDCLI(IPOIN2)
    !Index of the 3D node
    IPOIN3=NBOR3((IPLAN-1)*NPTFR2+IPTFR2)
    <...>
  ENDDO
ENDDO
```

As this is work in progress, the boundary conditions on the top of the step has not been properly imposed. Work needs to be done at corner node of both a vertical and a horizontal boundary. Furthermore, when calculating the evolution of the free surface, the vertical structures boundaries are taken into account in the same method as the other boundaries, and this might not be optimal.

E. New output variable for visualisation purposes

A new variable for VARIABLES FOR 3D GRAPHIC PRINTOUTS has been added. It is named VST, and is equal to 1 for all the nodes lying within the vertical structures and 2 for the boundaries of the vertical structures. This allows the user to remove the points inside vertical structures from the display.

III. Effect on computational times

Throughout the developments presented in section II, the impacts on the computational times were assessed. The validation case malpasset_large.cas was run with 10 planes on one of the computational clusters of EDF[1]. The simulations were run on a dedicated computational node on 28 processors. For each simulation run, the computational times of 5 different runs were averaged.

TABLE I: Computational time for a large test case without vertical structures.

Version	Averaged computational time
Original code	13 minutes 36 seconds
Modified 3D loops	13 minutes 53 seconds
All modifications	13 minutes 26 seconds

The sumary of the computational times can be found in Table I. Taking into account that averaging only five simulations still leaves some uncertainties in the computational times, this table shows that the developments have not increased the computational times.

IV. Qualitative test case

A. Geometry of the problem

These developments have been tested with a simple test case. In this case, two vertical structures are placed in a fluid domain of size $200 \times 100 \times 100$ meters (see Figure 6 for more details on the geometry). A flow rate of 500 m^3/s is imposed at the inflow boundary, and a constant water depth of 100 m is imposed at the outflow boundary.

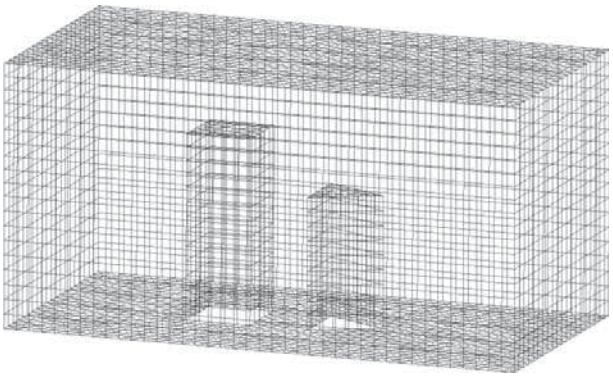

Fig. 5: Three-dimensional mesh of the test case.

The size of the 2D mesh elements is 5 m and there are 20 planes in the domain (the three-dimensional mesh is shown in Figure 5). The time step size is equal to 1 s and a zero

[1]The Porthos cluster, consisting of 585 computanional nodes of 28 "Intel R Xeon R CPU E5-2697 v3 @ 2.60GHz (Haswell)" processors.

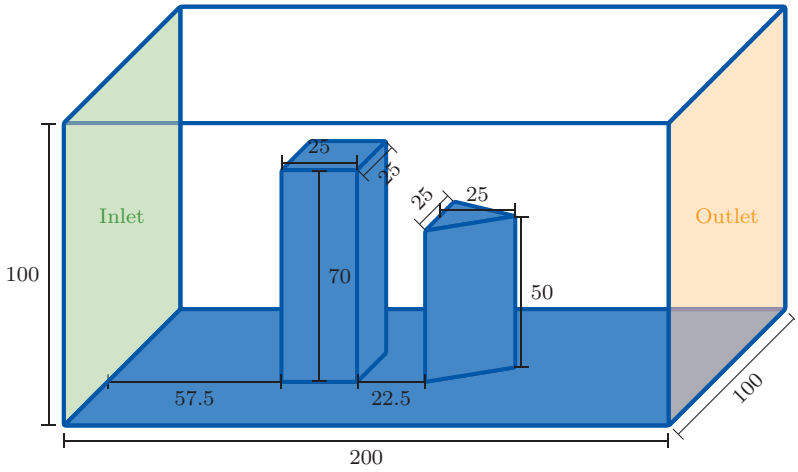

Fig. 6: Geometry of the test case. All dimensions are given in meters.

velocity is imposed on the bed and on the lateral boundaries of the vertical structures.

B. Numerical results

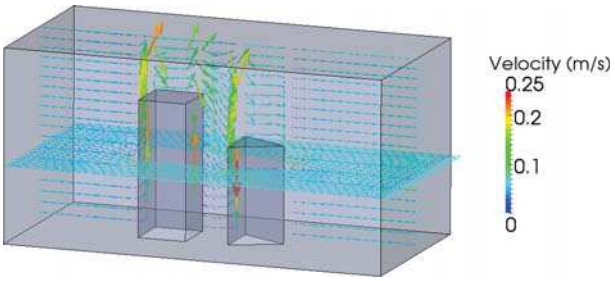

Fig. 7: Fluid velocities inside the test case after 100 time steps.

The results after 100 time steps are shown in Figure 7, where it is visible that the flow goes around these vertical structures. Therefore, the developments described in section II allow vertical structures to be modelled in Telemac-3D. However there remains a few issues to tackle. These can be seen in Figures 8 and 9.

In Figure 8, the vertical velocity along a slice of the model is plotted. It is clear in this figure that a checkerboarding effect of the vertical velocities appears for the nodes along and directly above the vertical boundaries of the vertical structures, which is a sign of instabilities. In fact, these instabilities would grow if the simulation was allowed to continue longer than 100 time steps, up to a point where horizontal planes would cross, crashing the simulation.

On the other hand, Figure 9 shows the velocities inside the vertical structures. As can be seen, the velocities along the boundaries are not equal to zero, which is in contradiction with the desired imposed velocities. It is the unclear if these velocities then diffuse to the elements inside, or if there remains a few loops that do not ignore those elements, as the plotted velocity vectors are not equal to zero.

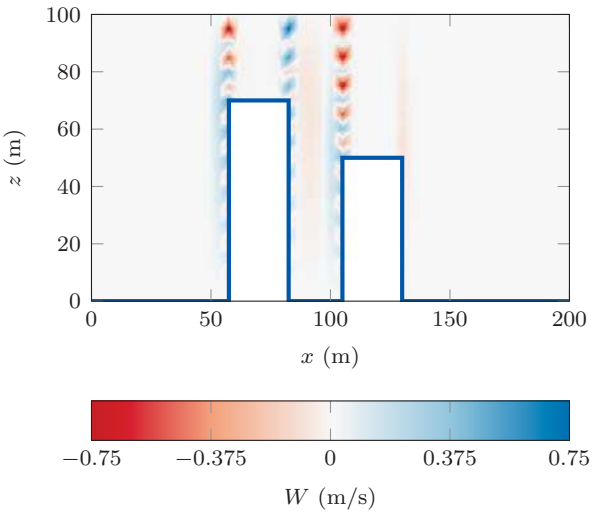

Fig. 8: Vertical velocities for a slice taken along the centre of the domain with the normal along the y-axis.

V. Concluding remarks

The work presented here shows the first steps achieved towards adding submerged structures with vertical walls on the bed of Telemac-3D simulations. These developments heavily modified the code: loops have been redefined to have a varying bed plane number, a two-dimensional mesh can now be read with boundary nodes defined inside, these nodes are then used to impose boundary conditions along the edges of a vertical structure and the nodes and elements inside such structures are ignored.

These modifications have been tested at each stage of development, and they have not modified the computational time or the results of simulations without vertical structures (further checks still need to be run). We are close to the simulation of vertical structures in Telemac-3D, even if a few issues remain.

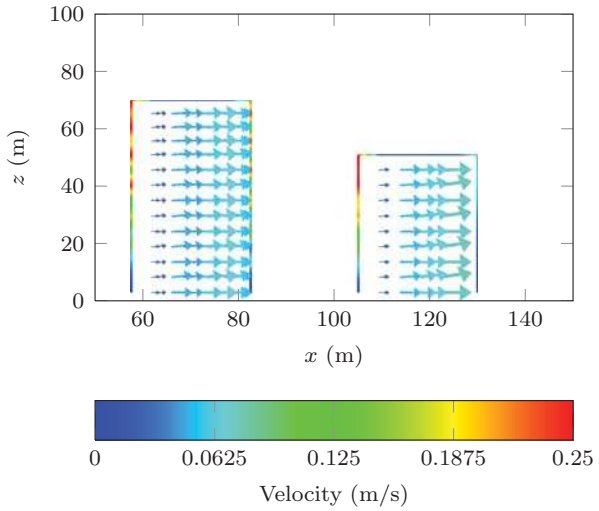

Fig. 9: Velocities inside the vertical structures on a slice taken along their centre with the normal along the y-axis. The line represents the magnitude of the velocities on the boundaries of structure and the arrows the velocity vectors for the nodes inside.

To list the most visible ones:

- numerical instabilities tend to develop directly above the vertical structures;
- boundary conditions along the vertical structures are not properly imposed (non-zero velocities are observed);
- the velocities inside the vertical structures are not equal to zero.

Therefore, additional work is required before these developments can be integrated in an official release of Telemac-3D.

REFERENCES

[1] P. Wang, "Extension du logiciel TELEMAC-3D pour des géométries 3D avec des tronçons verticaux," Master's thesis, Ecole Polytechnique de l'Université de Nice - Sophia Antipolis, 2016.

First improvements toward a reproducible Telemac-2D

Rafife Nheili
and Philippe Langlois
Univ. Perpignan Via Domitia
Digits, Architectures et Logiciels Informatiques,
Perpignan. France.
Univ. Montpellier, Laboratoire d'Informatique,
Robotique et de Microélectronique de Montpellier,
UMR 5506, Montpellier. CNRS. France.
Email: {rafife.nheili, langlois}@univ-perp.fr

Christophe Denis
ENS Cachan,
CMLA Research Center for Applied Maths,
Cachan. France.
Email: Christophe.Denis@cmla.ens-cachan.fr

***Abstract*—OpenTelemac suffers from numerical reproducibility failures. In parallel simulations, the domain distribution toward units computing with floating-point arithmetic may yield different numerical results. Numerical reproducibility is a requested feature to facilitate the debug, the validation and the test of industrial or large codes. We present how to apply compensation techniques to recover reproducibility in the finite element computation of a hydrodynamics simulation. Compensation is used in both the building and the resolution phases of the linear system which are not reproducible in the current version of the software. Here the building step relies on the element-by-element storage mode and the solving step applies the conjugated gradient algorithm. We also measure that the running time extra-cost of the reproducible version is reasonable enough in practice.**

I. Introduction

The openTelemac suite is a HPC code for the simulation at the industrial scale of free surface flows in 1D-2D-3D hydrodynamics. It is an integrated set of open source Fortran 90 modules developped since 20 years of international collaboration [11]. Like most large and complex applications, openTelemac introduces parallelism. The domain is distributed toward several processors which solve simultaneously their own sub-domains. In practice, the processors are not independent of each other, but each one needs the results from the others. This technology reduces the processing time since ideally using p processors divides by p the time to solve the same problem with only one processor.

An undesirable consequence of parallelism reported in openTelemac is the non-reproducibility of the results. The ability to reproduce the simulation results becomes a crucial property to improve the confidence in large scale numerical experiments. The changes of a simulation results must depend only on the changes of the simulations inputs, and not be accidentally affected by uncontrolled floating-point calculations. The non-deterministic propagation of the rounding errors and the dynamic reductions of parallel executions may yield to different outputs. Indeed, numerical reproducibility is a requested feature to facilitate the debugging and the testing of the code: it is not obvious to fix a bug nor to test a code when the results differ from one run to another. Moreover, critical simulations should verify this reproducibility to satisfy legal agreements.

We studied a schematic test case, called gouttedo, which is a 2D-simulation of a water drop fall in a square basin. The test case specificities are the EBE storage matrix, the uses of the wave equation system and of the conjugate gradient for the solving phase. This resolution runs for a triangular element mesh (8978 elements, 4624 nodes) and simulates several time steps of 0.2 sec. Figure 1 illustrates the gouttedo test case where we display the non reproducible behavior of the water depth simulation between the sequential and the 2 processor runs. The left plot shows the water depth values returned by the sequential simulation and the right one corresponds to the $p = 2$ parallel run. White spots exhibit the mesh elements where these latter results differ from the sequential ones.

The first task is to carefully identify the sources which produce the reproducibility failure and then to apply as few as possible modifications to limit their extra-cost. The difficulty in this work was to identify these sources. Figure 2 illustrates the main aspects we need to consider. First row shows how the results of a code, in different colors, are not reproducible when varying the number of processors. A convincing modified reproducible code should satisfied two criteria:
i) bit-wise *identical* result for every p-parallel run and for every $p \geq 1$, as showed in the second row in Figure 2 where the results share the same color. Reproducibility is measured as the relative error between the modified sequential simulation and the parallel ones (in green).
ii) the reproducible results must be within a reasonable range of differences compared to the original sequential simulation ones. This measure is important for the code developers who, in practice, trust their sequential results as a reference. The measure of the accuracy is the relative error between the original sequential simulation and the modified one (in red). The paper is organized as follows. In Section II we introduce floating-point arithmetic to explain the reasons of the non-reproducibility in parallel executions. In Section III, we summarize the compensation algorithms which are used in Telemac to recover the reproducibility. The sources

Figure 1: gouttedo: white spots are non reproducible water depth values between the sequential (left) and a 2 processors run (right). Time steps: 1, 2, . . . , 7, 8.

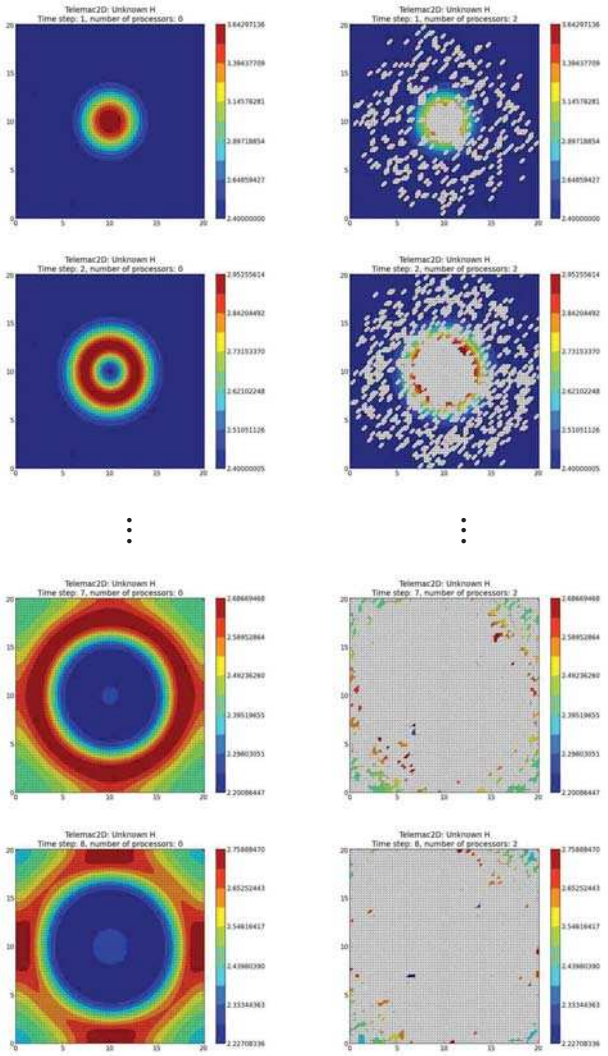

Figure 2: The two measures of a convincing modified reproducible code

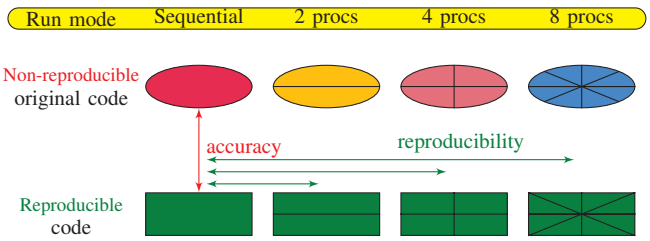

identification of the non-reproducibility and how we modify them by using compensation are detailed in Section IV. Section V presents the reproducible simulation. Finally the running time extra-cost of these modifications is analyzed in Section VI.

II. The sources of numerical non-reproducibility

A. Floating-point arithmetic features

Computer memory is limited so it cannot store the infinite precision of real numbers. The floating-point (FP) numbers are approximate real numbers. The IEEE-754 standard [5] defines the most common floating-point representation and the behavior of their arithmetic operations. It also defines the data formats, conversion rules, some special values, the rounding modes and the accuracy of basic operations. This standard aims to obtain predictable and portable programs which produce identical results when running on different machines.

1) Floating-point representation: It is based on the scientific notation to represent a floating-point number x as:

$$x = (-1)^s.m.\beta^e, \tag{1}$$

where $s \in \{0, 1\}$. The mantissa m is a string of integer digits which depends on the radix $\beta > 1$ ($0 \leq m_i < \beta$) and e (represented by w bits) acts as a scaling factor for floating-point number x. The number of mantissa digits is the precision of the floating-point number, denoted t. Figure 3 details each component for the binary case ($\beta = 2$).

Figure 3: Binary FP representation

sign	exponent	mantissa
$s \in \{0, 1\}$	$e_{min} \leq e \leq e_{max} \in \mathbb{Z}$	$m = 1.m_1m_2 \ldots m_{t-1}; 0 \leq m_i < 2$
1 bit	w bits	t bits

The IEEE-754 standard defines different precision where the most used ones are the binary single precision represented with 32 bits, and the binary double precision represented with 64 bits [5]. They correspond, respectively, to $(w, t) = (8, 24)$ or $(11, 53)$.

2) Rounding function: The rounding function, denoted $\circ$, applies to floating-point numbers and their operations. It is needed to represent one number or one operation result which can not be exactly represented by a floating-point number, e.g. the constants π or $1/10$. The rounded operation replaces these values by an approximating floating-point value. For a non representable number $x \in \mathbb{R}$, $\circ(x) = \hat{x}$ denotes the floating-point number $\hat{x} \in \mathbb{F}$ resulting from the rounding.

The IEEE-754 standard defines how any numerical value is rounded to a floating-point number by introducing several rounding modes. There are illustrate in Figure 4, where we distinguish the rounding to nearest (RN) which is the default rounding one, rounding toward $-\infty$ (RD), rounding toward $+\infty$ (RU) and rounding toward 0 (RZ). The standard forces the *correct* rounding for the basic operations (addition, subtraction, multiplication, division and square root). "Correct rounding" means that the returned result is computed as an infinitely precise result then it is rounded to the floating-point number, according to the chosen rounding mode. At each rounding, you lose a priori some accuracy which corresponds to the rounding error. This rounding error is bounded by the arithmetic precision. It is classic to denote $\mathbf{u}$ this working precision that verifies $\mathbf{u} = 2^{-t}$ for the RN rounding mode and $\mathbf{u} = 2^{1-t}$ for the other mode.

Figure 4: The rounding modes, $x, y > 0$.

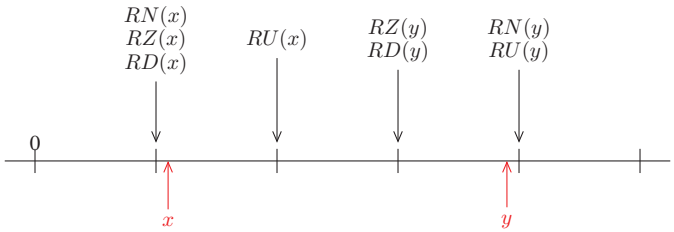

3) Relative errors: Whatever we work about accuracy or reproducibility of floating-point operation, we are interested in these rounding errors and more generally in approximation errors. Let $\hat{x} \in \mathbb{F}$ be the rounded value of $x \in \mathbb{R}$, the relative error is:

$$Err_{rel} = \frac{|\hat{x} - x|}{|x|}, \quad \text{if} \quad x \neq 0. \tag{2}$$

When a result is compared to the exact value x, Relation 2 measures the accuracy of the result $\hat{x}$. In our simulations we do not know the exact result. In this quest for reproducibility, we will compare the value $\hat{x}$ to a reference one, which is the sequential result, as explained in Figure 2.
The major problem of floating-point computation is the rounding errors propagation which occurs within a sequence of computations. Although one isolated operation returns the best possible result (the relative error is bounded by **u**), a sequence of calculations may lead to significant errors due to the accumulation of every single rounding error. It is well known that a final result of several operations may be far from the exact value, see [9] for details and numerous entries on the subject.

4) Non-associativity of floating-point arithmetic: Because of the rounding errors, the floating-point addition is not associative. So change in the addition order may produce different results: $(a + b) + c \neq a + (b + c)$. For instance, $\circ((-1+1)+\mathbf{u}) = \mathbf{u}$, which differs from $\circ((1+\mathbf{u})-1) = 0$. This phenomena is a consequence of the limited precision and range of the IEEE floating-point representation. Hence, depending on the computation order, the propagation of rounding errors differs to yield a different result.

B. Parallel computation and numerical reproducibility

Parallel computation is introduced by domain decomposition where each computing unit solve its own sub-domain. The sub-domains compute their local contributions, exchange and summed them to obtain the global value of the whole domain. In this procedure two causes may lead to non-reproducible results.
Firstly when the sub-domain number varies, the computation of the local contributions differs due to the different rounding errors propagation. In this case, even if the global value is summed in a static order (as it is the case in openTelemavc's `paraco`), it will differ when the number of sub-domain changes whereas being reproducible for successive runs with a fixed number of sub-domains.
Secondly, parallel computation may introduce collective communications where the arrival order of the local contributions differs because of dynamic scheduling or resource sharing for instance. That leads to different order of the computations and due to the non-associativity of the floating-point arithmetic, results are not reproducible. In this case, there is non-reproducibility even when the number of sub-domains does not change.

III. Compensation technique

Compensation is a way to increase the accuracy of results. We apply compensation techniques to recover the reproducibility in our context. The principle of this technique is to use error-free transformation (EFT) which computes the rounding errors generated by the elementary operations in floating point arithmetic. Many compensation algorithms have been developed using these transformations to compute the sum or the dot product of floating-point vectors [10].
The principle in these transformations is that, for an elementary operation $op \in \{+, -, *\}$ of two floating-point numbers $\hat{a}$ and $\hat{b}$, there are two floating-point numbers $\hat{x}, \hat{y}$ that verify:

$$\hat{a}\ op\ \hat{b} = \hat{x} + \hat{y}. \tag{3}$$

Here $\hat{x} = \circ(\hat{a}\ op\ \hat{b})$ is the rounded part of the result and $\hat{y}$ is the generated rounding error. It can also be respectively named the high-order and low-order parts of the result.

Now we present the EFT and the compensation algorithms that are useful in our context. Algorithm 1. 2Sum is one EFT of the addition proposed by Knuth [6] in 1969. It computes the high (x) and the low (y) parts of the sum of two floating-point numbers a and b, in $6flop$.

Algorithm 1 [x,y]=2Sum(a,b)

$x = RN(a + b)$
$a' = RN(x - b)$
$b' = RN(x - a')$
$\delta_a = RN(a - a')$
$\delta_b = RN(b - b')$
$y = RN(\delta_a + \delta_b)$

Algorithm 2. 2Product is one EFT of the multiplication introduced by Dekker in 1971 [1]. It starts by calling the Split algorithm proposed by Veltkamp [9]. This algorithm splits the inputs a and b into their high and lower parts, respectively a_h, b_h and a_l, b_l. The 2Product algorithm returns the two floating-point numbers $x = RN(a \times b)$ and the generated error y. It requires $17flop$. Another EFT for the product exists when a fused multiply and accumulate operator (FMA) is available [9].

Algorithm 2 [x,y]=2Product(a,b)

$[a_h, a_l] = \text{Split}(a)$
$[b_h, b_l] = \text{Split}(b)$
$x = RN(a \times b)$
$t_1 = RN(-r_1 + RN(a_h \times b_h))$
$t_2 = RN(t_1 + RN(a_h \times b_l))$
$t_3 = RN(t2 + RN(a_l \times b_h))$
$y = RN(t_3 + RN(a_l \times b_l))$

Algorithm 3. Sum2 is the compensation algorithm which approximates the sum of a vector using Algorithm 1. It was

proposed by Rump, Ogita and Oishi in 2005 [10]. The result res of this algorithm is as accurate as if it is computed in twice the working precision and finally rounded to the working precision. It requires $7(n-1)flop$.

Algorithm 3 res = Sum2(a)

$s_1 = a_1, \sigma_1 = 0$
for i=2 **to** n **do**
  $[s_i, q_i]$ =2Sum(s_{i-1}, a_i)
  $\sigma_i = RN(\sigma_{i-1} + q_i)$
end for
$res = RN(s_n + \sigma_n)$

Algorithm 4. Dot2 is a compensated dot product, that uses Algorithms 1 and 2 to compute a twice more accurate result. It requires $25n - 7flop$.

Algorithm 4 res = Dot2(a,b)

$[r, \epsilon]$ =2Product(a_1, b_1)
for i = 2 **to** n **do**
  $[p, \pi]$ =2Product(a_i, b_i)
  $[r, \sigma]$ =2Sum(r, p)
  $\epsilon = RN(\epsilon + RN(\sigma + \pi))$
end for
$res = RN(r + \epsilon)$

Sum2 and Dot2, are almost maximally accurate while their conditioning remains smaller than $1/\mathbf{u}$. The condition numbers for the sum and the dot product are respectively, $\sum |a_i| / |\sum a_i|$ and $\sum |a_i \cdot b_i| / |\sum a_i \cdot b_i|$. When this conditioning is larger than $1/\mathbf{u}$, the computation is ill-conditioned and one needs more than twice the working precision to remain accurate. Another levels of compensation can be applied, see [10] for instance.

IV. Necessary modifications to recover the reproducibility

We recover the numerical reproducibility for the gouttedo test case of Telemac-2D using the compensated algorithms presented in Section III. OpenTelemac applies the finite element library BIEF. This one includes many subroutines in Fortran 90 which provide the data structure and the subroutines to the building and the solving phases of the simulation. Almost all our subroutine modifications have been restricted to this library. We now describe 4 types of modifications: data structure, algebraic operations, building phase and solving phase. The unknowns at each node of the domain mesh are the depth of water (H) and the two velocity components (U, V). In the Introduction, it was reported that these results are not reproducible but the sources of this issue are unknown. Finite element method leads to build and solve a general sparse linear system. The strategy is to observe each component of the linear as the computation is performed. This system mixes the three sub-systems related to H, U, V. The sub-system components are computed from physic algebraic equations by taken into account all the physical condition inputs. In the case of the pseudo wave equation, the mixed system is simplified by eliminating the velocity from the continuity equation at the discrete level, more details of these transformations are detailled in [8]. So we obtain the decoupled system :

$$\begin{pmatrix} A_1 & 0 & 0 \\ 0 & A_2 & 0 \\ 0 & 0 & A_3 \end{pmatrix} \begin{pmatrix} H \\ U \\ V \end{pmatrix} = \begin{pmatrix} C_1 \\ C_2 \\ C_3 \end{pmatrix}, \tag{4}$$

where A_2 and A_3 become diagonal matrices thanks to the lumped-mass method. The matrix A_1 and the three second members are computed by algebraic transformations defined in [3]. It is important to note here that the two velocity second members C_2 and C_3 still depend on the H unknown. Hence, this procedure mixed the building and the resolution phases. System (4) is solved in two steps: H is first computed applying the conjugate gradient method to $A_1 H = C_1$. Then C_2 and C_3 derive from H, then the diagonal systems with A_2 and A_3 are solved to yield U and V.

In the following we distinguish the modified parts of the openTelemac code highlighting it on pink. The users choose the two following keywords in the test case file. The desired number of processors is defined by the keyword 'PARALLEL PROCESSORS' in English (or 'PROCESSEURS PARALLELES' in French). This correspond to the Fortran variable `NCSIZE` that takes value 0 for a sequential execution and p for a parallel one. The original computation or the reproducible ones is defined by the keyword "FINITE ELEMENT ASSEMBLY" in English (or "ASSEMBLAGE EN ELEMENTS FINIS" in French). This correspond to the Fortran variable `MODASS` that takes the values 1,2,3 respectively for the original, integer, compensated modes.

A. Modifications in the data structure

The main type in the BIEF library is `BIEF_OBJ` which may be a vector, a matrix or a block. This type contains many components that define the data, the size, the name *etc.* We write `V%R` the R component of the vector V which corresponds to the data. In the compensated version, these R values will be accompanied, when necessary, with the accumulation of their generated rounding errors. These errors will be stored in a component named E and we write `V%E` to access to them. The same way applies for the diagonal D of the matrix M: we write `M%D%R` for data and `M%D%E` for errors, *etc.*

Note: the code is not optimized to these modifications because the subroutine inputs/outputs are not always a `BIEF_OBJ` type, but sometimes double precision vectors. In other words, if the parameters of the subroutines were always of the `BIEF_OBJ` type, all the structure components would be accessible as `V%R` and `V%E`. But when the subroutine parameters are double precision vectors which refer to `V%R`, we had to manually add supplementary input/output parameter that refers to `V%E`.

B. Modifications in the building phase

The steps of the building phase which condition the reproducibility are the finite element assembly and its complement step in parallel, the interface node assembly. The finite element assembly is the main step that builds the linear system. It

recovers the finite elements values to express them on the nodal values computing:

$$V(i) = \sum_{ielem=1}^{nelem} W_{ielem}(i). \quad (5)$$

This process builds the global vector V of size $npoin$ by accumulating the elementary contributions W_{ielem} for every element $ielem$ in the mesh that contains the node i. This assembly is applied to the elementary vector, the diagonal of any matrix and in the EBE matrix-vector product process, see Section IV-D.

The domain decomposition in a parallel resolution introduces inner and interface mesh nodes. The latter ones belong to a common boundary between several sub-domains and are shared between several computing units. The interface node assembly is one of the main significant differences between the sequential and the parallel resolutions. It significantly affects the numerical reproducibility by a non-deterministic rounding errors propagation. Let V be an arbitrary vector extracted from the linear system, and let i an interface node that belongs to k sub-domains. $V^{d_k}(i)$ is one of the contribution of V in the sub-domain d_k at the interface node i (the computation of V^{d_k} only includes quantities related to d_k). Communications between the sub-domains $d_1, \ldots, d_k$ yield the final value $V(i)$ at every interface node i as the following reduction:

$$V(i) = \sum_{\text{sub-domains } d_k} V^{d_k}(i). \quad (6)$$

Accumulation (5) has the same order with respect to $ielem$ for inner nodes in the sequential and the parallel cases. Nevertheless, a given inner node i may become one interface node in another domain decomposition, *i.e.* when the number p of computing units varies. Hence this type of nodes suffers from a non-deterministic error propagation. // In practice, the computation of the vectors V or the diagonal of the matrix D is performed respectively in the subroutines `vectos` or `matrix`, which call the subroutine `assvec` to compute the finite element assembly process, *i.e.* Relation (5). In the compensated mode, the generated rounding errors of the assembly are calculated by subroutine 2Sum (Algorithm 1) which is added in BIEF. From Relation (5) we derive an assembly which now computes the rounding error of each node i:

$$[V(i), E_V(i)] = \text{ReprodAss}_{ielem=1,\ldots,nelem} W_{ielem}(i), \quad (7)$$

where:

$$(V(i), e_i) \quad = \quad \text{2Sum}(V(i), W_{el}(i)),$$

and $E_V(i)$ accumulates the errors e_i for all elements that include the node i.

In the subroutine `assvec` (Listing 1) this pair is accumulated with the errors generated by the assembly for each node $ile(ielem, idp)$.

We continue the modifications with the same idea to provide a reproducible interface point assembly. In practice this assembly is produced in the subroutine `paraco` which is called at several steps in the computation. It becomes `paraco_comp` in the compensated mode. In the original mode, the assembly of the sub-domains contributions (Relation 6) is an accumulation of the received data. In the compensated one, each sub-domain receives a pair [data, error] from every neighbor sub-domain.

Listing 1 FE assembly in `assvec`

```
1  DO IDP = 1 , NDP
2   DO IELEM = 1 , NELEM
3     IF (MODASS.EQ.1)
4  &   X(IKLE(IELEM,IDP)=X(IKLE(IELEM,IDP)
5  &   +W(IELEM,IDP)
6     ELSEIF (MODASS.EQ.3) THEN
7       CALL 2SUM(X(IKLE(IELEM,IDP)),
8  &    W(IELEM,IDP),X(IKLE(IELEM,IDP)),ERROR)
9       ERRX(IKLE(IELEM,IDP))= ERRX(IKLE(IELEM,IDP))
10 &    +ERROR
11    ENDIF
12  ENDDO
13 ENDDO
```

Then the assembly uses 2Sum to compute the rounding errors of the data accumulation. These generated rounding errors are accumulated and represent error contributions of the sub-domain. For all sub-domains d_k that share the interface node i, we compute:

$$[V(i), E_V(i)] = \bigoplus_{\text{sub-domains } d_k} [V^{d_k}(i), E_V^{d_k}(i)], \quad (8)$$

which derives from (6) using again the 2Sum error-free transformation for every d_k, as follows:

$$(V(i), e_k) \quad = \quad \text{2Sum}(V(i), V^{d_k}(i)), \quad (9)$$

$$E_V(i) \quad = \quad E_V(i) + E_V^{d_k}(i) + e_k. \quad (10)$$

Step (9) accumulates $V(i)$ and computes the generated rounding error e_k. Step (10) accumulates in $E_V(i)$ this e_k and the previous errors $E_V^{d_k}(i)$. Finally, compensation occurs after the last reduction of every interface node i to yield the whole vector V as:

$$V + E_V. \quad (11)$$

We stress that this compensation applies once to the vector of inner and interface nodes after the end of the interface node assembly (8). After this step, the compensated vector becomes reproducible.

We note that this procedure is applied to every vector and also for matrix the diagonal `M%D%R` which is a vector for the EBE storage: its accompanying error term `M%D%E` is calculated in a similar way.

C. Modifications in the algebraic operations

The rounding errors `V%E` must be updated for each algebraic operation on `V%R`. Each operation on block or vector is called by the subroutine `os` which only verifies the structure validation before calling the concerned subroutine `ov`. The latter computes the requested operation *op* for the passed vectors `X%R`, `Y%R`, `Z%R`. In the compensated mode, the new subroutine `ov_comp` is called: the data vectors are accompanied with their own error vectors `X%E`, `Y%E`, `Z%E` to also update them. Listing 2 contains some of these modified operations.

D. Modifications in the solving phase

In the gouttedo test case, the resolution phase applies the conjugate gradient (subroutine `gracjg`). The modifications impact the computations of the scalar product in function

Listing 2 Algebraic operations in `ov_comp`

```
!X,Y and Z correspond to the vector value
!!X_ERR,Y_ERR and Z_ERR correspond to the
vector errors
!For initialization
CASE('0  ')
DO I=1,NPOIN
  X(I) = 0.D0
  X_ERR(I)=0.D0
ENDDO
!For copy y to x
CASE('Y  ')
DO I=1,NPOIN
  X(I) = Y(I)
  X_ERR(I) = Y_ERR(I)
ENDDO
!For addition of two vectors
!In the original code: X(I) = Y(I) + Z(I)
DO I=1,NPOIN
  CALL TWOSUM(Y(I),Z(I),X(I),ERROR)
  X_ERR(I)=(Y_ERR(I)+Z_ERR(I))+ERROR
ENDDO
!For value by value vectors product
!In the original code: X(I) = Y(I) * Z(I)
DO I=1,NPOIN
  CALL TWOPROD(Y(I),Z(I),X(I),ERROR)
  X_ERR(I)=(Y(I) * Z_ERR(I))+(Y_ERR(I) * Z(I))
&        +(Y_ERR(I) * Z_ERR(I))
  X_ERR(I)=X_ERR(I)+ ERROR
ENDDO
```

`p_dots` and the matrix-vector product in subroutine `matrbl`, which are called by `gracjg`. We now describe these two modifications.

i) The scalar product $X \cdot Y$

According to the computation mode, the corresponding scalar product is called. In the original mode, the dot product of the whole domain is computed partially by each sub-domain, then the partial contributions are summed over all the sub-domains to compute the global scalar product. This reduction is computed by the MPI dynamic reduction which proceeds with an non-deterministic order. So for a given input results may differ. In the compensated mode, a twice more accurate scalar product is computed. In sequential, Dot2 (Algorithm 4) computes a such accurate sequential dot product. It accumulates both the dot product and the generated rounding errors (addition and multiplication) and finally compensates them together. In the parallel implementation, each sub-domain computes its local scalar product and the corresponding generated rounding errors. Hence a pair [data, error] is returned by `pdot2`. These local pairs are exchanged by the processors via MPI_ALLGATHER and are accurately accumulated by Sum2 (Algorithm 3) in every computing unit, see Listing 3.

ii) The matrix-vector product $M \times V$

The EBE storage and the EBE matrix-vector product are detailed in [3]. Matrix M is stored as `M%D` for its diagonal terms and `M%X` for its extra-diagonal ones. The result RES of the product $M \times V$, of size $npoin$, satisfies the following

Listing 3 The final sum on all the sub-domains

```
!In original version, MYPART is a scalar
!CALL MPI_ALLREDUCE(MYPART,P_DSUM,1,
MPI_DOUBLE_PRECISION,MPI_SUM,MPI_COMM_WORLD
,IER)
!In compensated version, MYPART is a pair
of scalar
CALL MPI_COMM_SIZE(MPI_COMM_WORLD,NUM_PROCS,IER)
ALLOCATE(ALL_PARTIAL_SUM(1:2*NUM_PROCS))
ALL_PARTIAL_SUM=0.D0
CALL MPI_ALLGATHER (MYPART,2,
MPI_DOUBLE_PRECISION,ALL_PARTIAL_SUM,2,
MPI_DOUBLE_PRECISION,MPI_COMM_WORLD,IER)
CALL SUM2(2*NUM_PROCS,ALL_PARTIAL_SUM,P_DSUMERR)
DEALLOCATE(ALL_PARTIAL_SUM)
```

equality:

$$RES = D.V + \sum_{ielem=1}^{nelem} X_{ielem}.V_{ielem}. \qquad (12)$$

The first operand is a vector R_1 (of size $npoin$) resulting from the Hadamard product $R_1(i) = D(i) \times V(i)$. The second operand is calculated in two steps:

1) firstly the multiplication of the extra-diagonal terms and the vector V_{ielem} via a mapping with the connectivity table from the global numbering i and the local ones $i_1, i_2, i_3 \in ielem$.
2) Secondly each term of the previous operation has to be assembled to a global vector R_2 of size $npoin$, in the corresponding node i, by the FE assembly step, *i.e.* applying Relation (5).

Finally, the two vectors are added to obtain the final result of the matrix-vector product: $RES = R_1 + R_2$.

In the compensated mode, this procedure is modified to also take care of the accompanied errors `M%D%E` and `V%E`, previously computed. The following modifications of the product (12) produce a reproducible $M \times V$ product because it ends with one interface point assembly step of the result. The diagonal part D is now associated with its errors E_D, so we compute the pair $[DV, E_D] \times V$. The finite element assembly in Relation (12) is now computed with the modified one (8). This updates the couple $[MV, E_{MV}]$ which is, finally, assembled on the interface nodes with Relation (8). The final step is the compensation $MV + E_{MV}$. So all the $M \times V$ products in the conjugate gradient iterations are now reproducible.

By achieving a reproducible EBE matrix-vector product and a reproducible dot product, the output H of the conjugate gradient becomes reproducible. It is important to note that there are still rounding errors in the conjugate gradient (generated by the divisions and the other operations) but they remain similar in both the sequential and the parallel executions.
Recovering the reproducibility of the last two sub-systems U and V is now straightforward. The U and V diagonal sub-systems depend on H. The second members C_2 and C_3 are built (from H) and are assembled at the interface nodes before the resolution. Reproducible members A_2, C_2, A_3 and C_3 lead

to the reproducible diagonal resolution of the U and V subsystems.

V. Reproducible results

Thanks to the previous modifications that rely on compensated techniques the results of the `gouttedo` test case are now reproducible.
Figure 5 displays two measures corresponding to Figure 2. The rep plot is the maximum relative error over the whole domain between the compensated parallel simulations and the compensated sequential one. The number of processors varies ($p = 2, 4, 8$) but all plots are superposed and constant at the precision level. This exhibits the reproducibility of the compensated simulations. The second plot acc displays the maximum relative difference between the original sequential Telemac-2D simulation and the compensated ones. Relative differences varies from 10^{-14} to 10^{-10}. This validates the compensated simulations that are very similar to the original sequential Telemac-2D simulation. As already mentioned, this latter is considered by the openTelemac developers as the reference simulation. Nevertheless since compensation provides more accuracy than the working precision computation, this curve certainly displays the increase of accuracy produced by the compensation.

Figure 5: Reproducibility (rep) of the compensated simulation and accuracy (rep) compared to the original Telemac-2D for the water depth in gouttedo. X-axis: time steps ($1 \ldots 20 \times 0.2$ sec). Y-axis: maximum relative difference. Number of processors: $p = 2, 4, 8$.

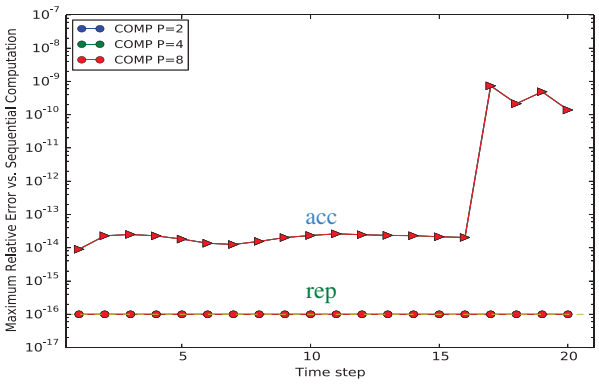

VI. Extra-cost reproducibility

In our context, we measure the extra-cost of the modifications that provide reproducible results compared to the original code. An appropriated method is to repeat the timing measurement several times and then to report the minimal.

We measure the running time extra-cost in cycles, on the version v7.2 of openTelemac. This measure are performed with the hardware counter, the Read-Time-Stamp Counter (RDTSC) instruction. For the parallel measurement, we synchronize the processors to be sure that we measure the minimal time between the processors, see Listing 4. In openTelemac and generally in any simulation, there are a lot of read/write data at both the pre- and post- simulation steps. It is not significant to measure the whole simulation: the extra-cost of the modifications is negligible beside the complete simulation cost. We only measure the modified parts compared to the original ones, which are both the building and the solving

Figure 6: gouttedo: Numerical reproducibility, no more white spots for the water depth values between the sequential (left) and a 2 processors run (right).
Time steps: 1, 2, ..., 7, 8.

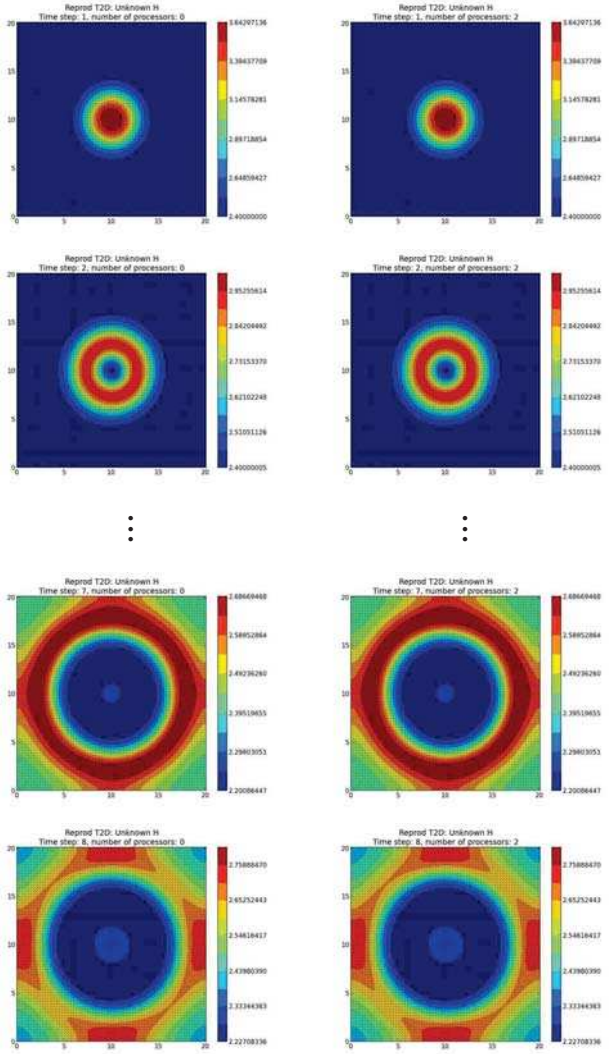

Listing 4 Synchronization of the processors in the performance test

```
! Beginning of the measure
  MPI_BARRIER()
  CALL RDTSC(Begin_Timer)
  !Time loop calculation...
  MPI_BARRIER()
  CALL RDTSC(End_Timer)
! End of the measure
  Total_Time = End_Timer - Begin_Timer
```

phases. So we measure from the begin to the end of the time loop that includes all the modifications and avoid to take into account the large amount of read/write process.
We compare 3 different meshes with 4624, 18225 and 72361 nodes to exhibit how the extra-cost depends on the magnitude of the problem. Table I presents the significant increasing number of interface nodes in these 3 meshes that also introduces a more important communication cost.

Table I: Number of interface nodes in 3 meshes when the number of computing units varies.

#IP		#nodes		
		4624 nodes	18225 nodes	72361 nodes
#procs	2 procs	72	143	280
	4 procs	304	674	1368
	8 procs	501	1152	2020

Figure 7 presents the running time (y-axis) and their ratios of the compensated version running time *vs.* the original version for a given time step and when varying the number of processors (x-axis). We remark that compensated algorithms double (more or less) the time of the core calculations. Cycles of the original code are represented as circles and the compensated ones as squares.
The simulation time increases as the number of mesh nodes because of the extra-computations of the construction and resolution of a larger system. In addition, the number of iterations of the conjugate gradient significantly increases depending on the number of the system unknowns. It is interesting to wrote that the extra-cost for reproducibility benefits from this time increase since our modifications impact the performance of the core simulation.
At the contrary, for a given mesh size, the ratio is larger when increasing the number of processors. This is due to the augmentation of the interface node number and to their extra-cost treatment in the compensated version, (Relation 8).

VII. Conclusion

We have presented how to recover the numerical reproducibility of the Telemac-2D simulation for the gouttedo test case using compensation techniques. The difficulties were to identify the sources of this non-reproducibility, *i.e.* where the rounding errors differ between the sequential and the parallel simulations, and to distinguish their implementations in this huge code. It was inevitable to manipulate three open-Telemac components: the Bief library, the parallel library and Telemac-2D module which include respectively 493, 46 and 192 subroutines. The modifications to obtain reproducibility were restricted to about 30 subroutines, mostly in BIEF. The first source is the non-deterministic error propagation at the interfaces nodes. We recall that this step is implicitly present in several parts of the computation (building and solving phases). It is sufficient to store and propagate these errors and finally compensate them into the computed value after every step of interface node assembly. These corrections are applied for both the parallel and the sequential simulations to yield the expected reproducibility. The second source is the dynamic reduction of the parallel implementation for the dot product in the conjugate gradient iterations. It is corrected by

Figure 7: Extra-cost running time and ratios of the compensated computation compared to the floating-point one, for the test case gouttedo in Telemac-2D. (Mesh size increases from bottom to top.)

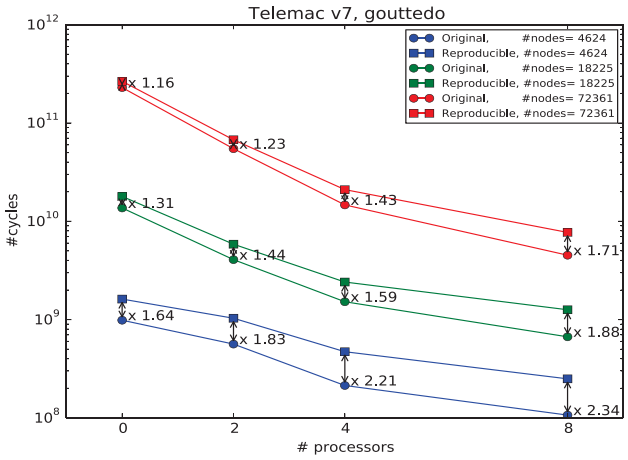

implementing a dot product that computes in about twice the working precision.
This approach is reasonable in term of running time extra-cost. We measured no significant extra-cost of the whole reproducible simulation compared to the original one (when the read/write data process are considered). Of course, as the computation core part takes about twice more time in the reproducible version, the extra-cost could be of the same order for larger cases.
The feasibility and the efficiency of the compensation have been compared to other solutions like integer conversion and reproducible sums [2]. These three techniques were applied to the *Nice* test case of the Tomawac module where the non-reproducibility source is only the finite element assembly step. The compensated solution appeared to be the more efficient one [7].

In this work, we track and modify the computation sequence of the test case gouttedo to make it reproducible. Modifications were only necessary to vector and EBE matrix operations. According to their experience, openTelemac developers are optimistic that no other source of non-reproducibility remains in the code [4]. The future development should integrate the same kind of modifications to other considered solving options, *e.g.* additional physical terms or other linear system solvers. At last, other structure operations should be corrected to obtain a whole reproducible code, *e.g.* operations on block structure, segment storage of matrices, *etc.* Up to our knowledge, these modifications seem easy to be integrated in future versions of a reproducible openTelemac.

Acknowledgment

We thank J.-M. Hervouet, EDR R&D (Chatou, France) for his valuable comments and his strong support to this work.

REFERENCES

[1] T. J. Dekker, "A floating-point technique for extending the available precision," *Numer. Math.*, vol. 18, pp. 224–242, 1971.

[2] J. W. Demmel and H. D. Nguyen, "Fast reproducible floating-point summation," in *Proc. 21th IEEE Symposium on Computer Arithmetic*. Austin, Texas, USA, 2013.

[3] J.-M. Hervouet, *Hydrodynamics of free surface flows: Modelling with the finite element method.* John Wiley & Sons, 2007.

[4] J.-M. Hervouet and al., "Private communication," Dec. 2015.

[5] *IEEE Standard for Binary Floating-Point Arithmetic, ANSI/IEEE Standard 754-1985*, IEEE Computer Society, New York, 1985, reprinted in SIGPLAN Notices, 22(2):9–25, 1987.

[6] D. E. Knuth, *The Art of Computer Programming, Volume 2, Seminumerical Algorithms*, 3rd ed. Reading, MA, USA: Addison-Wesley, 1998.

[7] P. Langlois, R. Nheili, and C. Denis, "Numerical Reproducibility: Feasibility Issues," in *NTMS'2015: 7th IFIP International Conference on New Technologies, Mobility and Security*. Paris, France: IEEE, IEEE COMSOC & IFIP TC6.5 WG, Jul. 2015, pp. 1–5.

[8] ——, "Recovering numerical reproducibility in hydrodynamic simulations," in *23rd IEEE International Symposium on Computer Arithmetic*, J. H. P. Montuschi, M. Schulte, S. Oberman, and N. Revol, Eds., no. ISBN 978-1-5090-1615-0. IEEE Computer Society, Jul. 2016, pp. 63–70, (Silicon Valley, USA. July 10-13 2016).

[9] J.-M. Muller, N. Brisebarre, F. de Dinechin, C.-P. Jeannerod, V. Lefèvre, G. Melquiond, N. Revol, D. Stehlé, and S. Torres, *Handbook of Floating-Point Arithmetic*. Birkhäuser Boston, 2010.

[10] T. Ogita, S. M. Rump, and S. Oishi, "Accurate sum and dot product," *SIAM J. Sci. Comput.*, vol. 26, no. 6, pp. 1955–1988, 2005.

[11] "Open TELEMAC-MASCARET. v.7.0, Release notes," www.opentelemac.org, 2014.

Application of Finite-Volume Schemes for the Bed Load Part of the Bed Evolution Equation

Bert Putzar
Consulting Engineer
Munich, Germany
Email: a61abepu@yahoo.com

***Abstract*—Numerical computations of coastal environments involving bed load transport can be demanding due to spurious oscillations in the numerical solution. On the other hand, predicting the morphological evolution of complex domains over several decades is mandatory in the context of integrated coastal management. This article would like to contribute to the improvement of long-term morphodynamic simulations. Four vertex-centered Finite-Volume schemes are presented. They are implemented into SISYPHE and applied to three different test cases: the dune propagation, the spreading of a sinusoidal hump and as a real world test case a numerical model of the German Bight. The flux-corrected scheme shows the best overall performance and is well suited for long-term morphodynamic simulations of complex domains. It turns out that this scheme represents a vast improvement for the numerical solution of the bed evolution equation.**

I. Introduction

The coastal zone is characterized by diverse ecosystems and a wide variety of natural resources. Complex sediment transport processes and the evolution of the seabed govern the natural morphology. On the other hand, the coastal zone faces major changes due to human uses. Predicting the morphologic evolution is mandatory to develop strategic visions or policies for the management of the coastal zone.

Numerical modeling systems like the TELEMAC system [7] can be used to simulate the sediment transport and the morphological evolution of such complex environments. Solving the bed evolution is one of the major difficulties in morphodynamic modeling due to spurious oscillations. Especially for large-scale simulations with complex topography and over a long-term period, as proposed e.g. by [4], it remains the difficulty to obtain satisfactory results.

Therefore, it was a demand to improve the numerical schemes for the bed load part of the Exner equation. Since this equation describes the propagation and transport of wave-like features, the numerical treatment is a challenge. A number of vertex-centered finite-volume schemes up to second order have been implemented in SISYPHE (Version v7p0) to solve the bed evolution equation: the central scheme, the upwind scheme, the Rusanov scheme and a flux-corrected scheme. They are applied to three different test cases: the dune propagation, the spreading of a sinusoidal hump and the German Bight model.

II. Physical Background

The bed evolution is described by the following partial differential equation:

$$\frac{\partial z_b}{\partial t} = -\frac{1}{\epsilon_n} \nabla \cdot \vec{q}_b \tag{1}$$

with z_b the bed elevation (vertical positive upward), t the time, $\epsilon_n = 1 - n$ the porosity term with n the sediment porosity and $\vec{q}_b = [q_{b,x}, q_{b,y}]^T$ the bed load discharge vector in the horizontal plane. The nabla operator is defined as $\nabla = [\partial_x, \partial_y]^T$. The bed load vector is pointing into the direction of the current

$$\vec{q}_b = q_b \frac{1}{\|\vec{v}\|} \vec{v} \tag{2}$$

where q_b denotes the absolute bed load discharge and $\vec{v} = [v_x, v_y]^T$ the current velocity vector.

To compute the bed load discharge, a wide variety of formulas do exits. For the analysis in this article the well-known formula according to the Meyer-Peter and Mueller [3] is used:

$$\frac{q_b}{\sqrt{g\,(s-1)\,d_s^3}} = m\,(\theta - \theta_{cr})^n \tag{3}$$

Herein, g is gravitational acceleration, $s = \rho_s/\rho$ with the sediment density $\rho_s = 2650\,\mathrm{kg/m^3}$ and the water density $\rho = 1000\,\mathrm{kg/m^3}$ and d_s the grain diameter. On the right hand side θ denotes the Shields parameter and θ_{cr} is the critical Shields parameter, which indicates the threshold for the initiation of sediment transport. The parameters are set to $m = 8$ and $n = 1.5$ for the Meyer-Peter and Mueller formula.

The non-dimensional bed shear stress θ reads as:

$$\theta = \frac{\tau_b}{(\rho_s - \rho)\,g d} \tag{4}$$

Herein, τ_b denotes the bed shear stress acting on the sediment grains. It is calculated according to Nikuradse's law and reads as:

$$\tau_b = \rho \frac{\kappa^2}{\log\left(\frac{12h}{k_s}\right)^2} \|\vec{v}\|^2 \tag{5}$$

Herein, κ is the von Karman constant and h the water depth. The parameter k_s denotes the bed roughness.

For all the results presented in this article one set of parameters have been used. The grain diameter is chosen to be $d_s = 1.5 \times 10^{-4}\,\mathrm{m}$ with a manually prescribed value for the critical shear stress of $\theta_{cr} = 0.047$. The porosity is set

to $n = 0.4$. The bed roughness k_s is equal to three times the sediment diameter. Furthermore, sediment supply is unlimited and only one sandy sediment fraction for bed load is taken into account.

III. Finite-Volume Method

To obatin the Finite-Volume formulation, the computational domain is divided into non-overlapping cells and the bed evolution equation is integrated over a computational cell. By introducing cell-averages for the time derivative and by applying the divergence theorem for the spatial derivatives, one obtains a numerical scheme that relates the rate of change of sediment volume to the fluxes across the cell boundary [6]. The Finite-Volume formulation with explicit time stepping for the bed evolution equation reads:

$$z_{b,i}^{n+1} = z_{b,i}^{n} - \frac{\Delta t}{\epsilon_n T_i} \sum_{j=1}^{ns} l_{ij}\phi_{ij} \quad \text{with } i = 1, .., ncell \tag{6}$$

where $z_{b,i}^{n+1}$ denotes the bed elevation at the new time step $n+1$, $z_{b,i}^{n}$ is the bed elevation at the previous time step n, Δt the time step and T_i the area of the Finite-Volume cell. Furthermore, ns is the number of surrounding sides (edges) of the cell and l_{ij} the edge length. The corresponding neighboring cell is denoted with j and $ncell$ is the number of cells of the computational domain. The numerical flux function ϕ_{ij} is the flux over the cell edge in or out of the Finite-Volume cell.

The method how the of the flux function is computed defines the final numerical scheme. In the following four different numerical flux functions are described. It should be remarked that they belong to the class of explicit schemes and hence they are subject to time step limitations. If the morphodynaimc model is coupled to the hydrodynamic model directly, the hydrodynamic time step is the decisive parameter for stability and therefore this issue is not addressed any further in this article.

A. Central Scheme (CDS)

The central scheme [6] reads as:

$$\phi_{ij}^{CDS} = \frac{1}{2}\left(\vec{F}_L + \vec{F}_R\right) \cdot \vec{n}_{ij} \tag{7}$$

Herein, the indices L and R denote the left (node i) and right (node j) state, respectively. The fluxes $\vec{F}_L$ and $\vec{F}_R$ correspond to $\vec{q}_{b,i}$ and $\vec{q}_{b,j}$. The unit normal vector n_{ij} is pointing outwards of cell i into the direction of cell j. The CDS-scheme is second order accurate in space and is unstable in the vicinity of shocks or sharp gradients.

B. Upwind Scheme (UPW)

One of the basic stable schemes is the UPW-scheme [6]. To circumvent instabilities that arise with a linear interpolation, the flux is chosen according to the direction the characteristic velocity. The flux is computed as:

$$\phi_{ij}^{UPW} = \frac{1}{2}\left(\vec{F}_L + \vec{F}_R\right) \cdot \vec{n}_{ij} - \frac{1}{2}\operatorname{sgn}(a_{ij})\left(\vec{F}_R - \vec{F}_L\right) \cdot \vec{n}_{ij} \tag{8}$$

where a_{ij} denotes the characteristic speed and the sign of a_{ij} defines the upwind direction, which is obtained as:

$$\operatorname{sgn}(a_{ij}) = \begin{cases} \operatorname{sgn}\left(\frac{q_{b,R}-q_{b,L}}{z_{b,R}-z_{b,L}}\right) & \text{if } z_{b,R} - z_{b,L} \neq 0 \\ \operatorname{sgn}\left(\phi_{ij}^{CDS}\right) & \text{otherwise} \end{cases} \tag{9}$$

with $q_{b,L} = \vec{q}_{b,i} \cdot \vec{n}_{ij}$ and $q_{b,R} = \vec{q}_{b,j} \cdot \vec{n}_{ij}$. Since a_{ij} can not be computed from the Rankine-Hugoniot jump condition if the bed level difference is nearly zero, the upwind direction is alternatively obtained from the bed load discharge vector. The UPW-scheme is know to suffer from significant numerical diffusion and a grid dependency of the computed results.

C. Rusanov Scheme (RUV)

Another stable and simple scheme is the Rusanov scheme [6], which is sometimes also named local Lax-Friedrichs scheme . The flux function is computed as:

$$\phi_{ij}^{RUV} = \frac{1}{2}\left(\vec{F}_L + \vec{F}_R\right) \cdot \vec{n} - \frac{1}{2}|a_{ij}|\left(z_{b,R} - z_{b,L}\right) \tag{10}$$

where the absolute value of the wave speed is estimated as

$$|a_{ij}| = \min\left(\left|\frac{q_{b,R} - q_{b,L}}{z_{b,R} - z_{b,L}}\right|, \frac{\Delta x}{\Delta t}\right) \tag{11}$$

with the Euclidean distance Δx between nodes i and j. The left term on the right hand side in (10) represents an diffusive term that stabilizes the numerical solution.

D. Flux-Correction (FCT)

Godunovs barrier theorem states that monotone schemes can be at most first order accurate [6]. As a result, higher order schemes tend to generate spurious oscillations. This issue can be overcome with the flux-corrected method. It was developed by [1] for the one-dimensional case and extended to multidimensions by [8]. This method combines the advantages of a stable, non-oscillatory first order scheme with the precision of an second order scheme by the help of an non-linear limiter function. In smooth regions the FCT-scheme uses the higher order flux, whereas in shock regions the stable low order scheme is used. The flux function read as:

$$\phi_{ij}^{FCT} = \phi_{ij}^{LO} + \alpha_{ij}\left(\phi_{ij}^{HI} - \phi_{ij}^{LO}\right) \tag{12}$$

where ϕ_{ij}^{LO} denotes a first order, non-oscillatory flux and ϕ_{ij}^{HI} a higher order flux. The factor α_{ij} is the results of a non-linear limiter; see [5] for the computation procedure for Finite-Volumes. For $\alpha_{ij} = 0$ the FCT-scheme is equal to the first order scheme and for $\alpha_{ij} = 1$ it is purely the higher order flux. For the results presented in the following the upwind scheme is used for the low order flux ($\phi_{ij}^{LO} = \phi_{ij}^{UPW}$) and for higher order flux the central scheme is applied ($\phi_{ij}^{HI} = \phi_{ij}^{CDS}$).

E. Implementation into SISYPHE

The Finite-Volumes schemes are implemented in a vertex-centered manner in the subroutine BED_LOAD_SOLVS_VF. The data structure as already available in SISYPHE is used. The keyword VFSCHEME has been introduced to switch between the numerical schemes easily. An edge-based algorithm is used for maximum performance and the whole program code is parallelized by the help of Message Passing Interface

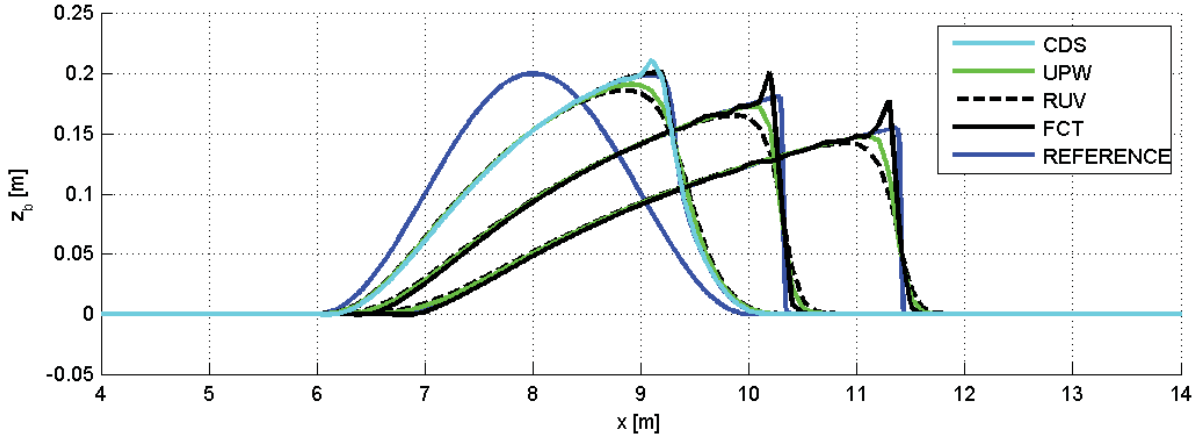

Fig. 1: Bed development for the dune test case after 5 h, 15 h and 30 h along the centerline of the channel. The initial bed level is shown for the reference simulation only.

(MPI) routines. At the open inflow boundaries, the bed level is prescribed. Free evolution is allowed on open outflow boundaries. For a closed wall, the flux through the boundary is zero but the evolution is free. The extension to sediment fractions and non-erodible bottom has been implemented as well, but the results are not discussed in this article.

IV. Verification

A. Dune Propagation

The propagation of a sand dune is one the most investigated test cases for numerical morphodynamic models. A variety of simulation setups do exist. For the following investigations the general parameters from the TELEMAC validation test case were adapted. The test case consist of a dune in a narrow channel with a unidirectional, constant discharge. The current is strong enough to move the sediment particles throughout the whole domain. With time, the dune is propagating downstream leading to a shock front. Without gravitational transport, the steep sharp front is further propagation downstream while reducing its height with time.

1) Model Setup: The geometry of the flume is defined with a length of $16\,\mathrm{m}$ and a width of $2\,\mathrm{m}$. The initial bed elevation (Figure 1) is prescribed as:

$$z_b = \begin{cases} 0.2\sin^2\left(\pi\frac{(x-6)}{4}\right) & x \in [6,10] \\ 0 & \text{otherwise} \end{cases} \tag{13}$$

The free surface elevation is equal to $z_s = 0.6\,\mathrm{m}$, yielding a water depth between $0.4\,\mathrm{m}$ and $0.6\,\mathrm{m}$. The specific discharge in x-direction is chosen to be $q_x = 0.2\,\mathrm{m}^2/\mathrm{s}$, which results in velocities between $0.33\,\mathrm{m/s}$ and $0.50\,\mathrm{m/s}$. Hence, the maximum Froude number is approximately $\mathrm{Fr}_{max} \approx 0.25$.

The simulations are carried out with the morphodynamic model SISYPHE. The steady state option is used to obtain the velocity field computed from the continuity correction for the steady discharge. The domain is discretized with 3911 nodes, forming 7432 triangular elements with a mean element edge length of $0.1\,\mathrm{m}$. The time step of $100\,\mathrm{s}$ is kept constant during the total simulation duration of 4 days.

To evaluate the numerical schemes, a reference solution (blue line in Figure 1) with a high resolution Finite-Volume upwind-method has been computed. Since the characteristic velocity is always pointing downstream for the presented test setup, the upwind direction is simply computed from the bed load discharge vector.

2) Results: Figure 1 shows the bed elevation after $5\,\mathrm{h}$, $15\,\mathrm{h}$ and $30\,\mathrm{h}$ along the centerline of the channel. The CDS-scheme shows instabilities as the dune propagates downstream. The bed evolution at $t = 5\,\mathrm{h}$ indicates this with wiggles at the top of the dune. Everywhere else the solution is smooth and compares well with the reference solution. After $5\,\mathrm{h}$ the simulation crashed due to increasing instabilities.

As expected, the UPW-scheme produces a smooth bed elevation for all time steps. On the other hand, near the shock front the solution is quite diffusive. Instead of a sharp front, the course of the bed is rounded in this region.

The RUV-scheme yields similar results than the UPW-scheme. Instead of a sharp front the course of the bed is rounded. Furthermore, it shows the strongest diffusion off all schemes, which reduces the height of the dune significantly.

A different behavior shows the FCT-scheme. The shock front is quite well captured and nearly as steep as the reference solution, but the method cannot prevent the appearance of small wiggles. Anyway, in smooth regions the solutions is similar to all the other schemes.

B. Hump Test Case

A two-dimensional test case is the migration of a Gaussian hump. In contrast to the dune propagation, the hump flattens out with time and develops into a star shape pattern. This problem has been proposed by [2], who also derived an analytical solution for the angle of spread.

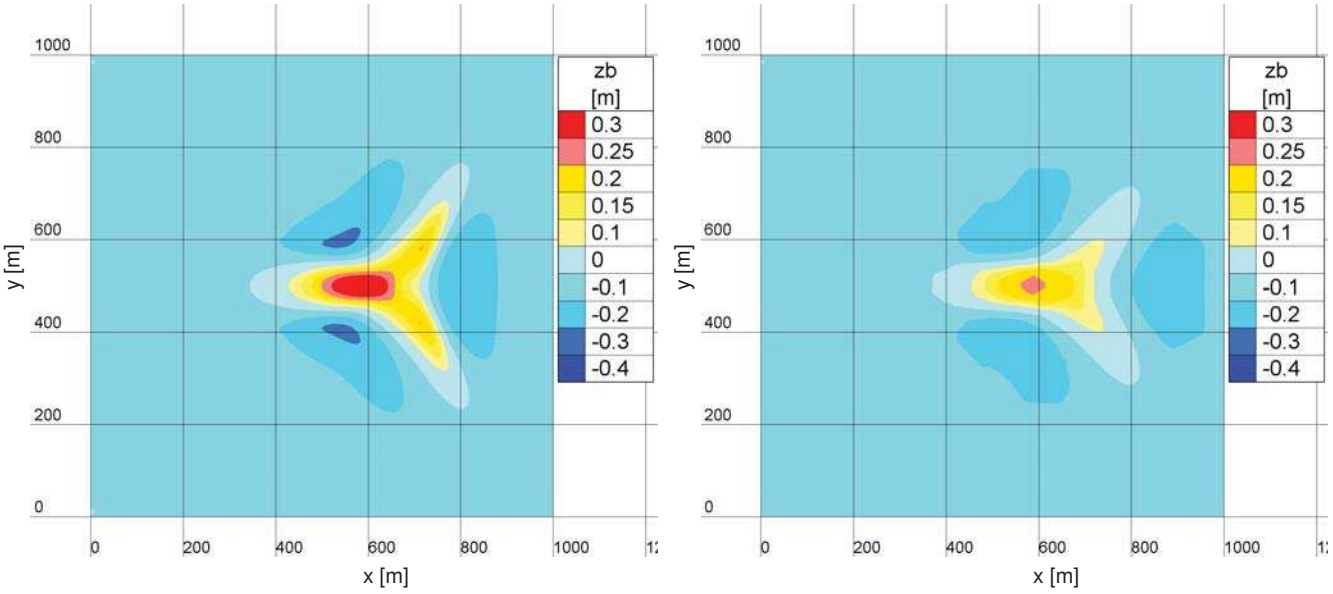

(a) CDS (b) UPW

(c) RUV (d) FCT

Fig. 2: Computed bed level after two days for the hump test case with flow direction form left to right.

1) Model Setup: The initial bed elevation is given by:

$$z_b = \begin{cases} \sin^2\left(\pi\frac{(x-300)}{200}\right)\sin^2\left(\pi\frac{(y-400)}{200}\right) & x \in [300, 500]\,, \\ & y \in [400, 600] \\ 20 & \text{otherwise} \end{cases} \tag{14}$$

The initial surface elevation is $z_{s,0} = 10\,\mathrm{m}$, yielding a water depth between $9\,\mathrm{m}$ and $10\,\mathrm{m}$. On the upstream boundary at $x = 0\,\mathrm{m}$ a constant inflow discharge of $Q_{x,in} = 50\,\mathrm{m}^3/\mathrm{s}$ is prescribed. The discharge in y-direction is set to zero. At the outflow boundary at $x = 1000\,\mathrm{m}$ free outflow conditions with a fixed surface elevation at $z_{s,out} = 10\,\mathrm{m}$ are defined. The lateral boundaries at $y = 0\,\mathrm{m}$ and $y = 1000\,\mathrm{m}$ are defined as closed walls with slip velocity conditions.

The simulations are carried out with the morphodynamic model SISYPHE coupled directly with the flow model TELEMAC-2D (Version v7p0). The bed evolution equation is solved without morphological acceleration techniques. Automatic time stepping for the TELEMAC-2D model has been used to ensure a flow Courant number of $Cr = 0.9$ in combination with the characteristics method for the advection. The quadratic domain is discretized with 12242 nodes. The mean element edge length of the 24082 triangular elements is $10\,\mathrm{m}$.

2) Results: The simulations results for the bed elevation after two days are presented in Figure 2.

The CDS-scheme in Figure 2a shows the typical star-shaped pattern. The spreading of the hump can be clearly observed. It is interesting to note that the CDS-scheme performs very well without producing any wiggles or instabilities.

A different picture draws the UPW-scheme. The diffusive character leads to a flattened bottom and hence the spreading is not as pronounced as for the CDS-scheme.

The RUV-scheme produces an even more flattened bottom, which is an effect of the additional term in the flux computation. As a result, the decay of the hump is largest of all schemes.

The FCT-scheme performs similar to the CDS-scheme. The decay of the hump is in the same order and much smaller as for the UPW-scheme and the RUV-scheme. The spreading of the hump is simulated very well.

V. Application

A. The North Sea Model

To evaluate the numerical schemes in terms of a realistic and complex setup, the numerical model of the German Bight (Figure 3a) as described in [4] has been applied. The simulation domain covers the North Sea, the English Channel and the adjoining area to the Baltic Sea. The unstructured finite element mesh consists of nearly $42\,000$ nodes forming ca. $80\,000$ triangular elements (Figure 3b). The models applied are the hydrodynamic model TELEMAC-2D [3] for calculating depth-averaged flow and the morphodynamic model SISYPHE [5] for the bed evolution.

Both models are coupled directly, meaning that data is exchanged each time step. Using the MPI abilities of the TELEMAC system has shortened the simulation time. With an AMD Opteron 32-core system it took approximately three days for a computation over a period of 50 years. The simulations are carried out with tidal forcing at the open boundaries and with unlimited sediment supply. Furthermore, no extra treatment of tidal flats for the Exner equation has been implemented.

In this article only the most south-eastern part of the German Bight is discussed (Figure 3a), which covers the estuaries of Elbe River and Weser River and large tidal flats. It should be remarked that the results presented do not represent real morphodynamic evolutions. The purpose is only the comparison of the numerical schemes.

B. Bed Evolution After One Year

Figure 4 shows the computed bed evolution after one year. The bed level is not shown since the evolutions after this time period are too small to visualize the different results at this scale satisfactory.

For the CDS-scheme, the evolutions are more less irregular and a pattern can hardly be observed. The highest values occur in the channels, especially in the Elbe Estuary. Here, the flow velocity is highest and the sediment dynamics is strongest.

The UPW-scheme produces completely different results. Even though the magnitude is nearly the same as for the CDS-scheme, a distinct pattern of erosion and deposition is present. In nearly every channel sediment deposition takes places, whereas the top of them are eroded. It is clear that this effect is unphysical and depends on the mesh topology.

The same can be observed for the RUV-scheme. The effect is more pronounced in the channels, since this scheme uses artificial diffusion to stabilize the computation. Hence, the bottom flattens out during the simulation especially at locations with high bed gradients.

The FCT-scheme, which is a blend of CDS-scheme and UPW-scheme, gives an bed evolution that is principally the same as the CDS-scheme.

C. Bed Evolution After 50 Years

The previous section shows that the UPW-scheme and the RUV-scheme produce unphysical solutions when applied to the real world test case German Bight. Hence, only the results of the CDS-scheme and the FCT-scheme for long term morphodynamic simulations are described in the following.

The results for bed elevation and bed evolution after 50 years of tide driven morphodynamics are shown in Figure 5. The bed elevation computed with the CDS-scheme (Figure 5a) seems to be satisfactory at the first sight. But a closer look reveals that at several nodes the bed level is significantly higher than at the surrounding area. Instabilities arise at these nodes that make the simulation unstable and the computational results unusable. Such local erroneous trend of the bed evolution is sometimes hard to detect and might develop at places where it is not expected. In contrast, the details in Figure 5a and Figure 5b in the Elbe Estuary show the typical - and expected - behavior of the unstable CDS-scheme. The bed evolutions range between $-20\,\mathrm{m}$ and $-20\,\mathrm{m}$ with an oscillating character along the estuary.

The FCT-scheme yields much better results for the bed elevation (Figure 5c) and the bed evolution (Figure 5d). Even though the overall impression is nearly equal to the CDS-scheme, one can observe that the local instabilities do not arise anymore. The bottom is smooth but not flattened out. The principal appearance compares very well with the initial bed elevation (Figure 3a) based on observations. The largest difference can be observed in the Elbe Estuary, which is shown in the details in Figure 5c and Figure 5d. The FCT-method successfully prevents instabilities and allows a stable as well as precise computation of the bed evolution over 50 years.

VI. Conclusion

Four Finite-Volumes schemes for the solution of the bed evolution equation on unstructured grids have been introduced and applied to three test cases.

The UPW-scheme and the RUV-scheme yield good results in situations with shock fronts but fail in real world conditions due to their diffusive character. Both generate similar results, whereas the RUV-scheme is the most diffusive one. The results show a significant dependence on the mesh topology. Hence, they are not suited for morphodynamic simulations of complex domains.

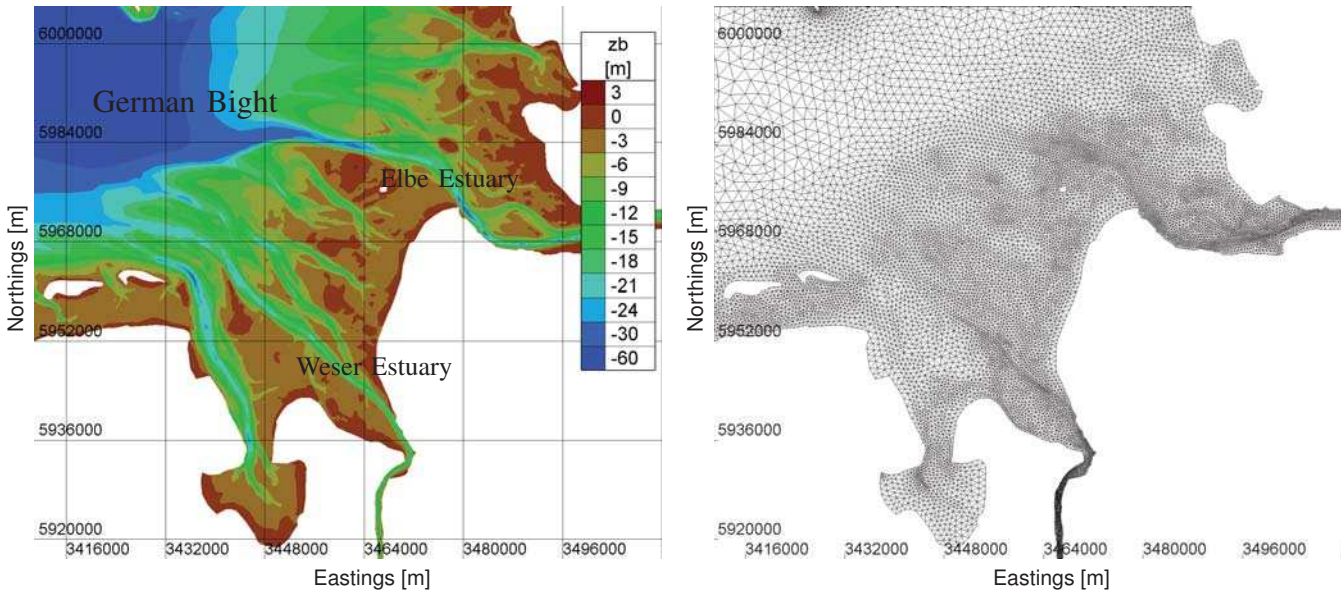

(a) initial bed level.

(b) triangular mesh

Fig. 3: South eastern part of the German Bight model, see [4] for more information.

Surprisingly, the unstable CDS-scheme works well in situation with smooth regions but it fails for the dune test case. Unfortunately, with long term simulations instabilities arise indicating that the CDS-scheme is inappropriate for simulations over decades.

The FCT-scheme combines the advantages of UPW-scheme and CDS-scheme. It produces stable solution even in the vicinity of shock front but is also well suited for the computation of smooth regions like in case of the spreading hump and complex domain like the German Bight. It works very well especially for long-term morphodynamic simulations.

The FCT-scheme fits excellently into the SISYPHE framework, since the data structure for the domain discretization and the boundary conditions can be used directly. Furthermore, the edge-based implementation allows the implementation of an efficient algorithm with moderate computational expense and is well suited for MPI acceleration.

In the next stage the FCT-scheme will be applied to the computation of fractionated bed load transport including the existence of a non-erodible bottom and the active layer concept. Furthermore, numerical simulations of coastal morphology under the influence of complex forcing with tide, wind and waves have to be carried out and the performance of the FCT-scheme has to be evaluated.

ACKNOWLEDGMENT

The presented work is based on the research project ”AufMod” (Development of an integrated model system for analyzing the long-term morphodynamics in the German Bight) [4], which was a project of the Association for Research in Coastal Engineering (grant number 03KIS085), financially supported by the German Ministry of Education and Research.

VII. REFERENCES

REFERENCES

[1] J. P. Boris and D. L. Book, “Flux corrected transport. 1. shasta, a fluid transport algorithm that works.” *Journal of Computational Physics*, vol. 11, p. 3869, 1973.

[2] H. J. De Vriend, “Analysis of horizontally two-dimensional morphological evolutions in shallow water,” *Journal of Geophysical Research: Oceans*, vol. 92, no. C4, pp. 3877–3893, 1987. [Online]. Available: http://dx.doi.org/10.1029/JC092iC04p03877

[3] Electricité de France, “Sisyphe User Manual Version 6.0,” Electricité de France, Direction des Etudes et Recherches, Chatou Cedex, Note technique, 2010.

[4] H. Heyer and K. Schrottke, “Aufbau von integrierten Modellsystemen zur Analyse der langfristigen Morphodynamik in der Deutschen Bucht (AufMod),” 2013, Gemeinsamer Abschlussbericht für das Gesamtprojekt mit Beiträgen aus allen 7 Teilprojekten.

[5] P. V. Slingerland, “An accurate and robust finite volume method for the advection diffusion equation,” 2007.

[6] E. Toro, *Riemann Solvers and Numerical Methods for Fluid Dynamics*. Berlin Heidelberg: Springer-Verlag, 2009.

[7] C. Villaret, J.-M. Hervouet, R. Kopmann, U. Merkel, and A. G. Davies, “Morphodynamic modeling using the telemac finite-element system,” *Computers & Geosciences*, vol. 53, pp. 105–113, 2013.

[8] S. T. Zalesak, “Fully multidimensional flux-corrected transport algorithms for fluids,” *Journal of Computational Physics*, vol. 31, no. 3, pp. 335 – 362, 1979. [Online]. Available: http://www.sciencedirect.com/science/article/pii/0021999179900512

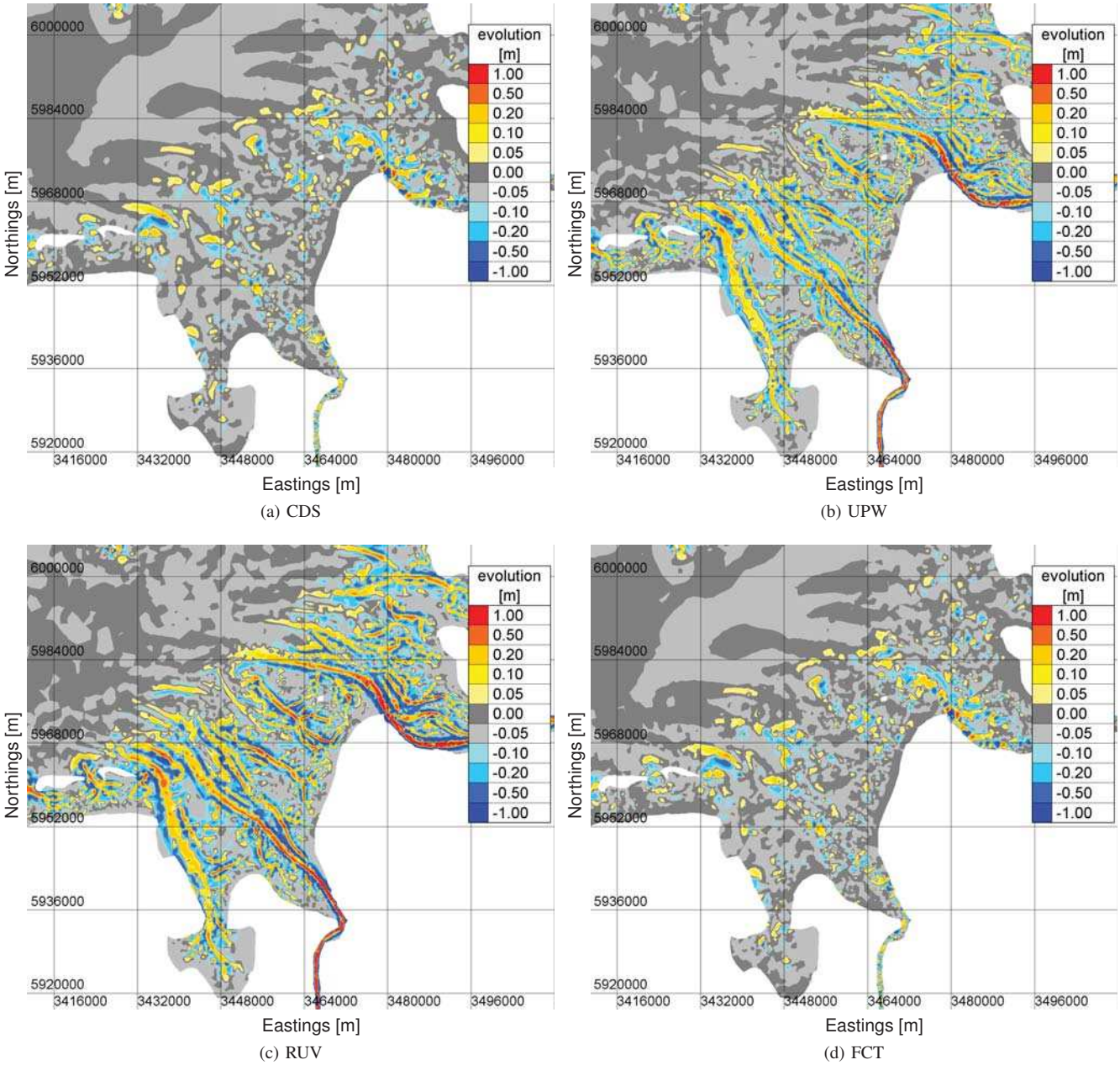

(a) CDS

(b) UPW

(c) RUV

(d) FCT

Fig. 4: Simulation results after 1 year.

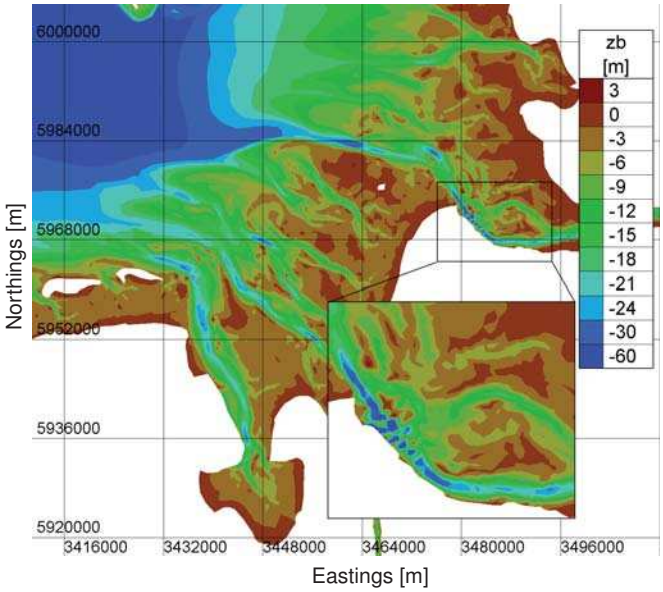

(a) CDS bed elevation

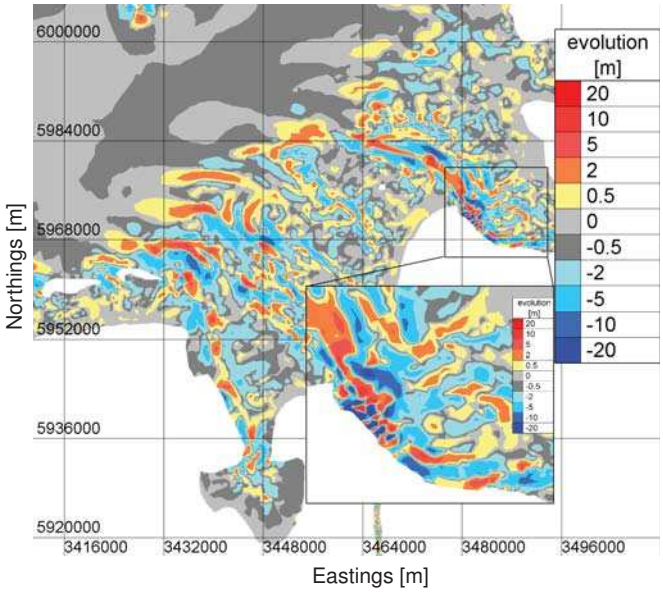

(b) CDS bed evolution

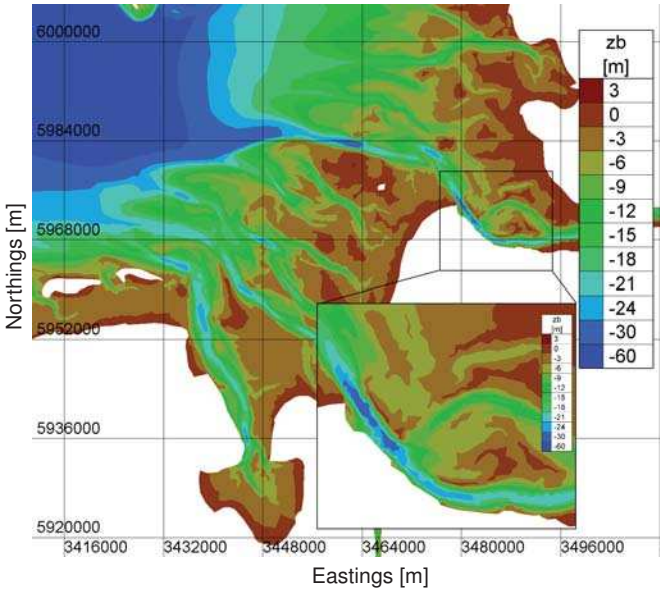

(c) FCT bed elevation

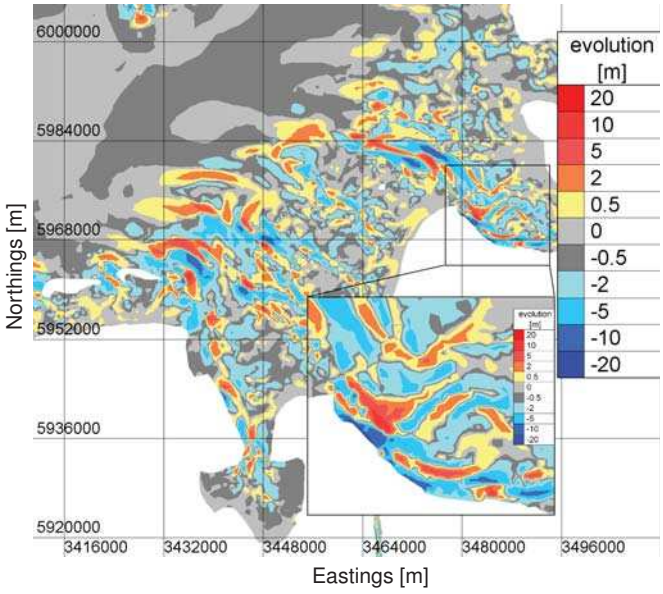

(d) FCT bed evolution

Fig. 5: Simulation results after 50 years.

Simulation of the flow around a submerged structure using the Immersed Boundary Method

Yue Yin*, Ming Li†, Charles Moulinec‡, David R. Emerson§
*School of Engineering, University of Liverpool
Email: yue.yin@stfc.ac.uk
†School of Engineering,University of Liverpool
Email: mingli@liverpool.ac.uk
‡Science and Technology Facilities Council
Daresbury Laboratory,Warrington, UK
Email: charles.moulinec@stfc.ac.uk
§Science and Technology Facilities Council
Daresbury Laboratory,Warrington, UK
Email:david.emerson@stfc.ac.uk

***Abstract*—In the current version of TELEMAC3D (7.0+), triangular 2-D unstructured body-fitted meshes are used to represent the computational domain as for example river banks or coastal lines. However due to the sigma mesh transformation in the vertical direction, flows around submerged obstacles with vertical walls can not be easily handled. In this study, the Immersed Boundary method is implemented to represent the obstacles in the water. The principle of the Immersed Boundary method is to simulate the flow around structures by applying forces which impede the flow along the solid boundaries. The numerical results are benchmarked with two laboratory scale cases, including the flow around a circular cylinder [12] and the flow over a submerged structure [8].**

I. Introduction

TELEMAC has been widely used to simulate river and maritime hydraulics. In the current version of the TELEMAC system (7.0+), and more specifically TELEMAC3D, triangular 2-D unstructured body-fitted meshes are used to represent the computational domain as for example river banks or coastal lines. However due to the sigma mesh transformation in the vertical direction, flows around submerged obstacles with vertical walls can not be easily handled.

The strategy based on triangular elements to mesh the bottom of the field, and using layers of triangle elements to simulate 3-D flows is a clear limitation to tackle flows around submerged obstacles, as each water column contains the same number of prisms. It is then possible to generate a mesh around obstacles such as island or bridge piles which go through the free surface, but not around submerged structures, for instance. In order to account for obstacles in water, an Immersed Boundary (IB) method has been used. The principle of the Immersed Boundary method is to simulate the flow around structures by applying forces which impede the flow along the solid boundaries. An additional IB force, which is to replace the actual reaction force on the solid surface, is applied in the momentum equations of the Navier-Stokes equations.

The IB method was firstly introduced by Peskin [9] in 1973 to simulate the blood flow in the heart. This approach was used to model elastic capillary and artery walls. Nowadays, a variety of approaches have been developed to simulate fluid-structure interaction (FSI) problems, for instance. The IB method used by Peskin [9] is a classic IB method in which IB forces are represented by appropriate constitutive laws depending on the realistic force condition. This approach is more suitable for the simulation of elastic boundaries as the spring feature of the boundary can be introduced by Hook's law. For a rigid boundary, the immersed boundary can be represented by a direct forcing method [4], [7]. The idea of this approach is to calculate the IB force based on the temporally discretised momentum equations. To incorporate direct forcing in the original diffused interface IB method, the quantities on the background and immersed boundary meshes can be materialised by employing discrete delta functions in the classical formulation.
Another commonly used IB method is the cut-cell method. In this approach, the mesh cells are cut at the interface to fit the immersed boundary. The fluxes across the faces of the cut-cells are reconstructed from the surrounding regular cells and immersed boundaries [3]. Due to the difficulty managing of the topology of the cut-cells (for instance, after cutting a rectangle cell, the shape of the remaining cell can be either a pentagon, a quadrangle or a triangle), this approach is easier to be used in 2-D [5], [13], [14] than in 3-D [1], [10].

In this study a direct forcing IB method has been developed and implemented in TELEMAC3D to simulate the structures submerged in the water. The 2-D mesh is generated in a way that the footprint of the obstacle on the bottom is accounted for. This allows to avoid adding extra interpolations when computing fluxes, for instance. The numerical results are compared with two laboratory scales experiment including the flow around a circular cylinder [12] and the flow over a submerged cylinder [8].

II. Numerical model

A. Governing equations

In this study, TELEMAC3D is used to simulate the flow impact on a full cylinder and a submerged cylinder respectively. TELEMAC3D is a three-dimensional computational

code which solves the 3-D Navier-Stokes equations using the Boussinesq approximation. The 3-D Navier-Stokes equations read:

$$\frac{\partial u_1}{\partial x_1} + \frac{\partial u_2}{\partial x_2} + \frac{\partial u_3}{\partial x_3} = 0 \tag{1}$$

$$\frac{\partial u_1}{\partial t} + u_1\frac{\partial u_1}{\partial x_1} + u_2\frac{\partial u_1}{\partial x_2} + u_3\frac{\partial u_1}{\partial x_3} = -\frac{1}{\rho}\frac{\partial p}{\partial x_1} + \nu\left(\frac{\partial^2 u_1}{\partial x_1^2} + \frac{\partial^2 u_1}{\partial x_2^2} + \frac{\partial^2 u_1}{\partial x_3^2}\right) + F_{x_1} \tag{2}$$

$$\frac{\partial u_2}{\partial t} + u_1\frac{\partial u_2}{\partial x_1} + u_2\frac{\partial u_2}{\partial x_2} + u_3\frac{\partial u_2}{\partial x_3} = -\frac{1}{\rho}\frac{\partial p}{\partial x_2} + \nu\left(\frac{\partial^2 u_2}{\partial x_1^2} + \frac{\partial^2 u_2}{\partial x_2^2} + \frac{\partial^2 u_2}{\partial x_3^2}\right) + F_{x_2} \tag{3}$$

$$\frac{\partial u_1}{\partial t} + u_2\frac{\partial u_3}{\partial x_1} + u_2\frac{\partial u_3}{\partial x_2} + u_3\frac{\partial u_3}{\partial x_3} = -\frac{1}{\rho}\frac{\partial p}{\partial x_3} - g + \nu\left(\frac{\partial^2 u_3}{\partial x_1^2} + \frac{\partial^2 u_3}{\partial x_2^2} + \frac{\partial^2 u_3}{\partial x_3^2}\right) + F_{x_3} \tag{4}$$

where (x_1, x_2, x_3) are the Cartesian coordinates, (u_1, u_2, u_3) is the velocity vector, t the time, ν is the dynamic viscosity, p is pressure, g is the gravity constant, $(F_{x_1}, F_{x_2}, F_{x_3})$ a potential extra force (it could be the wind, the Coriolis force, or an IB force for instance).

The pressure term is divided into hydrostatic pressure p_h and dynamic pressure p_d. The hydrostatic pressure is defined by the following equation:

$$p_h = p_{atm} + \rho_0 g(\eta - x_3) + \rho_0 g \int_{x_3}^{\eta} \frac{\Delta\rho}{\rho_0} dx_3 \tag{5}$$

where ρ_0 and $\Delta\rho$ are reference density (1,024kg/m3) and variation of density respectively; p_{atm} is the atmospheric pressure, η is the water surface elevation.

The dynamic pressure p_d is solved by Chorin and Teman projection scheme [2].

TELEMAC3D supports both hydrostatic and non-hydrostatic options. In the hydrostatic version, the pressure is only related to the water depth, i.e. Eqs. (1) (2) (3) (5) are solved. In the non-hydrostatic version, the full Navier-Stokes equations (Eqs. (1) (2) (3) (4)) with both hydrostatic pressure p_h and dynamic pressure p_d are solved.

In this study, the hydrostatic version is used to simulate the flow past a full cylinder and the non-hydrostatic version is used to simulate the flow past a submerged cylinder.

B. Immersed boundary condition

The Immersed Boundary method used here corresponds to a direct forcing method which relies on forces applied to some nodes of the mesh, which impedes the flow along the solid boundaries. The additional IB force replaces the actual reaction force on the solid surface and is activated by using source terms in the momentum equations of the Navier-Stokes equations. The forcing step is added in the pressure-continuity step which is the last step of solving the moment equations.

The forcing step in the current modified model can be represented as:

$$\frac{u_1^{n+1} - u_1^c}{\Delta t} = -g(\frac{\partial \eta}{\partial x_1}) + \nu\left(\frac{\partial^2 u_1}{\partial x_1^2} + \frac{\partial^2 u_1}{\partial x_2^2} + \frac{\partial^2 u_1}{\partial x_3^2}\right) + F_{x_1} \tag{6}$$

$$\frac{u_2^{n+1} - u_2^c}{\Delta t} = -g(\frac{\partial \eta}{\partial x_2}) + \nu\left(\frac{\partial^2 u_2}{\partial x_1^2} + \frac{\partial^2 u_2}{\partial x_2^2} + \frac{\partial^2 u_2}{\partial x_3^2}\right) + F_{x_2} \tag{7}$$

where u_i^c are the velocity components obtained from previous advection step of calculation and F_{x_i} contains the buoyancy terms

Following [6], the force terms are obtained by rearranging Eqs.[6] and Eqs.[7] and substituting u_1^{n+1}, u_2^{n+1}, u_3^{n+1} with the desired velocity at the solid node. By applying non-slip boundary conditions on the solid surface, the IB force terms are defined as:

$$f_{x_1}^{ibm} = \begin{cases} \dfrac{0 - u_1^c}{\Delta t} + g(\dfrac{\partial \eta}{\partial x_1}) \\ -\nu\left(\frac{\partial^2 u_1}{\partial x_1^2} + \frac{\partial^2 u_1}{\partial x_2^2} + \frac{\partial^2 u_1}{\partial x_3^2}\right) - F_{x_1} \text{ , on the boundary node} \\ 0 \text{ , elsewhere} \end{cases}$$

$$f_{x_2}^{ibm} = \begin{cases} \dfrac{0 - u_2^c}{\Delta t} + g(\dfrac{\partial \eta}{\partial x_2}) \\ -\nu\left(\frac{\partial^2 u_2}{\partial x_1^2} + \frac{\partial^2 u_2}{\partial x_2^2} + \frac{\partial^2 u_2}{\partial x_3^2}\right) - F_{x_2} \text{ , on the boundary node} \\ 0 \text{ , elsewhere} \end{cases}$$

TELEMAC3D uses the finite element method for the equation discretisation. The value of one node relies on the values of the surrounding nodes. Therefore, although the velocities on the IB nodes can be set to zero by applying the additional force (this is because of the assumption that the boundary of an obstacle is accounted for during meshing), small velocity fluctuations can still be observed inside the obstacle. In order to keep the model stable, a zero velocity condition is applied on all the nodes inside of the obstacle at each time-step. When dealing with submerged structures in the water, the vertical zero velocity condition is used at all Immersed Boundary nodes.

C. Turbulence modelling

In order to simulate more accurately the turbulence impact of a structure, focusing mainly on the wake, a two-eddy viscosity LES turbulence model was implemented by considering horizontal and vertical characteristic length-scales separately [11].

The two-eddy LES turbulence model shares similar ideas as the Smagorinsky model, but using different length-scales in the horizontal and vertical directions respectively. This approach is more suitable for highly anisotropic filtering cells rather than using a single characteristic length-scale. Two turbulence viscosities $\nu_{t,h}$ and $\nu_{t,v}$ are commonly used in geophysical fluid dynamics, with h and v representing the horizontal and the vertical components respectively. The diffusive term for the Navier-Stokes equations is calculated as:

$$D_i = \frac{\partial}{\partial x_1}\left(\nu_h \frac{\partial u_i}{\partial x_1}\right) + \frac{\partial}{\partial x_2}\left(\nu_v \frac{\partial u_i}{\partial x_2}\right) + \frac{\partial}{\partial x_3}\left(\nu_h \frac{\partial u_i}{\partial x_3}\right) \quad (8)$$

where $\nu_h = \nu + \nu_{t,h}$ and $\nu_v = \nu + \nu_{t,v}$, and ν is the water viscosity. Adopting the two-eddy LES model to reproduce the sub-grid stress through a Smagorinsky model gives:

$$\nu_{t,h} = (C_h L_h)^2 |S_h| \quad (9)$$

$$\nu_{t,v} = (C_v L_v)^2 |S_v| \quad (10)$$

where C_h and C_v are the coefficients of the model and L_h and L_v are 2 length-scales for the horizontal and vertical directions respectively. Here L_h and L_v are computed as:

$$L_h = \sqrt{\Delta_{x_1}^2 + \Delta_{x_2}^2} \quad (11)$$

$$L_v = \Delta_{x_3} \quad (12)$$

Δ_{x3} is obtained by calculating the vertical distance between two nodes. Because in the current code, the element volumes have been considered as the integral of test functions on the domain, L_h can be easily obtained by using an approximate value of $L_h = \sqrt{Volume/\Delta_{x3}}$

The strain rates tensor $|S_h|$ and $|S_v|$ are decomposed as:

$$|S_h| = \sqrt{2S_{11}^2 + 2S_{33}^2 + 2S_{13}^2} \quad (13)$$

$$|S_v| = \sqrt{2S_{12}^2 + 2S_{22}^2 + 2S_{23}^2} \quad (14)$$

where S_{ij} is calculated by the Einstein summation convention, reading as:

$$S_{ij} = \frac{1}{2}\left(\frac{\partial u_i}{\partial x_j} + \frac{\partial u_j}{\partial x_i}\right) \quad (15)$$

The coefficients of the model need calibration and this is still an open issue because of the lack of large range of available test cases. In this study, C_h and C_v are set to 0.005 and 0.25 respectively which is similar to the recommended value in [11].

III. CASE I: FLOW PAST A FULL CYLINDER

Firstly, a laboratory experiment (see Roulund [12]) is used to validate the implementation of the IB method. The numerical model is built to simulate the flow past a full cylinder in a flume.

A. Computational domain and mesh

Following Roulund's experiment [12], the simulation domain is set to be 50 m long by 4 m wide. The bed is assumed to be flat with a constant depth of 0.54 m. A cylinder with a diameter of 0.53 m (D) is placed at 13 m downstream the inlet as in figure 1.

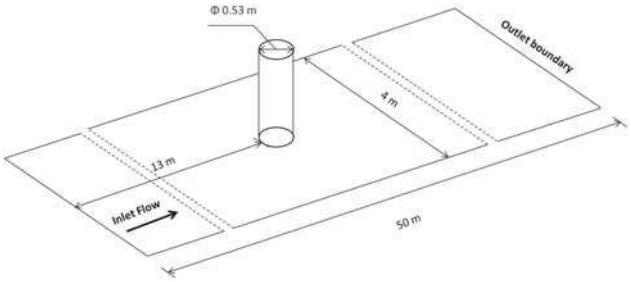

Fig. 1: Geometry of the computed domain

The area containing the cylinder and the wake part are refined. The mesh of the simulation domain contains 48,764 elements in 2-D and has 50 evenly distributed horizontal layers. As shown in figure 2, the hollow mesh is not used to represent the cylinder directly, however the boundary nodes of cylinder are marked as immersed boundary nodes which can be seen clearly (the boundary between blue mesh and red mesh is the immersed boundary).

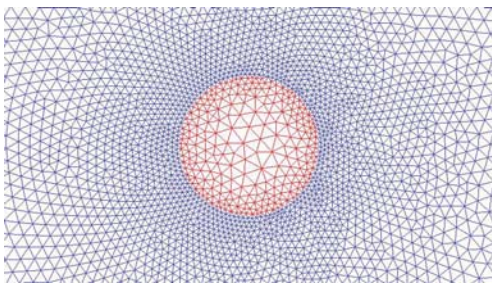

Fig. 2: Geometry of the computed domain with the immersed boundary

B. Model setup

Table I summrises the test conditions for the cylinder case. The smooth bed condtion from the experiment of [12] is used for the model testing.

In the table, Re is the Reynolds number based on the pile diameter,

$$Re = \frac{UD}{\nu} \quad (16)$$

Test	Flow past full cylinder
Bed	Rigid
Smooth bed/rough bed	Smooth
Water depth h (m)	0.54
Mean Flow velocity $U(ms^{-1})$	0.326
Pile diameter $D(m)$	0.53
Re Number	1.7×10^5
Fr Number	0.14

TABLE I: Test conditions for the numerical modelling

where U is the mean flow velocity and D is the diameter of the cylinder. Also in the table, Fr is the Froude number defined by

$$Fr = \frac{U}{\sqrt{gh}} \tag{17}$$

in which h is the water depth.

A time step of 0.01s is chosen to keep the maximum Courant below 0.8. The Courant number is defined as:

$$C = U\frac{\Delta t}{\Delta x} \tag{18}$$

where U is the depth-mean flow velocity and Δx is a given mesh size.

C. Results

The numerical model was run for 30 minutes and the last 100 seconds of the instantaneous results were collected for analysis and comparison.

The instantaneous horizontal flow distributions obtained from the numerical model are illustrated in figure 3. Three figures show the velocity profile at the surface, middle and bottom layer respectively. The oscillating flow due to the cylinder obstacle can be seen clearly in the surface and middle layers. All the figures show slow velocity regions in front of and behind the cylinder. A dramatic acceleration is also observed at each side of the cylinder. At the bottom layer, rather than the long oscillating wake, an accelerated velocity at the sides of the cylinder plays a more significant role in the flow structure.

In the further investigation of the horizontal flow distribution, the averaged horizontal velocity magnitude is calculated by averaging 100 instantaneous data. The result is represented in figure 4

As shown in this figure, the velocities inside the cylinder are kept to zero. The streamlines indicate the route of the flow past the cylinder. Under the effect of the immersed boundary forces which are applied on the cylinder boundary nodes, the upstream flow splits in front of the cylinder and then accelerates at each side. After stream detaching the cylinder, a pair of symmetric vortices is clearly found behind the cylinder.

The unsteady flow state is shown in figure 5 which covers a full vortex shedding period. From these figures, the unsteady behaviour of the wake is evident. The flow route is represented by both vectors and streamlines. The shedding of the vortices from the two sides of cylinder is clearly present.

Quantitatively, the numerical results obtained using the immersed boundary method are benchmarked with Roulund's

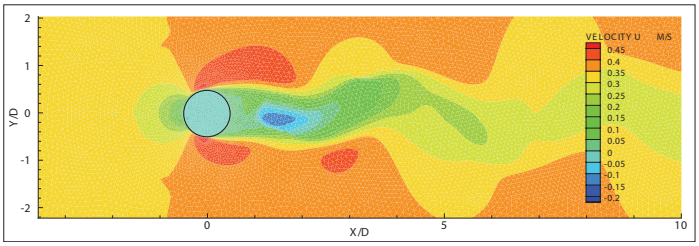

a: Surface

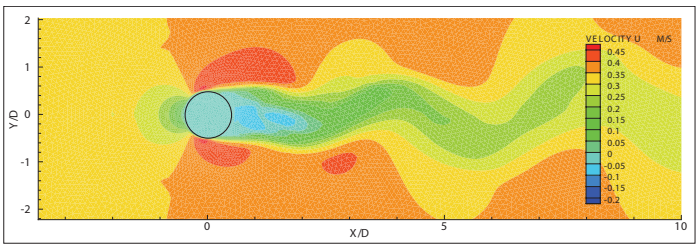

b: Z=-0.27m

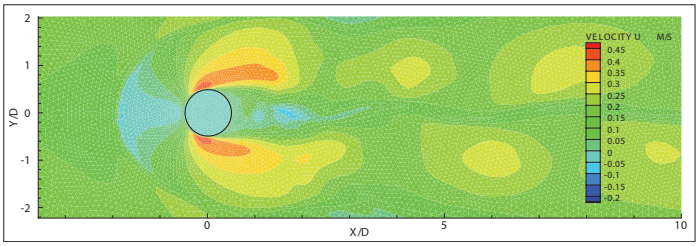

c: Bottom

Fig. 3: Horizontal velocity distribution at different layers

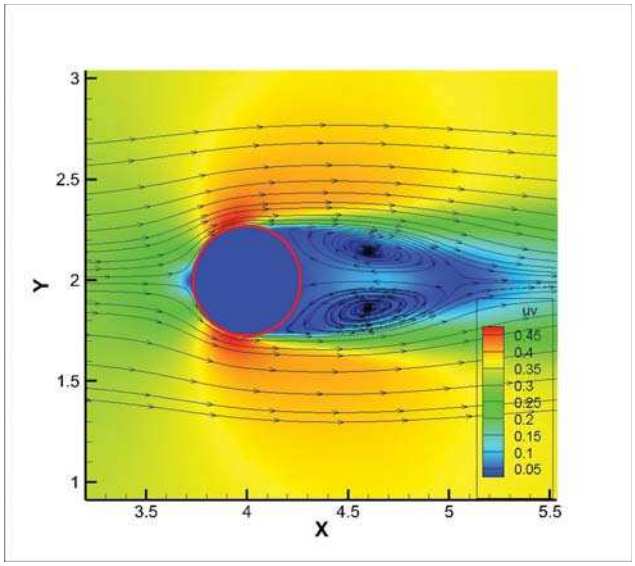

Fig. 4: Averaged horizontal velocity magnitude and streamlines at Z = -0.27 m

experiment [12]. Comparison results are shown in figures 6, 7:

The averaged horizontal and vertical velocities at layer Z=-0.34m are presented in the aformentioned figures. Experimen-

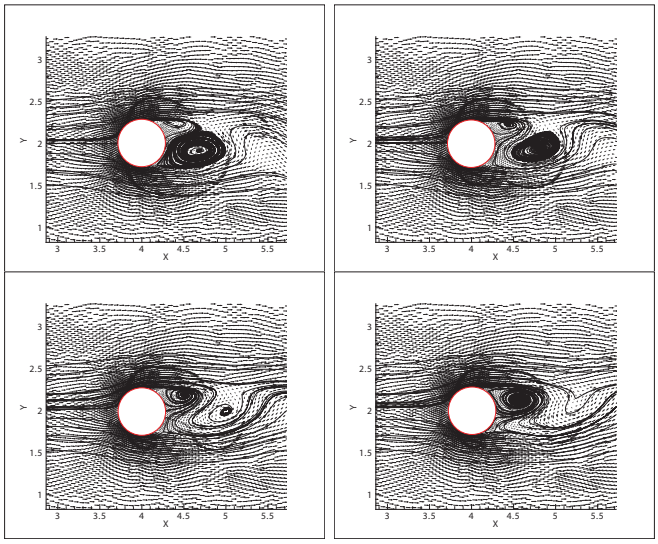

Fig. 5: Horizontal velocity vectors and streamlines for the unsteady flow simulation during one period of vortex shedding. Horizontal cross-section at z = -0.27 m

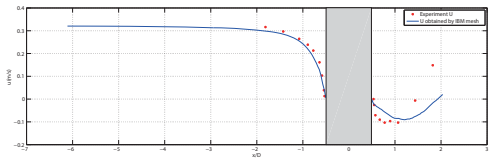

Fig. 6: Mean horizontal velocity at Z = -0.34m. Smooth rigid bed

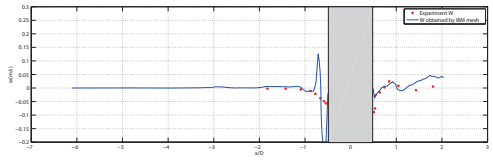

Fig. 7: Mean vertical velocity at Z = -0.34m. Smooth rigid bed

tal data and numerical model results are illustrated by red dots and blue curves respectively. The horizontal velocity distribution shows very good agreement between numerical model and experiment in front of the cylinder. The upstream flow reduces from about 0.32 ms^{-1} to approximately 0 ms^{-1} in front of the cylinder wall. Behind the cylinder, both experimental data and numerical model show a recovery flow, however the distance for recovery is slightly over-predicted by the numerical model. The vertical velocities obtained using the numerical model agree with the experiment measurement both in front of and behind the cylinder except for a big spike found in front of the cylinder. This spike is due to the water surface elevation raising in front of cylinder.

A comparison between the numerical results obtained by the immersed boundary condition and hollow mesh is presented in figure 8.The mean horizontal velocity obtained from the immersed boundary test and hollow mesh test are represented by a red line and a black line respectively. As shown in this figure, both IB test and hollow mesh test show the same result in front of the cylinder, although a small difference is found in the wake region. Between 0.5 D to about 18 D, the flow obtained by the immersed boundary test exhibits a faster recovery, however from 18D downstream on, the velocity predicted by the hollow mesh test is higher than the one of the IB test.

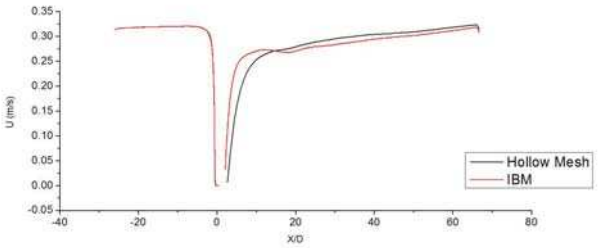

Fig. 8: Mean horizontal velocity along the center line at the layer of Z = -0.27

IV. CASE II: FLOW PAST A SUBMERGED CYLINDER (WITH FINITE HEIGHT)

In the second test case, the immersed boundary method is used to simulate the flow around a finite height cylinder. Following Palau-Salvador's experiment [8], cylinders with h=0.2 m height and two different diameters (0.040 m and 0.080 m respectively) are computed using the immersed boundary method.

A. Computational domain and mesh

Palau-Salvador's experiment [8] was performed in a tank with a constant water level of 3 meter and this water depth was also used in the numerical models. As shown in figure 9, the width and length of the numerical model was set to 4 h (0.8 m) and 13 h (2.6 m) respectively. The cylinder was placed at 3 h (0.6 m) downstream the inlet.

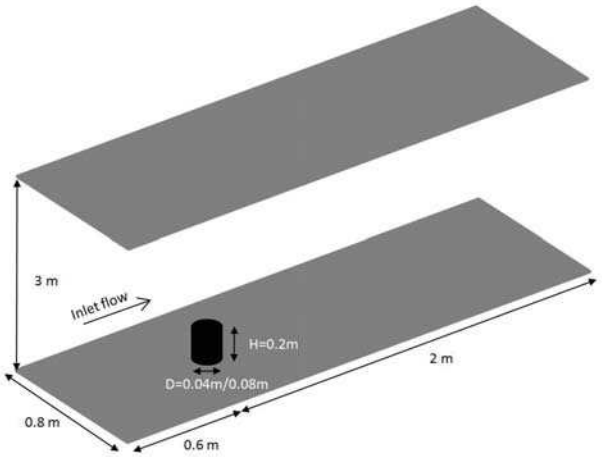

Fig. 9: Computational domain of the flow passing a finite height cylinder

Test	1	2
Bed condition	Smooth Rigid	Smooth Rigid
Water depth h (m)	3	3
Mean Flow velocity $U(ms^{-1})$	0.54	0.54
Pile diameter $D(m)$	0.04	0.08
Re Number	2.2×10^4	4.4×10^4

TABLE II: Test conditions for the numerical modelling

In total, the mesh of the numerical model contains 37,372 elements in 2-D and 50 layers in the vertical direction. Similar to the mesh used in case I, there are 100 nodes located on the cylinder boundaries. The mesh around the cylinder is refined. In the vertical direction, as shown in figure 10, the height of the first 30 layers from the bottom are fixed, thus the cylinder can maintain a constant height during the simulation.

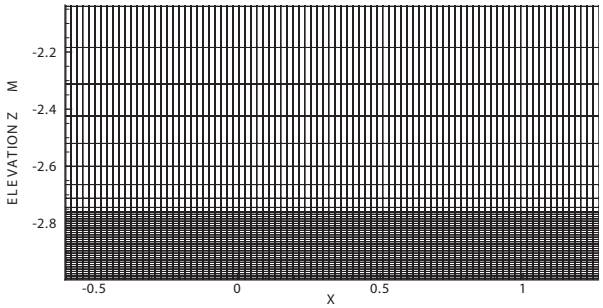

Fig. 10: Snapshot of the vertical mesh used in the numerical model of the flow passing a finite height cylinder

B. Model setup

The key parameters of the numerical model are summarised in table II.

A constant flow velocity of 0.54 ms^{-1} is set at the inlet boundary. The Reynolds number based on the pile diameter is 2.2×10^4 and 4.4×10^4 for both cylinders respectively. The time step equal to 0.001 s is chosen to keep the maximum Courant number below 0.6.

C. Results

The horizontal velocity distributions at the layer of $x_3 = h/2$ are illustrated in figure 11 and figure 12. The numerical results obtained from the 0.04 m diameter cylinder case and 0.08 m diameter cylinder case show similar pattern that the flow reduces speed in front of the cylinder and then recovers behind it. Streamlines in figures indicate that the upstream flow is separated by the structure and then pushed to the side of cylinder. After the flow detaches from the cylinder wall, small vortices are generated in the wake area. Comparing to the instantaneous pictures of Palau-Salvador's experiment, the width of the wake tail in the numerical results is slightly over-predicted.

The horizontal velocity distributions in the vertical cross-section along the centre line is shown in figure 13 . The numerical results show that the flow accelerates at the top of the cylinder and a deceleration is observed in the wake part. The vertical vortex behind the cylinder is seen clearly both in

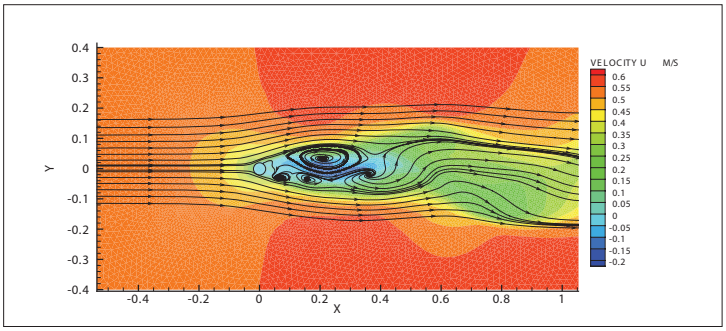

a: numerical model

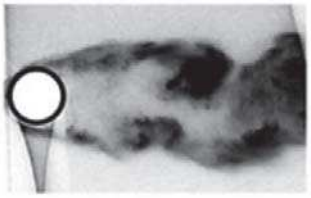

b: Experiment

Fig. 11: Horizontal velocity distribution at layer of $h/2$ of the cylinder d= 0.04m. (a)Numerical results. (b)Instantaneous pictures of Palau-Salvador's experiment [8]

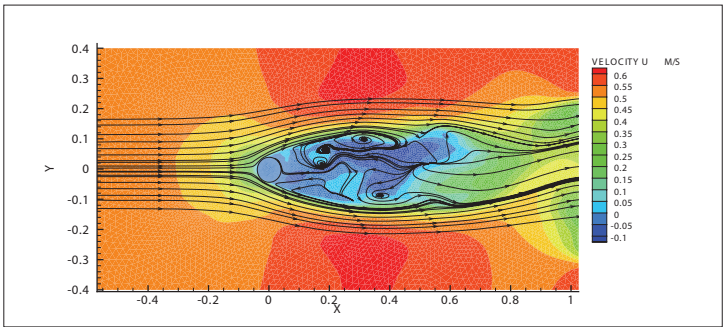

a: numerical model

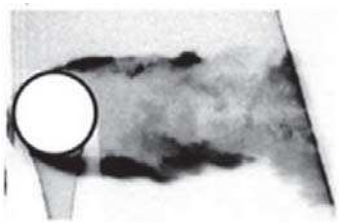

b: Experiment

Fig. 12: Horizontal velocity distribution at layer of $h/2$ of the cylinder d= 0.08m. (a)Numerical results. (b)Instantaneous pictures of Palau-Salvador's experiment [8]

the 0.04 m diameter cylinder case and 0.08 m diameter cylinder case. However in the figure of the 0.04m diameter cylinder result, the horizontal velocity colour bands indicate that there is a strong velocity fluctuation in front of the cylinder. The

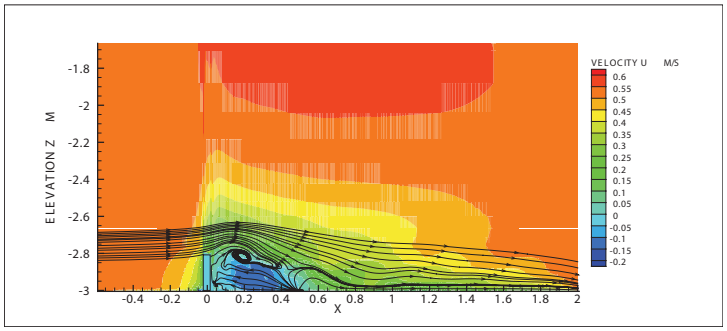

a: D=0.04m

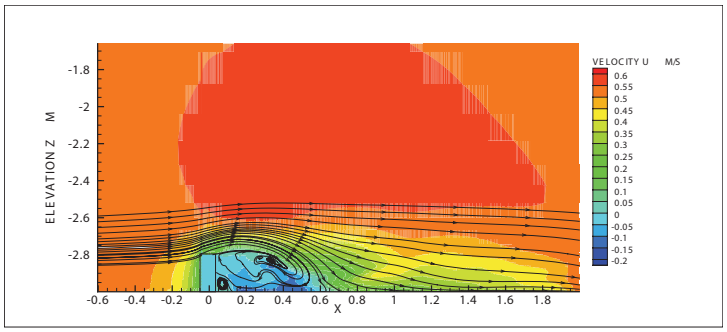

b: D=0.08m

Fig. 13: Horizontal velocity distribution along the center line in the vertical cross-section view.

reason of this impact is not clearly understood at the moment. Due to the same configuration used in both cylinder cases, this velocity fluctuation may come from the quality of the mesh used in the 0.04 m diameter cylinder case.

Figure 14 shows the Q-criterion to visualise the vortex structure obtained by both simulations. Q is the second scalar invariant of the velocity derivative tensor and has been widely used for vortex visualisation. The spike shown in Fig. 14 (a) proves the founding in Figure 13(a) that there is a strong velocity fluctuation in front of the cylinder. Exept this unknown phenomenon, the vortex structures including horseshoe vortex at the bottom in front of the cylinder, tip vortex above the cylinder and trailling vortex behind the cylinder are represented clearly in the simulations. Because the larger cylinder diameter case shows an increased Reynolds number based on the diameter, more vortices can be found in the result of the 0.08 m diameter cylinder case.

V. Conclusions - Perspectives

In this study, the Immersed Boundary method is implemented and applied to TELEMAC3D. Two laboratory scale cases including the flow passing a full cylinder and the flow passing a finite-height cylinder are simulated. In the full cylinder case, both instantaneous velocity profiles and mean velocity profiles are fairly well captured by the numerical model. In the finite-height cylinder test case, the general flow feature can be captured by the numerical model. The vortex structures can be seen clearly in the results.

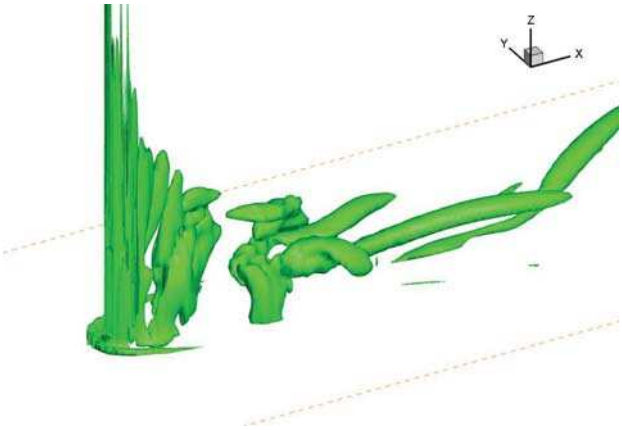

a: D=0.04m

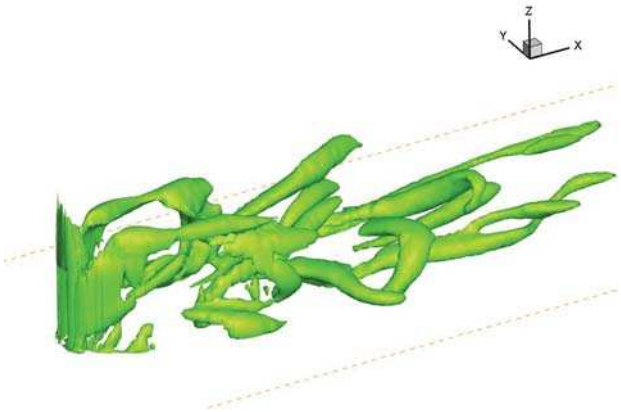

b: D=0.08m

Fig. 14: Horizontal velocity distribution along the center line in the vertical cross-section view

Generally, it is possible to couple the Immersed boundary method with TELEMAC3D to represent structures in the simulation. When dealing with an obstacle going from the bottom though the surface of the water, the immersed boundary method offers good accuracy in the prediction of surrounding flow structures. For the submerged obstacles, they can be simulated by TELEMAC3D by implementing immersed boundary method. Although the accuracy is limited currently, the result of the qualitative analysis can be still obtained from the numerical model.

In future works, the immersed boundary method used for submerged structure simulation will be further investigated. Not only qualitative analysis but also quantitative analysis will be done by benchmarking numerical results with laboratory measurement data.

Acknowledgment

The current study is supported by EPSRC and EDF Energy through an iCASE studentship. The technical supports from Computing Services of the University of Liverpool and from the Hartree Centre are also greatly appreciated.

VI. References

References

[1] A. S. Almgren, J. B. Bell, P. Colella, and T. Marthaler, "A cartesian grid projection method for the incompressible euler equations in complex geometries," *SIAM Journal on Scientific Computing*, vol. 18, no. 5, pp. 1289–1309, 1997.

[2] A. J. Chorin, "Numerical solution of the navier-stokes equations," *Mathematics of computation*, vol. 22, no. 104, pp. 745–762, 1968.

[3] D. K. Clarke, H. Hassan, and M. Salas, "Euler calculations for multi-element airfoils using cartesian grids," *AIAA journal*, vol. 24, no. 3, pp. 353–358, 1986.

[4] E. Fadlun, R. Verzicco, P. Orlandi, and J. Mohd-Yusof, "Combined immersed-boundary finite-difference methods for three-dimensional complex flow simulations," *Journal of computational physics*, vol. 161, no. 1, pp. 35–60, 2000.

[5] X. Hu, B. Khoo, N. A. Adams, and F. Huang, "A conservative interface method for compressible flows," *Journal of Computational Physics*, vol. 219, no. 2, pp. 553–578, 2006.

[6] J. Kim, D. Kim, and H. Choi, "An immersed-boundary finite-volume method for simulations of flow in complex geometries," *Journal of Computational Physics*, vol. 171, no. 1, pp. 132–150, 2001.

[7] J. Mohd-Yusof, "Combined immersed-boundary/b-spline methods for simulations of ow in complex geometries," *Annual Research Briefs. NASA Ames Research Center= Stanford University Center of Turbulence Research: Stanford*, pp. 317–327, 1997.

[8] G. Palau-Salvador, T. Stoesser, J. Fröhlich, M. Kappler, and W. Rodi, "Large eddy simulations and experiments of flow around finite-height cylinders," *Flow, turbulence and combustion*, vol. 84, no. 2, pp. 239–275, 2010.

[9] C. S. Peskin, "Flow patterns around heart valves: a numerical method," *Journal of computational physics*, vol. 10, no. 2, pp. 252–271, 1972.

[10] S. Popinet, "Gerris: a tree-based adaptive solver for the incompressible euler equations in complex geometries," *Journal of Computational Physics*, vol. 190, no. 2, pp. 572–600, 2003.

[11] F. Roman, G. Stipcich, V. Armenio, R. Inghilesi, and S. Corsini, "Large eddy simulation of mixing in coastal areas," *International Journal of Heat and Fluid Flow*, vol. 31, no. 3, pp. 327–341, 2010.

[12] A. Roulund, B. M. Sumer, J. Fredsøe, and J. Michelsen, "Numerical and experimental investigation of flow and scour around a circular pile," *Journal of Fluid Mechanics*, vol. 534, pp. 351–401, 2005.

[13] H. Udaykumar, R. Mittal, and W. Shyy, "Computation of solid–liquid phase fronts in the sharp interface limit on fixed grids," *Journal of computational physics*, vol. 153, no. 2, pp. 535–574, 1999.

[14] H. Udaykumar, W. Shyy, and M. Rao, "Elafint: a mixed eulerian–lagrangian method for fluid flows with complex and moving boundaries," *International journal for numerical methods in fluids*, vol. 22, no. 8, pp. 691–712, 1996.

TELEMAC model archive: Integrating open–source tools for the management and visualisation of model data

S. L. Mouradian*, A. Avdis*, M. D. Piggott*, C. T. Jacobs†, C. Villaret‡, D. R. de Mijolla§ and J. Lietava*
*Department of Earth Science and Engineering
Imperial College London, South Kensington, UK SW7 2BP
Email: simon.mouradian06@imperial.ac.uk
† Faculty of Engineering and the Environment
University of Southampton
‡ EDF-LNHE, France
§ Department of Physics
Imperial College London

***Abstract*—**

Reliable and robust archival of model set-ups and outputs, including input data is a major challenge. Failure to do this in a robust and sustainable manner could lead to increased set–up costs for new studies, duplication and possible inconsistencies in model outputs. In addition, comprehensive archival of input and output data is an important step in ensuring reproducibility of results. In order to address these challenges, the utilities presented in this paper facilitate the automatic archival of model data, and publication in a citable repositories.

The software is designed to offer data management, visualisation and database–entry functions for modelling with the TELEMAC suite. A purpose-built SALOME plugin is also presented, aimed at automatic file archival and publication. Visualisation is also provided through dedicated lightweight utilities using the crossplatform Google Earth desktop application.

The practice of transparent publication of model set–up and results is increasigly dictated by national legislation and will also lead to the collection of large databases, enabling the analysis of simulation set–ups as well as output. The ability to filter and analyse simulation set–ups can lead to the development of best–practice guidelines, as well as the opportunity to identify areas for the improvement of future simulations. Visualising all simulation set–ups together provides the big picture of research activities, and can offer the ability to identify trends in (perceived) optimal option choices, as well as identify regions where future opportunities might arise. Furthermore, as simulation set–ups from various parties can be collected together and visualised in a single framework, the ability to collaborate and spread knowledge internally within, and between, organisations is made possible through the presented tools.

I. Introduction

Over the past 30 years, numerical coastal modelling capabilities have increased substantially, reaching a point where they are an integral part of the planning phase for many coastal engineering projects. Ranging from the prediction of coastal flooding to sediment transport and environmental/ecological impact assessment studies, with many applications in between, the use of numerical coastal ocean modelling has become of paramount importance [3]. In such cases, it is generally the responsibility of the modeller (often in an ad hoc manner) to ensure archival of the model and its results. The (collectively) terabytes of data produced annually are often discarded, apart from a few summarising figures in reports and/or published articles, that can often not be used for recomputation and/or reanalysis at a later date. For many applications, archival of model results and data provenance records must be maintained for many years after the modelling phase of the project, as legislated by government bodies [2].

Within academic institutions, researchers were (and still are) traditionally credited based upon publications and citation rates, with minimal or no credit given for ensuring results are archived, reproducible and easily retrieved. Recentlty, rules published by the Research Council UK (RCUK) place particular emphasis on public accountability and open access [15], and on making all publically funded research data, samples and models accessible. It is therefore increasingly more important for institutions to adopt a reserach data management protocol.

The archival solution proposed here, by leveraging the PyRDM library [9], aims to make it easy for modellers to archive their work, as well as the option for providing each simulation setup and its results with a Digital Object Identifier (DOI). The DOI allows each simulation to be cited in reports and/or research papers, which can result in researchers being credited based on the amount of citations their simulations receive.

Large engineering companies often have groups spread geographically, or have several (academic or industrial) sub–contractors, all of whom produce numerical model setups and output data. This can result in inconsistent model setups and thus an inability to perform meaningful model comparisons, or can result in efforts being duplicated across groups. A centralised database that allows for a quick overview of current and previous numerical modelling activies can be a very useful tool used to streamline and optimise the process of setting up new simulations and comparing / benchmarking against similar studies, either by other research groups/teams, possibly based in different geographic locations.

When setting out to develop an archival system, we considered the following requirements: a) The entirety of files should be archived, to allow for the output data to be recomputed and reproduced; b) It must allow the results and setup to be readily retrieved; c) It must be very easy to use, with minimal user steps required, and fit within the workflow of the modeller. This is essential if the archival system is to be adopted and continually used. This is why we suggest our coastal model archiving tool be integrated in the SALOME modelling platform, in the form of a plugin (see section II-D for further details).

Archival of all of an institution's or community's coastal modelling activities in a cohesive, structured database also opens up the possibility for further analysis. In particular, it allows for a macro–scale analysis of these simulations, to obtain insight in the principles of setting up a model. For example, one can ask questions relating to how many sediment models use the two–dimensional shallow water formulation as their hydrodynamic solver, or which tidal simulations employ wind–forcing at the surface, or regularly used numerical or turbulence modelling choices.

Further insight can be obtained from an institution's research or consultancy activity by visualising coastal model domains on a map (for example, as in [4]), laid over satellite imagery. This allows for an analysis of the spatial distribution of coastal modelling activities. An organisation is able to, amongst other things, identify geographic hotspots of numerical modelling activity that could be consolidated, or identify geographic areas that may form new investment opportunities.

Motivated by the above, we describe an archival solution for coastal models that performs three distinct, yet integrated functions:

1) Packages a simulation setup and archives it on a file server hosted by a data repository service or institution. If the archived package is made public on an online repository, a DOI is generated for citation and easy retrieval.
2) Parses the simulation setup and populates a database with important parameters (and metadata, such as owner and time) that can be searched and analysed at a later date.
3) Converts the domain extent and result to a file format suitable for viewing in Geographical Information Systems (GIS) clients, such as Google Earth.

The resulting archival tool is a stand–alone, cross–platform desktop application with a graphical user interface, which we name AVoCadO (Archiving and Visualisation of Coastal Ocean models).

II. Methodology

The archival framework has been built upon the PyRDM library. PyRDM is a research data management library which features the ability to curate and publish data (and software) objects using various repository services, for example Figshare and Zenodo [9], [10]. The library implements the relevant API for each service, allowing data publication to be accomplished using a single codebase. These services, in turn, return a citable DOI that can be used for citing the relevant output.

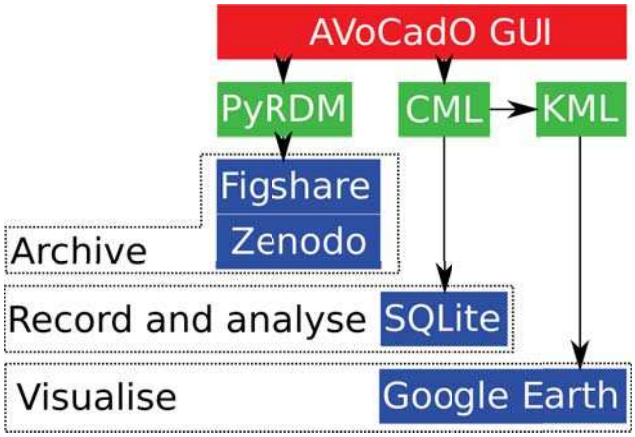

Fig. 1: AVoCadO toolchain. The user is exposed only to the graphical user interface. AVoCadO interfaces the PyRDM library [9] to archive software and data, and the CML library to generate SQL database entries and convert the mesh and results to the KML file format, suitable for visualisation in Google Earth.

Furthermore, AVoCadO is built on the CML library, which was developed specifically for this project, to handle the parsing of configuration files for adding entries to an SQL database, as well as generating GIS objects, to be visualised in software such as Google Earth. An overview of the toolchain is shown in Figure 1.

A. Archival

A large amount of automation is offered by PyRDM. We incorporate PyRDM's curation capabilities into the archiving workflow, which in turn allows AVoCadO to publish data to online, persistent repositories in a straight–forward, 'click of a button' manner. Such benefits of automated publishing tools have been demonstrated by e.g. [9], [10], and [8]. As a result of such advances in digital curation technology, this 'opening up' of data objects promotes more open research workflows and reproducibility best practices, and can also help ensure that research funding policies or government legislations are properly complied with [1], [11], [12], [14], [16].

We note that Figshare and Zenodo do not take ownership of any data published on their servers. The user uploading data is given the option of several licenses under which to publish their data. Figshare and Zenodo are data repositories that ensure the persistence and longevity of published output, and provide users with the ability to search for and obtain the published data. They also collect analytics for the user, such as views, downloads and citation rates.

A second archival option is provided within AVoCadO, whereby the data is archived on a private server. An encrypted connection is established using the secure shell protocol, and data is transferred from the modeller's workstation to an institution's file server. Using this archival method, a DOI is not generated, and thus the database holds a path to the hostname and location of the archived data on the file server. Whether a modeller archives simulation data and/or software to a public repository or a private server, the data is sent as an

archived package. A unique filename is obtained by naming each archived package with the *Simulation Name* provided by the user, appended by the MD5 hash.

B. Database

For the purposes of rapid prototyping the AVoCadO application, an SQLite database [7] is used, rather than a hosted, process based database server. We note the implementation is similar and only minor further development would be necessary to implement a mySQL or PostgreSQL database. These SQL servers would offer access control with user authentication, not currently offered by the embedded SQLite database.

A database entry is generated for each model archived. The database holds information that relates to retrieval of the archived input/output data (either a DOI or the hostname and location of the private file server). The database also holds information that is parsed from the model configuration file. For example, a database entry for the TELEMAC model would include information on whether a simulation used the finite element or finite volume discretisation method, or whether tidal flats were enabled.

A separate SQL table is used for each coastal modelling solver implemented in AVoCadO (currently only TELEMAC [6] (both 2D and 3D) and Fluidity [13]). Each table contains entries representing a single, archived model. For TELEMAC, the configuration (*.cas*) file is parsed using the parser utility that is provided in the TELEMAC source code. AVoCadO therefore has all the information that can be extracted from the configuration file at its disposal, and can record it in the database. A drawback of recording all the information includes inconsistencies between different versions of TELEMAC. A further significant note regarding the database entry, is that differences present in supplementary Fortran subroutines, or modifications made to the software source, are not recorded in the database (although the supplementary files and software source can be archived, if the modeller chooses to do so).

C. Visualisation

Visualisation is also provided by the CML library, developed as a part of AVoCadO. The CML library takes as input the directory in which the simulation resides and performs the following functions:

- *Establish numerical solver used*:
  Given the directory of model setup and results, CML attempts to determine whether the model uses TELEMAC or Fluidity as the numerical solver. This is established by checking the types of files within the directory. For example, the presence of a *.cas* file would suggest a TELEMAC model, whilst the presence of an *.flml* file the use of Fluidity.
- *Parse directory for files*:
  The directory is parsed to determine the configuration file, mesh file, results files and any supplementary files such as Fortran files, wind or tidal forcing. The modeller archiving the simulation can choose to override the automatically detected files, to only publish specific files, or replace certain files with files from a different directory. This AVoCadO feature of auto–selection of files ensures that minimal user input is required before a model can be archived. An example of the auto–populated interface is shown in Figure 2, where fields are populated with the TELEMAC example of the Monai Valley test case.
- *Extract mesh triagulation and results*:
  The input mesh is parsed to determine the boundary of the domain, as well as the triangulation. The points along the domain boundary are used to define a new line path in the KML format used by Google Earth, and the triangulation is used to define a network of lines, in the KML linestring format. The results file of the final timestep is parsed and used to produce an image in the *.png* file format. The domain boundary is used to *mask* the image, ensuring that the visualised result is only produced within the domain boundaries. Figure 3 shows example boundaries visualised in Google Earth.

For performance reasons, the initial visualisation only includes the outlines of archived models, as well as a placemark labelled with the name. This provides users with an overview of all archived simulations. A user is further able to enable/disable the visualisation of the mesh and/or the snapshot images generated from the results files. We note, however, that the memory requirement of Google Earth increases substantially when the mesh for multiple archived simulations is viewed at the same time. Figure 4 shows an example of the functionality of enabling/disabling field images, as well as how AVoCadO takes advantage of Google Earth's 'regioning' features. Regioning is the property whereby certain image overlays are only loaded and shown on screen when at low altitudes (zoomed in), thus avoiding densely populating the screen and limiting the memory required by Google Earth.

An important step in converting the mesh and results files to formats suitable for visualising in Google Earth, is applying the appropriate projection. Objects visualised in Google Earth are required to be in the World Geodetic System defined in 1984 (WGS 84). The transformation is realised by the use of the Python bindings of the GDAL library [5]. GDAL uses the spatial reference system identifiers as defined by the European Petroleum Survey Group (EPSG), and thus the EPSG code of the input coordinate reference system must be provided by the modeller. This input is labelled 'Coord system' and is given in the bottom right hand corner of the GUI, as seen in Figure 2. Generating a visualisation for Google Earth is only reasonable for numerical models on realistic geographical domain. Models that are performed on idealised domains in an arbitrary Cartesian coordinate system can not be projected for visualisation in Google Earth. An entry of zero (0) in this field will result in AVoCadO not producing the subsequent GIS objects, and will only use PyRDM for archiving.

D. SALOME plugin

The standalone application is currently able to parse input files from TELEMAC and Fluidity simulations, with a view to support more models in the future. The generality of AVoCadO as an archiving framework for coastal ocean models necessitates the use of a separate, stand–alone application. This, in

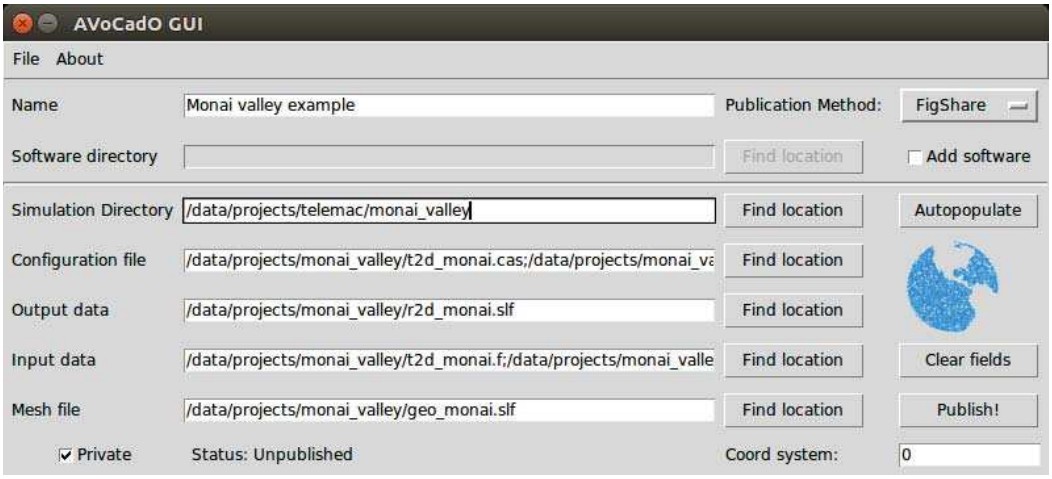

Fig. 2: The AVoCadO GUI after auto–populating with the TELEMAC example directory of the Monai Valley.

Fig. 3: Domain outlines and labeled placemarks for models of the Torness and Severn Estuary, two models archived using AVoCadO, visualised in Google Earth. Users have the ability to select the placemark, afterwhich more summary information about the model will appear on the screen. By default, only boundary lines are shown to ensure responsiveness, even with multiple archived simulations loaded in memory.

itself, could be a barrier to its adoption. Here, a TELEMAC specific archiving solution is also explored through integration within the SALOME framework. This solution is more integrated in the workflow of setting up a TELEMAC simulation and thus is more likely to be of use to the wider TELEMAC community in the longer term. To achieve integration with SALOME, the AVoCadO front–end is replaced by a front–end written in PyQT4 (the same graphical interface library used by SALOME), while using the same underlying Python modules as AVoCadO. This plugin allows for archival of models set up within the SALOME framework. The toolchain of the archival framework integrated within SALOME is illustrated in Figure 5.

In contrast to AVoCadO, the plugin does not require the modeller to provide the software with the directory in which the model setup resides. This is because the SALOME plugin is able to parse the SALOME configuration that specifies the files required for TELEMAC to run.

III. Discussion

AVoCadO is an archiving framework that brings the power of PyRDM [9] to the coastal modelling community. It lowers the complexity and time needed for archiving coastal model setups and their results, thus removing impediments for modellers to do so and encourages a more reproducible and open scientific workflow. Archival of model setups and results on a persistent, searchable, citable repository hosting service such as Figshare, that enables easy retrieval of data, is ‘added value’ to multiple parties. It is added value to the modellers themselves, as well as the modellers’ colleagues, who can look back upon previous simulations. This has the potential of lowering the time required to setup a new model, allows for improvements upon previous setups while also maintaining a historical record of configurations used for previous models. It can also provide the particular model with a citable DOI, which can be used to cite the modellers’ setup and results in reports, articles and presentations. This can potentially increase the exposure of the modeller within their respective community, and enable sharing of models, results and ideas. Such an archive also encourages collaboration across an institution’s departments or groups, often spanning multiple geographic locations, by ensuring a centralised database of archived models is available for everyone to access and review. It ensures that time and money is not wasted by setting up duplicate models and allowing modellers to become familiarised with modelling methodologies employed by colleagues.

A further benefit, realised by archiving the complete setup, is that it enables a more thorough comparison between different models. Very often, unfair comparisons are made between

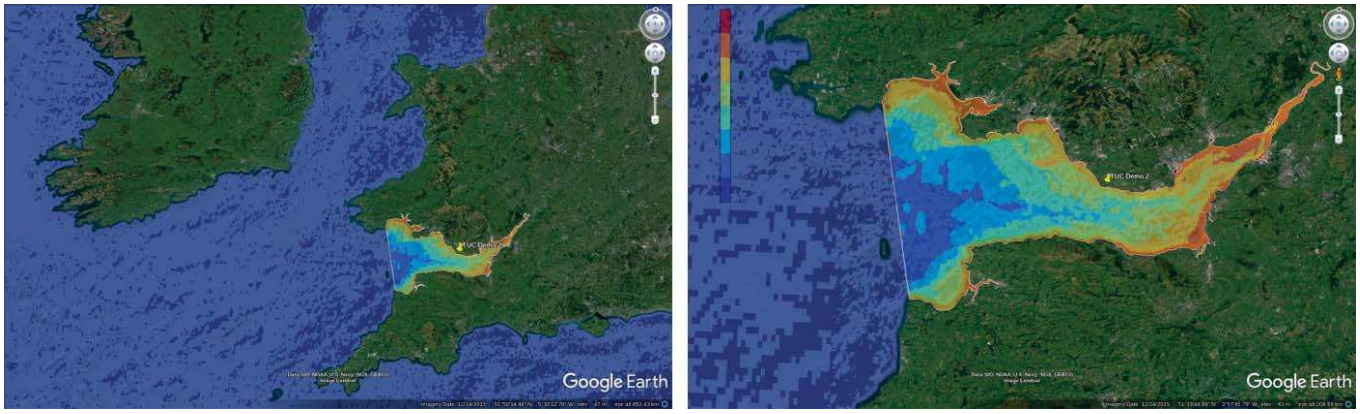

Fig. 4: Google Earth visualisation of a model of the Severn Estuary, as archived by AVoCadO. In these snapshots, the 'BOTTOM' field, depicting bathymetry, has been enabled. A *.png* image of bathymetry was generated and geographically placed by AVoCadO. The masking ensures that the bathymetry is only defined within the outline of the domain. The depiction on the right is zoomed closer to the model, at a level where a colourmap appears. KML files generated with AVoCadO take advantage of Google Earth's regioning, to ensure responsiveness even when multiple models are being visualised.

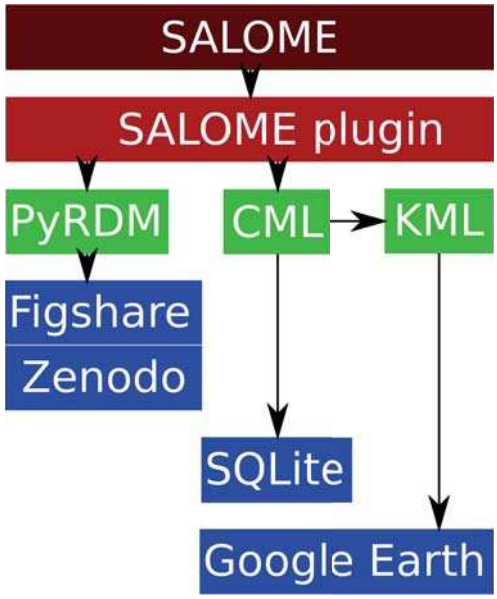

Fig. 5: SALOME plugin toolchain. The graphical user interface is now embedded within SALOME, and makes use of the same underlying Python libraries that AVoCadO does, providing the same capabilities to SALOME users.

models that employ different parameters, for example different forcing, or undocumented drag coefficients, or mesh resolution. Having access to the complete setup of previous studies one is comparing to allows for like–for–like comparisons.

A retrievable archive of previous modelling results, that allow recomputation and reanalysis, along with associated provenance (numerical model 'owner' and origin) is often required of an institution, either to comply with legislation, or the conditions set by a funding body. An archiving framework such as proposed in this paper can help institutions comply with such requirements.

The generation of a single database that contains entries and information on multiple simulation models makes obtaining insight into general modelling methodologies possible. Once a large number of simulations are recorded, possibly from various groups and/or using different underlying solvers, a statistical analysis of the database could lead to identification of common practices within the modelling community. These could result in guidelines of best practice, either automatically generated by mining the database and statistically identifying model setups, or with the meticulous direction of an expert.

The visualisation method described herein, provides an overview of all of an institution's coastal modelling activities. With regards to each particular model, the visualisation is coarse, simplified and often incomplete. This is because AVoCadO, in addition to an archiving tool, seeks to encourage collaboration between departments or groups within an institution, and the sharing of data, models and ideas. It does not seek to replace traditional data visualisation tools that are more powerful or better suited for producing animations from a model and have tools for analysis of the results.

The framework described offers the possibility of archiving models and software either publically on Figshare, or privately on a self–hosted file server. A further possibility is the use of the paid–for service 'Figshare for Institutions'. This provides institutions with an installation of Figshare, either on distributed cloud services such as Amazon Web Services, or on local institutional storage. This solution would offer institutions the benefits of Figshare, such as accurate metrics on shares, downloads, views and citations, but with the added benefit of being able to control where the data is stored and who has access to it. This is often necessary in cases where the data is commercially sensitive.

AVoCadO, as well as the described SALOME plugin, are free software released under the GNU GPL license. They are hosted on bitbucket.org, available to download, modify and redistribute, for both academic and commercial purposes. Installation instructions, along with a list of software requirements, as well as usage instructions, are provided in the manual

available with the source code.

IV. Conclusion

Data curation is often perceived to be an error–prone and time–consuming task and is typically treated as an afterthought leading to inconsistencies in the way data is stored, or even worse incomplete records. Herein we have presented AVoCadO, an archival framework for coastal ocean models, which encourages consistent data archival, aimed to form part of the model set–up and results visualisation processes. Consistency is achieved through automation, for example an automatic identification of the input and output data within SALOME, but also the integration of RDM utilities [9]. In addition, AVoCadO is built around a centralised database that holds information specific to each simulation model. As the database grows, it can be used for macro–scale analysis of various coastal modelling practices and be used as a valuable guide of best–practices. For models in a geographic domain, AVoCadO also offers the capability to illustrate the simulation overlaid on a map. More specifically for TELEMAC users, a similar archival strategy is presented that is embedded within SALOME as a plugin. At the expense of a single solution for multiple numerical solvers, the SALOME plugin offers TELEMAC users a way to archive their simulations with just a few clicks of a button.

Acknowledgment

Avdis and Mouradian would like to acknowledge the support of EPSRC Impact Acceleration Account EP/K503733/1, de Mijolla and Lietava the funding from Summer Research Projects from Imperial College London. The authors would also like to acknowledge the help of Z.Zachariadis for IT support during the project.

References

[1] A. A. Alsheikh-Ali, W. Qureshi, M. H. Al-Mallah, and J. P. A. Ioannidis, "Public Availability of Published Research Data in High-Impact Journals," *PLoS ONE*, vol. 6, no. 9, p. e24357, 2011.

[2] A. Avdis *et al.*, "Efficient unstructured mesh generation for marine renewable energy applications," , Manuscript in preparation.

[3] A. Avdis, C. T. Jacobs, S. L. Mouradian, J. Hill, and M. D. Piggott, "Meshing ocean domains for coastal engineering applications," in *VII European Congress on Computational Methods in Applied Sciences and Engineering*, 2016. [Online]. Available: https://www.eccomas2016.org/proceedings/pdf/7712.pdf

[4] G.-T. Chiang, T. O. White, M. T. Dove, C. I. Bovolo, and J. Ewen, "Geo-visualization fortran library," *Computers and Geosciences*, vol. 37, no. 1, pp. 65 – 74, 2011, virtual Globes in Science. [Online]. Available: http://www.sciencedirect.com/science/article/pii/S0098300410002177

[5] GDAL Development Team, *GDAL – Geospatial Data Abstraction Library, Version 2.1.0*, Open Source Geospatial Foundation, 2016. [Online]. Available: http://www.gdal.org

[6] J.-M. Hervouet, *Hydrodynamics of Free Surface Flows*. John Wiley and Sons, Ltd, 2007. [Online]. Available: http://dx.doi.org/10.1002/9780470319628

[7] R. Hipp *et al.*, "SQLite Development Team: SQLite," https://www.sqlite.org/download.html/, 2015.

[8] C. T. Jacobs and A. Avdis, "Git-RDM: A research data management plugin for the Git version control system," *Journal of Open Source Software*, vol. 29, 2016.

[9] C. T. Jacobs, A. Avdis, G. J. Gorman, and M. D. Piggott, "PyRDM: A Python-based library for automating the management and online publication of scientific software and data," *Journal of Open Research Software*, vol. 2, no. 1, p. e28, 2014.

[10] C. T. Jacobs, A. Avdis, S. L. Mouradian, and M. D. Piggott, "Integrating Research Data Management into Geographical Information Systems," in *Proceedings of the 5th International Workshop on Semantic Digital Archives*, 2015. [Online]. Available: http://hdl.handle.net/10044/1/28557

[11] R. J. LeVeque, I. M. Mitchell, and V. Stodden, "Reproducible Research for Scientific Computing: Tools and Strategies for Changing the Culture," *Computing in Science & Engineering*, vol. 14, no. 4, pp. 13–17, 2012.

[12] E. C. McKiernan, P. E. Bourne, C. T. Brown, S. Buck, A. Kenall, J. Lin, D. McDougall, B. A. Nosek, K. Ram, C. K. Soderberg, J. R. Spies, K. Thaney, A. Updegrove, K. H. Woo, and T. Yarkoni, "How open science helps researchers succeed," *eLife*, vol. 5, p. e16800, jul 2016. [Online]. Available: https://dx.doi.org/10.7554/eLife.16800

[13] M. Piggott, G. Gorman, C. Pain, P. Allison, A. Candy, B. Martin, and M. Wells, "A new computational framework for multi-scale ocean modelling based on adapting unstructured meshes," *International Journal for Numerical Methods in Fluids*, vol. 56, no. 8, pp. 1003–1015, 2008.

[14] V. Stodden, D. Bailey, J. Borwein, R. J. LeVeque, W. Rider, and W. Stein, "Setting the Default to Reproducible: Reproducibility in Computational and Experimental Mathematics," Institute for Computational and Experimental Research in Mathematics (ICERM), Tech. Rep., 2013. [Online]. Available: http://www.davidhbailey.com/dhbpapers/icerm-report.pdf

[15] R. C. UK, "RCUK Policy on Open Access and Supporting Guidance," Tech. Rep., 2013. [Online]. Available: http://www.rcuk.ac.uk/documents/documents/rcukopenaccesspolicy-pdf

[16] T. H. Vines, R. L. Andrew, D. G. Bock, M. T. Franklin, K. J. Gilbert, N. C. Kane, J.-S. Moore, B. T. Moyers, S. Renaut, D. J. Rennison, T. Veen, and S. Yeaman, "Mandated data archiving greatly improves access to research data," *The FASEB Journal*, vol. 27, no. 4, pp. 1304–1308, 2013.

Modelling complex vertical structures with TELEMAC-3D

Pierre-Louis Ligier,
Anders Söderström, Caroline Bohlin, Øyvind Lier
Sweco Energuide AB
Hydropower and Dams Department
Stockholm, Sweden
pierre-louis.ligier@sweco.se

***Abstract*— Two and three-dimensional hydrodynamic models based on an two-dimensional unstructured mesh, such as TELEMAC-2D and TELEMAC-3D, are well adapted to model vertical structures provided that the vertical geometry does not vary significantly. However, these models are less suitable if the geometry along the vertical axis is too complex. Nevertheless, TELEMAC-3D offers the possibility to include local head losses and varying atmospheric pressure giving more flexibility when dealing with complex vertical structures. Even though the program shows clear limitations compared with other CFD software able to solve more complex cases, it can easily be implemented on large scale computational domains. This article presents available methods that can be used to model certain types of vertical structures as well as application examples such as the modelling of bridge piers composed of tens of inclined piles, the influence of a debris boom on the flow conditions in a hydropower dam reservoir and the influence of floating docks on the current circulation in the vicinity of a marina.**

I. INTRODUCTION

Two and three-dimensional hydrodynamic models based on an two-dimensional unstructured mesh, such as TELEMAC-2D and TELEMAC-3D, are well adapted to model vertical structures provided that the vertical geometry does not vary significantly. However, these models are less suitable if the geometry along the vertical axis is too complex. Nevertheless, TELEMAC-3D offers the possibility to include local head losses and varying atmospheric pressure giving more flexibility when dealing with complex vertical structures.

This article is divided in two parts. The first parts presents TELEMAC-3D's limitations when modelling complex vertical structures. Available methods that can be used to overcome some modelling problems related to certain types of vertical structures are proposed and their validity is discussed. Finally, the last part of this article describes examples of applications where the proposed methods have been implemented.

The aim of this article is to present and share the experience gathered by Sweco from consulting assignments in which TELEMAC-3D has been used to model complex vertical structures. The methodology examples presented are not intended to be used as modelling standards.

II. AVAILABLE METHODS FOR MODELLING DISCONTINUOUS VERTICAL FEATURES

A. Overview

TELEMAC-3D solves the three-dimensional Navier Stockes equations in the field of free surface hydrodynamics for incompressible fluids [1, 2]. The main results are the three velocity components and the water depths solved at each time step.

The three-dimensional computational mesh is composed of a two-dimensional finite element mesh describing the bottom geometry that is duplicated several times along the vertical axis. This implies that only purely two-dimensional geometries can be modelled. Vertical faces are not allowed since such features cannot be represented in a two-dimensional horizontal mesh.

The principles followed by TELEMAC-3D do not allow modelling of complex three-dimensional geometries such as caves, culverts, tunnels etc. compared to other CFD software (FLUENT, FLOW-3D, COMSOL, openFOAM to name a few). However, the effect of certain types of vertical structures can be simulated by applying local head losses or pressure gradients in the computational mesh.

B. Local head losses

Local head losses can be applied at each computational node by defining the three components F_x, F_y and F_z of the source terms included in the three-dimensional momentum equations [2]. User defined source terms should be programmed in subroutine `source.f`. They are treated in an implicite way. Their expression is:

$$\begin{aligned} F_x &= S1U \cdot U \\ F_y &= S1V \cdot V \\ F_z &= S1W \cdot W \end{aligned} \quad (1)$$

With F_x, F_y and F_z the source terms in the three directions (m/s^2), $S1U$, $S1V$ and $S1W$ the intermediate terms to be defined in subroutine `source.f` (1/s) and U, V and W the three velocity components (m/s). For the sake of clarity, only the case corresponding to the x direction will be detailed in the following text.

The terms in the momentum equations can be defined as a force per unit volume divided by the fluid density (dimension m/s^2):

$$F_x = \frac{F}{Volume \cdot \rho} \quad (2)$$

With F being a force applied to the fluid (N), *Volume* the volume of application (m^3) and ρ the fluid density (kg/m^3). If the force F is defined as a drag force, (2) can be written as:

$$F_x = \frac{1}{2} \cdot \frac{Area \cdot C_D \cdot |U| \cdot U}{Volume} \quad (3)$$

With *Area* the area on which the force is applied (m^2), C_D the drag coefficient (-) and $|U|$ the velocity magnitude (m/s). From (1) and (3), *S1U* can then be defined as:

$$S1U = \frac{1}{2} \cdot \frac{Area \cdot C_D \cdot |U|}{Volume} = \frac{1}{2} \cdot \frac{C_D \cdot |U|}{dx} \quad (4)$$

With *dx* being the length of application of the drag force in the horizontal plane parallel to the flow direction (m). *S1V* and *S1W* are therefore equal to *S1U*.

Equation (2) can be used to apply head losses defined by other kind of forces. Another practical application is to apply a head loss corresponding to a friction loss at the free surface in order to model the flow resistance created by a rough surface in contact with the fluid. This is correct if one assumes that the free surface hydrodynamics equations remain valid. The corresponding equation is:

$$F_x = \frac{1}{2} \cdot \frac{Area \cdot C_f \cdot |U| \cdot U}{Volume} \quad (5)$$

With C_f the quadratic friction coefficient (-). From (1) and (5), *S1U* can then be defined as:

$$S1U = \frac{1}{2} \cdot \frac{Area \cdot C_f \cdot |U|}{Volume} = \frac{1}{2} \cdot \frac{C_f \cdot |U|}{dz/2} \quad (6)$$

With *dz* being the vertical distance between the two upper planes (m). In this case also, *S1V* and *S1W* are equal to *S1U*.

For Nikuradse's friction law and assuming that the velocity profile in the vicinity of the water surface can be considered as logarithmic, C_f can be expressed as [1, 2]:

$$C_f = 2 \cdot \left[\frac{\kappa}{ln\left(\frac{30 \cdot dz}{k_S}\right)} \right]^2 \quad (7)$$

With κ being the von Karman constant (0.4) and k_s the Nikuradse's roughness coefficient (m) also known as equivalent sand roughness.

C. Locally increased atmospheric pressure

Vertical obstacles located at the free surface, such as floating or fixed objects, can be modelled by applying a local atmospheric pressure gradient in order to lower the free surface. The locally increased atmospheric pressure can be defined at each computational node in subroutine `meteo.f` as:

$$P = P_0 + \rho g H \quad (8)$$

With P being the local atmospheric pressure (Pa), P_0 the reference atmospheric pressure (10^5 Pa), ρ the fluid density (kg/m^3), g the acceleration of gravity (9,81 m/s^2) and H the draught of the vertical structure (m). The keyword AIR PRESSURE should be set to "YES".

It can be noted that special initial conditions need to be defined accordingly regarding water depths in subroutine `condim.f` with the keyword INITIAL CONDITIONS set to "PARTICULAR".

D. Verifications and limitations

The methods described above are sensitive to mesh dimensions. When modelling head losses, (4) and (6) show that the intermediate source term *S1U* is dependent on horizontal and/or vertical mesh resolution. This needs to be taken into account in such applications.

The sensitivity to the mesh size has been estimated by modelling flow in a rectangular channel with the following set-up: bottom friction modelled with Nikuradse's friction law and for k_s = 0.01 m and with head loss applied at the free surface using the same friction law and friction coefficient as for the bottom. The channel is 20 m wide, 100 m long, has a flat bottom and an initial water depth of 5 m. The discharge applied is of 100 m^3/s to obtain an average flow velocity of 1.0 m/s. Three different vertical meshes have been defined with (i) 10 planes evenly distributed, (ii) 11 planes with an extra plane located 0.05 m below the water surface and with the other 10 planes located at the same levels than in the first case and (iii) same as before but the extra plane is located 0.05 m above the bottom. Turbulence was modelled with k-ε and the non-hydrostatic version was used. Results are presented as vertical velocity profiles from a point located in the central part of the channel in the downstream part, see Fig. 1. Result show that the vertical mesh size has a direct influence on the velocity in the vicinity of the refined zone but that the influence is limited at the other nodes. It can be noted that the vertical profile is nearly symmetrical which was an expected result since friction at the free surface has been defined in a similar way as the bottom friction. The fact that the profile is not entirely symmetrical might be due to the free surface

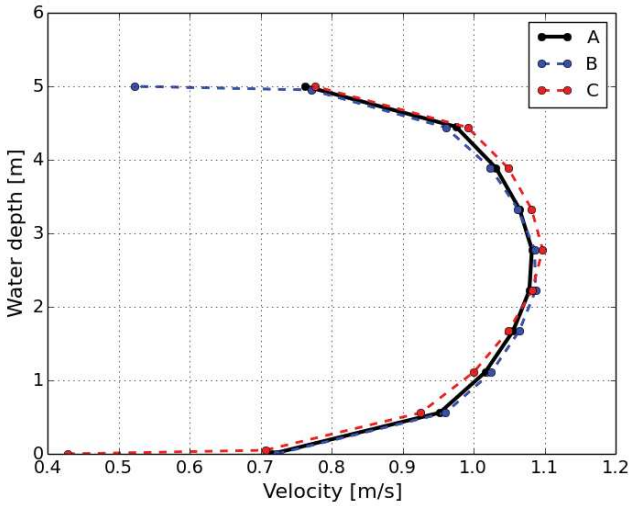

Figure 1. Sensitivity analysis to the vertical mesh resolution. Vertical velocity profiles. A: 10 planes evenly distributed; B: 11 planes with thin top layer; C: 11 planes with thin bottom layer.

slope observed for the results shown in Fig. 1 which was in the range of 8.10^{-5}.

The horizontal mesh resolution is also important when modelling local atmospheric pressure gradients. As mentioned above, a vertical gradient cannot be modelled with a two-dimensional mesh.

A simulation has been performed to assess the suitability of TELEMAC-3D for modelling head losses generated by a vertical contraction of the hydraulic section. The model geometry used is a 100 m long and 20 m wide channel. The initial water depth has been set to 20 m and the discharge has been chosen to 200 m^3/s so that the mean velocity is approximatively 0.5 m/s. The atmospheric has been locally increased to simulate a vertical contraction of 10 m with a gradient of 5.0 (distance of 2 m between the nodes with the normal atmospheric pressure and the nodes where the extra pressure is applied) so that the velocity in the contracted section is approximatively 1.0 m/s. Another simulation has been performed without increased atmospheric pressure but by increasing the bottom elevation of 10 m at the same location so that both cases can be considered as symmetrical, see Fig. 2. Bottom friction has been modelled using Nikuradse's law and with $k_s = 0.01$ m. The simulations have been performed with 10 evenly distributed vertical planes, with a constant viscosity turbulence model in the horizontal plane and with Prandtl's mixing length model in the vertical plane (velocity diffusivities have been set to 10^{-6} m^2/s in both cases) and with the non-hydrostatic version. Finally, the keyword FREE SURFACE GRADIENT COMPATIBILITY has been set to 1.0 to ensure a perfect balance between the free surface gradient and the computed velocities [1, 2]. The results show that the contractions generate head losses of 0.068 m and 0.064 m for the surface and bottom contraction, respectively. The difference might be due to the effects of bottom friction and turbulence between the bottom and the free surface. A theoretical head loss estimation using entrance and exit loss coefficients of 0.5 and 1.0 respectively, valid for abrupt geometry changes, gives a result of 0.076 m. This result is in good agreement with the model especially due to the fact that the atmospheric pressure and bottom gradient is not vertical (i.e. slightly smoother geometry changes). A theoretical head loss of 0.068 m is obtained if the entrance and exit loss coefficients are reduced by a factor 0.87. These results indicate that TELEMAC-3D reproduces correctly expected head losses due to the contraction of the hydraulic section by means of a locally increased atmospheric pressure.

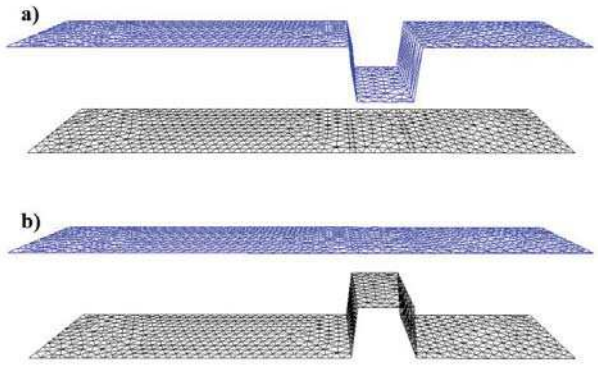

Figure 2. Model geometries used for the verification of head losses generated by a flow contraction (a: contraction at the free surface; b: contraction at the bottom). Only bottom and surface planes are visible.

Modelling obstacles with local head losses only allow to model their flow resistance. The flow acceleration occurring between these obstacles cannot be modelled in 3D. This can however be achieved in 2D by including element porosity [2].

III. EXAMPLES OF APPLICATION

A. The Getingmidjan Project, Stockholm (Sweden)

The railway line linking Stockholm Central and Stockholm South stations, called "Getingmidjan", has reached its technical life span and is in need of renovation. This line is one of the most trafficked railway axis of Sweden and a transport stop would have major consequences on railway transports in all the country. The renovation works will start once the new underground local railway tunnel of the new Citybanan project is in operation so that a part of the railway traffic using the Getingmidjan line can be diverted. Between Stockholm Central and Stockholm South stations, the Getingmidjan railway line crosses the Mälaren Lake on both sides of the Gamla Stan island (Old Town) on the Centralbron bridge, see Fig. 3a. Hydraulic modelling has been performed to assess flow conditions in the vicinity of the bridge in order to estimate the erosion risk, to provide support for work planning and to estimate environmental impacts of the renovation works.

The southern pass, called Söderström, is deep with maximal water depths of 20 m and with bottom material composed of loose sediments. The Centralbron bridge is composed of six piers founded using vertical and inclined piles reaching the bedrock, see Fig. 3b.

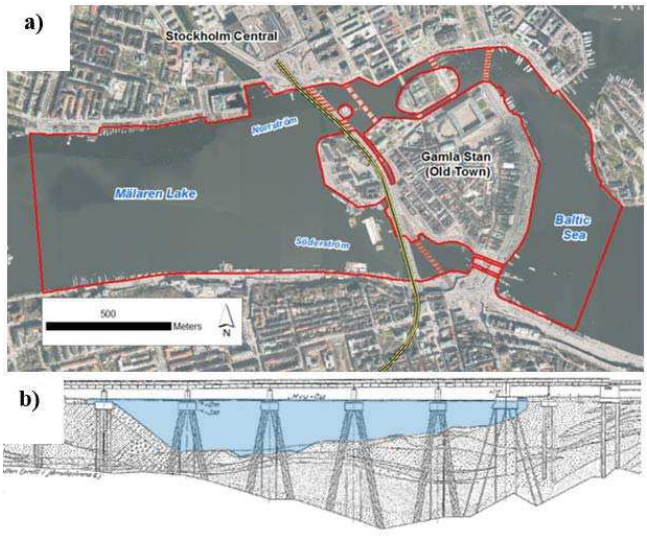

Figure 3. The Getingmidjan Project. a: situation map showing the extents of the hydraulic model (red) and the Getingmidjan railway line (yellow); b: cross section of the Centralbron Bridge over the Söderström pass on the southern side of Gamla Stan.

The model geometry is composed of a two-dimensional horizontal mesh totalling approximatively 82 400 elements and of 14 vertical planes. Turbulence has been modelled with the Smagorinsky model in the horizontal plane and with Prandtl's mixing length model in the vertical plane. TELEMAC-3D was run in its non-hydrostatic version (version 6.2).

Calibration has been performed against water levels measurements available from recent high flow events. Bottom friction was modelled with Strickler's law and the friction coefficient at the bridge location has been estimated to 50 $m^{1/3}/s$ from the calibration process.

It was not possible to model piles with the classic method by creating "islands" in the model due to the fact that the piles are inclined. The method chosen to model the piles' resistance to flow is inspired from the 2D drag force modelling (see the TELEMAC-2D dragfo validation case). Local head losses have been applied at the nodes located within the bridge pier and piles perimeter as intermediate implicite source terms in subroutine `source.f` using the following equation:

$$S1U = \frac{1}{2} \cdot \frac{nD}{A} \cdot C_D \cdot |U|$$

With n being the number of piles per pier (40), D the piles diameter (0.75 m), A the area of the zone within which the drag force term is applied (approximatively 350 m^2 for each pier), C_D the drag coefficient (dimensionless) and $|U|$ the magnitude of the flow velocity at each computational node (m/s).

No field measurement was available to calibrate the drag coefficient against. Hence, the drag coefficient value used has been taken equal to the one provided in the dragfo validation case valid for circular piles, C_D = 1,34 [2].

The effect of the added drag term on the velocity field through the bridge opening for the design flood is presented in Fig. 4. "Section S1" is located approximatively 10 m upstream of the bridge while "Section S2" is located along the bridge axis. The added drag term causes a contraction of the flow field between the piers and piles.

B. Fish migration at the Hunderfossen hydropower plant (Norway)

The Hunderfossen HPP is located on the Gudbrandsdalslågen River approximatively 15 km upstream of the city of Lillehammer in Norway. The reservoir is created by a concrete gravity dam equipped with spillway gates and with an ice spillway. The power plant is situated underground and is composed of two units. The intake structures is located near the ice spillway and the water is transferred to the units by two vertical shafts. A debris boom is located in the reservoir between the north bank and the ice spillway in order to divert the floating ice flakes out of the reservoir during the winter season. Following the installation of a new trashrack generating lower head losses, fish migration shifted from the ice spillway towards the power waterway, thereby increasing fish mortality. Following this, a study is being performed in order to identify solutions for diverting the fish migration from the power intake back to the ice spillway.

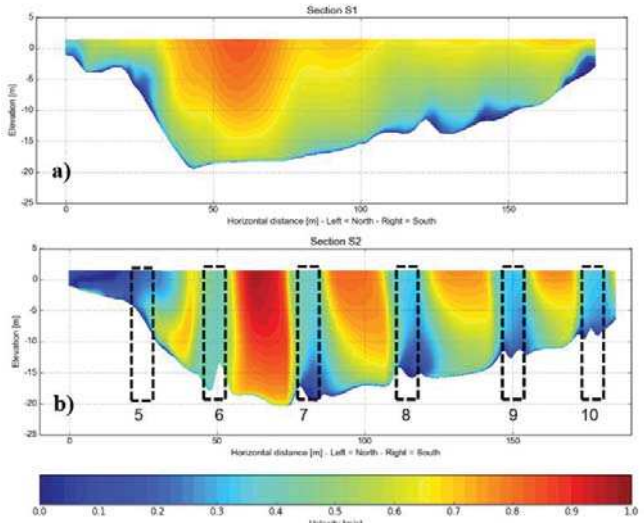

Figure 4. Vertical velocity profiles a: approximatively 10 m upstream the Centralbron Brdige; b: along the bridge axis. The black dashed lines represent the piers location.

A TELEMAC-3D model has been set-up covering the reservoir. The model geometry is composed of a two-dimensional horizontal mesh totalling approximatively 15 800 elements and of 17 vertical planes. The model has six open boundaries (inflow, outflow from ice spillway and from two of the spillway gates and two water level boundaries corresponding to the intake structure).

Bottom friction has been modelled using Strickler's law and with a friction coefficient of 30 $m^{1/3}/s$. The turbulence model used was k-ε. TELEMAC-3D was run in its non-hydrostatic version (version 7.1).

Flow resistance created by the debris boom has been modelled by applying a local head loss on the computational nodes corresponding to the boom location which was defined by two rows of aligned nodes in the horizontal mesh and by two horizontal planes with fixed elevations (in addition to the plane corresponding to the water surface) along the vertical axis. The boom geometry is composed of a vertical upstream face and of a 45-degree inclined downstream face. It extends to approximatively 0.3 m below the water surface. The main flow direction makes an angle of approximatively 67 degrees with the debris boom's axis so that the angle of attack is approximatively 33 degrees. The local head loss has been modelled as a drag force implemented as an implicite source term in subroutine `source.f`. The drag coefficient corresponding to the debris boom geometry can be estimated to approximatively 1.3 for flow perpendicular to the boom axis that has been corrected to approximatively 0.5 to account for the actual angle of attack [3]. The source term has been multiplied by a factor U_{ref}/U with U_{ref} being the velocity without the debris boom and U the velocity with the boom. This correction has been applied because the drag force formula is theoretically based on the undisturbed flow velocity.

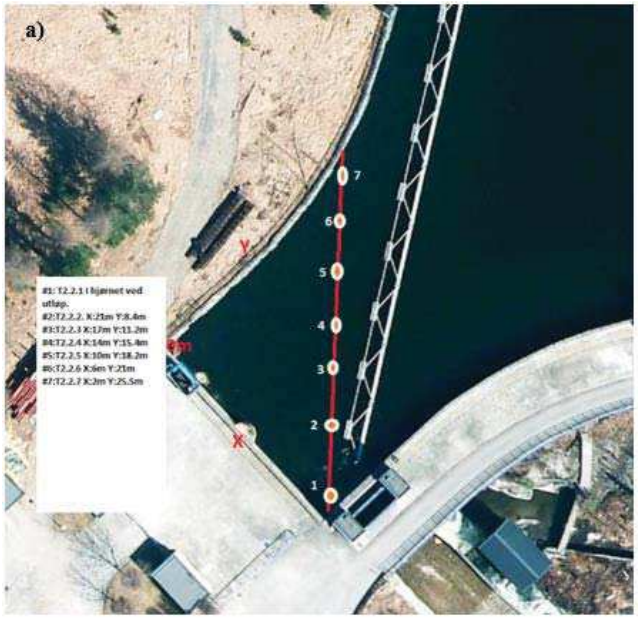

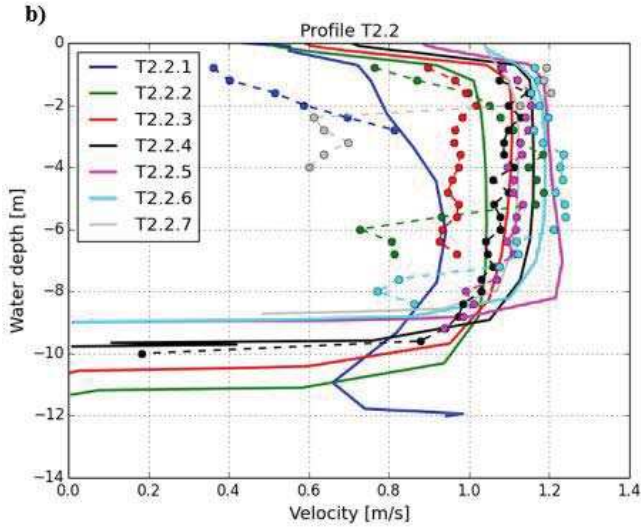

Figure 5. Velocity measurements and results from the hydraulic model. a: location of the measurement points; b: comparison between measurements and model results (vertical velocity profiles).

Flow velocity measurements have been performed in the vicinity of the debris boom with an acoustic Doppler device (Aquadopp Profiler by Nortek). The total discharge during the flow measurements was estimated to 403 m^3/s distributed with 67 m^3/s through the two radial gates, 14 m^3/s through the ice spillway and 322 m^3/s through the power station. Outflow from the radial gates has been modelled using a user defined vertical velocity profile enabling outflow at the correct water depth just above the bottom. Outflow from the ice spillway has been modelled by defining the bottom levels at the gate location so that the water depth at the boundary corresponds to the critical depth (surface spillway). The comparison between flow measurements performed downstream of the debris boom and the results from the hydraulic model is presented in Fig. 5. The model tends to underestimate somewhat the flow velocities in the central part of the canal

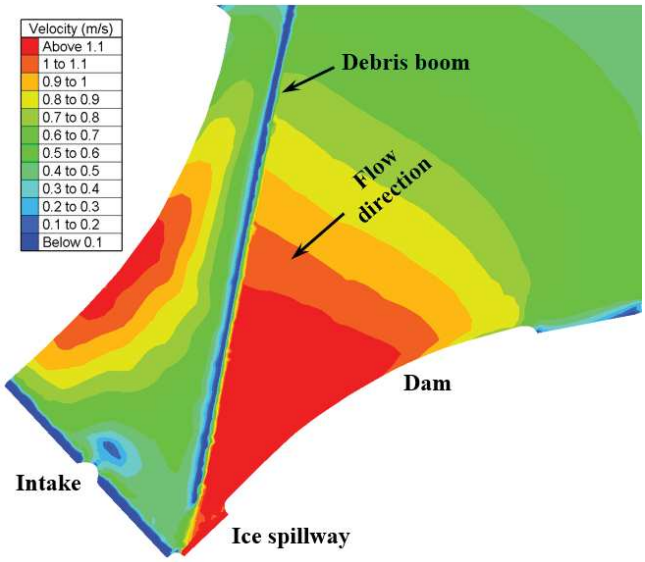

Figure 6. Surface current with debris boom.

(this might be due to inaccurate bottom levels) but reproduces the subsurface flow deceleration generated by the boom in a satisfying way. The simulated velocity profile at point T2.2.1 is likely influenced by the model boundaries (intake and ice spillway). Note that the flow measurements are considered to be uncertain for water depths greater than 2 to 6 m (due to lack of suspended particles in the water column). The simulated surface current is illustrated in Fig. 6. This study is ongoing and these results are therefore preliminary.

C. Flow resistance generated by floating docks (Sweden)

An environmental impact assessment study has been performed prior to the installation of new floating docks in a marina located in the Stockholm Archipelago. A hydraulic study has been performed with the aim of estimating the influence of the additional floating piers on the currents and the water circulation in the study area. Two types of floating docks are to be installed with inner docks composed of 2 m long rectangular pontoons every fourth meter (i.e. with a 2 m air space between two pontoons) and with outer docks composed of continuous concrete structures acting as a wave breaker. The draught of the inner and outer docks is of 0.4 m and 0.5 m respectively.

A TELEMAC-3D model has been set-up over the study area. The model geometry is composed of a two-dimensional horizontal mesh totalling approximatively 162 000 elements and of 12 vertical planes. The model has two open boundaries (water level boundaries at each end of the study area). Simulations were performed with wind forcing (average and extreme wind cases).

Bottom friction has been modelled using Strickler's law and with a friction coefficient of 35 $m^{1/3}/s$. The turbulence model used was k-ε. TELEMAC-3D was run in its non-hydrostatic version (version 7.1).

The effect of floating piers has been modelled by lowering locally the water surface to simulate the barrier created by the pontoons and by applying a friction loss term on the nodes

located at the interface between the pontoons and the water body. The lowering of the water surface was achieved by applying a locally increased atmospheric pressure corresponding to the pontoons' draught (meters of water column converted into Pascal) in subroutine `meteo.f` (initial conditions were defined in subroutine `condim.f`). It can be noted that the distance between nodes at the interface between free surface and the floating docks has been set to approximatively 0.1 to 0.2 m in order to obtain a free surface gradient as steep as reasonably possible. The friction loss term has been implemented as an implicite source term in subroutine `source.f` with the quadratic friction coefficient expressed in terms of Nikuradse's roughness coefficient k_s which has been set to 0.01 m. The vertical mesh has been defined with a classic Sigma repartition above level -0.6 (i.e. 0.1 m below the deepest docks) and with a user defined Sigma repartition (ZSTAR) between this level and the bottom. It can be noted that the effect of moored boats has been modelled using the same methodology and by assuming that the boats can be simulated as a continuous floating structure located along the docks with an average draught of 0.2 m. The two-dimensional mesh with information on floating docks' draught is depicted in Fig. 7. The initial water surface elevation has been defined in an additional variable stocked in the geometry file and read by the program thanks to the keywords NUMBER OF 2D PRIVATE ARRAYS and NAMES OF 2D PRIVATE VARIABLES.

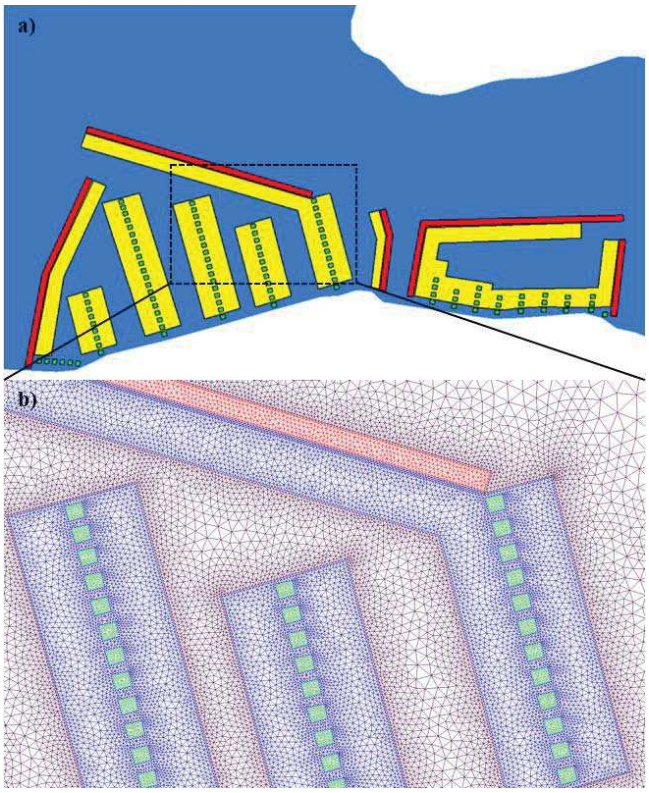

Figure 7. Modelling of floating docks and moored boats (a: overview of the structures with in yellow the moored boats, in green the inner docks and in red the outer docks; b: detailed view of the computational mesh with initial water surface values stocked in geometry file as an additional variable – note that the colors are not identical to a).

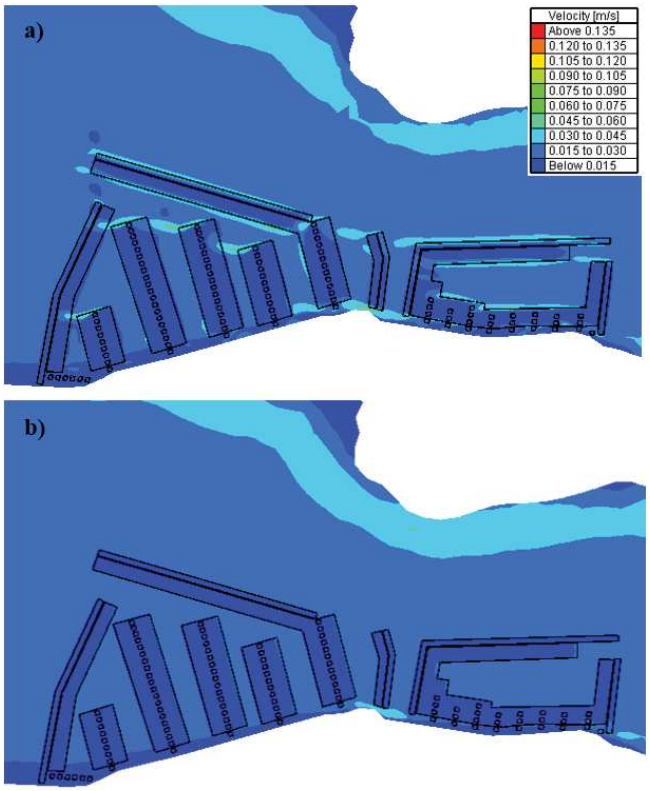

Figure 8. Sensitivity analysis on the keyword FREE SURFACE GRADIENT COMPATIBILITY (a: value 0.9; b: value 1.0). Surface current after a simulation time of 1 hour. The floating docks and moored boats are depicted with black lines.

A sensitivity analysis have shown that the value of the keyword FREE SURFACE GRADIENT COMPATIBILITY should be set to 1.0 in order to ensure a perfect balance between the free surface gradient and the computed velocities. Fig. 8 shows that erroneous currents are generated when using a value lower than 1.0 (for instance with the recommended value of 0.9).

Results in the vicinity of the marina are presented in Fig. 9 for an easterly wind blowing at 7.5 m/s. It can be seen that the surface current is reduced by floating docks and the moored boats. The differences are strongest in the western part of the marina which is in the lee (easterly wind and surface current) as well as in the vicinity of the outer docks (continuous barrier with a 0.5 m draught). Consequently, the surface current in the channel between the marina and the north shore is slightly increased. Results have shown that the flow in the sound is reduced by approximatively 8.4% due to the additional structures. A sensitivity analysis performed on the draught of the outer docks showed that the flow reduction can be lowered to 7,8% with a draught of 0.2 m indicating that their flow resistance is mainly linked to the number of additional pontoons (and therefore their associated friction) rather than to their draught (for the investigated geometries).

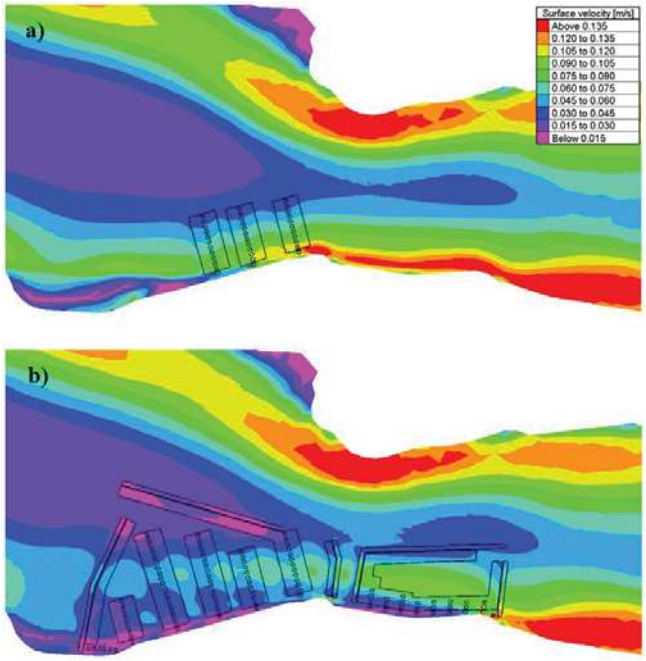

Figure 9. Stationary surface currents for the extreme wind case after a simulation time of 20 hours (a: reference configuration; b: with additional floating docks). The floating docks and moored boats are depicted with black lines.

IV. CONCLUSION

This article presents available methods for modelling certain types of complex vertical structures with the hydrodynamic software TELEMAC-3D. These methods are based on local head losses that can be applied at any computational node in order to model the flow resistance generated by a structure and on locally increased atmospheric pressure to simulate a vertical contraction of the water body at the free surface. The proposed methods have been discussed and their limitations highlighted. The aim of this article is however not to propose these methods as modelling standards as a more formal and in-depth verification and validation process would be needed. Finally, application examples have been described.

REFERENCES

[1] EDF R&D, TELEMAC-3D Software, Release 7.0, Operating manual, January 2016.

[2] J-M. Hervouet, Hydrodynamics of free surface flows, John Wiley & Sons, Ltd, 2007.

[3] R. D. Blevins, Applied fluid dynamics handbook, Kreiger Publishing Company, 2003.

Vortex streets behind bridge piers - Studies with Telemac-2D/3D & Telemac-AD

Christian Kessler
BERNARD Ingenieure ZT GmbH
Hall, Austria
christian.kessler@bernard-ing.com

Uwe Merkel
UHM River Engineering
Karlsruhe, Germany
info@uwe-merkel.com

***Abstract*— An existing bridge over the Danube River, the longest river in the European Union, will be expanded by two lateral bridges. Four additional bridge piers will potentially induce turbulence, side currents and vortex streets which must not influence the shipping route through and behind the bridge. Simulations with Telemac-2D and Telemac-3D and different pier shapes show Karman vortex streets behind the piers. The ongoing project uses Telemac-3D v7p1 and Telemac-AD to analyze the impact of the piers' shape. The necessary mesh density that is the basis for a reliable representation of the surrounding bathymetry was determined with tests against flume experiments and a mesh impact analysis with Telemac-AD. First results are discussed.**

I. INTRODUCTION

Obstacles in rivers are dangerous for swimmers, sport boats and sometimes even for cargo vessels. Currents near obstacles are different from the mainstream due to changes in fluid elevation, pressure and velocities.

High velocities frequently occur at the lateral face of bridge piers, whereas behind the pier backflow areas, side-currents and vortex streets develop, even if they are not always visible at the surface. At the front-face of an obstacle most of the water moves downward and may draw items down.

The main problem with the simulation of vortex streets is that a good representation is only possible if the mesh resolution is much smaller than the vortex diameters. In the case presented here, the vortex wake will have several hundred meters length, but the average vortex diameters will be below 1 meter at their origin. The necessary mesh resolution has to be small; some experts claim smaller than 1 cm resolution in 3D. But if one needs to simulate a larger river stretch with many bridge piers, a compromise resolution is necessary to keep calculation times acceptable.

Five steps are required to find a suitable mesh with necessary minimum density and to determine good Telemac parameter sets:

1. Straight flume experiments with various pier shapes (circle, ellipse, rectangular a.o.) were set up in different mesh densities. The meshes were programmed to control the mesh point density not only close to the obstacle but also with growing distance.
2. This has been tested with several Telemac setups and compared to classic empiric Kármán formulas for vortex approximations.
3. The mesh points that have an impact on the vortex have been identified with Telemac-AD. This marks the areas that have to be refined carefully.
4. The transfer of these rules to the real river model shows long Kármán vortex streets for academic circular piers and match the empiric formulas.
5. The prediction for the future pier shapes also shows Kármán vortex streets with small vorticity.

II. BOUNDARY CONDITIONS

A. The River and the Bridge

The Danube River (Figure 1) is, after the Volga, the second-longest river in Europe. It is located in central and eastern Europe. Its source is in Germany and the estuary is in Romania where it flows into the Black Sea. The Danube is an important international waterway. Dependent on the flow conditions, ships of up to 195 m in length and a width of up to 22.8 m navigate on the Danube, as do small recreational boats. For all of them strong side currents are a potential hazard.

From the total length of 2,888 km, 2,415 km are navigable, whereby 351 km are located in Austria. This section belongs to the "Upper Danube", which stretches from Kehlheim in Germany to Komárom in Hungary.

Figure 1: Overview of the Danube River

The Voest-bridge (Figure 2), named after the local steel producer, crosses the Danube at river-km 2,133.44. The bridge carries a highway with three traffic lanes and one bicycle lane in each direction. The cable-stayed bridge has one pier, which is permanently in water (Figure 3), on which the approx. 70 m high pylon is located.

Figure 2: Voest-bridge with additional side-bridges 6; project by consortium: Bernard Ingenieure, RWT plus ZT GmbH and Solid architecture.

Figure 3: Voest-bridge with existing bridge piers

There are two more piers in the floodplains; however, these are not of interest for shipping conditions. The shapes and the layout of the existing pier and the new river piers are shown in Figure 4 and Figure 5. The distance between the piers is 130m, which is sufficient space for 2 meeting cargo vessels of the size 195 m x 22.8 m. The free span width on the right side of the pier is approx. 215 m, on the left side approx. 72 m. The distance from pier to slope on the right is 185 m and on the left 60 m.

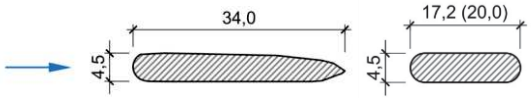

Figure 4: Shape of existing pier - Shape of new piers

In the course of the renovation of the Voest-bridge two additional side bridges will be built. Therefore four additional, new piers will be built in the regular flow section. The effect of the existing pier and the new piers in the regular flow section shall be investigated.

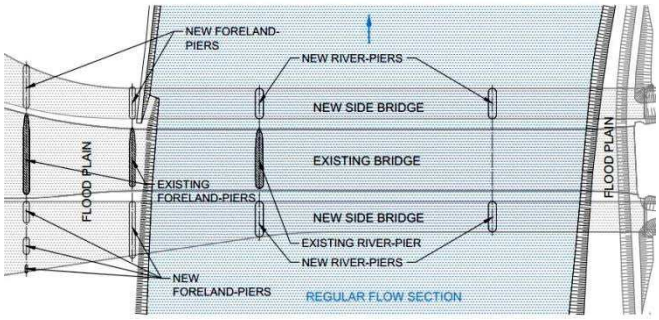

Figure 5: Layout

B. Simulation of Vortex Streets

Based on the research of Theodore von Kármán some empiric formulas and several laboratory examples are available for standard obstacle shapes, mainly for frontal symmetric approaching flow. These formulas, e.g., the vortex creation frequency (1), depend on the Strouhal-number.

$$f = \frac{S_R * V}{d} \tag{1}$$

where:

- S_R… Is the Strouhal number, approximately 0.2 for the problems discussed in this paper
- V… the steady velocity of the flow upstream of the obstacle
- d… diameter of the obstacle.

The “Body Reynolds Number” (2) influence is well known too, as shown too, as shown in

Figure 6 for the different stages of vortex development.

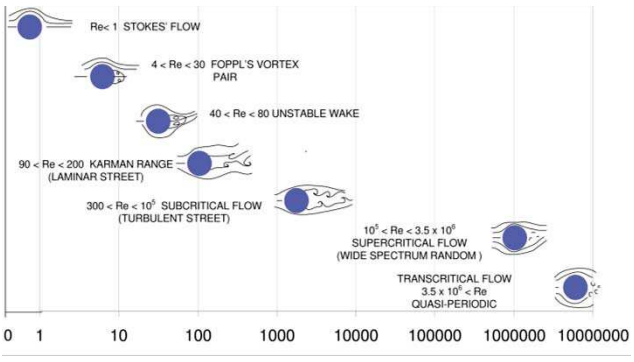

Figure 6: Body Reynolds Number and Vortex Formation [5]

$$\Re = V * d/v \quad (2)$$

where:

- d... the diameter of the cylinder
- V... the steady velocity of the flow upstream of the cylinder
- v... the kinematic viscosity of the fluid.

The separation point of vortices is the point at which the local wall shear stress disappears. Schlichting and Gersten [3] write that the angle of separation for a cylinder under a subcritical flow regime ($300<Re<10^5$) is approximately 80°.

Simulation by finite methods is more challenging to work with than the empiric formulas, as a low diffusion and dispersion is needed to prevent smoothening of the vortices. For Telemac the right advection scheme is known as a key feature. Additionally many scientific publications recommend a very small mesh resolution to keep the dispersion low. Throughout scientific literature, mesh resolution is chosen by the principle "high density, as widespread as the hardware allows us". But it is the nature of these numeric simulations that calculation time and costs are constraints.

The presented simulations in this paper test the abilities of Telemac-3D-v7p1 and Telemac-AD to integrate vortex movements in spatially large, inevitable coarser models.

Contrary to many former tests, the authors use Telemac-AD to quantify the mesh influence point by point in order to not bluntly densify meshes. The intent is to learn where to improve the resolution, where to save mesh points and to reveal unexpected interactions.

III. Tests with Telemac-3D v7p1

A. First tests vs. Observation in Nature

The first simulations of the existing Voest-bridge-piers did not show wake zones. So instead of the genuine shape a circular shape was modelled and consequently wake zones appeared. The question was raised if this is due to numerical reasons, or if there are no wake vortices for non-circular pier-shapes. Therefore the existing Voest-bridge pier and two comparable more non-circular piers at the Inn-river in Innsbruck were photographed and filmed. The results are shown in Figure 7.

All three observations showed wake zones behind the piers. They are not always obvious at first sight, but by studying pictures combined with tripod-filmed videos periodic patterns can be determined. Therefore it is assumed, that the absence of wake zones in simulations is due to numerical reasons.

The Voest-bridge-study covers a 2,900 m long section of the Danube River. The length was chosen based on considerations of calculation time and minimization of boundary conditions influence. The highest navigable discharge in the investigation area is 3670 m^3/s, which was chosen as boundary condition for the numerical simulations. The riverbed friction was defined with a Strickler-coefficient of 37.

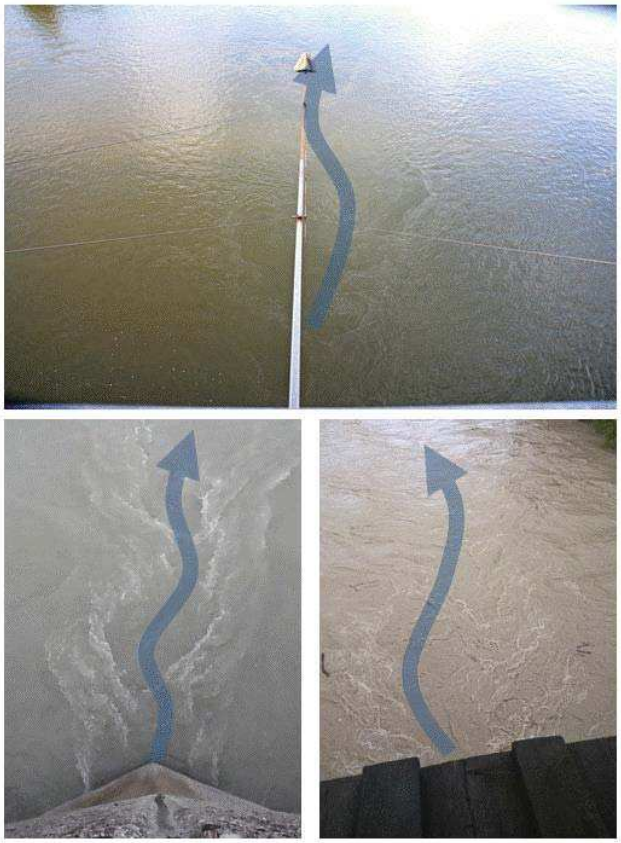

Figure 7: Observation of bridge-piers at the Danube/Voest-bridge (top), Inn-river in Innsbruck (lower-left) and Hall (lower right)

In order to study the effect of the pier, different shapes (Figure 8) were simulated with Telemac-2D v6p3 and v7p1. All parameters which influence the diffusivity were set to reduce it (e.g. velocity diffusivity). The calculation was performed nearly explicit (implicitation for velocity/depth = 0.9) in order to obtain less smoothing. Different advection-schemes and turbulence models with little smoothing were tested.

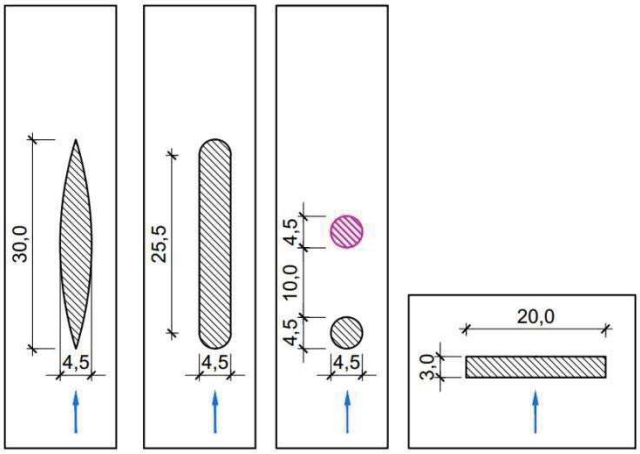

Figure 8: Studied pier shapes and arrangements

The results of the first simulation are shown in Figure 9. It was assumed, that the smoothing comes from dispersion, which is a problem of coarse meshes.

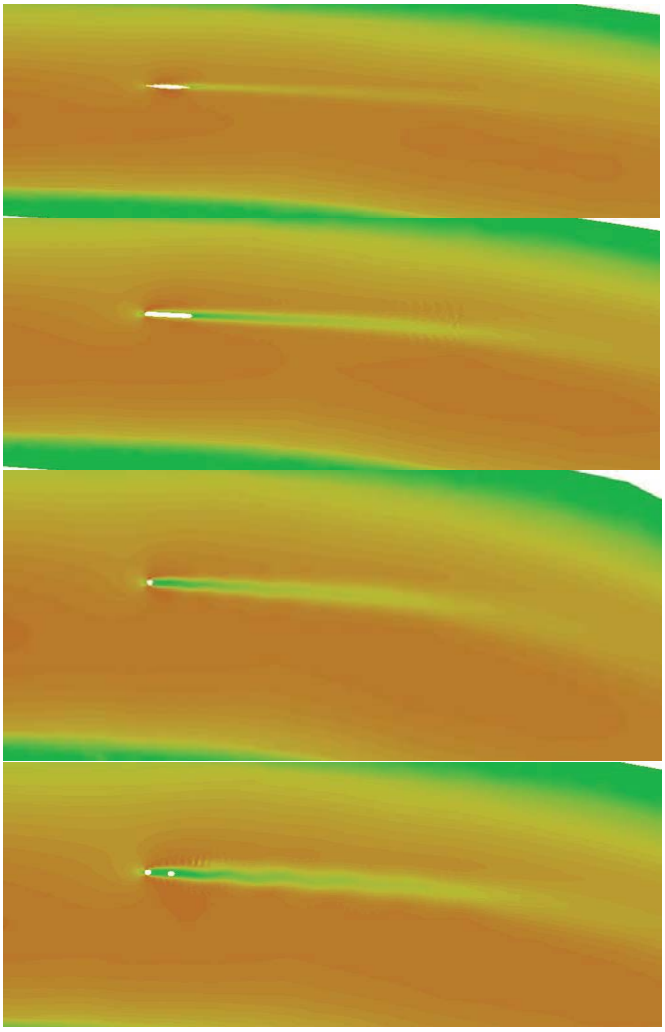

Figure 9: Wake zones vary with the pier shapes, but no Karman vortex streets are visible here.

B. Mesh Dependency and Telemac-AD

Two methods were chosen to find the right mesh / parameter combination:

- Manual densification until there is no further significant change in the results any more
- Selective densification based on Telemac-AD

For the first approach a series of flume meshes had been programmed with a Python script that instrumentalized Jonathan Shewchuk Triangle library [4]. Figure 10 shows meshes for a circle with r=1m and an ellipse with r1=1m and r2=4m. The displayed mesh densities are 180 (upper) and 40 (lower) points at the pier footprint and the triangle growth rate is 1.15 for every ring further away from the center. Despite of being clipped for Figure 10, the length upstream and downstream the pier is 50m, the total width is 20m. The first calculations showed a good vortex production for the circular mesh if used with the advection scheme "weak form of characteristics" and a small implicitation for depth and velocities. The vortex frequency could be reproduced exactly according to the Kármán law: 0.2Hz which equals one new vortex every 5 seconds. Additionally the separation point of vortices fits to Schlichting and Gersten's [3] experience. Figure 11 provides a good impression.

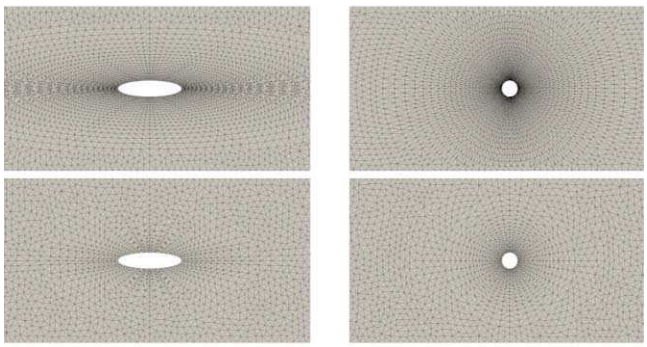

Figure 10: Meshes with controlled point density at the pier and guaranteed point distance growth of less than 1.15 times the neighbouring distance.

Mesh densities with less than 40 points around the circular pier didn't perform well. Starting with 40 points (which equals a boundary point distance of ~15cm) useful results were produced. With 160 points (which equals ~4 cm) the behaviour seemed to reach a tangent. 720 points did not change much, but increasing computational expenses. Therefore brute force densification came to its limits and already included too many nodes.

The second, smarter step was to use Telemac-AD to determine the right positions for high resolution mesh inserts.

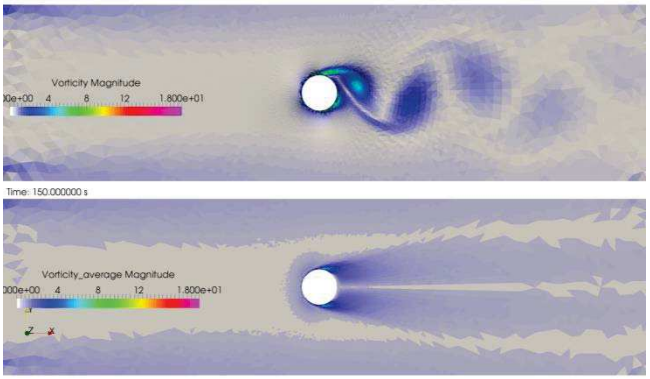

Figure 11: Upper Picture: Estimating vortex zones with the "weak form of characteristics" option produces results that comply with Kármán's formula for the vortex creation frequency. Lower picture: The time averaged vortex corridor.

Telemac-AD (T-AD) is a special sibling of Telemac, which is able to show the interaction between any calculation parameter, as long as it is of the Fortran data type "double precision". In this case, it is the mesh point's position on a user specified result: the vorticity behind the obstacle. The scientific background is explained in more detail in the TUC Proceedings of 2013[2].

T-AD is able to determine the influence of a large number of input variables on one single target variable in a single calculation. This means for the case presented in this paper, that 7,121 points in 2D have X, Y and Z coordinates, which are in total 21,363 variables, which might affect the one result: the vorticity behind the pier.

For this purpose a so called *cost function* is added to the Telemac Source code, like an internal post processing routine.

After every time step it processes a formula which quantifies the vorticity behind the pier. Several alternative cost functions were checked. The most useful among them were the standard deviation of the velocity components, the variability of U_y and the transfer velocity component. Figure 12 shows an orange frame which marks the examination zone for the displayed cost function. In Figure 13 this is the smaller purple zone.

T-AD v6p2 and v7p2 (so far unpublished) returned the adjoints (~ a kind of derivative) for the mesh variables X, Y and Z which are combined to generate the vector field (=arrows) in Figure 13. The arrows describe the direction and magnitude a mesh point should be shifted to increase the vorticity indicator (=cost function).

Note: This answer is the elementary input for a potential next step, the shape optimization. In the case presented here it means that if the Y-dimension of the pier would be bigger, the vorticity indicator would be stronger.

To return to the general question of "Which mesh point has influence on the vorticity and therefore needs to be treated with special care?"; in Figure 13 the adjoints' magnitude is colored as an answer. The logarithmic scale might mislead the interpretation. Boundary points have the greatest impact on the results, but the position of the inner points nearby (which are more numerous and cover a larger area) also have an impact on the results. This means, that the mesh dependency is still strong in an area of up to 50 % of pier radius or 50 cm away from the boundary nodes, even though the resolution is already < 6 cm in this zone. This means the initial recommendation was correct: cells have to be smaller here for scientific applications.

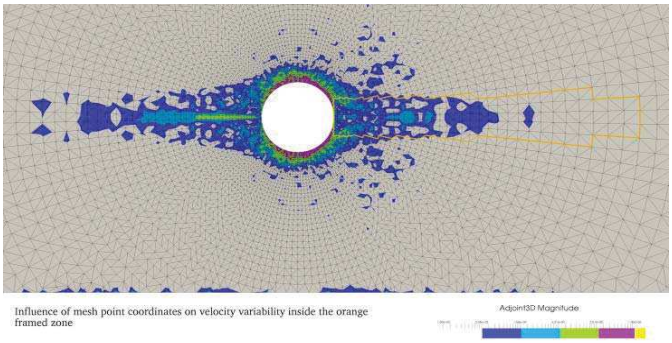

Figure 12: The magnitude of point coordinate adjoints clearly shows the dependency of the vorticity to non-boundary points. This means that shifting one of the coloured points in 2D will lead to slightly other results. Due to the logarithmic scale, the pink coloured boundary points have a 100 times stronger impact than the blue coloured surroundings. However, the blue area is up to 100 times larger.

Another interesting fact is the long influence zone directly upstream of the pier. The sensitivity of this area explains why fins or plates can disturb or even destroy the vortex system that efficiently.

Interpretation for the potential linear shift of an inner mesh point: As the bottom elevation is 0m for all points, the shift in X and Y direction wouldn't affect the bathymetry, but only the calculated velocity gradients close to the obstacle.

This obviously has no linear behavior and means that a different mesh point position would result in different velocity fields. More points would describe the V-field better, thus resulting in less impact for the single points.

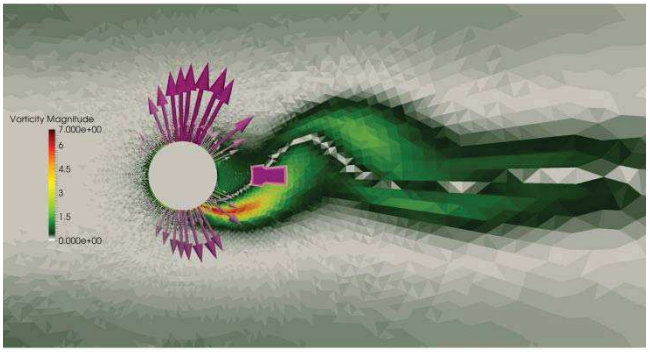

Figure 13: If the adjoints are displayed as arrows, they show the direction a mesh point has to be moved to increase the vorticity inside the pink selected area. The opposite direction would reduce it. In particular, the direct boundary points give the expected answer: Shift them to the inner side, and the vorticity will be reduced.

For practical purposes, the smaller differences of the results allow the authors a 15 cm resolution for the final flume-mesh. To understand why the upstream zone around the pillow is still that sensitive for the downstream vortex zone, Figure 14 (Telemac 3D-v7p1, here: 10 Levels in 3D) gives a visual explanation: The impact pillow on the upstream face and the side rolls are clearly visible and separated from the surrounding flow. The downward rotation is strongest at a distance of more than 0.5m to the obstacle itself. Outside of this zone, the impact (as calculated with Telemac-AD) decreases to a negligible magnitude.

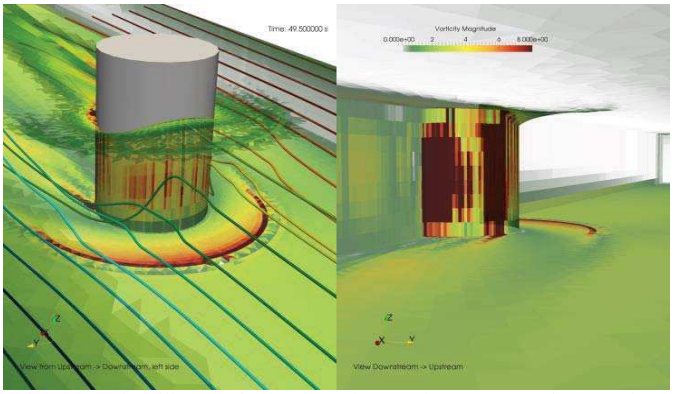

Figure 14: The pillow on the upstream face produces a strong downward drag with the strongest vorticity on the bottom and on the piers back. A fine mesh resolution is necessary for this area as well, as it is an essential component of the vortex building system. The downward drag starts up to 1m before the pier.

After many more comparisons between meshes, empirical formulae and literature, the step to the real scale model was made with the decision towards a mesh size of approx. 10cm along the circular piers rising by a factor of 1.15 to the next ring of cells. The first test with a circular pier returned the expected Kármán vortex street. The frequency is 0.035Hz, which equals the creation of one vortex every 28s. See fig. 15.

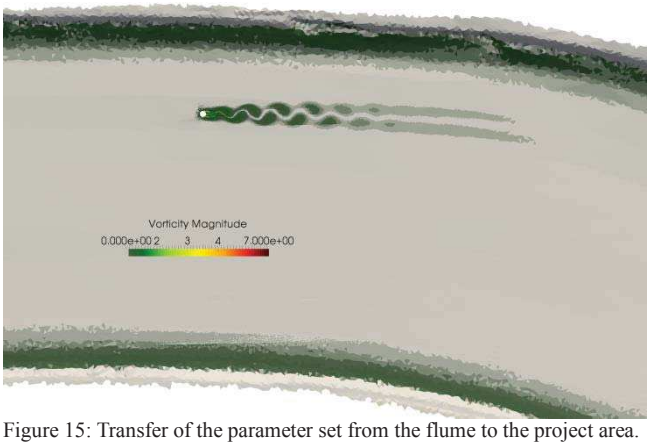

Figure 15: Transfer of the parameter set from the flume to the project area. The resulting vortex street complies with the empirical Kármán formulas.

The next step is the creation of the final mesh. It includes all 5 piers and uses the so far developed parameter setup and mesh densities, but there are no comparison values available anymore from literature or experiments.

With an further mesh-refinement to 5 cm edge length Kármán vortex streets with a small vorticity occur (Figure 16).

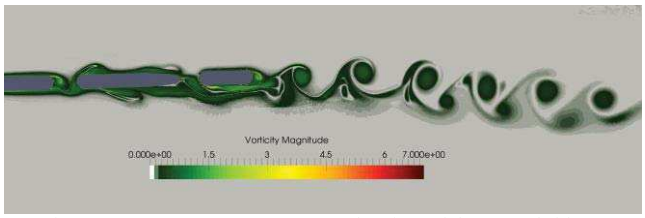

Figure 16: Kármán vortex streets at the piers of the Voest-bridge.

There are more questions to solve: What is the impact of diffusion? And what is the impact on small sport ships? At the time of writing, the answers to these questions are open, but we will publish some more results and a downloadable Telemac-AD example on the webpage

www.uwe-merkel.com/piers-and-eddies

IV. CONCLUSION

Vortex streets can be modeled well enough to comply with the well validated empirical formulas. It is important to avoid anything that induces artificial diffusion / dispersion. Two significant sources of dispersion are known beside some smoothing parameters: The mesh density and the type of advection. For the latter, the “weak form of characteristics” is the best possible answer in Telemac v7p1. For the first, the mesh density, the authors have not yet derived a universal empirical formula. However, in general results improved and met the Kármán frequency, when:

- the smallest cross section of the upstream pillow was resolved by at least 5 to 7 cells.
- and this resulting point density was used over a zone which starts at approx. 5 times the pier width before the pier until 10 times the width after the pier
- the triangle growth rate was kept <. 1,15
- the Delaunay criteria for the triangle shape was kept strictly
- the Courant-Friedrich-Levy criteria < 1 for the time step was kept.

Telemac-AD proved itself to be a reliable influence detection tool. It is particularly useful for more sophisticated pier shapes or groups (especially beyond the standard circular, elliptical, arrow or rectangular shapes).

Further parameters, such as resulting shear stress or scour development have not been investigated. Further fine-tuning will be necessary to meet the accuracy demands of the latter.

The width and dissipation of the wake is also mesh dependent, but in general less sensitive to the tested parameters.

ACKNOWLEDGEMENT

We thank Jan Riehme for the support on Telemac-AD and his work on it.

Further we thank the Amt der Oberösterreichischen Landesregierung, the Via Donau and the ASFINAG for their permissions and data.

REFERENCES

[1] ASFINAG. 2016. Neugestaltung Voestbrücke. Download 21.09.2016. www.asfinag.at

[2] Merkel, U. Riehme, J. 2013. Reverse engineering of initial & boundary conditions with TELEMAC and algorithmic differentiation. In: Proceedings – Telemac Users Club 10 / 2013, Karlsruhe

[3] Schlichting H. Gersten K. 2000, Boundary Layer Theory, 8th rev. and enl. ed., Springer, Berlin

[4] Shewchuk, J. R. Delaunay Refinement Algorithms for Triangular Mesh Generation, Computational Geometry: Theory and Applications 22, May 2000

[5] Xanthakos, P. 1995. Bridge Substructure and Foundation Design, Prentice Hall PTR, New Jersey

Study of ocean circulation by coupling with global ocean model

Adlane REBAÏ[1], Florence GANDILHON[1], Anne LEVASSEUR[1], Delphine LEBRIS[1], Olivier BERTRAND[1]
[1] ARTELIA Eau & Environnement – 6 rue de Lorraine 38130 ECHIROLLES - FRANCE

adlane.rebai@arteliagroup.com

***Abstract*—Most of the marine coastal models represent only the tidal currents. However, in many parts of the world, the coastal circulation is also driven by the global currents which are linked to climatology and atmospheric circulation. s. Through various studies around the world, and step by step, ARTELIA has developed a methodology to integrate the global circulation in TELEMAC numerical models; this methodology has evolved progressively according to data available and the requirements of the studies: port facilities, coastal development, cooling water systems, maritime renewable energy....This paper describes the methods and their evolution.**

I. INTRODUCTION

At the beginning, the global currents were only integrated as a flow rate at the TELEMAC model lateral boundaries. Then, a coupling with global ocean models has been implemented. This coupling involves the currents but also the salinity and the temperature. To have a good representation of the surface phenomena, the atmospheric forcing (wind stress, pressure field…) had to be added. The description of these developments is presented below in the context of the study site and its specificity.

II. SURFACE FLUX

The model has been developed in the framework of the construction and exploitation of a large scale transhipment containers terminal in the Republic of São Tomé e Príncipe. The area of the project has been selected by taking into account from one side, the existence of the deep-sea canyon which allows large draughts vessels to call and from the other side, the natural protection constituted by the island of São Tomé from major oceanic swells from SW and SE.

Currents in São Tomé, and more generally in the Gulf of Guinea, are marked by a variability occurring over wide ranges of time and space. The São Tomé island is located at the boundary area between the South-West Guinea current at the North and the West-North-West equatorial current at the South. Due to some seasonal fluctuations, this boundary is not constant. The variability of the current is due to the fact that it is essentially driven by atmospheric forcing and by seasonal changes in equatorial wind stress fields. Wind fields are directly related to the position and the intensity of the semi-permanent high pressure system in the South.

The study of the ocean circulation is based on the use and evaluation of a 3D local model of the Sao Tomé island. Boundary conditions of this local model have been determined by other models built on a regional scale.

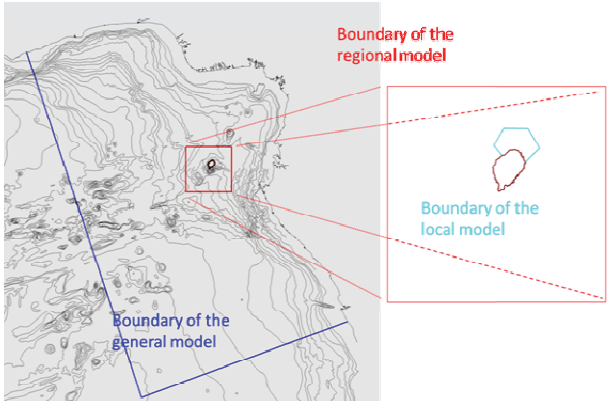

Figure 1 - Boundary of the general and regional model

To represent seasonal scenarios, combining the tidal effects to the global and local wind-driven currents, the sea level variations and tidal currents are computed by a specifically developed tidal hydrodynamic model. In order to add the global circulation currents to the tidal sea surface variations and currents, another model with nested grid has been built. This intermediate model integrates all the phenomena at these boundaries. This model, firstly build in 3D, has been simplified in 2D.

Finally, the local 3D model integrates the bathymetric data established from the survey around the site of the project and in particular those which describe the canyon and the water level and fluxes boundary conditions for the local model are transferred from the output of the intermediate model.

For the thermal and salt transport, only the local model is used. The initial and boundary conditions are based on the surveys and the wind data of the in-situ measurements in "Ilheu das Cabras" are applied as boundary conditions over the whole sea surface.

We have calibrated the hydrodynamic model on the results of measurements by tuning the bed resistance (which is not the dominating parameter for these depths), the eddy viscosity and the wind friction factor. We have put damping functions

inside the vertical viscosities, for the velocity and the tracers, to take into account of the impact of the stratification (thermal and saline stratification) on the results.

The time series of surface and bottom currents simulated by the model are calibrated against available in-situ measurements obtained from three stations (Figure 2). At the end of the tuning process, we may conclude that, in spite of some minor deviations, the agreement between the simulation results and the measurements is very good in general. So, we have assessed that the local model is calibrated successfully on the week of measurements and that the selected calibration parameters are the best compromise to reproduce the various hydro-meteorological situations simulated.

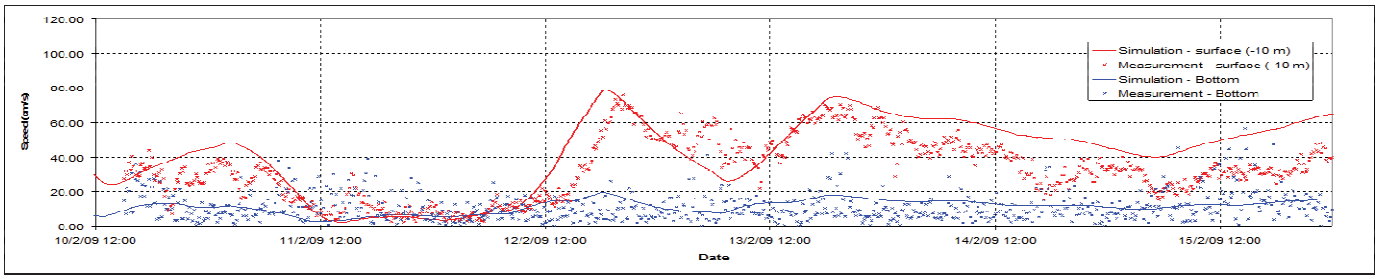

Figure 2 - Comparison model/measurement at surface (red) and bottom (blue)

III. GLOBAL CURRENTS

A. General description

In order to have a better representation of the currents in the areas where the global currents are predominant, it was decided to take them into account as input in the hydrodynamic model.

An ocean current is a continuous, directed movement of seawater generated by forces acting upon this mean flow, such as breaking waves, wind, the Coriolis effect, cabbeling, temperature and salinity differences, while tides are caused by the gravitational forces of the Sun and Moon. Depth contours, shoreline configurations, and interactions with other currents influence a current's direction and strength.

Since 2010, ARTELIA has fulfilled several hydrodynamic study in the Guinea gulf area. Thus global currents have been investigated in order to understand the circulation around the study area and then to provide input data into the model. Indeed, currents along the Guinea gulf coast are mainly driven by these complex global currents.

Analysis of currents implies a preliminary study of global currents in the Guinea Gulf. Indeed, even if these big ocean currents evolve offshore, they create global currents which can affect the local hydrodynamic at the superficial layers (0-100m).

In this area, global flows are complex and closely linked to climatology. On the one hand, atmospheric circulation (wind, rain, heat exchanges, anticyclonic cells …) generates currents, on the other hand, heat accumulated by the ocean in this area influence climate through marine currents.

B. Global currents in the Guinea Gulf

Main global currents, offshore the study area, are showed on Figure 3.

- The **South Equatorial Current (SEC)** is directly created by trade winds. It is a warm current going from east to west with a velocity between 0.2 to 1 m/s. Its maximum value appears during austral winter because of the Saint Helens anticyclone. It is found near the equator but its situation can move. The South Subtropical Current (parallel to the SEC) goes in the same direction (through the west) and is situated lightly south. The difference between these 2 currents is not clear.
- The **North Equatorial UnderCurrent (CCEN)** is situated on the north side of the equator. It evolves according to the Intertropical Convergence Zone (ITCZ) which corresponds to the part of the earth near the equator where atmospheric flows of the 2 hemispheres come together. Structure and position of this area evolves every day. It is stronger during austral winter.
- At the east, the North Equatorial Undercurrent gives birth to the main current of the Guinea Gulf: the **Guinea Current (GC)**; it flows easterly along the Guinea coast of the West Africa. Its mean speed is about 0.6 m/s, with a minimum value of about 0.25 m/s during austral summer (January - February), and a maximum value able to reach 1.5 m/s in austral winter (June – July). At the end of the Biafra Bay, it goes south to be partially integrated in the South Equatorial Current. Its extent is about 150 miles offshore with a thickness around 20 to 30m. Strong winds from North-East to East can create a switch of this current.

The limit between the Guinea Current and the South Equatorial Current is an area where; whirls, eddies appear.

- At the level of sub surface layers, complex circulations exist. The **Equatorial UnderCurrent (EUC)** is the

main flow; it goes easterly in the opposite direction of the SEC (bellow 100m depth). In the Guinea gulf, it divides into 2 branches: one through the south (which supplies the Congo-Gabon UnderCurrent) and the second one through the north towards the Biafra Bay which leads to the **Guinea UnderCurrent (GUC)** heading to the west. The size of these 2 branches is not well known because it depends on the position of EUC and its whirls near Sao Tome which evolve. During austral winter, EUC velocity reaches its maximum.

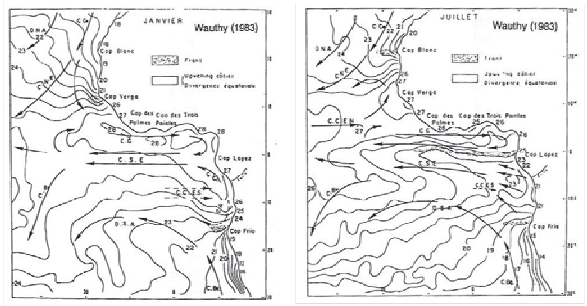

Figure 3 - Temperature and surface flow in January (austral summer) and July (austral winter)

C. *Global model*

Global Currents in the Gulf, which is one of the input data for the local hydrodynamic TELEMAC-3D model, have been derived from the MyOcean Products.

The MyOcean services provide information of currents, temperature, salinity on the Global Ocean, based on a combination of space and in situ observations and their assimilation into models.

For the present study, daily data of currents, temperature and salinity have been downloaded at a large scale and at various depth. They come from an operational Mercator global model analysis and forecast system which spatial resolution is at 1/12 degree horizontally and temporal resolution daily. The vertical discretization is composed of 50 layers (22 levels for the upper 100m).

Once the analysis is done, some of these data have been used as boundaries conditions for the hydrodynamic model.

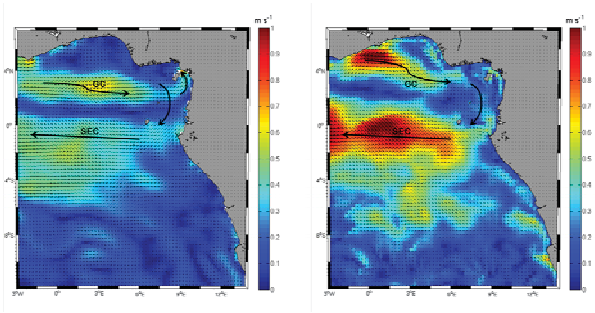

Figure 4 - Maps of global currents in the Guinea Gulf in February (left side) and July (right side)

Figure 4 shows the 2 main global currents at 2 different periods. As described previously, the Guinea Current is directed easterly whereas the South Equatorial Current goes toward the west. During the austral summer, the Guinea Current remains low because of the weakness of the North Equatorial Undercurrent; the South Equatorial Current, is also weak.

IV. GLOBAL CURRENTS AT THE SURFACE

In 2011, a study was conducted in Gabon in order to adress the issues of major coastal developments. A hydrodynamic model was built in order to reproduce the ocean circulation off Cap Lopez.

Maritime boundaries were controlled by water level (tide) and currents from the large-scale ocean model MERCATOR. The model proved to be unsatisfactory because it was unstable. This phenomenon is well known in modelling and is induced by a mismatch between the two sources of external data the Mercator model and the tidal model of the Gulf of Guinea) and the local model. These incompatibilities are usually of two types, namely differences in bathymetry and other source of external forcing such as wind.

To overcome this, it is necessary to bring this type of modelling to a number of degree of freedom to the limits that allow the model to adjust while integrating the external forcing provided at the boundary. Here, the flow is directed mainly to the north / south, thus the western boundary has been modified to only impose water levels. This change has resulted in some stability to the overall scale of the local model and modelled currents consistent with observations on the outskirts of Cap Lopez.

Despite this, the overall dynamics was not satisfactory, especially on the eastern boundary with the presence of a flux too important compared to the information available in the literature or from Mercator. In turn, this border has partially been modified to take into account only the water levels.

Finally, for each boundary, these forcing data have been implemented (Figure 5):

- Boundary 1: water level
- Boundary 2: water level and global current
- Boundary 3: water level
- Boundary 4; water level and global current

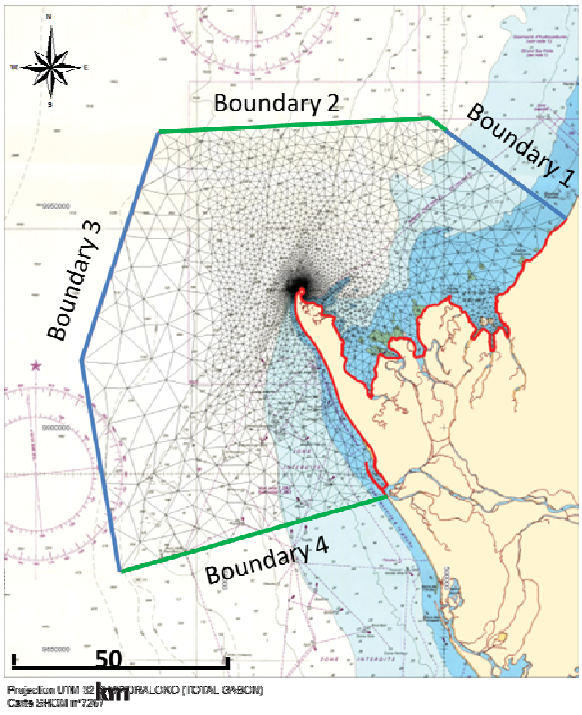

Figure 5 - Boundaries conditions

The energies involved in the model are consistent with the measurements. Indeed, the model alternates periods when the intensity is low (less than 0,2 m / s) and periods where the intensity is higher (several days around 0.30 to 0.40 m / s, which translates general currents supplied by the Mercator model) so that the measured velocity intensity is constant over the whole period. However, statistically, the model provides an average surface speed of about 13.5 cm / s compared with 14.5cm/ s for the observations. It is the same further with an average speed measured on the order of 13.1 cm / s 11,7cm / s speed modelled.

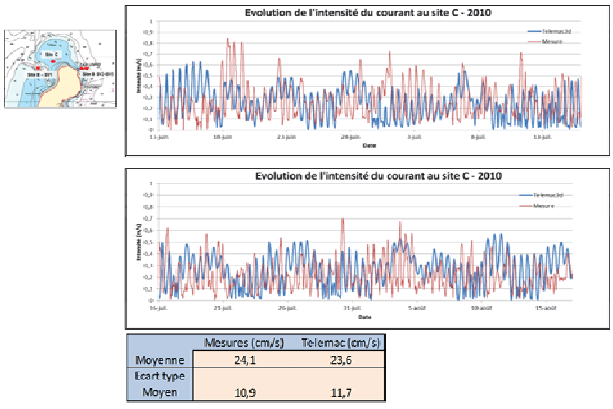

	Mesures (cm/s)	Telemac (cm/s)
Moyenne	24,1	23,6
Ecart type		
Moyen	10,9	11,7

Figure 6 - Comparison between model/measurements

In summary, for this study, only global currents at the surface are imposed. And then it's propagated on the vertical by using a Soulsby profile. So there no real 3D global current imposed. In order to have a better representation of the currents, 3D global currents must be taken into account. And to keep the 3D stratification, temperature and salinity have to be used in the model.

V. 3D GLOBAL CURRENTS, TEMPERATURE AND SALINITY

In 2014, ARTELIA has developed a model in order to develop the basis of design of a CLNG terminal project, which is located in an industrial/port development at about 30km South of the town of Kribi in Cameroon

Three maritime boundaries are considered (Figure 7).

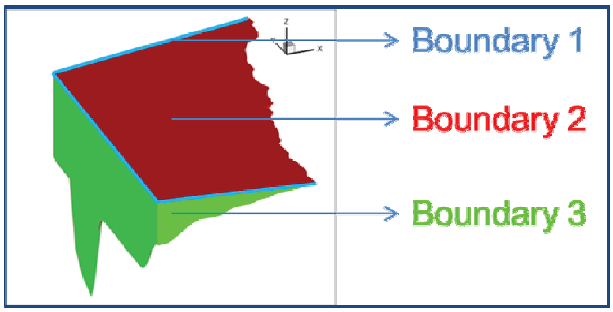

Figure 7 - The 3 hydrodynamic model boundaries

For each boundary, various forcing data have been implemented during the calibration step.

- Boundary 1 is the contours of the model at the surface, where tidal data are imposed as input.
- Boundary 2 corresponds to the surface layer where daily currents, temperature and salinity may be imposed as input data.
- Boundary 3 represents the 3D lateral conditions where daily currents, temperature and salinity may be imposed along the water column.

Then, during calibration process different input conditions have been imposed to the 3 boundaries, until a satisfactory reproduction of the measured current has been achieved.

This has been done in three steps (during each step, various tests have been realised). Finally, to improve model results, temperature and salinity are added, it is synthetized in Table 1.

TABLE 1 CALIBRATION CASES

Case	Boundaries						
	Boundary 1	Boundary 2			Boundary 3		
	Tide	Currents	Temperature	Salinity	Currents	Temperature	Salinity
Calibration Case 15	X	X			X		
Calibration Case 17	X	X			X		
Calibration Case 22	X		X	X	X	X	X
Calibration Case 23 (Final one)	X	X	X	X	X	X	X

The next figure shows the integral of speed amplitude for the different tests cases.

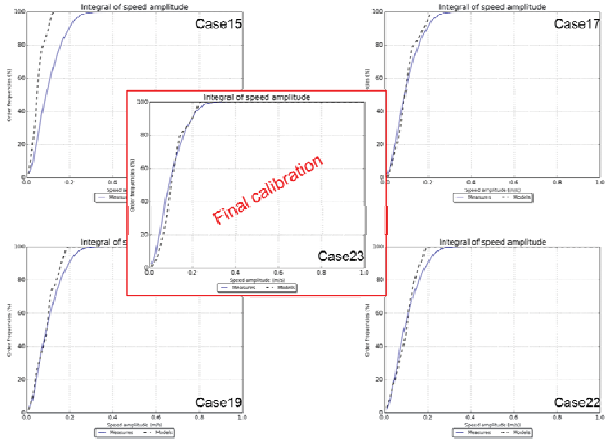

Figure 8 - Comparison between different tests cases

The statistical analyses show that the model is consistent with measurements both at the subsurface and the mid depth. Energy levels in the model are good. Local hydrodynamic circulation is correct even if sometimes the energy peaks are slightly weaker. It is worth noting that strong intensities represent a weak weight in global value of velocity. Distributions of speed amplitude (model and measures) are close.

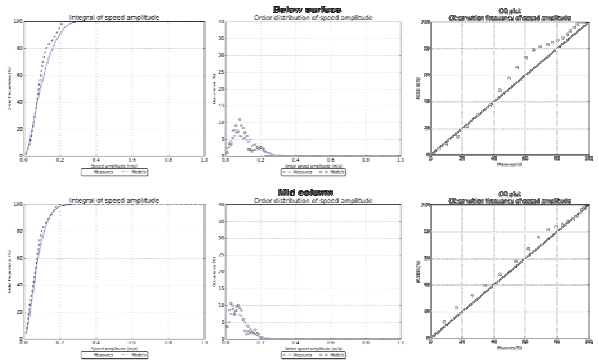

Figure 9 - Comparison model/measurements at the surface and mid column

This study shows how important it is to take into account all the parameters (global currents, temperature, salinity) when global currents are predominant.

VI. LONG TERM

In 2016, for an offshore project near the Martinique island, we have developed a three-dimensional model in order to model 20 years of currents, temperature and salinity. The size of the edges of the mesh is ¼° at the boundary for less than 200 m near the project. This size on the periphery is equivalent to the one of the structured grid of the NEMO model which is used to impose currents, temperature and salinity at the meso-scale and for the entire water column (boundary 3 in the figure below). TPXO is used for forcing the water depth with the tidal signal. Atmospheric conditions with air temperature, pressure, wind and evaporation are also imposed at the free surface.

In order to avoid a slow derive on the results, data assimilation is used on the bulk water for the two parameters salinity and temperature. The result of temperature evolution at different depth can be seen on Figure 10.

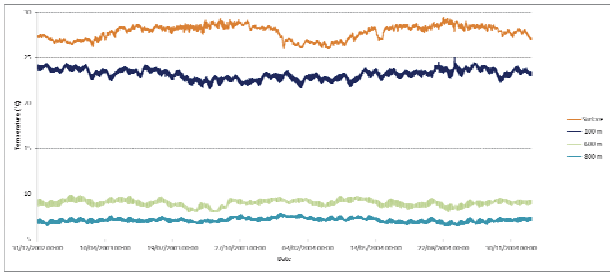

Figure 10 - Temperature evolution during 1 year

HR Wallingford
Working with water

Proceedings of the

XXIII[rd] TELEMAC-MASCARET User Conference

11 to 13 October 2016, Paris, France